

Non-Equilibrium Correlated Quantum Dynamics of Lattice Trapped Finite Bosonic Ensembles

Dissertation

zur Erlangung des Doktorgrades
an der Fakultät für Mathematik,
Informatik und Naturwissenschaften,
der Universität Hamburg,
Fachbereich Physik

vorgelegt von

Symeon Mystakidis

geboren am 13.01.1988 in Athen

Hamburg

2019

Eingereicht am:	06.08.2018
Gutachter der Dissertation:	Prof. Dr. Peter Schmelcher Prof. Dr. Ludwig Mathey
Datum der Disputation:	10.04.2019
Gutachter der Disputation:	Prof. Dr. Peter Schmelcher Prof. Dr. Ludwig Mathey Prof. Dr. Michael Potthoff Prof. Dr. Andreas Hemmerich Prof. Dr. Daniela Pfannkuche
Vorsitzende der Prüfungskommission:	Prof. Dr. Daniela Pfannkuche
Vorsitzender des Fach-Promotionsausschusses:	Prof. Dr. Wolfgang Hansen
Leiter des Fachbereichs Physik:	Prof. Dr. Michael Potthoff
Dekan des MIN-Fakultät:	Prof. Dr. Heinrich Graener

There are men who struggle for a day and they are good. There are men who struggle for a year and they are better. There are men who struggle many years, and they are better still. But there are those who struggle all their lives: These are the indispensable ones.

He who fights, can lose. He who doesn't fight, has already lost.

Bertolt Brecht.

To my Parents

Zusammenfassung

Ultrakalte Atome in optischen Gittern bilden eine vielseitige Umgebung für Vielkörperprobleme mit gut kontrollierbaren Parametern, die es uns erlauben, eine Vielzahl komplexer Quantensysteme im Labor zu simulieren, auch solche, die keine analytische Behandlung ermöglichen. Insbesondere die Nicht-Gleichgewichtsdynamik stark korrelierter Vielteilchensysteme ist eine der herausforderndsten Probleme der modernen Quantenphysik, mit Anwendungen die von Thermalisierungsdynamik über Transporteigenschaften bis hin zur Kontrolle von Korrelationen und der Dynamik reichen. Das Verständnis von Nichtgleichgewichtsphänomenen stark korrelierter Systeme ist eine weitreichende Aufgabe. Einblick in solche Systeme wird ermöglicht durch die Untersuchung von Systemen mit wenigen Teilchen, die nur eine kleine Anzahl relevanter Freiheitsgrade besitzen. Dennoch müssen Quantenkorrelationen zwischen den Teilchen berücksichtigt werden.

Die vorliegende Dissertation trägt zum Verständnis der Nichtgleichgewichtsdynamik stark korrelierter Quanten-Vielteilchensysteme bei, durch Untersuchung von Systemen mit wenigen Bosonen, die einer oder zwei Spezies zugehören und in optischen Gittern gefangen sind. Die Systeme werden aus dem Gleichgewicht gebracht, entweder durch einen Quench (plötzliche Änderung) eines Hamilton-Parameters oder durch eine zeitperiodischen Modulation der äußeren Begrenzung. Im Laufe einiger konsekutiven Untersuchungen zeigen wir verschiedene Möglichkeiten, die Nichtgleichgewichtsmoden zu koppeln, und enthüllen ihre korrelierte Natur und mikroskopische Herkunft. Um die Nichtgleichgewichtsdynamik zu simulieren, nutzen wir eine verfeinerte, hochflexible Ab-initio-Methode zur numerischen Lösung der zeitabhängigen Mehrkörper-Schrödinger-Gleichung namens "Multi-Layer Multi-Configuration Time-Dependent Hartree Method for Atomic Mixtures" (ML-MCTDHX).

Im ersten Teil untersuchen wir in sechs aufeinander folgenden Studien die korrelierte Nichtgleichgewichtsdynamik von Systemen, bestehend aus wenigen Bosonen, in eindimensionalen endlichen Gittern. Beginnend bei schwachen Wechselwirkungen wird gezeigt, dass eine abrupte Erhöhung der Interaktionsstärke eine globale Dichtewellentunneldynamik sowie Intra-Topf-Breathing und Cradle-ähnliche Prozesse in angeregten Bändern generiert. Der Cradle-Prozess ist ein dipolähnlicher Prozess, der durch den quench-induzierten Transport über die Barriere erzeugt wird und eines der zentralen Ergebnisse der vorliegenden Dissertation darstellt. Die Wechselwirkungs-Quenches koppeln auf bemerkenswerte Art und Weise die Dichtewellen- und Cradle-Moden, und induzieren Resonanzphänomene zwischen der Inter- und Intra-Topf-Dynamik. Wir zeigen weiter, dass die Cradle-Mode inhärent mit der anfänglichen Delokalisierung verknüpft ist und nach einem Quench von starken zu schwachen Wechselwirkungen nur für inkommensurable Konfigurationen mit Füllung größer als Eins angeregt werden kann. Alternativ wird eine plötzliche Verringerung der Gittertiefe eingesetzt, die die räumliche Delokalisierung begünstigt und die Cradle-Mode für Setups mit Füllung kleiner als Eins zugänglich macht. Durch Verwendung eines Protokolls mit mehreren Wechselwirkungs-Quenches beobachten wir den Anstieg von mehreren Tunnelmoden in den niedrigsten Bändern sowie die Cradle- und Breathing-Mode. Neben der Cradle-Mode sind alle anderen angeregten Moden in hohem Maße kontrollierbar und besitzen unterschiedliche Frequenzen während und zwischen den Quenches. In der Anregungsdynamik wird ein monoton

Verhalten mit zunehmender Quenchamplitude und eine nichtlineare Abhängigkeit von der Dauer der Anwendung der Quench-Wechselwirkungsstärke aufgedeckt. Zusätzlich wird ein periodischer Populationstransfer zwischen Impulsen für Quenches mit zunehmender Interaktion beobachtet, folgend einem Potenzgesetz für die Frequenz in Abhängigkeit von der Quenchamplitude. Lineare Wechselwirkungs-Quenches von einem suprafluiden zu einem Mott-Isolator-Zustand regen verschiedene Inter- und Intra-Band-Tunnelmoden an. Die Konkurrenz zwischen der Quenchrate und der Interpartikelabstoßung führt zu einer resonanten dynamischen Antwort bei moderaten linearen Quenchzeiten, die in Zusammenhang mit vermiedenen Kreuzungen im Vielkörpereigenespektrum steht. Es wird gezeigt, dass die resultierende Anregungsdynamik der höheren Bänder einem exponentiellen Zerfall unterliegt, der zwei unterschiedliche Zeitskalen besitzt mit variierender Rampenzeit. Bei der Untersuchung des Übergangs von flachen zu tiefen Gittern finden wir heraus, dass für einen diabatischen Quench der Anteil der angeregten Bänder abnimmt, während er im adiabatischen Limes ein nichtlineares Verhalten aufweist mit zunehmender Höhe der Potentialbarriere. Quenches von starken zu schwachen Wechselwirkungen führen zu einem Zusammenbruch des Mott-Isolators und zu vernachlässigbaren Anregungen höherer Bänder. Das Ausführen von Quenches des Wellenvektor oder der Phase eines räumlich abhängigen Interaktionsprofils löst eine Streuung in verschiedene Tunnelkanäle und eine reiche Anregungsdynamik aus, die bei höherer Inhomogenitätsamplitude verstärkt wird. Besonders wichtig ist dabei, dass der Phasen-Quench einen gerichteten Transport induziert, der es uns ermöglicht, zwischen ursprünglich energetisch entarteten Tunnelwege zu differenzieren. Anschließend beobachten wir einen periodischen Populationstransfer zwischen verschiedenen Impulsen für Quenches mit zunehmendem Wellenvektor und eine gerichtete Besetzung von höheren Impulsen nach einem Phasen-Quench. Wenn wir eine zusätzliche harmonische Falle von starker zu schwacher Frequenz quench, stellen wir fest, dass die Konkurrenz zwischen der anfänglichen Lokalisierung und der abstoßenden Wechselwirkung zu einer resonanten Reaktion des Systems führt, die in Zusammenhang mit vermiedenen Kreuzungen im Vielkörpereigenespektrum bei variierender Endfallfrequenz steht. Darüber hinaus zeigen wir, dass diese vermiedenen Kreuzungen genutzt werden können, um das System in einem Wunschzustand zu präparieren.

Der zweite Teil umfasst zwei Studien und widmet sich der Analyse der Nicht-Gleichgewichtsdynamik von ultrakalten bosonischen Ensembles in periodisch getriebenen eindimensionalen optischen Gittern. Für ein geschütteltes Gitter wird eine große Bandbreite von Treibfrequenzen abgedeckt und ein resonantes Verhalten der Intra-Band-Dynamik aufgedeckt, das mit einem reichen Intra-Band-Anregungsspektrum in Zusammenhang steht. Darüber hinaus wird gezeigt, dass für eine zunehmende Abstoßung eine starke Unterdrückung des Inter-Topf-Tunnelns und eine verstärkte Anregungsdynamik auftritt. Für ein vibrierendes Gitter führt ein zusätzlicher Wechselwirkungs-Quench zu Beimischungen verschiedener Anregungen in den äußeren Töpfen, einem verstärkten Breathing in der Mitte und einer Verstärkung der entstehenden Tunnelndynamik. Das Auftreten von mehrfachen Resonanzen zwischen der Inter- und Intra-Topf-Dynamik bei unterschiedlichen Quenchamplituden wird aufgezeigt, wobei die Position der Resonanzen über die Treibfrequenz abstimmbare ist und somit eine weitere Steuerung der Modenkopplung in optischen Gittern ermöglicht.

Im dritten und letzten Teil dieser Arbeit wird die Quenchdynamik einer Bose-Bose- und

einer Bose-Fermi-Mischung aufgeklärt. Unter Verwendung eines Interspezies-Interaktions-Quenchs überschreiten wir die Mischbarkeits-Unmischbarkeits-Schwelle in einer harmonisch begrenzten Bose-Bose-Mischung. Wir zeigen, dass eine Erhöhung des Interspezieswechselwirkungsstärke zu einer Filamentierung der Dichte jeder Spezies führt, wobei die spontan erzeugten Filamente stark korreliert sind und Domänenwandstrukturen aufweisen. Bemerkenswerterweise wird die Bildung von mehreren dunkel-antidunkel solitären Wellen beobachtet, wenn man dem umgekehrten Quench-Protokoll folgt, das heißt, wenn man die Interspezieswechselwirkungsstärke verringert. Diese solitären Wellenstrukturen zerfallen in die Vielkörperumgebung kurz nach ihrer Erzeugung, in scharfem Gegensatz zu den Vorhersagen der Mean-Field-Approximation. Um unsere Ergebnisse mit möglichen experimentellen Realisierungen zu verknüpfen, simulieren wir zum ersten Mal für binäre Mischungen Momentaufnahmen, die zeigen, dass die Wachstumsrate der Varianz einer Stichprobe von Momentaufnahmen den Grad der Verschränkung, inhärent im System, sondiert. Als nächsten Schritt untersuchen wir die Expansionsdynamik einer Bose-Fermi-Mischung mit gleicher Masse, die in einem eindimensionalen optischen Gitter gefangen ist, indem die verwendete harmonische Falle von stark zu schwach geschaltet wird. Indem wir die Interspezies-Interaktionsstärke verändern, realisieren wir die nicht mischbaren und mischbaren korrelierten Grundzustandsphasen. Wir zeigen weiter, dass die dynamische Reaktion des Systems entscheidend von der Anfangsphase abhängt und aus einer Ausdehnung aller Wolken und einer Inter-Topf-Tunnel-Dynamik besteht. Durch Variieren der Quenchamplitude wird eine Vielzahl von Reaktionsregimen im Bezug auf eine feste Phase enthüllt, die innerhalb der nicht mischbaren Phase reicher sind und durch unterschiedliche Expansionsstärken und Tunnelkanäle beschrieben werden. Schließlich wird in der Expansionsdynamik ein antikorreliertes Zwei-Körper-Verhalten zwischen den überwiegend besetzten Töpfen enthüllt.

Abstract

Ultracold atoms in optical lattices constitute a versatile many-body platform with highly tunable parameters, allowing us to emulate a multitude of complex quantum systems, in the laboratory, even those eluding analytical treatment. In particular, the nonequilibrium dynamics of strongly correlated many-body systems represents one of the most challenging problems of modern quantum physics, with applications ranging from thermalization dynamics and transport properties to the management of correlations and the control of the dynamics. Understanding nonequilibrium phenomena of strongly correlated systems is a formidable task. A very promising route to gain insight into such systems is to examine few-body setups which contain only a few relevant degrees of freedom, yet incorporating the quantum correlations between the particles.

The present dissertation contributes to the understanding of the nonequilibrium dynamics of strongly-correlated quantum many-body systems by exploring systems of few-bosons – of one or two species – trapped in optical lattices. The systems are driven out-of-equilibrium either by performing a quench of a Hamiltonian parameter or by considering a time-periodic modulation of the external confinement. In the course of several consecutive works, we showcase different ways to couple the nonequilibrium modes, while unveiling their correlated nature and microscopic origin. To simulate the nonequilibrium dynamics, a sophisticated, highly flexible ab-initio method for numerically solving the time-dependent many-body Schrödinger equation is utilized, namely the Multi-Layer Multi-Configuration Time-Dependent Hartree Method for Atomic Mixtures (ML-MCTDHX).

Within the first part we study in six consecutive works the correlated nonequilibrium dynamics of few-boson systems in one-dimensional finite lattices. Starting from weak interactions, it is shown that a sudden increase of the interaction strength generates a global density-wave tunneling dynamics as well as intrawell breathing and cradle-like excited-band processes. The cradle process is a dipole-like process generated by the quench-induced over-barrier transport and it is one of the central results of the present thesis. Remarkably enough, the interaction quenches couple the density-wave and cradle modes, inducing resonance phenomena between the inter and intrawell dynamics. We further show that the cradle mode is inherently related to the initial delocalization and, following a quench from strong-to-weak interactions, can be excited only for incommensurate setups with filling larger than unity. Alternatively, a sudden ramping down of the lattice depth which favors the spatial delocalization is employed to access the cradle mode for setups with filling smaller than unity. Following a multiple interaction quench protocol, we observe the rise of several lowest-band tunneling modes as well as the cradle and the breathing mode. Besides the cradle mode, all other excited modes are highly tunable possessing different frequencies during and in between the quenches. In the excitation dynamics a monotonic behavior with increasing quench amplitude and a non-linear dependence on the duration of the application of the quenched interaction strength is revealed. Additionally, a periodic population transfer between momenta for quenches of increasing interaction is observed, with a power-law frequency dependence on the quench amplitude. Linear interaction quenches from a superfluid to a Mott-insulator state excite various inter- and intraband tunneling modes. The competition between the quench rate and

the interparticle repulsion leads to a resonant dynamical response, at moderate ramp times, being related to avoided-crossings in the many-body eigenspectrum. The resultant higher-band excitation dynamics is shown to obey an exponential decay possessing two distinct time scales with varying ramp time. Inspecting the crossover from shallow to deep lattices we find that for a diabatic quench the excited-band fraction decreases, while approaching the adiabatic limit it exhibits a nonlinear behavior for increasing height of the potential barrier. Quenching from strong-to-weak interactions leads to a melting of the Mott-insulator and negligible higher-band excitations. Performing quenches either on the wavevector or the phase of a spatially dependent interaction profile triggers various tunneling channels and a rich excitation dynamics which is amplified for increasing inhomogeneity amplitude. Most importantly, the phase quench is shown to induce a directional transport enabling us to discern, otherwise, energetically degenerate tunneling pathways. Finally, a periodic population transfer between distinct momenta for quenches of increasing wavevector and a directed occupation of higher momenta following a phase quench is observed. Employing a quench of an additional harmonic trap from strong-to-weak confinement, we find that the competition between the initial localization and the repulsive interaction leads to a resonant response of the system related to avoided-crossings in the many-body eigenspectrum with varying final trap frequency. Furthermore, we show that these avoided-crossings can be utilized to prepare the system in a desired state.

The second part comprises two efforts and is devoted to the study of the nonequilibrium dynamics of finite ultracold bosonic ensembles in periodically driven one-dimensional optical lattices. For a shaken lattice, a wide range of driving frequencies is covered and a resonant behavior of the intrawell dynamics is revealed and found to be related to a rich intraband excitation spectrum. Moreover, it is shown that for increasing repulsion a strong suppression of the interwell tunneling and an enhanced excitation dynamics occurs. For a vibrating lattice, an additional interaction quench gives rise to admixtures of different excitations in the outer wells, an enhanced breathing in the center and an amplification of the emerging tunneling dynamics. The occurrence of multiple resonances between the inter- and intrawell dynamics at different quench amplitudes is revealed, with the position of the resonances being tunable via the driving frequency and thus allowing for further control of the mode coupling in optical lattices.

In the third and final part of this thesis we unravel the quench dynamics of a Bose-Bose and a Bose-Fermi mixture. Utilizing an interspecies interaction quench we cross the miscibility-immiscibility threshold in a harmonically confined Bose-Bose mixture. We show that increasing the interspecies repulsion coefficient results in a filamentation of the density of each species, with the spontaneously generated filaments being strongly correlated and exhibiting domain-wall structures. Strikingly, by following the reverse quench protocol, i.e., upon decreasing the interspecies interaction strength, the formation of multiple dark-antidark solitary waves is observed. These solitary wave structures are found to decay into the many-body environment, soon after their generation in sharp contrast to the predictions of the mean-field approximation. To relate our findings with possible experimental realizations, we simulate, for the first time for binary mixtures, single-shot images showcasing that the growth rate of the variance of a sample of single-shots probes the degree of entanglement inherent

in the system. As a next step we investigate the expansion dynamics of a mass balanced Bose-Fermi mixture confined in a one-dimensional optical lattice upon quenching an imposed harmonic trap from strong-to-weak confinement. Tuning the interspecies interaction strength we realize the immiscible and miscible correlated ground state phases. We further show that the system's dynamical response crucially depends on the initial phase and consists of an expansion of each cloud and an interwell tunneling dynamics. Varying the quench amplitude and referring to a fixed phase a multitude of response regimes is unveiled, being richer within the immiscible phase, which are described by distinct expansion strengths and tunneling channels. Finally, in the expansion dynamics a two-body anti-correlated behavior between the predominantly occupied wells is unveiled.

Contents

Preface	iii
1 Introduction	13
2 Theoretical Framework	19
2.1 Optical Lattices	19
2.1.1 AC Stark Shift and Dissipative Interaction	20
2.1.2 Bose-Hubbard Model	21
2.1.3 Extended Bose-Hubbard Models	25
2.2 Mean-Field Theory and the Gross-Pitaevskii Equation	27
2.3 Many-Body Methodological Approach: ML-MCTDHX	28
2.3.1 Many-body Wavefunction ansatz for Binary Mixtures	29
2.3.2 Limiting Cases and Convergence of the Many-Body Simulations	31
2.3.3 Wavefunction Ansatz for Scalar Bosons	32
2.4 Many-Body Eigenspectrum of Few-Bosons in a Triple-Well	33
2.4.1 The Multiband Wannier Number State Basis	34
2.4.2 Improved Relaxation Scheme	35
2.4.3 Eigenspectrum of Three and Four Bosons	35
2.5 Single-Shot Simulations in Binary Bosonic Mixtures and Scalar Bosons	38
2.5.1 Single-Shot Procedure	38
3 Outline of the Scientific Contributions	41
3.1 Hamiltonian of Few-Bosons in a Lattice	41
3.2 Basic Ground State Properties	42
3.3 Quench Dynamics in Scalar Few-Boson Ensembles	44
3.3.1 Quench Dynamics from Weak-to-Strong Interactions [[1]]	44
3.3.2 Quench Dynamics from Strong-to-Weak Interactions [[2]]	48
3.3.3 Dynamics after Multiple Interaction Quenches [[3]]	49
3.3.4 Dynamics Following a Linear Interaction Quench in Finite Optical Lattices of Unit Filling [[4]]	51
3.3.5 Quench Dynamics of Finite Bosonic Ensembles in Optical Lattices with Spatially Modulated Interactions [[5]]	53

CONTENTS

3.3.6	Quench-induced Resonant Tunneling Mechanisms of Bosons in an Optical Lattice with Harmonic Confinement [[6]]	55
3.4	Driven Lattices	56
3.4.1	Resonant Quantum Dynamics of Few Ultracold Bosons in Periodically Driven Finite Lattices [[7]]	56
3.4.2	Mode Coupling of Interaction Quenched Ultracold Few-Boson Ensembles in Periodically Driven Lattices [[8]]	58
3.5	Quench Dynamics in Binary Mixtures	59
3.5.1	Correlation Effects in the Quench-Induced Phase Separation Dynamics of a Two-Species Ultracold Quantum Gas [[9]]	60
3.5.2	Many-Body Expansion Dynamics of a Bose-Fermi Mixture Confined in an Optical Lattice [[10]]	61
4	Scientific Contributions	65
4.1	Quench Dynamics	66
4.1.1	Interaction Quench Induced Multimode Dynamics of Finite Atomic Ensembles	66
4.1.2	Negative-Quench-Induced Excitation Dynamics for Ultracold Bosons in One-Dimensional Lattices	83
4.1.3	Quantum Dynamical Response of Ultracold Few-Boson Ensembles in Finite Optical Lattices to Multiple Interaction Quenches	98
4.1.4	Bosonic Quantum Dynamics Following a Linear Interaction Quench in Finite Optical Lattices of Unit Filling	111
4.1.5	Quench Dynamics of Finite Bosonic Ensembles in Optical Lattices with Spatially Modulated Interactions	122
4.1.6	Quench-Induced Resonant Tunneling Mechanisms of Bosons in an Optical Lattice with Harmonic Confinement	137
4.2	Driven Lattices	151
4.2.1	Resonant Quantum Dynamics of Few Ultracold Bosons in Periodically Driven Finite Lattices	151
4.2.2	Mode Coupling of Interaction Quenched Ultracold Few-Boson Ensembles in Periodically Driven Lattices	167
4.3	Quench Dynamics in Binary Mixtures	184
4.3.1	Correlation Effects in the Quench-Induced Phase Separation Dynamics of a Two-Species Ultracold Quantum Gas	184
4.3.2	Many-Body Expansion Dynamics of a Bose-Fermi Mixture Confined in an Optical Lattice	203
5	Conclusions and Outlook	217
	Acknowledgments	227

Preface

This cumulative dissertation is based on the following sequence of publications, which throughout the thesis will be referenced with double brackets $[[\dots]]$.

List of publications this dissertation is based on

- [[1]] S.I. Mistakidis, L. Cao, and P. Schmelcher. Interaction quench induced multimode dynamics of finite atomic ensembles, *J. Phys. B: At. Mol. Opt. Phys.* **47**, 225303 (2014).
- [[2]] S.I. Mistakidis, L. Cao, and P. Schmelcher. Negative-quench-induced excitation dynamics for ultracold bosons in one-dimensional lattices, *Phys. Rev. A* **91**, 033611 (2015).
- [[3]] J. Neuhaus-Steinmetz, S.I. Mistakidis, and P. Schmelcher, Quantum dynamical response of ultracold few-boson ensembles in finite optical lattices to multiple interaction quenches, *Phys. Rev. A* **95**, 053610 (2017).
- [[4]] S.I. Mistakidis, G.M. Koutentakis, and P. Schmelcher. Bosonic quantum dynamics following a linear interaction quench in finite optical lattices of unit filling, *Chem. Phys.* (2017).
- [[6]] T. Plaßmann, S.I. Mistakidis, and P. Schmelcher. Quench Dynamics of Finite Bosonic Ensembles in Optical Lattices with Spatially Modulated Interactions, arXiv:**1802.06693** (2018).¹
- [[5]] G.M. Koutentakis, S.I. Mistakidis, and P. Schmelcher. Quench-induced resonant tunneling mechanisms of bosons in an optical lattice with harmonic confinement, *Phys. Rev. A* **95**, 013617 (2017).
- [[7]] S.I. Mistakidis, T. Wulf, A. Negretti, and P. Schmelcher. Resonant quantum dynamics of few ultracold bosons in periodically driven finite lattices, *J. Phys. B: At. Mol. Opt. Phys.* **48**, 244004 (2015).

¹This paper has been submitted to *Journal of Physics B: Atomic, Molecular and Optical Physics* and it is still under review.

CONTENTS

- [[8]] S.I. Mistakidis and P. Schmelcher. Mode coupling of interaction quenched ultracold few-boson ensembles in periodically driven lattices, *Phys. Rev. A* **95**, 013625 (2017).
- [[9]] S.I. Mistakidis, G.C. Katsimiga, , P.G. Kevrekidis, and P. Schmelcher. Correlation effects in the quench-induced phase separation dynamics of a two-species ultracold quantum gas, *New J. Phys.* (2018).
- [[10]] P. Siegl, S.I. Mistakidis, and P. Schmelcher. Many-Body Expansion Dynamics of a Bose-Fermi Mixture Confined in an Optical Lattice, *Phys. Rev. A* **97**, 053626 (2018).

Outline of this Thesis: Chapter 1 contains a general introduction to the field of trapped ultracold atoms, with emphasis on the intricate phenomena observed during the nonequilibrium dynamics of such systems. We provide the scientific context into which the above contributions are embedded. Additionally we discuss the basic theoretical framework that is needed to describe the nonequilibrium dynamics in optical lattices. To this end, the Bose-Hubbard model and the mean-field approximation are outlined while the main focus is given to the employed correlated many-body methodological approach. The latter method provides access to beyond Bose-Hubbard phenomena and it is employed in the present thesis to investigate the few-boson correlated out-of-equilibrium dynamics in finite optical lattices. To obtain a basic knowledge regarding the modes occurring for increasing interparticle repulsion in a lattice trapped few-body setup the many-body eigenspectrum of three and four bosons confined in a triple well is presented. Additionally, we briefly outline the basic ingredients of a novel computational algorithm that has been developed in the present thesis, enabling us to simulate single-shot absorption images. The latter are employed for the first time in the case of binary mixtures. An outline for each of the above-mentioned list of publications and their interconnections to the existing literature are discussed in Chapter 2. In Chapter 3 we present all the scientific contributions [[1-10]] as published. Finally, Chapter 4 provides a concluding discussion and some perspectives for future research.

Declaration of Personal Contributions to the Publications [[1-10]] The projects resulting in [[1,2]] were conducted entirely by myself, including the specification of the research questions, numerical simulations, approximate models and the writing of both manuscripts. Prof. Lushuai Cao has significantly contributed to the optimization of the presentation of our results. The publications [[3,6,10]] emerged from the Bachelor thesis projects of B.Sc. J. Neuhaus-Steinmetz, T. Plaßmann and P. Siegl, respectively, who have been supervised by myself to a great extent and also my supervisor Prof. Dr. Peter Schmelcher. I have been actively involved in the projects planning and provided as well as implemented most of the numerical analysis tools. Most of the simulations were carried out by B.Sc. J. Neuhaus-Steinmetz, T. Plaßmann and P. Siegl, respectively, and parts of them by myself. With the above B.Sc. students we discussed the physical interpretation of the results as well as technical issues almost on a daily basis. Finally, I have significantly contributed to the optimization of the presentation of our results and wrote all three manuscripts. The project [[5]] has been conceptualized by myself. All simulations have been carried out by M.Sc. Georgios Koutentakis. Through continuous detailed discussions I contributed to our understanding

of the results as reflected in the publication. Finally, I wrote parts of the manuscript and made substantial contributions to the overall presentation of our findings. The projects [[4,8]] have been conceptualized by myself and I have carried out all calculations and written both manuscripts. Project [[7]] has been invoked by myself. I performed the many-body simulations and data analysis, and also wrote the corresponding sections of the manuscript. The part concerning the Floquet analysis of the underlying single-particle dynamics has been performed by Dr. Thomas Wülf. The entire manuscript as well as the interpretation of all data was discussed among all authors. The publication resulting in [[9]] was invoked by Prof. Dr. Panayiotis Kevrekidis. All simulations and data analysis have been executed entirely by myself. All authors have contributed to the presentation of the results and the writing of the manuscript. In all cases, the project progress was discussed on a regular basis with Prof. Dr. Peter Schmelcher.

Further List of Publications:

- G.M. Koutentakis, S.I. Mistakidis, and P. Schmelcher. Probing Ferromagnetic Order in Few-Fermion Correlated Spin-Flip Dynamics, arXiv:**1804.07199** (2018).
- G.C. Katsimiga, S.I. Mistakidis, G.M. Koutentakis, P.G. Kevrekidis, and P. Schmelcher, Many-Body Dissipative Flow of a Confined Scalar Bose-Einstein Condensate Driven by a Gaussian Impurity, arXiv:**1805.08618**² .
- G.C. Katsimiga, S.I. Mistakidis, G.M. Koutentakis, P.G. Kevrekidis, and P. Schmelcher. Many-body quantum dynamics in the decay of bent dark solitons of Bose-Einstein condensates, *New J. Phys.* **19**, 123012 (2017).
- L. Cao, V. Bolsinger, S.I. Mistakidis, G.M. Koutentakis, S. Krönke, J.M. Schurer, and P. Schmelcher. A unified ab-initio approach to the correlated quantum dynamics of ultracold fermionic and bosonic mixtures, *J. Chem. Phys.* **147**, 044106 (2017).
- G.C. Katsimiga, G.M. Koutentakis, S.I. Mistakidis, P.G. Kevrekidis, and P. Schmelcher. Dark-Bright Soliton Dynamics Beyond the Mean-Field Approximation, *New J. Phys.* **19**, 073004 (2017).
- L. Cao, S.I. Mistakidis, X. Deng, and P. Schmelcher. Collective excitations of dipolar gases based on local tunneling in superlattices, *Chem. Phys.* **482**, 303 (2017).
- K. Karamanos, I.S. Mistakidis, and S.I. Mistakidis. Structure of the correlation function at the accumulation points of the logistic map, *Chaos Solitons and Fractals* **96**, 154 (2017).
- K. Karamanos, S.I. Mistakidis, T.J. Massart, and I.S. Mistakidis. Entropy production of entirely diffusional Laplacian transfer and the possible role of fragmentation of the boundaries, *Fractals* **23**, 1550026 (2015).

²Accepted in Physical Review A.

CONTENTS

- G. Kordas, S.I. Mistakidis, and A.I. Karanikas. Coherent state path integrals in the continuum, *Phys. Rev. A* **90**, 032104 (2014).
- K. Karamanos, I.S. Mistakidis, S.I. Mistakidis, and I.E. Sarris. Symbolic dynamics applied to velocity time-series in wind farms, *Advances in systems science and applications* **14**, 3 (2014).
- K. Karamanos, I.S. Mistakidis, and S.I. Mistakidis. Symbol-to-symbol correlation function at the Feigenbaum point of the logistic map, *Int. J. Bifurcation and Chaos* **23**, 1350118 (2013).
- I.S. Mistakidis, K. Karamanos, and S.I. Mistakidis. Statistical versus optimal partitioning for block entropies, *Kybernetes* **42**, 35 (2013).
- I.S. Mistakidis, K. Karamanos, and S.I. Mistakidis. Aspects of Arithmetic Experiments on Poincare Escape Time Statistics, *International Journal of Information Engineering* **2**, 97 (2012).
- K. Karamanos, I.S. Mistakidis, and S.I. Mistakidis. The many facets of Poincare recurrence theorem of the logistic map, *Kybernetes* **41**, 794 (2012).
- I.S. Mistakidis, S.I. Mistakidis, and K. Karamanos. Illuminating the Poincare Recurrence Theorem with Information Technology, *International Journal of Information Engineering* **1**, 1 (2011).

Chapter 1

Introduction

The experimental realization of Bose-Einstein condensates (BECs) in ultracold atoms [1–3] opened a new and highly attractive venue for studying correlated many-body systems in a controllable fashion within a clean and well-isolated environment. Major steps towards this level of control include e.g. the ability to precisely adjust both the sign and the strength of interparticle interactions by means of confinement-induced, optical and magnetic Fano-Feshbach resonances [4–8], the design of arbitrary potential landscapes or even the possibility to move the external confinement in a time-periodic manner [9]. Remarkably enough, recent advances in optical trapping even allow to control the size and atom number of these quantum systems providing access to few-body physics [10–14]. The above-mentioned characteristics make systems of ultracold atoms powerful quantum many-body platforms for simulating a diversity of physical phenomena, in part inspired from condensed matter physics, and emulating them in the laboratory.

Ultracold atoms in optical lattices constitute particularly appealing setups to assess the strongly correlated regime of interactions, where the system cannot be described by a simple mean-field approximation [15–18]. Optical lattices are periodic potentials created by the formation of a standing wave when a pair of counter-propagating laser beams interfere and are used to trap the atoms. The most popular theoretical model to describe both the static and the dynamical properties of such systems is the so-called Bose-Hubbard model [19,20] which rests upon the restriction of on-site interactions and nearest-neighbor tunneling processes. A basic feature of this model is the presence of two distinct phases: The Mott-insulator phase, where a constant number of atoms resides at each lattice site, and the superfluid phase, characterized by delocalized atoms across the system. In the presence of disorder, a third phase occurs, called Bose glass [16,21,22]. The quantum phase transition from a superfluid to a Mott-insulating state has been observed experimentally [23] for bosons in three-dimensional optical lattices, verifying in this way the predictions of the Bose-Hubbard Hamiltonian [20]. This hallmark experiment triggered a new era of theoretical and experimental investigations regarding strongly correlated quantum gases. A variety of phases with unique properties and increasing complexity has been realized with atoms confined in periodic potentials. These include one- and two-dimensional bosonic Mott phases [24,25], tunable Mott-insulator states [26], fermionic Mott-insulators [27,28], the Tonks-Girardeau gas [29,30], strongly paired

INTRODUCTION

fermions in lattice potentials [31–34], and unconventional superfluids involving excited-bands [35–38].

To gain a deeper understanding of the many-body state, a multitude of novel experimental methods have been further developed to probe the static and dynamical properties of strongly correlated quantum gases in optical lattices. For instance, in-situ imaging of the atomic cloud can be employed to detect the density distribution in real space [39, 40], time-of-flight images give access to the momentum distribution of trapped atoms [41], and density-density fluctuation measurements provide information about the system’s correlation functions [42–46]. Another paradigmatic example of recent experimental advances constitutes the so-called quantum gas microscope which allows for the detection of atoms in lattice systems with single-site resolution [47–49]. Even dynamical response functions can be obtained, via e.g. Radio-frequency [50, 51] or Bragg spectroscopy [52, 53]. Moreover, a great variety of unique lattice geometries has been realized, such as superlattices [54–56], cubic [57], hexagonal [59, 60], honeycomb [58] and Kagome lattices [61].

Despite the wide success of the Bose-Hubbard Hamiltonian to predict several physical phenomena which are also experimentally supported, there is a huge class of processes that lie beyond its applicability. These limitations stem from the inherent restrictions of this model and refer, for instance, to offsite interaction effects and the occupation of excited-bands. Apart from the purely theoretical interest in those effects, the aforementioned recent experimental advancements offer an excellent testbed to study many-particle physics beyond the lowest-band Bose-Hubbard approximation. Models operating beyond the standard Bose-Hubbard approximation are known as extended Hubbard models and can be employed to enter previously inaccessible regimes [62–64]. Indeed, a variety of quantum phases and dynamical phenomena have been based on mechanisms beyond the standard Hubbard model. For instance, offsite interactions give rise to novel experimentally confirmed correlated quantum phases such as the charge-density-wave insulator where the onsite occupancy alternates from site to site [65–73], unconventional superfluids [36, 37, 74] with a complex phase twist of the order parameter, dimerized insulators [75–79] possessing a unique excitation spectrum, or supersolids [67, 70, 73, 80–84] that involve diagonal and off-diagonal long range order. Moreover, density-induced tunneling processes [85–91] and effects of interaction-induced occupation of higher orbitals [64, 96] have been observed and found to affect the lattice band structure causing a significant shift of the superfluid to Mott-insulator phase boundary. Note that studies of extended Hubbard models have been conducted majorly relying on exact diagonalization techniques [92], strong-coupling expansion schemes [93, 94] and the Gutzwiller approximation [19, 95]. In the present dissertation, we use a variational approach, the Multi-Layer Multi-Configuration Hartree Method for Atomic Mixtures [97–100], which incorporates the system’s important correlation effects, to demonstrate among others the participation of beyond Hubbard processes of ultracold atoms trapped in optical lattices.

Besides the above-mentioned plethora of static phases, the nonequilibrium dynamics of such systems exhibits even more fascinating phenomena. Here, for instance, correlation induced mechanisms and collective excitations provide further insights into this new and burgeoning field. Owing to their unique experimental controllability, ultracold atoms in optical lattices provide an ideal setting for studying out-of-equilibrium quantum many-body

dynamics. The most frequently considered way to induce the nonequilibrium dynamics is a quantum quench [101–104]. Here, a many particle system initially prepared in a quantum state $|\Psi_0\rangle$, possessing certain correlation properties, of a Hamiltonian H_i evolves unitarily in time following the sudden change of an intrinsic system’s parameter (quench protocol) to a final Hamiltonian H_f . Considering a closed quantum system, the energy after the quench remains constant and is distributed among the various degrees of freedom during the unitary evolution. Dynamics generated by a quantum quench is an active field of research since it poses many fundamental questions such as the development of new correlations [105–111], the possible thermalization of the system [112–123], the scaling of defect formation when crossing a phase transition and the associated dynamical universality classes [124–133], as well as the controllability of the participating modes [134–141], to name only a few. It is the latter field of quench-induced dynamics that the present thesis mainly aims to address, providing further insight on the correlated mechanisms that take place in the out-of-equilibrium few-boson dynamics.

A series of consecutive experimental realizations on quench-induced phenomena evinced, further, the issue of thermalization [101, 112, 142–144] and the crossover between ballistic and diffusive expansion of atoms in optical lattices [145, 146] depending on the dimensionality and interaction strength. Moreover, peculiar transport phenomena of bosons and fermions [147–150], scaling properties of the defect density when crossing the superfluid to Mott-insulator transition [126–128, 151], and quench generated excitations [101, 152–155] have been revealed. Among the above studies, and as far as the notion of thermalization is concerned, a prominent example constitutes the collisional dynamics of two one-dimensional Tonks-Girardeau gases [142]. In this system no sign of thermalization has been observed, a behavior that is directly related to the integrability of the system. However, indications of relaxation dynamics have been observed when inspecting the evolution of one-dimensional condensates after their splitting [143, 144]. In this context of thermalization, a focal point of theoretical research has been the crossover from integrability to non-integrability and the consequent thermal or non-thermal behavior in relation to quantum chaos [112, 156–158, 365]. Its presence implies that simple observables are represented by random matrices in the eigenbasis of the Hamiltonian and thermalization occurs at the level of individual eigenstates. Thermalization in nonintegrable systems has also been formulated recently in terms of the eigenstate thermalization hypothesis [120, 159–161].

Despite the huge progress achieved over the past years on the theoretical side, the efficient simulation of nonequilibrium dynamics is still a challenging task and stresses the importance of developing novel theoretical approaches. The central problem is that the Hilbert space of a quantum many-body system grows exponentially with the number of its constituents and therefore obtaining analytical or numerically exact solutions becomes, in most cases, impossible already for small systems. Another complicating feature of the nonequilibrium dynamics is the presence of interactions leading to the appearance of strong interparticle correlations, at a level that often precludes the use of a perturbative analysis or mean-field approximations. In this respect, the dynamics beyond the paradigm of linear response theory has been a subject of growing theoretical interest [162–169], triggered also by the recent progress in ultracold atom experiments mainly focused on one-dimensional settings [10–14].

INTRODUCTION

A quench protocol inevitably excites the system and a number of defects, including correlated two-body processes and higher-band excitations, can be formed during the dynamics. For ultracold bosons confined in optical lattices, this implies the necessity to consider a multiband treatment [62, 63], in order to describe the emergent nonequilibrium correlated dynamics and to gain information about the higher-band excitation spectrum, inaccessible by the standard Bose-Hubbard model or mean-field methods. In the present dissertation, we provide a multimode treatment for the nonequilibrium dynamics of few-bosons confined in finite optical lattices in one spatial dimension, with all correlations taken into account. Among others, we demonstrate that such an approach is suitable for extracting information from the resulting many-body dynamics. In particular, we obtain the complete excitation spectrum, characterize the emergent various collective modes during the evolution, and provide, when possible, a scale-free universality of the system's dynamical response.

Yet another widely used technique to probe and study the out-of-equilibrium dynamics of ultracold atoms in optical lattices is the time periodic modulation, or driving, of either their position, e.g. shaken lattices, or their potential depth [9, 170, 171]. These modulations can be experimentally routinely achieved by controlling the phase or the intensity of the involved laser beams. In such systems the lattice band structure is modified during the driving which consequently affects the physical properties of the system, giving rise to a variety of intriguing effects. For instance, phase modulations have been used to address parametric amplification of matter waves [172], four-wave mixing [173, 174], coherent band coupling [175, 176], topological states of matter [177], coherent control of the superfluid to Mott-insulator phase transition [178], hybridization of the lattice band structure [172, 179], and even to engineer artificial gauge fields [180–183]. On the other hand, amplitude modulations of the lattice depth have been employed to probe the excitation spectrum of the system [24, 88, 184], the participating nearest-neighbor correlations [185] as well as to realize intriguing mechanisms such as photon-assisted tunneling [186] and orbital excitation blockade [187]. Furthermore lattice potentials can also be easily accelerated, creating inertial forces for the atoms in the co-moving reference frame. It has been shown [188–191] that within a time-averaged effective picture these oscillating forces lead to a renormalization of the tunneling matrix elements in both amplitude and sign. Representative processes here include Bloch-oscillations [192–195], Wannier-Stark ladders [196, 197], and Landau-Zener tunneling [195, 197].

As already argued, time-periodic modulations of optical lattices constitute an important concept towards the manipulation of the atomic motion [9, 171]. For instance, as it has recently been shown, the dynamics triggered by shaking an optical lattice can lead to an admixture of excited orbitals [198] or even induce dynamical instabilities caused by the interplay between the interparticle interactions and the external driving [199–202]. Accordingly, it is very important to carefully explore and design the relevant driving protocol so as to transfer the energy to the desired final degrees of freedom [134–139]. In the present dissertation, we study the dynamics of finite bosonic systems subjected to a shaken [[7]] or a vibrating [[8]] lattice potential with a particular emphasis on the microscopic characterization of the dynamical modes, their parametric coupling and thus their dynamical control.

Until now, we provided an overview of some intriguing effects arising in scalar, alias

single-component, bosonic ensembles. We have mainly focussed in their corresponding non-equilibrium properties induced either by a quench protocol or a time-periodic driving of the optical lattice in which they are trapped. Next, we shall turn our attention to the case of two-component mixtures mainly comprised of bosonic constituents and briefly report some of the outstanding phenomena observed in this field. Two-component Bose-Einstein condensates [1–3, 203–205] consisting e.g. by two alkali metals such as ^{23}Na - ^{87}Rb , two isotopes like ^{85}Rb - ^{87}Rb , or two hyperfine states of the same alkali metal, provide an ideal platform for studying intriguing and novel phenomena that cannot be addressed in a single-component setting. Three scattering lengths characterize the intra- and interspecies interaction between the atoms, being tunable with the aid of magnetic or optical Feshbach resonances [4–8]. The interplay between the inter- and intraspecies scattering has a direct consequence on several static properties of the condensate, such as its density profile and correlation properties. Correlation in interacting mixtures have been extensively studied [36, 206–210], revealing, for instance, altered phase separation regimes [211–214], the formation of quantum droplets [215–218], modified superfluid-insulator transitions [206, 219], composite fermionization [220], quantum emulsions [221], and spin-charge separation [222]. Moreover, instabilities [223] as well as new phases including paired or counterflow superfluidity [209] and twisted superfluidity in bi-spinor mixtures [36] have been observed. Additionally, quenching a binary mixture across the miscible-immiscible phase boundary has been a focal point of theoretical studies examining, for instance, the consequent scaling properties of the underlying correlation functions [224–226].

Besides the aforementioned two-component systems, also Bose-Fermi mixtures have been experimentally realized with the aid of sympathetic cooling [227–229]. This kind of mixtures serve as prototypical examples in which the intermingled particles obey different statistics [1, 2]. Indeed, *s*-wave interactions among spin-polarized fermions are prevented due to the Pauli exclusion principle. Such systems can be realized e.g. by a mixture of isotopes of ^7Li and ^6Li [230] or ^{171}Yb and ^{172}Yb [231, 232]. The complex interplay of Bose-Bose and Bose-Fermi interactions led to numerous theoretical studies of Bose-Fermi mixtures regarding, e.g., their phase separation process [233, 234] stability conditions [223, 235] and collective excitations [236, 237]. Bose-Fermi mixtures confined in optical lattices unveil a multitude of intriguing quantum phases including, among others, exotic Mott-insulator and superfluid phases [238–240], charge-density waves [241, 242], supersolid phases [243, 244] and polaron-like quasiparticles [242, 245].

The vast majority of the above-mentioned studies has been focused on a mean-field description, while the role of many-body effects, e.g. in the transition from the miscible to the immiscible phase, is much less understood. Recently, the inclusion of correlations in multi-component few-boson systems revealed altered phase separation processes [206, 219, 223, 246, 247], composite fermionization [220, 248, 249], or even the crossover between the two [250, 251]. Furthermore, the dynamical properties of such many-body ultracold mixtures have been studied, including the dependence of the tunnelling dynamics on the mass ratio [252, 253] and the intra- and interspecies interactions [254], as well as the emergence of Andersons orthogonality catastrophe upon quenching the interspecies repulsion [255]. However, far less emphasis has been placed on the many-body character of the

quench-induced dynamical phase separation phenomena. Our last two works [[9,10]] aim at partially addressing this latter apparent gap for both few and larger atomic ensembles. In particular, we study the dynamical phase separation of a repulsively interacting Bose-Bose mixture upon quenching the interspecies interaction coefficient across the phase boundary by initializing the system either in the phase miscible or the phase immiscible regime [[9]]. Finally, we move to a Bose-Fermi mixture confined in an optical lattice and examine, for the first time, the correlation effects in the many-body expansion dynamics of such a mixture residing either within the miscible or immiscible phase [[10]].

Objectives of this thesis

In this cumulative dissertation we theoretically study the zero-temperature nonequilibrium many-body quantum dynamics of repulsively short-range interacting few atomic ensembles and mixtures thereof confined in one-dimensional finite lattices. The correlated nonequilibrium dynamics is induced either by performing a quench on a system's parameter (e.g. the interaction strength) or via a periodic driving of the optical lattice. In particular, we theoretically explore the impact of correlations on the many-body quantum dynamics from various perspectives. By investigating a series of exemplary driving scenarios we demonstrate different ways to couple the triggered dynamical modes (such as single-particle or atom-pair tunneling) and reveal their corresponding correlation properties. Particularly, we mainly

- characterize the dynamical response of the system after the quench or during the periodic driving of the optical lattice;
- design the appropriate quench protocol in order to trigger certain dynamical modes;
- characterize the microscopic properties and reveal the correlated nature of the quench-induced modes;
- obtain a control of the non-equilibrium dynamics by coupling distinct dynamical modes;
- unveil novel higher-band excitations that participate in the nonequilibrium dynamics;
- provide experimental evidences of the observed dynamics by simulating single-shots absorption measurements.

We also clarify which processes can be obtained within a mean-field approximation or a lowest-band Bose-Hubbard model and which of them require the use of more elaborated methods that include interparticle correlations. These insights are obtained by utilizing the Multi-Layer Multi-Configuration Time-Dependent Hartree method for bosonic and fermionic mixtures, an ab-initio variational method designed for the treatment of the nonequilibrium quantum dynamics of ultracold multi-component systems.

Chapter 2

Theoretical Framework

2.1 Optical Lattices

Optical lattices are essentially artificial crystals of light generated by interfering optical laser beams. Atoms illuminated by a laser beam acquire a dipole moment, induced by the electric field of the laser, which in turn let them interact with the electric field. This interaction alters the energy of the atomic internal states depending on both the laser frequency and intensity. To confine the atoms within a periodic spatially dependent potential energy landscape a spatially dependent intensity is used. Such a periodic potential energy landscape that the atoms experience as a result of the standing wave pattern generated by the interference of laser beams is typically called an optical lattice, see Fig. 2.1 (a).

Ultracold atoms confined in optical potentials are reminiscent of solid state materials. For instance, the optical lattice can be perceived as playing the role of the crystal lattice in a solid while the atoms mimic the corresponding valence electrons. In that sense, the atoms are able to move within the lattice (quantum tunneling between the distinct sites) as the valence electrons move in the periodic energy landscape created by the positively charged ions in a crystal. Meanwhile, optical lattices possess several advantages with respect to solid state systems. They are largely free of defects and highly controllable systems by means of changing the laser properties. For instance the lattice depth can be tuned by changing the laser intensity, its spacing can be modified by the interference angle between the laser beams, its geometry is determined by the laser configuration and the entire configuration can be dynamically moved by changing the polarization of the light. Furthermore, atoms are much heavier than electrons which means that in order to probe the same physics occurring e.g. at a temperature of 100 Kelvins in a solid state setup one needs to cool atoms below a few nanokelvin. The latter requires the use of state-of-the-art cooling techniques which are nowadays available. In these systems it is possible to follow the dynamics of the atoms on time scales of the order of ms or even seconds. Finally and in sharp contrast to electrons, being charged particles and strongly coupled to their environment, atoms are neutral and almost completely isolated from their environment. Due to the above, ultracold atoms in optical lattices offer an ideal platform for simulating certain problems of condensed matter physics and constitute many-body systems exhibiting a diversity of physical phenomena.

THEORETICAL FRAMEWORK

Below, we first briefly outline the basic theory of optical lattices and discuss the single-particle properties of atoms in a periodic potential. Then, we introduce the so-called Bose-Hubbard Hamiltonian which is the simplest non trivial model that describes interacting bosons in an optical lattice.

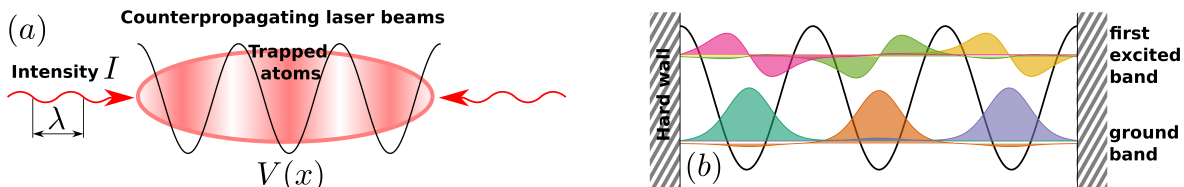


Figure 2.1: (a) Two counter propagating laser beams of intensity I and wavenumber λ forming a lattice potential $V(x)$. (b) Schematic representation of the Wannier functions of the first two energetically lowest-lying single-particle bands of a triple well.

2.1.1 AC Stark Shift and Dissipative Interaction

Neutral atoms interact with the light in a dissipative and a conservative manner. The conservative interaction originates from the interaction of the light field with the induced dipole moment of the atom resulting in a shift of the potential energy called AC-Stark shift. The dissipation is caused by the absorption of photons followed by a spontaneous emission event. Spontaneous emission processes can be neglected only for fairly large detunings providing a case where the energy shift can be used to create a conservative trapping potential. We shortly explain both processes below.

Let us consider a two-level atom with internal states $|g\rangle$ and $|e\rangle$ being energetically separated by $\hbar\omega_0$. The atom is further illuminated by a classical monochromatic electromagnetic field $E(x) = E_0(x)e^{i\omega t} + E_0^*(x)e^{-i\omega t}$ with amplitude $E_0(x)$ and frequency ω . This electromagnetic field induces a dipole moment (\hat{d}) to the atom which then interacts with $E(x)$ as $H_I = -\hat{d} \cdot E$. Here $\hat{d} = \sum_{\alpha, \beta=g,e} \langle \alpha | \hat{d} | \beta \rangle | \alpha \rangle \langle \beta |$ with $\sum_{\alpha} | \alpha \rangle \langle \alpha | = 1$, $\langle \alpha | \hat{d} | \alpha \rangle = 0$ and $\mu_{eg} = \langle e | \hat{d} | g \rangle \neq 0$ because the atoms do not have a permanent dipole moment. Then, $\hat{d} = \mu_{eg} | e \rangle \langle g | + \mu_{eg}^* | g \rangle \langle e |$ and the Hamiltonian of the total system reads

$$\hat{H} = \hbar\omega_0 | e \rangle \langle e | - (\mu_{eg} | e \rangle \langle g | + \mu_{eg}^* | g \rangle \langle e |) (E_0(x)e^{-i\omega t} + E_0^*(x)e^{i\omega t}). \quad (2.1)$$

This Hamiltonian can be transformed into a time-independent one by performing the rotating wave approximation which is valid in the limit of small detunings, $|\delta| \equiv |\omega - \omega_0| \ll |\omega + \omega_0|$. The rotating frame of the laser is determined by the unitary transformation $\hat{U}(t) = e^{-i\omega \hat{\sigma}_z t/2}$, where $\hat{\sigma}_z = | e \rangle \langle e | - | g \rangle \langle g |$ is the Pauli matrix, and the Hamiltonian transforms according to $\hat{H} \rightarrow \hat{U}^\dagger \hat{H} \hat{U} + i\hbar \frac{\partial \hat{U}^\dagger}{\partial t} \hat{U}$. Neglecting processes with a rapidly oscillating phase, $e^{\pm i(\omega + \omega_0)t}$ and considering only the near resonant frequency processes the Hamiltonian is reduced to

$$\hat{H} = -\frac{\hbar\delta}{2} \hat{\sigma}_z - \left(\frac{\hbar\Omega(x)}{2} | e \rangle \langle g | + \frac{\hbar\Omega^*(x)}{2} | g \rangle \langle e | \right), \quad (2.2)$$

where $\Omega(x) = 2E_0(x)\mu_{eg}/\hbar$ is the so-called Rabi frequency. Employing second order perturbation theory which is applicable in the limit that the detuning is large compared to the Rabi frequency i.e. $|\delta| \gg \Omega$ we can determine the effect of atom-light interaction on the states $|e\rangle$, $|g\rangle$. Then, the energy shift $E_{eg}^{(2)}$ reads

$$E_{eg}^{(2)} = \pm \hbar \frac{\Omega^2(x)}{4\delta}, \quad (2.3)$$

where \pm refers to the states $|g\rangle$ and $|e\rangle$ respectively. This latter energy shift is known as the AC-Stark shift and defines the optical potential that atoms in the state $|g\rangle$ experience. Of course, in the case that the atoms are illuminated by superimposed counter propagating laser beams which interfere they experience a standing wave pattern resulting from this interference. The resulting periodic landscape of the energy experienced by the atoms is the optical lattice potential. The simplest possible lattice geometry is that of a one-dimensional optical lattice [see Fig. 2.1 (a)]. The latter can be generated by creating a standing wave interference pattern by the retroreflection of a single laser beam with Rabi frequency Ω_0 . This results in a Rabi frequency $\Omega(x) = 2\Omega_0 \sin(kx)$ yielding the periodic potential

$$V(x) = \frac{\hbar\Omega_0^2}{\delta} \sin^2(kx), \quad (2.4)$$

where $k = 2\pi/\lambda$ denotes the magnitude of the laser wavevector and $V_0 = \frac{\hbar\Omega_0^2}{\delta}$ is the lattice depth. This potential possesses a lattice constant, $a = \lambda/2$, determined by $V(x+a) = V(x)$ for every x .

Up to now, we have assumed that the excited state possesses an infinite life time since we neglected its decay due to the spontaneous emission of photons. This latter effect can be modelled phenomenologically by attributing to the excited state a complex valued energy. Indeed, when the excited state has a life time $1/\Gamma_e$, the energy of the perturbed ground state becomes $E_g^{(2)} = V(x) + i\gamma(x)$ where

$$V(x) \approx \hbar \frac{\Omega^2(x)}{4\delta} \quad \text{and} \quad \gamma \approx \hbar \frac{\Omega^2(x)\Gamma_e}{8\delta^2}. \quad (2.5)$$

Here $V(x)$ (real part of the energy) corresponds to the optical potential. Most importantly, the sign of the detuning δ determines the sign of $V(x)$. For $\delta > 0$ (blue detuning) $V(x) > 0$ resulting in a repulsive potential whose minima correspond to the points with zero light intensity (atoms are repelled from the high intensity regions). For $\delta < 0$ (red detuning) $V(x)$ is attractive and its minima correspond to the regions with maximum light intensity where atoms are likely to reside. We remark here that the cases of blue and red detuning are also often called as “weak field seekers” and ”strong field seekers” respectively. On the other hand, $\gamma(x)$ (imaginary part of the energy) refers to the loss rate of atoms from the ground state.

2.1.2 Bose-Hubbard Model

The Hubbard model, originally introduced in 1963 by J. Hubbard [256], has been derived for describing the behaviour of strongly-correlated electrons in solids. It has been used

THEORETICAL FRAMEWORK

to describe a multitude of systems in solid state physics such as short correlation length superconductors, Josephson arrays and the critical behavior of ^4He . More surprisingly, since more than a decade now, variations of this model are routinely being implemented with ultracold atoms in optical lattices, allowing for their study in a clean and almost perfectly isolated (defect-free) environment. In the following, our aim is to briefly outline the derivation of the Hubbard model for ultracold bosons in optical lattices and discuss its limitations as well as its possible extensions.

In second quantization, the Hamiltonian for a three-dimensional dilute interacting bosonic gas confined in an optical lattice potential $V(\mathbf{r})$ reads

$$H = \int d\mathbf{r} \Psi^\dagger(\mathbf{r}) \left(-\frac{\hbar^2}{2m} \nabla^2 + V(\mathbf{r}) \right) \Psi(\mathbf{r}) + \frac{1}{2} \int d\mathbf{r} d\mathbf{r}' \Psi^\dagger(\mathbf{r}) \Psi^\dagger(\mathbf{r}') V_I(\mathbf{r}, \mathbf{r}') \Psi(\mathbf{r}) \Psi(\mathbf{r}'), \quad (2.6)$$

where $\Psi^\dagger(\mathbf{r})$, $\Psi(\mathbf{r})$ denote the bosonic creation, annihilation field operators respectively and m is the bosonic mass. The isotropic short-range pseudopotential $V_I(\mathbf{r}, \mathbf{r}')$ modelling s -wave interactions

$$V_I(\mathbf{r} - \mathbf{r}') = \frac{4\pi\hbar^2 a_s}{m} \delta(\mathbf{r} - \mathbf{r}') \frac{\partial}{\partial |\mathbf{r} - \mathbf{r}'|} |\mathbf{r} - \mathbf{r}'|. \quad (2.7)$$

Here a_s is the s -wave scattering length which characterizes the interparticle interactions through low-energy elastic collisions between neutral atoms, independently of the actual two-body potential. Indeed, for ultracold atoms the de Broglie wavelength is much larger than the effective extension of the interaction potential, implying that the interatomic potential can be replaced by a pseudopotential. For a non-singular $\Psi(\mathbf{r})$ this pseudopotential is equivalent to a contact interaction

$$V_I(\mathbf{r} - \mathbf{r}') = \frac{4\pi\hbar^2 a_s}{m} \delta(\mathbf{r} - \mathbf{r}') \equiv g\delta(\mathbf{r} - \mathbf{r}'). \quad (2.8)$$

The above approximation is valid when long-range contributions are negligible. For a more elaborated discussion about the scattering theory see for instance [257,258]. Note that positive values of a_s account for repulsive interactions while negative values for attractive ones.

The natural energy scale of the Hamiltonian of Eq. (2.6) is the recoil energy $E_R = \frac{\hbar^2 k^2}{2m}$, with $k = 2\pi/\lambda$ and λ being the wavelength of the optical lattice. The optical lattice potential is typically $V(x, y, z) = V_{0,x} \sin^2(k_x x) + V_{0,y} \sin^2(k_y y) + V_{0,z} \sin^2(k_z z)$. If $V_{0,x} \ll V_{0,y} = V_{0,z}$ then a setup for a one-dimensional optical lattice is obtained, namely excitations to the y and z directions are highly suppressed and the system may be considered as a series of independent one-dimensional tubes along the x direction. In what follows, we assume that the above condition is fulfilled and therefore the analysis refers to one spatial dimension.

Within the weakly interacting regime, lattice trapped bosonic atoms are well described by a Bose-Hubbard Hamiltonian [20]. Let us therefore explain how the Bose-Hubbard Hamiltonian is derived from the many-body Hamiltonian of Eq. (2.6) by simply expanding the field operators onto single-particle Wannier modes [266]. We remind that the field operators $\hat{\Psi}(x)$ can always be expanded in the basis of Bloch functions $\phi_{n,\kappa}(x)$, which are the eigenfunctions of the single-particle Hamiltonian consisting of only the kinetic term and the lattice potential

$$\hat{\Psi}(x) = \sum_{n,\kappa} \hat{b}_{n,\kappa} \phi_{n,\kappa}(x). \quad (2.9)$$

The indices κ , n of the Bloch functions denote the quasi-momentum and the band number respectively. Intuitively κ might be viewed as a quantum number characteristic of the translational symmetry of the periodic potential, just as the momentum is a quantum number characterizing the translational symmetry in free space. Of course in a strict sense κ is not the same as the momentum, but it turns out that it plays the same fundamental role in the dynamics within a lattice potential as the momentum does in the absence of the lattice. To emphasize this similarity κ is called the quasimomentum. For sufficiently deep lattice potentials and at low temperatures the band gap between the lowest and the first excited-band may be fairly large so that the second and higher-bands will not be populated and therefore can be disregarded. Within the lowest Bloch band of the optical lattice the field operators can be expanded into an orthonormal Wannier basis. This basis consists of functions being localized around the lattice sites. We remark here that Wannier orbitals are a unitary transformation of the Bloch functions and constitute an equivalent representation to describe such a periodic system. Moreover, they constitute a more appropriate representation than the Bloch functions, as the lattice depth (or equivalently the interaction) is increased and the atoms become progressively more localized at individual lattices sites. The Wannier functions will be denoted in the following as $w_i(x) \equiv w(x - x_i)$ with x_i corresponding to the minima of the lattice potential and i is the site index. The expansion of the field operator in terms of this basis is known as the tight-binding approximation and it is justified when the temperature is sufficiently low and the typical interaction energies are not strong enough to excite energetically higher-band modes. The corresponding expansion reads

$$\hat{\Psi}(x) = \sum_i \hat{b}_i w_i(x), \quad (2.10)$$

where \hat{b}_i (\hat{b}_i^\dagger) refers to the annihilation (creation) operator of a boson localized at the i -th lattice site and obey the standard canonical commutation relations $[\hat{b}_i, \hat{b}_j^\dagger] = \delta_{ij}$. For simplicity in the following we will omit the hat symbol from the operators. Inserting the above expansion into the Hamiltonian of Eq. (2.6) we obtain the celebrated lowest-band Bose-Hubbard model

$$H = - \sum_{\langle i,j \rangle} J_{ij} b_i b_j^\dagger + \frac{U}{2} \sum_i [n_i(n_i - 1) - \mu n_i], \quad (2.11)$$

where $\langle ij \rangle$ indicates that the sum is performed over nearest neighbors. Note that each pair (i, j) appears twice in the summation ensuring in this way the hermiticity of the first term. Furthermore, $n_i = b_i b_i^\dagger$ is the boson number operator at site i and μ denotes the chemical potential being introduced to control the total number of atoms. The corresponding tunneling matrix elements between adjacent sites read

$$J_{ij} = - \int dx w_i^*(x) \left[-\frac{\hbar^2}{2m} \frac{\partial^2}{\partial x^2} + V(x) \right] w_j(x). \quad (2.12)$$

Moreover, the strength of the two-body on-site interactions U for a contact potential is given by

$$U = g \int dx |w_i(x)|^4. \quad (2.13)$$

THEORETICAL FRAMEWORK

Finally we remark here that in the presence of an additional external potential, V_M , one more term has to be included in the Bose-Hubbard Hamiltonian accounting for a potential energy $H_M = \sum_i \epsilon_i n_i$ with $\epsilon_i = \int dx V_M(x) |w_i(x)|^2$. This latter term essentially describes an energy offset for each lattice site and typically is absorbed into a site-dependent chemical potential $\mu_i = \mu + \epsilon_i$.

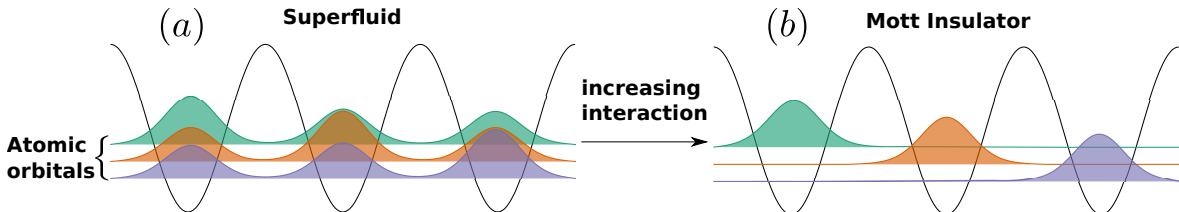


Figure 2.2: Schematic representation of the transition from (a) a superfluid phase to (b) a Mott insulating state of three bosons confined in a triple well for increasing interparticle repulsion. Note that the degree of the on-site excitation is the same for all wells.

The Bose-Hubbard Hamiltonian [Eq. (2.11)] predicts a quantum phase transition from a superfluid to a Mott-insulator state. This transition has already been observed experimentally for bosons confined in a three-dimensional optical lattice [23]. In particular, the Bose-Hubbard model exhibits two different quantum phases depending on the ratio between the tunneling energy and the on-site repulsion energy. A superfluid, compressible, gapless phase occurs when the tunneling term dominates, $J \gg U$, while an incompressible Mott-insulator ground state exists when the on-site interaction dominates i.e. $J \ll U$. For a schematic representation of these two phases see also Fig. 2.2. The onset of superfluidity is a consequence of the competition between the kinetic energy, which favors particle delocalization, and the interaction energy, which promotes particle localization resulting in small particle-number fluctuations. Within the superfluid phase the kinetic energy term dominates the Hamiltonian of Eq. (2.11). Then, quantum correlations can be neglected and the system can be described by a macroscopic wavefunction. The many-body state is almost a product over identical single-particle wavefunctions

$$\Psi_{SF}^{U=0}(x_1, \dots, x_N) = \prod_{i=1}^N \phi(x_i), \quad (2.14)$$

where $\phi(x)$ obeys the mean-field Gross-Pitaevskii equation (for a detailed description of this equation see Sec. (2.2)). For increasing interaction the average kinetic energy required for an atom to tunnel between adjacent lattice sites becomes insufficient to overcome the potential energy cost. The atoms tend to be localized at individual lattice sites and the particle-number fluctuations almost vanish. This is the Mott-insulator phase where the ground state of the system consists of localized atomic wavefunctions with a fixed number of atoms per lattice site. The corresponding ground state is a product of Fock states

$$\Psi_{MI}^{J=0}(x_1, \dots, x_N) = \prod_i |n_0\rangle_i, \quad (2.15)$$

where n_0 denotes the number of bosons per lattice site i in the Mott-insulator state. The corresponding lowest-lying excitations that conserve the particle number are the so-called particle-hole excitations being obtained by adding and removing a particle from the system. This phase is characterized by the existence of an energy gap which is determined by the energy necessary to create one particle-hole pair. For further details regarding the properties of the above-mentioned phase transition we refer the interested reader to [19,20]. Here we only mention that the Bose-Hubbard model and its phase transition has been studied extensively both analytically and numerically. On the theoretical side many different techniques have been employed such as mean-field approximations [259–261], renormalization group theories [20] and strong-coupling expansions [93,94]. On the numerical side, most of the studies have been conducted with quantum Monte Carlo methods and density matrix renormalization techniques [15,18,262–265,311].

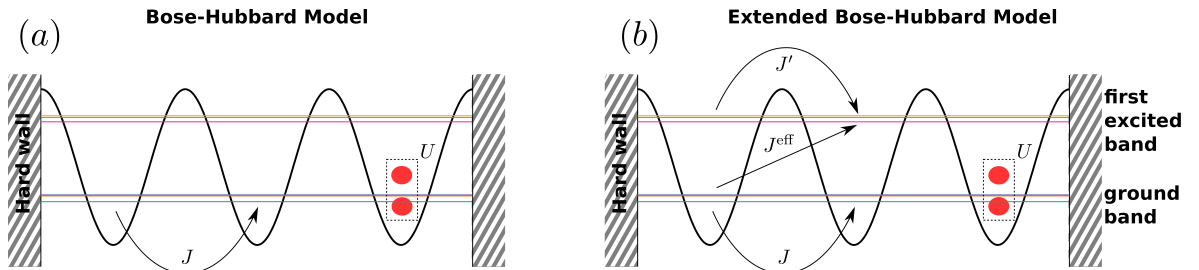


Figure 2.3: Schematic representation of the basic underlying mechanisms within (a) the Bose-Hubbard and (b) an extended Bose-Hubbard model. The symbols J , J' and J^{eff} refer to the intraband within the lowest-band interwell, first excited-band and the corresponding interband tunneling amplitudes respectively. U denotes the onsite repulsion energy.

2.1.3 Extended Bose-Hubbard Models

As already discussed above, within the Bose-Hubbard model only the energetically lowest single-particle band is assumed to be occupied since higher excited-bands are energetically well separated. However, it turns out that such a single band approximation is often insufficient, e.g. for strong interparticle interactions or shallow lattices, and that contributions of higher-bands can not be neglected. Taking into account higher-bands is an important extension of the standard Bose-Hubbard model. For instance, in strongly correlated systems, the interaction induced coupling between the distinct orbital bands becomes fairly strong so that higher-bands are mixed with the lowest-band. Due to the dominant contribution of energetically higher-bands to the total energy, the orbital occupation is determined by on-site interaction processes. Following a mean-field treatment it can be shown [62,63] that the occupation of higher orbitals results in a modified on-site wave function of the particles in order to minimize the on-site interaction energy. The contribution of higher orbitals also alters the wavefunction overlap between neighboring lattice sites, leading to a modified tunneling amplitude which becomes occupation dependent.

Let us then formulate a multiorbital Bose-Hubbard model. We first expand the field

THEORETICAL FRAMEWORK

operator $\Psi(x)$ taking explicitly excited-bands into account

$$\Psi(x) = \sum_{i,\alpha} b_i^\alpha w_i^\alpha(x), \quad (2.16)$$

where $w_i^\alpha(x)$ denotes a Wannier function of the band α being localized at site i . b_i^α , $b_i^{\alpha\dagger}$ are the annihilation, creation operators for a boson located at site i and energy band α . Inserting Eq. (2.16) into the many-body Hamiltonian [see Eq. (2.6)] we obtain the tunneling matrix elements

$$J_{ij}^\alpha = - \int dx w_i^{\alpha*}(x) \left[-\frac{\hbar^2}{2m} \frac{\partial^2}{\partial x^2} + V_{ext}(x) \right] w_j^\alpha(x). \quad (2.17)$$

By construction $J_{ij}^{\alpha\beta} = 0$ for $\alpha \neq \beta$. Furthermore for sufficiently deep lattices it is enough to restrict the hopping to nearest neighbor sites, since the tunneling amplitudes are exponentially damped with the hopping distance. However, for shallow lattices the inclusion of next nearest neighbor hoppings might be necessary [114]. The energies in the different orbitals are given by

$$\epsilon^\alpha = \int dx w_i^{\alpha*}(x) \left[-\frac{\hbar^2}{2m} \frac{\partial^2}{\partial x^2} + V_{ext}(x) \right] w_i^\alpha(x), \quad (2.18)$$

while the corresponding interaction integrals by

$$U_{ijkl}^{\alpha\beta\gamma\delta} = \int dx dx' w_i^{\alpha*}(x) w_j^{\beta*}(x') V(x-x') w_k^\gamma(x) w_l^\delta(x). \quad (2.19)$$

Combining all the above terms we obtain the full multiorbital Bose-Hubbard model described by the many-body Hamiltonian

$$H = - \sum_{\alpha,i,j} J_{ij}^\alpha b_i^{\alpha\dagger} b_j^\alpha + \sum_{\alpha\dots\delta,i\dots l} U_{ijkl}^{\alpha\beta\gamma\delta} b_i^{\alpha\dagger} b_j^{\beta\dagger} b_k^\gamma b_l^\delta + \sum_{\alpha,i} (\epsilon^\alpha - \mu) n_i^\alpha. \quad (2.20)$$

The full description of lattice and orbital degrees of freedom captured by the multiorbital Bose-Hubbard model leads to an extremely complex many-particle problem. In addition to that for very strong interactions such a description might lead to convergence problems [see [63] and references therein]. It follows from the above that the key point for the description of a many-body bosonic system trapped in an optical lattice is the implementation of an effective multiorbital Hubbard model in order to restrict the corresponding computational costs and also take the important, for the system under consideration, effects into account. In this direction extended Hubbard models have been constructed including, for instance, correlated and occupation dependent tunneling contributions within the lowest-band as well as correlated tunnelings and occupation of higher-bands. A multitude of such extended Hubbard models have already been suggested and are also summarized in various reviews e.g. see [62–64]. As a final remark let us list some of the effects predicted by such models and also observed in the past decade in many different experiments: i) modifications of on-site interactions [26, 187, 267–269], ii) observation of density-induced tunneling [64, 85–91, 270], iii) effects of excited-bands [38, 271–276], iv) shift of the Mott-insulator transition in a Bose-Fermi mixture [86, 88, 277, 278] and v) dynamical spin effects [279–281] to name a few.

2.2 Mean-Field Theory and the Gross-Pitaevskii Equation

Within the weakly interacting regime and large particle number limit, quantum fluctuations can be neglected to a good approximation. In this regime most of the atoms occupy the same condensate wavefunction [1–3, 282]. This latter assumption essentially reduces the many-body problem to an effective single-particle one, where all interaction effects solely manifest themselves in the deformation of the associated single-particle orbital.

As already discussed in Sec. 2.1.2 a sufficiently dilute ultracold atomic gas, composed by N interacting bosons each of mass m and confined by an external potential $V_{ext}(x)$ is described by the many-body Hamiltonian of Eq. (2.6). The mean-field approximation is based on the assumption that only one single-particle state $\phi(x)$ is mainly occupied in a macroscopic way, i.e. its occupation number N_0 is of the order of the number of bosons N . Then, the state of the total system is given by

$$\Psi(x_1, \dots, x_N) = \prod_{i=1}^N \phi(x_i), \quad (2.21)$$

where x_i labels the spatial coordinate of the atoms. For simplicity below we shall use the notation $x_i \equiv x$. According to the above, within the mean-field realm it makes sense to consider the following separation of the macroscopic (condensate) contribution from the bosonic field operator

$$\Psi(x) = \langle \Psi(x) \rangle + \delta\Psi(x), \quad (2.22)$$

where $\langle \Psi(x) \rangle \equiv \Psi(x)$ is known as the macroscopic wavefunction of the condensate, while $\delta\Psi(x)$ describes its non-condensed part and accounts for quantum and thermal fluctuations [1, 2]. Operating in the low energy limit where $V(x - x') = g\delta(x - x')$ with $g = 4\pi\hbar^2 a/m$, the zeroth order theory (i.e. ignoring quantum and thermal fluctuations described by $\delta\Psi(x)$) for the underlying bosonic system can be obtained e.g. by means of the Heisenberg equation of motion $i\hbar\frac{\partial\Psi}{\partial t} = [H, \Psi]$. Such a consideration leads to the famous Gross-Pitaevskii equation

$$i\hbar\frac{\partial\Psi(x, t)}{\partial t} = \left[-\frac{\hbar^2}{2m}\frac{\partial^2}{\partial t^2} + V_{ext}(x) + g|\Psi(x, t)|^2 \right] \Psi(x, t). \quad (2.23)$$

Here $\Psi(x, t)$ is normalized to the number of atoms, namely $N = \int dx |\Psi(x, t)|^2$ and the non-linearity introduced by the interatomic interactions is characterized by the s -wave scattering length a with $a > 0$ ($a < 0$) for repulsive (attractive) interatomic interactions respectively. It is worth mentioning that the Gross-Pitaevskii equation can also be obtained by following a variational procedure, namely by imposing the stationarity condition $\delta S = 0$ to the action $S = \int dt dx (i\hbar\Psi^* \frac{\partial}{\partial t} \Psi) + \int dt \mathcal{E}$ with $\mathcal{E} = \int dx \left[\frac{\hbar^2}{2m} |\Psi|^2 + V_{ext} |\Psi|^2 + \frac{g}{2} |\Psi|^4 \right]$ being the energy functional. While the Gross-Pitaevskii theory describes a perfect Bose-Einstein condensed state with all atoms occupying the same single-particle orbital, small deviations can be taken into account in the large particle limit $N \gg 1$ via a perturbative approach known as the Bogoliubov theory [1, 2, 283]. Indeed, decomposing the bosonic field operator as in Eq. (2.22), the Hamiltonian can be expanded up to quadratic order with respect to $\delta\Psi$ assuming that

this term is small when compared to the condensate orbital. The resulting Hamiltonian is then diagonalized using the so-called Bogoliubov transformation [see details in [282, 283]] leading to a non-interacting theory of quasi-particles with a pair-correlated ground state [284, 285]. This approach can provide valuable information for the breakdown of the mean-field approximation [286–294]. However, its first basic assumption of small quantum depletion cannot be systematically checked, while the requirement $N \gg 1$ makes this approach not suitable for studying few-body systems as well as the crossover from few- to many-body physics.

The Gross-Pitaevskii framework can naturally be generalized to describe a weakly interacting bosonic mixture consisting of species A and B each one being governed by its own wavefunction $\Psi_A(x, t)$ and $\Psi_B(x, t)$ respectively [1–3]. Considerations similar to the ones discussed in the single component case yield, for instance, the corresponding energy functional of the mixture of the two condensates. Then, following a variational principle leads to the coupled Gross-Pitaevskii equations

$$\begin{aligned} i\hbar \frac{\partial \Psi_A(x, t)}{\partial t} &= \left[-\frac{\hbar^2}{2m_A} \frac{\partial^2}{\partial t^2} + V_{ext}^A(x) + g_A |\Psi_A(x, t)|^2 + g_{AB} |\Psi_B(x, t)|^2 \right] \Psi_A(x, t) \\ i\hbar \frac{\partial \Psi_B(x, t)}{\partial t} &= \left[-\frac{\hbar^2}{2m_B} \frac{\partial^2}{\partial t^2} + V_{ext}^B(x) + g_B |\Psi_B(x, t)|^2 + g_{AB} |\Psi_A(x, t)|^2 \right] \Psi_B(x, t). \end{aligned} \quad (2.24)$$

Here m_A, m_B denote the mass of each component subjected to the external potentials $V_{ext}^A(x)$ and $V_{ext}^B(x)$ respectively. Furthermore, $g_A = 4\pi\hbar^2 a_A/m_A$, $g_B = 4\pi\hbar^2 a_B/m_B$ and $g_{AB} = 4\pi\hbar^2 a_{AB}/m_{AB}$ refer to the intra and interspecies coupling constants with a_A, a_B, a_{AB} the corresponding scattering lengths and $1/m_{AB} = 1/m_A + 1/m_B$.

Concluding, the mean-field Gross-Pitaevskii approximation has been proved very successful in describing phenomena in various areas of physics concerning weakly interacting bosonic gases and mixtures thereof. For instance, within the Gross-Pitaevskii framework the formation, interactions and dynamics of various types of excitations in a Bose-Einstein condensate such as dark [283, 295, 296], bright [3, 297, 298] and dark-bright solitons [299–302] or vortices (see Refs. [303–308]) have been described. However, alterations on the properties of these structures have already been reported when correlations are taken into account. Some of the most prominent examples of such alterations include the decay and splitting of quantum dark [286–294] and dark-bright solitons [309], interactions between bright solitons embedded in a many-body environment [334] and the smearing effect of a vortex core [310].

2.3 Many-Body Methodological Approach: ML-MCTDHX

The field of ultracold atoms constitutes nowadays a major challenge for theoretical approaches due to the enormous variety of relevant scenarios that can be considered involving a broad range of interaction strengths and particle numbers, the presence of more than a single species, various trapping potential landscapes and different dimensionalities. Recently, there are many highly sophisticated computational methods to treat the nonequilibrium quantum dynamics of many-body systems (see e.g. Ref. [311] and references therein). Here, we are not aiming at reviewing all these methods but rather mention only a few of them. Well

celebrated examples of such many-body methods include but are not limited to the exact diagonalization approach [246, 247, 250, 251, 312], the density matrix renormalization group methods (DMRG) [313–316], field-theoretical approaches [317–319], the Monte Carlo methods [320, 321] and variational methods [322].

In the following, we focus on a variational approach, namely the Multi-Layer Multi-Configuration Time-Dependent Hartree method for atomic mixtures (ML-MCTDHX) [97–100] employed in Refs. [[1-10]]. ML-MCTDHX is a wave packet dynamical approach tailored to treat finite size systems of bosons and atomic mixtures and it is therefore perfectly suited for our studies. Moreover, it naturally allows for studying the dynamics as well as the ground state of an ultracold atom system. This method originates from the quantum chemistry Multi-Configuration Time-Dependent Hartree method (MCTDH) [323, 324] designed for molecular dynamics. It has recently been applied successfully also to few-boson systems [325–328]. MCTDH has been initially designed for handling distinguishable particles, a fact that limits its efficiency in simulations of indistinguishable bosonic systems. New methods have been developed based on MCTDH to conquer this limitation by taking into account the permutation symmetry of the bosons on the very fundamental level of the working equations, and these new methods, e.g. MCTDHB [329–332], have been successfully applied to various bosonic systems [333–339]. To extend the research to macroscopic bosonic and fermionic mixtures of arbitrary number of species, ML-MCTDHX has been recently developed [97–100]. This method does not only takes into account the permutation symmetry of the bosons (fermions) in the working equations, but also utilizes the multilayer scheme for the system wave vector expansion, a fact that grants the method the flexibility of studying bosonic and fermionic mixtures of arbitrary species in all spatial dimensions and internal degrees of freedom, e.g. spin components [340, 341].

Next, we explicate the working principles of ML-MCTDHX by providing the wavefunction ansatz for an atomic mixture and elaborate on the significance of the involved reduced density matrices. Finally, we provide a short discussion on the convergence of the method. For a more detailed discussion on this method, however, we refer the interested reader to Refs. [97, 98].

2.3.1 Many-body Wavefunction ansatz for Binary Mixtures

ML-MCTDHX [97–100] is a flexible variational method for solving the time-dependent many-body Schrödinger equation of atomic mixtures. It relies on expanding the total many-body wavefunction with respect to a time-dependent and variationally optimized basis. The latter enables us to capture the important correlation effects using a computationally feasible basis size. In this way, we can obtain converged results with a reduced number of basis states compared to expansions relying on a time-independent basis. Finally, its multi-layer ansatz for the total wavefunction allows us to account for intra and interspecies correlations when simulating the dynamics of e.g. bipartite systems.

A binary ultracold atomic setup is a bipartite composite system residing in the Hilbert space $\mathcal{H}^{AB} = \mathcal{H}^A \otimes \mathcal{H}^B$, with \mathcal{H}^σ being the Hilbert space of the σ species. To take into account correlations between the different (inter-) or the same (intra-) species, M distinct species functions for each species are introduced obeying $M \leq \min(\dim(\mathcal{H}^A), \dim(\mathcal{H}^B))$. In this way, the many-body wavefunction Ψ_{MB} can be expressed according to the truncated

THEORETICAL FRAMEWORK

Schmidt decomposition [342, 343] of rank M

$$\Psi_{MB}(\mathbf{x}^A, \mathbf{x}^B; t) = \sum_{k=1}^M \sqrt{\lambda_k(t)} \Psi_k^A(\mathbf{x}^A; t) \Psi_k^B(\mathbf{x}^B; t). \quad (2.25)$$

The Schmidt weights $\lambda_k(t)$ in decreasing order are referred to as the natural species populations of the k -th species function Ψ_k^σ of the σ species. Note that $\{\Psi_k^\sigma\}$ forms an orthonormal N_σ -body wavefunction set in a subspace of \mathcal{H}^σ . To quantify the presence of interspecies correlations or entanglement we use the eigenvalues λ_k of the species reduced density matrix

$$\rho^{N_\sigma}(\mathbf{x}^\sigma, \mathbf{x}'^\sigma; t) = \int d^{N_{\sigma'}} x^{\sigma'} \Psi_{MB}^*(\mathbf{x}^\sigma, \mathbf{x}'^\sigma; t) \Psi_{MB}(\mathbf{x}'^\sigma, \mathbf{x}^\sigma; t) \quad (2.26)$$

where $\mathbf{x}^\sigma = (x_1^\sigma, \dots, x_{N_\sigma-1}^\sigma)$, and $\sigma \neq \sigma'$. In case that multiple eigenvalues of ρ^{N_σ} are macroscopically populated the system is referred to as species entangled or interspecies correlated, otherwise it is said to be non-entangled. Evidently [see also Eq. (2.25)], the system is entangled [342, 344, 345] when at least two distinct $\lambda_k(t)$'s are finite, which implies that the corresponding many-body state cannot be expressed as a direct product of two states stemming from \mathcal{H}^A and \mathcal{H}^B . Therefore the quantity $1 - \lambda_1(t)$ offers a measure for the degree of the system's entanglement. A particular configuration of A species $\Psi_k(\mathbf{x}^A; t)$ is always accompanied by a particular configuration of B species $\Psi_k(\mathbf{x}^B; t)$ and vice versa. Indeed, measuring one of the species states e.g. $\Psi_{k'}^A$ collapses the wavefunction of the other species to $\Psi_{k'}^B$ thus manifesting the presence of bipartite entanglement [342, 346, 347]. Summarizing, the above many-body wavefunction ansatz Ψ_{MB} constitutes an expansion in terms of different interspecies modes of entanglement, where $\sqrt{\lambda_k(t)} \Psi_k^A(\mathbf{x}^A; t) \Psi_k^B(\mathbf{x}^B; t)$ corresponds to the k -th entanglement mode.

To include interparticle correlations each of the species functions $\Psi_k^\sigma(\mathbf{x}^\sigma; t)$ is expanded using the permanents (determinants) of m^σ distinct time-dependent bosonic (fermionic) single-particle functions (SPFs) $\varphi_1, \dots, \varphi_{m^\sigma}$

$$\Psi_k^\sigma(\mathbf{x}^\sigma; t) = \sum_{\substack{n_1, \dots, n_{m^\sigma} \\ \sum n_i = N}} c_{k, (n_1, \dots, n_{m^\sigma})}(t) \sum_{i=1}^{N_\sigma!} \text{sign}(\mathcal{P}_i)^\zeta \mathcal{P}_i \left[\prod_{j=1}^{n_1} \varphi_1(x_j; t) \cdots \prod_{j=1}^{n_{m^\sigma}} \varphi_{m^\sigma}(x_j; t) \right]. \quad (2.27)$$

$\zeta = 0, 1$ refers to the case of bosons and fermions respectively and $\text{sign}(\mathcal{P}_i)$ denotes the sign of the corresponding permutation. \mathcal{P} is the permutation operator exchanging the particle configuration within the SPFs. $c_{k, (n_1, \dots, n_{m^\sigma})}(t)$ are the time-dependent expansion coefficients of a particular determinant (for fermions) or permanent (for bosons), and $n_i(t)$ denotes the occupation number of the SPF $\varphi_i(\mathbf{x}; t)$. Furthermore, the SPFs are expanded within a time-independent primitive basis $|k\rangle$ of dimension M_{pr} . For the physical systems presented in this thesis, within our implementation we use a sine discrete variable representation as a primitive basis for the SPFs. Following a variational principle, such as the Lagrangian [348], McLachlan [349] or the Dirac Frenkel [350, 351], for the generalized ansatz [see Eqs. (2.25), (2.27)]

yields the ML-MCTDHX equations of motion [97, 98]. For bosonic mixtures, these consist of a set of M^2 ordinary (linear) differential equations of motion for the coefficients $\lambda_k(t)$, coupled to a set of $M \left[\frac{(N_A+m^A-1)!}{N_A!(m^A-1)!} + \frac{(N_B+m^B-1)!}{N_B!(m^B-1)!} \right]$ non-linear integrodifferential equations for the species functions, and $m_A + m_B$ non-linear integrodifferential equations for the SPFs. We note here that e.g. for Bose-Fermi mixtures, the non-linear integro-differential equations for the species functions are $M \left[\frac{(N_B+m^B-1)!}{N_B!(m^B-1)!} + \frac{m^F!}{N_F!(m^F-N_F)!} \right]$, where the indices B, F denote the corresponding bosonic and fermionic component respectively. A detailed derivation of these equations of motion can be found in [97–100].

The corresponding one-body reduced density matrix of the σ species can be expanded [see Eq. (2.25)] as

$$\begin{aligned} \rho^{(1),\sigma}(x, x'; t) &= \int d^{N_\sigma-1} \bar{x}^\sigma d^{N_{\sigma'}} x^{\sigma'} \Psi_{MB}^*(x, \bar{\mathbf{x}}^\sigma, \mathbf{x}^{\sigma'}; t) \Psi_{MB}(x', \bar{\mathbf{x}}^\sigma, \mathbf{x}^{\sigma'}; t) \\ &= \sum_{k=1}^M \lambda_k(t) \rho_k^{(1),\sigma}(x, x'; t), \end{aligned} \quad (2.28)$$

where $\sigma \neq \sigma'$, $\bar{x}^\sigma = (x_1^\sigma, x_2^\sigma, \dots, x_{N_\sigma-1}^\sigma)$, and

$$\rho_i^{(1),\sigma}(x, x'; t) = \int d^{N_\sigma-1} \bar{x}^\sigma \Psi_i^{*\sigma}(x, \bar{x}^\sigma; t) \Psi_i^\sigma(x', \bar{x}^\sigma; t) \quad (2.29)$$

denotes the one-body density matrix of the i -th species function. We remark here that the bosonic (fermionic) subsystem is termed intraspecies correlated if more than one (N_σ) eigenvalue(s) of $\rho^{(1),\sigma}(x, x')$ are macroscopically occupied, otherwise it is fully coherent (Hartree-Fock correlated).

Moreover, the eigenfunctions of the σ -species one-body density matrix, $\rho^{(1),\sigma}(x, x')$, are the so-called σ -species natural orbitals, $\phi_i^\sigma(x; t)$. For our purposes, here, we consider them to be normalized to their corresponding eigenvalues

$$n_i^\sigma(t) = \int dx |\phi_i^\sigma(x; t)|^2. \quad (2.30)$$

$n_i^\sigma(t)$ are known as the natural populations and for bosons $1 - n_1^\sigma(t)$ [$1 - \sum_i n_i^\sigma(t)$ with $i = 1, \dots, N_\sigma$ for N_σ fermions] serves as a measure of the degree of the σ species inter-particle correlations [352–355]. Finally, it can be easily shown that in a bosonic [fermionic] system when $n_1^\sigma(t) = N^\sigma$, $n_{i \neq 1}^\sigma(t) = 0$ [$\sum_i n_i^\sigma(t) = N^\sigma$, $n_{i > N_\sigma}^\sigma(t) = 0$] the first [first N_σ] natural orbital(s) $\phi_1^\sigma(x^\sigma; t)$ [$\phi_i^\sigma(x^\sigma; t)$, $i = 1, \dots, N_\sigma$] reduces to the mean-field [Hartree Fock] wavefunction.

2.3.2 Limiting Cases and Convergence of the Many-Body Simulations

A major challenge for many-body simulations is to achieve a desirable degree of convergence. To judge the quality of the ML-MCTDHX ansatz one has to carefully examine the truncation order of the total system's Hilbert space which is indicated by the used numerical configuration space $C = (M; m_A; m_B; M_{pr})$. Here, $M = M_A = M_B$ refers to the number of

THEORETICAL FRAMEWORK

species functions and m_A, m_B denote the amount of SPFs for each of the species while M_{pr} is the size of the employed primitive basis. It is also worth mentioning at this point that ML-MCTDHX can operate in different approximation orders. As such when choosing $m_\sigma = M_{pr}$ and $M_\sigma = \frac{(N_\sigma + m_\sigma - 1)!}{N_\sigma!(m_\sigma - 1)!}$, our wavefunction ansatz is of full configuration-interaction type thus covering the complete system's Hilbert space. In the other extreme case of neglecting all correlations by setting $M = 1$ and $m_\sigma = 1$ for bosons ($m_\sigma = N_\sigma$ for fermions), the ML-MCTDHX equations of motion reduce to coupled Gross-Pitaevskii (Hartree-Fock) equations of motion, depending on the statistics of the components. In between the above-mentioned extreme cases, i.e. for not too strong inter and intraspecies correlations, one expects that it is sufficient to consider only a few species functions and orbitals, a fact that leads to a much higher efficient representation of the many-body state. Therefore employing ML-MCTDHX, m_σ and M need to be chosen according to the dominant correlations in the system under consideration such that the many-body expansion becomes efficient, i.e. it involves as few coefficients as possible, while capturing all relevant correlations.

To infer about the convergence of a many-body simulation, one has to systematically increase m_σ, M and M_{pr} , namely enlarge the subspace within which ML-MCTDHX finds the variationally optimal solution, and compare the results for the observables of interest, e.g. the variance of the density distribution or the total energy of the system. Additionally, in distinct situations, there are observables which can provide analytical estimations, e.g. the center of mass variance given that the center of mass motion is decoupled. Such observables, although limited, can also be employed to judge the convergence of the ML-MCTDHX simulations [97]. Let us emphasize here that increasing the number of basis functions of the ML-MCTDHX method implies that the corresponding many-body simulations become computationally costly and at some point prohibitive. An auxiliary indicator for the obtained numerical accuracy is provided by the population of the lowest occupied species functions and natural orbitals for each species which should be kept below 1%. Therefore, if there are species functions and natural orbitals which are barely populated, one can assume to have supplied a large enough basis for the calculation [97–100]. In this sense, a negligibly occupied lowest natural population $\lambda_M^\sigma(t) [n_{m_\sigma}^\sigma(t)]$ means that the corresponding species function NSF [natural orbital] essentially does not contribute to the numerically obtained $|\Psi_{MB}(t)\rangle$. Such a convergence investigation provides in practice a good indicator for the considered basis being sufficiently large, however it cannot be considered as a strict convergence criterion [356, 357]. In summary, the degree of convergence in general depends on the observable of interest, of course.

2.3.3 Wavefunction Ansatz for Scalar Bosons

We remark that in the case of structureless (scalar) bosons the above outlined ML-MCTDHX computational package reduces to the Multi-Configuration Time-Dependent Hartree method for bosons (MCTDHB) [329–332]. The latter has already been applied for a wide set of nonequilibrium bosonic settings, e.g. see [333–339]. Therefore in order to solve the many-body Schrödinger equation $(i\hbar\partial_t - H)|\Psi(t)\rangle = 0$ of the interacting bosons as an initial value problem $|\Psi(0)\rangle = |\Psi_0\rangle$, we rely on MCTDHB.

As already outlined for ML-MCTDHX, the MCTDHB allows for a variationally optimal

truncation of the Hilbert space as we employ a time-dependent moving basis where the system can be instantaneously optimally represented by time-dependent permanents. Consequently, the many-body wavefunction $|\Psi_{MB}(t)\rangle$ is expanded in terms of the bosonic number states $|n_1, n_2, \dots, n_M; t\rangle$, that built upon time-dependent single-particle functions (SPFs) $|\phi_i(t)\rangle$, $i = 1, 2, \dots, M$, and time-dependent weights $C_{\mathbf{n}}(t)$

$$|\Psi_{MB}(t)\rangle = \sum_{\mathbf{n}} C_{\mathbf{n}}(t) |n_1, n_2, \dots, n_M; t\rangle. \quad (2.31)$$

In the last expression M denotes the number of SPFs and the summation \mathbf{n} is over all the possible combinations n_i such that the total number of bosons N is conserved. Within our numerical implementation, the SPFs are expanded on a so-called primitive basis $\{|k\rangle\}$ of dimension M_{pr} . In all presented contributions [[1-10]] we use as a primitive basis for the SPFs a sine discrete variable representation which intrinsically introduces hard-wall boundaries at both ends of the potential.

To determine the time-dependent many-body wavefunction $|\Psi_{MB}(t)\rangle$ we need to calculate the equations of motion for the expansion coefficients $C_{\mathbf{n}}(t)$ and the SPFs $|\phi_i(t)\rangle$. To obtain these MCTDB equations of motion [329, 330, 358] we follow a variational principle such as the Dirac-Frenkel [350, 351]

$$\langle \delta\Psi_{MB} | i\partial_t - \hat{H} | \Psi_{MB} \rangle = 0. \quad (2.32)$$

The aforementioned equations consist of a set of M non-linear integrodifferential equations of motion for the SPFs which are coupled to the $\frac{(N+M-1)!}{N!(M-1)!}$ linear equations of motion for the coefficients $C_{\mathbf{n}}(t)$. Finally, let us note that in the limit in which $M = M_{pr}$ the above expansion is equivalent to a full configuration interaction approach. Moreover, in the case of $M = 1$ the many-body wavefunction is given by a single permanent $|n_1 = N; t\rangle$ and the method reduces to the time-dependent Gross-Pitaevskii mean-field approximation.

2.4 Many-Body Eigenspectrum of Few-Bosons in a Triple-Well

A major focus of the present cumulative thesis is to unravel the microscopic processes of few lattice trapped bosons when exposed to a particular quench protocol. For our investigations and in sharp contrast to the discrete Bose-Hubbard model we employ a continuum space Hamiltonian [see for instance Eq. (2.33) below] which enables us to resolve quench-induced higher-band excitations. For the sake of completeness let us note that the Bose-Hubbard model remains an adequate approximation for the theoretical description of the quench dynamics in deep lattices and for relatively small quench amplitudes when compared to the lattice band gap. To expose the underlying physical processes that can lead to the emergence of such many-body excited states [[1-6]] we mainly follow two pathways. First, we invoke the corresponding many-body eigenspectrum of the system. Such a calculation is, of course, computationally prohibitive for large systems however it is feasible for few-body ensembles trapped in a finite lattice. Furthermore, in order to comprehend the microscopic processes that participate in the quench-induced dynamics we employ the notion of non-interacting multiband Wannier number states.

Below we first explicate the formalism of the multiband expansion and categorize the number states of two representative few-body ensembles consisting respectively of three and four bosons in a triple well. Then we briefly discuss our numerical approach, within MCTDHB, to obtain the many-body eigenspectrum and finally we showcase the many-body eigenspectrum of three and four bosons confined in a triple well as a function of the interparticle repulsion.

2.4.1 The Multiband Wannier Number State Basis

The understanding of the spatial localization of states in lattice systems renders the use of multiband Wannier number states crucial as the latter enables the interpretation of both intraband and interband processes involving also information about the population of excited-bands. Generally, such a representation becomes valid when the lattice potential is deep enough so that the Wannier states between different wells possess a fairly small overlap in space for not too high energetic excitations. In this way, each localized Wannier function can be adequately assigned to a certain well and the respective band-mixing is fairly small.

As already mentioned in Section 2.3.3, MCTDHB exploits a wavefunction expansion in terms of time-dependent variationally optimized SPFs namely $\Psi_{MB}(t) = \sum_{\mathbf{n}} C_{\mathbf{n}} |n(t)\rangle$. However, for the analysis of the induced dynamics in lattice systems, it is more intuitive to rely on a time-independent basis instead of a time-dependent one. To this end, we project the numerically obtained MCTDHB wavefunction on a time-independent number state basis and thus make the connection with the multiband Wannier functions. This time-independent basis is constructed by single-particle Wannier states localized on each lattice site. We provide as many non-interacting Wannier states as required in order to ensure that during the dynamics the new basis is complete. To enable the above projection we have developed in the framework of ML-MCTDHB a fixed basis analysis package in terms of which we use a time-independent basis for the expansion of the system's wavefunction. Summarizing, in order to identify the modes participating in the dynamics we project the numerically obtained many-body correlated MCTDHB wavefunction on a time-independent number state basis consisting of single-particle Wannier states being localized on each lattice site. This expansion allows us to study inter- and intraband transitions [[1-8]].

The many-body bosonic wavefunction of a system with N bosons, m -wells and j localized single particle states [[1-6]] reads

$$|\Psi\rangle = \sum_{\{\mathbf{n}_i\}} C_{\{\mathbf{n}_i\}} |\mathbf{n}_1, \mathbf{n}_2, \dots, \mathbf{n}_m\rangle, \quad (2.33)$$

where $|\mathbf{n}_1, \mathbf{n}_2, \dots, \mathbf{n}_m\rangle$ is the multiband Wannier number state, the element $\mathbf{n}_i = n_i^{(1)} \otimes n_i^{(2)} \otimes \dots \otimes n_i^{(j)}$ and the occupation of the Wannier orbital $n_i^{(k)}$ refers to the number of bosons which reside at the i -th well and k -th band. Due to the fixed number of bosons N the total number of configurations is constrained by $\sum_{i=1}^m \sum_{\lambda=1}^{j-1} n_i^{(\lambda)} = N$. For instance, in a setup with $N = 4$ bosons confined in a triple well ($m = 3$) which includes $j = 3$ single-particle states, the state $|1^{(0)}, 1^{(1)} \otimes 1^{(1)}, 1^{(0)}\rangle$ indicates that in the left and right wells one boson occupies the Wannier orbital of the energetically lowest-band while the remaining two bosons are in the middle

well, residing in the Wannier orbital of the first excited-band. For simplicity, in the following, we shall omit the zero index when referring to the energetically lowest (i.e. zeroth) band.

Below, we shall calculate the eigenspectrum with respect to the interparticle repulsion for the characteristic cases of three and four bosons in a triple well. To analyze the corresponding eigenspectra it is instructive to energetically categorize the involved number states. In this way, for the three particle case one can realize three different energetic classes of number states with respect to the interparticle repulsion. Namely, the triples $\{|3, 0, 0\rangle + \circ\}$ (T), the single pairs $\{|2, 1, 0\rangle + \circ\}$ (SP) and the singles $\{|1, 1, 1\rangle + \circ\}$ (S), where \circ stands for all corresponding permutations. For later convenience we further classify the excited-band energetic classes into single-particle excitation (SE) and higher excited (HE) classes. The former [latter] class involves states of single [double] occupancy in every site with one excitation to the first excited-band e.g. $\{|1, 1^{(1)}, 1\rangle + \circ\}$ [$\{|1 \otimes 1^{(1)}, 1, 0\rangle + \circ\}$ and $\{|1^{(1)}, 2, 0\rangle + \circ\}$]. Accordingly, for the case of four particles in a triple well and regarding the zeroth band states four distinct energetic classes of number states can be realized. Namely, the single pairs (SP) $\{|2, 1, 1\rangle + \circ\}$, double pairs (DP) $\{|2, 0, 2\rangle + \circ\}$, triples (T) $\{|3, 1, 0\rangle + \circ\}$ and quadruples (Q) $\{|4, 0, 0\rangle + \circ\}$.

2.4.2 Improved Relaxation Scheme

To obtain the n -th many-body eigenstate we rely on the so-called improved relaxation scheme implemented within MCTDHB. This numerical scheme can be summarized according to the following procedure

- Initialize the system with an ansatz set of SPFs $\{|\phi_i^{(0)}\rangle\}$.
- Diagonalize the Hamiltonian within a basis spanned by the SPFs.
- Set the n -th obtained eigenvector as the $C_{\mathbf{n}}(0)$ -vector.
- Propagate the SPFs in imaginary time within a finite time interval $d\tau$.
- Update the SPFs to $\{|\phi_i^{(1)}\rangle\}$.
- Repeat the above-mentioned steps until the energy of the state converges within the prescribed accuracy.

To explore the dynamics, we propagate the many-body wavefunction (obtained via the improved relaxation scheme) by utilizing the appropriate Hamiltonian within the MCTDHB equations of motion.

2.4.3 Eigenspectrum of Three and Four Bosons

The eigenspectrum of a lattice system provides invaluable information about the participating states for a given set of Hamiltonian parameters. In particular, inspecting the system's eigenspectrum several unique properties inherent to the system under consideration can be

THEORETICAL FRAMEWORK

revealed, such as the bandwidth, the band gap and possible avoided or exact crossings between different many-body eigenstates [362]. Such a knowledge equips us with information that is necessary in order to understand and analyze the microscopic mechanisms being responsible e.g. for the corresponding quantum quench dynamics [[4,6]]. Next, let us discuss the eigenspectrum of three and four bosons trapped in a relatively deep triple well system for varying interparticle repulsion.

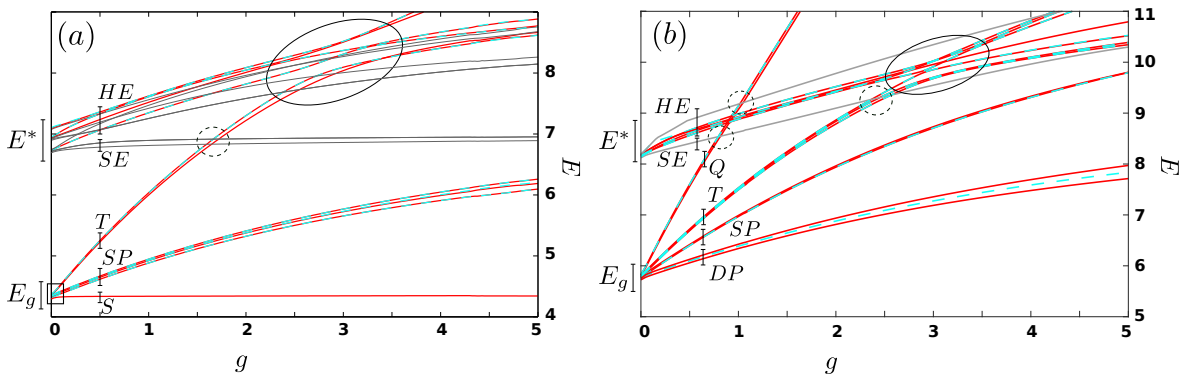


Figure 2.4: (a) Dependence of the lowest 25 eigenenergies E_i on the interparticle repulsion g for three bosons confined in a triple well with a potential depth $V_0 = 10$. The solid boxes indicate the superfluid to Mott-insulator transition. (b) The same as in (a) but for the case of four bosons trapped in a triple well. In both panels solid (dashed) lines indicate the parity even (odd) eigenenergies, while the existing wide (narrow) avoided-crossings possessing a width $\delta E > 0.01$ ($\delta E < 0.01$) are marked by solid (dashed) circles. The eigenenergies of the eigenstates that do not contribute to any wide avoided-crossing are shown in grey. Finally, the energy regions E_g , E^* and the subbands possessing zero, single and more than one excited states are indicated by the respective bars.

We first focus on the case of three bosons confined in a relatively deep triple well, namely $V_0 = 10.0 E_R$. The corresponding eigenenergy spectrum of the first 25 lowest-lying eigenenergies for increasing interparticle repulsion is depicted in Fig. 2.4 (a). As it can be seen, close to the non-interacting limit, $g \simeq 0$, the many-body eigenstates are energetically categorized according to their corresponding particle configuration in terms of single-particle bands. Indeed, the eigenstates of the system are predominantly bunched onto two energy regions denoted by E_g and E^* in Fig. 2.4 (a) respectively. Namely, the eigenstates lying within E_g do not possess any higher-band excitations, while those bunched onto E^* refer to states with one single-particle excitation to the first excited-band. The width of the aforementioned energy regions defines the so-called bandwidth, and depends on the tunneling coupling between the different sites. Note that the term tunneling coupling refers to the corresponding inverse tunneling rate [19, 20, 93, 94]. Furthermore, the distance between E^* and E_g is characterized by the band gap between the ground and the first excited-band of the non-interacting system. Concerning the decomposition of each eigenstate in terms of spatially localized Wannier number states [see Eq. (2.33)] it turns out that it is an admixture of all the energetic classes S , SP and T . The latter is a consequence, of course, of the spatial delocalization of the bosons

within the triple well, and therefore manifests the few-body analogue of the superfluid phase for small interaction strengths.

For increasing repulsion the energy expectation value of the number states belonging to the SP and T classes increases. As a consequence, the same holds for the eigenenergies of the eigenstates to which the aforementioned number states are contributing. In particular, for $0 < g \lesssim 0.5$ a multitude of avoided-crossings is observed, see Fig. 2.4 (a), which essentially indicate the tunneling coupling between the S , SP and T number states of the same parity. This interaction regime corresponds in our few-boson system to the region where the transition from the superfluid to the Mott-insulator phase occurs. Turning to $g \geq 0.5$ the eigenenergies of the lowest-band become well separated into three subbands according to the energetic class of their dominant number state [see Fig. 2.4 (a)]. Here, the ground state of the system is dominated by the S class manifesting in this way the few-body analogue of the Mott-insulator phase. Moreover, the SP and T class eigenstates are also bunched together forming the SP and T subbands, while the eigenstates of the T subband (being the most sensitive to interparticle repulsion) experience wide (see solid circles) and narrow (see dashed circles) avoided crossings with the eigenstates possessing a higher-band excitation. Let us note here in advance, that the wide avoided-crossings are related to the onset of the cradle mode, described in [[1,2]], and are a consequence of the interaction induced decay of an SP or T state caused by the scattering of one of the bosons that reside in the same well to the first excited state of an adjacent site. This process generates the so-called cradle mode which represents a dipole-like intrawell oscillation in the outer wells of the finite lattice.

A similar behavior to the above is also observed when inspecting the many-body eigen-spectrum of four bosons confined in a relatively deep triple well, $V_0 = 10 E_R$, for increasing interaction strength [see Fig. 2.4 (b)]. However, here the number of the involved eigenstates is higher since there exist more possible particle configurations when compared to the three boson case. Most importantly, a transition from a superfluid to a Mott insulating state is prohibited due to the incommensurate filling factor. Fig. 2.4 (b) presents the eigenenergy spectrum of the first 20 lowest-lying eigenenergies for increasing g . For very weak interactions the many-body eigenstates are energetically categorized according to their corresponding particle configuration in terms of single-particle bands. In particular, they majorly reside within two energetically different regions denoted by E_g and E^* . The eigenstates within E_g do not possess any higher-band excitations, while those lying in E^* correspond to states with one single-particle excitation to the first excited-band. Remarkably enough, we observe the occurrence of an exact crossing between the Q class eigenstate with the eigenstates possessing a single higher-band excitation at $g \approx 0.8$. Moreover the T class exhibits exact (avoided) crossings with states referring to a higher-band excitation at $g \approx 2.4$ ($g \approx 3$ and $g \approx 4.3$). Let us finally mention in advance that within [[1,2]] the observed interaction quench dynamics is mainly a consequence of these exact and avoided-crossings between the many-body eigenstates at distinct interparticle repulsions.

2.5 Single-Shot Simulations in Binary Bosonic Mixtures and Scalar Bosons

Single-shot experimental measurements of ultracold quantum quantum gases probe the spatial configuration of the atoms which is dictated by sampling the many-body probability distribution. In particular, an experimental image refers to a convolution of the spatial particle configuration with a point spread function. This point spread function describes the response of the imaging system to a point-like absorber (atom). Such single shots images can be successfully simulated when having the many-body wavefunction at hand as is the case of operating within ML-MCTDHX.

Quantum mechanically the positions (x_1, \dots, x_N) of N particles measured in an experiment are distributed according to the N -particle probability density $P(x_1, \dots, x_N) = |\Psi_{MB}(x_1, \dots, x_N)|^2$, where $\Psi_{MB}(x_1, \dots, x_N)$ refers to the many-body wavefunction of the system. In general, when the probability $\Psi_{MB}(x_1, \dots, x_N)$ is known, single shots can be simulated by drawing the positions of all particles from $P(x_1, \dots, x_N)$, resulting in a vector of positions (x'_1, \dots, x'_N) that we refer to in the following as a single shot. The main difficulty to perform the above procedure stems from the fact that the functional form of the many-body wavefunction is generally not known in many-body dynamics. To sample $P(x_1, \dots, x_N)$ one needs to realize that

$$P(x_1, \dots, x_N) = P(x_1)P(x_2|x_1) \dots P(x_N|x_{N-1}, \dots, x_1). \quad (2.34)$$

$P(x_2|x_1)$, for instance, denotes the conditional probability to detect an atom at position x_2 if another one is located at x_1 . The key point in this procedure is to draw the positions of all N particles. In this way, we first draw x'_1 from $P(x_1)$, then x'_2 from $P(x_2|x'_1)$, next x'_3 from $P(x_3|x'_2, x'_1)$ and so on. Following the above-mentioned procedure we obtain a histogram of a single-shot (x'_1, \dots, x'_N) , which is analogous to an experimental image. Here we provide an algorithm to simulate single shots for a binary bosonic mixture from the $(N_A + N_B)$ -body ML-MCTDHX wavefunction [see also Eq. (2.25)] obtained by numerically solving the time-dependent many-body Schrödinger equation $(i\hbar\partial_t - H) |\Psi(t)\rangle = 0$. Moreover we show how this single-shot algorithm can also be used to perform such simulations in a scalar bosonic ensemble using the corresponding N -body wavefunction ansatz [see Eq. (2.32)].

2.5.1 Single-Shot Procedure

Referring to a two-species bosonic mixture our aim is to mimic the corresponding experimental procedure and simulate single shot images for both species A [namely $\mathcal{A}^A(\tilde{x}; t_{im})$] and species B [i.e. $\mathcal{A}^B(\tilde{x}'|\mathcal{A}^A(\tilde{x}; t_{im}))$] at each instant of the many-body evolution when we consecutively image at time $t = t_{im}$ first the A and then the B species. To achieve this we rely on the many-body wavefunction being accessible within the ML-MCTDHX framework. It is important to remark that for the modelling of the point spread function, being related to the experimental resolution, we use a Gaussian possessing a width w which is commonly much smaller than the typical length scale (e.g. in a harmonic trap this is the harmonic oscillator length) of the system.

As already mentioned, our single-shot simulation procedure relies on a sampling of the many-body probability distribution [310, 359–361] which is accessible via ML-MCTDHX. For a two-species bosonic ensemble and when inter and intraspecies correlations are taken into account, the degree of entanglement between the distinct species is crucial for the image ordering. Indeed, the role of entanglement between the species is manifested by the Schmidt decomposition [see Eq. (2.25)] and in particular is incorporated in the Schmidt coefficients λ_k 's. Let us first analyze the situation where first the species A is imaged and then the species B .

In order to image first the A and then the B species we consecutively annihilate all the N_A particles. Referring to a certain time instant of the imaging, t_{im} , a random position is drawn satisfying the constraint $\rho_{N_A}^{(1)}(x'_1) > l_1$ where l_1 is a random number within the interval $[0, \max\{\rho_{N_A}^{(1)}(x; t_{im})\}]$. Next, we project the $(N_A + N_B)$ -body wavefunction to the $(N_A - 1 + N_B)$ -body one, by using the operator $\frac{1}{\mathcal{N}}(\hat{\Psi}_A(x'_1) \otimes \hat{\mathbb{1}}_B)$. $\hat{\Psi}_A(x'_1)$ is the bosonic field operator that annihilates an A species boson at position x'_1 and \mathcal{N} is a normalization constant. The above-mentioned process directly affects the λ_k coefficients (entanglement weights) and thus despite the fact that the B species has not been imaged yet, both $\rho_{N_A-1}^{(1)}(t_{im})$ and $\rho_{N_B}^{(1)}(t_{im})$ are altered. The latter can be easily shown by carefully inspecting the Schmidt decomposition. Indeed after the first measurement the form of the many-body wavefunction reads

$$|\tilde{\Psi}_{MB}^{N_A-1, N_B}(t_{im})\rangle = \sum_i \sqrt{\tilde{\lambda}_{i, N_A-1}(t_{im})} |\tilde{\Psi}_{i, N_A-1}^A(t_{im})\rangle |\Psi_i^B(t_{im})\rangle. \quad (2.35)$$

$|\tilde{\Psi}_{i, N_A-1}^A\rangle = \frac{1}{N_i} \hat{\Psi}_A(x'_1) |\Psi_i^A\rangle$ refers to the $(N_A - 1)$ species wavefunction. The constant $N_i = \sqrt{\langle \Psi_i^A | \hat{\Psi}_A^\dagger(x'_1) \hat{\Psi}_A(x'_1) | \Psi_i^A \rangle}$ denotes the corresponding normalization factor and $\tilde{\lambda}_{i, N_A-1} = \lambda_i N_i / \sum_i \lambda_i N_i^2$ are the Schmidt coefficients referring to the $(N_A - 1 + N_B)$ -body wavefunction. To obtain a single-shot image we repeat the above-mentioned procedure for $N_A - 1$ steps. The resulting distribution of positions $(x'_1, x'_2, \dots, x'_{N_A-1})$ is convoluted with a point spread function and leads to a single-shot $\mathcal{A}^A(\tilde{x}) = \sum_{i=1}^{N_A} e^{-\frac{(\tilde{x}-x'_i)^2}{2w^2}}$ for the A species. Here, \tilde{x} refers to the spatial coordinates within the image and w is the width of the point spread function. It is also worth mentioning that before annihilating the last of the N_A particles, the many-body wavefunction possesses the form

$$|\tilde{\Psi}_{MB}^{1, N_B}(t_{im})\rangle = \sum_i \sqrt{\tilde{\lambda}_{i, 1}(t_{im})} |\Phi_{i, 1}^A(t_{im})\rangle |\Psi_i^B(t_{im})\rangle, \quad (2.36)$$

where $|\Phi_{i, 1}^A(t_{im})\rangle$ refers to a single-particle wavefunction characterizing the A species. It can be easily shown that annihilating the last A species particle the many-body wavefunction becomes

$$|\tilde{\Psi}_{MB}^{0, N_B}(t_{im})\rangle = |0\rangle \otimes \sum_i \frac{\sqrt{\tilde{\lambda}_{i, 1}(t_{im})} \langle x | \Phi_{i, 1}^A \rangle}{\sum_j \sqrt{\tilde{\lambda}_{j, 1}(t_{im})} |\langle x | \Phi_{j, 1}^A \rangle|^2} |\Psi_i^B(t_{im})\rangle. \quad (2.37)$$

THEORETICAL FRAMEWORK

Here $\langle x|\Phi_{j,1}^A\rangle$ is the single-particle orbital of the j -th mode. Evidently, performing this last step the entanglement between the species is destroyed while the wavefunction of the B species $|\Psi_{MB}^{N_B}(t_{im})\rangle$ corresponds to the second term of the cross product on the right hand side of Eq. (2.37). Therefore, $|\Psi_{MB}^{N_B}(t_{im})\rangle$ obtained after the annihilation of all N_A atoms is a non-entangled N_B -particle many-body wavefunction and its corresponding single-shot procedure reduces to the single species case [310, 359].

The latter process is well-established and benchmarked in several works that consider the correlated nonequilibrium quantum dynamics of ultracold scalar bosonic ensembles [310, 359–361]. Let us therefore only briefly outline the underlying process below. Focussing on a specific time instant of the imaging, $t = t_{im}$, we first calculate $\rho_{N_B}^{(1)}(x; t_{im})$ from the many-body wavefunction $|\Psi_{N_B}\rangle \equiv |\Psi(t_{im})\rangle$. Next we draw a random position x_1'' which obeys $\rho_{N_B}^{(1)}(x_1''; t_{im}) > l_2$ where l_2 is a random number lying within the interval $[0, \rho_{N_B}^{(1)}(x; t_{im})]$. Then, one particle located at a position x_1'' is annihilated and $\rho_{N_B-1}^{(1)}(x; t_{im})$ is calculated from $|\Psi_{N_B-1}\rangle$. Subsequently, a new random position x_2'' is drawn from $\rho_{N_B-1}^{(1)}(x; t_{im})$. In total, this procedure is repeated for $N_B - 1$ steps and finally we obtain the distribution of positions $(x_1'', x_2'', \dots, x_{N_B-1}'')$ which is then convoluted with a point spread function. The above results in a single-shot $\mathcal{A}^B(\tilde{x}'|\mathcal{A}^A(\tilde{x}))$, where \tilde{x}' denote the spatial coordinates within the image. We note once more that for the employed point spread function a Gaussian of width w is used.

Let us emphasize here that the same overall procedure has to be followed in order first to image the B and then the A species. The latter imaging process results in the corresponding single-shots $\mathcal{A}^B(\tilde{x})$ and $\mathcal{A}^A(\tilde{x}'|\mathcal{A}^B(\tilde{x}))$.

In the next section and in particular within the outline of our first scientific contribution [[1]] we discuss an application of the single-shots simulations during the nonequilibrium dynamics of four scalar bosons confined in a triple well. Moreover, within [[9]] we provide paradigmatic single-shot simulations for the case of a harmonically trapped Bose-Bose mixture subjected to an interspecies interaction quench.

Chapter 3

Outline of the Scientific Contributions

In the present chapter, we summarize our scientific contributions published in Refs. [[1-10]]. The basic underlying concept of all contributions is the characterization of the nonequilibrium dynamics of few-bosons confined in finite optical lattices. The nonequilibrium situation is induced either by performing a quench [[1-6]] on a parameter of the Hamiltonian or by considering a time-periodic driving of the optical lattice [[7-8]]. Additionally we investigate the correlation properties in the quench-induced dynamics of a harmonically confined Bose-Bose mixture [[9]] and the many-body expansion dynamics of a lattice trapped Bose-Fermi mixture [[10]]. In all contributions we are aiming to microscopically characterize the quench-induced processes, reveal their correlated nature and obtain a coupling between the distinct triggered modes, thus providing a way to control the resulting nonequilibrium dynamics.

3.1 Hamiltonian of Few-Bosons in a Lattice

The many-body Hamiltonian of N identical bosons each of mass M confined in an one-dimensional m -well optical lattice reads

$$H = \sum_{i=1}^N \left[-\frac{\hbar^2}{2M} \frac{\partial^2}{\partial x_i^2} + V_{ext}(x_i) \right] + \sum_{i<j} V_I(x_i - x_j). \quad (3.1)$$

The lattice potential $V_{ext} = V_0 \sin^2(kx)$ is characterized by its depth V_0 and periodicity l . In this respect $k = 2\pi/l$ denotes the wave vector of the counterpropagating lasers forming the optical lattice. Within the ultracold regime, the short-range interaction potential $V_I(x_i - x_j) = g\delta(x_i - x_j)$ between particles located at positions x_i , can be adequately described by s -wave scattering. The effective one-dimensional coupling strength [363] $g = \frac{2\hbar^2 a^s}{Ma_{\perp}^2} (1 - |\zeta(1/2)| a^s / \sqrt{2} a_{\perp})^{-1}$, where ζ denotes the Riemann zeta function at $x = 1/2$.

The transversal length scale is given by $a_{\perp} = \sqrt{\hbar/M\omega_{\perp}}$, where ω_{\perp} stands for the frequency of the transversal confinement, while a^s denotes the free space s -wave scattering length. The interaction is tunable by a^s with the aid of Feshbach resonances [5,6] or by means of ω_{\perp} [7,363].

OUTLINE OF THE SCIENTIFIC CONTRIBUTIONS

In the following we consider only the dynamics of repulsively interacting bosons, implying that $g > 0$. To restrict the infinitely extended trapping potential to a finite one with m wells and length L , we impose hard-wall boundary conditions at the appropriate positions, $x_{\pm m} = \pm \frac{m\pi}{2k}$.

Below, the many-body Hamiltonian is rescaled in units of the recoil energy $E_R = \frac{\hbar^2 k^2}{2M}$. Then the corresponding length, time, frequency and interaction strength scales are given in units of k^{-1} , $\omega_R^{-1} = \hbar E_R^{-1}$, ω_R and $2E_R k^{-1}$ respectively. For convenience we shall also set $\hbar = M = k = 1$ so that all quantities below are given in dimensionless units.

3.2 Basic Ground State Properties

Before exploring the dynamics, let us shortly comment on the ground state properties of a lattice system for different filling factors $\nu = N/m$, where N denotes the particle number and m the number of the wells. In the commensurate case, i.e. $\nu = 1, 2, \dots$, the ground state for increasing interparticle interaction is known to exhibit the superfluid to Mott-insulator phase transition [19, 20] which has been addressed extensively in the past years, see also Fig. 3.1 (a). However, for a system characterized by an incommensurate filling, $\nu \neq 1, 2, \dots$, the main feature is the existence of a delocalized fraction of particles which forbids the occurrence of a Mott state [see Fig. 3.1 (b)]. Here, one can distinguish two physical situations. The case $\nu > 1$ where on-site interaction effects prevail and the case $\nu < 1$ in which the main feature is the redistribution of the particles over the sites as the interaction strength increases. We note that such a delocalized phase has been explained in terms of the particle hole states using a strong coupling expansion [93, 94].

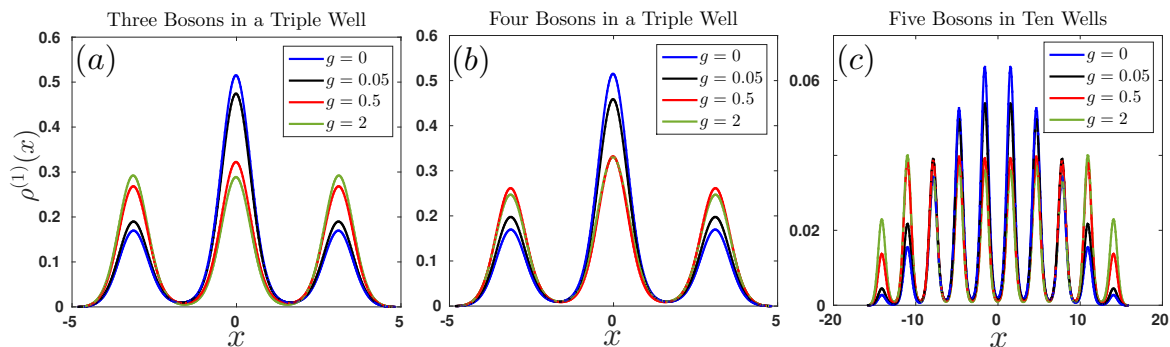


Figure 3.1: One-body density for the ground state of (a) three and (b) four bosons confined in a triple well and (c) five bosons in a ten well lattice potential. Different lines refer to distinct interparticle repulsions (see legends).

Let us first briefly summarize the ground state properties for increasing interactions for a setup consisting of four atoms in three wells, i.e. one extra particle on a Mott background. For a more elaborated discussion on the eigenspectrum of this system see Section 2.4.3. The main characteristic of the initial state is the competition between delocalization and on-site interaction effects. The single-particle density for the non-interacting case $g = 0$ is largest in

the middle site and decreases for the outer ones due to the hard-wall boundary conditions that render the middle and outer sites non-equivalent [Fig. 3.1 (b)]. Entering the weak interaction regime we observe a tendency towards a uniform population due to the repulsion of the bosons. For further increasing repulsion a trend towards the repopulation of the central well occurs. For strong interparticle repulsion, the state can be interpreted as a fraction $N \bmod m$ of extra delocalized particles being on a commensurate background of localized particles. On the one-body density level the on-site populations are quite similar, which is attributed to the localized background, while their slight observed discrepancy is caused by the non-uniform distribution of the extra particle in the first excited-band, preventing the formation of a perfect insulator phase even for strong repulsion, see Fig. 3.1 (b).

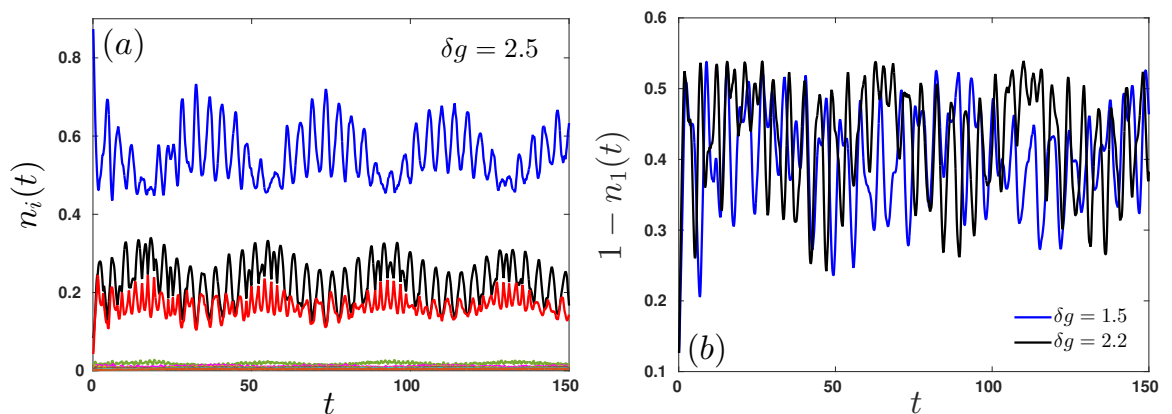


Figure 3.2: (a) Evolution of the populations of the first nine natural orbitals for four bosons confined in a triple well after an interaction quench with amplitude $\delta g = 2.5$. (b) Deviation from unity of the population of the first natural orbital following interaction quenches of different amplitudes δg (see legend). In all cases the system is initialized in the ground state of four weakly interacting, $g = 0.05$, bosons in a triple well. $\delta g = g_f - g_{in}$ with g_f , g_{in} referring to the post and pre quench interaction strengths respectively.

Turning to the ground state for systems with filling factor $\nu < 1$, the most important aspect is the spatial redistribution of the atoms as the interaction strength increases. The non-interacting ground state ($g = 0$) is the product of the single-particle eigenstates spreading across the entire lattice, while due to the hard-wall boundary conditions the two central wells of the potential are slightly more populated. For increasing repulsion within the weak interaction regime the atoms are pushed to the outer sites which gain and lose population in the course of increasing g , while the particle number fluctuations are more pronounced for the wells with a lower population [364]. Summarizing, for $\nu < 1$ the one-body density remains asymmetric even for strong interactions due to the low population, while the delocalized fraction of particles permits the presence of long-range one particle correlations even in the strongly repulsive regime [364]. A paradigmatic example of the ground state properties on the one-body density level for increasing repulsion in such a system is shown in Fig. 3.1 (c) for five particles confined in ten wells.

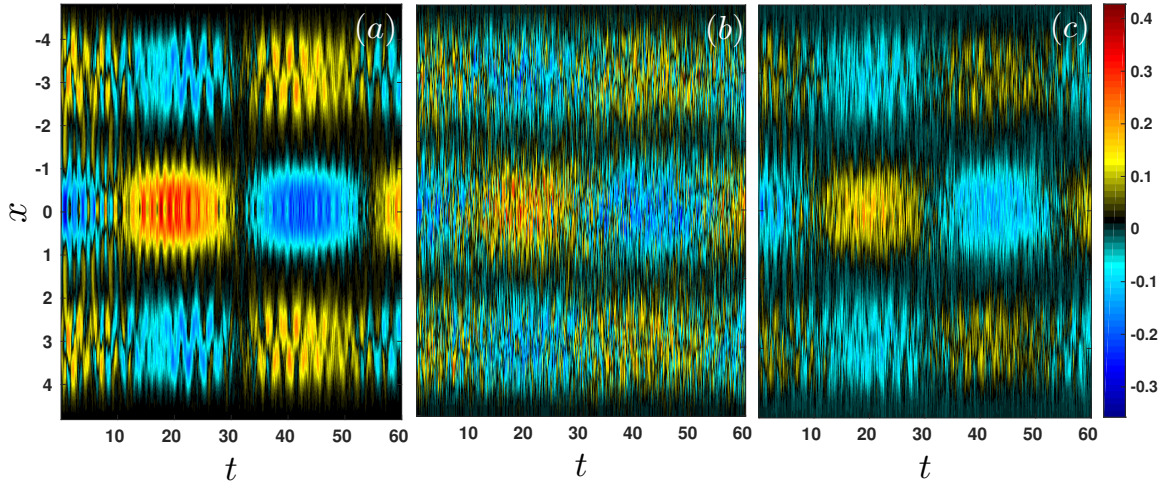


Figure 3.3: (a) Evolution of the one-body density temporal fluctuations $\delta\rho^{(1)}(x, t)$ following an interaction quench with amplitude $\delta g = 2$. (b), (c) Temporal fluctuations of the averaged images $\delta\bar{A}(x, t) = \bar{A}(x, t) - (1/T) \int_0^T dt \bar{A}(x, t)$ over $N_{shots} = 100$ and $N_{shots} = 500$ after an interaction quench with amplitude $\delta g = 2$ within the many-body approach. In all cases the system consists of four bosons confined in a triple well and it is initialized in its ground state with $g = 0.05$.

3.3 Quench Dynamics in Scalar Few-Boson Ensembles

3.3.1 Quench Dynamics from Weak-to-Strong Interactions [[1]]

In [[1]] we investigate the correlated nonequilibrium dynamics of few-bosons confined in one-dimensional finite lattices subjected to a sudden change in the interaction strength. Focusing on highly non-perturbative situations by considering weak-to-strong interaction quenches with respect to the initial state, we drive the system to a regime where the interparticle interactions dominate in comparison to the kinetic energy. By considering strong quench amplitudes and examining representative few-body setups for incommensurate filling factors, our treatment lies beyond the validity of the lowest-band Bose-Hubbard model [19, 20] which, in this regime of interactions, provides at most a qualitative description of the system's dynamics. To support our arguments we show in Fig. 3.2 the contribution of the consecutive populated natural orbitals [see also Eq. (3.2)] during the nonequilibrium dynamics of four bosons in a triple well after an interaction quench. Similar investigations, although restricted to the weak interaction regime, have been performed within the realm of the Bose-Hubbard model showcasing the dynamics of one-body inter and intra-site correlations [365–368]. Contrary to those studies, here, we are mainly interested on the microscopic characterization of inter and intrawell quench-induced modes as well as on their controllability.

Starting from the weakly interacting ground state of the system we perform a quench towards the strongly interacting regime. To avoid suppression of tunneling due to Mott-

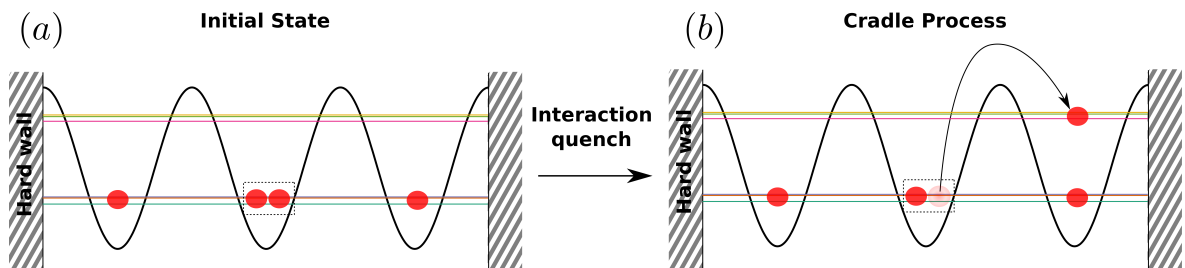


Figure 3.4: Visualization of the cradle process generated by the over-barrier transport. The system is (a) prepared in a weakly repulsively interacting superfluid ground state which is (b) then subjected to a sudden interaction quench. A boson initiated in the central well can overcome the lattice barrier and move to its neighboring well, resulting in a cradle motion due to the interaction quench.

insulator phases arising for strong interactions we study setups of incommensurate filling factors. Following an interaction quench we demonstrate the emergence of excited-band modes linked to certain interband processes, namely the breathing and the cradle modes, as well as the rise of the density-wave tunneling mainly corresponding to a lowest-band intraband phenomenon. To identify the dominant microscopic mechanisms during the dynamics in terms of a band structure we employ the concept of a multi-band Wannier number state basis. To inspect the overall response of our system on the one-body level we resort to the temporal fluctuations of the single-particle density, namely $\delta\rho^{(1)}(x,t) = \rho^{(1)}(x,t) - \langle\rho^{(1)}(x)\rangle_T$ with $\langle\rho^{(1)}(x)\rangle_T = \int_0^T dt \rho^{(1)}(x,t)/T$ being the time-averaged single-particle density over evolution time T , see also Fig. 3.3 (a). A density-wave spatial pattern occurs which evolves in time and reflects the tunneling dynamics after the quench namely the mode that transfers population among the middle and the outer wells. More explicitly, this mode refers to an effective breathing of the “global wavepacket” that reflects the instantaneous density distribution of the trap. Intuitively, under an interaction quench the bosons tend to repel each other and the cloud expands and contracts, mimicking this way the breathing dynamics of the bosons as known in the harmonic trap. Recently [369] this mode has also been examined in the framework of the Bose-Hubbard model for a quench on the lattice frequency. The findings of the latter work suggest that such a “global” breathing mode also exists for many-body systems in optical lattices where instead of our hard-wall boundaries a weak harmonic confinement imposed to the lattice geometry renders the sites of the optical lattice non-equivalent. To investigate in more detail the tunneling dynamics we employ the fidelity spectrum [370, 371] for varying interaction strength. In this spectrum we identify three different tunneling pathways which refer to single and atom pair tunneling. We remark that atom-pair tunneling has already been observed for few-atoms confined in a driven double-well [54, 134].

Additionally in the intrawell dynamics two distinct excited modes occur. Namely the middle well exhibits a breathing mode, due to the lattice symmetry, which can be identified as an expansion and contraction of the bosonic cloud. For recent investigations on the properties of the breathing mode as well as its dependence on the particle number and the interaction

strength we refer the reader to Refs. [372–375]. The second mode we observe, generated in the outer wells, is the so-called cradle mode, manifested as a “dipole-like” oscillation of the localized wavepacket. The generation of this mode is accompanied by an initial over-barrier transport of the particles from the central well to the outer ones due to the release of energy into the system and the consequent collisions with the respective atoms in the outer sites, rerepresented schematically in Fig. 3.4. During the dynamical process, regions of density dips (or dark cradles) in the outer sites are accompanied by enhanced breathing dynamics in the middle site. Each of the above modes possesses different characteristic frequencies. For a qualitative description of these modes we rely on the intrawell dynamics of $\delta\rho(x, t)$ analyzing in particular the Fourier spectra of representative intrawell observables. More explicitly, the intrawell asymmetry within each of the outer wells and the variation of the center of mass coordinate for the cases of the cradle and the breathing mode, respectively. In this manner, we have found representative cradle and breathing mode states which refer to a superposition of the first two and three single-particle bands respectively. Most importantly, we show that one can tune the frequency of the energetically highest tunneling branch in resonance with the frequency of the cradle mode by varying the quench amplitude. In turn, this resonance is associated with an avoided-crossing in the frequency spectrum of these modes, resulting in their enhancement so that the system features a dominant beating. This enables us to control the interwell dynamics by triggering the intrawell dynamics via the quench amplitude in optical lattices. To complement our study an effective Hamiltonian that describes the observed spectral properties and the resonant dynamical behaviour is derived, by numerically identifying the relevant minimal Fock space. Finally, and in order to generalize our findings for larger systems we investigate a system with a filling factor smaller than unity. Here, among others, we demonstrate that the cradle and breathing modes can also be observed in the intrawell dynamics of a setup comprising of ten wells.

Single-Shot Simulations of the Lattice Trapped Few-Boson Interaction Quench Dynamics: Let us now demonstrate how the correlated nature of the quantum dynamics of lattice trapped finite bosonic ensembles subjected to an interaction quench can be inferred by simulating in-situ single-shot measurements [310, 359–361]. As discussed in Section 2.5, the single-shot simulation procedure is based on a sampling of the many-body probability distribution, being accessible within the MCTDHB framework. Note that for all single-shot simulations to be presented below, the employed spread function consists of a Gaussian possessing a width $w = 1$. However, our observations remain valid also for smaller widths.

We first investigate whether the presence of correlations, and as a consequence the fragmentation of the bosonic ensemble, can be deduced by inspecting the time evolution of the variance of single-shot measurements. The variance of a sample of single-shot measurements $\{\mathcal{A}_k(\tilde{x})\}_{k=1}^{N_{shots}}$, where \tilde{x} refers to the spatial coordinates within the image, reads

$$\mathcal{V}(t_{im}) = \int dx \frac{1}{N_{shots}} \sum_{k=1}^{N_{shots}} [\mathcal{A}_k(\tilde{x}; t_{im}) - \bar{\mathcal{A}}(\tilde{x}; t_{im})]^2, \quad (3.2)$$

with $\bar{\mathcal{A}}(\tilde{x}; t_{im}) = 1/N_{shots} \sum_{k=1}^{N_{shots}} \mathcal{A}_k(\tilde{x}; t_{im})$. $\mathcal{V}(t)$ is shown in Fig. 3.5 for $N_{shots} = 500$ both

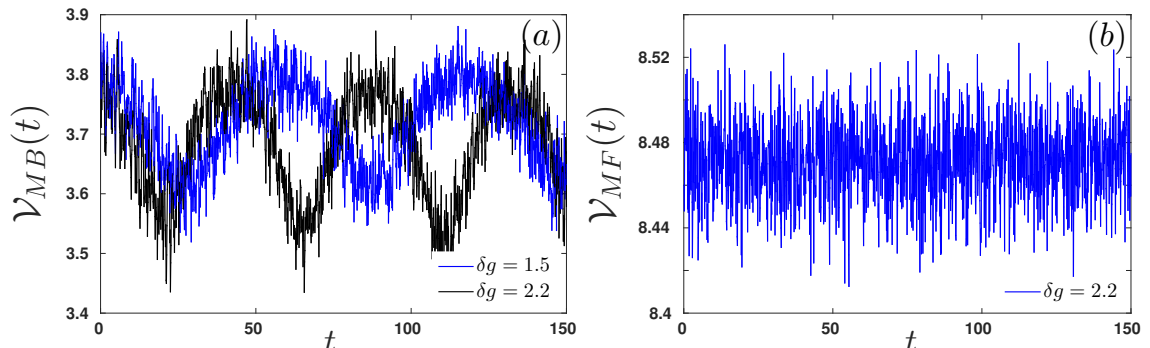


Figure 3.5: Evolution of the variance $\mathcal{V}(t)$ obtained from the simulation of in-situ single-shot measurements within (a) the many-body approach and (b) the mean-field approximation. The system is initialized in the weakly interacting, $g = 0.05$, ground state and to induce the dynamics we perform an interaction quench of amplitude δg (see legends).

at the mean-field and the many-body level. As it can be seen by inspecting Fig. 3.5 (b), within the mean-field approximation, $\mathcal{V}(t)$ is mainly constant exhibiting negligible amplitude fluctuations. On the contrary, when correlations are taken into account $\mathcal{V}(t)$ undergoes large amplitude oscillations [Fig. 3.5 (a)], resembling in this manner the density-wave tunneling mode, also identified as the “global” breathing of the entire bosonic cloud [compare Fig. 3.3 (a) and Fig. 3.5 (a)]. In particular for $t < 25$ the bosons travel towards the outer wells of the triple well (reflected by the negative $\delta\rho^{(1)}(x, t)$ in these regions) and the variance decreases, while for $25 < t < 50$ the bosons tend to bunch in the central well (negative $\delta\rho^{(1)}(x, t)$ in the middle well) and \mathcal{V} increases. This behavior of the variance observed in the many-body scenario can be explained as follows. In a coherent condensate i.e. $n_1(t) = 1$, where the mean-field approximation is valid, $\mathcal{V}(t)$ is essentially constant during the time evolution as all the atoms in the corresponding single-shot measurement are selected from the same single-particle function, see Eq. (2.21). In contrast, when referring to a many-body system where fragmentation is possible the corresponding many-body state is a superposition of several mutually orthonormal single-particle functions, see Eq. (2.31). In this way, $\mathcal{V}(t)$ is drastically altered from its mean-field counterpart as the atoms are picked from the above-mentioned superposition and thus the distribution of the atoms in the cloud depends strongly on the position of the already imaged atoms. We remark that the above-described behavior of $\mathcal{V}(t)$ persists also for smaller samplings of single-shot measurements, e.g. $N_{shots} = 200$ (not shown here for brevity).

Having established that the correlated character and the density-wave tunneling mode can be deduced from $\mathcal{V}(t)$, we next examine whether the on-site motion including the cradle and breathing mode can be directly observed by performing an averaging over several single-shot images. It is important to remark here that due to the diluteness of the considered bosonic gas ($N = 4$) the observation of the one-body density dynamics through a single-shot image is not possible. To properly capture the dynamics of the single-particle density within a single-shot image a much higher particle number, e.g. $N \sim 10^4$ is required. However

OUTLINE OF THE SCIENTIFIC CONTRIBUTIONS

such a calculation is computationally feasible only for the two orbital case in which the numerical convergence on the many-body level can not be ensured. To directly assign the few-boson dynamics observed in the temporal fluctuations of the one-body density $\delta\rho^{(1)}(x, t)$ we measure $\delta\bar{A}(x, t) = \bar{A}(x, t) - (1/T) \int_0^T dt \bar{A}(x, t)$. Figures 3.3 (b), (c) present $\delta\bar{A}(x, t)$ for different number of single-shot samplings namely $N_{shots} = 100$ and $N_{shots} = 500$ respectively. As it is evident $\delta\bar{A}(x, t)$ is able to capture the dynamics of both intrawell modes, a result that becomes even more prominent for increasing number of shots, compare Figs. 3.5 (a), (b) and (c). We remark here that for larger samplings e.g. $N_{shots} = 1000$ the $\delta\bar{A}(x, t)$ resembles almost perfectly $\delta\rho^{(1)}(x, t)$ (results not shown).

Our first study of the nonequilibrium dynamics following a sudden raise of the interparticle repulsion of initially weakly interacting superfluids revealed the existence of the on-site cradle and breathing excited modes. Most importantly the occurrence of a resonance between a tunneling channel and the cradle allowing for a controllability between the inter and intrawell dynamics has been unveiled. Another remarkable finding was the detection of the cradle mode, attributed to the over-barrier transport of bosons residing in neighboring wells, caused by the import of energy into the system. A natural question that arises is whether this cradle mode can be excited when quenching the system from strong-to-weak interactions thus exerting energy from the system. An important aspect here is to explore how the initial ground state configuration, reflected by the filling factor of the system, affects the generation of the quench-induced excited modes or enables us to resonantly couple them.

3.3.2 Quench Dynamics from Strong-to-Weak Interactions [[2]]

As a next step we proceed to the investigation of the nonequilibrium dynamics of strongly repulsive bosonic ensembles in one-dimensional finite lattices induced by interaction quenches and/or a ramp of the lattice potential height [[2]]. Recent theoretical studies of strongly correlated quantum gases have been devoted, for instance, to the study of transport properties and the formation or melting of Mott domains [39, 377–379] after a quantum quench. In contrast, our study [[2]] focusses on the controllable excitation of certain higher-band modes depending on both the quench protocol and the filling factor, their properties in terms of the tunable parameters of the Hamiltonian and the characterization of the overall system's dynamical response. To this end, we study from a few-body perspective the dynamical effects resulting from an abrupt or a time-dependent quench, focussing on the few-body collective excitations and the control of the respective dynamics.

We explore the quantum dynamics of strongly interacting bosons following a quench to a weakly interacting final state. It is important to remark here that a quench from strong-to-weak interactions minimizes the unavoidable heating processes [376] that might have been present in [[1]] especially for large quench amplitudes. Such a quench triggers several normal modes of the system including distinct lowest-band tunneling pathways, an on-site breathing and a cradle mode. The dominant number state configuration of each mode is identified, within the concept of multiband Wannier number states, showing the participation of excited-band contributions. In this manner, conceptual differences concerning the ingredients of each mode and its emergent excitation process when compared to the case of weak-to-strong interaction quenches [[1]] have been demonstrated. Recall that the local breathing mode refers

to an expansion and contraction dynamics of the bosons in an individual well. Interestingly enough, it is observed that the cradle mode can be excited only for setups with filling larger than unity for a quench from strong-to-weak interactions. Indeed, as argued in [[1]] this mode refers to a dipole-like oscillation and it is generated via an over-barrier transport. Naturally for strong interactions such a transport is inherently related to the initial delocalization of the particles, reflecting in this way the filling factor of the system under consideration. Its underlying generation mechanism can be summarized as follows. Due to the strong interparticle repulsion the initial spatial configuration corresponds to one localized boson in each well and one delocalized (over the three wells) energetically close to the lattice barrier. Then, a negative change in the interaction strength yields a high probability for the delocalized particle to overcome the barrier and move to a neighboring well, where it collides with the initially localized particle, resulting in a cradle process. Therefore for other filling factors this effect disappears and the consequent dynamics, when quenching from strong-to-weak interactions, is dominated by the interwell tunneling. This constitutes a major difference in comparison to a positively interaction quenched superfluid where due to release of energy into the system we allow for the over-barrier transport independently of the filling factor. Furthermore, by considering time-dependent quenches, namely different quench rates, or the modulation of various potential parameters of the Hamiltonian we suggested scenarios to control the cradle and breathing modes by means of manipulating their frequencies. Inspecting the fidelity evolution we also studied the system's dynamical response and its long time evolution with respect to the quench amplitude, as well as demonstrated the dynamical crossover from a sudden to an adiabatic parameter change by employing time-dependent variations of the interaction strength. Here, the persistence of the excited modes for finite-ramp rates has been demonstrated.

To excite the cradle mode in setups characterized by filling smaller than unity we enforce the spatial delocalization of the atoms by quenching the height of the potential barrier to lower values. Indeed, ramping-down the optical potential depth drives the system to a region where the kinetic energy of the atoms dominates in comparison to the potential energy. To further enhance the dynamical contribution of this mode in systems with filling smaller than unity we showcase that one needs to rely on a combined quench protocol comprising of a barrier and a simultaneous interaction quench to smaller values.

Up to now we have analyzed the nonequilibrium dynamics of finite bosonic ensembles confined in optical lattices following a quench from strong-to-weak interactions and vice versa. These studies allowed us to characterize on the microscopic level the triggered lowest and excited-band modes, resonantly couple them by tuning the quench strength and unveil under what circumstances they can be excited. Evidently, in order to steer the dynamics the considered quench protocol plays a key role. Therefore, adopting a quench that enables us to dynamically control the various excited modes of the bosonic system is highly desirable.

3.3.3 Dynamics after Multiple Interaction Quenches [[3]]

In [[3]] we follow a generalized quench protocol, namely a multiple interaction quench (MIQ) scenario, consisting of different sequences of single quenches. In particular, the protocol comprises of a quench followed by its “inverse” namely by going back to the original interaction

OUTLINE OF THE SCIENTIFIC CONTRIBUTIONS

strength (single pulse). The latter, enables the system to dynamically return to its original Hamiltonian within certain time intervals. An important question here is to what extent certain properties induced by the quench persist during the quantum mechanical evolution. In a recent study [380] the effects of the MIQ protocol in a three-dimensional ultracold Bose gas have been investigated using the time-dependent Bogoliubov approximation. It has been demonstrated that the system produces more elementary excitations with increasing number of MIQs, while the one and two-body correlation functions tend to a constant value for long evolution times. Here, we aim to dynamically manipulate the quench-induced excited modes and offer controllable schemes of certain excitation processes.

We study the correlated nonequilibrium quantum dynamics following a multiple interaction quench protocol for few-bosonic ensembles confined in one-dimensional finite optical lattices. Our protocol can be summarized as follows. At $t = 0$ the interparticle repulsion is quenched from the initial value g_{in} to a final one g_f , maintaining g_f (positive half) for time τ (pulse width). Then, the interaction strength is quenched back, i.e. from g_f to g_{in} , maintaining this value g_{in} (negative half) for time τ . This latter procedure is repeated according to the number of the pulses n_p . The system is prepared within the weak interaction regime and sequences of interaction quenches to strong interactions and back are performed. We focus on the intermediate interaction strength regime, where current state of the art analytical approaches are not applicable. In order to characterize the impact of the multiple pulses we study the interplay between the quench amplitude and the pulse width during the evolution. The quenches give rise to a variety of interwell tunneling channels and excite the cradle and the breathing modes. By systematically investigating the different time intervals of the MIQ protocol we identify the frequency branch of each process and the time intervals for which it occurs.

The lowest-band tunneling dynamics consists of three distinct energy channels occurring in the positive halves of the MIQ. When the system is quenched back only one tunneling mode survives. This opens the possibility to dynamically manipulate the tunneling dynamics within the different time intervals of the MIQ protocol. Utilizing, for instance, different pulse widths we can switch on and off for chosen time intervals certain tunneling modes of the system. The intrawell excited motion is described by the cradle and the breathing modes being initiated by the over-barrier transport as a consequence of the quench to stronger interactions. The cradle mode persists during the time evolution since it has already been initialized during the first pulse. As a consequence the coupling between the cradle mode and one of the tunneling modes, discussed in [[1]], disappears when $g = g_{in}$ and arises only for $g = g_f$. Therefore, using a MIQ protocol one can switch on and off this mode resonance. Meanwhile, the breathing mode shows a strong dependence on the instantaneous interatomic repulsion. Within the positive halves of the MIQ it possesses an interaction-dependent frequency branch, whilst in the corresponding negative halves the latter branch disappears and two new frequency branches appear which are interaction independent. Therefore, the system in the course of the MIQ turns from the δg -dependent to the δg -independent branch providing additional controllability. Moreover, we inspect the consequent excitation dynamics and analyze its dependence on the quench amplitude focussing on a fixed pulse width and a varying final interaction strength. We observe that the quench-induced excitation dynamics

depends almost linearly on the quench amplitude, i.e. for increasing amplitude of the quench the amount of excitations increase. Regarding the dependence of the excitation dynamics on the pulse width we unveil a non-linear dependence. The above imply that the interplay between the quench amplitude and the pulse width yields a tunability of the higher-band excitation dynamics, indicating a substantial degree of controllability of the system under a MIQ protocol. Another prominent signature of the impact of the quenches is revealed by resorting to the evolution of the one-body momentum distribution. It is shown that within the positive halves of the MIQ protocol a periodic population transfer of lattice momenta takes place accompanied by a transition to a side peak structure within the negative halves of the MIQ. This periodic population transfer of lattice momenta constitutes an alternative signature of the excited energy channels within the positive halves of the MIQ protocol. We note that similar observations have been made experimentally in a variety of quenched setups [142, 172, 381]. Finally, the frequency of the above-mentioned periodicity possesses a power-law dependence on the quench amplitude.

The study of the nonequilibrium dynamics after multiple interaction quenches enabled us to controllably excite and de-excite certain processes during the time evolution. Another intriguing question that emerges towards the direction of controllable excitation processes is to what extent one can gain insights into the largely unexplored scaling of the few-body defect density, including the formation and melting of Mott domains and the excited to higher-band fraction participating in the dynamics. To this end, we next examine the nonequilibrium dynamics of few-boson ensembles confined in finite optical lattices upon dynamically crossing the superfluid-to-Mott-insulator state, utilizing a linear interaction quench.

3.3.4 Dynamics Following a Linear Interaction Quench in Finite Optical Lattices of Unit Filling [[4]]

In [[4]] we explore the nonequilibrium quantum dynamics following a linear interaction quench (LIQ) protocol in repulsively interacting few-boson ensembles confined in one-dimensional finite optical lattices. We focus on unit filling setups such that the ground state of the system for increasing interaction strength exhibits a transition from a superfluid to a Mott-insulator phase. To dynamically probe this transition, quench dynamics of ultracold bosons confined in optical lattices has been vastly used in order to examine e.g. the Kibble-Zurek mechanism [124–133], the approach to the adiabatic response limit [39, 377, 378, 382–385], the formation and melting of Mott domains [39, 377–379] and the growth of interparticle correlations [105–109]. As finite bosonic systems do not serve as a platform to confirm the Kibble-Zurek scaling hypothesis due to their finite size [386], here, we unravel the scaling of the few-body defect density including the excited to higher-band fraction which have been largely ignored in all previous investigations.

We consider few-bosons confined in an optical lattice of unit filling. To realize the few-body analogue of the superfluid to Mott-insulator phase transition the many-body eigenspectrum for varying interparticle repulsion is calculated, revealing the existence of narrow and wide avoided-crossings between states of the zeroth and the first excited-band. Performing a LIQ we cross the phase boundary dynamically, with a finite ramp rate, either from weak-to-strong interactions (positive LIQ) or inverserly (negative LIQ), covering in both cases the

OUTLINE OF THE SCIENTIFIC CONTRIBUTIONS

diabatic-to-nearly-adiabatic crossing regimes. The employed LIQ protocol consists of two time scales. At $t = 0$ the interatomic interaction is quenched from the initial value g_i to a final one g_f in a linear manner for time $t \in [0, \tau]$ and then it remains a constant at a value g_f , namely $g(t, \tau) = g_i + \delta g \frac{t}{\tau}$. $\delta g = g_f - g_i$ denotes the quench amplitude of the LIQ and g_i (g_f) is the effective one-dimensional interaction strength before (after) the quench. The system's dynamical response caused by the LIQ and in particular its dependence on several system parameters, such as the height of the potential barrier is subsequently examined. Overall, the induced dynamical response consists of the lowest-band tunneling and higher-band excitations.

In particular, when crossing the weak-to-strong interaction regimes we find an enhanced dynamical response at moderate quench rates rather than in the abrupt or almost adiabatic regimes. The resulting lowest-band tunneling dynamics comprises of first and second order transport [54,134]. These modes can be manipulated by tuning either the interaction strength after the quench or the height of the potential barriers in the optical lattice. Moreover, a rich interband tunneling dynamics takes place possessing mainly a single excitation to the first or second excited-band of the finite lattice. We further analyze the excited to higher-band fraction examining its dependence on the quench ramp rate and barrier height. It is shown that following a LIQ the excited to higher-band fraction obeys a bi-exponential decay for decreasing quench rate. This introduces two different time scales in the excitation dynamics, which are directly related to the diabatic or adiabatic crossing of the transition respectively and the width of the existing avoided-crossings in the many-body eigenspectrum. The excited to higher-band fraction follows a more complex scaling for varying height of the potential barrier. Namely for diabatic quenches it reduces withn increasing barrier, while for large ramp times it shows a non-linear behavior exhibiting a maximum at a certain height of the potential barrier. This latter behavior manifests the strong dependence of the excited to higher-band fraction on the quench rate both for shallow and deep lattices. Additionally, the higher-band dynamics depends strongly on the postquench state, namely when we tend to the region of an existing avoided-crossing it is characterized by a non-linear growth, while for larger quench amplitudes it increases in an almost linear manner.

The overall dynamical response following a LIQ from strong-to-weak interactions is suppressed, when compared to the inverse scenario, and it mainly consists of the lowest-band tunneling dynamics. Here the melting of the Mott-insulator state is observed. In this case the quench triggers only a few tunneling modes and the excited to higher-band fraction is negligible, obeying an exponential decay both with varying ramp time and potential height. As a consequence, the lowest-band approximation can adequately describe the induced dynamics. Finally, we made an attempt to generalize our results for both positive and negative LIQs by considering larger systems, showcasing the robustness of the above-mentioned scalings, as well as the enhancement of the excited to higher-band fraction for increasing system size. This latter observation suggests that larger setups of unit filling can be driven out-of-equilibrium more efficiently which is a manifestation of the Anderson orthogonality catastrophe [255,387,388].

All the above discussed contributions have been devoted to the nonequilibrium dynamics induced by a quench on the constant effective one-dimensional interaction strength. Recently,

the advent of optical Feshbach resonances which utilize an optical coupling between bound and scattering states, enables us to design complex spatial interaction strength distributions across the atomic sample. Remarkably enough, the intensity and detuning of the participating optical fields can be rapidly changed and allow even for nanometer scale modulations of the resulting scattering length [389]. Motivated by these advancements we next investigate the nonequilibrium dynamics of finite bosonic ensembles which experience a spatially modulated interaction strength and are confined in finite optical lattices. Such a study allows us to create peculiar ground state configurations, not accesible in the constant interaction strength case, and to further steer the resulting out-of-equilibrium dynamics.

3.3.5 Quench Dynamics of Finite Bosonic Ensembles in Optical Lattices with Spatially Modulated Interactions [[5]]

In [[5]] we study the ground state properties and the nonequilibrium quantum dynamics of few-bosons experiencing a spatially modulated interaction strength and confined in a finite lattice potential. Being experimentally accessible via the optical Feshbach resonance technique, spatially inhomogeneous interaction patterns introduce in the system a periodic structure which is known as non-linear optical lattice [390–392]. In this context theoretical studies have recently unveiled, among others, altered properties of the emerging non-linear excitations e.g. see [394–398], the existence of a delocalizing transition of bosons in one-dimensional optical lattices [401], optimal control schemes to stimulate transitions into excited modes of a condensate [402] and a particle localization phenomenon at the regions where the scattering length vanishes [403, 404]. However, all the above-mentioned investigations have been performed within the mean-field realm while evidences regarding the occurrence of fragmentation when considering spatially inhomogeneous interactions in bosonic systems have already been reported in few-boson ensembles [405, 406] showcasing, for instance, resonant interband tunneling mechanisms [407, 408]. Contrary to the above, in the present investigation we explore, for the first time, the quench-induced few-boson correlated dynamical response in a combined linear and non-linear optical lattice. Our major scope is to create certain ground state particle distributions, identify their correlated nature and provide ways to steer the dynamics within the same or energetically distinct single-particle bands.

We employ a spatially modulated interaction strength of sinusoidal type, $C_{int}(x, g, a, k_1, \phi) = g [1 + a \cos^2(k_1 x + \phi)]$, which is characterized by its wavevector k_1 , inhomogeneity amplitude a , interaction offset g and a phase ϕ . We remark that $\phi \neq 0$ and fixed k_1 yields an interaction strength imbalance between all lattice wells, while for varying k_1 and $\phi = 0$ C_{int} is on average the same only for the parity symmetric outer sites. Besides the use of an optically induced Feshbach resonance [389, 409–411], such an interaction profile can be achieved employing holographic beam shaping techniques, e.g. a digital micromirror device [412]. In our investigation we focus on setups possessing fillings larger than unity in order to profit from the competition between delocalization and on-site interaction effects and thus avoid suppression of tunneling.

For the ground state of the system we show that by varying either the wavevector or the phase of the interaction, the density distribution can be effectively displaced to regions of decreasing interaction strength. The inhomogeneity amplitude being of the order of half the

OUTLINE OF THE SCIENTIFIC CONTRIBUTIONS

lattice depth is kept fixed, while the interaction offset is unity. In particular, for small values of the wavevector the spatially averaged in each well interaction strength is larger within the central well when compared to the outer ones and becomes equal for increasing spatial periodicity. This causes a spatial redistribution of the atoms from the outer to the central wells for increasing wavevectors and the ensemble remains superfluid. A phase shift yields an interaction imbalance between all lattice wells and enables us to displace the single-particle density distribution in a preferred direction, achieving Mott-like states.

Following a quench of the wavevector, the dynamics is characterized by enhanced response regions, located at fractional values of the wavevector, in which bosons at distinct wells are subjected to different spatially averaged interaction strengths. These enhanced response regions become gradually less transparent for an increasing wavenumber as the interaction profile tends to a uniform configuration. The quench yields the excitation of a multitude of tunneling modes consisting of single and two particle transport which can be further amplified or shifted by adjusting the interaction offset or the inhomogeneity amplitude respectively. A breathing dynamics of the bosonic cloud also occurs and it is characterized by interband tunneling processes which possess a single excitation to the second or fourth excited-band. The corresponding momentum distribution reveals a periodic population transfer of momenta during the dynamics, while inspecting the one-body coherence function we observe that partially coherent regions occur between the wells that are predominantly populated during the evolution.

Employing a phase quench an interaction strength imbalance between all lattice wells is imposed, yielding a directed transport along the finite lattice as it accounts for a spatial shift of the entire interaction profile. The induced tunneling modes are of single-particle and atom pair type. Most importantly, a phase quench enables us to discriminate, otherwise, energetically degenerate tunneling channels. Such a paradigmatic example is the single-particle lowest-band tunneling from the middle to the left or the right well. For increasing inhomogeneity amplitudes the quench-induced modes become more discernible, namely their energy difference is intensified. The above-mentioned directional transport is also reflected in the one-body momentum distribution where a directed consecutive population of higher momenta occurs. From a one-body correlation perspective the predominantly populated wells form a partially incoherent region which is shifted in the preferred tunneling direction. Last but not least a phase quench yields a noticeable over-barrier transport giving rise to a global breathing motion of the bosonic cloud and a cradle mode in the outer wells. These modes refer to single-particle interband processes to the first or second excited-band respectively.

Until now we have analyzed several aspects of the correlated nonequilibrium dynamics of interaction quenched few-boson ensembles confined in finite optical lattices. Another intriguing question that still remains is whether one can achieve to a certain extent an initial state preparation and consequently obtain a direct control of the many-body evolution. To investigate this scenario we next unravel the expansion dynamics of finite bosonic ensembles confined in a composite potential landscape, comprising of a finite lattice and an imposed harmonic oscillator potential. In contrast to the above studies this investigation will permit us to gain insights into the competition between the initial localization of the atoms and the repulsive interaction strength during the many-body dynamics and subsequently infer about

specific resonant processes.

3.3.6 Quench-induced Resonant Tunneling Mechanisms of Bosons in an Optical Lattice with Harmonic Confinement [[6]]

In the present contribution [[6]] we study the nonequilibrium dynamics of few-bosons confined in a one-dimensional optical lattice upon quenching the frequency of an imposed harmonic trap from strong-to-weak confinement. Besides the static properties of such systems [413–415, 415,416] a recent experimental investigation examined the dependence of the quench-induced ballistic expansion rate of a bosonic Mott-insulator on the interparticle interaction [145], while on the theoretical side it has been demonstrated [369] that in the limit of low-filling factors the dynamics is equivalent to that of harmonically trapped bosons with a lattice-dependent effective mass. Both of the aforementioned effects emerge when the harmonic confinement is relatively weak compared to the interparticle repulsion. In contrast, here, we shall examine effects that arise due to the competition between the harmonic confinement and the interaction strength, thus favoring different spatial configurations. Exploiting this competition we will achieve a high level of mode controllability by utilizing specific state preparations.

Investigating the many-body eigenspectrum for a varying trap frequency we reveal the existence of narrow and wide avoided-crossings between the many-body eigenstates. Focussing on the case of a strong harmonic confinement the eigenstates become well-separated and are dominated by a single Wannier number state. Having analyzed the static properties of the system we turn our attention to the quench-induced dynamics for varying final trap frequency. Within the non-interacting limit, a pronounced tunneling dynamics occurs only for the case of a weak final harmonic trapping. Referring to intermediate interactions different response regimes are observed, depending on the postquenched confinement strength. This behavior is caused by the multiple avoided-crossings present with varying harmonic oscillator frequency in the many-body eigenspectrum which can be exploited in order to reveal a rich dynamics after quenching the trap frequency. Indeed, for relatively small quench amplitudes we observe Rabi oscillations caused by the wide avoided-crossings between the ground and the first excited states. Turning to intermediate quench amplitudes the narrow avoided-crossings, which solely involve excited states, can be utilized to selectively couple the initial state to a desired final state. Here, the dynamics is characterized by multiple frequencies one of which is particularly slow and can be used to drive the system to a desired final state. Large quench amplitudes give rise to a multimode dynamical response of small amplitude. In this regime of quenches the number state with the dominant contribution to the initial state is an eigenstate of the final system, while the other contributions to the initial state give rise to the observed multimode dynamics. Moreover, we showcase that the deterministic preparation of the system in a desired Wannier number state is hindered by the fact that more tunneling modes are induced by additional contributions to the initial state. As a final attempt, the dynamics of states lying at stronger interparticle interactions, possessing admixtures of a single excitation to the first excited-band which do not couple in the eigenstate spectrum, have been examined. In the many-body eigenspectrum avoided-crossings appear at higher trap frequencies and are narrower. The consequent dynamics significantly differs from the case of

weak interactions, with higher-band effects being more prominent and lowest-band tunneling being suppressed. In conclusion, we can infer that for increasing quench amplitude the system exhibits regions of a pronounced dynamical response in the vicinity of wide avoided-crossings and sharper response peaks closely related to the existing narrow avoided-crossings in the many-body eigenspectrum. Thus, an appropriate selection of the postquench confinement enables us to couple the initial state to a desired final one, allowing for a low-frequency and efficient population transfer between the two eigenstates. Finally, we have shown that the quench-induced many-body dynamics alters significantly with varying particle number and interparticle repulsion, as the positions and widths of the avoided-crossings are shifted, giving rise to further controllability of the dynamics.

3.4 Driven Lattices

A very important ingredient, as outlined above, towards the manipulation of the dynamics is the proper design of the relevant driving protocol in order to transfer the energy to the desired final degrees of freedom. As a next step, in the following two works we shall examine the nonequilibrium dynamics induced by a time-periodic modulation of the finite optical lattice. Our major scope is to demonstrate the high level of controllability that one can achieve also in a driven lattice scenario and to characterize the modes participating in the dynamics.

3.4.1 Resonant Quantum Dynamics of Few Ultracold Bosons in Periodically Driven Finite Lattices [[7]]

In [[7]] we unravel the nonequilibrium quantum dynamics of finite ultracold bosonic ensembles confined in a periodically driven, and in particular shaken, one-dimensional optical lattice. Similar recent studies on shaken optical lattices demonstrated the participation of excited orbitals in the course of the dynamics [198] and even the presence of parametric dynamical instabilities due to the interplay of the interparticle interactions and the external driving [199–202]. Our investigation, which has been conducted before Refs. [198–202], showcases the inescapable necessity to include excited-band states for the accurate description of the nonequilibrium dynamics, the parametric coupling of the respective excitations and their microscopic characterization. Most importantly, the occurrence of a parametrically induced resonance is elucidated.

We examine the correlated nonequilibrium quantum dynamics of few-body bosonic ensembles subjected to a time-periodic driving of a finite-size optical lattice. The driven optical lattice is modelled with the sinusoidal function $V_{sh}(x, t) = V_0 \sin^2[k_0(x - A \sin \omega_D t)]$. It is characterized by the barrier depth V_0 , a lattice wave-vector k_0 , the amplitude A and the frequency $\omega_D = 2\pi/T_D$ of the driving field. Such a scheme has been implemented in the experiment of e.g. Ref. [172], where the retroreflecting mirrors that are used to form the lattice can be moved periodically in space. Alternatively, a frequency difference between the counterpropagating laser beams can be induced by means of acousto-optical modulators [417] which renders the lattice time-dependent. We particularly focus on the regimes of large lattice depths and small driving amplitudes in order to limit the degree of induced excitations

that would otherwise lead to heating processes.

Initializing the few-body system in its weakly or strongly interacting ground state we examine, in a systematic manner, i.e. covering a wide range of driving frequencies the time evolution of the system induced by a shaken optical lattice. The driving enforces the bosons residing in distinct wells to oscillate in-phase and to exhibit a dipole-like intrawell mode. We showcase that the system's dynamical evolution is mainly governed by the interwell tunneling and the intrawell dipole-like mode. The periodically driven dynamics of the system in the non-interacting regime has been firstly analyzed within the framework of the Floquet theory, i.e. at the single-particle level, providing an accurate description of the observed processes. However, for finite particle numbers and interaction strengths such a single-particle description is shown to be inadequate for the explanation of the observed dynamics and a multimode treatment becomes necessary. The deep optical lattice and the small driving amplitude render the interwell tunneling weak. However, a quite rich excitation spectrum is observed. We remark here that such higher-lying excitations, which lead to a coupling between the two energetically lowest energy bands, have already been exploited for the realization of single- and two-qubit gates, where the quantum bit is encoded into the localized Wannier functions of the two lowest energy bands of each lattice site [418]. The local dipole mode is identified from the intrawell oscillations of bosons in the individual wells. Most importantly, it has been found that by adjusting the driving frequency the intrawell dynamics experiences a resonant behaviour, elucidating that it can be controlled by tuning the driving frequency. This resonantly driven dynamics is manifested e.g. by the periodic formation of enhanced density oscillations (giant dipole oscillations) or from the periodic population of additional lattice momenta in the momentum distribution of the one-body density. The population of the energetically higher momenta is reminiscent of the parametric amplification of a matter-wave phenomenon [172]. Additionally, utilizing the Floquet theory it has been shown that in the proximity of this resonance the first two Floquet modes are dominantly contributing. Away from resonance the dynamics can be described by only the first Floquet mode. To comprehend the enhanced population of the second Floquet mode in the vicinity of the resonance the corresponding quasienergy spectrum has been employed, revealing avoided-crossings between the first two Floquet modes at certain driving frequencies. To identify the frequencies referring to the intrawell and interwell tunneling dynamics the frequencies associated with the interference terms between the Floquet modes have been employed, showing pronounced on-site oscillations and an enhancement of the interwell tunneling mode in the vicinity of the resonance. Turning to an ensemble consisting of few-bosons we examined the influence of the interatomic interactions both for the inter- and intrawell generated modes. It has been shown that the interparticle repulsion affects each of the above-mentioned modes, yielding a destruction of the interwell tunneling dynamics in the strongly interacting regime and an enhancement of the excitations namely an increased contribution of energetically higher-band states. To gain further insights into the intrawell atomic motion we employ the spectrum of the local one-body density and of the on-site density oscillations. Inspecting these spectra with respect to the driving frequency we have identified all the relevant dynamical frequencies, such as those referring to the intrawell oscillations and the emergent tunneling dynamics. Finally, all the above outlined findings are confirmed for different filling factors, lattice potentials, and

boundary conditions, showcasing a type of universality for the observed dynamics.

Collecting the knowledge obtained from all the above contributions we can arrive to the following two main conclusions. By shaking an optical lattice a tunable on-site dipole mode and a resonant intrawell dynamics can be realized, while a sudden increase of the interparticle repulsion in a non-driven lattice gives rise to a rich lowest-band as well as intraband dynamics which can be further coupled for certain quench amplitudes. Then, a natural question that arises is how a combination of periodic driving and interaction quenches can be used to steer the overall dynamics of the system and as a consequence also the coupling of the interwell and intrawell modes. In this direction within our next scientific contribution we explore the dynamics of interaction quenched finite bosonic ensembles confined in periodically driven lattice systems.

3.4.2 Mode Coupling of Interaction Quenched Ultracold Few-Boson Ensembles in Periodically Driven Lattices [[8]]

In [[8]] we investigate the quantum dynamics of interaction quenched few-boson ensembles trapped in one-dimensional periodically driven finite optical lattices. Our study provides deep insights on the activation of certain energy channels, by using distinct driving protocols, and the microscopic origin of the quench induced nonequilibrium processes. The periodic modulation consists of a lattice vibration with amplitude δ and an angular frequency $\omega_D = 2\pi f_D$, namely $V_{br}(x; t) = V_0 \sin^2[k_x(1 + \delta \sin(\omega_D t))x]$. V_0 denotes the lattice depth and $k_x = \frac{\pi}{l}$ the corresponding wavevector, where l denotes the distance between successive potential minima. To experimentally realize such a potential acousto-optical modulators [417] can be employed which induce a frequency difference among the involved counterpropagating laser beams that form the lattice potential. Focussing on a deep lattice potential and small driving amplitudes we aim to minimize the degree of excitations that could, otherwise, lead to the creation of the cradle motion [[1]] or even to heating processes.

Starting from the ground state of a weakly interacting few-boson ensemble, we unravel the system's time evolution in the periodically driven finite lattice by performing a simultaneous interaction quench. We first showcase that in an exclusively driven lattice one can induce out-of-phase local dipole modes in the outer wells, and an on-site breathing mode in the central well. Recall that this is in direct contrast to a shaken lattice, where only on-site in-phase dipole modes are generated [[7]]. To unravel the regime from adiabatic to high frequency driving we cover a wide range of driving frequencies. It is observed that within the intermediate frequency regime, which is intractable by current analytical methods, the system can be driven to a highly nonequilibrium state when compared to the other driving frequency regions. More importantly, a resonance of the intrawell dynamics takes place, characterized by an enhanced tunneling dynamics, thus opening a multitude of energetically higher-lying interwell tunneling pathways. This resonance is mainly of single-particle character and it survives upon increasing interaction acquiring additional features, the most remarkable of which being the co-tunneling of an atom pair [54, 134]. Within this resonantly driven regime an intensified loss of coherence occurs, providing this way an independent and potentially experimentally tractable signature of the resonant dynamics.

To induce a correlated many-body dynamics we employ an interaction quench upon the

periodically driven lattice for various driving frequencies. In this manner we can trigger more effectively the interwell as well as the intrawell dynamics and drive the system towards strongly out-of-equilibrium regimes. Consequently, the tunneling and the on-site breathing mode are amplified, while in the outer wells the bosons experience an admixture of a dipole and a breathing component. The latter, in turn leads to oscillations around the minimum of the well and a simultaneous contraction and expansion dynamics. Our investigation indicates that the interaction quench can be used to manipulate the tunneling frequency, rendering the single-particle tunneling dominant even at resonant driving, and to amplify the emergent intrawell modes yielding also a strong influence on the excitation dynamics.

Next, the dynamics of the periodically driven lattice, i.e. for a fixed driving frequency, with varying quench amplitude has been studied. It has been shown that the lowest-band tunneling dynamics contains three channels, the breathing mode possesses two frequency branches and the aforementioned admixture occurring in the outer lattice wells involves three branches: one stemming from the breathing motion and two others referring to the dipole component. Therefore, the combination of different driving protocols can excite distinct inter- and intrawell modes and manifest various energetically distinct components of a mode. Remarkably enough, five distinct resonances between the lowest-band tunneling dynamics and the intrawell dynamics are revealed. In particular, the lowest-band tunneling experiences a resonance with the breathing component of the central well, two resonances with the breathing motion of the outer wells and two resonances with the dipole motion of the outer wells. We show that these resonances can be further manipulated via the frequency of the periodic driving, allowing for further control of the mode coupling in optical lattices. The observed resonances between various inter- and intrawell modes demonstrate the richness of the system, while their dependence e.g. on the driving frequency exposes the tunability of the system.

3.5 Quench Dynamics in Binary Mixtures

In all the above-mentioned scientific contributions we argued about possible coupling schemes between the distinct modes that are present in the nonequilibrium, quenched or periodically driven, dynamics of single-component bosonic ensembles and revealed the correlated nature of these modes. A step forward to advance our understanding on the correlated nature of the nonequilibrium dynamics is to study multicomponent systems. Indeed multicomponent setups are novel systems, whose behavior is very different with respect to their single-component counterparts. In this context, quantum correlations possess a distinct role as their interplay gives rise to novel phases of matter and peculiar dynamical phenomena [203, 204]. Possible manifestations of the latter are complex tunneling processes [407, 408] or collective modes [248]. In view of the importance of quantum correlations for various physical systems, a large part of the corresponding field aims at developing a decisive understanding of the controllability of the tunneling dynamics by engineering the correlation properties. While such ambitions have already been highly successful for single-component systems [134–139], the corresponding investigations in two component setups remains a major challenge for the field, which calls for novel approaches that are conceptually beyond the single-orbital or lowest-band approximations. Within the next two works we aim to reveal the correlated

mechanisms during the interaction quench-induced dynamical phase separation process in a two-component harmonically trapped Bose-Bose mixture and also expose the correlated nature of the expansion dynamics of a Bose-Fermi mixture confined in an optical lattice.

3.5.1 Correlation Effects in the Quench-Induced Phase Separation Dynamics of a Two-Species Ultracold Quantum Gas [[9]]

In [[9]] we investigate the quench-induced phase separation dynamics of a harmonically trapped repulsively interacting binary bosonic ensemble both within and beyond the mean-field approximation. It is known that binary bosonic mixtures exhibit a second-order phase transition from a miscible to an immiscible state based on the interaction strength characterizing the system. If the strength of the interspecies interaction exceeds that of the intraspecies interaction, then energy considerations show that the two species prefer to be in a phase separated, alias immiscible state [10, 14], otherwise the system resides in the miscible phase, see also Fig. 3.6. A multitude of recent studies in multicomponent few-boson systems evinced, for instance, altered phase separation processes [206, 219, 223, 246, 247], composite fermionization [220, 248, 249], and the dependence of the tunnelling dynamics on the mass ratio [252, 253] or the intra- and interspecies interactions [254]. On the contrary, here, we focus on the many-body character of the quench-induced dynamical phase separation process.

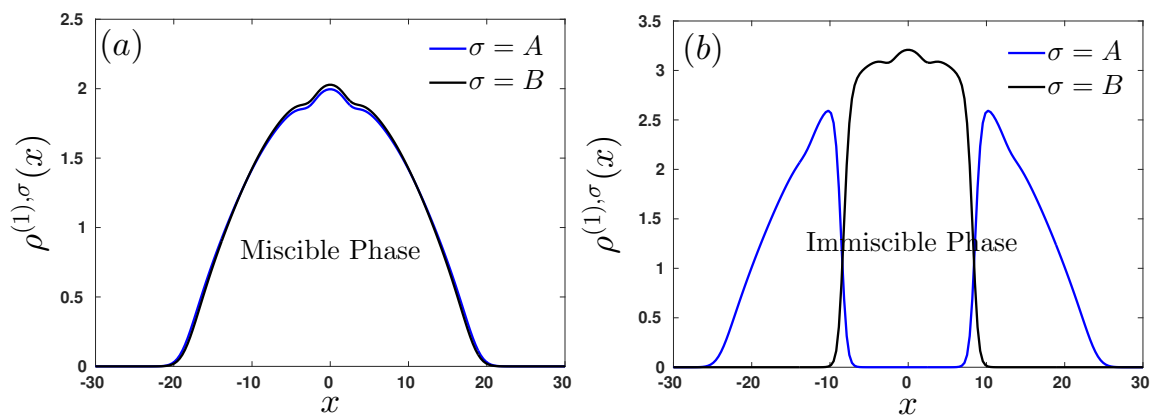


Figure 3.6: Ground state one-body densities for a Bose-Bose mixture comprising of $N_A = N_B = 50$ atoms. The intraspecies interactions correspond to $g_{AA} = 1.004$ and $g_{BB} = 0.9544$ and the interspecies interaction strengths are (a) $g_{AB} = 0.1$ and (b) $g_{AB} = 1.4$.

We first initialize our system into the miscible phase fixing the intraspecies interactions to the experimentally measured values for a binary bosonic ensemble of ^{87}Rb atoms prepared in the internal states $|F = 1, m_F = -1\rangle$ and $|F = 2, m_F = 1\rangle$ [419], while the interspecies interaction is zero. To realize the miscible-to-immiscible transition the intraspecies interactions are held fixed and the interspecies repulsion is quenched to larger values that exceed that of the intraspecies. A filamentation of the one-body density during the dynamics of each of the two species takes place in both the mean-field and the correlated approach with the filaments

formed undergoing collective breathing oscillations. The dominant wavenumber associated with the emerging phase separated state appears to be higher in the mean-field case and it is found to be in excellent agreement with the analytical predictions available in this limit. It is shown that increasing the interspecies repulsion accelerates the filamentation process, gives rise to a larger number of filaments formed and leads to an almost complete phase separation. Referring to the same interaction strengths and examining few-boson systems we find that phase separation is absent in the many-body case, while it is still present within the mean-field framework.

A correlation analysis on both the one- and the two-body level further signifies the phase separation process as the miscibility-immiscibility threshold is crossed. Indeed, on the one-body level prominent losses of coherence are observed between filaments residing around the center of the trap with the longer distant ones lying at the periphery of the bosonic cloud, verifying the fragmented nature of the system. Remarkably enough, at the two-body level domain-wall-like structures are revealed, i.e. interfaces that separate the distinct filaments [420–422] formed, since the inner filaments in both species are found to be anti-correlated with their respective outer ones. To offer a link with potential experimental realizations of the above-observed dynamics we utilized, for the first time for binary mixtures, single-shot simulations. The presence of both the entanglement and the fragmentation are related to the variance of single-shot images. In particular, it is shown that the growth rate of the variance resembles the growth rate of the entanglement while the fragmented nature of the binary system is captured by the deviations in the variance measured in the course of the dynamics with respect to each of the two species.

Turning to the reverse quench scenario, namely quenching from the immiscible towards the miscible phase multiple dark-antidark solitary waves, i.e. density humps on top of the bosonic background, are spontaneously generated at both the mean-field and the many-body level which are found to decay within the latter framework [309]. Indeed, we showcase that at the many-body level many decay events increase the production of dark-antidark solitary waves, with the product of each decay consisting of a slow and a fast dark-antidark structure [309]. This increasement results in multiple collisions and interference events between the involved matter waves, with most of being lost during evolution. Utilizing the variance of single-shot measurements we reveal the presence of an enhanced entanglement, since the system in this case is strongly correlated on the many-body level. Finally, we consider quenches within the immiscible regime and reveal the one-dimensional analogue of the so-called “ball” and “shell” structure that appears in higher-dimensional binary systems [423].

3.5.2 Many-Body Expansion Dynamics of a Bose-Fermi Mixture Confined in an Optical Lattice [[10]]

In our final contribution [[10]] we study the quench-induced expansion dynamics of a mass-balanced Bose-Fermi mixture confined in an one-dimensional optical lattice with an imposed harmonic trap upon considering quenches from strong-to-weak confinement. The expansion dynamics in similar trapped geometries has been investigated mainly for the single component case revealing, for instance, the dependence of the expansion strength on the interatomic interactions [145], a lowest-band global breathing mode [369], the occurrence of a resonant

OUTLINE OF THE SCIENTIFIC CONTRIBUTIONS

dynamical response [[6]] and a temperature-dependent long-range order [424–427]. Here we provide a systematic study of the expansion dynamics for particle imbalanced Bose-Fermi mixtures with a particular emphasis on how the interspecies correlations, which reflect the initial phase of the system [428–431], affect the expansion dynamics of the mixture.

Referring to the ground state properties of the system we showcase that by tuning the ratio between the inter- and intraspecies interaction strengths two distinct ground state configurations can be entered, namely the miscible and immiscible phases. These phases are characterized by a complete or vanishing overlap of the bosonic and fermionic single-particle density distributions respectively. Operating within the weak interaction regime, we perform a quench from strong-to-weak confinement and unravel the resulting dynamical response within each of the above-mentioned phases for varying final harmonic trap frequency. We deduce that each individual phase exhibits a characteristic response consisting of an overall expansion of both atomic clouds and an interwell tunneling dynamics which can be manipulated by adjusting the quench amplitude.

Inspecting the quench-induced dynamics within the immiscible phase we observe the occurrence of a resonant-like response of both components at moderate quench amplitudes in contrast to what it is expected upon completely releasing the imposed harmonic trap. This observation is in accordance with the single-component expansion dynamics discussed in [[6]]. A systematic analysis of the Bose-Fermi mixture expansion dynamics shows the existence of different bosonic response regimes, accompanied by a lesser amount of fermionic ones for decreasing confinement strength. We find that for varying quench amplitude the bosons either perform a breathing dynamics or solely expand. Meanwhile, the fermions undergo tunneling between the nearest neighbor outer wells being located at the edges of the bosonic cloud or show a delocalized behavior over the entire lattice. Comparing the findings with the mean-field approximation we are able to identify the many-body characteristics of the expansion dynamics. Indeed, it is shown that within the single-orbital approximation the tunneling dynamics of both components cannot be adequately captured. The bosonic expansion is significantly suppressed and the diffusive character of the fermions is replaced by an expansion of two almost localized density branches to the outer wells for large quench amplitudes. The many-body character of the induced expansion is further elucidated by studying the evolution of the distinct orbitals. The first one resembles the mean-field approximation while the higher-orbital contributions are responsible for the observed correlated dynamics. Finally, the one and two-body coherence functions for each species show that during the evolution the predominantly occupied wells are one-body incoherent and two-body anti-correlated among each other while within each well a correlated behavior for bosons and an anti-correlated one for fermions occurs.

Turning to the miscible phase the dynamical response of the Bose-Fermi mixture is greatly altered when compared to the immiscible one. Here, the bosons majorly perform interwell tunneling reaching an almost steady state for long evolution times, while the fermions expand until the edges of the surrounding bosonic cloud where they are partly transmitted and partly reflected back towards the central wells. Neglecting all correlations the bosonic tunneling dynamics is found to be enhanced and remains undamped, whilst the fermionic expansion resembles adequately the many-body case.

OUTLINE OF THE SCIENTIFIC CONTRIBUTIONS

Finally, the dependence of the Bose-Fermi mixture expansion strength on the mass imbalance between the two components and the potential barrier height has been examined. It has been shown that for mass imbalanced mixtures the heavy component remains almost unperturbed, while upon increasing the height of the potential barrier the expansion dynamics is suppressed.

Chapter 4

Scientific Contributions

4.1 Quench Dynamics

4.1.1 Interaction Quench Induced Multimode Dynamics of Finite Atomic Ensembles

PAPER

Interaction quench induced multimode dynamics of finite atomic ensembles

To cite this article: S I Mistakidis *et al* 2014 *J. Phys. B: At. Mol. Opt. Phys.* **47** 225303

View the [article online](#) for updates and enhancements.

Related content

- [Resonant quantum dynamics of few ultracold bosons in periodically driven finite lattices](#)
S I Mistakidis, T Wulf, A Negretti *et al.*
- [Interaction-driven interband tunneling of bosons in the triple well](#)
Lushuai Cao, Ioannis Brouzos, Sascha Zöllner *et al.*
- [The impact of spatial correlation on the tunneling dynamics of few-boson mixtures in a combined triple well and harmonic trap](#)
Lushuai Cao, Ioannis Brouzos, Budhaditya Chatterjee *et al.*

Recent citations

- [Phases, many-body entropy measures, and coherence of interacting bosons in optical lattices](#)
R. Roy *et al*
- [Bosonic quantum dynamics following a linear interaction quench in finite optical lattices of unit filling](#)
S.I. Mistakidis *et al*
- [Quench-induced resonant tunneling mechanisms of bosons in an optical lattice with harmonic confinement](#)
G. M. Koutentakis *et al*

Interaction quench induced multimode dynamics of finite atomic ensembles

S I Mistakidis¹, L Cao^{1,2} and P Schmelcher^{1,2}

¹Zentrum für Optische Quantentechnologien, Universität Hamburg, Luruper Chaussee 149, D-22761 Hamburg, Germany

²The Hamburg Centre for Ultrafast Imaging, Universität Hamburg, Luruper Chaussee 149, D-22761 Hamburg, Germany

Received 31 July 2014, revised 8 September 2014

Accepted for publication 16 September 2014

Published 3 November 2014

Abstract

The correlated non-equilibrium dynamics of few-boson systems in one-dimensional finite lattices is investigated. Starting from weak interactions we perform a sudden interaction quench and employ the numerically exact multi-layer multi-configuration time-dependent Hartree method for bosons to obtain the resulting quantum dynamics. Focusing on the low-lying modes of the finite lattice we observe the emergence of density-wave tunneling, breathing and cradle-like processes. In particular, the tunneling induced by the quench leads to a ‘global’ density-wave oscillation. The resulting breathing and cradle modes are inherent to the local intrawell dynamics and connected to excited-band states. Moreover, the interaction quenches couple the density-wave and the cradle modes allowing for resonance phenomena. These are associated with an avoided-crossing in the respective frequency spectrum and lead to a beating dynamics for the cradle. Finally, complementing the numerical studies, an effective Hamiltonian in terms of the relevant Fock states is derived for the description of the spectral properties and the related resonant dynamics.

Keywords: interaction quench, non-equilibrium dynamics, higher-band effects, density-wave tunneling, cradle mode, breathing mode, avoided crossing

(Some figures may appear in colour only in the online journal)

1. Introduction

Ultracold atoms in optical lattices are regarded as an ideal tool to study properties of quantum many-body systems in a controllable manner [1–4]. This is experimentally manifested by handling independently the lattice potential and the interaction strength between the atoms. The former is achieved by tuning counter-propagating lasers and the latter by means of optical, magnetic or confinement-induced Fano-Feshbach resonances [5–10]. Currently one of the main focus of many-body physics is to comprehend quantum phase transitions (QPTs) and to unravel their internal mechanisms. In this direction, the experimental progress yielded the realization and explanation of superfluid (SF) to Mott insulating (MI) states, complementing the theoretical efforts within the Bose–Hubbard (BH) framework [11, 12]. Furthermore, other exotic quantum phases like the Bose Glass phase or Mott shells have been realized in disordered systems [13–16].

These and other QPTs raise new prospects for theory and experiment, most notably the inescapable necessity of taking quantum effects into account.

Apart from the experimental efforts in the investigation of the ground state properties in many-body systems, recently it became possible, using trapped ultracold atomic gases, to explore the evolution of isolated strongly correlated systems [17] after being quenched. In a corresponding experiment, the system is originally prepared in the ground state $|\psi_0\rangle$ of the Hamiltonian \hat{H}_i , and then driven out of equilibrium at time $t = 0$ by a sudden change of either the trapping frequency or the interaction strength, yielding a new Hamiltonian \hat{H}_f evolving the system in time. The resulting non-equilibrium situation triggers challenging conceptual questions concerning the unitary evolution, such as the not yet fully understood connection of quantum ergodicity to the integrability of a system [18, 19]. The experimental applications in this field includes the realization of a quantum version of Newton’s

cradle [20], the quenching of a ferromagnetic spinor condensate [21], the light-cone effect in the spreading of correlations [22, 23], as well as the collapse and revival of a BEC [24]. Also, a recent experiment on quenched atomic SFs reports the realization of Sakharov oscillations which are known to emerge from the large-scale correlations in galaxies [25].

From another perspective, the inclusion of higher-band contributions results in an additional orbital degree of freedom yielding novel phenomena such as unconventional condensation [26–28] and anisotropic tunneling. Indeed, excited-band populations caused by interactions have already been observed either by sweeping the magnetic field across a Feshbach resonance [29] or via Raman transitions which couple directly the zeroth band to the first excited p -band of the lattice [30]. Other experimental achievements indicate the observation of a 2D SF in the p -band [31] and the orbital excitation blockade [32] when exciting atoms to higher orbitals as well as supersolid quantum phases in cubic lattices [33, 34]. The aforementioned aspects have led, among others, to the construction of multiflavor and multiorbital models [35–38]. Motivated by the previous studies here we investigate the higher-band dynamics of interaction quenched SFs focussing on the resulting low-lying collective modes, which are nowadays of great experimental interest.

In the present study, we examine the response of a finite atomic ensemble confined in one-dimensional (1D) finite lattices subjected to a sudden change in the interaction strength. More precisely, we focus on highly non-perturbative situations by considering weak-to-strong interaction quenches with respect to the initial state. In this manner, we drive the system to a regime where the interparticle interactions dominate in comparison to their kinetic energy. For weak interactions, the single-band approximation, namely the BH model, provides quantitative predictions of the system dynamics; for strong interactions, however, it yields at most a qualitative description. In this manner, by considering strong quench amplitudes and examining representative few-body setups for incommensurate filling factors, our treatment goes beyond the validity of the BH model. The numerical method which we employ in order to study the dynamical properties of our 1D finite setups is the recently developed multi-layer multi-configuration time-dependent Hartree method for Bosons (ML-MCTDHB) [39, 40], based on MCTDHB which has been developed and applied successfully previously [41–44]. Both methods are very efficient in treating bosonic systems both for static properties and in particular their dynamics (see next section), while they are equivalent for the case of a single species treated here.

We demonstrate the emergence of higher-band modes, namely the breathing and the cradle modes as well as the rise of the density-wave tunneling, following interaction quenches. Especially the observation of the cradle mode which refers to a localized wave-packet oscillation is arguably one of our central results. The dynamical properties of incommensurate setups are investigated by examining the time-evolution of the corresponding one-body densities and their respective fluctuations. In addition, we analyze the Fourier

spectra of representative intrawell observables and the variation of the center of mass coordinate for the cases of the cradle and breathing modes, respectively. More specifically, the occurrence of a resonance between the cradle and one of the tunneling modes, being manifested by an avoided crossing in the frequency spectrum, is observed here. This opens the possibility to control the interwell dynamics by triggering the intrawell dynamics via the quench amplitude in optical lattices. Additionally, the construction of an effective Hamiltonian describing the dynamical behaviour is provided and the minimal Fock space required to produce the cradle process is derived.

The work is organized as follows. In section 2 we introduce our setup, explaining also the ML-MCTDHB method, the quench protocol and the number state representation. In section 3 we report on the quench dynamics for different incommensurate filling factors and demonstrate the emergent modes that arise due to the interaction quench. We summarize our findings and give an outlook in section 4.

2. Setup and analysis tools

2.1. The model

Our system consists of N neutral short-range interacting bosons in a 1D trap. The many-body Hamiltonian reads

$$H = \sum_{i=1}^N \left(\frac{p_i^2}{2M} + V(x_i) \right) + \sum_{i<j} V_{\text{int}}(x_i - x_j), \quad (1)$$

where the one-body part of the Hamiltonian contains the 1D lattice potential $V(x_i) = V_0 \sin^2(kx_i)$ which is characterized by its depth V_0 and periodicity l , with $k = \pi/l$ being the wave vector of the lasers forming the optical lattice. Furthermore, in order to restrict the infinite trapping potential $V(x_i)$ to a finite one with m sites and length L , we impose hard wall boundary conditions at the appropriate positions. On the other hand, we model the short range two-body interaction potential as $V_{\text{int}}(x_i - x_j) = g_{1D} \delta(x_i - x_j)$ with the effective coupling strength $g_{1D} = \frac{2\hbar^2 a_0}{M a_{\perp}^2} \left(1 - |\zeta(1/2)| \frac{a_0}{\sqrt{2} a_{\perp}} \right)^{-1}$ [10]. The coupling g_{1D} depends on the 3D s-wave scattering length a_0 , the oscillator length $a_{\perp} = \sqrt{\frac{\hbar}{M \omega_{\perp}}}$ of the transverse trapping potential and the mass M of the atom. From the above expression it is obvious that we can tune the interaction strength by the scattering length a_0 or the frequency of the confinement ω_{\perp} via Feshbach resonances [8, 9] or confinement induced resonances [45–47] respectively. Additionally, for reasons of computational convenience we will rescale the above Hamiltonian in units of the recoil energy $E_R = \hbar^2 k^2 / 2M$ by setting $\hbar = M = 1$. In this manner, the rescaled interaction strength can be rewritten as $g = \frac{g_{1D}}{E_R}$, whereas the spatial and temporal coordinates are given in units of k^{-1} and E_R^{-1} respectively. Therefore, all quantities below are in dimensionless units.

In a BH model which we address here for reasons of comparison, the Hilbert space is truncated with respect to the localized lowest-band Wannier states which form a complete set of orthogonal basis functions. This represents an alternative and more convenient way for discussing phenomena in which the spatial localization of states plays an important role. Our *ab initio* simulation goes beyond the single-band approximation and requires higher-band states to describe the real and site independent ($J_{ij} = J_{ji}^* \equiv J$) tunneling strength. Notice also, that the hard wall boundaries we consider here imply zero tunnel coupling between the first and the last sites (in contrast to periodic boundary conditions which result in a certain coupling for all sites). In our *ab initio* simulations we use a sufficiently large lattice depth $V_0 = 4.5$ such that each well includes two localized single-particle Wannier states, i.e. the ground and first-excited states, while the higher excited states are taken into account as delocalized states.

2.2. The computational method : ML-MCTDHB

The ML-MCTDHB constitutes a variational numerically exact *ab initio* method for investigating both the stationary properties and in particular the non-equilibrium quantum dynamics of bosonic systems covering the weak and strong correlation regimes. Its multi-layer feature enables us to deal with multispecies bosonic systems, multidimensional or mixed dimensional systems in an efficient manner. Also, the multiconfigurational expansion of the wavefunction in the ML-MCTDHB method takes into account higher-band effects which renders this approach unique for the investigation of systems governed by temporally varying Hamiltonians, where the system can be excited to higher bands especially during the dynamics. An important characteristic of the ML-MCTDHB approach is the representation of the wavefunction by variationally optimal (time-dependent) single particle functions (SPFs) and expansion coefficients $A_{i_1 \dots i_S}(t)$. This renders the truncation of the Hilbert space optimal when employing the optimal time-dependent moving basis. Also, the requirement for convergence demands a sufficient number of SPFs such that the numerical exactness of the method is guaranteed. Therefore, the number of SPFs has to be increased until the quantities of interest acquire the corresponding numerical accuracy. This constitutes a numerically challenging and time-consuming task especially for strong interactions where the use of more SPFs to ensure convergence is unavoidable.

Let us elaborate. In a generic mixture system consisting of N_σ bosons of species $\sigma = 1, 2, \dots, S$ the main concept of the ML-MCTDHB method is to solve the time-dependent Schrödinger equation

$$i \left| \dot{\Psi} \right\rangle = \hat{H} \left| \Psi \right\rangle$$

$$\left| \Psi(0) \right\rangle = \left| \Psi_0 \right\rangle, \quad (2)$$

as an initial value problem by expanding the total wave-

function in terms of Hartree products

$$\left| \Psi(t) \right\rangle = \sum_{i_1=1}^{M_1} \sum_{i_2=1}^{M_2} \dots \sum_{i_S=1}^{M_S} A_{i_1 \dots i_S}(t) \left| \psi_{i_1}^{(1)}(t) \right\rangle \dots \left| \psi_{i_S}^{(S)}(t) \right\rangle. \quad (3)$$

Here each species state $\left| \psi_i^{(\sigma)} \right\rangle$ ($i = 1, 2, \dots, M_\sigma$) corresponds to a system of N_σ indistinguishable bosons, which in turn can be expanded in terms of bosonic number states $\left| \vec{n}(t) \right\rangle^\sigma$ as follows

$$\left| \psi_i^{(\sigma)} \right\rangle = \sum_{\vec{n} \parallel \sigma} C_{i, \vec{n}}^\sigma(t) \left| \vec{n}(t) \right\rangle^\sigma, \quad (4)$$

where each σ boson can occupy m_σ time-dependent SPFs $\left| \varphi_j^{(\sigma)} \right\rangle$. The vector $\left| \vec{n} \right\rangle = \left| n_1, n_2, \dots, n_{m_\sigma} \right\rangle$ contains the occupation number n_j of the j th SPF that obeys the constraint $n_1 + n_2 + \dots + n_{m_\sigma} = N_\sigma$.

Here we focus on the case of a single species in one-dimension where the ML-MCTDHB is equivalent to MCTDHB [41–44, 48]. To be self-contained, let us briefly discuss the ansatz for the many-body wavefunction and the procedure for the derivation of the equations of motion. The many-body wavefunction is a linear combination of time-dependent permanents

$$\left| \Psi(t) \right\rangle = \sum_{\vec{n}} C_{\vec{n}}(t) \left| n_1, n_2, \dots, n_M; t \right\rangle, \quad (5)$$

where M is the number of SPFs and the summation is again over all possible combinations which retain the total number of bosons. Notice that in the limit in which M approaches the number of grid points the above expansion becomes exact in the sense of a full configuration interaction approach. On the other hand, the permanents in (5) can be expanded in terms of the creation operators $a_j^\dagger(t)$ for the j th orbital $\varphi_j(t)$ as follows

$$\left| n_1, n_2, \dots, n_M; t \right\rangle = \frac{1}{\sqrt{n_1! n_2! \dots n_M!}} \times \left(a_1^\dagger \right)^{n_1} \left(a_2^\dagger \right)^{n_2} \dots \left(a_M^\dagger \right)^{n_M} \left| \text{vac} \right\rangle, \quad (6)$$

which satisfy the standard bosonic commutation relations $\left[a_i(t), a_j(t) \right] = \delta_{ij}$, etc. To proceed further, i.e. to determine the time-dependent wave function $\left| \Psi \right\rangle$, we have to find the equations of motion for the coefficients $C_{\vec{n}}(t)$ and the orbitals (which are both time-dependent). For that purpose one can employ various schemes such as the Lagrangian, McLachlan [49] or the Dirac–Frenkel [50, 51] variational principle, each of them leading to the same result. Following the Dirac–Frenkel variational principle

$$\langle \delta \Psi | i \partial_t - \hat{H} | \Psi \rangle = 0, \quad (7)$$

we can determine the time evolution of all the coefficients $C_{\vec{n}}(t)$ in the ansatz (5) and the time dependence of the orbitals $\left| \varphi_j \right\rangle$. These appear as a coupled system of ordinary differential equations for the time-dependent coefficients $C_{\vec{n}}(t)$ and nonlinear integrodifferential equations for the time-dependent orbitals $\varphi_j(t)$. The aforementioned equations constitute the well-known MCTDHB equations of motion [41–44].

Note that for the needs of our implementation we have used a discrete variable representation for the SPFs (or

orbitals $|\varphi_j\rangle$, specifically a sin-DVR which intrinsically introduces hard-wall boundaries at both ends of the potential (i.e. zero value of the wave function on the first and the last grid point). For the preparation of our initial state we therefore relax the bosonic wavefunction in the ground state of the corresponding m -well setup via imaginary time propagation in the framework of ML-MCTDHB. Subsequently, we change abruptly the interaction strength and explore the time evolution of $\Psi(x_1, x_2, \dots, x_N; t)$ using ML-MCTDHB. Finally, note that in order to justify the convergence of our simulations, e.g. for the triple well, we have used up to 10 SPFs finally confirming the convergence. Another criterion for convergence is the population of the natural orbital with the lowest population which is kept for each case below 0.1%.

2.3. Quantum quench protocol

Our approach to study the non-equilibrium dynamics follows a so-called quantum quench. According to this the system is originally prepared at $t = 0$ in the ground state $|\psi_0\rangle$ of some initial Hamiltonian $H_{in} = H(\zeta_{in})$, where ζ_{in} is a system parameter associated to the perturbation such as the interaction strength or the height of the barrier. Then for times $t > 0$ we suddenly quench the parameter ζ to a final value ζ_f and examine the subsequent evolution of the system under the new Hamiltonian $H_f = H(\zeta_f)$.

In the general case, the final Hamiltonian assumes the form $H_f = H_{in} + \lambda H_r$, where H_r is a dimensionless perturbing operator and λ , which possesses the dimensionality of an energy, is the so-called quench amplitude. In our case the quench protocol consists of tuning the interaction strength between the particles which appears in the two-body part (V_{int}) of the Hamiltonian (1). Therefore, we assume as the initial state $|\psi_0\rangle$ (at $t = 0$) the ground state of the Hamiltonian $H_{in} = H(g_{in})$ and we explore its dynamical behaviour for $t > 0$ subject to the Hamiltonian $H_f = H(g_f)$. Under this protocol the time evolution of the system according to the Schrödinger picture is $|\psi(t)\rangle = e^{-\frac{i}{\hbar}H_f t} |\psi_0\rangle$ while the evolution of the expectation value of a system operator \hat{A} obeys

$$\langle \psi(t) | \hat{A} | \psi(t) \rangle = \sum_{f, f'} C_f C_{f'} e^{-i\frac{E_f - E_{f'}}{\hbar} t} \langle f | \hat{A} | f' \rangle, \quad (8)$$

where $|f\rangle$ refers to the eigenstates and E_f the respective eigenvalues of the final Hamiltonian $H_f = H(g_f)$. Thus, for our system the new Hamiltonian governing the dynamics can be written as follows

$$H(g_f) = H(g_{in}) + \frac{\delta g}{g_{in}} \sum_{k < j} V_{int}(x_k - x_j), \quad (9)$$

with $\frac{\delta g}{g_{in}}$ being the corresponding quench amplitude.

2.4. Number state representation

Using ML-MCTDHB we calculate the wavefunction with respect to a time-dependent basis of SPFs. Therefore the expansion of the wavefunction in general reads $|\psi(t)\rangle = \sum_{\vec{n}} A_{\vec{n}}(t) |n(t)\rangle$. On the

analysis side, however, it is preferable to analyze our results in a time-independent basis and make the connection with the multi-band Wannier functions. In this respect, we have developed in the framework of ML-MCTDHB a fixed basis analysis package in terms of which we use a time-independent basis for the expansion of the wavefunction, i.e. $|\psi(t)\rangle = \sum_{\vec{m}} \tilde{A}_{\vec{m}}(t) |\vec{m}\rangle$.

In addition, in order to interpret our results we will use as an explanatory tool the concept of a generalized number state representation with multiband Wannier states. To use this representation we assume that the lattice potential is deep enough such that the Wannier functions belonging to different wells have very small overlap for not too high energetic excitation. Within this framework we can analyze the inter-band processes as well as the intraband tunneling. As a specific example, let us elaborate for the case of a triple well system the corresponding wavefunction in terms of these states which encode the allocation of the n bosons among the individual wells

$$|\psi\rangle = \sum_{n, I} C_{n, I} |n_L, n_M, n_R\rangle_I. \quad (10)$$

Here n_L, n_M, n_R are the number of bosons localized in the left, middle, and right well respectively which satisfy the condition $n_L + n_M + n_R = n$. The summation is over all the different arrangements of the n bosons in the triple well as well as the different necessary excited states (index I) that we must take into account according to their energetical order. In this manner, we use an expansion in terms of the number states of the non-interacting bosons, i.e. products of non-interacting single particle Wannier functions. Finally, it is important to notice that such an expansion is valid also in the strong interaction regime but needs then a large number of excited configurations.

The notion of the generalized number states will be one of our basic tools for the analysis of the non-equilibrium dynamics. For illustration, let us analyze in some detail the case of four bosons in a triple well which will be one of the considered setups in the following. Here, in terms of the number states we can realize four different categories. The quadruple mode $\{|4, 0, 0\rangle_I, |0, 4, 0\rangle_I, |0, 0, 4\rangle_I\}$ that refers to four bosons in the same well, as well as the triple mode $\{|3, 1, 0\rangle_I, |0, 3, 1\rangle_I, |1, 0, 3\rangle_I, |1, 3, 0\rangle_I, |0, 1, 3\rangle_I, |3, 0, 1\rangle_I\}$ which implies that three bosons are localized in the same well and the fourth resides in one of the remaining wells. In addition, there is the pair mode that can be separated into two categories: the double pair mode $\{|2, 2, 0\rangle_I, |0, 2, 2\rangle_I, |2, 0, 2\rangle_I\}$ where the bosons are divided into two pairs each of them occupying a different well and the single pair mode $\{|2, 1, 1\rangle_I, |1, 2, 1\rangle_I, |1, 1, 2\rangle_I\}$ which contains a pair and two separated bosons.

Let us comment on the relation between the different categories of number states and the eigenstates of the system. The number states of a particular category with the same intrawell energetical index i share a similar ‘on-site’ energy and they will significantly contribute to the same eigenstates. In this manner, the eigenstates can be also classified with respect to the dominantly contributing number states, e.g. the single-pair (SP), the double-pair (DP), the triple (T) and the quadruple (Q) mode. To be concrete, in the following we will

use the notation $|i\rangle_{\alpha,I}$ to characterize the eigenstates, where the index α refers to the spatial occupation, i.e. the SP ($\alpha = 1$), DP ($\alpha = 2$), T ($\alpha = 3$) and Q ($\alpha = 4$), the index I denotes the respective energetical level and i stands for the index within each group. For instance $\{|i\rangle_{1,0}\}$ represent the eigenstates which are dominated by the set of SP states $\{|2, 1, 1\rangle_0, |1, 2, 1\rangle_0, |1, 1, 2\rangle_0\}$, where the index i take values from 1 to 3.

Finally, note that for the second system which we consider, consisting of five bosons in ten wells, the same analysis in terms of number states is straightforward. More precisely, one can realize seven different categories of number states. Namely, the single mode $\{|1, 1, 1, 1, 1, 0, \dots\rangle_{I, \dots}\}$, the SP mode $\{|2, 1, 1, 1, 0, \dots\rangle_{I, \dots}\}$, the DP mode $\{|2, 2, 1, 0, \dots\rangle_{I, \dots}\}$, the first triple mode $\{|3, 1, 1, 0, \dots\rangle_{I, \dots}\}$, the second triple mode $\{|3, 2, 0, \dots\rangle_{I, \dots}\}$ the quadruple mode $\{|4, 1, 0, \dots\rangle_{I, \dots}\}$ and the fifth mode $\{|5, 0, \dots\rangle_{I, \dots}\}$. Here, each mode can be characterized using similar arguments as we did for the case of the triple-well.

3. Quench dynamics

The main characteristic of a system with incommensurate filling ν is the existence of a delocalized fraction of particles [52]. Therefore, the most important feature is the absence of a Mott insulating state since there is a SF fraction on top of a Mott insulator phase. Below we consider both the case $\nu > 1$ where on-site interaction effects prevail and $\nu < 1$ in which the main concern is the redistribution of particles over the sites as the interaction increases. In the following, we proceed for each case with a brief discussion of the ground state properties and then we focus on the quantum dynamics resulting after an interaction quench.

3.1. Filling factor $\nu > 1$

Our initial state is the ground state for a given interaction strength in the weak-interaction regime. Therefore, let us briefly summarize the ground state properties for weak interactions for a setup consisting of four atoms in three wells, i.e. one extra particle on a Mott background. For this case of incommensurability we encounter two main aspects: delocalization and on-site interaction effects. The particle density for the non-interacting case $g = 0$ is largest in the middle site and decreases for the outer ones due to the hard-wall boundary conditions that render the middle and outer sites non-equivalent. In the low-interaction regime we observe a tendency towards a uniform population for $g \approx 0.2$ due to the repulsion of the bosons. For further increasing repulsion such as $g = 0.8$ we note a trend towards the repopulation of the central well again.

In the following, we study the quench dynamics for $t > 0$ of the above setup by means of an abrupt change in the repulsive interaction strength at $t = 0$. In order to investigate out-of-equilibrium aspects in our system we first examine the response of the one-body density. Therefore, we perturb our system starting from a SF ground state with $g_{in} = 0.05$ where

the atoms are bunching in the central well. As a consequence of the quench the system gains energy. Figures 1(a) and (b) show the time-evolution of the relative density in the triple well trap for weak and strong quench amplitudes, namely $\delta g = 0.8$ and $\delta g = 2.0$ respectively. We define the deviation of the instantaneous density from the average value up to time T for each grid point x as $\delta\rho(x, t) = \rho(x, t) - \langle\rho(x)\rangle_T$ where the quantity $\langle\rho(x)\rangle_T = \int_0^T dt \rho(x, t)/T$ refers to the corresponding mean single-particle probability density. Therefore, $\langle\rho(x)\rangle_T$ refers to the average behaviour of the one-body density while $\delta\rho(x, t)$ is the respective fluctuating part. According to our simulations the ratio $\frac{|\delta\rho(x, t)|}{\langle\rho(x)\rangle_T}$ is of the order of 10^{-1} .

As can be seen in figure 1, at each time instant $\delta\rho(x, t)$ exhibits a density-wave like spatial pattern. This density wave also evolves in time, changing between a peak-valley-peak and a valley-peak-valley pattern, where the peak and valley refer to a positive and negative relative density in a certain well, respectively. The evolution of this pattern reflects the tunneling dynamics under a quench, and will be termed in the following as density-wave tunneling. Note that the density-wave tunneling refers exclusively to the mode that transfers population among the middle and the outer wells. Additionally the inner-well dynamics which can be seen in figure 1(c) is described by two excited modes: the middle well exhibits a breathing mode due to the lattice symmetry, while in the left and right wells we observe the so-called cradle mode, manifested as a ‘dipole-like’ oscillation of the localized wavepacket. A close comparison of figures 1(a) and (b) reveals a transition from a multifrequency to a single frequency spectrum for weak to strong interaction quenches respectively. In the following, we will discuss in some detail each of the aforementioned dynamical modes and their significant role in the overall non-equilibrium dynamics.

3.1.1. Density-wave tunneling and breathing mode. Let us first focus on the explanation of the density-wave tunneling as an effective breathing of the ‘global wavepacket’ described by the envelope of the density distribution in the triple well. According to this, we illustrate in figure 2(a) some intersections of the one-body density for different time instants and define an envelope function for the triple-well which is the quadratic function that encloses the corresponding instantaneous peaks of the density. As we have already mentioned, the density-wave reflects the tunneling dynamics of bosons confined in the optical lattices, which is dominated in the present case by the states of the lowest-band. In turn, the dynamical tunneling is constituted by the contraction and expansion of the envelope in the course of the dynamics induced by the interaction quench. Intuitively, under an interaction quench the bosons tend to repel each other and the envelope will expand and then contract, which mimics the breathing dynamics of the bosons as known in the harmonic trap. In a recent study [53] this mode has been examined in the framework of the BH model for a quench in the lattice frequency. This suggests that

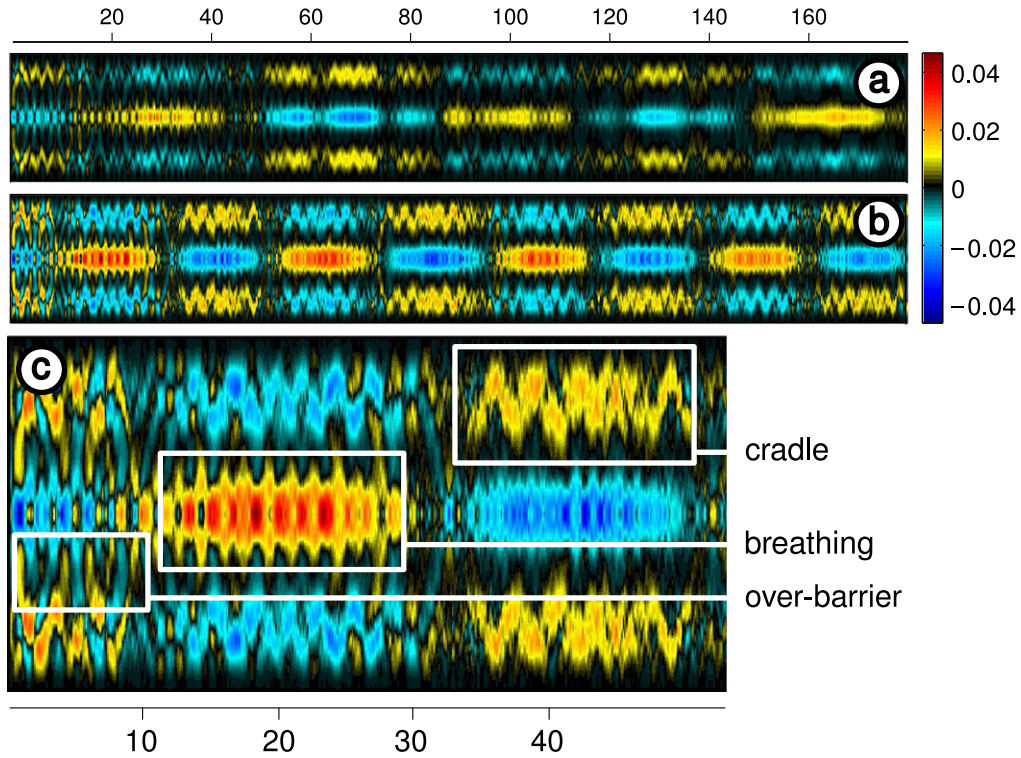


Figure 1. The fluctuations $\delta\rho(x, t)$ of the one-body density caused by an abrupt quench of the inter-particle repulsion. The initial state of each setup is the ground state of $N = 4$ bosons confined in a triple-well trap with $g_{in} = 0.05$. The space-time evolutions of the density are depicted for different quench amplitudes (a) $\delta g = 0.8$, (b) $\delta g = 2.0$. In (c) we show an inset of (b) for the first $t = 50$ time units where we demonstrate the cradle, breathing and over-barrier modes. Note that the spatial extent of each well is $(-3\pi/2: -\pi/2)$, $(-\pi/2: \pi/2)$, $(\pi/2: 3\pi/2)$ for the left, middle and right wells respectively. The vertical axis represents the spatial extent of the trap whereas the horizontal axis denotes the propagation time t .

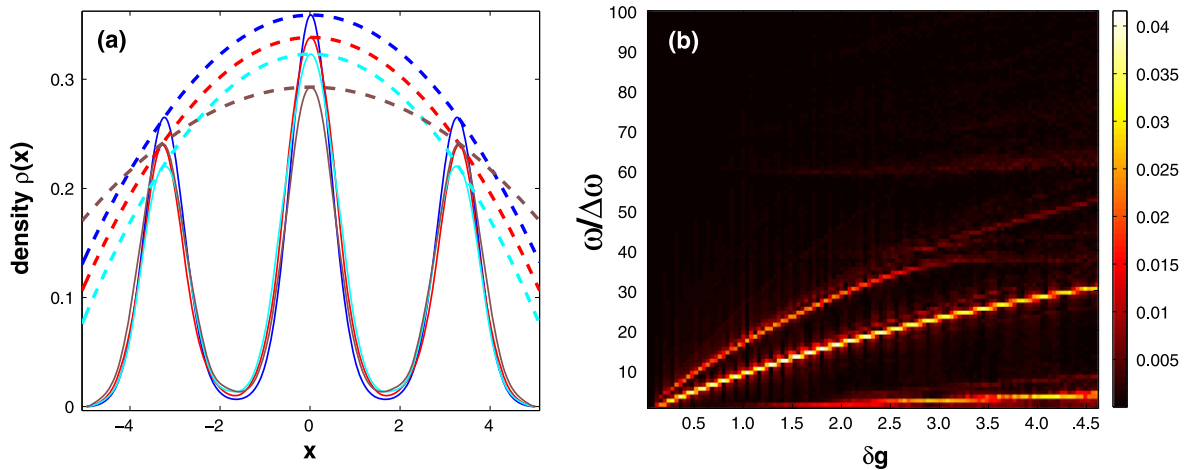


Figure 2. (a) Evolution of the one-body density $\rho(x, t)$ induced by an abrupt change of the inter-particle repulsion with amplitude $\delta g = 2.8$. The initial state is the superfluid ground state of $N = 4$ bosons with $g_{in} = 0.05$ confined in a triple-well trap. We observe spatio temporal oscillations constituting the density waves (see also figure 1). Shown is also the envelope of the one-body density (dashed lines) at different time instants: $t = 1$ (blue), $t = 10.3$ (red), $t = 18.8$ (light blue) and $t = 26.2$ (brown). The spectrum of the interwell tunneling modes can be obtained from the spectrum of the fidelity $F(t) = |\langle \psi(0) | \psi(t) \rangle|^2$ which is shown in (b) as a function of the quench amplitude δg . Here the vertical axis refers to normalized frequency units $\omega/\Delta\omega$, where $\Delta\omega = 2\pi/T$ and T being the respective propagation time.

it also exists for many-body systems in optical lattices where instead of our hard-wall boundaries a weak harmonic confinement renders the sites of the optical lattice non-equivalent.

Let us further investigate the properties of the tunneling modes due to their significance for the above-discussed effects. The tunneling properties can be identified in terms of the overlap of the instantaneous wavefunction during the

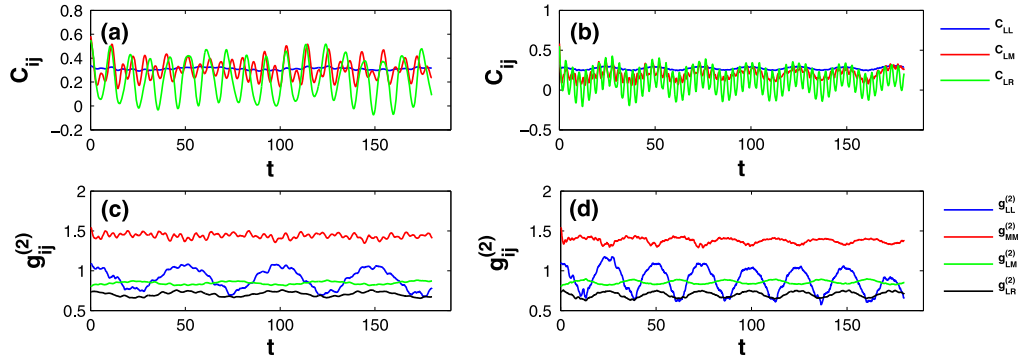


Figure 3. The time evolution of the one-body correlation function C_{ij} and the density correlations $g_{ij}^{(2)}$ for a quench from $g_{in} = 0.05$ to (a) $g_f = 1.0$ and (b) $g_f = 4.2$ (see text). For the density correlations we demonstrate the situation of (c) a weak quench $\delta g = 0.6$ and (d) a strong quench $\delta g = 4.0$.

dynamics and the initial state (see equation (11) below) which we denote as $D(t) = \langle \psi(0) | \psi(t) \rangle$. Then, the quantity that we are interested in is the probability that the states of the unperturbed and perturbed system are the same during the time evolution which can be expressed through the fidelity $F(t) = |D(t)|^2$. The identification of the interwell tunneling branches can be achieved via the frequency spectrum of the fidelity $F(\omega) = \frac{1}{\pi} \int dt F(t) e^{i\omega t}$ which provides us with the evolution of the frequencies of the tunneling modes for different quench amplitudes. Figure 2(b) therefore shows $F(\omega)$ with varying quench amplitude where we can identify three interwell tunneling branches. Note that the lowest one dominates for strong interaction quenches and this can be linked to the transition from a multifrequency to a single frequency behaviour that we have observed above in figures 1(a) and (b).

Next, in order to obtain a quantitative description of the multiband behaviour we adapt the number state basis (section 2.4) where the four different categories consist of: the Q, the T, the DP and the SP mode. Indeed, let $|\psi(0)\rangle = \sum_{i;\alpha;I} C_i^{\alpha;I} |i\rangle_{\alpha;I}$ be the initial wavefunction in terms of the eigenstates $|i\rangle_{\alpha;I}$ of the final Hamiltonian. Then the fidelity reads

$$|\langle \psi(0) | \psi(t) \rangle|^2 = \sum_{i;\alpha;I} |C_i^{\alpha;I}|^4 + \sum_{i,j;\alpha,\beta;I} |C_i^{\alpha;I}|^2 |C_j^{\beta;I}|^2 \cos(\epsilon_i^{\alpha;I} - \epsilon_j^{\beta;I})t, \quad (11)$$

where the indices α, β specify the particular groups of number states introduced in section 2.4 i, j is the internal index within each group and I denotes the band index. For the density-wave mode that we examine here we have $I = 0$. Moreover, in the above expansion the terms of the second sum represent the different tunneling branches whose Fourier transforms are shown in figure 2(b). The eigenstate $|i\rangle_{\alpha;I}$ may belong to one of the four existing categories of number states with a corresponding eigenenergy. In particular, the lowest branch in the Fourier spectrum corresponds to the energy difference $\Delta\epsilon$ within the energetically lowest states of the SP mode, i.e. intraband tunneling from the state $|1, 2, 1\rangle_0$ to $|2, 1, 1\rangle_0$ etc.

The second branch refers to the next energetically closest different modes. The tunneling process is here from the energetically lowest state of a SP mode to the energetically lowest DP mode, e.g. from $|1, 2, 1\rangle_0$ to $|2, 2, 0\rangle_0$. Finally the third branch refers to a tunneling process from a SP mode to a T mode, e.g. from $|2, 1, 1\rangle_0$ to $|3, 1, 0\rangle_0$. The remaining tunneling branches as for instance a transition from a DP mode to a T mode do in principle exist but they are negligible in comparison to the above ones due to the respective energy differences and therefore we can hardly identify them in figure 2(b). Note that the same spectrum could also be found from the frequency spectrum of the local density of a certain well, e.g. from $\rho_L(\omega)$.

According to the above the tunneling dynamics here is mainly an intraband phenomenon. To verify this we have also employed the respective single-band BH model where we have identified each branch in the weak interaction regime. Within this framework, we can observe the interwell tunneling processes but have to restrict ourselves to the weak interaction regime where the single-band approximation is valid. On the contrary, we can not observe either of the onsite breathing or cradle motion (see next section) which include higher-band contributions and are intrinsically linked to the intrawell structure.

Another important tool in order to explore the interwell tunneling is to examine how correlations among different sites react after an interaction quench. We examine two different types of correlations, the single particle correlations $C_{ij}(t) = \langle \psi | b_i^\dagger b_j | \psi \rangle / N$ and the second order normalized correlation function (or coherence) $g_{ij}^{(2)}(t) = \langle n_i n_j \rangle / \langle n_i \rangle \langle n_j \rangle$. Here, b_i^\dagger (b_i) denotes the corresponding creation (annihilation) operator of a particle located at site i in the lowest-band, while $n_i = b_i^\dagger b_i$ is the number operator for the site i . Notice that we mainly focus on the lowest-band description as the present tunneling mode is dominated by the lowest-band contributions, thus filtering out the influence from higher-bands. In figures 3(a) and (b) we illustrate the time evolution for the various types of one-body correlations associated with the left well for different quench amplitudes $\delta g = 0.95$ and $\delta g = 4.15$ each time starting from the SF regime ($g_{in} = 0.05$). The single

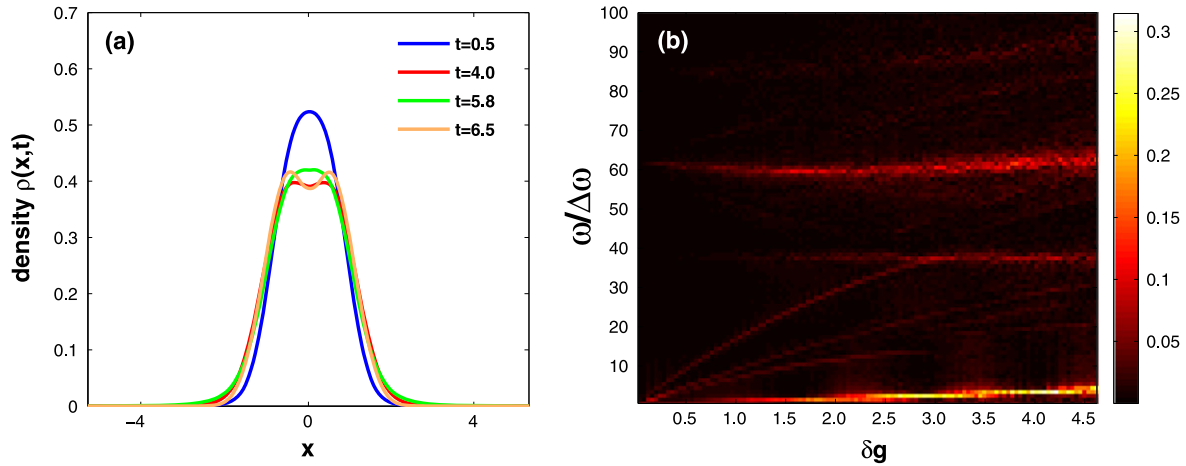


Figure 4. (a) One-body density profiles at different time instants after an interaction quench. The system consists of $N = 2$ bosons confined in a harmonic trap with $g_{in} = 0.05$, while the quench amplitude is $\delta g = 2.8$. The reshaping of the density indicates the breathing mode while the oscillatory structure demonstrates the contribution of excited states during the dynamics. On the other hand, in (b) we present the Fourier spectrum as a function of the quench amplitude for the quantity $\sigma_M^2(\omega)$ referring to the breathing mode. We observe that the breathing frequency is predominantly constrained to a narrow band. Note that we use normalized frequency units $\omega/\Delta\omega$, with $\Delta\omega = 2\pi/T$ and T being the whole propagation time.

particle correlations oscillate even for long time scales which can be attributed to the finite-size of our system. The diagonal term C_{LL} reflects the density oscillations of the left well which are relatively small. Moreover, we observe the change in the periods T of the tunneling, that is as we increase the interaction quench we obtain a decrease of the respective period denoted by rapid small amplitude oscillations. However, the non-diagonal terms C_{ij} with $i \neq j$ exhibit a non-vanishing oscillatory behaviour with an amplitude much larger than the density oscillations, i.e. C_{LL} . The latter shows more frequencies than the density which illustrates the emergence of more dynamical structures. This indicates that even a weak tunneling can transport substantial off-site correlations in the system.

On the other hand, the two-body correlation function $g_{ij}^{(2)}$ can be used to measure density fluctuations in the system under consideration. A basic property of this function is that $g_{ij}^{(2)} > 1$ refers to bunching whereas $g_{ij}^{(2)} < 1$ indicates antibunching. Ensembles with $g_{ij}^{(2)} = 1$ are referred to as fully second order coherent whereas for bunched particles one can infer that they have the tendency to reside together and vice versa for the antibunched case. Figures 3(c) and (d) illustrate various components of the second order correlation function for different interaction quenches. For the diagonal terms that refer to the middle well we observe that $g_{MM}^{(2)} > 1$ for the whole propagation time while for the left (or right) well we find that $g_{LL}^{(2)}$ oscillates around unity. The latter indicates a dynamical transition from bunching to antibunching and vice versa which has an impact also on the $g_{MM}^{(2)}$ component. In particular, for small quenches we can see that $g_{MM}^{(2)}$ is almost unchanged during the dynamics while $g_{LL}^{(2)}$ oscillates around unity and spends more time below unity. This means that for small quenches we can not affect significantly the initial distribution and two bosons are more likely to reside in the middle well. Increasing the quench

amplitude we observe that the two components are anticorrelated i.e. for the time intervals where $g_{LL}^{(2)}$ is smaller than unity the corresponding component $g_{MM}^{(2)}$ for the middle well is enhanced. Here the reduction of the $g_{LL}^{(2)}$ component is more pronounced than the enhancement of the $g_{MM}^{(2)}$ which might indicate an impact of the initial distribution. The off-diagonal terms $g_{LR}^{(2)}, g_{LM}^{(2)}$ with respect to the left well are always lower than 1 and anticorrelated. Also, for every time during the dynamics $g_{LM}^{(2)} > g_{LR}^{(2)}$ holds, indicating that it is more likely for two bosons to be one in the left and one in the middle site than one in the left and one in the right. On the other hand, the oscillatory behaviour of $g_{ij}^{(2)}$ can again be attributed to the finite size of our system. Concluding this part we can infer that the one-body and two-body correlations as shown in figure 3 demonstrate a rich phenomenology in terms of correlation dynamics. This might pave the way for further investigations on how a weak density-wave tunneling can transport significant correlation oscillations.

As the density-wave tunneling has been understood to lead to the ‘envelope breathing’ with the character of a breathing mode, let us now turn our attention to the study of the on-site or local breathing mode. In general, the breathing mode then refers to a uniform expansion and contraction of the local wavepacket. For a recent study concerning the dependence of the breathing mode frequency on the particle number as well as on the interaction strength see [54], while for further related and recent investigations we refer the reader to [55–58]. As we shall discuss briefly here, this local breathing mode can also be triggered by a quench of the interaction strength in a harmonic trap. To this end, figure 4(a) shows snapshots of the one-body density of a system consisting of two bosons in a single harmonic trap (with $g_{in} = 0.05$) after an interaction quench $\delta g = 2.8$ which mimics the dynamics within the middle well of the triple-well system. Here, we observe the reshaping of the density

profile for different time instants as well as the formation of oscillatory structures which indicate the existence of higher-band effects.

Coming back to the triple well, the local breathing mode refers to a contraction and expansion dynamics of the wavepacket in a single well, i.e. intrawell breathing induced by an interaction quench. In order to quantify the local breathing frequency in the triple-well setup we define the coordinate of the center of mass of the respective well

$$X_{\text{cm}}^{(i)} = \frac{\int_{d_i}^{d_{i+1}} dx (x - x_0^{(i)}) \rho_i(x)}{\int_{d_i}^{d_{i+1}} dx \rho_i(x)}. \quad (12)$$

Here $i = R, M, L$ stands for the right, middle and left well respectively whereas $x_0^{(i)}$ refers to the middle point of the corresponding well. On the other hand, d_i are the coordinates of the edge points of an individual well and $\rho_i(x)$ the corresponding single-particle densities. From this point of view the preferable quantity to identify the breathing process is the variance of the coordinate of the center of mass

$$\text{var}[x^{(i)}(t)] = \sigma_{(i)}^2 = \int_{d_i}^{d_{i+1}} dx \rho_i(x) (x - X_{\text{cm}}^{(i)})^2. \quad (13)$$

Therefore, the breathing frequency of the middle well can be obtained from the spectrum of the second moment $\sigma_M^2(\omega) = \frac{1}{\pi} \int dt \sigma_M^2(t) e^{i\omega t}$. In figure 4(b) we observe a dominant frequency, located at $\omega \approx 60\Delta\omega$ (with $\Delta\omega = 2\pi/T$ and T being the total propagation period) which is approximately two times the trapping frequency of a harmonic approximation to a single well. This frequency depends only weakly on the interaction quench and it is related to the breathing frequency. There occur additional low frequency branches in figure 4(b) which are related e.g. to the tunneling dynamics.

3.1.2. The cradle mode induced by the over-barrier transport. For a qualitative description of the cradle mode one has to rely on the intrawell dynamics of $\delta\rho(x, t)$ for the left or right well as shown in figure 1. In particular, the generation of this mode is accompanied by a direct over-barrier transport as a consequence of the interaction quench. This results in a cradle mode which represents a dipole-like oscillation. In the following, let us first illustrate the main mechanism and then analyze in some detail the cradle mode.

Initially, in terms of its dominating spatial configuration our system consists of two bosons in the middle well and two others each of them localized in one of the outer wells. Then we perform a sudden change in the interaction strength which raises the energy as mentioned previously. As a consequence with high probability at least one particle from the central well gains enough energy to overcome the barrier (over-barrier transport), and directly moves to the outer wells where it performs an inelastic collision with the preexisting particle initially localized in the neighboring site. The two-particle collision leads to a cradle dynamics and to the dipole-like density oscillation as visualized in Figure 5. According to our simulations we observe significant over-barrier transport for $\delta g > 0.24$. This process is most significant for the first few

periods of the cradle motion as for later times due to inelastic collisions in the left well the atom loses part of its initial energy and can predominantly tunnel through the barrier.

Therefore, the cradle mode as a localized wave-packet oscillation can be produced via a variation in the respective interaction strength. Moreover as already mentioned, is reminiscent of the dipole oscillation in the one-body density evolution while a detailed analysis demonstrates a major difference between the two. Indeed, the cradle mode which is of two-body nature possesses two intrinsic frequencies that refer to the center of mass and the relative frame of the harmonic oscillator. As we prove in the appendix up to a good approximation this can be modeled by a coherent state of the center of mass and relative coordinates. Finally, note that during the evolution we can identify regions of bright and dark cradles which are associated with an enhanced or reduced tunneling of the density from the respective well (see also figure 1).

Especially, as the cradle mode breaks the local reflection symmetry of the one-body density in each well, we divide for a further investigation of this mode (neglecting the breathing mode) each well into two equal parts left and right of the center with corresponding integrated densities $\rho_{a,1}(t)$ and $\rho_{a,2}(t)$. Here the index a refers to the corresponding well, i.e. $a = L, M, R$ for the left, middle and right well respectively. In the following, we use as a measure of the intrawell wavepacket asymmetry (referring to the cradle motion) the quantity $\Delta\rho_a(t) = \rho_{a,1}(t) - \rho_{a,2}(t)$. Furthermore, in order to investigate the impact of different quenches on the system we compute the Fourier transformation of the quantity $\Delta\rho_a(\omega) = \frac{1}{\pi} \int dt \Delta\rho_a(t) e^{i\omega t}$ which will provide us with the evolution of the frequencies of the respective modes for different quench amplitudes. Figure 6(a) presents the resulting frequencies from the $\Delta\rho_L(\omega)$ versus the respective interaction quench δg for 110 different quenches from weak-to-strong interactions, where the amplitude δg varies from 0.04 to 4.5.

Firstly, from figure 6(a) we can identify one dominant branch which is insensitive to the quench amplitude and its frequency is that of the cradle mode. This branch corresponds to the cradle intrawell oscillation and will be referred to in the following as the cradle branch. A modulation of the frequency of the cradle motion can be achieved by tuning the barrier height, i.e. we can reduce its frequency using lower barriers and vice versa.

Besides the cradle branch, three interwell tunneling branches show up in the spectrum of $\Delta\rho_L(\omega)$ with a relatively weak amplitude. Among them we can distinguish the contribution of the highest frequency tunneling branch. The latter together with the branch of the cradle experience an avoided-crossing at $\delta g \simeq 2.8$ in the course of which both amplitudes are enhanced.

For a more detailed analysis of the above observations, let us assume that initially the state of the system in terms of the eigenstates of the final Hamiltonian is given by a linear superposition of the form $|\psi(0)\rangle = \sum_{i;\alpha;l} C_i^\alpha |l\rangle_{\alpha,l}$. Then at an arbitrary time instant t the expectation value of the

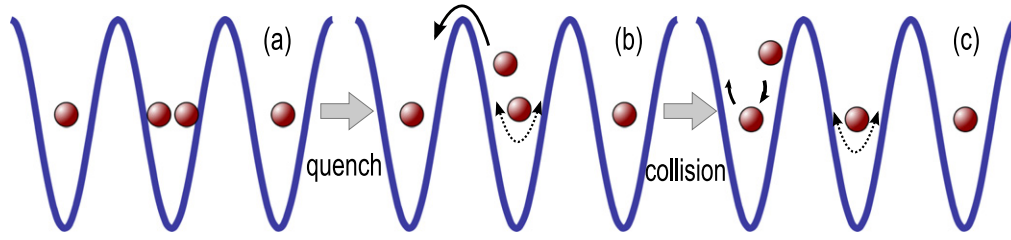


Figure 5. Visualization of the cradle process induced by the over-barrier transport. In this scenario, the system which is (a) initially in a superfluid ground state is subjected to an abrupt interaction quench. In this manner, a boson initiated in the middle well can overcome the barrier (b) and move to the neighboring well resulting in a cradle motion (c) due to the quench in the inter-particle repulsion.

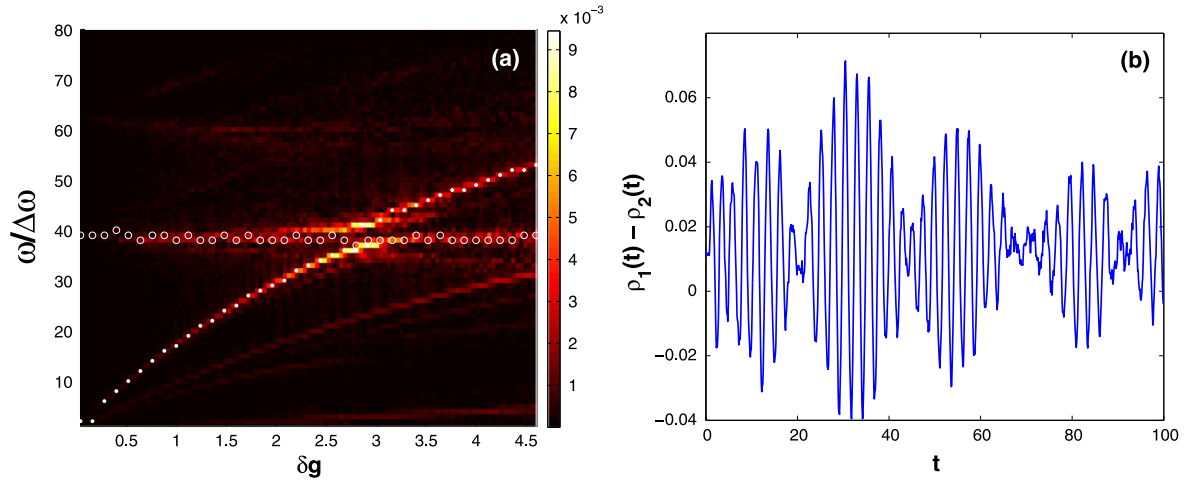


Figure 6. (a) Fourier spectrum as a function of the interaction quench of the intrawell asymmetry $\Delta\rho_L(\omega)$ for the left well (see text). The same spectrum can be obtained for the right well. The frequency units $\omega/\Delta\omega$ are normalized with $\Delta\omega = 2\pi/T$ and T being the respective propagation period. An avoided crossing takes place between the tunneling and the cradle modes where we observe an enhancement of the mode amplitudes at least for finite time propagation periods. The full white dots in the tunneling branch correspond to the intraband frequency $\Delta\omega_1$ between the states $|2, 1, 1\rangle_0$ and $|3, 0, 1\rangle_0$, whereas the empty circles in the branch of the cradle mode refer to the frequency $\Delta\omega_2$ for the states $|2, 1, 1\rangle_0$ and $|2, 1, 1\rangle_1$ describing the cradle-like process (see text). As a consequence we notice the occurrence of a beating (b) for the cradle in the region of the avoided crossing.

intrawell asymmetry operator can be expressed as

$$\begin{aligned} \langle \psi | \Delta\hat{\rho} | \psi \rangle = & \sum_{i;\alpha;l} |C_i^{\alpha;l}|^2 \langle i | \Delta\hat{\rho} | i \rangle_{\alpha;l} \\ & + 2 \sum_{i \neq j} \text{Re} \left(C_i^{\alpha;l} C_j^{\beta;l} \right)_{l;\alpha} \langle i | \Delta\hat{\rho} | j \rangle_{\beta;l} \\ & \times \cos \left[\left(\omega_i^{\alpha;l} - \omega_j^{\beta;l} \right) t \right]. \end{aligned} \quad (14)$$

Here, the first term refers to the average part whereas the second term demonstrates an oscillatory behaviour. In the following, we will concentrate on the oscillatory term of this expectation value which essentially describes the cradle motion. As also illustrated in the analytical expression for the cradle mode (see appendix) the dominant oscillation terms ${}_{\alpha;l} \langle i | \Delta\hat{\rho} | j \rangle_{\beta;l} \neq 0$ are given by the eigenstates $|i\rangle_{1;0}$ and $|i\rangle_{1;1}$ within which $|2, 1, 1\rangle_0$ and $|2, 1, 1\rangle_1$ significantly contribute respectively. Consequently, the corresponding oscillation frequency matches the energy difference between these eigenstates which is to a good approximation given by the energy difference ($\Delta\epsilon$) between $|2, 1, 1\rangle_0$ and $|2, 1, 1\rangle_1$. Meanwhile, $|2, 1, 1\rangle_1$ also contributes to the eigenstates $|i\rangle_{2;0}$ and $|i\rangle_{3;0}$ of the DP and T modes respectively thus

leading to a non-zero ${}_{1;0} \langle i | \Delta\hat{\rho} | j \rangle_{2(3);0} \neq 0$, and therefore to the observed tunneling branches. The above mechanism is resonant between $|2, 1, 1\rangle_0$ and $|2, 1, 1\rangle_1$ for a particular quench amplitude δg .

To verify our statements, let us calculate the number state energy differences between the aforementioned states and compare them with the eigenenergy difference in the full spectrum (figure 6(a)). In this manner we indeed find good agreement. We illustrate the δg -dependence of these frequencies in figure 6(a) with the white full dots and open circles on top of the exact avoided-crossing implying the reliability of our above statements. Indeed, we observe only very minor deviations of numerical ML-MCTDHB results and the description via equation (14). However, the intensities do differ significantly, see figure 6(a).

In conclusion, the avoided crossing and the accompanying enhancement indicate that the local intrawell dynamics can couple to the interwell dynamics. In turn, this induces a resonance between the two dynamical processes which can enhance the local and long-range dynamics. The fact that the cradle mode can be coupled with a mode of the interwell tunneling is remarkable. This gives rise to the possibility of controlling the ‘global dynamics’ by triggering the ‘local

dynamics'. Especially, we can tune the characteristic frequency of the tunneling mode to become resonant with the corresponding frequency of the cradle mode by means of tuning the quench amplitude. Increasing further the quench amplitude we can drive the system again out of resonance.

As a consequence of this avoided crossing the intrawell asymmetry $\Delta\rho$ dynamics features a beating, as shown in figure 6(b), which corresponds to two dominant frequencies in the $\rho_1(\omega) - \rho_2(\omega)$ spectrum. Indeed, let $\Delta\omega_1(\delta g) = E_\alpha - E_\beta$ be the frequency of the respective intraband tunneling ($|2, 1, 1\rangle_0 \rightarrow |3, 0, 1\rangle_0$). Assume further that $\Delta\omega_2(\delta g) = E_\gamma - E_\sigma$ refers to a frequency of a process that includes a ground and the first excited state of the SP mode taking into consideration that we refer to one of the outer wells (left or right) so we need two particles there. In this manner, there exists a region of critical quench amplitudes δg_{cr} which corresponds to the avoided crossing where $\Delta\omega_1(\delta g_{\text{cr}}) \approx \Delta\omega_2(\delta g_{\text{cr}})$ and the system features a degeneracy between the states $|3, 0, 1\rangle_0$ and $|2, 1, 1\rangle_1$.

From the above discussion, one can infer that a representative wavefunction describing the cradle process in terms of Fock states for the left well (and similarly for the right) can in principle be written as

$$|\varphi\rangle_L^{\text{cradle}} = C_0(\delta g, t)|2, 1, 1\rangle_0 + C_1(t)|2, 1, 1\rangle_1 \equiv |2, 1, 1\rangle_L^D, \quad (15)$$

where the coefficients C_0 and C_1 denote the probability amplitudes for the corresponding state. Note also that the amplitude of the zeroth state $|2, 1, 1\rangle_0$ depends on the quench while the one for the first-excited state $|2, 1, 1\rangle_1$ is essentially constant, i.e. independent of δg .

Taking advantage of the previous description we can construct an effective Hamiltonian for this process. Thus, if we denote by $\{|\vec{n}_0\rangle\}$ the corresponding truncated basis vectors, the effective Hamiltonian obtained from (1) in this subspace will be of the form

$$H_{\text{eff}} = \sum_{\vec{n}_0} \epsilon_{\vec{n}_0} |\vec{n}_0\rangle \langle \vec{n}_0| + \sum_{\vec{n}_0, \vec{m}_0} J_{\vec{n}_0, \vec{m}_0} |\vec{n}_0\rangle \langle \vec{m}_0|, \quad (16)$$

where $J_{\vec{n}_0, \vec{m}_0} = \langle \vec{n}_0 | H_{\text{eff}} | \vec{m}_0 \rangle$ is the effective tunneling amplitude and $\epsilon_{\vec{n}_0} = \langle \vec{n}_0 | H_{\text{eff}} | \vec{n}_0 \rangle$.

Therefore the representative subspace providing the mode-coupling within a minimal model consists of the states $|2, 1, 1\rangle_0, |3, 0, 1\rangle_0, |2, 1, 1\rangle_1$. In terms of the corresponding effective Hamiltonian the respective term for the cradle mode is $|2, 1, 1\rangle_1 \langle 2, 1, 1|$ whereas the term $|2, 1, 1\rangle_0 \langle 3, 0, 1|$ reflects the tunneling process. Thus from the Hamiltonian (16) one can realize a three-level system consisting of the states according to their energetical order: $|2, 1, 1\rangle_0 \equiv |1\rangle, |3, 0, 1\rangle_0 \equiv |2\rangle, |2, 1, 1\rangle_1 \equiv |3\rangle$. In this manner, we take into account an energy detuning Δ between the states $|2\rangle$ and $|3\rangle$ whereas due to the fact that the level $|1\rangle$ is weakly coupled with the other levels we neglect the respective tunneling amplitudes, i.e. $J_{12} = J_{13} = 0$. Therefore, we can reduce our problem to a two level system realizing the Hamiltonian $H_{\text{eff}} = \sum_{i=1}^3 \epsilon_i |i\rangle \langle i| + J_{23} |2\rangle \langle 3| + \text{h.c.}$ which

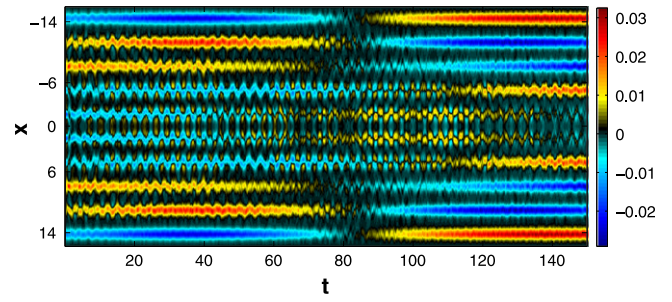


Figure 7. The fluctuations $\delta\rho(x, t)$ of the one-body density for five atoms in ten wells. Initially we observe the emergence of the over-barrier transport and subsequently the cradle and the tunneling modes. The setup is initially prepared in the superfluid ground state with $g_{in} = 0.05$ and is suddenly quenched with $\delta g = 4.0$.

is known to exhibit an avoided level crossing and can be solved analytically.

In the remaining part of this section, we proceed to the investigation of a system with filling factor $\nu < 1$ in order to generalize our findings. More precisely, among others we demonstrate that the cradle mode can also be found in the inner-well dynamics for a setup with ten wells, which reveals in particular that it is independent of the employed hard-wall boundaries.

3.2. Filling factor $\nu < 1$

Let us consider here the case of five bosons in a ten-well finite lattice. Concerning the ground state analysis with filling factor $\nu < 1$, the most important aspect is the spatial redistribution of the atoms as the interaction strength increases. The non-interacting ground state ($g = 0$) is the product of the single-particle eigenstates spreading across the entire lattice, while due to the hard-wall boundary conditions the two central wells of the potential are slightly more populated. As the repulsion increases within the weak interaction regime the atoms are pushed to the outer sites which gain and lose population in the course of increasing g , while the particle number fluctuations are more pronounced for the wells with a lower population [52]. It is also important to notice that in such a setup the one-body density will not become uniform even for strong interactions. In addition, the particle number fluctuations saturate to a relatively high value (for $g \approx 3.5$) in accordance with the existence of the delocalized phase. Also, in such a case of incommensurability due to the delocalized fraction of particles the long-range one-particle correlations do not vanish even for strong interactions.

In the following, we explore the dynamics following a sudden interaction quench at time $t = 0$ which is applied to the ground state in the weak interaction regime, $g_{in} = 0.05$. Figure 7 demonstrates the response of the system on the one-body level namely $\delta\rho(x, t)$ after a strong interaction quench $\delta g = 4.0$, from which we can easily identify the emergence of three modes. Initially we observe an over-barrier transport and then the cradle and the tunneling modes. The lattice symmetry (even number of wells) leads to the lack of the local breathing mode. Concerning the cradle mode, this would be a

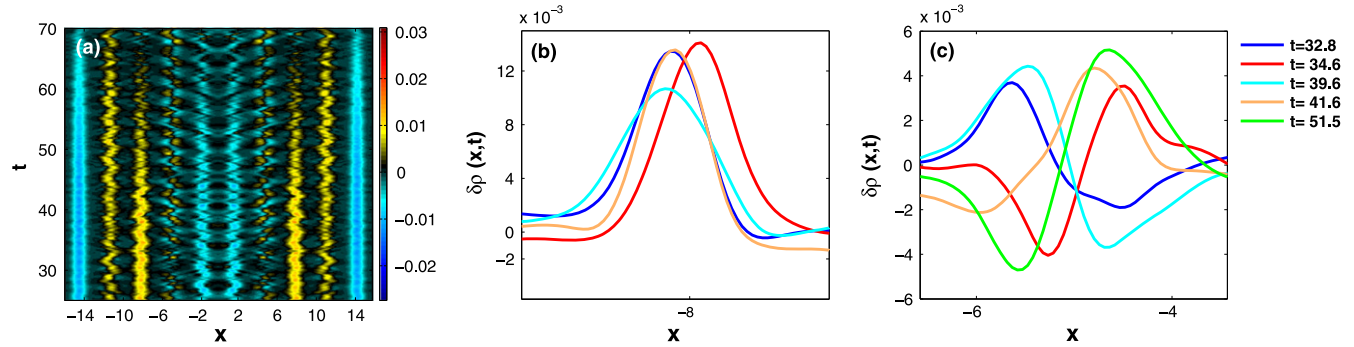


Figure 8. The response of the fluctuating part $\delta\rho(x, t)$ of the one-body density after an abrupt change in the inter-particle repulsion. The setup consists of five particles in ten wells and the initial state corresponds to interaction strength $g_{in} = 0.05$. Shown are $\delta\rho(x, t)$ for (a) a given time period of the cradle-like process for $\delta g = 2.4$ and the respective fluctuating one-body density profiles at different time instants for (b) the second well indicating the ground state of the cradle state and (c) the fourth well demonstrating the first-excited state of the cradle process. The nodal structure indicates the occupation of excited Wannier states in the respective well whereas the oscillatory behaviour visualizes the cradle process.

superposition of the states $|1, 1, 2, 0, 0, 0, 0, \dots\rangle_0 + \text{permut}$ and $|1, 1, 2, 0, 0, 0, 0, \dots\rangle_i + \text{permut}$ with $i \neq 0$, where *permut* stands for the spatial permutation of the occupations inside the ket vector. Here, one can consider the minimal subspace consisting of the above states with $i = 1$ in order to proceed in an effective approach as we did for the case $\nu > 1$.

Additionally, in order to visualize the cradle process from a one-body perspective we demonstrate in figure 8 for a specific quench $\delta g = 3.4$ the density fluctuations $\delta\rho(x, t)$ for different time instants. Figure 8(a) illustrates the evolution of the fluctuations for a specific time interval following up on the over-barrier transport, where we can observe the cradle process in each well. Subsequently, in figures 8(b) and (c) we show intersections of $\delta\rho(x, t)$ focussing on the second and the fourth wells in order to visualize the higher-band contributions to the mode. Indeed, in figure 8(b) we observe that the profile of the fluctuations corresponds to almost localized wave-packets inside the well which are spatially shifted with time. This process demonstrates the motion of the cradle and corresponds to the ground state of this mode. However, figure 8(c) illustrates the same profile $\delta\rho(x, t)$ but for a different well, where the appearance of at least one node indicates the occupation of the first excited Wannier state in the well. This behaviour together with the shift of the wave-packet indicates the first-excited state of the cradle mode.

Also, in the Fourier spectrum we can find the avoided-crossing between the cradle and the tunneling frequency where the critical region of quench amplitudes is $\delta g_{cr} = 4.2 - 4.3$ with equal cradle frequency as for the triple well case due to the same barrier height $V_0 = 4.5$. In turn, the avoided crossing here, if we refer to the third well, can be explained from the dominant number states $|1, 1, 2, 0, \dots\rangle_0$, $|1, 1, 2, 0, \dots\rangle_1$ for the cradle and $|1, 1, 2, 0, \dots\rangle_0$, $|1, 0, 3, 0, \dots\rangle_0$ for the tunneling process. Therefore, we can conclude that by tuning the interaction quench we can again realize a resonance between the aforementioned modes.

An important observation is that as we increase the interaction quench the tunneling process can be altered. Indeed, this behaviour can be attributed to the fact that the

higher the quench amplitude, the larger the energy of the system becomes. From this point of view we expect a strong link of the change of the spatial distribution of the atoms in the lattice and the quench amplitude. The above behaviour is a main characteristic of setups with filling factor $\nu < 1$ where on-site effects are not manifested. In order to quantify our arguments concerning the spatial redistribution process we will rely on an analysis of the one-body reduced density matrix $\rho^{(1)}(x, x'; t)$ of the dynamics provided by ML-MCTDHB. Its off-diagonal parts can be used as a measure of the coherence as they indicate off-diagonal long-range order in an infinite lattice. Although, for our finite setups we cannot conclude upon true off-diagonal long-range order this term refers to the appearance of short and long range one-body correlations. Thus, this quantity can be directly linked to the tunneling process. In figure 9, we depict the one-body density matrix for three different quenches namely $\delta g = 1.4, 2.6, 3.8$ at two different time instants $t_1 = 7.0$ (a), (b), (c) and $t_2 = 42.8$ (e), (f), (g) of the propagation in order to indicate the change in the tunneling process. The off-diagonal contributions fade out with increasing quench amplitude and a tendency for concentration close to the diagonal is observed at equal times which implies an alteration of the character of the tunneling process. In addition, the off-diagonal part cannot vanish completely even for strong quenches since the particles always remain delocalized. This is a main characteristic of incommensurate setups.

Going beyond the above examined finite setups, one can suggest a generalization for the wavefunction of the cradle state for a many-body system. Let N be the number of sites and n the total number of bosons. Then the corresponding generalized number state would be of the form $|n_1, n_2, \dots, n_N\rangle_i$ whereas the minimum representative wavefunction for the cradle that refers to the first well can be written as

$$|\psi\rangle^{\text{cradle}} = d_1(t)|2, n_2, \dots, n_N\rangle_0 + d_2(t)|2, n_2, \dots, n_N\rangle_1, \quad (17)$$

where $n_2 + n_3 + \dots + n_N = n - 2$ with $n > 2$ and d_1, d_2 denotes the amplitudes for each contribution in the above expansion. An additional constraint is that for an even number

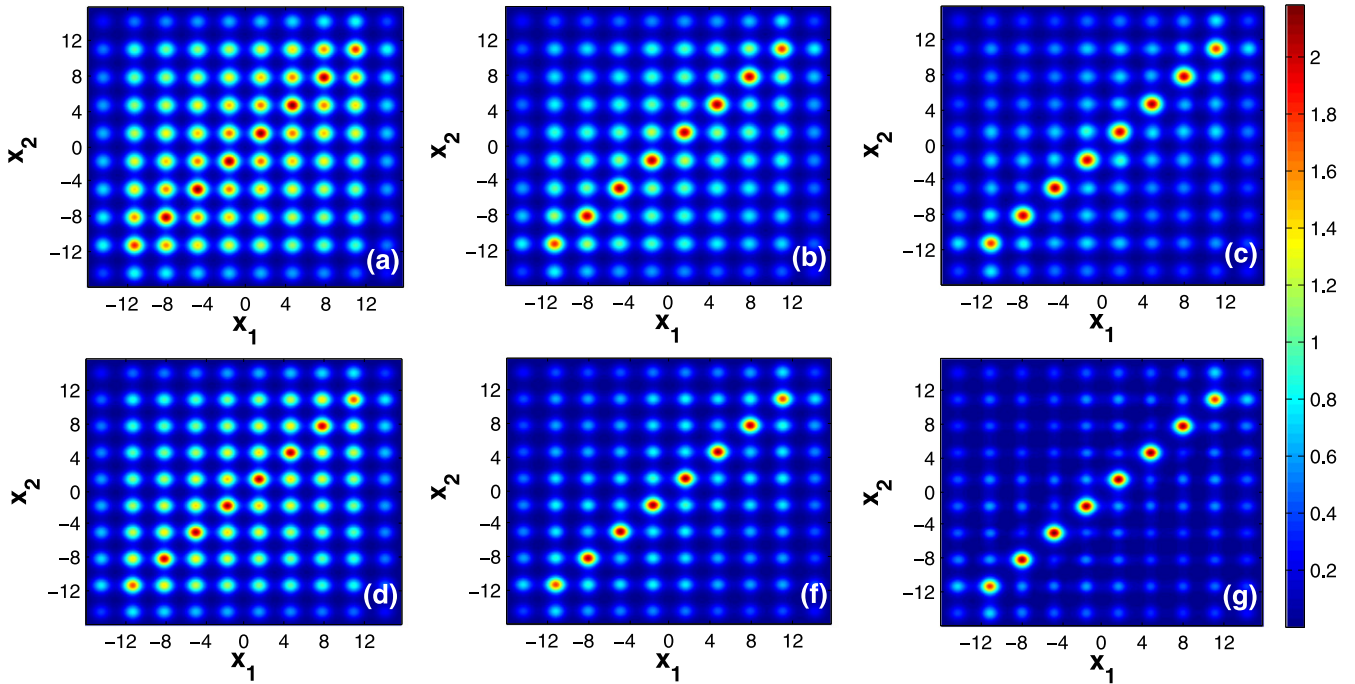


Figure 9. Off-diagonal one-body reduced density matrix $\rho^{(1)}(x, x'; t_1)$ for five particles in 10 wells for two different time instants $t_1 = 7.0$ (a), (b), (c) and $t_2 = 42.8$ (e), (f), (g) during the evolution. Shown are three values of the interaction quench (a), (d) $\delta g = 1.4$, (b), (f) $\delta g = 2.6$ and (c), (g) $\delta g = 3.8$. The elimination of the off-diagonal spots for strong quench amplitudes indicates the difference in the tunneling process.

of sites N this relation holds for all permutations, while for odd N the permutation that corresponds to a state with two particles in the middle well indicates the presence of the local breathing motion. The extension to cradles in the remaining wells is straightforward.

4. Summary and conclusions

We have explored the influence of sudden interaction quenches on small bosonic ensembles in finite 1D multi-well traps. In particular, we have mainly focussed on setups with incommensurate filling factors in order to avoid the suppression of tunneling due to MI phases for strong interactions. Starting from the SF regime, we change abruptly the effective coupling strength from weak to strong interactions. In this manner, we observe the emergence of tunneling, breathing and cradle processes. Furthermore for the explanation of the dynamical behaviour of our system in terms of a band structure we employ the concept of generalized multi-band Wannier number states which are meaningful for sufficiently large barrier heights V_0 . Although these have been constructed numerically, such a treatment is valid even in the strong interaction regime where perturbative methods fail.

The density-wave tunneling has been linked to an effective breathing of the ‘global wavepacket’ that refers to the instantaneous density distribution of the trap. The local breathing mode has been identified as an expansion and contraction dynamics of bosons in the individual wells. Moreover, in terms of a number state analysis of the observed dynamics it is necessary to include higher-band contributions

to describe it. On the other hand, the cradle process, as we have pointed out, exists in almost every site of the lattice and refers to a localized wave-packet oscillation. This mode is a consequence of the initial over-barrier transport of the particles from the central well to the outer ones due to the sudden import of energy into the system and the consequent inelastic collisions with the respective atoms in the outer sites. Therefore, we can describe this process via the coherent states of the harmonic oscillator referring here to the center of mass and the relative coordinate (see appendix). The aforementioned modes are always accompanied by a tunneling process which is mainly a lowest-band phenomenon. During the dynamical process, regions of density dips or dark cradles in the outer sites are accompanied by enhanced breathing dynamics on the middle site. Each of the above modes possesses different characteristic frequencies. In particular, we show that one can tune the frequency of the highest branch of the tunneling mode in resonance with the frequency of the cradle mode by varying the quench amplitude. In turn, this resonance is associated with an avoided crossing in the frequency spectrum of these modes resulting in an enhancement of both of them. In this case, the system features a dominant beating.

We have computed, the dominant Fock states in the expectation value of the asymmetry operator in order to describe the dynamics associated with the avoided-crossing. In this manner, we have found a representative cradle state which is a superposition of the first two bands, as well as the number state most responsible for the tunneling mode that couples with the cradle in the avoided crossing.

There are at least two ways that one might pursue as a follow-up direction. A first possible extension is to consider smooth time-dependent interaction quenches in order to unravel the behaviour of the system in such a non-equilibrium continuously driven case or to find similarities with the so-called Kibble–Zurek mechanism [59–64]. A second path in this direction would be the study of mixtures consisting of different bosonic species.

Acknowledgments

LC and PS gratefully acknowledge funding by the Deutsche Forschungsgemeinschaft (DFG) in the framework of the SFB 925 Light induced dynamics and control of correlated quantum systems. The authors would like to thank P Giannakeas, C Morfonios and S Krönke for fruitful discussions. We also thank J Stockhofe for a careful reading of the manuscript.

Appendix. Remarks on the cradle state

In this appendix we will briefly discuss the derivation of the cradle state. This state, as we have already mentioned in the main text, refers to an oscillation of two wavepackets of minimal uncertainty in a single well which we model as a harmonic trap. The creation of the two-particle cradle state in a single well corresponds to the collision between a particle injected to the well with another particle which is initially localized in the minimum of the well. We further model each particle as a localized one, where the first one is centered in the trap and the other one is displaced from the minimum by an amount x_0 . In this manner, taking advantage of the exactly solvable model of the harmonic oscillator, we can derive the initial wavefunction of the cradle state. In the following, we will use the natural units $m = \hbar = 1$. Due to the harmonic potential approximation we can separate the motion into the relative $X_r = (x_1 - x_2)/\sqrt{2}$ and center-of-mass $X_c = (x_1 + x_2)/\sqrt{2}$ coordinates. Adopting these coordinates the initial wavefunction reads

$$\psi_0(X_c, X_r; 0) = \left(\frac{\omega}{\pi}\right)^{1/2} e^{-\frac{\omega}{2}\left(X_c - \frac{x_0}{\sqrt{2}}\right)^2} \times \left(e^{-\frac{\omega}{2}\left(X_r + \frac{x_0}{\sqrt{2}}\right)^2} + e^{-\frac{\omega}{2}\left(X_r - \frac{x_0}{\sqrt{2}}\right)^2} \right). \quad (\text{A.1})$$

Thus, the intrawell oscillation can be separated into two parts: (a) the center-of-mass motion which is an effective one-body problem and (b) the relative motion that refers to a reduced two-body problem. Therefore, we can easily show that the wavefunction of the center-of-mass at any time $t > 0$ is described by

$$\psi(X_c; t) = \frac{1}{\sqrt{\sqrt{\pi}}} e^{-\frac{1}{2}(X_c - x_0 \cos \omega t) - i\left(\frac{\omega t}{2} + X_c x_0 \sin \omega t\right)}, \quad (\text{A.2})$$

which is the well-known coherent state solution of the harmonic oscillator. This wave-packet oscillates around the minimum of the potential in a simple harmonic trap without

changing its shape while it satisfies the minimum-uncertainty, i.e. $\Delta p \Delta x = \hbar/2$. On the other hand, the corresponding wavefunction of the relative frame reads

$$\psi(X_r; t) = \sum_n C_{2n} e^{i\omega_{2n} t} \varphi_{2n}, \quad (\text{A.3})$$

where φ_{2n} are the even eigenstates of the trapping potential $V(x) = \frac{1}{2}m\omega^2 x^2 + g\delta(x)$. These eigenfunctions are known as the Weber functions. Thus, we can conclude that the cradle state contains two characteristic frequencies: (a) the frequency $\omega_c = \omega$ that refers to the motion of the center-of-mass and (b) the frequency $\omega_r = \omega_{2n+2} - \omega_{2n} \approx 2\omega$ of the relative frame. The above comments lead us to the conclusion that the major difference between the cradle state that we have found here and the dipole state of a many-body system is that our state contains the two frequencies ω_c and ω_r while the many-body collective state has just one.

Comparing the analytical results with the exact numerical ones obtained from the ML-MCTDHB method we conclude that in our case we observe only the center-of-mass oscillation in the frequency spectrum. This is a consequence of the fact that the quantity $\Delta\rho = \rho_1 - \rho_2$ that we have used to measure the intrawell asymmetry can describe only the motion of the center-of-mass.

References

- [1] Bloch I 2005 *Nat. Phys.* **1** 23–30
- [2] Bloch I, Dalibard J and Zwerger W 2008 *Rev. Mod. Phys.* **80** 885
- [3] Pitaevskii L and Stringari S 2003 *Bose–Einstein Condensation* (Oxford: Oxford University Press)
- [4] Jaksch D and Zoller P 2005 *Ann. Phys.* **315** 52–79
- [5] Petsas K I, Coates A B and Grynberg G 1994 *Phys. Rev. A* **50** 5173
- [6] Grimm R, Weidemüller M and Ovchinnikov Y B 2000 *Adv. At. Mol. Opt. Phys.* **42** 95–170
- [7] Santos L, Baranov M A, Cirac J I, Everts H U, Fehrmann H and Lewenstein M 2004 *Phys. Rev. Lett.* **93** 030601
- [8] Kohler T, Goral K and Julienne P S 2006 *Rev. Mod. Phys.* **78** 1311
- [9] Chin C, Grimm R, Julienne P and Tiesinga E 2010 *Rev. Mod. Phys.* **82** 1225
- [10] Olshanii M 1998 *Phys. Rev. Lett.* **81** 938
- [11] Jaksch D, Bruder C, Cirac J I, Gardiner C W and Zoller P 1998 *Phys. Rev. Lett.* **81** 3108
- [12] Fisher M P, Weichman P B, Grinstein G and Fisher D S 1989 *Phys. Rev. B* **40** 546
- [13] Batrouni G G, Rousseau V, Scalettar R T, Rigol M, Muramatsu A, Denteneer P J H and Troyer M 2002 *Phys. Rev. Lett.* **89** 117203
- [14] Rey A M, Pupillo G, Clark C W and Williams C J 2005 *Phys. Rev. A* **72** 033616
- [15] Rigol M, Batrouni G G, Rousseau V G and Scalettar R T 2009 *Phys. Rev. A* **79** 053605
- [16] Lühmann D S, Bongs K and Pfannkuche D 2009 *J. Phys. B: At. Mol. Opt. Phys.* **42** 145305
- [17] Polkovnikov A, Sengupta K, Silva A and Vengalattore M 2011 *Rev. Mod. Phys.* **83** 863
- [18] Trotzky S, Chen Y A, Flesch A, McCulloch I P, Schollwöck U, Eisert J and Bloch I 2012 *Nat. Phys.* **8** 325–30

- [19] Rigol M, Dunjko V, Yurovsky V and Olshanii M 2007 *Phys. Rev. Lett.* **98** 050405
- [20] Kinoshita T, Wenger T and Weiss D S 2006 *Nature* **440** 900–3
- [21] Sadler L E, Higbie J M, Leslie S R, Vengalattore M and Stamper-Kurn D M 2006 *Nature* **443** 312–5
- [22] Langen T, Geiger R, Kuhnert M, Rauer B and Schmiedmayer J 2013 *Nature* **9** 640–3
- [23] Cheneau M, Barmettler P, Poletti D, Endres M, Schauß P, Fukuhara T, Gross C, Bloch I, Kollath C and Kuhr S 2012 *Nature* **481** 484–7
- [24] Greiner M, Mandel O, Hänsch T W and Bloch I 2002 *Nature* **419** 51–54
- [25] Hung C L, Gurarie V and Chin C 2013 *Science* **341** 1213–5
- [26] Cai Z, Duan L M and Wu C 2012 *Phys. Rev. A* **86** 051601
- [27] Cai Z and Wu C 2011 *Phys. Rev. A* **84** 033635
- [28] Kuklov A B 2006 *Phys. Rev. Lett.* **97** 110405
- [29] Köhl M, Günter K, Stöferle T, Moritz H and Esslinger T 2006 *J. Phys. B: At. Mol. Opt. Phys.* **39** S47
- [30] Müller T, Fölling S, Widera A and Bloch I 2007 *Phys. Rev. Lett.* **99** 200405
- [31] Wirth G, Ölschläger M and Hemmerich A 2010 *Nat. Phys.* **7** 147–53
- [32] Bakr W S, Preiss P M, Tai M E, Ma R, Simon J and Greiner M 2011 *Nature* **480** 500–3
- [33] Scarola V W and Sarma S D 2005 *Phys. Rev. Lett.* **95** 033003
- [34] Scarola V W, Demler E and Sarma S D 2006 *Phys. Rev. A* **73** 051601
- [35] Isacsson A and Girvin S M 2005 *Phys. Rev. A* **72** 053604
- [36] Chen G H and Wu Y S 2003 *Phys. Rev. A* **67** 013606
- [37] Altman E, Hofstetter W, Demler E and Lukin M D 2003 *New J. Phys.* **5** 113
- [38] Kuklov A, Prokof'ev N and Svistunov B 2004 *Phys. Rev. Lett.* **92** 050402
- [39] Cao L, Krönke S, Vendrell O and Schmelcher P 2013 *J. Chem. Phys.* **139** 134103
- [40] Krönke S, Cao L, Vendrell O and Schmelcher P 2013 *New J. Phys.* **15** 063018
- [41] Alon O E, Streltsov A I and Cederbaum L S 2007 *J. Chem. Phys.* **127** 154103
- [42] Streltsov A I, Alon O E and Cederbaum L S 2007 *Phys. Rev. Lett.* **99** 030402
- [43] Alon O E, Streltsov A I and Cederbaum L S 2008 *Phys. Rev. A* **77** 033613
- [44] Broeckhove J, Lathouwers L, Kesteloot E and van Leuven P 1988 *Chem. Phys. Lett.* **149** 547–50
- [45] Kim J I, Melezhik V S and Schmelcher P 2006 *Phys. Rev. Lett.* **97** 193203
- [46] Bergeman T, Moore M G and Olshanii M 2003 *Phys. Rev. Lett.* **91** 163201
- [47] Giannakeas P, Diakonou F K and Schmelcher P 2012 *Phys. Rev. A* **86** 042703
- [48] Beck M H, Jäckle A, Worth G A and Meyer H D 2000 *Phys. Rep.* **324** 1
- [49] McLachlan A D 1964 *Mol. Phys.* **8** 39–44
- [50] Frenkel J 1934 *Wave Mechanics* (Oxford: Oxford University Press) pp 423–28
- [51] Dirac P A 1930 *Proc. Camb. Phil. Soc.* vol 26 (Cambridge: Cambridge University Press) pp 376–85
- [52] Brouzos I, Zöllner S and Schmelcher P 2010 *Phys. Rev. A* **81** 053613
- [53] Tschischik W, Moessner R and Haque M 2013 *Phys. Rev. A* **88** 063636
- [54] Schmitz R, Krönke S, Cao L and Schmelcher P 2013 *Phys. Rev. A* **88** 043601
- [55] Abraham J W and Bonitz M 2014 *Contrib. Plasma Phys.* **54** 27–99
- [56] Bauch S, Balzer K, Henning C and Bonitz M 2009 *Phys. Rev. B* **80** 054515
- [57] Abraham J W, Balzer K, Hochstuhl D and Bonitz M 2012 *Phys. Rev. B* **86** 125112
- [58] Abraham J W, Bonitz M, McDonald C, Orlando G and Brabec T 2014 *New J. Phys.* **16** 013001
- [59] Kibble T W 1976 *J. Phys. A: Math. Gen.* **9** 1387
- [60] Zurek W H 1985 *Nature* **317** 505–8
- [61] Zurek W H, Dorner U and Zoller P 2005 *Phys. Rev. Lett.* **95** 105701
- [62] Dziarmaga J 2005 *Phys. Rev. Lett.* **95** 245701
- [63] Damski B 2005 *Phys. Rev. Lett.* **95** 035701
- [64] Damski B and Zurek W H 2006 *Phys. Rev. A* **73** 063405

**4.1.2 Negative-Quench-Induced Excitation Dynamics for Ultracold Bosons
in One-Dimensional Lattices**

Negative-quench-induced excitation dynamics for ultracold bosons in one-dimensional latticesS. I. Mistakidis,¹ L. Cao,^{1,2} and P. Schmelcher^{1,2}¹Zentrum für Optische Quantentechnologien, Universität Hamburg, Luruper Chaussee 149, 22761 Hamburg, Germany²Hamburg Centre for Ultrafast Imaging, Universität Hamburg, Luruper Chaussee 149, 22761 Hamburg, Germany

(Received 3 December 2014; revised manuscript received 6 February 2015; published 10 March 2015)

The nonequilibrium dynamics following a quench of strongly repulsive bosonic ensembles in one-dimensional finite lattices is investigated by employing interaction quenches and/or a ramp of the lattice potential. Both sudden and time-dependent quenches are analyzed in detail. For the case of interaction quenches we address the transition from the strong repulsive to the weakly interacting regime, suppressing in this manner the heating of the system. The excitation modes such as the cradle process and the local breathing mode are examined via local density observables. In particular, the cradle mode is inherently related to the initial delocalization and, following a negative interaction quench, can be excited only for incommensurate setups with filling larger than unity. Alternatively, a negative quench of the lattice depth which favors the spatial delocalization is used to access the cradle mode for setups with filling smaller than unity. Our results shed light on possible schemes to control the cradle and the breathing modes. Finally, employing the notion of fidelity we study the dynamical response of the system after a diabatic or adiabatic parameter modulation for short and long evolution times. The evolution of the system is obtained numerically using the *ab initio* multilayer multiconfiguration time-dependent Hartree method for bosons, which permits us to follow nonequilibrium dynamics including the corresponding investigation of higher-band effects.

DOI: [10.1103/PhysRevA.91.033611](https://doi.org/10.1103/PhysRevA.91.033611)

PACS number(s): 03.75.Lm, 67.85.Hj

I. INTRODUCTION

The realization of ultracold atomic gases has opened up exciting possibilities for the study of the nonequilibrium quantum dynamics of many-body systems [1,2]. The high degree of tunability and the good isolation from the environment renders ultracold gases a versatile tool to realize systems far from equilibrium as they remain coherent for sufficiently long time scales, allowing us to probe them experimentally [3–5]. In particular, the dynamical response of a closed quantum system can be investigated via a sudden change (i.e., a rapid perturbation compared to any other characteristic time scale of the system) of a Hamiltonian parameter called “quantum quench.” Typically, in such a scenario the many-body system is initially prepared in a characteristic state which is not an eigenstate of the perturbed Hamiltonian, and the subsequent time evolution is explored. In this way, important aspects can be studied such as the connection between the final and initial states or the emergence of a steady state [6]. Despite recent theoretical advances (see Ref. [2] and references therein), our understanding of strongly correlated quantum gases after a quench is far from complete and constitutes an appealing problem of modern quantum physics [7–13].

In a previous work [14] following a sudden raise of the interparticle repulsion (positive quench) we explored the dynamics of initially weakly interacting superfluids. As a consequence a cradle mode generated by the over-barrier transport of bosons residing in neighboring wells and caused by the import of energy to the system has been detected. This mode has further been identified as a two-body intrawell collision which was dipolelike [15,16]. In addition, a local-breathing mode reminiscent to the usual breathing mode in a harmonic trap [17–22] has been observed. The occurrence of a resonance between a tunneling mode and the cradle giving rise to the controllability between the inter- and intrawell dynamics has also been revealed. However, the above scenario can also

give rise to unavoidable heating processes, especially for large quench amplitudes. To overcome this ambiguity, i.e., minimize the heating [23], one can start from strong interparticle repulsion and quench back to weak interactions called negative interaction quench. A negative quench may lead to a drastically different dynamical behavior as the filling factor ν is expected to play a crucial role. Here an intriguing aspect would be to explore how the initial spatial configuration of the system, reflected by the corresponding filling factor, affects the system dynamics and as a consequence the generation of the emergent excited modes. This investigation will permit us to gain a deeper understanding of the on-site excited modes (especially the cradle mode), the underlying microscopic mechanisms, and their controllability in terms of the tunable parameters of the Hamiltonian.

In this work a systematic *ab initio* analysis of the nonequilibrium dynamics of strongly repulsive interacting bosons in one-dimensional (1D) lattices is carried out. To this end, we study from a few-body perspective the dynamical effects resulting from an abrupt quench or time-dependent modulation of a Hamiltonian parameter, focusing on the few-body collective excitations and the control of the dynamics. In particular, we start from strong repulsive interactions and perform negative quenches either on the interparticle repulsion or on the optical lattice depth. This permits us to unravel the transport properties and the emergent excitation modes, i.e., the local breathing and the cradle processes. Especially, for the case of a negative interaction quench we demonstrate that the cradle mode can be excited only for incommensurate setups with filling factor $\nu > 1$, exploiting the initial delocalization. On the other hand, for filling $\nu < 1$ in order to access this mode we use as a tool a barrier quench, thereby enforcing the over-barrier transport, which in turn can generate the cradle mode. The persistence of the dynamical modes for finite-ramp rates and long evolution times accessible in recent experiments

is also shown. The concept of fidelity is extensively applied in order to study the response of the quenched system and the transition from the diabatic to the adiabatic limit. The resulting nonperturbative dynamics (large quench) is explored using the recently developed numerically exact multilayer multiconfiguration time-dependent Hartree method for bosons [24,25] (ML-MCTDHB), which reduces in our case of a single species to MCTDHB [26,27].

This article is organized as follows. In Sec. II we explain the setup, the basic observables, and the representation of the wave function. Section III is devoted to a detailed study of the nonequilibrium quantum dynamics for two different quench protocols for incommensurable setups. We summarize and give an outlook in Sec. IV. Our computational method ML-MCTDHB is described in the Appendix.

II. THEORETICAL FRAMEWORK

We consider N identical bosons of mass m trapped within an n -site optical lattice along the x direction modeled by the potential $V_{\text{tr}}(x) = V_0 \sin^2(\frac{\pi x}{l})$ where l is the distance between successive potential minima, supplied with hard-wall boundaries at $x = \pm nl/2$. Transversally, the bosonic system is trapped by a uniform harmonic trapping potential with energy spacing $\hbar\omega_{\perp}$ and oscillator length $a_{\perp} = \sqrt{\hbar/m\omega_{\perp}}$, yielding an effective 1D coupling strength [28] $g_{1D} = \frac{2\hbar^2 a_0}{ma_{\perp}^2} (1 - \frac{|\xi(1/2)|a_0}{\sqrt{2}a_{\perp}})^{-1}$ for s -wave scattering, a_0 being the three-dimensional s -wave scattering length. The many-body Hamiltonian then reads

$$H = \sum_{i=1}^N -\frac{\hbar^2}{2m} \frac{\partial^2}{\partial x_i^2} + V_{\text{tr}}(x_i) + \sum_{i<j} V_{\text{int}}(x_i - x_j) \quad (1)$$

with the short-range contact interaction potential $V_{\text{int}}(x_i - x_j) = g_{1D} \delta(x_i - x_j)$ between bosons located at positions x_i, x_j represented by a Dirac δ function. The interaction strength can thereby be tuned by varying a_0 via a Feshbach resonance [28–31] or by altering the extent a_{\perp} of the transversal confinement [28,32,33]. In the following, for reasons of universality as well as of computational convenience, we shall use dimensionless units. To this end, the Hamiltonian (1) is rescaled in units of the recoil energy $E_r = \frac{\hbar^2 k^2}{2m}$. For our simulations we have used a sufficiently large lattice depth $V_0 = 6.0$, which is of the order of 3.0 to 4.0 E_r (depending on k), such that each well contains at least two localized single-particle Wannier states. The spatial and temporal coordinates are given in units of k^{-1} and $\hbar E_r^{-1}$, respectively.

A quench is performed by varying, abruptly or slowly, a parameter λ of the system (here the interaction strength g_{1D} or the lattice depth V_0 , or generally both) from an initial value $\lambda_0 = \lambda(t=0)$ to a final value λ_q according to a given scheme $\lambda(t)$. The ground state $|\Psi_0\rangle$ of the initial Hamiltonian $H_0 = H(\lambda_0)$ then evolves into $|\Psi_{\lambda}(t)\rangle = U_{\lambda}(t)|\Psi_0\rangle = \exp(-iH_{\lambda}t/\hbar)|\Psi_0\rangle$ at time t under the λ -quenched Hamiltonian. The overlap between the time-evolved states of the system in the presence (via U_{λ}) and absence (via $U_0 = e^{-iH_0 t/\hbar}$) of the quench,

$$f_{\lambda}(t) = \langle \Psi_0(t) | \Psi_{\lambda}(t) \rangle, \quad (2)$$

yields the fidelity (or Loschmidt echo [34])

$$F_{\lambda}(t) = |f_{\lambda}(t)|^2, \quad (3)$$

which provides a time-resolved measure for the effect of the quench on the system.

Using the ML-MCTDHB method outlined in the Appendix, we obtain the reduced one-body density matrix

$$\rho^{(1)}(x, x'; t) = \sum_{\alpha=0}^{M-1} n_{\alpha}(t) \varphi_{\alpha}(x, t) \varphi_{\alpha}^*(x', t) \quad (4)$$

in its (diagonal) spectral representation by natural orbitals $\varphi_{\alpha}(x, t)$, where $\alpha = 0, 1, \dots, M-1$ and M being the number of the considered orbitals. The corresponding population eigenvalues $n_{\alpha}(t) \in [0, 1]$ characterize the fragmentation of the system [35–38]: If there is only one macroscopically occupied orbital the system is said to be condensed, otherwise it is fragmented.

To explore the spatially resolved system dynamics we use the deviation

$$\delta\rho(x, t) = \rho(x, t) - \langle \rho(x) \rangle_T \quad (5)$$

of the one-body density $\rho(x, t) \equiv \rho^{(1)}(x, x; t)$ from its time average $\langle \rho(x) \rangle_T = \int_0^T dt \rho(x, t)/T$ over the considered time of propagation T . In this sense, we treat $\delta\rho(x, t)$ as the temporal fluctuation of the density around its “macroscopic” component along the lattice.

To incorporate the information of excited bands, we further analyze the dynamics by projecting the many-body wave function Ψ to the multiband Wannier number state basis as

$$|\Psi\rangle = \sum_{N, I} C_{N, I} |N_1 N_2 \dots N_n\rangle_I, \quad (6)$$

where $\{|N_1 N_2 \dots N_n\rangle_I\}$ is the multiband Wannier number state with $N = \sum_i N_i$, and I indexing the energetic (excitation) order [14]. This representation proves convenient for lattice systems when describing intraband and interband processes where the spatial localization of states plays a significant role and remains valid in the strong interaction regime for a sufficient number of supplied single-particle functions. Table I presents the excitation decomposition (the occupation of excited levels in each lattice site) of some number states frequently used in the following analysis.

TABLE I. Energetic decomposition of some frequently used number states for $n = 3$ lattice sites. The index I refers to the excitation order and is used as a compact notation instead of the detailed decomposition. Each element N^i in a decomposition refers to the i th energy level (superscript) of N noninteracting bosons in the corresponding site.

Index I	$ 2, 1, 1\rangle_I$	$ 1, 2, 1\rangle_I$
$I = 0$	$ 2^0, 1^0, 1^0\rangle$	$ 1^0, 2^0, 1^0\rangle$
$I = 1$	$ 1^0 \otimes 1^1, 1^0, 1^0\rangle$	$ 1^1, 2^0, 1^0\rangle$
$I = 2$	$ 2^0, 1^1, 1^0\rangle$	$ 1^0, 1^0 \otimes 1^1, 1^0\rangle$
$I = 3$	$ 2^0, 1^0, 1^2\rangle$	$ 1^0, 2^0, 1^1\rangle$
$I = 4$	$ 1^1 \otimes 1^2, 1^0, 1^0\rangle$	$ 1^2, 2^0, 1^0\rangle$
$I = 5$	$ 2^0, 1^2, 1^0\rangle$	$ 1^0, 1^0 \otimes 1^2, 1^0\rangle$

Note that the eigenstates can be ordered with respect to the single particle excitation and the spatial occupation of the particles. The eigenstates of the same category form an energetical band. Following this categorization we label the eigenstates as $|\zeta\rangle_{\alpha;I}$, where α and I denote the spatial occupation and energetical order, respectively [14]. For instance, $\alpha = 1$ refers to a single-pair state, $\alpha = 2$ to a two-pair state, etc., while ζ sorts the eigenstates within each category according to the eigenenergy.

III. QUENCH DYNAMICS

Before exploring the dynamics, some remarks concerning the ground states in the lattice for different filling factors $\nu = N/n$, where N denotes the particle number and n the number of the wells, are in order. For the commensurate case ($\nu = 1, 2, \dots$), concerning the ground state it is known that for increasing interparticle interaction one can realize the superfluid to the Mott insulator phase transition [39], which has been addressed extensively in the past few years. On the other hand, for a system with an incommensurate filling $\nu \neq 1, 2, \dots$ the main feature is the existence of a delocalized fraction of particles which forbids the occurrence of a Mott state. Here one can distinguish two physical situations: (1) the case $\nu > 1$ where on-site interaction effects prevail and (2) $\nu < 1$ in which the main concern is the redistribution of the particles over the sites as the interaction increases. This delocalized phase can also be explained in terms of the particle hole states using a strong coupling expansion [40,41].

In the present study we consider the quench dynamics for setups with site occupancy different from unity and therefore exclude the Mott state physics. We proceed with a short reference to the ground state and consequently analyze the dynamical process following each quench protocol.

A. Quench from strong to weak interactions for filling $\nu > 1$

In this section, we focus on a system consisting of four strongly interacting bosons in a triple well, i.e., with filling $\nu > 1$. The initial state before the quench is characterized by the competition between delocalization and on-site interaction effects. For strong interparticle repulsion, as we consider here ($g = 5.0$), this state can be interpreted as a fraction $N \bmod n$ of extra delocalized particles being on a commensurate background of localized particles. On the one-body level the on-site populations are quite similar, which can be attributed to the localized background, while their slight discrepancy is due to the nonuniform distribution of the extra particle in the first excited band. The latter prevents the formation of a perfect insulator phase even for strong repulsion. Our goal is to investigate the dynamical processes following a negative quench of the interaction strength, thereby approaching the weakly interacting regime. For an interaction quench protocol the final Hamiltonian H_f can be constructed as a sum of a part H_0 , which provides the prequenched state of the system and an additional part that denotes the perturbation

$$H_f(g_f, V) = H_0(g_{in}, V) + \frac{\delta g}{g_{in}} \sum_{k < j} V_{int}(x_k - x_j), \quad (7)$$

where g_{in} and g_f are the initial and final interaction strengths, respectively, and $\delta g = g_f - g_{in}$ is the quench amplitude focusing here on $\delta g < 0$ and $|\frac{\delta g}{g_{in}}| \sim 1$.

In the following subsections we first proceed with a brief fragmentation analysis inspired from the perspective of natural orbitals. Then we explain in some detail the response of the system and investigate each of the emergent normal modes consisting of a local breathing mode and a dipolelike cradle mode. A study for the manipulation of the excited modes and their presence for the case of a finite ramp is also provided.

1. Dynamical fragmentation

In this subsection, we analyze the role of dynamical fragmentation, i.e., the occurrence of more than one significantly occupied quantum states during the evolution, with a varying quench amplitude. Especially, the fragmentation in the nonequilibrium dynamics of trapped finite systems is known to depend strongly on the particle number [37,42], the interaction strength, and the evolution time. The spectral decomposition of the one-body reduced density matrix offers a measure of fragmentation via the populations $n_a(t)$ of the natural orbitals $\phi_a(t)$ [see Eq. (4)]. In particular, a nonfragmented (condensed) state requires the occupation of $n_0(t)$ to be close to unity [38].

Figure 1(a) shows the evolution of the natural populations of the three highest occupied natural orbitals for different quench amplitudes. The population of the first orbital $n_0(t)$ is always significantly below unity which confirms the fragmentation process, while the three most occupied natural orbitals add up to more than 90% of the population. Focusing on the first orbital we note that the temporal average of the fragmentation reduces as the quench amplitude increases and vice versa. Especially, for final interactions close to a noninteracting state we observe a tendency for a nonfragmented state at least for certain time periods. This constitutes a major difference between a negative and a positive interaction quench scenario. In the latter case the fragmentation process is enhanced for larger quench amplitudes, which can be attributed to the consequent raise of the interparticle repulsion during the process. However, here we face the inverse behavior because in the initial strongly interacting state the interparticle repulsion is already significant and tends to be reduced after the quench. Moreover, the second and third orbitals take on a compensatory role to the first, e.g., in the time periods where $n_0(t)$ is enhanced $n_1(t)$ and $n_2(t)$ are reduced. Finally, note that for smaller quenches the latter populations possess smaller amplitude oscillations, whereas strong quenches introduce large amplitude variations of the populations.

Figure 1(b) illustrates the response of the first natural orbital $\phi_0(x, t)$ at different time instants during the evolution after a quench to $g_f = 0.05$. As can be seen $\phi_0(x, t)$ exhibits spatial oscillations in the outer wells and an on-site broadening in the middle well which accounts for interaction effects. Another important remark is that the band structure is effectively reflected by the population of the natural orbitals; i.e., the orbitals $\phi_0(x)$, $\phi_1(x)$, and $\phi_2(x)$ correspond to the effective first single-particle band, orbitals $\phi_3(x)$, $\phi_4(x)$, and $\phi_5(x)$ to the second band, etc. Thus, the lowest orbital $\phi_0(x, t)$ follows quite well the evolution of the quenched one-body density.

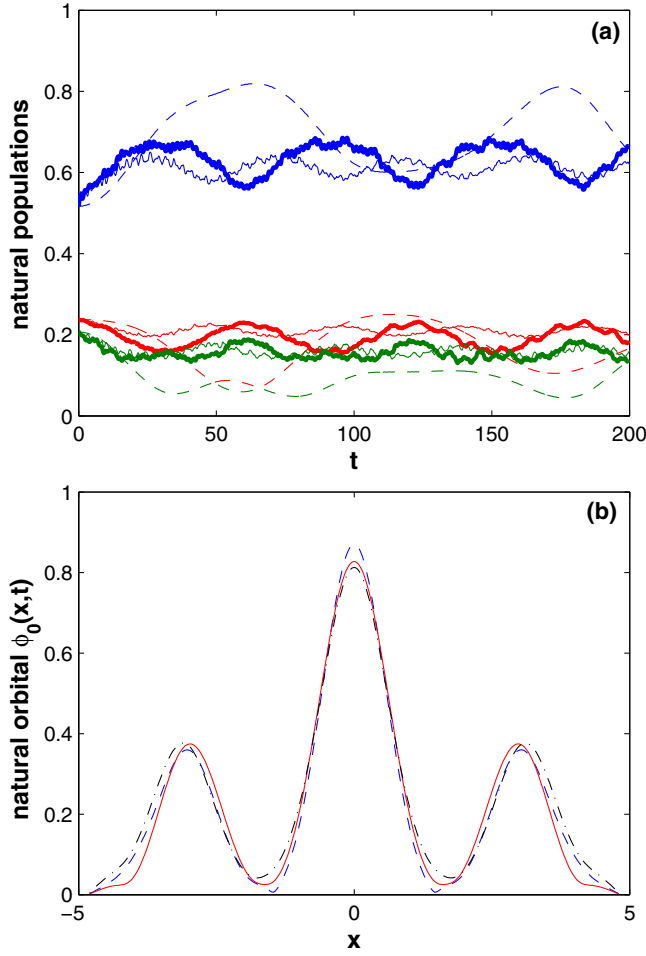


FIG. 1. (Color online) Fragmentation analysis for a system of four bosons in a triple well with $g_{in} = 5.0$. Shown are (a) the time evolution of the first three occupations $n_0(t)$ (upper panel blue lines), $n_1(t)$ (lower panel red lines), and $n_2(t)$ (lower panel green lines), for different quench amplitudes $\delta g = -4.9$ (dashed lines), $\delta g = -4.0$ (thick solid lines), and $\delta g = -2.5$ (thin solid lines). (b) Profiles of the lowest natural orbital $\phi_0(x,t)$ for a quench amplitude $\delta g = -4.95$ and different time instants during the evolution $t_1 = 0.9$ (blue dashed), $t_2 = 2.6$ (red solid), and $t_3 = 7.0$ (black dashed-dotted).

2. Dynamical response and transport properties

To investigate the dynamical response of the system we use the above-discussed fidelity $F_\lambda(t)$ [see Eq. (3)]. This quantity is shown in Fig. 2(a) as a function of the final interaction strength and the time. We mainly note the appearance of two different regions as a function of the quench amplitude. The first one corresponds to quenches from a strong repulsive state with $g_{in} = 5.0$ to intermediate interactions where $3.4 < g_f < 5.0$. Here the overlap during the dynamics is rather large with minimal percentage up to 85%, and therefore the system is quite insensitive to the quench. In the second region where the final state belongs to weak or even to the noninteracting regime, i.e., $0 < g_f < 3.4$, we observe the formation of an oscillatory pattern in the fidelity evolution. This pattern indicates the sensitivity of the system to these type of quenches, meaning that the system can be driven far from the initial state, while the minimal overlap for the extreme case of $g_f \rightarrow 0$ can even

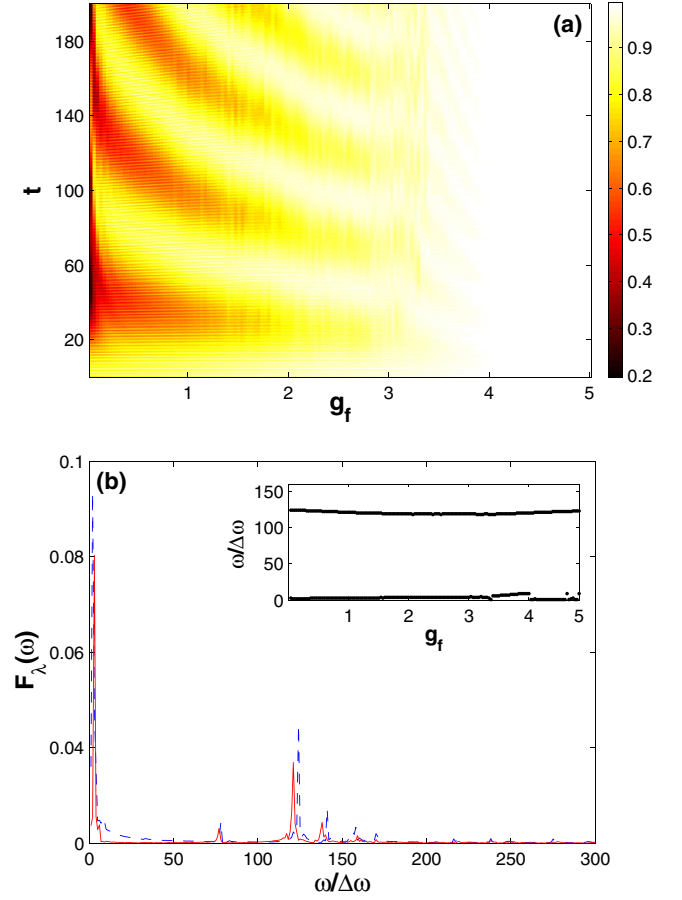


FIG. 2. (Color online) (a) Fidelity evolution following negative interaction quenches for $g_{in} = 5.0$. (b) The frequency spectrum of the fidelity for $g_f = 0.6$ (blue dashed) and $g_f = 1.0$ (red solid), which indicates the tunneling modes. The inset shows the dependence of each tunneling branch with respect to the final interaction strength after the quench. We incorporate 150 quenches in the range of $0 < g_f < 5.0$. The frequency units are normalized as $\omega/\Delta\omega$, with $\Delta\omega = 2\pi/T$ and T being the considered evolution time.

be of the order of 20%. The emergence of the above regions is universal in the system in the sense that it weakly depends on the height of the barrier. Thus, for an increasing barrier height the second region (larger quenches) will become narrower due to the larger potential energy, which inhibits a possible departure of the system from the initial state.

In order to identify the tunneling modes participating in the dynamics we use as a measure the spectrum of the fidelity $F_\lambda(\omega) = \frac{1}{\pi} \int dt F_\lambda(t) e^{i\omega t}$. Indeed, Fig. 2(b) shows $F_\lambda(\omega)$ for different final interactions where we observe two dominant tunneling peaks. To proceed with a more quantitative description of the tunneling dynamics we shall expand the wave function in terms of the number states. To this end, let $|\Psi(0)\rangle = \sum_{\zeta;\alpha;I} C_{\zeta}^{\alpha;I} |\zeta\rangle_{\alpha;I}$ be the initial wave function in terms of the eigenstates $|\zeta\rangle_{\alpha;I}$ of the final Hamiltonian [14]. Then the expansion of the fidelity reads

$$|\langle\Psi(0)|\Psi(t)\rangle|^2 = \sum_{\zeta_1;\alpha;I} |C_{\zeta_1}^{\alpha;I}|^4 + \sum_{\zeta_1,\zeta_2;\alpha,\beta;I} |C_{\zeta_1}^{\alpha;I}|^2 \times |C_{\zeta_2}^{\beta;I}|^2 \cos(\epsilon_{\zeta_1}^{\alpha;I} - \epsilon_{\zeta_2}^{\beta;I})t, \quad (8)$$

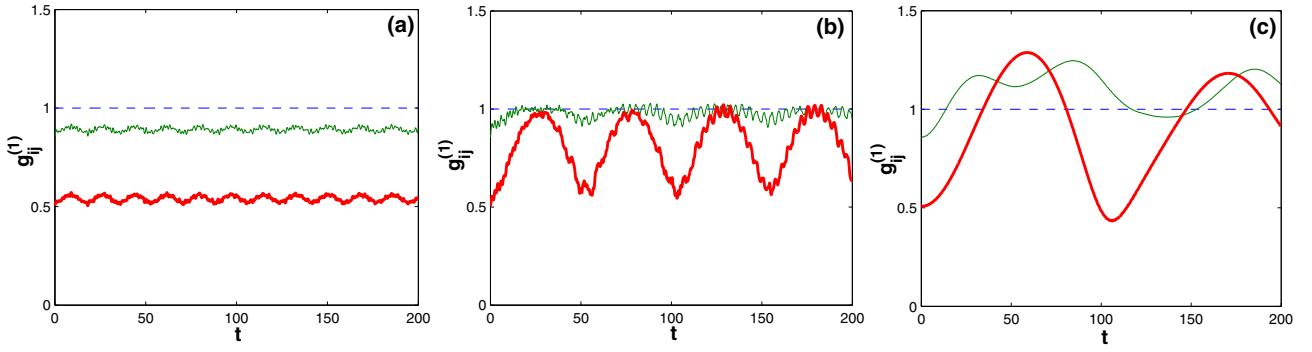


FIG. 3. (Color online) The time evolution of the normalized one-body correlation function $g_{ij}^{(1)}$ after various negative interaction quenches for $g_{in} = 5.0$. Shown are different components of the correlation function $g_{ij}^{(1)}$ with respect to the left well $g_{LL}^{(1)}$ (blue dashed line), $g_{LM}^{(1)}$ (green thin solid line), and $g_{LR}^{(1)}$ (red thick solid line) for final interactions (a) $g_f = 3.8$, (b) $g_f = 1.6$, and (c) $g_f = 0.05$.

where the second term contains the separate contributions from each tunneling branch. The indices α, β indicate a particular set of number states, ζ_i is the intrinsic index within each set, I denotes the respective energetical level, and $\epsilon_{\zeta_i}^{\alpha:I}$ refers to the eigenfrequency of a particular eigenstate. In particular, the first peak at frequency $\omega_1 \approx 3\Delta\omega$ (with $\Delta\omega = 2\pi/T$ and T denotes the propagation time) corresponds to the energy difference $\Delta\epsilon$ within the energetically lowest states of the single pair mode. Therefore the process corresponds to an intraband tunneling, e.g., from the state $|1,2,1\rangle_0$ to $|2,1,1\rangle_0$, etc. However, the second peak located at $\omega_2 \approx 125\Delta\omega$ refers to an interband transition between the states $|1,2,1\rangle_2$ and $|1,2,1\rangle_0$, which reflects the initial strongly correlated state. In the inset we present the δg dependence of the location of the aforementioned peaks. As can be seen, the two branches are mainly steady as a function of the interaction quench and their frequencies are constrained in a narrow band, while their amplitude (see main figure) reduces significantly for weak quenches.

In the course of the investigation of the tunneling dynamics one fundamental question that has to be addressed is how correlations propagate [43] in the quenched system. Here, in order to distinguish genuine interwell correlations from density oscillation effects we explore the response of the normalized single particle correlations $g_{ij}^{(1)}(t) = \langle \Psi | b_i b_j^\dagger | \Psi \rangle / \sqrt{\langle \Psi | b_i b_i^\dagger | \Psi \rangle \langle \Psi | b_j b_j^\dagger | \Psi \rangle}$ [44]. b_i^\dagger denotes the creation operator of a particle at the i th well, while the diagonal elements $g_{ii}^{(1)} = 1$ by definition. An important property of this function is that for $g_{ij}^{(1)} > 1$ (< 1) the corresponding detection probabilities at positions i and j are correlated (anticorrelated), while the case $g_{ij}^{(1)} = 1$ is referred to as fully first order coherent. Figures 3(a)–3(c) illustrate the time evolution for different components of the one-body correlations for various negative interaction quenches. As expected the diagonal terms correspond to a straight line at unity for all quench amplitudes. The nondiagonal terms $g_{ij}^{(1)}$, $i \neq j$ exhibit a nonvanishing oscillatory behavior, while for increasing quench amplitude a substantial built-up of correlations is observed. In particular, approaching the noninteracting limit $g_{LM}^{(1)}(t) > 1$ for most of the time, whereas $g_{LR}^{(1)}(t)$ oscillates around unity, indicating a transition from an anticorrelated to a correlated situation.

3. The local breathing mode

The breathing mode can be used in order to measure some key quantities of a trapped system such as its kinetic and interaction energy or the coupling strength [17,17–19]. It refers to an expansion and contraction of the bosonic cloud and can be excited either via a variation of the interparticle interaction or a modulation of the frequency of the trapping potential.

In a similar manner, our quenched system exhibits local breathing oscillations which are most prominent in the subsystem corresponding to the middle well. To detect the frequencies of this normal mode we examine the variance of the coordinate of the center of mass for a particular well. The center of mass for the i th well is defined as $X_{CM}^{(i)} = \int_{d_i}^{d_i'} dx (x - x_0^{(i)}) \rho_i(x) / \int_{d_i}^{d_i'} dx \rho_i(x)$. The index $i = R, M, L$ corresponds to the right, middle, and left well, respectively, while $x_0^{(i)}$ refers to the central point of the corresponding well. The limits of the wells are denoted by d_i and d_i' , whereas $\rho_i(x)$ is the respective single particle density. For the identification of the breathing process we define the operator of the second moment $\sigma_M^2(t) = \langle \Psi | (x - X_{CM}^{(i)})^2 | \Psi \rangle$. The latter serves as a measure for the instantaneous spreading of the cloud in the i th well and can also be used experimentally in order to probe the expansion velocity of a quenched condensate [5]. Then, if we connect the initial wave function with the eigenstates $|\zeta\rangle_{\alpha:I}$ of the final Hamiltonian H_f , we obtain

$$\begin{aligned} \sigma_M^2(t) = & \sum_{\alpha:\zeta_1:I} |C_{\zeta_1}^{\alpha:I}|^2 \langle \zeta_1 | (x - X_{CM}^{(i)})^2 | \zeta_1 \rangle_{\alpha:I} \\ & + 2 \sum_{\substack{\zeta_1 \neq \zeta_2 \\ \alpha:\zeta_1:I, \beta:\zeta_2:I}} \text{Re}(C_{\zeta_1}^{\beta:I*} C_{\zeta_2}^{\alpha:I}) \langle \zeta_1 | (x - X_{CM}^{(i)})^2 | \zeta_2 \rangle_{\alpha:I} \\ & \times \cos(\omega_{\zeta_1}^{\beta:I} - \omega_{\zeta_2}^{\alpha:I})t. \end{aligned} \quad (9)$$

To identify the frequencies of the local breathing mode, Fig. 4 shows the frequency spectrum of the second moment $\sigma_M^2(\omega) = \frac{1}{\pi} \int dt \sigma_M^2(t) e^{i\omega t}$, which refers to the middle well, for different quench amplitudes. Three main peaks can be observed. The lowest of these three peaks refers to a tunneling mode being identified from the energy difference within the energetically lowest states of the single pair mode. The appearance of this peak in the spectrum is due to the fact that the tunneling can

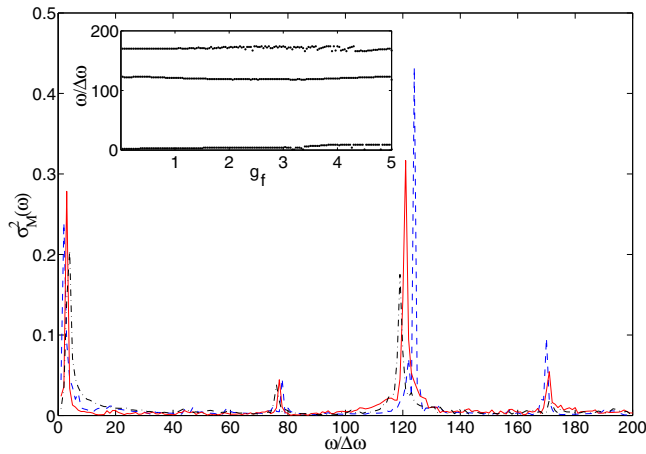


FIG. 4. (Color online) Fourier spectrum of the second moment $\sigma_M^2(\omega)$ for the local breathing mode for different quench amplitudes. The initial state corresponds to $g_{in} = 5.0$, and the final interactions are $g_f = 0.15$ (blue dashed), $g_f = 0.8$ (red solid), and $g_f = 1.7$ (black dashed-dotted). In the inset we show the δg dependence of each breathing branch, where we incorporate 150 quenches in the range of $0 < g_f < 5.0$. Note that the frequency units are normalized with respect to $\omega/\Delta\omega$, where $\Delta\omega = 2\pi/T$ and T is the respective propagation time.

induce a change in the width of the local wave packet. The second and third peaks refer to interband processes and are related to higher-band transitions. In particular, the second peak is located at $\omega_2 \approx 125\Delta\omega$ and refers to a transition from $|1,2,1\rangle_0$ to $|1,2,1\rangle_2$, whereas the third one with frequency $\omega_3 \approx 170\Delta\omega$ corresponds to a transition from $|1,2,1\rangle_0$ to $|1,2,1\rangle_5$. To illustrate the dependence of the above three peaks on the interaction quench we show in the inset the evolution of the location of each peak with respect to the final interaction strength g_f after the quench. We observe that the branches are more sensitive for a quench to $2.0 < g_f < 4.0$, otherwise they are mainly constant.

4. The cradle mode

This mode refers to a dipolelike oscillation generated via an over-barrier transport due to the initially delocalized state

between neighboring wells. In the present case it is induced by an interaction quench. From a one-body perspective the cradle mode is demonstrated by the inner well dynamics of the one-body density fluctuations $\delta\rho(x,t)$. Figure 5 shows the evolution of the system through the relative density after a sudden negative interaction quench from $g_{in} = 5.0$ to $g_f = 0.07$. The emergence of the cradle mode in the outer wells manifested as a dipolelike oscillation and the local breathing in the central well as a contraction and expansion dynamics is observed.

The initial spatial configuration due to the strong interparticle interaction corresponds to one localized boson in each well and one delocalized (over the three wells) energetically close to the barrier. In turn, the negative change in the interaction strength yields a high probability for the delocalized particle to overcome the barrier (over-barrier transport) and move to a neighboring well, where it performs a collision with the initially localized particle. This results in the cradlelike mode inside the respective neighboring site and refers to a localized wave-packet oscillation [14]. Note that the cradle is inherently related to the initial delocalization and after a negative interaction quench of a strongly correlated system can be excited only for incommensurate systems with filling factor $\nu > 1$. For other fillings it disappears and the consequent dynamics is dominated by the interwell tunneling.

In the following, in order to quantitatively examine the inner-well dynamics we proceed with a local density analysis. For that purpose we divide a particular well from the center into two equal sections with $\rho_{a,1}(t)$ and $\rho_{a,2}(t)$ being the respective integrated densities of the left and right parts during the evolution. The index $a = L, M, R$ stands for the left, middle, and right well, respectively. In this manner, a measure of the intrawell asymmetry which captures the cradle motion is the quantity $\Delta\rho_a(t) = \rho_{a,1}(t) - \rho_{a,2}(t)$. Figure 6(a) shows the frequency spectrum of the above quantity for the left well, i.e., $\Delta\rho_L(\omega) = \frac{1}{\pi} \int dt \Delta\rho_L(t) e^{i\omega t}$ for various negative interaction quenches. From the spectrum we can identify two dominant peaks located at the positions $\omega_2 \approx 79\Delta\omega$ and $\omega_3 \approx 125\Delta\omega$. These two frequency branches correspond to the cradle mode. In addition, we observe a low-frequency peak related to the interwell tunneling at frequency $\omega_1 \approx 3\Delta\omega$. The inset shows the δg dependence of the above three frequency peaks. The location of each branch remains essentially independent of

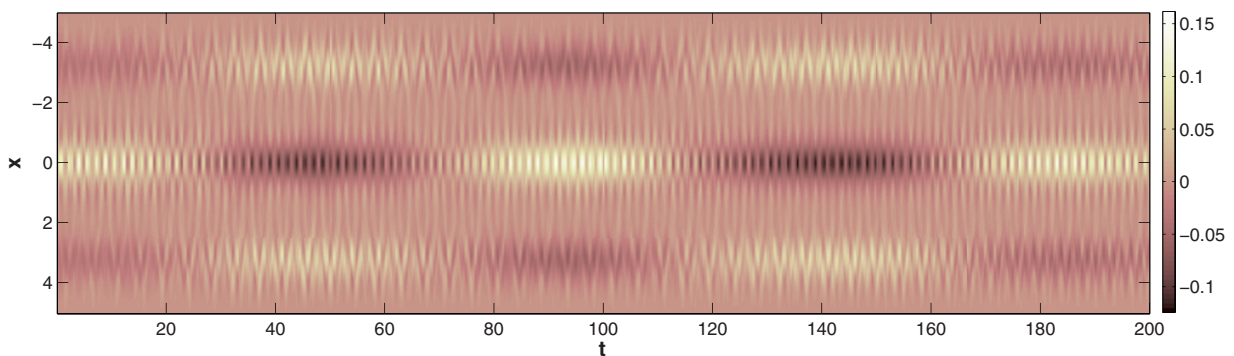


FIG. 5. (Color online) Space-time evolution of the fluctuations $\delta\rho(x,t)$ after a sudden negative quench of the interparticle repulsion from $g_{in} = 5.0$ to $g_f = 0.07$, thereby approaching the noninteracting limit. We observe the cradle mode in the left and right wells, the local breathing mode in the middle well and the interwell tunneling during the evolution.

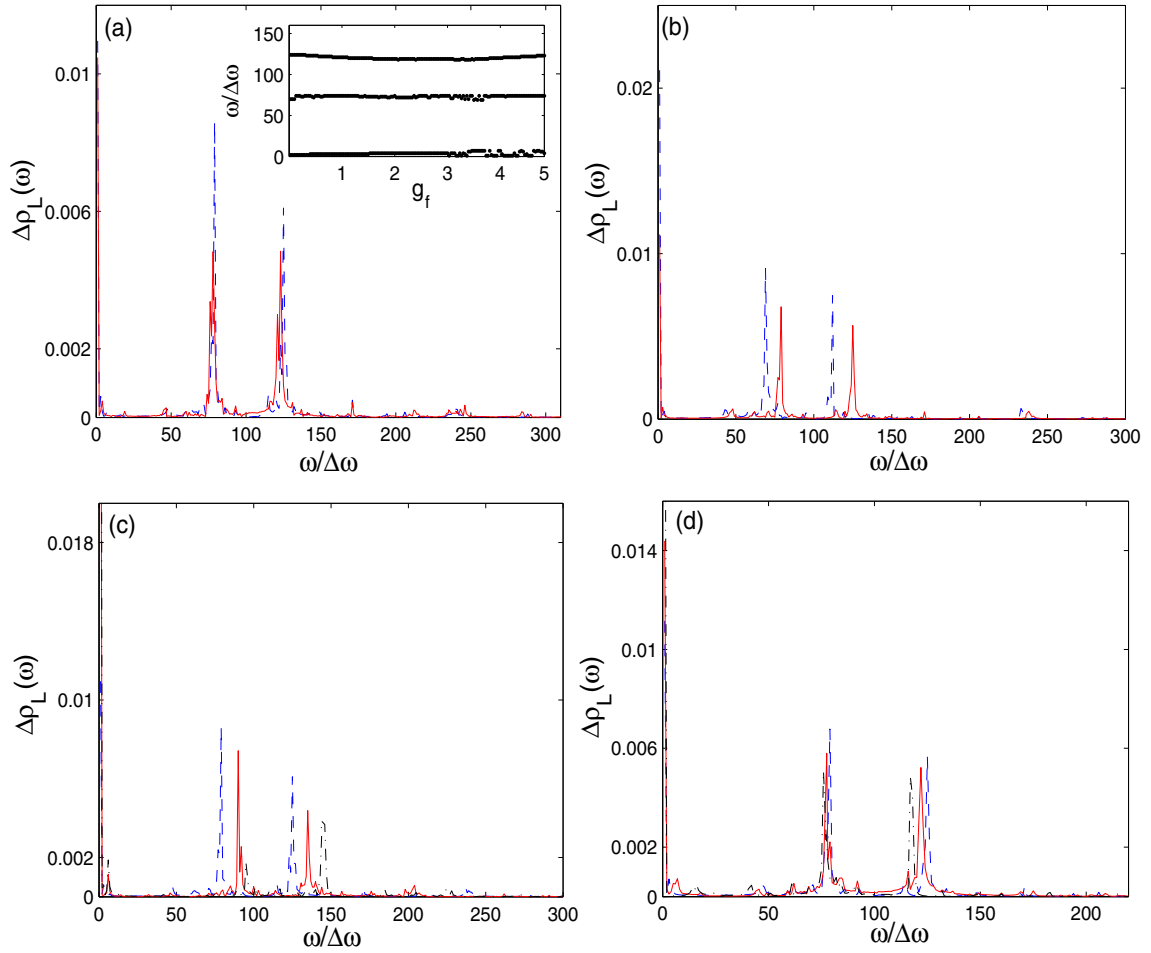


FIG. 6. (Color online) The frequency spectrum of the intrawell asymmetry $\Delta\rho_L(\omega)$. (a) The final state of the system is obtained after a sudden negative interaction quench from $g_{in} = 5.0$ to $g_f = 0.1$ (blue dashed) and $g_f = 0.45$ (red solid). The inset shows the evolution of each peak that refers to the cradle as a function of the quench amplitude (we incorporate 150 quenches in the range $0 < g_f < 5.0$). (b) The spectrum $\Delta\rho_L(\omega)$ for the same quench amplitude, $\delta g = -4.95$, and different barrier heights $V_0 = 5.5$ (red solid) and $V_0 = 3.5$ (blue dashed). (c) Sudden quench to $g_f = 0.4$ and the hard-wall boundaries located at $x_\sigma = \pm 3\pi/2$ (blue dashed), $x_\sigma = \pm 5\pi/4$ (red solid), and $x_\sigma = \pm 11\pi/8$ (black dashed-dotted). (d) It is illustrated the spectrum of $\Delta\rho_L(\omega)$ for an imposed harmonic trap $V_{\text{harm}} = 0$ (blue dashed), $V_{\text{harm}} = 0.02x^2$ (red solid), and $V_{\text{harm}} = 0.05x^2$ (black dashed-dotted) on top of the lattice. Finally, note that in each case we use normalized frequency units $\omega/\Delta\omega$, with $\Delta\omega = 2\pi/T$ and T being the respective evolution time.

the strength of the interaction quench, and it is therefore constrained to a corresponding narrow band.

To gain a deeper understanding of the cradle mode we again refer to a number state analysis and expand the initial state of the system in terms of the eigenstates of the final Hamiltonian as $|\Psi(0)\rangle = \sum_{\zeta;\alpha;I} C_\zeta^{\alpha;I} |\zeta\rangle_{\alpha;I}$. Then the expectation value of the asymmetry operator reads

$$\begin{aligned} \langle \Psi | \Delta \hat{\rho}(t) | \Psi \rangle &= \sum_{\zeta_1; \alpha; I} |C_{\zeta_1}^{\alpha; I}|^2 {}_{I; \alpha} \langle \zeta_1 | \Delta \hat{\rho} | \zeta_1 \rangle_{\alpha; I} \\ &+ 2 \sum_{\zeta_1 \neq \zeta_2} \text{Re}(C_{\zeta_1}^{\alpha; I*} C_{\zeta_2}^{\beta; I}) {}_{I; \alpha} \langle \zeta_1 | \Delta \hat{\rho} | \zeta_2 \rangle_{\beta; I} \\ &\times \cos[(\omega_{\zeta_1}^{\alpha; I} - \omega_{\zeta_2}^{\beta; I})t]. \end{aligned} \quad (10)$$

Here the terms of the second sum in the above expression which demonstrate an oscillatory behavior describe the cradle mode. Therefore, we need to detect the eigenstates $(|\zeta\rangle_{\alpha; I})$

of the dominant oscillation terms, i.e., ${}_{\alpha; I} \langle \zeta | \Delta \hat{\rho} | \zeta \rangle_{\beta; I} \neq 0$. A direct numerical analysis indicates that the respective eigenstates are $|\zeta\rangle_{1;0}$, $|\zeta\rangle_{1;1}$, $|\zeta\rangle_{1;2}$, whereas the corresponding significantly contributing number states are $|2, 1, 1\rangle_0$, $|2, 1, 1\rangle_1$, and $|2, 1, 1\rangle_4$ due to the fact that the corresponding oscillation frequency matches the energy difference between these eigenstates.

Let us now investigate possible control protocols of the cradle mode via a modulation of its frequency by means of a varying potential parameter or via an external forcing. An efficient way to manipulate the frequency is to tune the height of the potential barriers. In this way, the cradle frequency can be reduced using a more shallow lattice (thereby making the excitation of the cradle mode more easy). Indeed, within the harmonic approximation it can be easily shown that the effective frequencies for two lattices with different potential depths $V_{0;1}$ and $V_{0;2}$, respectively, obey $\omega_{\text{eff};1} = (V_{0;1}/V_{0;2})^{1/4} \omega_{\text{eff};2}$. This situation is illustrated

in Fig. 6(b) where the frequency spectrum of the inner-well asymmetry with the same quench amplitude but different barrier heights $V_0 = 5.5$ (red solid) and $V_0 = 3.5$ (blue dashed) is shown. We observe a negative shift of each frequency peak for a decreasing lattice depth which confirms our previous arguments. Alternatively, a similar manipulation of the cradle frequency can be achieved by comparing lattices with the same height of the potential barrier but different frequencies. Then, the respective effective frequencies are related via $\omega_{\text{eff},1} = (l_2/l_1)^{1/2}\omega_{\text{eff},2}$, where l is the distance between two successive potential minima.

In a similar manner, one can pose the question how the cradle mode frequency depends on g_{in} for fixed g_f . According to our simulations (omitted here for brevity) each peak remains essentially unchanged, indicating that the system does not keep any memory from the particular strongly correlated initial microscopic configuration.

A further question is to ask for the impact of the boundary conditions. Hence, we assume a fixed height for the barrier but changing the position of the hard wall boundary conditions. Then we expect that as the wall is closer to the center of the right or left well the cradle would be more enhanced because effectively the frequency of the local harmonic oscillator is larger and so the period of the cradle reduces. Indeed, Fig. 6(c) illustrates for the same quench amplitude the Fourier spectrum of the intrawell asymmetry $\Delta\rho_L(\omega)$ imposing the hard-wall boundaries at different positions, namely, at $x_\sigma = \pm 3\pi/2$ (blue dashed), $x_\sigma = \pm 5\pi/4$ (red solid), and $x_\sigma = \pm 11\pi/8$ (black dashed-dotted). The frequency peaks of the cradle mode are shifted by a positive value for a closer to the center hard wall. As a final attempt we impose a harmonic trap on top of the triple well, which increases the potential energy of the edge wells. Then the on-site energy of the Wannier states at the edges becomes larger than that (of the same degree of energetical excitation) in the central well. This in turn renders the initialization of the cradle mode more difficult, and for strong superimposed harmonic traps its excitation for a fixed quench amplitude becomes impossible. Accordingly, Fig. 6(d) shows a scenario with the same quench amplitude but different superimposed harmonic traps. We observe negative variations and a reduction of the intensity of each peak for a stronger harmonic trap, thereby confirming our above discussion.

In the next subsection we explore the excitation modes induced by a time-dependent modulation of the interaction strength and establish their presence also for this case.

5. Finite ramping

The present subsection is devoted to the study of the dynamics induced by time-dependent interaction quenches with a finite ramp rate. In particular, we attempt to investigate quenches with the same amplitude but evolving on different time scales, in order to gain a further insight into the dynamical response of the system with relevance to the experimentally occurring time scales. To this end, let us adopt a time-dependent quench scenario of the form

$$g(t; \tau) = g_{in} + (g_f - g_{in}) \tanh(t/\tau). \quad (11)$$

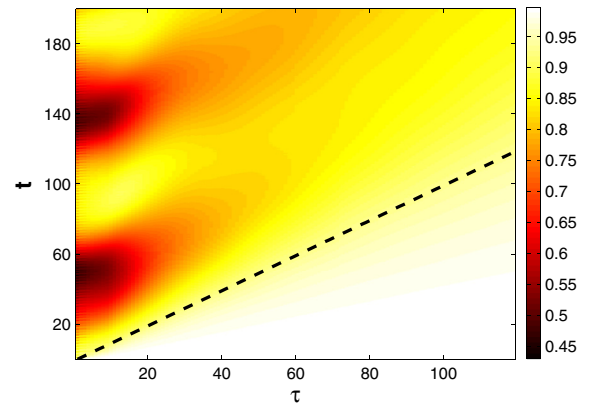


FIG. 7. (Color online) Fidelity evolution for $g_{in} = 5.0$ and $g_f = 0.1$ as a function of the ramp rate τ measured in units of the Heisenberg time τ_H (see text). The black dotted line correspond to the situation with $t = \tau$.

Here g_{in}, g_f are the interaction strength for the initial and final state respectively, whereas τ denotes the finite ramp rate of the performed quench. Focusing now on a strong nonequilibrium postquench state with $g_f = 0.1$, Fig. 7 shows the dynamical crossover, for finite evolution times, from an abrupt to an adiabatic interaction modulation for increasing ramp rates τ . To interpret the resulting behavior on a relevant time scale we define the Heisenberg time $\tau_H \sim 1/\Delta\epsilon(\delta g)$, where $\Delta\epsilon(\delta g) = \epsilon(g_{in}) - \epsilon(g_f)$ refers to the energy difference between the ground state of the system before and after a sudden interaction quench. As is shown for times $t < \tau$ (region under the black dotted line in Fig. 7) the system essentially remains in the initial ground state of the unperturbed Hamiltonian. On the other hand, in the region with $t > \tau$, which spreads for decreasing τ (thereby approaching the sudden quench), the system starts to significantly depart from the initial state. Remarkably enough for $\tau < 30\tau_H$ we observe the appearance of black lobes (overlap of the order of 40%) during the evolution, which indicate the persistence of the excitation modes in this region. For $\tau > 30\tau_H$ we have a transition to a smoother dynamical departure of the system from the initial state and as a consequence the elimination of the excitation modes. In particular, for $\tau > 85\tau_H$ the Hamiltonian changes sufficiently slowly, i.e., the system tends to remain in the instantaneous ground state, and therefore the modulation is almost adiabatic for the whole evolution time. For a smaller quench the adiabatic regime can be reached for sufficiently smaller time scales due to the reduced impact of the quench to the system. These statements are also valid for a linear quench protocol of the form $g(t; \tau) = g_{in} + (g_f - g_{in})t/\tau$ for $t \leq \tau$, and $g(t; \tau) = g_f$ for $t > \tau$.

As a next step we study the effect of the time-dependent interaction quench on the excitation modes, i.e., the breathing and cradle processes. To give further insight in the overall nonequilibrium process, Fig. 8 illustrates the evolution of $\delta\rho(x, t)$, for the same relevant interactions as in Fig. 5 where we considered a sudden quench, implementing now the time-dependent scenario of Eq. (11) with a finite rate $\tau = 0.8\tau_H$. The above-discussed modes still persist but with reduced intensity, which is larger when the quench is faster.

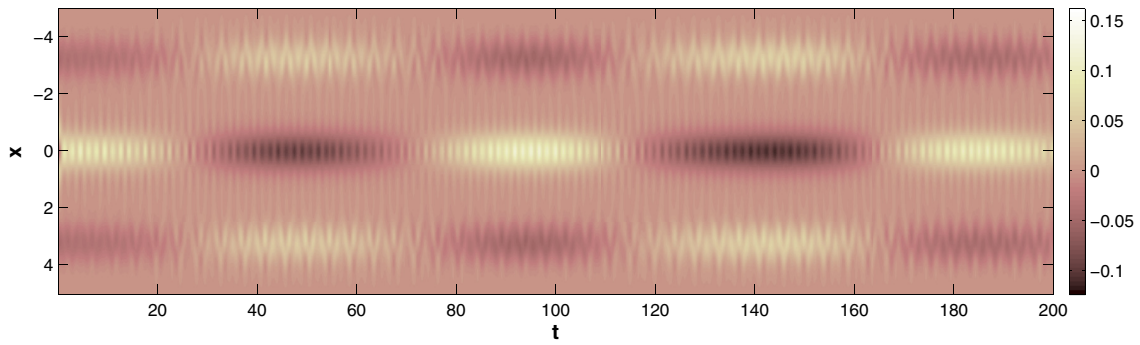


FIG. 8. (Color online) The fluctuations $\delta\rho(x,t)$ of the one-body density caused by a negative time-dependent quench of the interparticle repulsion to $g_f = 0.07$ ($g_{in} = 5.0$) with a finite ramp rate $\tau = 0.8\tau_H$. For a direct comparison the quench parameters, here, have been chosen similar with Fig. 5, which refers to the respective sudden quench scenario. We observe that the cradle mode in the left and right wells, the local breathing mode in the middle well, and the interwell tunneling during the evolution persist.

According to this let us investigate how one can manipulate the local breathing mode via the quench rate τ . Figure 9(a) shows the frequency spectrum of the local breathing mode

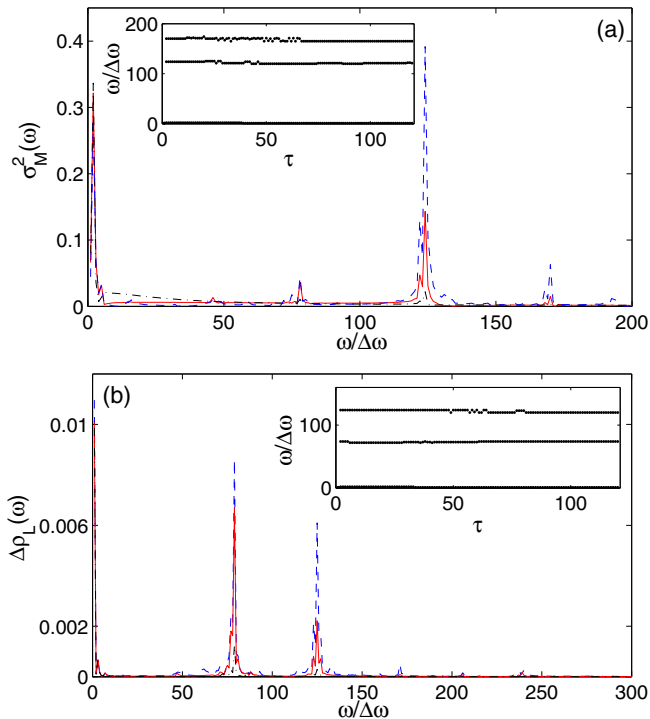


FIG. 9. (Color online) (a) Frequency spectrum of the variance $\sigma_M^2(\omega)$ for time-dependent quenches of the form of Eq. (11) with final interaction $g_f = 0.1$ and rates $\tau = 0\tau_H$ (blue dashed), $\tau = 0.8\tau_H$ (red solid), and $\tau = 3.0\tau_H$ (black dashed-dotted). The inset shows each branch of the local breathing mode as a function of the quench rate τ (we incorporate 160 different rates in the range $0 < \tau < 120$). In (b) we present the spectrum of the intrawell asymmetry $\Delta\rho_L(\omega)$ for a time-dependent scenario with quench amplitude $\delta g = -4.90$ and rates $\tau = 0\tau_H$ (blue dashed), $\tau = 0.8\tau_H$ (red solid), and $\tau = 3.0\tau_H$ (black dashed-dotted). The inset demonstrates the dependence of each branch of the cradle mode as a function of the quench rate τ . Finally, note that we have used normalized frequency units $\omega/\Delta\omega$, with $\Delta\omega = 2\pi/T$ and T being the respective evolution time.

obtained for the same amplitude $\delta g = -4.9$ and different quench rates τ . As it can be seen the position of each peak remains the same but its intensity decreases significantly for larger rates. To further probe the position of each branch with respect to the quench rate τ we present in the inset the τ dependence of each peak (without taking into account its intensity). It is obvious that each branch is quite insensitive to the interaction quench while in terms of its intensity [Fig. 9(a)], one can infer that by considering larger rates can gradually obliterate each frequency branch, i.e., for a faster quench the spectrum is more rich. Especially, one finds that for $\tau > 30\tau_H$ this mode can essentially be eliminated, which means that the intensity of each peak is negligible (in our case $\leq 10^{-5}$).

Finally, we study the effect of the finite ramping on the cradle mode. Figure 9(b) presents the spectrum of the intrawell asymmetry $\Delta\rho_L(\omega)$ for an abrupt quench in the interparticle repulsion and two different quenches obeying the above time-dependent law with different rates τ but same final interaction as in the abrupt case. Moreover, in the inset we demonstrate the evolution of each peak (without taking into account its intensity) as a function of the ramp rate τ . We observe that for larger rates τ the location of each frequency peak remains essentially the same (inset) but the respective amplitude tends to decrease, while for $\tau > 9.0\tau_H$ the third peak that refers to the second excited state in the left well has already been eliminated. Increasing further the rate $\tau > 30\tau_H$ one can eliminate the cradle (intensity $\leq 10^{-5}$) approaching the adiabatic region as also shown in Fig. 7.

In the following section we turn to the study of the quench dynamics induced by a modulation of the optical lattice depth examining its dynamical response and the consequent excitation modes.

B. Quench of the optical potential depth for filling $\nu < 1$

Here we consider a quench protocol which consists of a ramp-down of the optical potential depth, thereby driving the system to a region where the kinetic energy of the atoms dominates in comparison to the potential energy. As we shall demonstrate, following this protocol one can excite the cradle mode also for setups with filling $\nu < 1$. The system consists of five particles in an eight-well setup, but our conclusions can be easily generalized for arbitrary filling factors. To be

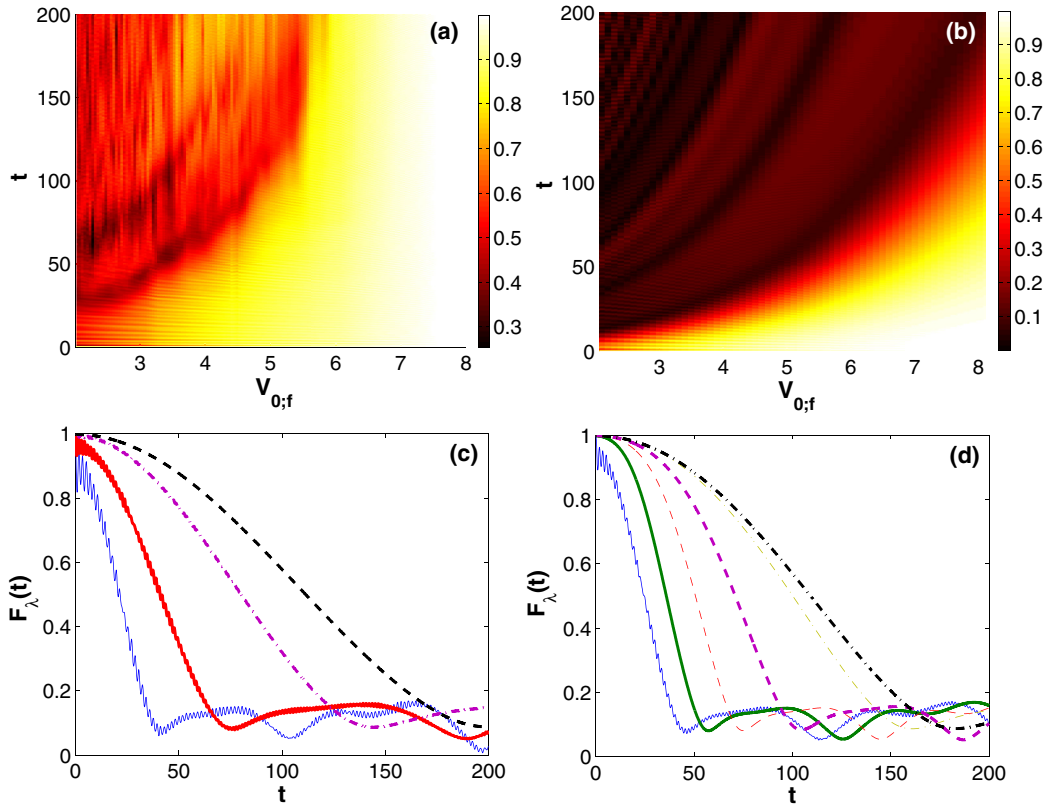


FIG. 10. (Color online) (a) Fidelity evolution as a function of different sudden negative quenches of the optical lattice depth. The system consists of five strongly interacting bosons ($g = 5.0$) in an eight-well potential with $V_{0;in} = 8.0$. (b) Same but for different quenches of the lattice depth and a simultaneous interaction quench to $g_f = 0.02$. (c) Profiles of the fidelity evolution for different quench amplitudes $\delta V_0 = -3.8$ (blue thin solid), $\delta V_0 = -2.5$ (red thick solid), $\delta V_0 = -0.9$ (magenta dashed-dotted), $\delta V_0 = -0.2$ (black dashed), and a simultaneous interaction quench to $g_f = 0.02$. In (d) we present profiles of the fidelity following a negative time-dependent quench of the potential depth to $V_{0,f} = 4.0$ with different ramp rates $\tau = 0.4\tau_H$ (blue thin solid), $\tau = 15.0\tau_H$ (green thick solid), $\tau = 40.0\tau_H$ (red thin dashed), $\tau = 100.0\tau_H$ (magenta thick dashed), $\tau = 400.0\tau_H$ (yellow thin dashed-dotted), and $\tau = 800.0\tau_H$ (black thick dashed-dotted) and a simultaneous interaction quench to $g_f = 0.02$.

self-consistent with the previous study we start from a strongly interacting initial state with $g_{in} = 5.0$, while the lattice is assumed to be initially deep enough with a depth $V_{0;in} = 8.0$ to include the first three Wannier energy levels. As usual, in order to interpret the dynamics induced by the quench we should be aware of the characteristics of the initial ground state. For a system with filling $\nu < 1$ the one-body density remains asymmetric even for strong interactions due to the low population, while the delocalized fraction of particles permits the presence of long-range one-particle correlations even in the strongly repulsive regime [45].

Let us firstly analyze the nonequilibrium dynamics induced by a sudden ramp-down of the optical potential depth at time $t = 0$. The final Hamiltonian that governs the dynamics following the above scenario is given by

$$H_f(g, V_{0,f}) = H_0(g, V_{0;in}) + \frac{\delta V_0}{V_{0;in}} \sum_{k=1}^N V_{tr}(x_k), \quad (12)$$

with $V_{0;in}$, $V_{0,f}$ being the initial and final potential depth, respectively, $\delta V_0 = V_{0,f} - V_{0;in} < 0$ due to the reduction of the barrier, and V_{tr} being the lattice potential.

To examine the response of the system after the quench we initially rely on the fidelity $F_\chi(t)$. We consider quenches of the barrier down to $V_{0,f} = 2.0$, where the lattice is quite shallow and includes only the first Wannier energy level while the others are considered as delocalized. Indeed, Fig. 10(a) shows in a transparent way the instantaneous fidelity as a function of the final lattice depth. The rise of two different dynamical regions is observed. In the first region ($5.0 < V_{0,f} < 8.0$) the overlap is rather large with a minimum of the order of 80%, while in the second region ($2.0 < V_{0,f} < 5.0$) it can even reach 25% during the evolution. As we shall demonstrate below, the response of the system following this protocol is drastically different from that obtained through an interaction quench for fillings $\nu < 1$ where the dynamics is dominated by the interwell tunneling. In particular, one can excite more on-site dynamical modes and even use a barrier quench on top of an interaction quench in order to excite the cradle mode. To indicate the latter and also to trigger more efficiently the dynamical modes from here on we mainly proceed by performing a simultaneous barrier and an interaction quench to weak interactions, i.e., $g_f = 0.02$. Figure 10(b) presents the fidelity during the dynamics induced by different quenches of the lattice depth and a simultaneous interaction quench

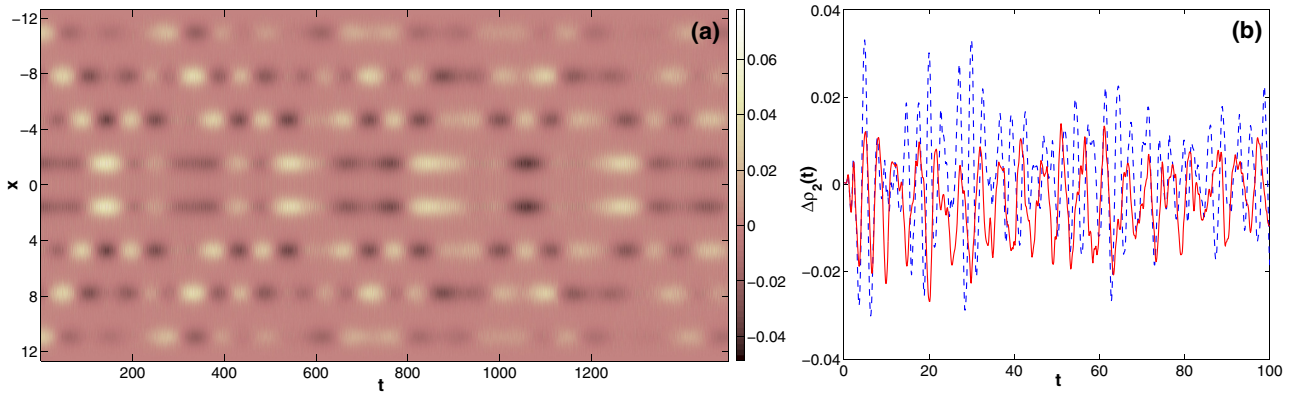


FIG. 11. (Color online) (a) The fluctuations $\delta\rho(x,t)$ of the one-body density, for an eight-well setup with $N = 5$, caused by a sudden negative barrier quench from $V_{0,in} = 8.0$ to $V_{0,f} = 4.0$ and a simultaneous interaction quench from $g_{in} = 5.0$ to $g_f = 0.02$. (b) The intrawell asymmetry $\Delta\rho_2(t)$ for the second well of the eight-well setup for a barrier quench (red solid curve) to $V_{0,f} = 4.0$ and for the combined quench scenario, i.e., barrier and interaction quench, with final parameters $V_{0,f} = 4.0$ and $g_f = 0.02$ (blue dashed curve).

to $g_f = 0.02$. The dynamical response of the system shows four different regions during the evolution. In the first (white part) the system is close to the initial state with minimal percentage up to 80%, while the second (yellow) and the third (light-red) regions indicate that the system significantly departs from the initial state with a percentage of the order of 50% and 30%, respectively. The latter regions correspond to transition states following the combined quench. Finally, in the fourth section (dark-red) the system is driven to a completely different state possessing a maximal overlap of the order of 10%. In particular, for a fixed overlap a quadratic response of the system as a function of the quench amplitude is observed.

To analyze further the response of the system, Fig. 10(c) illustrates some profiles of the fidelity in the course of the dynamics for different quenches. The fidelity exhibits a quadratic decay for short times, while after a characteristic time $\tau_c(\delta V_0)$ it oscillates around a constant value $F_0(\delta V_0)$, which depends on the quench amplitude such that it is larger for a smaller quench. The observed short-time quadratic behavior can be easily explained as follows. Let $|\Psi_0\rangle$ be the initial eigenstate of H_0 , and $|\Psi(\delta t)\rangle$ the corresponding state after a short-time interval δt . Then the short-time expansion of the overlap reads

$$|\langle\Psi_0|\Psi(\delta t)\rangle|^2 = 1 - (\delta t/\tau_c)^2 + O[(\delta t)^4], \quad (13)$$

$\tau_c^{-1} = [\langle\Psi(\delta t)|H_f^2|\Psi(\delta t)\rangle - \langle\Psi(\delta t)|H_f|\Psi(\delta t)\rangle^2]^{1/2}$ is the quench characteristic time $\tau_c(\delta V_0)$ or so-called Zeno time [34,46]. Especially, we observe that the time $\tau_c(\delta V_0)$ depends on the quench amplitude; i.e., for smaller quenches it becomes larger due to the smaller energy difference between the pre- and postquench states, and the system cannot equilibrate fast. Furthermore, the rapid small amplitude oscillations during the decay are a consequence of the quantum interference and are predominantly due to the overbarrier transport induced by the quench. Thus, they are also a presignature of the cradle mode, which is discussed below. The fact that at least some frequencies of the cradle mode could be indirectly observed in the fidelity spectrum is not surprising. Indeed, from the expansion of the fidelity [see Eq. (8)] in terms of the number states it is obvious that when the contribution of the excited band states, that refer to the cradle, is significant

the mode should also be observed in the fidelity spectrum. For smaller quenches these amplitude oscillations fade out, thereby indicating that the cradle is very weak.

Furthermore, in order to unravel the crossover between a diabatic and an adiabatic quench, let us consider a time-dependent scenario of the form $V(t;\tau) = V_{0,in} + (V_{0,f} - V_{0,in}) \tanh(t/\tau)$. To obtain the physically relevant time scales, let us rescale the time t in units of the quench characteristic time scale $\tau_H(\delta V_0) \sim 1/\Delta\epsilon(\delta V_0)$, where $\Delta\epsilon = \epsilon(V_{0,in}; g_{in}) - \epsilon(V_{0,f}; g_f)$ is the energy difference between the prequench and the postquench system. Figure 10(d) demonstrates the fidelity in the course of the dynamics for an interaction quench to $g_f = 0.02$ and the same final potential depth $V_{0,f} = 4.4(V_{in} = 8.0)$ for different ramp rates τ . A direct observation, here, is that the system has a similar quadratic response (for short times) with respect to the quench, being accompanied by small amplitude oscillations especially for fast quenches, $\tau < 28\tau_H$. This indicates that the characteristics of the dynamics, such as the excitation modes, remain also for finite rates. By considering large rates τ the switch on of the energy difference is sufficiently slow, and an eigenstate of the initial Hamiltonian becomes approximately an eigenstate for the instantaneous final Hamiltonian. In this manner, we tend to approach the adiabatic limit and the system equilibrates in a slower manner while the small amplitude fast oscillations tend to disappear. Note that for smaller relative quench amplitudes the adiabatic limit is attained for smaller ramp rates due to the reduced impact of the quench.

The reduction of the lattice depth allows for an initially delocalized boson to overcome the barrier if its kinetic energy dominates with respect to the potential energy. Then it is possible to perform a collision with a second particle on the neighboring site and a cradle state can be generated. Figure 11(a) illustrates from the perspective of the relative density $\delta\rho(x,t)$ the evolution of the system after a negative change of the lattice depth from $V_{0,in} = 8.0$ to $V_{0,f} = 4.0$ and a simultaneous interaction quench from $g_{in} = 5.0$ to $g_f = 0.02$. The dynamics shows the propagation of interwell tunneling via the population transport along the lattice, following the evolution of the bright regions. The corresponding propagation velocity is smaller for a smaller quench of the barrier.

Furthermore, locally we observe the emergence of the cradle mode for the inner-well dynamics as a consequence of the overbarrier transport. However, this mode is hardly visible in Fig. 11(a) due to the presented long evolution time and possesses a small amplitude as we shall demonstrate below.

The cradle mode refers to the inner-well oscillations between at least two bosons in the same well. The dominant number states for such a process exemplified using the first well are $|2,0,1,1,1,0,\dots\rangle_0$ and $|2,0,1,1,1,0,\dots\rangle_1$, with a straightforward extension for the remaining wells. To identify the presence of the cradle mode for the present setup we show in Fig. 11(b) the intrawell asymmetry $[\Delta\rho_\alpha(t)]$, for the second well of the lattice, as a function of time, and two different quench scenarios, i.e., an instantaneous ramp-down of the lattice depth (red solid curve) and its combination with a simultaneous interaction quench to $g_f = 0.02$ (blue dashed curve). In the latter case the resulting amplitude is larger, which is due to the simultaneous interaction quench. For an incommensurate setup with filling $\nu > 1$ this amplitude is even more larger as the initially delocalized particles, energetically close to the barrier, render the system sensitive even to a small perturbation.

IV. CONCLUSIONS AND OUTLOOK

We have investigated the quantum dynamics of strongly interacting bosons following a quench either to a weakly interacting final state or to a lattice with lowered barriers. The observed normal modes consist of the interwell tunneling, a local breathing, and a cradle mode. Each of these modes have been explained in detail, among others, within the concept of multiband Wannier number states which capture the population of excited states. The dominant Fock space for each mode has been identified showing the inclusion of higher-band contributions. In this manner, conceptual differences concerning the ingredients of each mode as well as the corresponding excitation process in comparison with the case of positive interaction quenched [14] superfluids have been demonstrated.

The interwell tunneling refers mainly to a direct population transport among the individual wells. On the other hand, the local breathing mode refers to expansion and contraction dynamics of the bosons in an individual well. The cradle mode corresponds to a localized wave packet oscillation. For the interaction quench scenario where we start from a strongly interacting state and quench back to weak interactions it is shown that the generation of the cradle mode is due to the initial delocalization. Therefore it can be observed only for setups with filling $\nu > 1$, while for the case of $\nu \leq 1$ it can be excited only with the aid of a barrier quench. This is a major difference in comparison to a positively interaction quenched superfluid where due to import of energy in the system we allow for the over-barrier transport independently of the filling factor. The fidelity function has been employed in order to investigate the response of the system and its long-time evolution with respect to the quench amplitude, as well as to show the dynamical crossover from a sudden to an adiabatic parameter change. By considering time-dependent quenches, i.e., different quench rates, or the modulation of various potential parameters of

the Hamiltonian we proposed scenarios to control the excited modes by manipulating their frequencies.

Our developed understanding of the excitation modes as well as the tunneling dynamics may pave the way to a control of the nonequilibrium dynamics of such strongly correlated systems. For instance, the finite ramp rate of a time-dependent quench may allow for the control of the normal modes or the transport of a definite number of atoms. There are many ways to proceed in this direction. As an example we mention the nonequilibrium dynamics of mixtures of different bosonic species in order to unravel their excitation modes or to create schemes for selective transport of an individual bosonic component.

ACKNOWLEDGMENTS

S.M. would like to thank P. Giannakeas, C. Morfonios, and M. Mark for fruitful discussions. S.M. also thanks the Hamburgisches Gesetz zur Förderung des wissenschaftlichen und künstlerischen Nachwuchses (HmbNFG) for a Ph.D. scholarship. L.C. and P.S. gratefully acknowledge funding by the Deutsche Forschungsgemeinschaft (DFG) in the framework of the SFB 925 Light Induced Dynamics and Control of Correlated Quantum Systems.

APPENDIX: THE COMPUTATIONAL METHOD, ML-MCTDHB

Our analysis has been performed via the multilayer multi-configuration time-dependent Hartree method for bosons (ML-MCTDHB) [24,25], which constitutes an *ab initio* method for the stationary properties but in particular the nonequilibrium quantum dynamics of bosonic systems. For a single species it is identical to MCTDHB, which has been established [26,27,47] and applied extensively [47–50].

The advantage of the MCTDH-type methods [51] in comparison to other exact computational methods is the representation of the wave function by a set of variationally optimal time-dependent orbitals. In turn, this implies the truncation of the total Hilbert space to an optimal one by employing a time-dependent moving basis in which the system can be instantaneously optimally represented by time-dependent Hartree products. The use of time-dependent orbitals is the key for the numerically exact treatment, i.e., we need a much smaller set of time-adaptive orbitals in order to achieve the same level of accuracy compared to the case of a static basis. To be self-contained let us briefly introduce the basic concepts of the method and discuss how it can be adapted to our purposes.

The main underlying idea of the MCTDHB method is to solve the time-dependent Schrödinger equation $(i\hbar\partial_t - H)\Psi(x,t) = 0$ as an initial value problem. The expansion of the many-body wave function which is a linear combination of time-dependent permanents reads

$$|\Psi(t)\rangle = \sum_{\vec{n}} C_{\vec{n}}(t) |n_1, n_2, \dots, n_M; t\rangle, \quad (\text{A1})$$

where M is the number of orbitals and the summation is over all possible combinations which retain the total number of bosons. The permanents in terms of the creation operators

$a_j^\dagger(t)$ for the j th orbital $\varphi_j(t)$ are given by

$$\begin{aligned} & |n_1, n_2, \dots, n_M; t\rangle \\ &= \frac{1}{\sqrt{n_1! n_2! \dots n_M!}} (a_1^\dagger)^{n_1} (a_2^\dagger)^{n_2} \dots (a_M^\dagger)^{n_M} |\text{vac}\rangle, \quad (\text{A2}) \end{aligned}$$

which satisfy the standard bosonic commutation relations $[a_i(t), a_j(t)] = \delta_{ij}$, etc. To proceed further, i.e., to determine the time-dependent wave function $|\Psi\rangle$ we have to find the equations of motion for the coefficients $C_{\vec{n}}(t)$ and the orbitals (which are both time-dependent). For that purpose one can employ various schemes such as the Lagrangian, McLachlan [52], or the Dirac-Frenkel [53,54] variational principle. Following the Dirac-Frenkel variational principle $\langle \delta\Psi | i\partial_t - \hat{H} | \Psi \rangle = 0$ we can determine the time evolution of all the coefficients $C_{\vec{n}}(t)$ in the ansatz (A1) and the time dependence for the orbitals $\{\varphi_j\}$. In this manner, we end up with a set of M nonlinear integrodifferential equations of motion for the orbitals, which are coupled to the $\frac{(N+M-1)!}{N!(M-1)!}$ linear equations of motion for the coefficients. These equations are the well-known MCTDHB equations of motion [26,27,47,55].

In terms of our implementation we have used a discrete variable representation for the orbitals and a sin-DVR which intrinsically introduces hard-wall boundaries at both ends of the potential (i.e., zero value of the wave function on the first and the last grid point). For the preparation of our initial state we rely on the so-called relaxation method in terms of which we can obtain the lowest eigenstates of the corresponding n -well setup. The key idea is to propagate some initial wave function $\Psi^{(0)}$ by the nonunitary $e^{-H\tau}$ (propagation in imaginary time). As $\tau \rightarrow \infty$, this exponentially damps out any contribution but that stemming from the ground state like $e^{-E_m\tau}$. In turn, we change either the initial interparticle interaction or the depth of the optical lattice abruptly or in a time-dependent manner in order to study the evolution of $\Psi(x_1, x_2, \dots, x_N; t)$ in the n -well potential within MCTDHB. Finally, note that in order to ensure the convergence of our simulations, e.g., for the triple well, we have used up to 11 single particle functions, thereby observing a systematic convergence of our results for sufficiently large spatial grids. Another criterion for ensuring convergence is the population of the lowest occupied natural orbital, which is kept for each case below 0.1%.

-
- [1] I. Bloch, J. Dalibard, and W. Zwerger, *Rev. Mod. Phys.* **80**, 885 (2008).
- [2] A. Polkovnikov, K. Sengupta, A. Silva, and M. Vengalattore, *Rev. Mod. Phys.* **83**, 863 (2011).
- [3] M. Weidemüller, A. Hemmerich, A. Görlitz, T. Esslinger, and T. W. Hänsch, *Phys. Rev. Lett.* **75**, 4583 (1995).
- [4] C. L. Hung, X. Zhang, L. C. Ha, S. K. Tung, N. Gemelke, and C. Chin, *New J. Phys.* **13**, 075019 (2011).
- [5] J. P. Ronzheimer, M. Schreiber, S. Braun, S. S. Hodgman, S. Langer, I. P. McCulloch, F. Heidrich-Meisner, I. Bloch, and U. Schneider, *Phys. Rev. Lett.* **110**, 205301 (2013).
- [6] M. Rigol, V. Dunjko, and M. Olshanii, *Nature (London)* **452**, 854 (2008).
- [7] M. Cheneau, P. Barmettler, D. Poletti, M. Endres, P. Schauß, T. Fukuhara, C. Gross, I. Bloch, C. Kollath, and S. Kuhr, *Nature (London)* **481**, 484 (2012).
- [8] S. S. Natu and E. J. Mueller, *Phys. Rev. A* **87**, 053607 (2013).
- [9] E. Altman and A. Auerbach, *Phys. Rev. Lett.* **89**, 250404 (2002).
- [10] D. Chen, M. White, C. Borries, and B. DeMarco, *Phys. Rev. Lett.* **106**, 235304 (2011).
- [11] H. Elmar, R. Hart, M. J. Mark, J. G. Danzl, L. Reichsöllner, M. Gustavsson, M. Dalmonte, G. Pupillo, and H.-C. Nägerl, *Nature (London)* **466**, 597 (2010).
- [12] K. W. Mahmud, L. Jiang, P. R. Johnson, and E. Tiesinga, *New J. Phys.* **16**, 103009 (2014).
- [13] S. Campbell, M. A. Garcia-March, T. Fogarty, and T. Busch, *Phys. Rev. A* **90**, 013617 (2014).
- [14] S. I. Mistakidis, L. Cao, and P. Schmelcher, *J. Phys. B* **47**, 225303 (2014).
- [15] W. Kohn, *Phys. Rev.* **123**, 1242 (1961).
- [16] M. Bonitz, K. Balzer, and R. vanLeeuwen, *Phys. Rev. B* **76**, 045341 (2007).
- [17] J. W. Abraham and M. Bonitz, *Contrib. Plasma Phys.* **54**, 27 (2014).
- [18] S. Bauch, K. Balzer, C. Henning, and M. Bonitz, *Phys. Rev. B* **80**, 054515 (2009).
- [19] S. Bauch, D. Hochstuhl, K. Balzer, and M. Bonitz, *J. Phys.: Conf. Series* **220**, 012013 (2010).
- [20] J. W. Abraham, K. Balzer, D. Hochstuhl, and M. Bonitz, *Phys. Rev. B* **86**, 125112 (2012).
- [21] R. Schmitz, S. Krönke, L. Cao, and P. Schmelcher, *Phys. Rev. A* **88**, 043601 (2013).
- [22] S. Peotta, D. Rossini, M. Polini, F. Minardi, and R. Fazio, *Phys. Rev. Lett.* **110**, 015302 (2013).
- [23] P. Makotyn, C. E. Klauss, D. L. Goldberger, E. A. Cornell, and D. S. Jin, *Nat. Phys.* **10**, 116 (2014).
- [24] L. Cao, S. Krönke, O. Vendrell, and P. Schmelcher, *J. Chem. Phys.* **139**, 134103 (2013).
- [25] S. Krönke, L. Cao, O. Vendrell, and P. Schmelcher, *New J. Phys.* **15**, 063018 (2013).
- [26] O. E. Alon, A. I. Streltsov, and L. S. Cederbaum, *J. Chem. Phys.* **127**, 154103 (2007).
- [27] O. E. Alon, A. I. Streltsov, and L. S. Cederbaum, *Phys. Rev. A* **77**, 033613 (2008).
- [28] M. Olshanii, *Phys. Rev. Lett.* **81**, 938 (1998).
- [29] R. Grimm, M. Weidemüller, and Y. B. Ovchinnikov, *Adv. At. Mol. Opt. Phys.* **42**, 95 (2000).
- [30] R. A. Duine and H. T. Stoof, *Phys. Rep.* **396**, 115 (2004).
- [31] C. Chin, R. Grimm, P. Julienne, and E. Tiesinga, *Rev. Mod. Phys.* **82**, 1225 (2010).
- [32] J. I. Kim, V. S. Melezhik, and P. Schmelcher, *Phys. Rev. Lett.* **97**, 193203 (2006).
- [33] P. Giannakeas, F. K. Diakonou, and P. Schmelcher, *Phys. Rev. A* **86**, 042703 (2012).
- [34] T. Gorin, T. Prosen, T. H. Seligman, and M. Žnidarič, *Phys. Rep.* **435**, 33 (2006).
- [35] R. W. Spekkens and J. E. Sipe, *Phys. Rev. A* **59**, 3868 (1999).

- [36] S. Klaiman, N. Moiseyev, and L. S. Cederbaum, *Phys. Rev. A* **73**, 013622 (2006).
- [37] E. J. Mueller, T. L. Ho, M. Ueda, and G. Baym, *Phys. Rev. A* **74**, 033612 (2006).
- [38] O. Penrose and L. Onsager, *Phys. Rev.* **104**, 576 (1956).
- [39] M. P. A. Fisher, P. B. Weichman, G. Grinstein, and D. S. Fisher, *Phys. Rev. B* **40**, 546 (1989).
- [40] J. K. Freericks and H. Monien, *Europhys. Lett.* **26**, 545 (1994).
- [41] J. K. Freericks and H. Monien, *Phys. Rev. B* **53**, 2691 (1996).
- [42] K. Sakmann, A. I. Streltsov, O. E. Alon, and L. S. Cederbaum, *Phys. Rev. A* **89**, 023602 (2014).
- [43] S. Bravyi, M. B. Hastings, and F. Verstraete, *Phys. Rev. Lett.* **97**, 050401 (2006).
- [44] K. Sakmann, A. I. Streltsov, O. E. Alon, and L. S. Cederbaum, *Phys. Rev. A* **78**, 023615 (2008).
- [45] I. Brouzos, S. Zöllner, and P. Schmelcher, *Phys. Rev. A* **81**, 053613 (2010).
- [46] A. Peres, *Am. J. Phys.* **48**, 931 (1980).
- [47] A. I. Streltsov, O. E. Alon, and L. S. Cederbaum, *Phys. Rev. Lett.* **99**, 030402 (2007).
- [48] A. I. Streltsov, K. Sakmann, O. E. Alon, and L. S. Cederbaum, *Phys. Rev. A* **83**, 043604 (2011).
- [49] O. E. Alon, A. I. Streltsov, and L. S. Cederbaum, *Phys. Rev. A* **76**, 013611 (2007).
- [50] O. E. Alon, A. I. Streltsov, and L. S. Cederbaum, *Phys. Rev. A* **79**, 022503 (2009).
- [51] M. H. Beck, A. Jäckle, G. A. Worth, and H.-D. Meyer, *Phys. Rep.* **324**, 1 (2000).
- [52] A. D. McLachlan, *Mol. Phys.* **8**, 39 (1964).
- [53] J. Frenkel, in *Wave Mechanics* 1st ed. (Clarendon Press, Oxford, 1934), pp. 423–428.
- [54] P. A. M. Dirac, *Proc. Cambridge Philos. Soc.* **26**, 376 (1930).
- [55] J. Broeckhove, L. Lathouwers, E. Kesteloot, and P. Van Leuven, *Chem. Phys. Lett.* **149**, 547 (1988).

**4.1.3 Quantum Dynamical Response of Ultracold Few-Boson Ensembles
in Finite Optical Lattices to Multiple Interaction Quenches**

Quantum dynamical response of ultracold few-boson ensembles in finite optical lattices to multiple interaction quenches

J. Neuhaus-Steinmetz,¹ S. I. Mistakidis,¹ and P. Schmelcher^{1,2}

¹*Zentrum für Optische Quantentechnologien, Universität Hamburg, Luruper Chaussee 149, 22761 Hamburg, Germany*

²*The Hamburg Centre for Ultrafast Imaging, Universität Hamburg, Luruper Chaussee 149, 22761 Hamburg, Germany*

(Received 10 March 2017; published 10 May 2017)

The correlated nonequilibrium quantum dynamics following a multiple interaction quench protocol for few-bosonic ensembles confined in finite optical lattices is investigated. The quenches give rise to an interwell tunneling and excite the cradle and a breathing mode. Several tunneling pathways open during the time interval of increased interactions, while only a few occur when the system is quenched back to its original interaction strength. The cradle mode, however, persists during and in between the quenches, while the breathing mode possesses distinct frequencies. The occupation of excited bands is explored in detail revealing a monotonic behavior with increasing quench amplitude and a nonlinear dependence on the duration of the application of the quenched interaction strength. Finally, a periodic population transfer between momenta for quenches of increasing interaction is observed, with a power-law frequency dependence on the quench amplitude. Our results open the possibility to dynamically manipulate various excited modes of the bosonic system.

DOI: [10.1103/PhysRevA.95.053610](https://doi.org/10.1103/PhysRevA.95.053610)

I. INTRODUCTION

Ultracold atoms in optical lattices offer the opportunity to realize a multitude of systems and to study their quantum phenomena [1–5]. Moreover, recent experimental advances in optical trapping allow one to control the size and atom number of these quantum systems, and furthermore include the tunability of the atomic interactions via Feshbach resonances [6–8]. A promising research direction in this context is the nonequilibrium quantum dynamics for finite atomic ensembles. Here, the most frequently considered setting is a quantum quench (see Refs. [9–11] and references therein), where one explores the quantum evolution after a sudden change of an intrinsic system parameter such as the interaction strength [12–15]. A complicating feature of the nonequilibrium dynamics is the presence of interactions at a level that often precludes the use of a perturbative analysis and/or mean-field (MF) approximation. Specifically, the dynamics beyond the paradigm of linear response has been a subject of growing theoretical interest [16–24] triggered by the recent progress in ultracold atom experiments particularly in one spatial dimension [25–28].

Referring to few-body systems in finite optical lattices, it has been shown [14,15] that following an interaction quench several tunneling pathways can be excited as well as collective behavior such as the cradle or breathing mode are observed. Furthermore, a sudden raise of the interactions [14] couples one of the tunneling modes with the cradle mode giving rise to a resonant behavior. On the other hand, a sudden decrease of the interparticle repulsion [15] excites the cradle mode only for setups with a filling larger than unity and no mode coupling can be observed. From this it is evident that in order to steer the dynamics the considered quench protocol plays a key role. Naturally, one can then generalize the underlying protocol to a multiple interaction quench (MIQ) scenario, which consists of different sequences of single quenches. A specific case would be a quench followed by its “inverse,” namely by going back to the original interaction strength (single pulse). This enables the system to dynamically return to its original Hamiltonian within certain time intervals and the question emerges what properties

induced by the quench persist during the longer time evolution. Very recently [29], a study of the effects of the MIQ protocol on the one- and two-body correlation functions of a three-dimensional ultracold Bose gas has been performed using the time-dependent Bogoliubov approximation. It has been shown that the system produces more elementary excitations with increasing number of MIQs, while the correlation functions tend to a constant value for long evolution times.

In the present work, we provide a multimode treatment of few bosons in finite optical lattices in one spatial dimension, where all correlations are taken into account. Such an approach is very appropriate in order to extract information on the resulting many-body dynamics and in order to obtain the complete excitation spectrum. This will allow us to explore how the MIQ protocol, reflected by the different temporal interaction intervals, affects the system dynamics and as a consequence the persistence of the emergent various collective modes during the evolution.

Several protocols varying the number of quenches are hereby investigated. Our focus is on the regime of intermediate interaction strengths, where current state of the art analytical approaches are not applicable. The lowest-band tunneling dynamics involves several channels following a quench of increasing interaction, while only a few persist when the system is quenched back. Furthermore, the intrawell excited motion is described by the cradle and the breathing modes being initiated by the overbarrier transport which is a consequence of the quench to increased interactions. We find that in the course of the MIQ the cradle mode persists for all times, while the breathing mode possesses distinct frequencies depending on the different time intervals of the MIQ. In contrast to the single quench scenario [14,15] here by tuning the parameters of the MIQ we can manipulate both the interwell tunneling and the intrawell excited modes. Moreover, the higher-band excitation dynamics is explored in detail. A monotonic increase of the excited to higher-band fraction for larger quench amplitudes is observed and a nonlinear dependence on the time interval of a single quench (pulse width) is revealed. Remarkably, the interplay between the quench amplitude and the pulse width

yields a tunability of the higher-band excitation dynamics. This observation indicates a substantial degree of controllability of the system under a MIQ protocol, which is an important result of our work. Moreover, it is shown that in the course of a certain pulse the presence of increased interactions leads to a periodic population transfer between different lattice momenta, while for the time intervals of the initial interaction strength this does not happen. The frequency of the above-mentioned periodicity possesses a power-law dependence on the quench amplitude.

This work is organized as follows. In Sec. II we introduce the quench protocol and the multiband expansion as an analysis tool. Section III focuses on the detailed investigation of the impact of the MIQ on the quantum dynamics for filling factors larger than unity, whereas Sec. IV presents the dynamics for filling factors smaller than unity. We summarize our findings and present an outlook in Sec. V. The Appendix describes our computational method and delineates the convergence of our numerical results.

II. QUENCH PROTOCOL AND MULTIBAND EXPANSION

We consider N identical bosons each of mass M confined in an m -well optical lattice. The many-body Hamiltonian reads

$$H = \sum_{i=1}^N \left(\frac{p_i^2}{2M} + V_{\text{tr}}(x_i) \right) + \sum_{i < j} V_{\text{int}}(x_i - x_j, \tau, n_p, t), \quad (1)$$

where the one-body part of the Hamiltonian builds upon the one-dimensional lattice potential $V_{\text{tr}}(x) = V_0 \sin^2(kx)$. The latter is characterized by its depth V_0 and periodicity l , with $k = \pi/l$ denoting the wave vector of the counterpropagating lasers which form the optical lattice. To restrict the infinitely extended trapping potential $V_{\text{tr}}(x)$ to a finite one with m wells and length L , we impose hard wall boundary conditions at the appropriate positions, $x_m = \pm \frac{m\pi}{2k}$. Furthermore, $V_{\text{int}}(x_i - x_j, t, \tau, n_p) = g(t, \tau, n_p) \delta(x_i - x_j)$ corresponds to the contact interaction potential between particles located at positions $\{x_i\}$ with $i = 1, 2, \dots, N$.

To trigger the dynamics we employ a MIQ protocol. At $t = 0$ the interatomic interaction is quenched from the initial value g_{in} to a final amplitude g_f , maintaining g_f (positive half) for time τ (pulse width). Then, the interaction strength is quenched back from g_f to its initial value g_{in} , maintaining this value g_{in} (negative half) for time τ . This procedure is repeated according to the number of the pulses n_p ; see Fig. 1 for the case of three pulses. Therefore, our protocol reads

$$g(t, \tau, n_p) = g_{\text{in}} + (g_f - g_{\text{in}}) \times \sum_{i=0}^{n_p-1} [\Theta(t - 2i\tau) \Theta((2i+1)\tau - t)]. \quad (2)$$

Here, each pulse is modeled by a temporal step function depending on the parameters n_p and τ which refer to the number of the considered pulses and the pulse width, respectively. Moreover, $\delta g = g_f - g_{\text{in}}$ denotes the quench amplitude of the MIQ. Experimentally, the effective interaction strength in one dimension can be tuned either via the three-dimensional scattering length by using a Feshbach resonance [8,30] or by a change of the corresponding transversal confinement frequency ω_{\perp} [31–33].

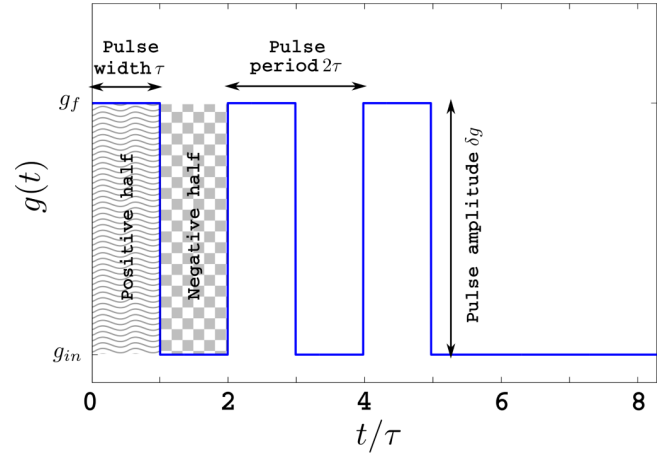


FIG. 1. Sketch of a triple pulse MIQ protocol, $g(t)$, with pulse width τ . g_{in} (g_f) refer to the pre-(post-) quenched interaction strength and $\delta g = g_f - g_{\text{in}}$ is the pulse or quench amplitude.

For reasons of simplicity we rescale the Hamiltonian (1) in units of the recoil energy $E_R = \frac{\hbar^2 k^2}{2M}$. Thus the length, time, and frequency scales are given in units of k^{-1} , $\omega_R^{-1} = \hbar E_R^{-1}$, and ω_R , respectively. To include three localized single-particle Wannier states in each well we employ a sufficiently large lattice depth of $V_0 = 10.0 E_R$. Finally, for convenience we set $\hbar = M = k = 1$. Hence all quantities below are given in dimensionless units.

To solve the underlying many-body Schrödinger equation we employ the multiconfiguration time-dependent Hartree method for bosons (MCTDHB) [34,35]. In contrast to the MF approximation, within this method we take all correlations into account and employ a variable number of variationally optimized time-dependent single-particle functions (see the Appendix for more details). Below, when comparing with the MF approximation we will refer to MCTDHB as the correlated approach. For the interpretation and analysis of the induced dynamics it is preferable to rely on a time-independent many-body basis rather than the time-dependent one used for our numerical calculations. We therefore project the numerically obtained wave function on a time-independent number state basis consisting of single-particle states localized on each lattice site. Thus the total wave function is expanded in terms of noninteracting multiband Wannier number states. The Wannier states between different wells possess a fairly small overlap for not too high energetic excitation as the employed lattice potential ($V_0 = 10.0 E_R$) is deep enough. Then, a many-body bosonic wave function for a system of N bosons, m wells, and j localized single-particle states [14,15] reads

$$|\Psi(t)\rangle = \sum_{\vec{n}} C_{\vec{n}}(t) |\vec{n}\rangle, \quad (3)$$

where $|\vec{n}\rangle \equiv |\otimes_{\lambda=0}^{j-1} n_1^{(\lambda)}, \otimes_{\lambda=0}^{j-1} n_2^{(\lambda)}, \dots, \otimes_{\lambda=0}^{j-1} n_m^{(\lambda)}\rangle$ denotes the multiband Wannier number state. Each element can be decomposed as $\otimes_{\lambda=0}^{j-1} n_i^{(\lambda)} = n_i^{(0)} \otimes n_i^{(1)} \otimes \dots \otimes n_i^{(j-1)}$, where $n_i^{(\lambda)}$ denotes the number of bosons being localized in the i th well, and λ th band satisfying the closed subspace constraint $\sum_{i=1}^m \sum_{\lambda=0}^{j-1} n_i^{(\lambda)} = N$. For instance, in a setup

with $N = 4$ bosons confined in a triple well $m = 3$, which is our workhorse in the following, which includes $\lambda = 3$ single-particle states, the state $|1^{(0)}, 1^{(0)} \otimes 1^{(1)}, 1^{(0)}\rangle$ indicates that in every well one boson occupies the zeroth excited band, but in the middle well there is one extra boson localized in the first excited band. For this setup we can identify four different energetic classes of number states. The single pairs $\{|2^{(I_1)}, 1^{(I_2)}, 1^{(I_3)}\} + \odot\}$ (SP), the double pairs $\{|2^{(I_1)}, 2^{(I_2)}, 0^{(I_3)}\} + \odot\}$ (DP), the triples $\{|3^{(I_1)}, 1^{(I_2)}, 0^{(I_3)}\} + \odot\}$ (T), and the quadruples $\{|4^{(I_1)}, 0^{(I_2)}, 0^{(I_3)}\} + \odot\}$ (Q), where \odot stands for all corresponding permutations and $\mathbf{I} = (I_1, I_2, I_3)$ indicates the order of the degree of excitation. For our purposes we only consider the corresponding subclass with isoenergetic states, e.g., for the double pairs $\{|2^{(I_1)}, 2^{(I_2)}, 0^{(I_3)}\}, |0^{(I_1)}, 2^{(I_2)}, 2^{(I_3)}\}, |2^{(I_1)}, 0^{(I_2)}, 2^{(I_3)}\}$. To characterize the eigenstates in terms of number states we adopt the compact notation $|s\rangle_{\alpha, \mathbf{I}}$, where s denotes the spatial occupation and α relates to each of the above classes. For instance, $\{|s\rangle_{1, \mathbf{I}}\}$ with $\mathbf{I} = (1, 1, 0)$ represents

$$\begin{aligned} & \{|2^{(1)}, 1^{(1)}, 1^{(0)}\}, |2^{(1)}, 1^{(0)}, 1^{(1)}\}, |1^{(0)}, 2^{(1)}, 1^{(1)}\}, \\ & |1^{(0)}, 1^{(1)}, 2^{(1)}\}, |1^{(1)}, 1^{(0)}, 2^{(1)}\}, |1^{(1)}, 2^{(1)}, 1^{(0)}\} \end{aligned}$$

and s runs from 1 to 6.

III. QUENCH DYNAMICS FOR FILLING $\nu > 1$

In this section the nonequilibrium dynamics following the MIQs for a system with filling factor $\nu > 1$ is analyzed. The system is initially prepared in the ground state of four bosons confined in a triple well with interparticle repulsion $g_{\text{in}} = 0.1$. It is thus dominated by the number state $|1^0, 2^0, 1^0\rangle$. To induce the dynamics we focus on a double and five pulse quench protocol [see Eq. (2) for $n_p = 2$ or $n_p = 5$ and $\tau = 50$ or $\tau = 25$, respectively] and compare with the results for a single interaction quench.

A. Tunneling dynamics

To investigate the dynamical response we employ the fidelity evolution $F(t; \tau) = |\langle \Psi(0) | \Psi(t; \tau) \rangle|^2$, which is the overlap between the instantaneous and the initial wave function [36–39]. Following a single quench, see Fig. 2(a), two different dynamical regions arise in the fidelity evolution. For $0.1 \leq g_f \leq 1.0$ the system is only weakly perturbed since $F(t) \approx 1$. For $g_f \geq 1.0$ the fidelity deviates significantly from unity and exhibits in time an oscillatory pattern. These oscillations are amplified with increasing quench amplitude and characterized both by a higher amplitude and frequency due to the increasing deposition of energy into the system. For the double pulse protocol the dynamical response is altered, as compared to the single quench scenario, and it is characterized by four distinct temporal regions; see Fig. 2(b). For $t < \tau$ the same pattern as for the single quench is, of course, observed as the two protocols are identical within this time interval, i.e., $g(t < \tau) = g_f$. At $t = \tau$ the system is quenched back to g_{in} and the oscillation of the fidelity almost vanishes. Then, $F(\tau < t < 2\tau) \approx F(t = \tau)$, where the value $F(t = \tau)$ depends strongly on the phase of the oscillation at $t = \tau$ and therefore on δg . During the positive half of the second pulse $2\tau < t < 3\tau$ an oscillatory pattern is observed, possessing the

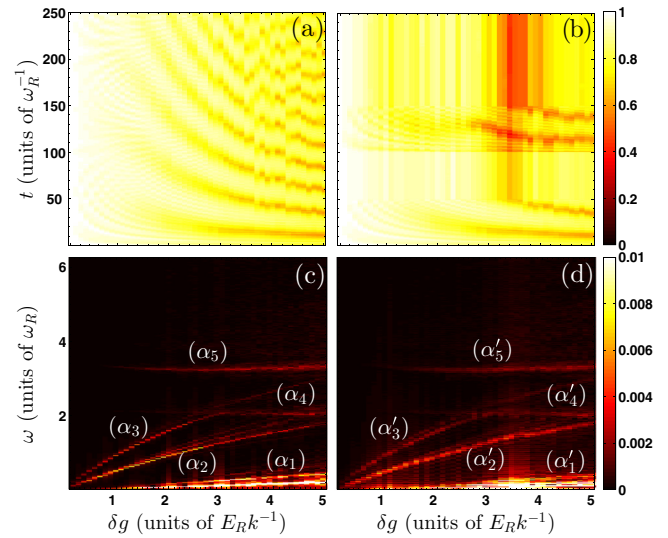


FIG. 2. As a function of the quench amplitude δg are shown the following: (a),(b) fidelity evolution for a single quench and a double pulse ($n_p = 2$) MIQ, respectively, and (c),(d) the corresponding fidelity spectra. Parameter values are $g_{\text{in}} = 0.1$, $\tau = 50$, and $N = 4$.

same frequencies with those occurring during the positive half of the first pulse. The system is driven further away from the initial state as more energy is added. Note that the dominant frequency of the oscillation depends on δg as in the single quench scenario; see Fig. 2(a). At $t = 3\tau$ the system is quenched back to g_{in} and the oscillatory behavior of the response again vanishes. Hereafter, $F(t > 3\tau) \approx F(t = 3\tau)$. Remarkably enough, for $3.2 \leq g_f \leq 3.7$, the fidelity reduces significantly after the second pulse to the value $F(t > 3\tau) = 0.44$ at $g_f = 3.4$. The existence of such strong response regions for certain combinations of δg and τ is caused by the MIQ scenario and will be addressed below in more detail.

To identify the corresponding tunneling modes that participate in the dynamics we inspect the spectrum of the fidelity [14,15,40] for the single quench [Fig. 2(c)] and the double pulse [Fig. 2(d)] protocols. Both scenarios excite the same frequency modes possessing though some differences, caused by the fact that in the finite time intervals that the system is quenched back within the double pulse protocol, the response remains mainly stable. The observed modes triggered by a single (double-pulsed) quench can be energetically categorized as follows: (α_1) [(α'_1)] tunneling within the SP category, (α_2) [(α'_2)] tunneling between the SP and DP categories, and (α_3) [(α'_3)] tunneling between the SP and T categories. The latter two processes are reminiscent of the atom pair tunneling which has been experimentally detected in driven optical lattices [41,42]. To gain more insight into the spectrum of the double pulse scenario we have splitted the evolution into the different temporal regions that the protocol imposes, i.e., $g = g_f$ or $g = g_{\text{in}}$. As nearly no oscillations occur in the negative halves of the double pulse ($\tau < t < 2\tau$ and $t > 3\tau$) all tunneling branches except a_1 are then suppressed. Note here that, in principle, for $g = g_{\text{in}}$ all branches possess very small and nearly equal frequencies which are resolvable in the case of a large enough τ . However, for $t < \tau$ (positive half of the first pulse) and $2\tau < t < 3\tau$ (positive half of the second pulse) the

above-mentioned three modes occur; see also Fig. 2(d). The latter enables us to dynamically manipulate or even switch on and off certain tunneling processes due to the presence or absence of increased interactions. Finally, we remark that the branches denoted, e.g., by $(\alpha_4), (\alpha_5)$ refer to higher-band excitations and will be addressed below.

B. Dominant intrawell excitations: The cradle and the breathing modes

Let us focus on the cradle and the breathing mode in the following. The cradle mode represents a dipolelike intrawell oscillation in the outer wells of the finite lattice. Following an interaction quench it is induced by an overbarrier transport of a boson initially residing in the central well (for a detailed description on the generation of this mode, see [14,15]). It breaks the parity symmetry within the outer wells and can thus be quantified by the corresponding intrawell asymmetry of the wave function. For instance, in the left well $\Delta\rho_L(t) = \rho_{L,1}(t) - \rho_{L,2}(t)$, where $\rho_{L,1}(t)$ and $\rho_{L,2}(t)$ denote the spatially integrated densities of the left and the right half of the well. To investigate the frequencies that characterize the cradle mode and how they are influenced by the different quench protocols we employ the spectrum $\Delta\rho_L(\omega) = 1/\pi \int dt e^{i\omega t} \Delta\rho_L(t)$. Previously [14] it has been shown that following a single interaction quench $\Delta\rho_L(\omega)$, as a function of the quench amplitude, possesses mainly two distinct frequency branches [see Fig. 3(a)]. The latter refer to a tunneling mode $|2^{(0)}, 1^{(0)}, 1^{(0)}\rangle \equiv |3^{(0)}, 0^{(0)}, 1^{(0)}\rangle$ [see branch b_2 in Fig. 3(a)] and an interband overbarrier process $|1^{(0)}, 2^{(0)}, 1^{(0)}\rangle \equiv |1^{(0)} \otimes 1^{(1)}, 1^{(0)}, 1^{(0)}\rangle$ [see branch b_3 in Fig. 3(a)] being identified as the cradle mode. Remarkably,

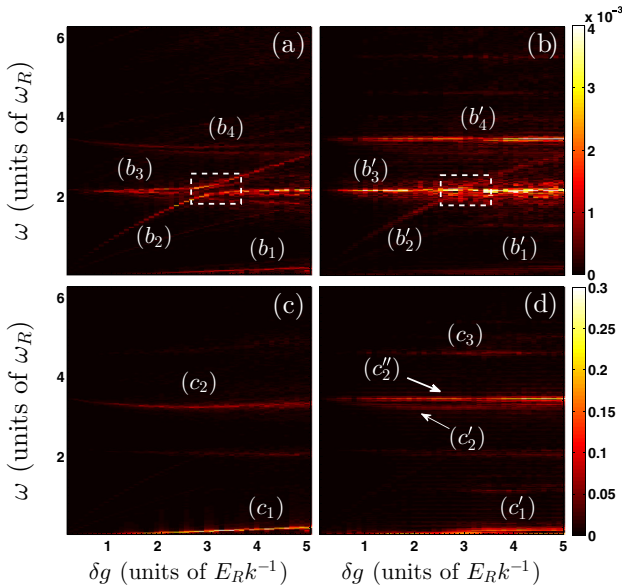


FIG. 3. As a function of the quench amplitude δg are shown the following: (a),(b) spectrum of the intrawell asymmetry $\Delta\rho_L(\omega)$ following a single quench and a double pulse ($n_p = 2$) MIQ, respectively. Spectrum of $\sigma_M^2(\omega)$ following (c) a single quench and (d) a double pulse MIQ protocol. Parameter values are $g_{\text{in}} = 0.1$, $\tau = 50$, and $N = 4$.

these two modes come into resonance in a certain region of quench amplitudes [see the dashed rectangle in Fig. 3(a)], and therefore it is possible to couple the interwell (tunneling) with the intrawell (cradle) dynamics. However, following a double pulse, see Fig. 3(b), the aforementioned resonance is hardly visible as the tunneling mode is less pronounced compared to the single quench scenario [compare also Figs. 2(c) and 2(d)]. Indeed, the tunneling mode [see branch b'_2 in Fig. 3(b)] is present only when $g(t) = g_f$, while the cradle mode [see branch b'_3 in Fig. 3(b)] persists also after we quench back to g_{in} . The above can be explained as follows: when the interaction strength is reduced, the bosons do not possess the required energy to perform a second-order tunneling process, and therefore the SP to T tunneling mode, see b'_2 , is absent when we quench back. On the contrary, the cradle mode persists also when $g(t) = g_{\text{in}}$, $t > 0$ as it is an intrawell mode and has already been initialized previously. Therefore, a tunneling process is required to initialize the cradle mode but is not a prerequisite for it to persist. As a consequence the coupling between the cradle mode and the SP to T tunneling mode disappears when $g = g_{\text{in}}$ and occurs only for $g = g_f$. Thus, using a MIQ protocol, one can switch on and off the above described mode resonance [see also the dashed rectangle in Fig. 3(b)]. Finally, we note that the energetically lower visible branch, e.g., b_1 , refers to tunneling within the SP mode [see also Fig. 2(c)], while the energetically upper branch in both spectra located at $\omega \approx 3.5$ belongs to the breathing mode and is explained below in detail.

The breathing mode refers to an expansion and contraction of the bosonic cloud and can be excited by varying the interaction strength or the frequency of the trapping potential [43–45]. Here, due to the lattice symmetry it is expected [14,15] to be more prone in the central well. To identify the breathing mode we employ the second moment $\sigma_M^2(t) = \langle \Psi(t) | \hat{P}_M(x - X_{\text{c.m.}}^{(M)})^2 \hat{P}_M | \Psi(t) \rangle$ within the spatial region of the middle well (denoted by the index M). Here, the operator $\hat{P}_M = \int_{-\pi/2}^{\pi/2} dx |x\rangle \langle x|$ projects onto the spatial region of the middle well and $X_{\text{c.m.}}^{(M)} = \int_{-\pi/2}^{\pi/2} dx (x - x_0^M) \rho_M(x) / \int_{-\pi/2}^{\pi/2} dx \rho_M(x)$, x_0^M , and $\rho_M(x)$ refer to the center of mass, the center position, and the single-particle density of the middle well, respectively. To investigate the frequency spectrum of the breathing mode we employ $\sigma_M^2(\omega) = 1/\pi \int dt e^{i\omega t} \sigma_M^2(t)$ [46–48]. For a single interaction quench, it has been shown [14] that $\sigma_M^2(\omega)$ possesses two distinct frequency branches, shown in Fig. 3(c). The upper branch (denoted as c_2) refers to the second-order process $|1^0, 1^0, 1^0 \otimes 1^2\rangle \equiv |1^0, 2^0, 1^0\rangle \equiv |1^0 \otimes 1^2, 1^0, 1^0\rangle$, which indicates the presence of a global interwell breathing mode induced by the overbarrier transport. The fact that the breathing mode is also visible in the intrawell asymmetry spectrum [see Fig. 3(a)] of the left (right) well is another indication that it is indeed a global mode. The lower branch (denoted as c_1) corresponds to the interwell tunneling mode $|1^0, 2^0, 1^0\rangle \equiv |2^0, 1^0, 1^0\rangle$. Both of the above branches weakly depend on the quench amplitude δg . Turning to the double pulse [Fig. 3(d)], the above two branches now indicated by c'_1 and c'_2 persist but also two additional and g_f -independent branches marked by c''_2 and c_3 appear above c'_2 . Note here that $\omega_{c''_2} = \lim_{g_f \rightarrow g_{\text{in}}} \omega_{c'_2}$ showing

that these branches stem from the same eigenfrequencies, while the branch c'_3 refers to an admixture of higher-band states. Importantly, the g_f -independent branches exist only during the time intervals of g_{in} , i.e., for $\tau < t < 2\tau$ and $t > 3\tau$, whereas the g_f dependence occurs only during the positive halves of the MIQ, i.e., for $g = g_f$. To conclude, the double pulse MIQ protocol gives rise to two additional g_f -independent branches of breathing dynamics. The latter suggests that by tuning the intrinsic parameters of the MIQ protocol one can steer the induced breathing dynamics.

C. Excitation dynamics

To gain a deeper understanding of the excitation dynamics, we investigate in the following the occupation of higher-band states during the time evolution. We consider the probability to find $N_0 < N$ bosons in the λ th band

$$P_{N_0}^{(\lambda)}(t; \tau) = \sum_{\vec{n} \in \mathcal{N}_{N_0}^{(\lambda)}} |\langle \vec{n} | \Psi(t; \tau) \rangle|^2, \quad (4)$$

where the notation $\vec{n} \in \mathcal{N}_{N_0}^{(\lambda)}$ denotes that the sum is performed over the configurations $\mathcal{N}_{N_0}^{(\lambda)} \equiv \{\vec{n} : \sum_{i=1}^3 \sum_{\lambda=0}^{j-1} n_i^{(\lambda)} = 4 \text{ and } \sum_{i=1}^3 n_i^{(\lambda)} = N_0\}$ that belong to the Hilbert space consisting of four particles from which N_0 reside in the λ th band.

The case of $\lambda = 0$ and $N_0 = N = 4$ refers to the probability to find all four bosons within the ground band, i.e., the energetically lowest band. Then, the above excitation probability reduces to $P_N^{(0)}(t; \tau) = \sum_{\vec{n} \in \mathcal{N}_{N_0}^{(0)}} |\langle \vec{n} | \Psi(t; \tau) \rangle|^2$. To investigate the impact of the quench amplitude δg we show in Fig. 4(a) $P_N^{(0)}(t; \tau)$ following a five pulse MIQ protocol [see Eq. (2) for $n_p = 5$ and $\tau = 25$]. We observe that for $g_f \leq 1$ the occupations $P_N^{(0)}(t; \tau = 25)$ are approximately unity and thus within this regime only to a minor degree excitations occur. However, for $g_f > 1.0$ an oscillatory pattern in time is formed [see also Fig. 2(c)], indicating the consecutive formation of higher-band excitations. In particular, within a positive half of the MIQ, i.e., $\ell\tau < t < (\ell + 1)\tau$, $\ell = 0, 2, 4, 6, 8$, large amplitude oscillations of $P_N^{(0)}(t; \tau = 25)$ occur, while in the negative halves of the MIQ, i.e., $\ell\tau < t < (\ell + 1)\tau$, $\ell = 1, 3, 5, 7$ and $t > 9\tau$, the oscillatory behavior of $P_N^{(0)}(t; \tau = 25)$ almost vanishes thereby forming an excitation plateau; see also Fig. 4(a₁) which presents $P_N^{(0)}(2\tau < t < 4\tau)$. In addition, focusing on $t > 9\tau$ a nearly linear decrease of $P_N^{(0)}(t > 9\tau; \tau = 25)$ with increasing δg is observed. This can be attributed to the fact that by using higher quench amplitudes we import more energy to the system and thus more excitations can be formed, though some small deviations from this tendency exist, for instance, we find a slightly lower $P_N^{(0)}(t; \tau)$ for $g_f = 3.8$ than for $g_f = 3.9$ [hardly visible in Fig. 4(a)]. To demonstrate the necessity of correlations for the description of the excitation dynamics we perform a comparison with the MF approximation. Figure 4(b) presents $P_N^{(0)}(t; \tau = 25)$ within the MF approximation for varying δg . A similar qualitative overall behavior compared to the above analysis is observed. For $g_f < 1$ the occupations $P_N^{(0)}(t; \tau = 25) \approx 1$, while for $g_f \geq 1$, $P_N^{(0)}(t; \tau = 25)$ form oscillatory patterns within the positive halves of the MIQ

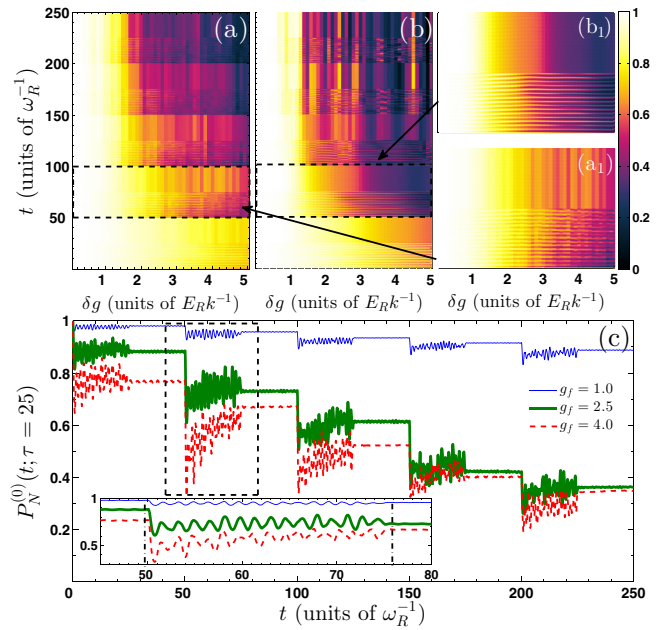


FIG. 4. Time evolution of the probability $P_N^{(0)}(t; \tau = 25)$ to find all four bosons within the ground band with respect to the quench amplitude δg following a five pulse ($n_p = 5$) MIQ protocol. (a),(b) $P_N^{(0)}(t; \tau = 25)$ for varying δg including correlations and for the MF approximation, respectively. The insets (a₁),(b₁) show $P_N^{(0)}(t; \tau = 25)$ of (a),(b), respectively, only within the second pulse. (c) Profiles of $P_N^{(0)}(t; \tau = 25)$ for different δg (see legend). For better visibility of the oscillatory behavior during the positive half of the second pulse we show in the inset $P_N^{(0)}(45 < t < 80; \tau = 25)$. The system consists of four initially weakly interacting, $g_{\text{in}} = 0.1$, bosons confined in a triple well.

and remain steady in the negative halves of the MIQ [see also Fig. 4(b₁)]. However, $P_N^{(0)}(t; \tau = 25)$ is always lower when compared to the correlated approach; see Figs. 4(a) and 4(b) and in particular Figs. 4(a₁) and 4(b₁), which show $P_N^{(0)}(t; \tau)$ during the second pulse. Obviously, the oscillation amplitudes during the positive halves of the MIQ as well as the values of $P_N^{(0)}(t; \tau)$ for $g = g_{\text{in}}$ are larger within the MF approximation than the correlated approach. In addition, the linear dependence of $P_N^{(0)}(t > 9\tau; \tau = 25)$ is lost within the MF approximation and therefore we cannot observe an overall tendency of the excitation probability with increasing interparticle repulsion. To explicitly demonstrate the excitation process we show in Fig. 4(c) various profiles of $P_N^{(0)}(t, \tau)$, taken from Fig. 4(a), for different δg . For very short times $P_N^{(0)}(t, \tau)$ drops to a lower value and subsequently oscillates with an amplitude smaller than the initial decrease exhibiting multiple frequencies. Note that both the initial decrease as well as the amplitude and the oscillation frequency depend on δg ; see also branch c'_2 in Fig. 3(d). During the positive halves of the MIQ, i.e., $\ell\tau < t < (\ell + 1)\tau$, $\ell = 0, 2, 4, 6, 8$, $P_N^{(0)}(t; \tau)$ oscillates with a decreasing amplitude (particularly for larger δg), but $\bar{P}_N^{(0)}(\tau) = 1/T \int_{\ell\tau}^{(\ell+1)\tau} dt P_N^{(0)}(t; \tau)$ increases [e.g., see the dashed red line in the inset of Fig. 4(c)]. To gain more insight into the oscillation frequencies during the positive half of the MIQ protocol, we calculate the spectrum $P_N^{(0)}(\omega) =$

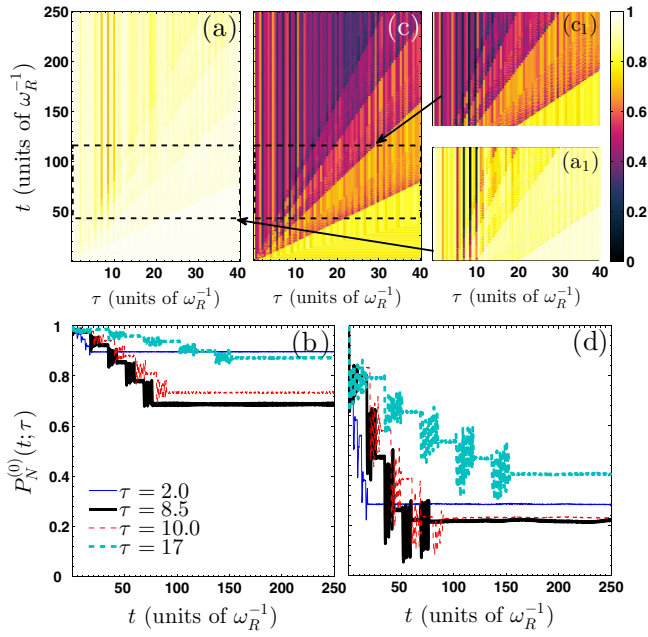


FIG. 5. (a) Time evolution of the probability to find all four bosons within the ground band $P_N^{(0)}(t; \tau)$ for varying pulse width τ following a five pulse $n_p = 5$ MIQ protocol with $\delta g = 1.0$. (b) The corresponding profiles of $P_N^{(0)}(t; \tau)$ for different values of τ (see legend). (c),(d) The same as above but for $\delta g = 2.9$. The insets (a₁),(c₁) show $P_N^{(0)}(40 < t < 120; \tau = 25)$ of (a),(c). The system consists of four initially weakly interacting $g_{\text{in}} = 0.1$ bosons in a triple well.

$1/\pi \int_0^T dt P_N^{(0)}(t) e^{i\omega t}$. The latter shows two dominant branches from which the first one matches the frequency of the cradle mode [see branch b'_3 in Fig. 3(b)] and the other one corresponds to the frequency of the weakly δg -dependent breathing mode [see branch c'_2 in Fig. 3(d)]. At the end of the positive half, the amplitude of the above-mentioned oscillation suddenly decreases and $P_N^{(0)}(t; \tau)$ remains almost steady exhibiting only tiny oscillations (excitation plateaus). We again remark that the value of $P_N^{(0)}(t; \tau)$ in a negative half of a certain pulse, where the excitation plateaus appear, strongly depends on the phase of the oscillation at $t = \ell\tau$, $\ell = 1, 3, \dots, 9$ (see also below).

Next, we focus on the impact of the pulse width τ on the excitation dynamics. Fig. 5(a) shows $P_N^{(0)}(t; \tau)$ for varying pulse width and employing a five pulse MIQ protocol with $g_f = 1.0$. Overall, we observe that $P_N^{(0)}(t; \tau)$ for fixed τ exhibits a similar oscillatory pattern as before within the positive halves of the MIQ and the formation of the excitation plateaus within the negative halves of the MIQ, see also Fig. 5(a₁). Also, $P_N^{(0)}(t; \tau)$ decreases with each additional pulse and remains almost steady after the last pulse. To illustrate the latter behavior, several profiles of $P_N^{(0)}(t; \tau)$ are shown in Fig. 5(b). In contrast to the approximately linear δg -dependence of $P_N^{(0)}(t > 9\tau; \tau)$, we observe here that the fraction $1 - P_N^{(0)}(t; \tau)$ of excitations depends on the pulse width in a non-linear manner, i.e. increasing τ does not necessarily lead to a smaller $P_N^{(0)}(t > 9\tau; \tau)$. For instance, $P_N^{(0)}(t > 9\tau; \tau = 2.0) \approx 0.89$, $P_N^{(0)}(t > 9\tau; \tau = 8.5) \approx 0.68$ whereas $P_N^{(0)}(t > 9\tau; \tau = 10.0) \approx 0.73$

[see Fig. 5(b)]. It is also important to note that while δg is the same for all pulses, the corresponding oscillation amplitude of $P_N^{(0)}(t; \tau)$ during a certain positive half of the MIQ is not fixed, indicating that it is not only affected by the quench amplitude but also depends on the pulse width. To further elaborate on the effects of the combination of δg and τ , Fig. 5(c) shows $P_N^{(0)}(t; \tau)$ for $g_f = 2.9$ and varying τ . As the quench amplitude is increased the system produces more excitations and after the pulses $\bar{P}_N^{(0)}(\tau)$ is much lower than in the case of $g_f = 1.0$ [compare Figs. 5(a₁) and 5(c₁)]. Overall, $P_N^{(0)}(t; \tau)$ behaves similar as in the case of $g_f = 1.0$, see also the corresponding profiles in Fig. 5(d), and the non-linear dependence on the pulse width is again present. The oscillation amplitudes of $P_N^{(0)}(t; \tau)$ within the positive halves of the MIQ protocol are larger as compared to the case of $g_f = 1.0$. This δg -dependence of the oscillation amplitude has been observed also for other quench amplitudes (results not shown here). Finally, $P_N^{(0)}(t > 9\tau; \tau)$ remains almost steady, while a larger δg leads in general to a lower $P_N^{(0)}(t > 9\tau; \tau)$. However, exceptions do in principle exist indicating the significance of the optimal combination of δg and τ .

To gain a deeper understanding of the underlying excitation processes during the evolution we explore the probability of finding $N_0 < N$ bosons within the λ -th band, see Eq. (4). For instance, $P_{N_0}^{(\lambda)}(t; \tau) = \sum_{\vec{n} \in N_{N_0}^{(\lambda)}} |\langle \vec{n} | \Psi(t; \tau) \rangle|^2$, for $\lambda = 1, 2$ represent the probability to find N_0 bosons within the first or second excited band respectively. More precisely, below, we investigate the probability to have one or two bosons in the first, second or third excited band as higher-lying states are not significantly occupied in our system. First we shall study the effect of δg on the different excitation processes by considering a five pulse MIQ protocol with fixed pulse width $\tau = 25$ and varying δg . Figs. 6(a)–6(c) show the probability to find one or two bosons in the first, second or third excited band. For all shown cases, the same overall excitation pattern [e.g. see $P_N^{(0)}(t; \tau)$ in Fig. 4(c)] is observed. Within a positive half of the MIQ $P_{N_0}^{(\lambda)}(t)$ oscillates, while in the negative halves of the MIQ it remains almost steady (excitation plateaus) possessing only tiny amplitude oscillations. Each pulse increases the value of $P_{N_0}^{(\lambda)}(t)$ and larger values of δg lead to larger excitation probabilities as more energy is added to the system. Overall, we observe that a single-particle excitation to the second excited band $P_1^{(2)}(t; \tau)$, which refers to the breathing mode, possesses the main contribution. However, for increasing δg also other and mainly higher excitation processes start to play a role and contribute significantly to the dynamics as shown in Figs. 6(b) and 6(c). These higher order excitations correspond to single and two-particle excitations in the first, second and third excited band possessing comparable amplitudes. Note that excitations higher than a two-particle excitation to the third excited band are negligible.

Next, let us inspect the role of τ on $P_{N_0}^{(\lambda)}(t; \tau)$ employing the five pulse MIQ protocol with $g_f = 4.0$. For $\tau = 2.0$, see Fig. 6(d), we observe a competition between $P_1^{(2)}(t; \tau)$, $P_2^{(1)}(t; \tau)$ and $P_1^{(3)}(t; \tau)$ possessing also the highest contributions after the pulses, namely $P_1^{(2)}(t > 9\tau) \approx 0.28$, $P_2^{(1)}(t > 9\tau) \approx 0.23$ and $P_1^{(3)}(t > 9\tau) \approx 0.18$

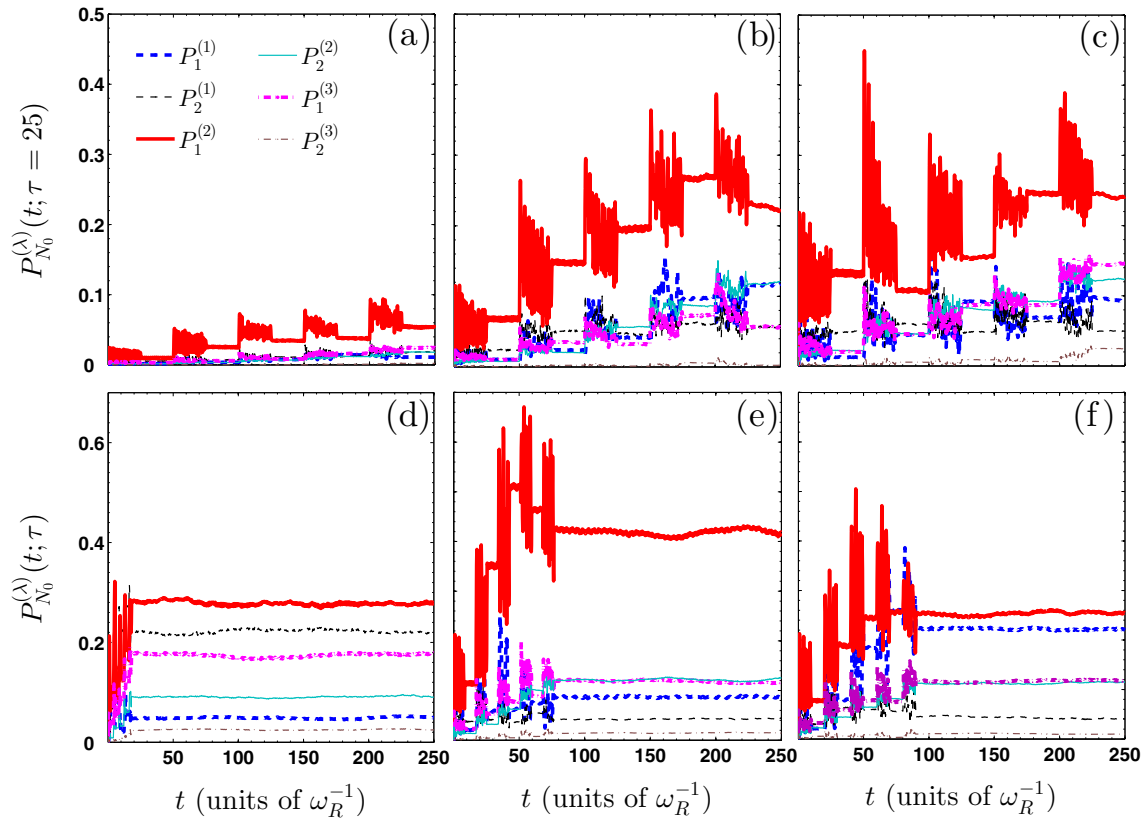


FIG. 6. Time evolution of the probability to find one or two bosons in higher bands (see legend) following a five pulse MIQ protocol with fixed pulse width $\tau = 25.0$ and varying amplitude (a) $\delta g = 1.0$, (b) $\delta g = 2.5$, and (c) $\delta g = 4.0$. (d),(e),(f) The same as above but for fixed quench amplitude $\delta g = 4.0$ and varying pulse width (d) $\tau = 2$, (e) $\tau = 8.5$, and (f) $\tau = 10$. The system consists of four bosons initially prepared in the ground state with $g_{\text{in}} = 0.1$ of a triple well.

respectively. $P_2^{(2)}(t; \tau)$ is to a lesser extent contributing with an amplitude $P_2^{(2)}(t > 9\tau) \leq 0.1$. All the other excitations are significantly below $P_2^{(2)}(t; \tau)$. The final state after the last pulse, $t > 9\tau$, exhibits many different excited modes. For $\tau = 8.5$, see Fig. 6(e), $P_1^{(2)}(t; \tau)$ clearly possesses the dominant contribution after the last pulse with $P_1^{(2)}(t > 9\tau) \approx 0.42$. In addition, $P_2^{(2)}(t; \tau)$ and $P_1^{(3)}(t; \tau)$ are significantly smaller with comparable contributions around 0.1. All the remaining states are negligible and their contributions are below 0.1. Therefore, the parameter values $\tau = 8.5$ and $g_f = 4.0$ appear to be a good combination in order to achieve a single-particle excitation to the second excited band. For $\tau = 10.0$, see Fig. 6(f), $P_1^{(1)}(t; \tau)$ that mainly refers to the cradle mode and $P_1^{(2)}(t; \tau)$ are the dominant contributions with $P_1^{(1)}(t > 9\tau) \approx 0.22$ and $P_1^{(2)}(t > 9\tau) \approx 0.25$, respectively. A less dominant interplay is observed for the states $P_2^{(2)}(t; \tau)$ and $P_1^{(3)}(t; \tau)$ which fluctuate around 0.15. The remaining excitation processes, e.g., $P_2^{(1)}(t; \tau)$, contribute below 0.05. In this case we observe that the final state includes single-particle excitations to the first, second, and third excited bands as well as a two-particle excitation to the second band. Other excitation processes are distributed below 0.05 and do not contribute essentially to the final state. The above discussion suggests that for a fixed δg (pulse width τ) different excited states can be targeted by employing different pulse widths τ (quench amplitudes δg). Therefore,

one can achieve a particular band occupation by choosing a specific combination of τ and δg . We remark that this picture is confirmed by employing different combinations of the number of pulses, pulse widths, and final interaction strengths.

To demonstrate the applicability of our results for larger systems, in the following section we proceed to the investigation of a system with filling factor $\nu < 1$. In particular, we shall show that the character of the excitation dynamics induced by a MIQ exhibits similar characteristics to the triple well case.

IV. DYNAMICS FOR FILLINGS $\nu < 1$

Let us now focus on a setup of three bosons confined in a lattice potential consisting of eight wells. For the ground state with filling factor $\nu < 1$ a spatial redistribution of the atoms occurs with increasing interaction strength, i.e., the atoms are pushed from the central to the outer wells [49]. Here, the initial state is the ground state for $g = 0.1$, where the particles are predominantly localized in the center of the multiwell trap. Then, the ground state is dominated by Wannier number states of the form $|0,0,0,1,2,0,0,0\rangle$, $|0,0,0,1,1,1,0,0\rangle$, $|0,0,0,0,3,0,0,0\rangle$ and their corresponding parity symmetric states, e.g., $|0,0,0,2,1,0,0,0\rangle$, due to the underlying spatial symmetry of the system.

To induce the dynamics a five pulse MIQ protocol with $\tau = 50$ is applied for $t > 0$. Figure 7(a) presents the fidelity evolution $F(t; \tau)$ for varying quench amplitude δg . The overall

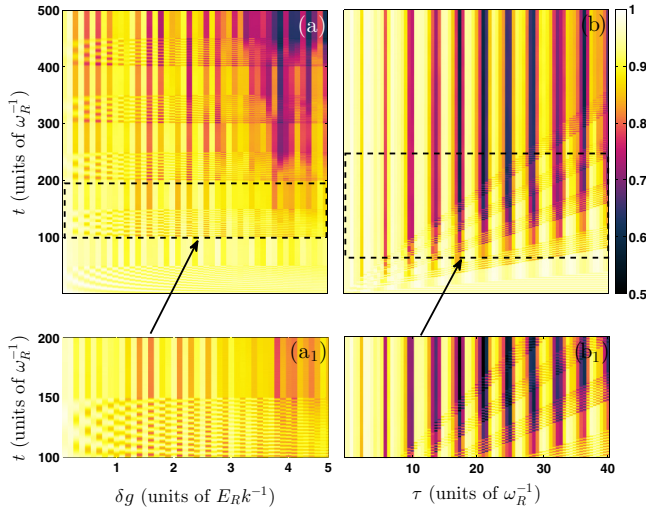


FIG. 7. (a) Fidelity evolution with varying δg , employing a five pulse $n_p = 5$ MIQ protocol with $\tau = 50$. The inset (a₁) depicts $F(t; \tau = 50)$ of (a) only within the duration of the second pulse. (b) The same as in (a) but with varying pulse width τ and $\delta g = 2.9$. The inset (b₁) shows $F(80 < t < 250; \tau)$ of (b). The system consists of three bosons confined in an eight well potential.

dynamical behavior is similar to the triple well case (see Sec. III). Indeed, during the positive halves of the MIQ the system is driven far from its initial ground state, while when it is quenched back it tends to a steady state. Each additional pulse drives the system further away from its initial state. To visualize better the response of the system during a certain pulse Fig. 7(a₁) illustrates $F(2\tau < t < 4\tau; \tau = 50)$, i.e., during the second pulse as a function of δg . The fidelity shows an oscillatory pattern during the positive half and an almost fixed value in the corresponding negative half. Note here that the oscillatory pattern of $F(t; \tau)$ possesses multiple frequencies which mainly correspond to the different tunneling modes triggered by the MIQ. These frequencies become larger for increasing δg . Let us next examine the impact of the pulse width τ on the response of the system, namely we consider a five pulse MIQ with fixed $g_f = 2.9$ and vary the pulse width; see Fig. 7(b). The dynamical response of the system resembles that for the triple well case (see Sec. III). It exhibits an oscillatory pattern within the positive halves of the MIQ protocol, tends to a steady state when $g(t) = g_{in}$, and increases with each additional pulse. The above description is illustrated in a transparent way in Fig. 7(b₁) where $F(80 < t < 250; \tau)$ is shown. Note here that $F(t; \tau)$ exhibits multiple frequencies during the evolution that refer to the induced tunneling dynamics. Finally, $F(t > 9\tau; \tau)$ shows a nonlinear dependence on τ .

To understand whether signatures of parametric amplification of matter waves can be observed during the evolution we inspect the momentum distribution

$$n(k, t) = \frac{1}{2\pi} \iint dx dx' \rho_1(x, x', t) e^{-ik(x-x')}, \quad (5)$$

where $\rho_1(x, x', t)$ denotes the one-body reduced density matrix, which is obtained by tracing out all the bosons but one in the N -body wave function. We remark that the momentum

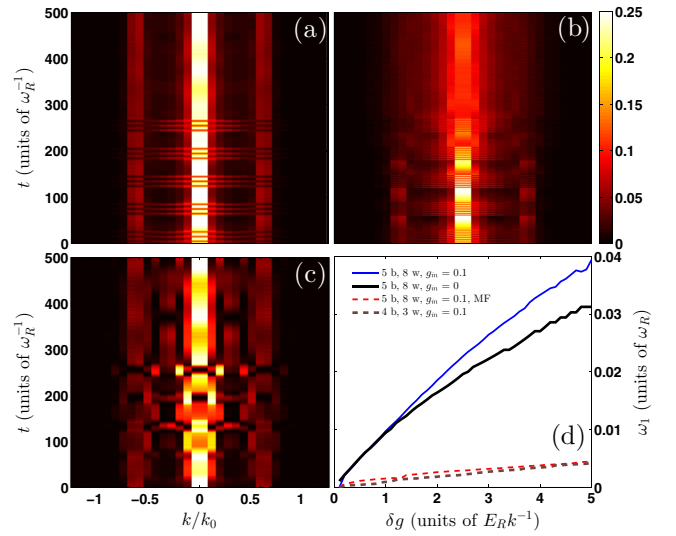


FIG. 8. Momentum distribution as a function of time for (a) $\delta g = 1.0$ and (b) $\delta g = 2.9$. (c) The same as (a) but within the MF approximation. The horizontal axis represents the lattice momenta in units of the inverse lattice vector $k_0 = \pi/l$. The system consists of an eight well lattice potential with five bosons being subjected to a five pulse ($n_p = 5$) MIQ characterized by $\tau = 25$. (d) Dominant oscillation frequency ω_1 that appears in the momentum distribution for varying quench amplitude δg . Different curves correspond to different initial conditions, approximations, and system size (see legend).

distribution can be observed experimentally as it is accessible via time-of-flight measurements [3,50,51]. Figure 8(a) presents the time evolution of the momentum distribution for an eight well lattice potential with five bosons that are subjected to a MIQ of small quench amplitude and pulse width, namely $\delta g = 1.0$ and $\tau = 25$. As shown, employing a MIQ protocol the momentum distribution exhibits in time a periodically modulated pattern when $g = g_f$; e.g., see Fig. 8(a) for $0 < t < 25$. Indeed, within the positive half of the MIQ $n(k, t)$ oscillates with frequency ω_1 between the momenta $k_0 = 0, \pm k_0/2 \approx \pm 1.57$, i.e., it is gradually transformed from a side peak structure (peaks at $k_0 = 0, \pm k_0/2$) to a broad maximum around $k_0 = 0$. On the contrary, in the negative halves of the MIQ [$\ell\tau < t < (\ell + 1)\tau$, $\ell = 1, 3, 5, 7, 9$] as well as after the last pulse $t > 10\tau$ this side peak structure is preserved. Note here that the frequency ω_1 does not depend on the considered pulse width. However, one can tune the time intervals of the periodic modulation by considering pulses with different τ 's. The observed periodic population transfer between the $k_0 = 0, \pm k_0/2$ momenta is reminiscent of the parametric amplification of matter waves. Similar observations have been made experimentally in different setups in Refs. [26,50,52]. This might pave the way for a more elaborate study of this process in the future, also for higher particle numbers and lattice potentials, but it is clearly beyond the scope of this work. We remark here that in the case of a single interaction quench only the above-mentioned periodic modulation within the positive half of the MIQ protocol can be achieved. Furthermore, the momentum distribution for a stronger interparticle repulsion, i.e., $g_f = 2.9$, shown in Fig. 8(b), exhibits a similar structure as above but with an

increasing frequency within the positive halves of the MIQ. However, for large evolution times this behavior is blurred as an effect of the strong interaction which decreases the degree of coherence. Comparing with the MF calculation, shown in Fig. 8(c), we observe that the periodic modulation of the populated lattice momenta within the positive halves of the MIQ is essentially lost and no clear signature of the effect of a pulse can be seen in $n(k,t)$. However, the activation of the additional lattice momenta is present but not in a systematic manner. This indicates the inescapable necessity of taking into account correlations for the description of the out-of-equilibrium dynamics. We remark here that in the case of larger filling factors where the presence of interparticle correlations is more dominant the failure of the MF approximation to capture certain features of the dynamics is even more prominent (results not shown here for brevity). Summarizing, the coherent MIQ dynamics leads to a periodic population transfer between different lattice momenta within a positive half of the MIQ and a side peak structure when the system is quenched back.

To shed further light on the possible control of the dynamics we finally examine the dependence of the frequency ω_1 of the periodic modulation during a positive half of the MIQ on several system parameters. Figure 8(d) presents ω_1 with varying quench amplitude δg . As shown, ω_1 depends strongly on the interparticle repulsion and in particular for increasing δg it possesses a power-law behavior, namely

$$\omega_1(g_f; N, g_{\text{in}}) = \alpha g_f^b + c, \quad (6)$$

where α, b, c are positive constants. This is also in line with our previous observations on the evolution of the momentum distribution; see Figs. 8(a) and 8(b). Although the periodic modulation of lattice momenta within the positive halves of the MIQ protocol is essentially lost within the corresponding MF approximation we also present the dominant frequency of $n(k,t)$ as a function of δg in Fig. 8(d). The obtained frequency dependence retains the above-mentioned power-law behavior but the corresponding frequencies for fixed δg are smaller even for low quench amplitudes. The latter is another manifestation of the failure of the single orbital approximation to accurately describe the induced dynamics. An additional intriguing question is whether ω_1 depends on the initial interparticle repulsion and therefore possesses a many-body nature. Starting from a broader initial wave packet, i.e., $g_{\text{in}} = 0$ shown in the same figure, ω_1 is lower especially for $1.5 < g_f < 5$, where the system is significantly perturbed from its initial state [see also $\bar{F}(\tau) = 1/T \int_0^T dt F(t; \tau) < 0.8$ in Fig. 7(a)]. To show that the general trend of ω_1 is valid also for other system sizes, Fig. 8(d) illustrates the obtained δg dependence for four bosons confined in a triple well considering the same values for the initial system parameters [see also Fig. 4(a)]. Indeed, a similar functional form is observed, while the frequencies ω_1 for the same δg are reduced when compared to the eight well case.

V. CONCLUSIONS AND OUTLOOK

We have explored the nonequilibrium quantum dynamics of multiply interaction quenched few boson ensembles confined in a finite optical lattice. Initially the system is within the weak interaction regime and sequences of interaction quenches to

strong interactions and back are performed. To characterize the impact of the multiple pulses we study the interplay between the quench amplitude and the pulse width during the evolution. A variety of lowest-band interwell tunneling modes, a cradle mode, and different breathing modes are excited. Focusing on the different time intervals of the MIQ protocol we identify the frequency branch of each process and the time intervals for which they exist. To further illustrate the peculiarity of a MIQ protocol we compare with the single quench scenario. We have analyzed the dynamical behavior by applying multiband Wannier number states and identified for each of the above-mentioned processes the transitions between the dominant number states.

The lowest-band interwell tunneling dynamics consists of three different energy channels which exist in the positive halves of the MIQ. When the system is quenched back only one tunneling mode survives. This raises the possibility to manipulate the tunneling dynamics within the different time intervals of the MIQ protocol. For instance, using different pulse widths we can switch on and off for chosen time intervals certain tunneling modes of the system.

We then turned to the excited modes, i.e., the cradle and the breathing modes. The cradle mode ‘‘ignores’’ the multipulse nature of the quench protocol and persists during the time evolution. However, the breathing mode shows a strong dependence on the instantaneous interatomic repulsion. Indeed, within the positive halves of the MIQ it possesses an interaction dependent frequency branch. However, in the negative halves of the MIQ the latter branch disappears and two new frequency branches appear which are interaction independent. As a result the system turns from the δg -dependent to the δg -independent branch providing further controllability. Furthermore, the excitation dynamics is investigated in detail. To analyze the dependence on the quench amplitude we focus on a fixed pulse width and vary the final interaction strength. It is shown that the excitation dynamics possesses a linear dependence on the quench amplitude, i.e., for increasing amplitude of the quench the amount of excitations as seen in the fidelity increase. For the dependence of the excitation dynamics on the pulse width we observe a nonlinear dependence, i.e., there is no monotonic behavior of the produced excitations with varying pulse width. The latter implies that in order to control the excitation dynamics one has to use an optimal combination of the quench amplitude and the pulse width. Another prominent signature of the impact of the quenches is revealed by inspecting the momentum distribution. A periodic population transfer of lattice momenta within the positive halves of the MIQ protocol and a transition to a side peak structure in the negative halves of the MIQ are observed. This periodic population transfer of lattice momenta constitutes an independent signature of the excited energy channels within the positive halves of the MIQ protocol, allowing one to study it from another perspective and to potentially measure it in corresponding experiments.

Let us comment on a possible experimental realization of our setup. In a corresponding experiment weakly interacting bosons should be trapped in a one-dimensional optical superlattice being formed by two retroreflected laser beams. To form each supercell of the superlattice the first beam possesses a large wave number and intensity when

compared to the second beam which forms each cell of the supercell. The above-mentioned wave numbers should be commensurate. Then, the potential landscape of each supercell is similar to the one considered in the present study. Such an experimental implementation may be achieved either by the use of holographic masks [53] or by the modulation of the wave number [54]. The interatomic repulsion can be tuned with the aid of a magnetic Feshbach resonance. The corresponding dynamical properties can then be probed with the recently developed single-site resolved imaging techniques (quantum microscope) [55–57]. We also remark that double occupancies can also be identified via Feshbach molecule formation [58–60], while triple occupancies can be measured by inducing three-body recombination [61–63].

Finally, we provide an outlook onto possible future investigations. The achieved understanding of the nonequilibrium dynamics induced by multiple pulses of the interatomic repulsion may inspire similar investigations in other more complicated systems. A possible direction would be to apply our protocol to repulsively interacting dipolar systems and/or to include modulations of the lattice geometry. Certainly for larger particle numbers and sizes the question whether thermalization [64,65] occurs for long evolution times after the system has been quenched to its initial Hamiltonian is an intriguing one.

ACKNOWLEDGMENTS

The authors gratefully acknowledge funding by the Deutsche Forschungsgemeinschaft (DFG) in the framework of the SFB 925 “Light induced dynamics and control of correlated quantum systems.” S.I.M. thanks G. M. Koutentakis for fruitful discussions.

APPENDIX: COMPUTATIONAL METHOD MCTDHB

To solve the time-dependent many-body Schrödinger equation $(i\hbar\partial_t - H)\Psi(x,t) = 0$ we apply the multiconfiguration time-dependent Hartree method for bosons [34,35,66] (MCTDHB). This method has been used extensively in the literature to explore the bosonic quantum dynamics; see for instance [66–71]. The key idea of MCTDHB is to exploit time-dependently variationally optimized single-particle functions (SPFs) to form many-body states and thus to achieve an optimal truncation of the Hilbert space. The ansatz for the many-body wave function is taken as a linear combination of time-dependent permanents $|\vec{n}(t)\rangle$ with time-dependent weights $A_{\vec{n}}(t)$. Each time-dependent permanent $|\vec{n}(t)\rangle$ corresponds to a certain configuration of bosons that occupy M variationally optimized SPFs $|\phi_j(t)\rangle$. In turn, the SPFs are expanded using a primitive time-independent basis $\{|\chi\rangle\}$ of dimension M_{pr} . The time evolution of the N -body wave function for the Hamiltonian under consideration reduces to the determination of the A -vector coefficients and the SPFs which obey the variationally obtained MCTDHB equations of motion [34,35,66]. We also remark that in the limiting case of $M = 1$, MCTDHB reduces to the time-dependent Gross Pitaevski equation.

For our implementation we have used a sine discrete variable representation as a primitive basis for the SPFs. To

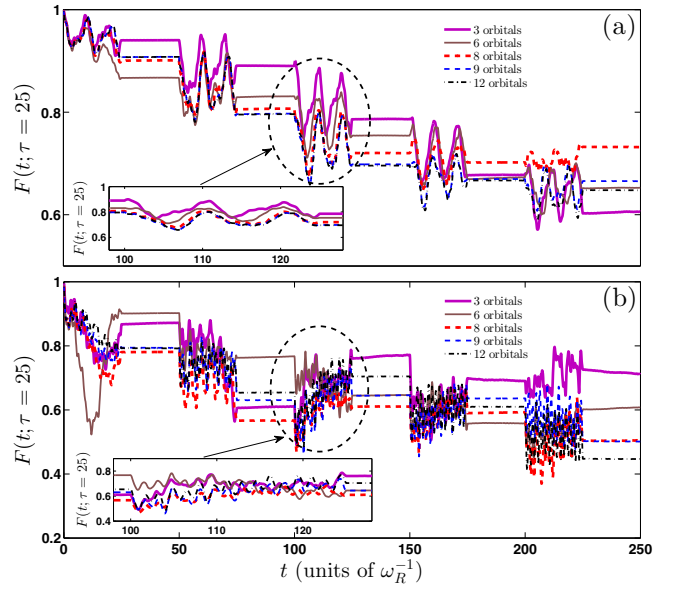


FIG. 9. $F(t; \tau = 25)$ for a varying number of SPFs (see legend) following a five pulse ($n_p = 5$) MIQ with (a) $\delta g = 1$ and (b) $\delta g = 3.0$. For better visibility of the evolution within the positive halves of the MIQ protocol, we show in the insets $F(t; \tau = 25)$ only during the third pulse.

prepare the system in the ground state of the Hamiltonian H , we rely on the relaxation method. The key idea is to iteratively propagate some initial ansatz wave function $|\Psi^{(0)}\rangle$ in imaginary time. This exponentially damps out all contributions but the one stemming from the ground state like $\sim e^{-(E_m - E_0)\tau}$ and therefore the system relaxes to the ground state (within the prescribed accuracy) after a finite time. To study the dynamics, we propagate the wave function by utilizing the appropriate Hamiltonian within the MCTDHB equations of motion. Finally, let us remark that for our implementation we employed the multilayer multiconfiguration Hartree method for bosons [72,73] (ML-MCTDHB), which reduces to MCTDHB for the case of a single bosonic species as considered here.

To maintain the accurate performance of the numerical integration of the MCTDHB equations of motion we ensured that $|\langle\Psi(t)|\Psi(t)\rangle - 1| < 10^{-8}$ and $|\langle\varphi_i(t)|\varphi_j(t)\rangle - \delta_{ij}| < 10^{-9}$ for the total wave function and the SPFs, respectively. To conclude about the convergence of our simulations, we increase the number of SPFs and primitive basis states, thus observing a systematic convergence of our results. In particular, we have used $M_{\text{pr}} = 300$, $M = 9$ ($M_{\text{pr}} = 600$, $M = 8$) for the triple well (eight wells). To be more concrete, in the following we shall briefly demonstrate the convergence procedure for the triple well simulations with increasing number of SPFs. Figures 9(a) and 9(b) present $F(t; \tau = 25)$ for different number of SPFs following a five pulse MIQ with small ($\delta g = 1$) and large ($\delta g = 3$) quench amplitudes, respectively. In both cases a systematic convergence of the fidelity evolution (for $M > 8$) is observed for an increasing number of SPFs. Indeed for small quench amplitudes, see Fig. 9(a), the maximum deviation observed in the fidelity evolution between the 9 and 12 orbital cases is of the order of 3% for large evolution times

$t > 225$, that is, after the fifth pulse. As expected, the case of a larger quench amplitude, presented in Fig. 9(b), shows a more demanding convergence behavior. However, also in this case a decreasing relative error between different approximations for increasing M is illustrated. For instance, the maximum deviation observed in the fidelity evolution calculated using 9 and 12 SPFs, respectively, is of the order of 8% for large evolution times ($t > 200$). Summarizing, it is important to comment that in both of the above-mentioned cases even the calculation with 6 SPFs is not able to quantitatively

predict the dynamics. For better visibility of the relative error between different approximations within a positive half of the MIQ protocol, we show in the corresponding insets of Fig. 9 the dynamics during the positive half of the third pulse. Note here that the same analysis has also been performed for the dynamics in the eight well potential (omitted here for brevity) showing a very similar behavior. Another indicator of convergence is the population of the lowest occupied natural orbital, which is kept below 0.01% for all of our simulations.

-
- [1] O. Morsch and M. Oberthaler, *Rev. Mod. Phys.* **78**, 179 (2006).
- [2] M. Lewenstein, A. Sanpera, V. Ahufinger, B. Damski, A. Sen, and U. Sen, *Adv. Phys.* **56**, 243 (2007).
- [3] I. Bloch, J. Dalibard, and W. Zwerger, *Rev. Mod. Phys.* **80**, 885 (2008).
- [4] M. Lewenstein, A. Sanpera, and V. Ahufinger, *Ultracold Atoms in Optical Lattices: Simulating Quantum Many-body Systems* (Oxford University Press, Oxford, 2012).
- [5] V. I. Yukalov, *Laser Phys.* **19**, 1 (2009).
- [6] G. Zürn, F. Serwane, T. Lompe, A. N. Wenz, M. G. Ries, J. E. Bohn, and S. Jochim, *Phys. Rev. Lett.* **108**, 075303 (2012).
- [7] F. Serwane, G. Zürn, T. Lompe, T. B. Ottenstein, A. N. Wenz, and S. Jochim, *Science* **332**, 336 (2011).
- [8] C. Chin, R. Grimm, P. Julienne, and E. Tiesinga, *Rev. Mod. Phys.* **82**, 1225 (2010).
- [9] A. Polkovnikov, K. Sengupta, A. Silva, and M. Vengalattore, *Rev. Mod. Phys.* **83**, 863 (2011).
- [10] P. Calabrese, *EPJ Web Conf.* **90**, 08001 (2015).
- [11] T. Langen, R. Geiger, and J. Schmiedmayer, *Annu. Rev. Condens. Matter Phys.* **6**, 201 (2015).
- [12] C. Kollath, A. M. Läuchli, and E. Altman, *Phys. Rev. Lett.* **98**, 180601 (2007).
- [13] A. Läuchli and C. Kollath, *J. Stat. Mech.: Theory Exp.* (2008) P05018.
- [14] S. I. Mistakidis, L. Cao, and P. Schmelcher, *J. Phys. B* **47**, 225303 (2014).
- [15] S. I. Mistakidis, L. Cao, and P. Schmelcher, *Phys. Rev. A* **91**, 033611 (2015).
- [16] A. L. Fetter and J. D. Walecka, *The Quantum Mechanics of Many-Particle Systems* (McGraw-Hill, New York, 1971).
- [17] J. Kinnunen and P. Törmä, *Phys. Rev. Lett.* **96**, 070402 (2006).
- [18] N. Proukakis, S. Gardiner, M. Davis, and M. Szymaska, *Quantum Gases: Finite Temperature and Non-Equilibrium Dynamics* (World Scientific, Singapore, 2013), Vol. 1.
- [19] J. Grond, A. I. Streltsov, L. S. Cederbaum, and O. E. Alon, *Phys. Rev. A* **86**, 063607 (2012).
- [20] J. Grond, A. I. Streltsov, A. U. J. Lode, K. Sakmann, L. S. Cederbaum, and O. E. Alon, *Phys. Rev. A* **88**, 023606 (2013).
- [21] O. E. Alon, A. I. Streltsov, and L. S. Cederbaum, *J. Chem. Phys.* **140**, 034108 (2014).
- [22] O. E. Alon, *J. Phys.: Conf. Ser.* **594**, 012039 (2015).
- [23] M. Theisen and A. I. Streltsov, *Phys. Rev. A* **94**, 053622 (2016).
- [24] R. Beinke, S. Klaiman, L. S. Cederbaum, A. I. Streltsov, and O. E. Alon, [arXiv:1612.06711](https://arxiv.org/abs/1612.06711).
- [25] T. Kinoshita, T. Wenger, and D. S. Weiss, *Science* **305**, 1125 (2004).
- [26] T. Kinoshita, T. Wenger, and D. S. Weiss, *Nature (London)* **440**, 900 (2006).
- [27] E. Haller, M. Gustavsson, M. J. Mark, J. G. Danzl, R. Hart, G. Pupillo, and H. C. Nägerl, *Science* **325**, 1224 (2009).
- [28] B. Paredes, A. Widera, V. Murg, O. Mandel, S. Fölling, I. Cirac, G. V. Shlyapnikov, T. W. Hänsch, and I. Bloch, *Nature (London)* **429**, 277 (2004).
- [29] L. Chen, Z. Zhang, and Z. Liang, *Mod. Phys. Lett. B* **30**, 1650367 (2016).
- [30] T. Köhler, K. Goral, and P. S. Julienne, *Rev. Mod. Phys.* **78**, 1311 (2006).
- [31] M. Olshanii, *Phys. Rev. Lett.* **81**, 938 (1998).
- [32] J. I. Kim, V. S. Melezhik, and P. Schmelcher, *Phys. Rev. Lett.* **97**, 193203 (2006).
- [33] P. Giannakeas, F. K. Diakonou, and P. Schmelcher, *Phys. Rev. A* **86**, 042703 (2012).
- [34] O. E. Alon, A. I. Streltsov, and L. S. Cederbaum, *J. Chem. Phys.* **127**, 154103 (2007).
- [35] O. E. Alon, A. I. Streltsov, and L. S. Cederbaum, *Phys. Rev. A* **77**, 033613 (2008).
- [36] L. Campos Venuti and P. Zanardi, *Phys. Rev. A* **81**, 022113 (2010).
- [37] T. Gorin, T. Prosen, T. H. Seligman, and M. Žnidarič, *Phys. Rep.* **435**, 33 (2006).
- [38] S. Campbell, M. A. Garcia-March, T. Fogarty, and T. Busch, *Phys. Rev. A* **90**, 013617 (2014).
- [39] M. Á. García-March, T. Fogarty, S. Campbell, T. Busch, and M. Paternostro, *New J. Phys.* **18**, 103035 (2016).
- [40] S. I. Mistakidis and P. Schmelcher, *Phys. Rev. A* **95**, 013625 (2017).
- [41] S. Fölling, S. Trotzky, P. Cheinet, M. Feld, R. Saers, A. Widera, T. Müller, and I. Bloch, *Nature (London)* **448**, 1029 (2007).
- [42] Y. A. Chen, S. Nascimbéne, M. Aidelsburger, M. Atala, S. Trotzky, and I. Bloch, *Phys. Rev. Lett.* **107**, 210405 (2011).
- [43] J. W. Abraham and M. Bonitz, *Contrib. Plasma Phys.* **54**, 27 (2014).
- [44] J. W. Abraham, K. Balzer, D. Hochstuhl, and M. Bonitz, *Phys. Rev. B* **86**, 125112 (2012).
- [45] S. Bauch, D. Hochstuhl, K. Balzer, and M. Bonitz, *J. Phys.: Conf. Ser.* **220**, 012013 (2010).
- [46] S. Klaiman and O. E. Alon, *Phys. Rev. A* **91**, 063613 (2015).
- [47] S. Klaiman, A. I. Streltsov, and O. E. Alon, *Phys. Rev. A* **93**, 023605 (2016).
- [48] S. Klaiman, A. I. Streltsov, and O. E. Alon, *J. Phys.: Conf. Ser.* **826**, 012020 (2017).

- [49] I. Brouzos, S. Zöllner, and P. Schmelcher, *Phys. Rev. A* **81**, 053613 (2010).
- [50] S. Will, D. Iyer, and M. Rigol, *Nat. Commun.* **6**, 6009 (2015).
- [51] R. Bücker, J. Grond, S. Manz, T. Berrada, T. Betz, C. Koller, U. Hohenester, T. Schumm, A. Perrin, and J. Schmiedmayer, *Nat. Phys.* **7**, 608 (2011).
- [52] N. Gemelke, E. Sarajlic, Y. Bidel, S. Hong, and S. Chu, *Phys. Rev. Lett.* **95**, 170404 (2005).
- [53] J. F. Sherson, C. Weitenberg, M. Endres, M. Cheneau, I. Bloch, and S. Kuhr, *Nature (London)* **467**, 68 (2010).
- [54] T. Li, H. Kelkar, D. Medellin, and M. Raizen, *Opt. Express* **16**, 5465 (2008).
- [55] P. M. Preiss, R. Ma, M. E. Tai, J. Simon, and M. Greiner, *Phys. Rev. A* **91**, 041602(R) (2015).
- [56] T. Fukuhara, S. Hild, J. Zeiher, P. Schauß, I. Bloch, M. Endres, and C. Gross, *Phys. Rev. Lett.* **115**, 035302 (2015).
- [57] M. Miranda, R. Inoue, Y. Okuyama, A. Nakamoto, and M. Kozuma, *Phys. Rev. A* **91**, 063414 (2015).
- [58] F. Meinert, M. J. Mark, E. Kirilov, K. Lauber, P. Weinmann, M. Gröbner, A. J. Daley, and H. C. Nägerl, *Science* **344**, 1259 (2014).
- [59] K. Winkler, G. Thalhammer, F. Lang, R. Grimm, J. H. Denschlag, A. J. Daley, A. Kantian, H. P. Büchler, and P. Zoller, *Nature (London)* **441**, 853 (2006).
- [60] J. G. Danzl, M. J. Mark, E. Haller, M. Gustavsson, R. Hart, J. Aldegunde, J. M. Hutson, and H. C. Nägerl, *Nat. Phys.* **6**, 265 (2010).
- [61] B. D. Esry, C. H. Greene, and J. P. Burke, Jr., *Phys. Rev. Lett.* **83**, 1751 (1999).
- [62] T. Kraemer, M. Mark, P. Waldburger, J. G. Danzl, C. Chin, B. Engeser, A. D. Lange, K. Pilch, A. Jaakkola, H. C. Nägerl, and R. Grimm, *Nature (London)* **440**, 315 (2006).
- [63] S. Knoop, F. Ferlaino, M. Mark, M. Berninger, H. Schöbel, H. C. Nägerl, and R. Grimm, *Nat. Phys.* **5**, 227 (2009).
- [64] M. Srednicki, *Phys. Rev. E* **50**, 888 (1994).
- [65] M. Rigol, V. Dunjko, and M. Olshanii, *Nature (London)* **452**, 854 (2008).
- [66] A. I. Streltsov, O. E. Alon, and L. S. Cederbaum, *Phys. Rev. Lett.* **99**, 030402 (2007).
- [67] A. I. Streltsov, K. Sakmann, O. E. Alon, and L. S. Cederbaum, *Phys. Rev. A* **83**, 043604 (2011).
- [68] O. E. Alon, A. I. Streltsov, and L. S. Cederbaum, *Phys. Rev. A* **76**, 013611 (2007).
- [69] O. E. Alon, A. I. Streltsov, and L. S. Cederbaum, *Phys. Rev. A* **79**, 022503 (2009).
- [70] G. M. Koutentakis, S. I. Mistakidis, and P. Schmelcher, *Phys. Rev. A* **95**, 013617 (2017).
- [71] S. I. Mistakidis, T. Wulf, A. Negretti, and P. Schmelcher, *J. Phys. B* **48**, 244004 (2015).
- [72] L. Cao, S. Krönke, O. Vendrell, and P. Schmelcher, *J. Chem. Phys.* **139**, 134103 (2013).
- [73] S. Krönke, L. Cao, O. Vendrell, and P. Schmelcher, *New J. Phys.* **15**, 063018 (2013).

**4.1.4 Bosonic Quantum Dynamics Following a Linear Interaction Quench
in Finite Optical Lattices of Unit Filling**



Bosonic quantum dynamics following a linear interaction quench in finite optical lattices of unit filling

S.I. Mistakidis^{a,*}, G.M. Koutentakis^{a,b}, P. Schmelcher^{a,b}

^aZentrum für Optische Quantentechnologien, Universität Hamburg, Luruper Chaussee 149, 22761 Hamburg, Germany

^bThe Hamburg Centre for Ultrafast Imaging, Universität Hamburg, Luruper Chaussee 149, 22761 Hamburg, Germany

ARTICLE INFO

Article history:

Received 23 August 2017

In final form 30 November 2017

Available online 2 December 2017

Keywords:

Nonequilibrium dynamics

Linear interaction quench

Superfluid to Mott insulator phase transition

Interband tunneling

Intraband tunneling

ABSTRACT

The nonequilibrium ultracold bosonic quantum dynamics in finite optical lattices of unit filling following a linear interaction quench from a superfluid to a Mott insulator state and vice versa is investigated. The resulting dynamical response consists of various inter and intraband tunneling modes. We find that the competition between the quench rate and the interparticle repulsion leads to a resonant dynamical response, at moderate ramp times, being related to avoided crossings in the many-body eigenspectrum with varying interaction strength. Crossing the regime of weak to strong interactions several transport pathways are excited. The higher-band excitation dynamics is shown to obey an exponential decay possessing two distinct time scales with varying ramp time. Studying the crossover from shallow to deep lattices we find that for a diabatic quench the excited band fraction decreases, while approaching the adiabatic limit it exhibits a non-linear behavior for increasing height of the potential barrier. The inverse ramping process from strong to weak interactions leads to a melting of the Mott insulator and possesses negligible higher-band excitations which follow an exponential decay for decreasing quench rate. Finally, independently of the direction that the phase boundary is crossed, we observe a significant enhancement of the excited to higher-band fraction for increasing system size.

© 2017 Elsevier B.V. All rights reserved.

1. Introduction

During the past two decades, ultracold atoms in optical lattices emerged as a versatile system to investigate many-body (MB) phenomena [1–4]. A prominent example is the experimental observation of the superfluid (SF) to Mott insulator (MI) quantum phase transition [5,6] which, among others, demonstrated a pure realization of the Bose-Hubbard model [7,8]. Moreover, lattice systems constitute ideal candidates for studying nonequilibrium quantum phase transitions [9–14], where a number of defects, induced by time-dependent quenches [15,16], appear in the time evolving state. The Kibble-Zurek mechanism of such defect formation [15,17–20], originally addressed in the context of classical phase transitions [21,22], has been tested in different ultracold MB settings [23–28] and refers to the rate of topological defect formation induced by quenches across phase transitions.

Quench dynamics of ultracold bosons confined in an optical lattice covering the MI-SF transition in both directions has been vastly used to examine both the Kibble-Zurek mechanism [19,25,26,29–32] and the approach to the adiabatic response limit

[29,33–43,45]. Referring to the Kibble-Zurek mechanism, recent studies [30,31] of a linear quench across the MI-SF and back in the one-dimensional Bose-Hubbard model demonstrated that the excitation density and the correlation length satisfy the Kibble-Zurek scaling for limited ranges of quench rates. On the other hand and focussing on the slow quench dynamics across the MI-SF transition many recent works evinced the formation and melting of Mott domains [34,37–40], the growth of interparticle correlations [32,41–44] and the consequent equilibration process [16,35,45].

Despite the enormous theoretical and experimental efforts in this field, the response of such systems subjected to abrupt or quasi-adiabatic quenches has not been completely understood and deserves further investigation. In particular, a nonadiabatic quench inevitably excites the system, and a number of defects including higher-band excitations can be formed during the dynamics. The latter implies the necessity to consider a multiband treatment [46] of the nonequilibrium correlated dynamics and to obtain information about the higher-band excitation spectrum [47–52] being inaccessible by the lowest Bose-Hubbard model or mean-field (MF) methods. Promising candidates for such investigations constitute few-body systems [53,54] being accessible by current state of the art experiments [55–58]. In this context, it is possible to track the microscopic quantum mechanisms [59–62]

* Corresponding author.

E-mail address: smistaki@physnet.uni-hamburg.de (S.I. Mistakidis).

consisting of intraband and interband tunneling, namely tunneling within the same or between energetically different single-particle bands respectively, and to avoid finite temperature effects. Such few-body systems do not serve as a platform to confirm the Kibble-Zurek scaling hypothesis due to their finite size [43]. However, they provide useful insights into the largely unexplored scaling of few-body defect density including the formation and melting of Mott domains and the excited to higher-band fraction participating in the dynamics.

In the present work we consider few bosons confined in an optical lattice of unit filling. Thereby, the ground state for increasing interaction strength experiences the few-body analogue of the SF to MI transition. We first analyze the MB eigenspectrum for varying interparticle repulsion, revealing the existence of narrow and wide avoided crossings between states of the zeroth and first excited band. Then, we apply a linear interaction quench (LIQ) protocol either from weak to strong interactions (positive LIQ) or inversely (negative LIQ) covering in both cases the diabatic to nearly adiabatic crossing regimes. As a consequence we observe a dynamical response consisting of the lowest band tunneling and higher-band excitations. Overall, we find an enhanced dynamical response at moderate quench rates rather than in the abrupt or almost adiabatic regimes. The lowest band dynamics consists of first and second order tunneling [63–65]. These modes can be further manipulated by tuning either the interaction strength after the quench (postquench interaction) or the height of the potential barriers in the optical lattice. Furthermore, we show that following a positive LIQ the excited to higher-band fraction obeys a bi-exponential decay for varying ramp time. The latter decay law possesses two time scales being related to the width of the existing avoided crossings in the eigenspectrum. However, the interband tunneling [66,67], with varying height of the potential barrier exhibits a more complex behavior. For diabatic quenches it decreases, while for smaller quench rates it scales non-linearly possessing a maximum at a certain height of the potential barrier. The latter behavior manifests the strong dependence of the excited to higher-band fraction on the quench rate. Moreover, the excited fraction for a varying postquench interaction strength features different scaling laws. Approaching the region of the corresponding avoided crossing it exhibits a non-linear growth, while for stronger interactions it increases almost linearly. On the contrary, for a negative LIQ we observe the melting of the MI. Here, the lowest band transport (intraband tunneling) is reduced when compared to the inverse scenario, while the excited fraction is negligible obeying an exponential decay both with varying ramp time and potential height. Finally, for both positive and negative LIQs the higher-band fraction is significantly enhanced for increasing system size.

This work is organized as follows. In Section 2 we introduce our setup and outline the multiband expansion being used for a microscopic analysis of the dynamics. Section 3 presents the resulting dynamics induced by a LIQ connecting the weakly to strongly correlated regimes and back in a triple well of unit filling. To extend our findings in Section 4 we discuss the LIQ dynamics for larger lattice systems of unit filling. We summarize and discuss future perspectives in Section 5. Appendix A describes our computational methodology.

2. Setup and analysis tools

The Hamiltonian of N identical bosons each of mass M confined in a one-dimensional m -well optical lattice employing a LIQ protocol reads

$$H = \sum_{i=1}^N \left(\frac{p_i^2}{2M} + V_0 \sin^2(kx_i) \right) + g(t, \tau) \sum_{i < j} \delta(x_i - x_j). \quad (1)$$

The lattice potential is characterized by its depth V_0 and periodicity l , with $k = 2\pi/l$ being the wave vector of the counterpropagating lasers forming the optical lattice. To restrict the infinitely extended trapping potential to a finite one with m wells and length L , we impose hard wall boundary conditions at the appropriate positions, $x_m = \pm \frac{m\pi}{2k}$.

Within the ultracold regime, the short-range interaction potential between particles located at positions x_i , can be adequately described by s -wave scattering. To trigger the dynamics we follow a LIQ protocol. At $t = 0$ the interatomic interaction is quenched from the initial value g_i to a final one g_f in a linear manner for time $t \in [0, \tau]$ and then it remains a constant g_f . Therefore, our protocol reads

$$g(t, \tau) = g_i + \delta g \frac{t}{\tau}. \quad (2)$$

Here, $\delta g = g_f - g_i$ denotes the quench amplitude of the linear quench, while g_i (g_f) is the effective one-dimensional interaction strength before (after) the quench. The effective one-dimensional interaction strength [68] is given by $g_{1D} = \frac{2\hbar^2 a_0}{Ma_{\perp}^2} \left(1 - |\zeta(1/2)| a_0 / \sqrt{2} a_{\perp} \right)^{-1}$. Here $a_{\perp} = \sqrt{\hbar/M\omega_{\perp}}$ is the transverse harmonic oscillator length with ω_{\perp} the frequency of the two-dimensional confinement and a_0 denotes the free space 3D s -wave scattering length. Experimentally, the effective interaction strength can be tuned either via a_0 with the aid of Feshbach resonances [69,70] or via the corresponding transversal confinement frequency ω_{\perp} [68,71,72].

In the following, the Hamiltonian (1) is rescaled in units of the recoil energy $E_R = \frac{\hbar^2 k^2}{2M}$. Then, the corresponding length, time and interaction strength scales are given in units of k^{-1} , $\omega_R^{-1} = \hbar E_R^{-1}$ and $E_R k^{-1}$, respectively.

To simulate the nonequilibrium dynamics we employ the Multi-Configuration Time-Dependent Hartree method for Bosons (MCTDHB) [73,74] which exploits an expansion in terms of time-dependent variationally optimized single-particle functions (see Appendix A for more details). In contrast to the MF approximation, within this approach we account for the system's interparticle correlations and hence we will refer to MCTDHB simply as the MB approach. However, for the analysis of the induced dynamics in lattice systems, it is more intuitive to rely on a time-independent MB basis instead of a time-dependent one. Here, we project the numerically obtained wavefunction on a time-independent number state basis being constructed by the single-particle Wannier states localized on each lattice site. The MB bosonic wavefunction of a system with N bosons, m -wells and j localized single particle states [59,60] reads

$$|\Psi\rangle = \sum_{\{\vec{n}_i\}} C_{\{\vec{n}_i\}} |\vec{n}_1, \vec{n}_2, \dots, \vec{n}_m\rangle, () \quad (3)$$

where $|\vec{n}_1, \vec{n}_2, \dots, \vec{n}_m\rangle$ is the multiband Wannier number state, the element $\vec{n}_i = |n_i^{(1)}\rangle \otimes |n_i^{(2)}\rangle \otimes \dots \otimes |n_i^{(j)}\rangle$ and the Wannier orbital $|n_i^{(k)}\rangle$ refers to the number of bosons which reside at the i -th well and k -th band. For instance, in a setup with $N = 3$ bosons confined in a triple well i.e. $m = 3$, which includes $k = 3$ single-particle states, the state $|1^{(0)}, 1^{(1)}, 1^{(0)}\rangle$ indicates that in the left and right wells one boson occupies the Wannier orbital of the zeroth excited band while in the middle well there is one boson in the Wannier orbital of the first excited band. Below, when we refer to a boson that resides within the zeroth (ground) band we shall omit the zero index. Here, one can realize three different energetic classes of number states with respect to the interparticle repulsion. Namely, the triples $\{|3, 0, 0\rangle + \odot\}$ (T), the single pairs $\{|2, 1, 0\rangle + \odot\}$ (SP)

and the singles $\{|1, 1, 1\rangle + \odot\}$ (S), where \odot stands for all corresponding permutations. For later convenience, on the analysis part, we further classify the excited band energetic classes into single-particle excitation (SE) and higher excited (HE) classes. The former [latter] class involves states of single [double] occupancy in every site with one excitation to the first excited band e.g. $\{|1, 1^{(1)}, 1\rangle + \odot\}$ [$\{|1 \otimes 1^{(1)}, 1, 0\rangle + \odot\}$ and $\{|1^{(1)}, 2, 0\rangle + \odot\}$].

Moreover, according to the above expansion the time averaged probability for bosons to lie in a higher single-particle band reads

$$\bar{P}_{exc}(\tau) = 1 - \frac{1}{T} \int_0^T dt P_0(t; \tau). \quad (4)$$

Here, $P_0(t; \tau) = \sum_{\{n_i\}} |\langle n_1, n_2, n_3 | \Psi(t) \rangle|^2$, $i = 1, 2, 3$ denotes the probability for all particles to reside within the zeroth band, while T refers to the considered finite evolution time where $\bar{P}_{exc}(\tau)$ has converged to a certain value. The above probability amplitude will be a main tool for the investigation of the scaling of the excited to higher-band fraction with respect to τ .

3. LIQ dynamics in a triple well of unit filling

To analyze the LIQ induced dynamics of our system, it is instructive first to demonstrate the dependence of the eigenstates on the interparticle repulsion. Thus, we first investigate the eigenspectra of the system with varying interaction strength [Section 3.1], which are subsequently related to the LIQ dynamics [Sections 3.2 and 3.3].

3.1. Eigenspectra

In contrast to the discrete Bose-Hubbard model, here we employ a continuum space Hamiltonian [see Eq. (1)], which allows us to resolve quench induced higher-band excitations [75]. For completeness we note that the Bose-Hubbard model is adequate for the theoretical description of the quench dynamics in deep lattices (i.e. large V_0) and for relatively small quench amplitudes when compared to the band gap. To expose the underlying physical processes that lead to the emergence of such MB excited states [49–52] we examine, below, the eigenenergies of three particles confined in a triple well potential as a function of the interaction strength g .

First we focus on the case of a relatively shallow triple well, namely $V_0 = 4.0$, see Fig. 1(a). For very small interactions, $g \simeq 0$, the MB eigenstates are energetically categorized according to their corresponding particle configuration in terms of single-particle bands. For instance, Fig. 1(a) shows that the eigenstates of the system are predominantly bunched onto two energy regions denoted by E_g and E^* respectively. The eigenstates lying within E_g possess zero higher-band excitations, while those bunched onto E^* refer to states with one single-particle excitation to the first excited band. The width of the aforementioned energy regions (bandwidth) depends on the tunneling coupling between the different sites. Note here that the term tunneling coupling refers to the corresponding inverse tunneling rate [7,8]. The distance between E^* and E_g (band gap) is characterized by the band gap between the ground and the first excited band of the non-interacting system. Regarding the decomposition of each eigenstate in terms of (localized) Wannier number states [see Eq. (3)] it turns out that it is an admixture of all the energetic classes S, SP and T . The latter indicates the spatial delocalization of the bosons within the triple well, and therefore manifests the few-body analogue of the SF phase for low interactions.

For increasing interaction strength the energy expectation value of the number states belonging to the SP and T classes increases strongly. The same holds for the eigenenergies of the eigenstates

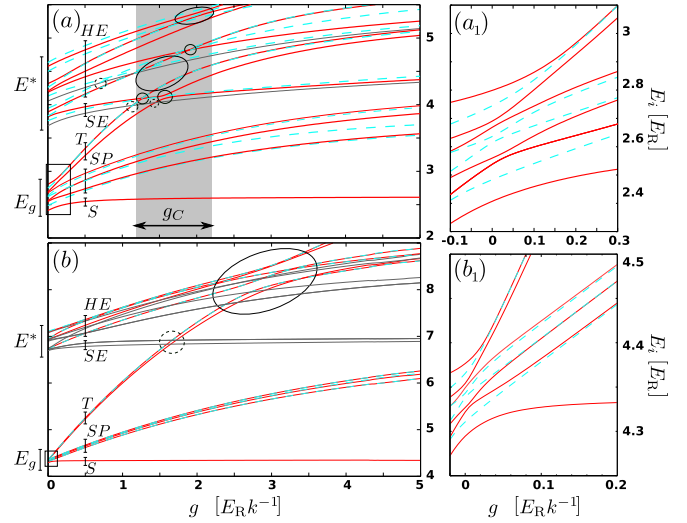


Fig. 1. Dependence of the lowest 25 eigenenergies E_i on the interaction strength g . The system consists of three bosons confined in a triple well with potential depth (a) $V_0 = 4$ and (b) $V_0 = 10$. Solid (dashed) lines represent parity even (odd) E_i 's. Wide (narrow) avoided crossings possessing a width $\delta E > 0.01$ ($\delta E < 0.01$) are denoted by solid (dashed) circles. The eigenenergies of the eigenstates that do not contribute to any wide avoided crossing are shown in grey. The energy regions E_g, E^* and the subbands S, SP, T, SE and HE are marked by the respective bars. The grey scaled interaction interval g_C in (a) denotes the region of avoided crossings between the SE and T as well as the T and HE classes for the case of a shallow lattice $V_0 = 4$. The solid boxes indicate the SF to MI transition. For better visibility of the avoided crossings in the vicinity of $g = 0$ (see solid boxes), (a₁) and (b₁) provide the lowest 10 eigenenergies of (a) and (b) respectively.

to which the aforementioned number states are contributing. For $0 < g \lesssim 0.5$ several avoided crossings are observed, see Fig. 1 (a₁). These avoided crossings manifest the tunneling coupling between the S, SP and T number states of the same parity [66,75]. The aforementioned interaction regime corresponds in our few-body system to the region where the transition from the SF to the MI phase takes place. For $g \geq 0.5$ the eigenenergies of the lowest band become well separated into three subbands according to the energetic class of their dominant number state, see Fig. 1(a). The ground state of the system is dominated by the S class manifesting the few-body analogue of the MI phase. The SP and T class dominated eigenstates are also bunched together forming the SP and T subbands. Moreover, the eigenstates of the T subband (being the most sensitive to interparticle repulsion) experience wide (see solid circles) and narrow (see dashed circles) [76] avoided crossings with the eigenstates possessing a higher-band excitation. The wide avoided crossings are related to the onset of the cradle mode [59,60] and are a consequence of the interaction induced decay of an SP or T state caused by the scattering of one of the bosons that reside in the same well to the first excited state of an adjacent site [77]. This latter process gives rise to the so-called cradle mode which represents a dipole-like intrawell oscillation in the outer wells of the finite lattice (for a detailed description on the generation and properties of this mode see [59,60]).

The same overall behavior can be observed for deeper lattices, see for instance in Fig. 1(b) the case of $V_0 = 10$. As shown, the differences between shallow and deep lattices are mainly quantitative [78]. The bandwidth of each subband decreases as a consequence of the reduced tunneling coupling, while the corresponding subband energy gap increases. Most importantly, the transition from the SF to the MI state is realized for smaller interactions when compared to the case of $V_0 = 4$ [see in particular Fig. 1 (a₁) and (b₁)]. Moreover, as a consequence of the increased band gap, the positions of the avoided crossings related to the cradle mode (see solid circles in Fig. 1) occur at larger interparticle

repulsions g . Concluding, all differences in the eigenspectrum caused by V_0 can be traced back to the increased intrawell localization of the particles for deeper lattices.

In the following sections, we study the dynamical response induced by a LIQ from $g_i = 0$ to $g_f = 2$ and back. The choice of $g_i = 0$ ensures that the initial state within a positive LIQ consists of an admixture of all energetic classes, while due to the post-quench interaction, $g_f = 2$, the system remains adequately detuned from the cradle mode even in the fully diabatic (i.e. abrupt) limit. Moreover, following a negative LIQ from $g_i = 2$ to $g_f = 0$ the system initially resides in a MI state and finally in an admixture of several lowest band states. Taking advantage of the above presented eigenspectra, we expect that the higher-band dynamics strongly depends on the ramping rate of the SF to MI transition resulting in a different population of the T class (eigen) states.

3.2. Quench dynamics from SF to MI phase

Let us first focus on the positive LIQ dynamics to strong interactions, namely from $g_i = 0$ to $g_f = 2$, of a system consisting of three initially non-interacting bosons confined in a triple well. The initial MB state is an admixture of the available lowest band number states [see also Fig. 1(a)], where the main contribution stems from the SP category due to the hard wall boundary conditions. To gain an overview of the system's dynamical response induced by the LIQ we employ the fidelity $F(t; \tau) = |\langle \Psi_\tau(0) | \Psi_\tau(t) \rangle|^2$, being the overlap between the time evolved and the initial (ground) state [79–81]. Fig. 2(a) presents $F(t; \tau)$ for a shallow lattice ($V_0 = 4$) with varying ramp time τ . As it can be seen, $F(t; \tau)$ performs oscillations in time with multiple frequencies, while for increasing ramp time the system significantly departs from its initial state [i.e. $F(t; \tau)$ overall decreases]. Interestingly enough, for intermediate τ 's the fidelity fluctuates more prominently, see e.g. $15 < \tau < 35$, indicat-

ing an enhanced dynamical response. The same overall response is observed for deeper lattices, see for instance Fig. 2(d), but the corresponding signatures of enhanced response for larger τ 's become more faint due to the increased energy gap in the respective MB eigenspectra [see also Fig. 1]. To further elaborate on the overall response of the system induced by the LIQ we show in Fig. 2(b) the time averaged fidelity of Fig. 2(a) for different ramp times, namely $\bar{F}(\tau) = \frac{1}{T-\tau} \int_\tau^T dt F(t; \tau)$, where $T = 500$. We observe that for increasing τ , $\bar{F}(\tau)$ mainly decreases possessing also some small amplitude deformations displayed as dips in $\bar{F}(\tau)$. This overall decrease of $\bar{F}(\tau)$ implies that the system departs more prominently from its initial state for increasing τ and it is a manifestation of the Landau–Zener mechanism [19,82,83]. Namely, the more adiabatically we drive the system it departs stronger from its initial state. Finally, it is observed that for large enough τ , namely $\tau > 70$, \bar{F} tends to a constant value which indicates a tendency to approach the adiabatic ramping rate. The small amplitude deformations in $\bar{F}(\tau)$ refer to different resonant response regions at specific intervals of τ . These strong response regions indicate that the specific combination of τ 's and quench amplitude are more efficient to cross the existing avoided crossings [see Fig. 1] and as a consequence to depart from the initial state. This latter behavior is already imprinted in $F(t; \tau)$ at the final instant of the ramping, i.e. $t = \tau$. Indeed, within the τ intervals that $\bar{F}(\tau)$ exhibits dips (humps) the system departs significantly (negligibly) from its initial state at time $t = \tau$, see also Fig. 2(a). A careful inspection of the eigenspectra, shown in Fig. 1(a), indicates that for smaller V_0 's the gap between the different energetic subbands reduces and therefore the corresponding tunneling processes can be more pronounced. The latter suggests that for shallower [deeper] lattices the system is perturbed more efficiently [inefficiently] resulting in an enhanced [reduced] dynamical response. To examine in more detail the dynamical response, induced by the LIQ, we employ the normalized variance of the fidelity

$$K(\tau) = \frac{\sqrt{\sigma_F^2(\tau)}}{\bar{F}(\tau)}, \quad (5)$$

where $\sigma_F^2(t) = \frac{1}{T-\tau} \int_\tau^T dt [F(t; \tau) - \bar{F}(\tau)]^2$ denotes the temporally integrated variance of the fidelity. $K(\tau)$ serves as a measure for the mean fidelity variation from its mean value and it is bounded to take values within the interval $[0, 1]$. Then, when $K(\tau) \rightarrow 1$ [$K(\tau) \rightarrow 0$] the system possesses the maximum [minimum] fluctuation from its mean final state. Clearly, within the ramping intervals $\tau \in (5, 10)$, $(15, 35)$ the system can be driven away from its initial state in the most prominent manner [$K(\tau)$ increases] and therefore the dynamical response is maximized (see also below).

To identify the participating tunneling modes induced by the positive LIQ, we inspect the fidelity spectrum [61,62], see Fig. 2(e). As shown the LIQ triggers five distinct tunneling modes onto the system. The first four modes located at $\omega_{1,2,3,4} \approx 0.2, 1, 1.8, 2.9$ for $V_0 = 10, g_f = 2$ refer to intraband tunneling within the SP class, $SP \rightarrow S, SP \rightarrow T$, and $T \rightarrow S$ categories respectively. The mode at $\omega_5 \approx 3.75$ indicates interband interaction assisted tunneling between the S and HE states. Note here that the $SP \rightarrow S$, and $T \rightarrow S$ lowest band modes refer to second order tunneling [63–65], while the others denote single-particle transport. The positions of these frequency branches remain insensitive to varying τ , see the inset in Fig. 2(e). It is also worth mentioning at this point that the dominant dynamical modes $SP \rightarrow S$ and $SP \rightarrow T$ are responsible for the maximized dynamical response [see Fig. 2(c)] within the ramping intervals $\tau \in (5, 10)$ and $(15, 35)$ respectively. To highlight the correlated MB character of the above mentioned tunneling processes we also show the corresponding fidelity

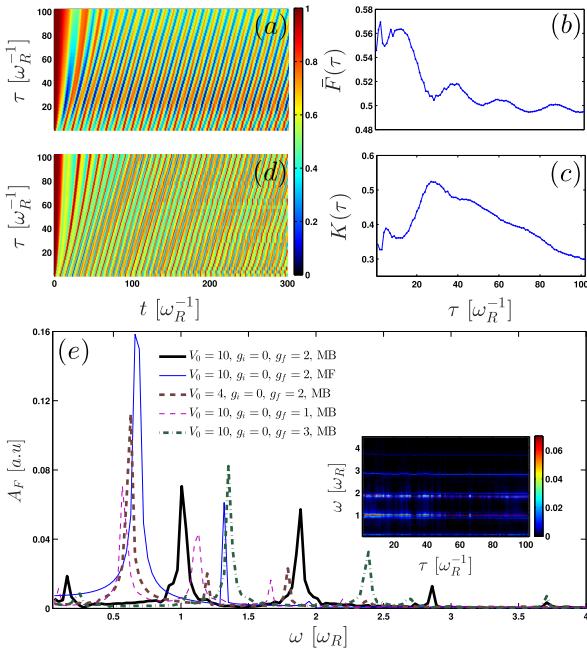


Fig. 2. Fidelity evolution for varying ramp time τ after a LIQ from $g_i = 0$ to $g_f = 2$. Shown are the cases of (a) a shallow $V_0 = 4$ and (d) a deep $V_0 = 10$ triple well. (b) Mean fidelity $\bar{F}(\tau)$ and (c) normalized variance of the fidelity $K(\tau)$ in the case of a shallow lattice for varying τ . (e) Spectrum of the fidelity $F(\omega)$, following a LIQ with $\tau = 8$ for different barrier heights, initial and final interactions within the MB approach or the MF approximation (see legend). Inset: $F(\omega)$ following a LIQ from $g_i = 0$ to $g_f = 2$ for varying ramp time τ . The system consists of three initially non or weakly interacting bosons (see legend) confined in a triple well.

spectrum calculated within the MF approximation. Here, we observe that the system features only the first two tunneling modes, namely transport within the SP and $SP \rightarrow S$ categories. These mode frequencies are also positively shifted namely $\omega'_{1,2} \approx 0.65, 1.35$ when compared to the MB approach. As a next step, let us demonstrate possible control protocols of the tunneling dynamics. An efficient way to manipulate the transport frequency is to tune the height of the potential barriers. Then, the tunneling frequency can be enhanced by using a shallow lattice as the corresponding energy gaps between the different subbands become smaller [compare Fig. 1(a), (b)], thereby making each tunneling process more favorable. Indeed, as shown in Fig. 2(e) the single-particle tunneling modes for $V_0 = 4$ are located at larger frequencies $\omega'_{1,2} \approx 0.6, 1.2$ when compared to $V_0 = 10$ with the former being the most energetically favorable as it possesses the highest amplitude. On the other hand, the two particle transport modes, namely $SP \rightarrow S$ and $S \rightarrow T$, are negatively shifted with respect to their corresponding frequencies for $V_0 = 10$. The latter is a consequence of the decreasing subband energy gap occurring for shallower lattices, see also Fig. 1. Alternatively, a similar manipulation of the tunneling frequency can be achieved by tuning the postquenched state, by e.g. the value of g_f . We observe that for smaller (larger) g_f 's the corresponding tunneling branches are negatively (positively) shifted when compared to $g_f = 2$ and $V_0 = 10$ [see Fig. 2(e)]. It is important to note here that the frequency peaks located at $\omega''_{1,2} \approx 0.6, 1.1$ refer to tunneling between energetically different SP states and the S class. Summarizing, it has been shown that by tuning either the height of the potential barrier or the postquenched state via g_f we can manipulate the location and the intensity of the tunneling frequency branches.

Next we investigate the excitation dynamics, and in particular the time averaged probability of finding at least one boson within a single-particle state of a higher-band [see also Eq. (4)]. Fig. 3(a) presents $\bar{P}_{exc}(\tau)$ for varying τ . As it is evident and further confirmed by a direct numerical fit, the mean excitation probability obeys the bi-exponential law

$$\bar{P}_{exc}(\tau) = Ae^{-\tau/\tau_1} + Be^{-\tau/\tau_2}, \quad (6)$$

where A, B are positive constants. Here, the two time scales introduced by the positive constants τ_1, τ_2 of the bi-exponential are necessary in order to describe accurately the mean excitation dynamics covering the sudden to adiabatic interaction quench regimes. The existence of these two time scales can be explained by the behavior of the number states that contribute to the MB state at each ramping interval. For convenience let us refer to the ramping time at the border between diabatic and moderate to nearly adiabatic ramping as τ_a [see also Fig. 3(a)]. Then, following the LIQ for $\tau < \tau_a$ where $\bar{P}_{exc}(\tau)$ exhibits a rapid decay, the avoided crossing located at $g = 0$ in the eigenspectra is crossed diabatically and the MB state after the quench consists of a superposition of all lowest band number state classes. However for $\tau > \tau_a$, where $\bar{P}_{exc}(\tau)$ features a slow decay, the crossing at $g = 0$ is traversed in a more adiabatic manner and the system after the quench is again in a superposition of the above mentioned states but now the state $|1, 1, 1\rangle$ possesses the main contribution. Alternatively, the above description can be explained by the fact that the SP and T categories for varying τ exhibit different scalings. Indeed, for $\tau \ll \tau_a$ the population of the SP increases while the T slowly decreases for increasing τ . However, for $\tau \geq \tau_a$ both categories decay in favor of the S state. Having described the mechanism behind this bi-exponential decay of $\bar{P}_{exc}(\tau)$ let us demonstrate whether this law is robust also within the MF approximation or upon varying the initial state of the system. As it can be seen in Fig. 3(a) $\bar{P}_{exc}(\tau)$ exhibits the same bi-exponential law also within the MF approximation but the predicted

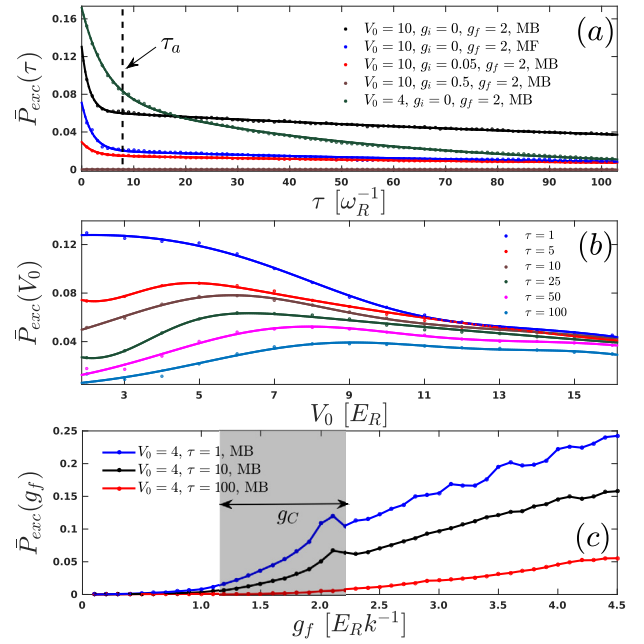


Fig. 3. Mean excitation probability of at least one boson to reside in an excited band for varying (a) ramp time τ of the LIQ, (b) barrier height V_0 and (c) postquench interaction strength g_f . In all cases we consider a LIQ from an initially non to a final strongly correlated state unless stated otherwise (see legends). Different curves correspond to different parameter values (see legend), while the lines belong to a numerical fitting and provide a guide to the eye. The time-scale τ_a denotes the border between diabatic and moderate to nearly adiabatic ramping for $V_0 = 10$. The grey scaled interaction interval in (c) denoted by g_C refers to the region of avoided crossings when $V_0 = 4$ between the SE and T as well as the T and HE categories, see also Fig. 1 (a).

amount of excitations is lesser when compared to the MB approach. Therefore, we can infer that the MF approximation predicts the qualitative decay of excitations but fails to capture the quantitative amount of excitations. Turning again to the MB approach, we observe that by initializing the system in a weakly interacting state $\bar{P}_{exc}(\tau)$ shows the same decay law but fewer excitations are produced than starting from $g_i = 0$. This can be explained by the fact that the population of the T category in the initial state is strongly suppressed for increasing g_i . Additionally, Fig. 3(a) shows $\bar{P}_{exc}(\tau)$ for a shallower lattice. $\bar{P}_{exc}(\tau)$ again exhibits a bi-exponential decay but most importantly it is observed that at $\tau \approx 19$ the curves for $V_0 = 10$ and $V_0 = 4$ cross each other. As a consequence for $\tau < 19$ [$\tau > 19$] $\bar{P}_{exc}(\tau)$ is larger [smaller] for the shallower lattice. The above-mentioned crossing between the $\bar{P}_{exc}(\tau)$ for different heights of the potential barriers serves as a starting-point for investigating in the following the behavior of the mean excitation probability for varying V_0 and fixed τ , see Fig. 3(b). A compatible double

Gaussian fit $\bar{P}_{exc}(V_0) = A_1 e^{-\left(\frac{V_0 - C_1}{C_2}\right)^2} + B_1 e^{-\left(\frac{V_0 - D_1}{D_2}\right)^2}$ (where $A_1, B_1, C_1, C_2, D_1, D_2$ refer to positive constants) is provided as a guide to the eye. As it can be seen, the scaling of $\bar{P}_{exc}(V_0)$ depends strongly on the considered ramping time τ . Indeed, proximally to the diabatic limit, e.g. see $\tau = 1$, $\bar{P}_{exc}(V_0)$ decreases for increasing V_0 . Interestingly enough, for larger τ , e.g. see $\tau = 25$, $\bar{P}_{exc}(V_0)$ exhibits a completely different behavior. Initially it increases for increasing V_0 until it reaches a maximum value and then decreases for larger V_0 . For instance, at $\tau = 25$ $\bar{P}_{exc}(V_0)$ increases until $V_0 \approx 6$ where it exhibits a maximum and then decreases for $V_0 > 6$. We also remark here that the maximum of $\bar{P}_{exc}(V_0)$ is displaced for varying τ , e.g. for $\tau = 10$ is located at $V_0 \approx 5.5$ while for $\tau = 50$ is at $V_0 \approx 8$. The above described alternating behavior of $\bar{P}_{exc}(V_0)$ for the different τ regions

can be traced back to the previously observed crossing of $\bar{P}_{\text{exc}}(\tau)$ for different V_0 , shown in Fig. 3(a) at $\tau = 19$. Indeed, for $\tau < 19$ ($\tau > 19$) $\bar{P}_{\text{exc}}(\tau)$ decreases (increases) for increasing V_0 , i.e. $\bar{P}_{\text{exc}}(\tau(19, V_0 = 4)) > \bar{P}_{\text{exc}}(\tau(19, V_0 = 10))$. This is due to the fact that the fast (slow) decay process described by τ_1 (τ_2) being related to the $T \rightarrow SP$ ($SP \rightarrow S$) mode is stronger (weaker) for increasing V_0 , see also Fig. 3(a). Comparing $\bar{P}_{\text{exc}}(V_0)$ for a fixed V_0 and varying τ , we observe that $\bar{P}_{\text{exc}}(V_0)$ decreases in a uniform manner for increasing τ , a result that is in accordance with our previous observations for the $\bar{P}_{\text{exc}}(\tau)$ bi-exponential decay, see Fig. 3(a). However, for deeper lattices ($V_0 > 12$) the decrease of $\bar{P}_{\text{exc}}(V_0)$ almost halts after a certain τ_0 (mainly $\tau_0 > 10$).

Finally, we study the impact of the postquench interaction strength on the higher-band excited fraction, see Fig. 3(c). $\bar{P}_{\text{exc}}(g_f)$ exhibits two distinct response regions with respect to g_f . These regions are classified by the location g_c of the existing avoided crossings between the SE and T as well as HE categories in the corresponding MB eigenspectrum, see the grey scaled area which incorporate the solid ellipses in Fig. 1(a). Indeed, when g_f approaches g_c $\bar{P}_{\text{exc}}(g_f)$ exhibits a non-linear growth as shown in the grey scaled interaction interval of Fig. 3(c), while for $g_f > g_c$ it increases in a linear manner. Overall, $\bar{P}_{\text{exc}}(g_f)$ grows for larger g_f 's as we import more energy to the system and thus excite more higher-band states. On the contrary, $\bar{P}_{\text{exc}}(g_f)$ reduces for larger τ 's because for more adiabatic LIQs the effect of the existing avoided crossings is smeared out.

In the next subsection we examine the negative LIQ dynamics, within the triple well system, from the MI to the SF correlated regimes. In particular, we shall elaborate in detail how such a negative LIQ alters the overall response of the system consisting of inter and intraband tunneling dynamics.

3.3. Quench dynamics from MI to SF phase

The system is initialized within the strongly correlated regime, $g_i = 2$, and therefore the ground state corresponds to the spatial contribution $|1, 1, 1\rangle$. To induce the dynamics we perform a negative LIQ to a weakly or non-interacting state and examine the dynamical response of the system. Fig. 4(a) presents $F(t; \tau)$ in a shallow triple well, $V_0 = 4$, for varying ramp time τ and $g_f = 0$. As in the positive LIQ scenario $F(t)$ exhibits oscillations during the evolution possessing here, however, only a few small value frequencies. The fact that $F(t; \tau) < 1$ indicates the melting of the MI phase [34]. The MB state after the quench consists of a superposition of the S, SP and T classes, see also Fig. 1(a). To justify the latter, we resort to the probability of specific number states that belong to the above classes. Indeed, Fig. 4(c), (d) and (e) present $P_1(t) = |\langle 1, 1, 1 | \Psi(t) \rangle|^2$, $P_2(t) = |\langle 1, 2, 0 | \Psi(t) \rangle|^2 = |\langle 0, 2, 1 | \Psi(t) \rangle|^2$ and $P_3(t) = |\langle 0, 3, 0 | \Psi(t) \rangle|^2$ respectively. We observe that for diabatic LIQs the three modes are almost equally populated, while for large τ 's the SP mainly contributes to the dynamics and the other states possess a decaying amplitude in time. The reduced amplitude of $|1, 1, 1\rangle$ for larger τ indicates that the system is significantly perturbed for proximally adiabatic LIQs. To further elaborate on the system's dynamical response, Fig. 4(f) illustrates the corresponding normalized variance of the fidelity $K(\tau)$ for varying τ . We observe an almost monotonic decrease of $K(\tau)$ for increasing τ , especially for $\tau > 10$, suggesting that the dynamical response is enhanced in the abrupt limit and reduces when the adiabatic limit is approached. The same overall response is also observed for a deeper triple well, see Fig. 4(b). However, the corresponding decaying response for increasing τ is more faint due to the increased energy gap between the MB eigenstates, see also Fig. 1.

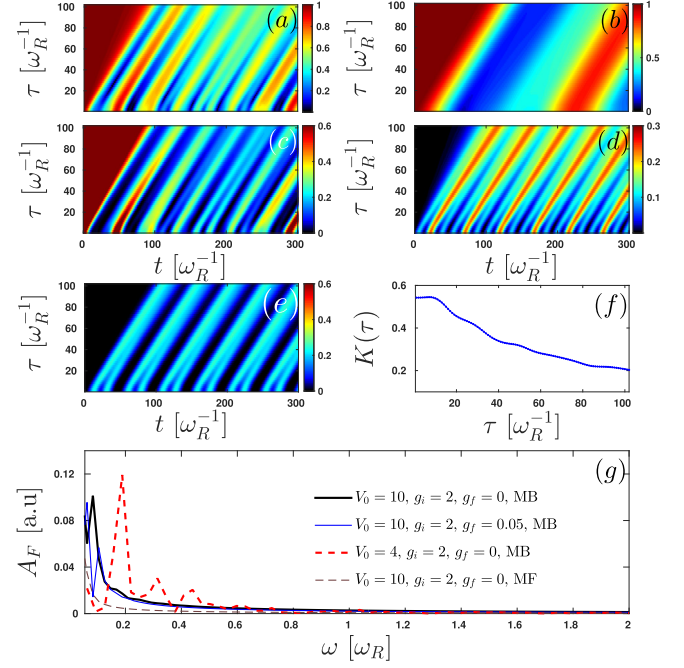


Fig. 4. Fidelity evolution for varying ramp time τ after a LIQ from $g_i = 2$ to $g_f = 0$. Shown are the cases of (a) a shallow $V_0 = 4$ and (b) a deep $V_0 = 10$ triple well. Probabilities of specific number state configurations during the evolution, namely (c) $P_1(t) = |\langle 1, 1, 1 | \Psi(t) \rangle|^2$, (d) $P_2(t) = |\langle 1, 2, 0 | \Psi(t) \rangle|^2 = |\langle 0, 2, 1 | \Psi(t) \rangle|^2$ and (e) $P_3(t) = |\langle 0, 3, 0 | \Psi(t) \rangle|^2$. (f) Normalized variance of the fidelity $K(\tau)$ in the case of a shallow lattice for varying ramp time τ . (g) Spectrum of the fidelity following a LIQ with $\tau = 8$ for different barrier heights, initial and final interactions within the MB approach or the MF approximation (see legend). The system consists of three initially strongly interacting bosons (see legend) confined in a triple well.

To investigate the tunneling dynamics we rely on the fidelity spectrum, see Fig. 4(g). It is observed that, in the case of a deep lattice ($V_0 = 10$), following a LIQ to $g = 0$ only the $S \rightarrow SP$ tunneling mode is excited which is located at $\omega \approx 0.1$. Employing the corresponding MF approximation this tunneling mode hardly survives with frequency $\omega' = 0.001$ [hardly visible in Fig. 4(g)]. Turning again to the MB correlated approach, we investigate the influence on the tunneling dynamics of the postquench state and the dependence on the potential barrier. Examining first the situation of a weakly correlated postquench state, namely $g_f = 0.05$, we observe that two lowest band tunneling modes exist. The first mode located at $\omega_1 \approx 0.02$ refers to the transport $S \rightarrow SP$ and the second at $\omega_2 \approx 0.11$ to tunneling $S \rightarrow T$. On the other hand, following a LIQ in a shallow lattice to a non-interacting final state mainly three tunneling modes are triggered. The first located at $\omega'_1 = 0.2$ refers to transport $S \rightarrow SP$, while the remaining two possess frequencies $\omega'_2 = 0.35$ and $\omega'_3 = 0.45$ which correspond to tunneling between the S and different states belonging to the T class. Note that higher frequency peaks, e.g. at $\omega_3 \approx 0.62$, refer to higher order lowest band transitions, for instance $SP \rightarrow T$, and possess reduced amplitudes.

To complement our study, let us explore the mean amount of higher-band excitations induced by a negative LIQ. As in the previous section we examine the impact of the mean excitation dynamics as a function of the ramping time τ [see Fig. 5(a)] or the height of the potential barrier V_0 [see Fig. 5(b)]. Here, we observe that the mean excitation dynamics for varying ramp time obeys an exponential decay

$$\bar{P}_{\text{exc}}(\tau) = A_3 e^{-\tau/\tau_3}, \quad (7)$$

where A_3, τ_3 correspond to positive constants, and τ_3 characterizes the rate of the decay. As shown the amount of produced excitations is negligible for all ramp times, see Fig. 5(a). It reduces for a LIQ to a

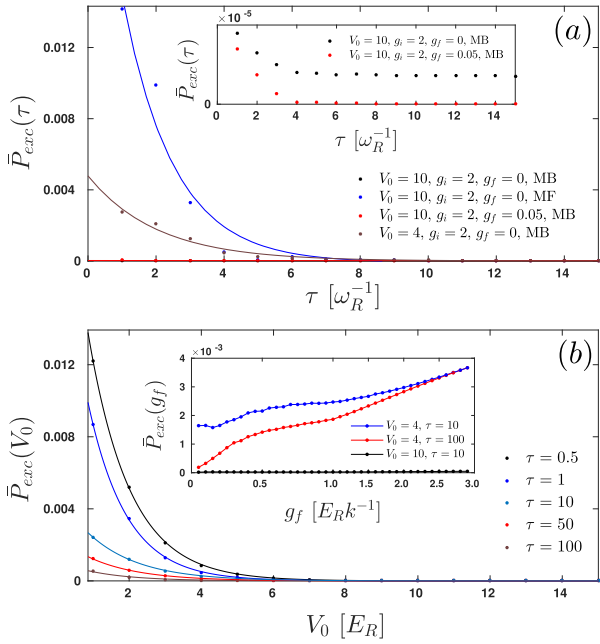


Fig. 5. Mean excitation probability of at least one boson to reside in an excited band for varying (a) ramp time τ of the LIQ (see a magnified version in the inset), (b) barrier height V_0 and in the inset of (b) postquench interaction strength g_f with $g_i = 3$. In all cases we consider a LIQ from an initially strongly to a final non correlated state unless stated otherwise (see legends). Different curves correspond to different parameter values (see legend), while the lines stem from a numerical fitting and provide a guide to the eye.

weakly correlated instead of the non-interacting state [see the inset of Fig. 5(a)] and it is enhanced for shallower lattices. Finally, the corresponding MF approximation shows the same qualitative behavior but quantitatively fails to predict the correct amount of excitations. In addition, we find that the mean excitation dynamics follows again an exponential decay with respect to the barrier height, namely

$$\bar{P}_{exc}(V_0) = A_4 e^{-V_0/V_1}, \quad (8)$$

where A_4, V_1 refer to positive constants and V_1 is the inverse rate of the decay. As it can be deduced from Fig. 5(b) again the produced amount of excitations is negligible and reduces even further when a larger ramp time is considered. Finally, let us examine the dependence of the excited to higher-band fraction on the postquench state for fixed ramping rate, shown in the inset of Fig. 5(b). We observe that the population of excited states is overall negligible, and in particular it is greatly reduced when we enter the SF regime namely $g_f < 0.5$ as well as in the case of deep optical lattices. Concluding, we can infer that the excitation dynamics following a LIQ from a MI-like to a weakly or even non-interacting final state is negligible. Therefore the lowest band approximation provides an adequate description of the system's dynamics.

To demonstrate the robustness of our results for larger optical lattices, in the following section, we proceed to the investigation of unit filling systems which contain higher number of bosons confined in multiwell traps. In particular, we show that the dynamical response induced by a LIQ exhibits similar characteristics to the triple well case.

4. LIQ Dynamics in extensive unit filling lattice systems

Let us now investigate the dynamical response for larger unit filling setups. Here, we mainly focus on a five well optical lattice and

consider a LIQ from a SF to a MI-like state and vice versa. Concerning the initial state of the system in the SF phase it consists of an admixture of the Wannier number states $|0, 1, 3, 1, 0\rangle, |0, 2, 3, 0, 0\rangle, |0, 2, 2, 1, 0\rangle, |1, 1, 2, 1, 0\rangle, |1, 1, 1, 1, 1\rangle$, while in the MI phase the dominant contribution stems from the $|1, 1, 1, 1, 1\rangle$ state. Note also that due to the underlying spatial symmetry of the system all the corresponding parity symmetric states contribute as well.

To trigger the dynamics we employ either a positive or a negative LIQ protocol. Fig. 6(a) shows $F(t; \tau)$ following a positive LIQ for varying τ . As in the triple well case, we observe that $F(t; \tau)$ exhibits an oscillatory behavior in time possessing also multiple frequencies which mainly correspond to lowest band transport and a few interband tunneling modes. The amplitude of the $F(t; \tau)$ oscillation becomes larger for increasing τ when referring to a fixed time instant t . This indicates that the system maximally departs from its initial state in the proximity of an adiabatic LIQ. Then by exploiting τ we can adjust the sweeping rate of the avoided crossings in the corresponding MB eigenspectrum (not shown here for brevity) and thus control the population of the resulting excitations. Interestingly enough and in contrast to the triple well system here $\bar{F}(t > \tau; \tau) < 0.3$, suggesting that larger unit filling setups can be driven out-of-equilibrium in a more efficient manner which is a manifestation of the Anderson orthogonality catastrophe [84,85,81]. As a consequence more modes can be triggered pointing also to the opportunity for enhanced interband tunneling (see below). To demonstrate the MB character of the dynamics we next present $F(t; \tau)$ employing the corresponding MF approximation, see Fig. 6(b). Despite the overall tendency for enhanced dynamical response for increasing τ , $F(t; \tau)$ differs significantly from the MB approach. Indeed, a reduced number of modes is participating most of which refer to single-particle transport while $0.35 < \bar{F}(t > \tau; \tau) < 0.8$ in direct contrast to Fig. 6(a). The existing

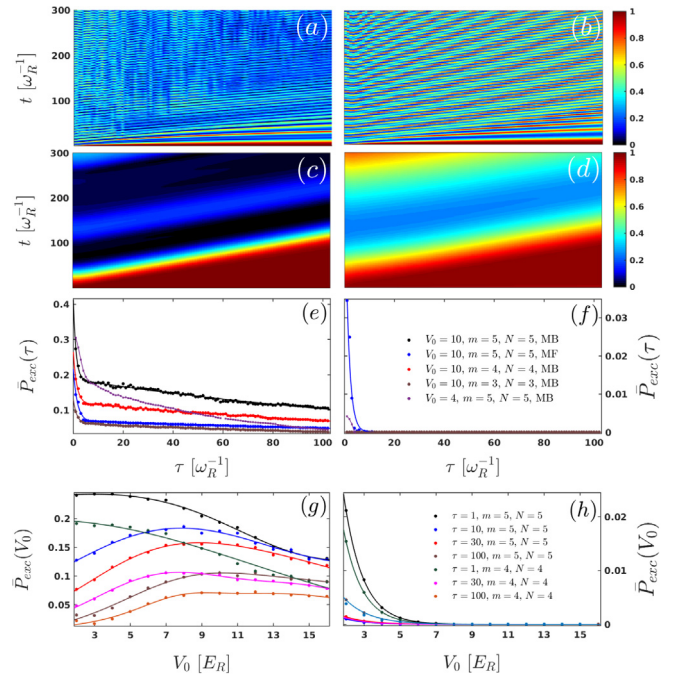


Fig. 6. Fidelity evolution for varying ramp time τ after a positive LIQ from $g_i = 0$ to $g_f = 2$ within (a) the MB approach and (b) the MF approximation. (c), (d) The same as (a), (b) but following a negative LIQ from $g_i = 2$ to $g_f = 0$. The system consists of five initially (a), (b) non and (c), (d) strongly interacting bosons confined in five wells. $\bar{P}_{exc}(\tau)$ for varying ramp time τ of the (e) positive and (f) negative LIQ. (g), (h) The same as (e), (f) but for varying barrier height V_0 . Different curves correspond to different parameter values (see legends), while the lines stem from a numerical fitting and provide a guide to the eye. The legend shown in (f) [(h)] is the same also for (e) [(g)].

modes possess positive shifted frequencies, when compared to the MB approach.

Next we examine the dynamical response induced by a negative LIQ, namely the MI melting, employing again $F(t; \tau)$, see Fig. 6(c). We observe that $F(t; \tau)$ performs oscillations of both large amplitude and period, while for larger τ 's the system becomes more perturbed [hardly visible in Fig. 6(c)]. After the LIQ the MB state consists of a superposition of several lowest band number states among which the states of double occupancy, e.g. $|0, 2, 2, 1, 0\rangle$, possess the main contribution and become dominant as we tend to an adiabatic ramping. The above result is in agreement with the negative LIQ dynamics of the triple well, however here $F(t; \tau)$ performs oscillations of both larger amplitude and period. Within the corresponding MF approximation, see Fig. 6(d), $F(t; \tau)$ shows the same overall qualitative decrease for larger τ 's but quantitatively the dynamical response is altered significantly. For instance, $F(t; \tau)$ and its oscillation frequencies are larger when compared to the MB approach.

Turning to the investigation of the induced interband tunneling we employ the mean excitation probability $\bar{P}_{exc}(t; \tau)$ for varying τ . Following a positive [negative] LIQ $\bar{P}_{exc}(\tau)$ obeys a bi-exponential [an exponential] decay law, see Fig. 6(e) [Fig. 6(f)] similar to the triple well case. Note also that, as before, following a negative LIQ $\bar{P}_{exc}(\tau)$ is negligible. Additionally, $\bar{P}_{exc}(\tau)$ is enhanced for larger unit filling setups, while the MF approximation predicts a smaller (enhanced) amount of excitations for positive (negative) LIQs. Following a positive LIQ there is a crossing point (here at $\tau = 8$) between $\bar{P}_{exc}(\tau)$'s, as in the triple well case, that refer to different V_0 's. This behavior of $\bar{P}_{exc}(\tau)$ seems to be quite robust in different setups and suggests the existence of two excitation time scales concerning the ramping rate and V_0 . Namely, within a positive diabatic (adiabatic) LIQ the excited to higher-band fraction is larger (smaller) for shallower lattices. To complement our study on the excitation dynamics we investigate $\bar{P}_{exc}(V_0)$ for varying V_0 both for a positive LIQ, see Fig. 6(g), as well as a negative LIQ, see Fig. 6(h). We observe that within a positive LIQ scenario $\bar{P}_{exc}(V_0)$ strongly depends on τ . In agreement to the triple well case, $\bar{P}_{exc}(V_0)$ decreases for small τ [e.g. see $\tau = 1$ in Fig. 6(g)], while for larger rampings $\bar{P}_{exc}(V_0)$ shows a maximum at a specific region of V_0 [e.g. see $\tau = 10$ in Fig. 6(g)]. However, for a negative LIQ $\bar{P}_{exc}(V_0)$ follows an exponential decay with respect to V_0 . Overall, in both positive and negative LIQs the excited to higher-band mean fraction increases for a more diabatic ramping and also for larger systems of unit filling. Finally, let us note that for the five well system $\bar{P}_{exc}(V_0)$ is not negligible suggesting that for more extensive unit filling lattices the occupation of higher-band states might be unavoidable even in the course of the negative LIQ dynamics.

5. Conclusions and outlook

We have explored the nonequilibrium quantum dynamics following a linear interaction quench protocol in repulsively interacting few boson ensembles confined in finite optical lattices. The focus has been on unit filling such that the ground state of the system for increasing interaction strength exhibits the transition from a SF to a MI phase. To realize this transition and obtain the interaction dependence of the occupation of the number states, we first calculate the many-body eigenspectrum for varying interparticle repulsion. Here, the existence of multiple avoided crossings before and after the transition is elucidated. To induce the dynamics we perform a LIQ and cross dynamically, with a finite ramp rate, the aforementioned transition from both directions. Subsequently, we explore the dynamical response caused by the LIQ and in particular examine its dependence on several system parameters, such

as the height of the potential barrier. It is important to note here that within our multiband treatment the dynamical response consists of both the lowest band tunneling and the excited to higher-bands fraction.

Crossing the weak to strong interaction regimes yields the excitation of several lowest band tunneling pathways consisting of single and two particle transport. Furthermore, a rich interband tunneling dynamics is observed possessing mainly a single excitation to the first or second excited band. Analyzing in more detail the excited to higher-band fraction we examine its dependence on the quench ramp rate and barrier height. We find that it exhibits a bi-exponential decay for decreasing quench rate. This decay law introduces two different time scales in the excitation dynamics, which are directly related to the diabatic or adiabatic crossing of the transition respectively and can be further explained by the behavior of the participating number states. Furthermore, the excited fraction follows a more complex scaling for varying height of the potential barrier. For diabatic quenches it reduces, while for larger ramp times it exhibits a non-linear behavior. The latter can be explained by exploiting the dependence on the ramp time of the excited fraction for shallow and deep lattices. Finally, the higher-band dynamics strongly depends on the postquench state, namely when we tend to the region of an existing avoided crossing it is described by a non-linear growth, while for larger quench amplitudes it increases in an almost linear manner.

In contrast to the above, the dynamical response following a LIQ from strong to weak interactions is reduced and mainly comprises of the lowest band tunneling dynamics. Indeed, in this case following the quench we can excite only a few tunneling modes, while the excited to higher-band fraction is negligible and obeys an exponential decay for varying ramp time. Here, the lowest band approximation seems to describe the induced dynamics accurately. Finally, we made an attempt to generalize our results by considering larger systems, e.g. a five well setup, and showing the robustness of the above mentioned scalings as well as the enhancement of the excited to higher-band fraction.

Finally, let us comment on possible future extensions of our work. An interesting alternative of the present work would be to investigate the dynamical response induced by a LIQ in repulsively interacting dipolar bosons [86] upon crossing the corresponding SF to supersolid transition point. Certainly, the study of bosonic or fermionic spinor ensembles confined in an optical lattice is an intriguing perspective. Here, the inclusion of the spin degree of freedom enriches the phase diagram [1,87,88] and as a consequence it might alter significantly the dynamical response.

Acknowledgments

The paper is dedicated to Professor Hans-Dieter Meyer, a dear colleague, on the occasion of his 70th birthday. It was and it is always a great pleasure to interact with him. The authors gratefully acknowledge funding by the Deutsche Forschungsgemeinschaft (DFG) in the framework of the SFB 925 “Light induced dynamics and control of correlated quantum systems” and by the excellence cluster “The Hamburg Centre for Ultrafast Imaging-Structure, Dynamics and Control of Matter at the Atomic Scale”.

Appendix A. The computational approach: MCTDHB

To solve the many-body (MB) Schrödinger equation $(i\hbar\partial_t - H)|\Psi(t)\rangle = 0$ of the interacting bosons as an initial value problem $|\Psi(0)\rangle = |\Psi_0\rangle$, we rely on the Multi-Configuration Time-Dependent Hartree method for Bosons (MCTDHB) [73,74,89]. The latter has already been applied for a wide set of nonequilibrium bosonic settings, e.g. see [59–62,75,89–93]. This method allows

for a variationally optimal truncation of the Hilbert space as we employ a time-dependent moving basis where the system can be instantaneously optimally represented by time-dependent permanents. The MB wavefunction is expanded in terms of the bosonic number states $|n_1, n_2, \dots, n_M; t\rangle$, that built upon time-dependent single-particle functions (SPFs) $|\phi_i(t)\rangle, i = 1, 2, \dots, M$, and time-dependent weights $C_{\vec{n}}(t)$

$$|\Psi(t)\rangle = \sum_{\vec{n}} C_{\vec{n}}(t) |n_1, n_2, \dots, n_M; t\rangle. \quad (\text{A1})$$

Here M is the number of SPFs and the summation \vec{n} is over all the possible combinations n_i such that the total number of bosons N is conserved. Note that in the limit in which M approaches the number of grid points the above expansion is equivalent to a full configuration interaction approach. Furthermore, in the case of $M = 1$ the MB wavefunction is given by a single permanent $|n_1 = N; t\rangle$ and the method reduces to the time-dependent Gross Pitaevskii mean-field approximation.

To determine the time-dependent wave function $|\Psi(t)\rangle$ we calculate the equations of motion for the coefficients $C_{\vec{n}}(t)$ and the SPFs $|\phi_i(t)\rangle$. Following the Dirac-Frenkel [94,95] variational principle, $\langle \delta\Psi | i\partial_t - \hat{H} | \Psi \rangle = 0$, we obtain the well-known MCTDHB equations of motion [73,74,89]. These equations consist of a set of M non-linear integrodifferential equations of motion for the SPFs being coupled to the $\frac{(N+M-1)!}{N!(M-1)!}$ linear equations of motion for the coefficients $C_{\vec{n}}(t)$. Finally, let us remark that in terms of our implementation we use an extended version of MCTDHB being referred to in the literature as the Multi-Layer Multi-Configuration Time-Dependent Hartree method for bosonic and fermionic Mixtures (ML-MCTDHX) [96–98]. This computational package is particularly suitable for treating systems consisting of different bosonic, fermionic species, while for the case of a single bosonic species it reduces to MCTDHB.

For the numerical implementation, the SPFs are expanded within a so-called primitive basis $\{|k\rangle\}$ of dimension M_p . As a primitive basis for the SPFs we have used a sine discrete variable representation, which intrinsically introduces hard-wall boundaries at both ends of the potential. To obtain the n -th MB eigenstate we rely on the so-called improved relaxation scheme, being summarized as follows. First, we initialize the system with an ansatz set of SPFs $\{|\phi_i^{(0)}\rangle\}$, diagonalize the Hamiltonian within a basis spanned by the SPFs and set the n -th obtained eigenvector as the $C_{\vec{n}}^{(0)}$ -vector. Then, we propagate the SPFs in imaginary time within a finite time interval $d\tau$, update the SPFs to $\{|\phi_i^{(1)}\rangle\}$ and repeat the above steps until the energy of the state converges within the prescribed accuracy. In turn, we perform a time-dependent quench on the strength of the interparticle repulsion and study the evolution of $|\Psi(t)\rangle$ in the m -well potential by utilizing the appropriate Hamiltonian within the MCTDHB equations of motion.

To track the numerical error and guarantee the accurate performance of the numerical integration for the MCTDHB equations of motion we impose the following overlap criteria $|\langle \Psi | \Psi \rangle - 1| < 10^{-9}$ and $|\langle \phi_i | \phi_j \rangle - \delta_{ij}| < 10^{-10}$ for the total wavefunction and the SPFs respectively. The dimension of the used primitive basis consists of 300 spatial grid points in the case of a triple well and 500 spatial grid points for the five well potential. Furthermore, to ensure the convergence of our simulations we have used up to 9 (10) optimized single particle functions for the triple (five) well, thereby observing a systematic convergence of our results. An auxiliary indicator for convergence is provided by the population of the lowest occupied natural orbital kept always below 0.1%.

References

- [1] M. Lewenstein, A. Sanpera, V. Ahufinger, B. Damski, A. Sen, U. Sen, *Adv. in Phys.* 56 (2007) 243.
- [2] I. Bloch, J. Dalibard, W. Zwerger, *Rev. Mod. Phys.* 80 (2008) 885.
- [3] V.I. Yukalov, *Laser Phys.* 19 (2009) 110.
- [4] M. Lewenstein, A. Sanpera, V. Ahufinger, *Ultracold Atoms in Optical Lattices: Simulating Quantum Many-Body Systems*, Oxford University Press, Oxford, 2012.
- [5] M. Greiner, O. Mandel, T. Esslinger, T.W. Hänsch, I. Bloch, *Nature (London)* 415 (2002) 39.
- [6] M. Greiner, O. Mandel, T.W. Hänsch, I. Bloch, *Nature (London)* 419 (2002) 51.
- [7] M.P. Fisher, P.B. Weichman, G. Grinstein, D.S. Fisher, *Phys. Rev. B* 40 (1989) 546.
- [8] D. Jaksch, C. Bruder, J.I. Cirac, C.W. Gardiner, P. Zoller, *Phys. Rev. Lett.* 81 (1998) 3108.
- [9] W.H. Zurek, U. Dörner, P. Zoller, *Phys. Rev. Lett.* 95 (2005) 105701.
- [10] A. Polkovnikov, *Phys. Rev. B* 72 (2005) 161201.
- [11] D. Chowdhury, U. Divakaran, A. Dutta, *Phys. Rev. E* 81 (2010) 012101.
- [12] K. Sengupta, D. Sen, S. Mondal, *Phys. Rev. Lett.* 100 (2008) 077204.
- [13] V. Mukherjee, A. Dutta, D. Sen, *Phys. Rev. B* 77 (2008) 214427.
- [14] A. Dutta, R.R.P. Singh, U. Divakaran, *EPL* 89 (2010) 67001.
- [15] A. Polkovnikov, K. Sengupta, A. Silva, M. Vengalattore, *Rev. Mod. Phys.* 83 (2011) 863.
- [16] N. Andrei, arXiv:1606.08911 (2016).
- [17] T.W.B. Kibble, *Phys. Today* 60 (2007) 47.
- [18] A. Del Campo, W.H. Zurek, *Int. J. Mod. Phys. A* 29 (2014) 1430018.
- [19] J. Dziarmaga, *Adv. Phys.* 59 (2010) 1063.
- [20] J. Beugnon, N. Navon, *J. Phys. B: At. Mol. Opt. Phys.* 50 (2017) 0222002.
- [21] T.W. Kibble, *J. Phys. A* 9 (1976) 1387.
- [22] W.H. Zurek, *Nature (London)* 317 (1985) 505.
- [23] G. Lamporesi, S. Donadello, S. Serafini, F. Dalfovo, G. Ferrari, *Nat. Phys.* 9 (2013) 656.
- [24] M. Anquez, B.A. Robbins, H.M. Bharath, M. Boguslawski, T.M. Hoang, M.S. Chapman, *Phys. Rev. Lett.* 116 (2016) 155301.
- [25] L.W. Clark, L. Feng, *Chin. Science* 354 (2016) 606.
- [26] D. Chen, M. White, C. Borries, B. DeMarco, *Phys. Rev. Lett.* 106 (2011) 235304.
- [27] K. Meldgin, U. Ray, P. Russ, D. Chen, D.M. Ceperley, B. DeMarco, *Nature Phys.* 12 (2016) 646.
- [28] M. Aidelsburger, J.L. Ville, R. Saint-Jalm, S. Nascimbéne, J. Dalibard, J. Beugnon, *Phys. Rev. Lett.* 119 (2017) 190403.
- [29] R. Schützhold, M. Uhlmann, Y. Xu, U.R. Fischer, *Phys. Rev. Lett.* 97 (2006) 200601.
- [30] B. Gardas, J. Dziarmaga, W.H. Zurek, *Phys. Rev. B* 95 (2017) 104306.
- [31] J. Dziarmaga, W.H. Zurek, *Sci. Rep.* 4 (2014) 5950.
- [32] S. Braun, M. Friesdorf, S.S. Hodgman, M. Schreiber, J.P. Ronzheimer, A. Riera, M. del Rey, I. Bloch, J. Eisert, U. Schneider, *Proc. Nat. Acad. Sci.* 112 (2015) 3641.
- [33] S.R. Clark, D. Jaksch, *Phys. Rev. A* 70 (2004) 043612.
- [34] J.S. Bernier, D. Poletti, P. Barmettler, G. Roux, C. Kollath, *Phys. Rev. A* 85 (2012) 033641.
- [35] C.L. Hung, X. Zhang, N. Gemelke, C. Chin, *Phys. Rev. Lett.* 104 (2010) 160403.
- [36] S.D. Huber, E. Altman, H.P. Büchler, G. Blatter, *Phys. Rev. B* 75 (2007) 085106.
- [37] L. Vidmar, S. Langer, I.P. McCulloch, U. Schneider, U. Schollwöck, F. Heidrich-Meisner, *Phys. Rev. B* 88 (2013) 235117.
- [38] N. Gemelke, X. Zhang, C.L. Hung, C. Chin, *Nature* 460 (2009) 995.
- [39] M. Rigol, R.T. Scalettar, P. Sengupta, G.G. Batrouni, *Phys. Rev. B* 73 (2006) 121103.
- [40] P. Sengupta, M. Rigol, G.G. Batrouni, P.J.H. Denteneer, R.T. Scalettar, *Phys. Rev. Lett.* 95 (2005) 220402.
- [41] Y. Yanay, E.J. Mueller, *Phys. Rev. A* 93 (2016) 013622.
- [42] C. Kollath, A.M. Läuchli, E. Altman, *Phys. Rev. Lett.* 98 (2007) 180601.
- [43] F.M. Cucchiatti, B. Damski, J. Dziarmaga, W.H. Zurek, *Phys. Rev. A* 75 (2007) 023603.
- [44] P. Navez, R. Schützhold, *Phys. Rev. A* 82 (2010) 063603.
- [45] S.S. Natu, K.R. Hazzard, E.J. Mueller, *Phys. Rev. Lett.* 106 (2011) 125301.
- [46] M. Lacki, D. Delande, J. Zakrzewski, *New J. Phys.* 15 (2013) 013062.
- [47] J. Kinnunen, P. Törmä, *Phys. Rev. Lett.* 96 (2006) 070402.
- [48] N. Proukakis, S. Gardiner, M. Davis, M. Szymaska, *Quantum Gases: Finite Temperature and Non-Equilibrium Dynamics*, Vol. 1, World Scientific, 2013.
- [49] J. Grond, A.I. Streltsov, L.S. Cederbaum, O.E. Alon, *Phys. Rev. A* 86 (2012) 063607.
- [50] J. Grond, A.I. Streltsov, A.U. Lode, K. Sakmann, L.S. Cederbaum, O.E. Alon, *Phys. Rev. A* 88 (2013) 023606.
- [51] M. Theisen, A.I. Streltsov, *Phys. Rev. A* 94 (2016) 053622.
- [52] R. Beinke, S. Klaiman, L.S. Cederbaum, A.I. Streltsov, O.E. Alon, *Phys. Rev. A* 95 (2017) 063602.
- [53] D. Blume, *Physics* 3 (2010) 74.
- [54] D. Blume, *Rep. Progr. Phys.* 75 (2012) 046401.
- [55] G. Zürn, F. Serwane, T. Lompe, A.N. Wenz, M.G. Ries, J.E. Bohn, S. Jochim, *Phys. Rev. Lett.* 108 (2012) 075303.
- [56] F. Serwane, G. Zürn, T. Lompe, T.B. Ottenstein, A.N. Wenz, S. Jochim, *Science* 332 (2011) 336.
- [57] A.N. Wenz, G. Zürn, S. Murmann, I. Brouzos, T. Lompe, S. Jochim, *Science* 342 (2013) 457.
- [58] A.M. Kaufman, B.J. Lester, M. Foss-Feig, M.L. Wall, A.M. Rey, C.A. Regal, *Nature* 527 (2015) 208.

- [59] S.I. Mistakidis, L. Cao, P. Schmelcher, *J. Phys. B: At. Mol. Opt. Phys.* **47** (2014) 225303.
- [60] S.I. Mistakidis, L. Cao, P. Schmelcher, *Phys. Rev. A* **91** (2015) 033611.
- [61] J. Neuhaus-Steinmetz, S.I. Mistakidis, P. Schmelcher, *Phys. Rev. A* **95** (2017) 053610.
- [62] S.I. Mistakidis, P. Schmelcher, *Phys. Rev. A* **95** (2017) 013625.
- [63] S. Fölling, S. Trotzky, P. Cheinet, M. Feld, R. Saers, A. Widera, T. Müller, I. Bloch, *Nature* **448** (2007) 1029.
- [64] F. Meinert, M.J. Mark, E. Kirilov, K. Lauber, P. Weinmann, M. Gröbner, A.J. Daley, H.C. Nägerl, *Science* **344** (2014) 1259.
- [65] Y.A. Chen, S. Nascimbene, M. Aidelsburger, M. Atala, S. Trotzky, I. Bloch, *Phys. Rev. Lett.* **107** (2011) 210405.
- [66] L. Cao, I. Brouzos, S. Zöllner, P. Schmelcher, *New J. Phys.* **13** (2011) 033032.
- [67] L. Cao, I. Brouzos, B. Chatterjee, P. Schmelcher, *New J. Phys.* **14** (2012) 093011.
- [68] M. Olshanii, *Phys. Rev. Lett.* **81** (1998) 938.
- [69] T. Köhler, K. Goral, P.S. Julienne, *Rev. Mod. Phys.* **78** (2006) 1311.
- [70] C. Chin, R. Grimm, P. Julienne, E. Tiesinga, *Rev. Mod. Phys.* **82** (2010) 1225.
- [71] J.I. Kim, V.S. Melezhik, P. Schmelcher, *Phys. Rev. Lett.* **97** (2006) 193203.
- [72] P. Giannakeas, F.K. Diakonov, P. Schmelcher, *Phys. Rev. A* **86** (2012) 042703.
- [73] O.E. Alon, A.I. Streltsov, L.S. Cederbaum, *J. Chem. Phys.* **127** (2007) 154103.
- [74] O.E. Alon, A.I. Streltsov, L.S. Cederbaum, *Phys. Rev. A* **77** (2008) 033613.
- [75] G.M. Koutentakis, S.I. Mistakidis, P. Schmelcher, *Phys. Rev. A* **95** (2017) 013617.
- [76] The selection rule leading to the formation of exact crossings is the intrawall parity symmetry. The latter prohibits transitions from the ground state of a particular site (parity even) to the first excited state of the same site (parity odd). This selection rule is weakly violated for the edge sites due to the hard wall boundary conditions leading to very narrow avoided crossings possessing a width $\delta E \lesssim 0.01 E_R k^{-1}$ Koutentakis.
- [77] The described process is a result of the couplings $U_{s,s\pm 1}^{0,0,1} = \int dx |w_s^{(0)}(x)|^2 w_s^{(0)}(x) w_{s\pm 1}^{(1)}(x) \neq 0$ which do not fall under the restriction described in Note 1.
- [78] The only striking qualitative difference is that the wide avoided crossings between the T and SE eigenstates exhibited for shallow lattices [see Fig. 1fig: eigenspectra (a)] become narrow in the case of deep lattices [see Fig. 1fig: eigenspectra (b)]. The latter results from the fact that a transition from a T to a SE number state requires a tunneling mediated virtual transition to an SP state, which is suppressed for deep lattices.
- [79] L.C. Venuti, P. Zanardi, *Phys. Rev. A* **81** (2010) 022113.
- [80] T. Gorin, T. Prosen, T.H. Seligman, M. Žnidarič, *Phys. Rep.* **435** (2006) 33.
- [81] S. Campbell, M. García-March, T. Fogarty, T. Busch, *Phys. Rev. A* **90** (2014) 013617.
- [82] L.D. Landau, *Phys. Sov. Un.* **2** (1932) 2.
- [83] C. Zener, *Proc. R. Soc. London A* **137** (1932) 6.
- [84] P.W. Anderson, *Phys. Rev. Lett.* **18** (1967) 1049.
- [85] M. Knap, A. Shashi, Y. Nishida, A. Imambekov, D.A. Abanin, E. Demler, *Phys. Rev. X* **2** (2012) 041020.
- [86] B. Chatterjee, I. Brouzos, L. Cao, P. Schmelcher, *J. Phys. B: At. Mol. Opt. Phys.* **46** (2013) 085304.
- [87] S. Tsuchiya, S. Kurihara, T. Kimura, *Phys. Rev. A* **70** (2004) 043628.
- [88] M. Rizzi, D. Rossini, G. De Chiara, S. Montangero, R. Fazio, *Phys. Rev. Lett.* **95** (2005) 240404.
- [89] A.I. Streltsov, O.E. Alon, L.S. Cederbaum, *Phys. Rev. Lett.* **99** (2007) 030402.
- [90] A.I. Streltsov, K. Sakmann, O.E. Alon, L.S. Cederbaum, *Phys. Rev. A* **83** (2011) 043604.
- [91] O.E. Alon, A.I. Streltsov, L.S. Cederbaum, *Phys. Rev. A* **76** (2007) 013611.
- [92] O.E. Alon, A.I. Streltsov, L.S. Cederbaum, *Phys. Rev. A* **79** (2009) 022503.
- [93] G.C. Katsimiga, S.I. Mistakidis, G.M. Koutentakis, P.G. Kevrekidis, P. Schmelcher, *New J. Phys.* (2017), <https://doi.org/10.1088/1367-2630> (in press).
- [94] J. Frenkel, *Wave Mechanics*, 1st ed., Clarendon Press, Oxford, 1934, pp. 423–428.
- [95] P.A. Dirac, (1930, July). *Proc. Camb. Phil. Soc.* **26**, 376. Cambridge University Press.
- [96] L. Cao, S. Krönke, O. Vendrell, P. Schmelcher, *J. Chem. Phys.* **139** (2013) 134103.
- [97] S. Krönke, L. Cao, O. Vendrell, P. Schmelcher, *New J. Phys.* **15** (2013) 063018.
- [98] L. Cao, V. Bolsinger, S.I. Mistakidis, G.M. Koutentakis, S. Krönke, J.M. Schurer, P. Schmelcher, *J. Chem. Phys.* **147** (2017) 044106.

4.1.5 Quench Dynamics of Finite Bosonic Ensembles in Optical Lattices with Spatially Modulated Interactions

Quench Dynamics of Finite Bosonic Ensembles in Optical Lattices with Spatially Modulated Interactions

T. Plaßmann,¹ S. I. Mistakidis,¹ and P. Schmelcher^{1,2}

¹*Zentrum für Optische Quantentechnologien, Universität Hamburg,
Luruper Chaussee 149, 22761 Hamburg, Germany*

²*The Hamburg Centre for Ultrafast Imaging, Universität Hamburg,
Luruper Chaussee 149, 22761 Hamburg, Germany*

(Dated: February 20, 2018)

The nonequilibrium quantum dynamics of few boson ensembles which experience a spatially modulated interaction strength and are confined in finite optical lattices is investigated. Performing quenches either on the wavevector or the phase of the interaction profile an enhanced imbalance of the interatomic repulsion between distinct spatial regions of the lattice is induced. Following both quench protocols triggers various tunneling channels and a rich excitation dynamics consisting of a breathing and a cradle mode. All modes are shown to be amplified for increasing inhomogeneity amplitude of the interaction strength. Especially the phase quench induces a directional transport enabling us to discern energetically, otherwise, degenerate tunneling pathways. Moreover, a periodic population transfer between distinct momenta for quenches of increasing wavevector is observed, while a directed occupation of higher momenta can be achieved following a phase quench. Finally, during the evolution regions of partial coherence are revealed between the predominantly occupied wells.

I. INTRODUCTION

Ultracold atoms in optical lattices have emerged as powerful quantum many-body platforms with highly tunable parameters enabling us to emulate in the laboratory a multitude of complex systems [1–3]. Due to the remarkable experimental progress it is nowadays possible to create arbitrarily shaped potential landscapes [4], and to realize besides many-body also highly controllable few-body systems [5–8]. Moreover the advent of magnetic [9, 10] and optical Feshbach resonances [11–17] offer the possibility of tuning the elastic interatomic interaction strength with unprecedented level of accuracy. In particular optical Feshbach resonances, utilizing optical coupling between bound and scattering states, provide the flexibility to design complex spatial interaction strength distributions across the atomic sample. The corresponding intensity and detuning of the participating optical fields can be rapidly changed and allow even for nanometer scale modulations of the resulting scattering length [15].

Spatially inhomogeneous interaction patterns introduce in the system a periodic structure which is known as nonlinear optical lattice [18–21]. This concept reinvigorated the theoretical interest of diverse topics ranging from the simulation of sonic black holes [22, 23] to altered properties of the emerging nonlinear excitations [21, 24]. In this latter context a plethora of new phenomena have been revealed such as emission of solitons or trains thereof [25, 26], Bloch oscillations of solitary waves [27–29], adiabatic compression [29, 30] and dynamical trapping [31] of matter waves to name a few. Moreover, the existence of a delocalizing transition of bosons in one-dimensional optical lattices [32], optimal control schemes to stimulate transitions into excited modes of a condensate [33], a particle localization phenomenon at the re-

gions where the scattering length vanishes [34, 35] and the emergence of Faraday waves [36] have been demonstrated.

The above-mentioned investigations have been performed within the mean-field realm resting under the premise of a macroscopic wavefunction which is composed of a single orbital. Meanwhile there is evidence that when considering spatially inhomogeneous interactions in bosonic systems fragmentation, namely the occupation of more than a single-particle state, occurs [37, 38]. In this context and referring to few boson ensembles confined in optical lattices different resonant interband tunneling mechanisms [39, 40] have been unveiled. Independently and following a linear or a sudden homogeneous interaction quench in lattice trapped few boson systems it has been shown that the quench inevitably leads to the population of higher lying band states [41], it generates collective modes such as the breathing and the cradle processes [42, 43] and couples the lowest and excited band states [42, 44, 45]. For a lattice setting the spatial interaction pattern (nonlinear lattice) can give rise to a preferred interaction imbalance of the bosons between the distinct lattice sites and therefore particular particle configurations can be formed [46]. In this context it is particularly interesting to examine whether a certain particle distribution can be displaced in a controlled way upon an interaction quench leading to a steered tunneling within the same or energetically different bands and collective modes such as e.g. the cradle mode, during the evolution. To address this question in the present work we employ the Multi-Configurational Time-Dependent Hartree method for Bosons (MCTDHB) [47, 48] being a multimode treatment which enables us to capture the important correlation effects and account for several energetically distinct single-particle bands [49]. In this way we investigate, for the first time, the quench induced few

boson correlated dynamical response in a combined linear and nonlinear optical lattice. Our spatially modulated interaction strength is of sinusoidal type being characterized by its wavevector, inhomogeneity amplitude, interaction offset and a phase.

Regarding the ground state of the system we show that by tuning either the wavevector or the phase, the density distribution can be effectively displaced to regions of decreasing interaction strength. In particular, for distinct wavevectors the ensemble remains superfluid while a phase shift leads to a displacement of the particles in a preferred direction enabling for the existence of Mott-like states. The corresponding system's dynamical response upon quenching either the wavevector or the phase of the spatial interaction strength is enhanced for quenches that yield a non-negligible interaction imbalance of bosons located in different wells. Both quench scenarios yield the excitation of a multitude of lowest band interwell tunneling modes composed of single-particle and atom pair [50–52] transport. The manipulation of these modes by adjusting the interaction offset or the inhomogeneity amplitude will also be analyzed and discussed. Importantly, by performing a phase quench a directed tunneling along the finite lattice is achieved. The latter allows to discriminate between the parity symmetric tunneling modes, e.g. single-particle lowest band tunneling from the middle to the left or the right well, which would be otherwise energetically equal. Besides the lowest band tunneling dynamics both quenches give rise to an over-barrier transport (being significantly increased when following a phase quench) which in turn generates a cradle mode in the outer wells and a global breathing motion of the bosonic cloud. These modes are related to single-particle interband processes [41, 53] to the first, second and fourth excited band respectively, and are found to be enhanced for increasing inhomogeneity magnitude. Inspecting the one-body momentum distribution a periodic (consecutive) population transfer to higher momenta during the dynamics occurs when quenching the wavevector (phase) of the spatially inhomogeneous interaction profile. Finally the one-body coherence function reveals a partial coherence between the predominantly occupied wells during the evolution.

This work is structured as follows. In Sec. II we introduce the employed spatially-dependent interaction strength and the multiband expansion which we use for the interpretation of the quench induced dynamics. Sec. III presents briefly the ground state properties of a system composed of four inhomogeneously interacting bosons in a triple well. Then, we focus on the resulting dynamics caused by a quench of the wavevector (Sec. IV) or the phase (Sec. V) of the spatial interaction strength. In Sec. VI we discuss the quench induced dynamics for a five well lattice system of filling larger than unity. We provide an outlook and discuss future perspectives in Sec. VII. Finally, Appendix A describes our computational methodology.

II. SETUP AND MULTIBAND EXPANSION

The many-body Hamiltonian of N identical bosons possessing mass M and confined in a one-dimensional m -well optical lattice reads

$$H = \sum_{i=1}^N \left(\frac{p_i^2}{2M} + V_0 \sin^2(k_0 x_i) \right) + \sum_{i<j} V_{int}(x_i - x_j, g, a, k_1, \phi). \quad (1)$$

The external potential is characterized by its barrier depth V_0 and wavevector $k_0 = \pi/l$, where l denotes the distance between successive potential minima. In a corresponding experimental setup k_0 is the wavevector of the counterpropagating laser beams that form the confining optical lattice.

The interatomic interaction is modelled by a spatially-dependent short-ranged contact pseudopotential $V_{int}(x_i - x_j, g, a, k_1, \phi) = C_{int}(g, a, k_1, \phi, x_i) \delta(x_i - x_j)$ between particles located at positions x_i , $i = 1, 2, \dots, N$. The effective one-dimensional spatially-dependent interaction strength reads

$$C_{int}(x, g, a, k_1, \phi) = g [1 + a \cos^2(k_1 x + \phi)], \quad (2)$$

where g refers to an average interaction offset. k_1 denotes the wavevector of the periodic modulation, a is the amplitude of the inherent inhomogeneity and ϕ is a constant phase shift. Note that $\phi \neq 0$ and fixed k_1 yields an interaction strength imbalance between all lattice wells, while for varying k_1 and $\phi = 0$ C_{int} is on average the same only for the parity symmetric, with respect to the center ($x = 0$), outer sites. Due to periodicity ϕ takes values within the interval $[0, \pi/2]$. Several interaction profiles of Eq. (2) for varying wavevector k_1 or phase ϕ are presented in Fig. 1 together with the underlying triple well potential $V_0 \sin^2(k_0 x)$. Experimentally such a spatially modulated interaction profile can be achieved with the aid of optically induced Feshbach resonances [11, 12, 17, 54], e.g. by a laser field tuned near a photoassociation transition. Alternatively a technique of holographic beam shaping can be used, e.g. a digital micromirror device [55], to engineer wavefronts of arbitrary phase, amplitude and wavelength [56, 57].

For simplicity, the Hamiltonian is rescaled in units of the recoil energy $E_R = \frac{\hbar^2 k_0^2}{2M}$. Thus the frequency, spatial and temporal scales are given in units of ω_R , k_0^{-1} and $\hbar E_R^{-1}$ respectively. In addition we set $\hbar = M = k_0 = 1$. The confinement of the bosons in the m -well system is ensured by the use of hard-wall boundary conditions at $x_m = \pm \frac{m\pi}{2k_0}$. Finally, the lattice depth is fixed to $V_0 = 6E_R$ including this way two localized single-particle Wannier states per lattice site.

To examine the static properties and the quench induced dynamics upon varying the wavevector k_1 or the phase ϕ of C_{int} we employ MCTDHB [47, 48]. In contrast

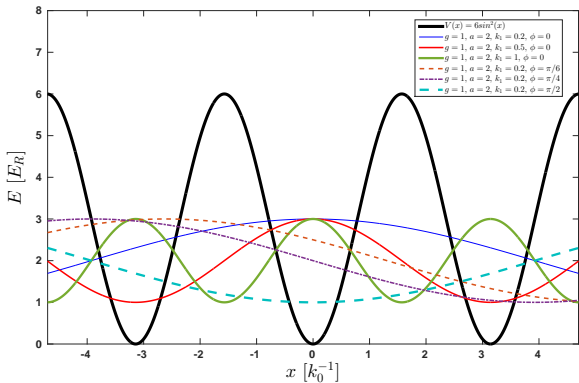


Figure 1. Different configurations of the spatially-dependent interaction strength $C_{int}(x, g, a, k_1, \phi)$ in a triple well potential $V_0 \sin^2(k_0 x)$ for $k_0 = 1$, $V_0 = 6$ (see legend).

to the mean-field approximation, within this approach we exploit an expansion in terms of many variationally optimized time-dependent single-particle functions (for more details, see also Appendix A). The latter allows for the investigation of the emergent interparticle correlations revealing the many-body properties of the system. To identify the modes participating in the dynamics we project the numerically obtained many-body correlated MCTDHB wavefunction on a time-independent number state basis consisting of single-particle Wannier states being localized on each lattice site. Such an expansion offers the possibility to study inter- and intraband transitions [42]. The many-body bosonic wavefunction of N bosons in an m -well potential which includes j localized Wannier states reads

$$|\Psi(t)\rangle = \sum_{\vec{n}} C_{\vec{n}}(t) |\vec{n}\rangle. \quad (3)$$

The multiband Wannier number state $|\vec{n}\rangle = |\otimes_{\lambda=0}^{j-1} n_{\lambda}^{(\lambda)}, \dots, \otimes_{\lambda=0}^{j-1} n_m^{(\lambda)}\rangle$ while the Wannier occupation number $n_i^{(\lambda)}$ indicates the number of bosons that reside in the Wannier orbital $|n_i^{(\lambda)}\rangle$ of the i -th well and λ -th energy band. Due to the fixed number of bosons N the total number of configurations is constrained by $\sum_{i=1}^m \sum_{\lambda=1}^{j-1} n_i^{(\lambda)} = N$. For a setup of $N = 4$ bosons confined in a triple well $m = 3$, which will be our workhorse in the following, e.g. the state $|1^{(0)}, 1^{(1)} \otimes 1^{(1)}, 1^{(0)}\rangle$ indicates that in the left and right wells one boson occupies the Wannier orbital of the energetically lowest band while the remaining two atoms are in the middle well, residing in the Wannier orbital of the first excited band. For simplicity, below, we shall omit the zero index when referring to the energetically lowest (zeroth) band.

We note that in the case of a homogeneous contact interaction and regarding the zeroth band states one can realize four distinct energetic classes of number states. Namely, the single pairs (SP) $\{|2, 1, 1\rangle + \circlearrowleft\}$, double pairs (DP) $\{|2, 0, 2\rangle + \circlearrowleft\}$, triples (T) $\{|3, 1, 0\rangle + \circlearrowleft\}$ and

quadruples (Q) $\{|4, 0, 0\rangle + \circlearrowleft\}$, where \circlearrowleft denotes all corresponding permutations. However, in the presence of a spatially inhomogeneous interaction, each energy class is further energetically splitted depending on the combination of the corresponding occupation number n_i and the spatially averaged interaction strength in the i -th well. Here we distinguish two cases. For varying k_1 and $\phi = 0$ each energy class splits into a subclass containing the states with the lowest occupancy in the middle well and another one which includes all the other states of the original energy class. As an example the SP class separates into the $\{|2, 1, 1\rangle, |1, 1, 2\rangle\}$ and $\{|1, 2, 1\rangle\}$ subclasses. Moreover, since the phase shift ϕ yields distinct C_{int} in each well all states of a certain class become energetically individual.

III. GROUND STATE PROPERTIES

Before investigating the dynamics, let us elaborate on the ground state properties of a system with filling $\nu = N/m > 1$ (here $N = 4$ and $m = 3$) under the influence of the spatially-dependent interaction profile [see Eq. (2)]. Referring to the case of a homogeneous contact interaction the ground state characteristics of a lattice setup depends strongly on the system's filling factor. For commensurate fillings ($\nu = 1, 2, \dots$) and increasing interatomic repulsion one can realize the superfluid to Mott insulator phase transition [58, 59], while for incommensurate fillings ($\nu \neq 1, 2, \dots$) the delocalized fraction of particles forbids the occurrence of a Mott state due to prevailing on-site interaction effects. On the other hand, spatially varying interactions can influence mainly systems consisting of sufficiently overlapping atoms (namely $\nu \geq 1$) as the emergent on-site interactions effects can be highly exploited in this case. In the following we explore the ground state properties for $N = 4$ bosons in a triple well either for varying wavevector k_1 or phase ϕ but for fixed interaction offset, $g = 1$, and inhomogeneity amplitude $a = 2$.

We first inspect the dependence of the ground state configuration on the wavevector k_1 of the interaction strength C_{int} for $\phi = 0$. The one-body reduced density matrix $\rho^{(1)}(x, x') = \langle x | \hat{\rho}^{(1)} | x' \rangle$ is obtained by tracing out all bosons but one in the N -body density operator $\hat{\rho}^{(N)} = |\Psi\rangle\langle\Psi|$ of the N -body system. Fig. 2 (a) shows the one-body density $\rho^{(1)}(x) = \rho^{(1)}(x, x' = x)$ for different spatial periodicities $k_1 = 0, 0.5, 0.75$ and 1 of C_{int} . The various k_1 values lead to distinct spatially averaged interaction strengths for the central and the outer wells. For $k_1 = 1$ the bosons residing in each well are subject to the same average interaction strength, see also Fig. 1. A slightly increased particle density in the middle well when compared to the outer ones is observed due to the hard-wall boundary conditions. This situation resembles a homogeneously interacting system i.e. $k_1 = 0$ with $C_{int} = g + a$, see Fig. 2 (a). On the contrary, $k_1 = 0.5$ yields a spatially varying interaction strength exhibiting

a peak within the central well [see Fig. 1] which forces the ensemble to preferably populate the outer wells. Other values of k_1 yield an intermediate behavior of the particle density, e.g. see $\rho^{(1)}(x)$ for $k_1 = 0.75$ in Fig. 2 (a).

To cast light on the non-local properties of the system's ground state from a one-particle perspective we employ the first order coherence function [60, 61] $g^{(1)}(x, x') = \rho^{(1)}(x, x') / \sqrt{\rho^{(1)}(x)\rho^{(1)}(x')}$. Here $\rho^{(1)}(x, x')$ is the one-body reduced density matrix and $|g^{(1)}(x, x')|$ takes values within the interval $[0, 1]$. Two distinct spatial regions \mathcal{D} , \mathcal{D}' , with $\mathcal{D} \cap \mathcal{D}' = \emptyset$, where $|g^{(1)}(x, x'; t)| = 0$, $x \in \mathcal{D}$, $x' \in \mathcal{D}'$ ($|g^{(1)}(x, x'; t)| = 1$, $x \in \mathcal{D}$, $x' \in \mathcal{D}'$) are said to be fully incoherent (coherent). For bosonic ensembles in optical lattices it is known that if within a well $|g^{(1)}(x, x'; t)| = 1$ (diagonal elements) while between different wells $0 \ll |g^{(1)}(x, x'; t)| \leq 1$ [$|g^{(1)}(x, x'; t)| = 0$] (off-diagonals) the appearance of superfluid-like [Mott-like] one-body correlations are indicated. In this sense the above-described ground state single-particle density distributions caused by C_{int} for $k_1 = 1$ and $k_1 = 0.5$ possess superfluid-like one-body correlations, see Figs. 2 (c) and (d) respectively. Therefore we can infer that the ensemble under the influence of different spatial periodicities k_1 with all the other parameters of C_{int} kept fixed exhibits a superfluid behavior, being an anticipated result since $\nu > 1$. Moreover, the difference with respect to the magnitude of the off-diagonal $|g^{(1)}|^2$ elements reflects essentially the particular density imbalance between the different wells induced by k_1 , see also Fig. 2 (a). Namely, the most occupied wells with the larger spatially integrated density exhibit stronger coherence losses with the lower populated ones than the latter among each other.

To infer about the effect that finite phase terms have on the ground state properties of the system we consider in the following the case $\phi \neq 0$. As it can be easily seen from Eq. (2) a phase $\phi > 0$ accounts for a spatial shift of the interaction profile C_{int} yielding an imbalance of the interparticle repulsion between all lattice wells. With the aid of such spatially-dependent interaction strengths a directed shift of the single-particle density distribution can be achieved. For instance, the choice $k_1 = 0.2$ and $\phi = \pi/4$ corresponds to a spatial interaction strength with a minimum (maximum) in the vicinity of the right (left) well [see also Fig. 1]. As a result two atoms mainly populate the right well and one resides in each of the left and middle wells, see Fig. 2 (b). Therefore an important contribution to the ground state configuration stems from the number state $|1, 1, 2\rangle$. Moreover, setting $k_1 = 0.2$ and $\phi = \pi/2$ yields a C_{int} which is minimized around the middle well and maximized in each of the outer wells. Then, a bunching of the atoms is observed in the central lattice region and the one-body density is described by the state $|1, 2, 1\rangle$, see Fig. 2 (b). Summarizing, the low values of C_{int} in the neighborhood of either the middle ($\phi = \pi/2$) or the right ($\phi = \pi/4$) well gives rise to double occupation in these wells of the lattice and to a single occupation in the other wells. The possibility to create such almost localized single-particle density distributions

by tuning the phase ϕ of the interaction profile C_{int} enables us to emulate spatially inhomogeneous Mott insulator like states. The latter can be firstly confirmed by employing the corresponding one-body coherence function $|g^{(1)}(x, x')|$, shown in Figs. 2 (e) and (f). Indeed, $|g^{(1)}(x, x')|$ exhibits almost vanishing off-diagonal contributions which suggest the emergence of Mott-like correlations. To further ensure the existence of the Mott insulator like state we rely on the two-body coherence function $g^{(2)}(x_1, x_2) = \rho^{(2)}(x_1, x_2) / \rho^{(1)}(x_1)\rho^{(1)}(x_2)$ [62]. The two-body density $\rho^{(2)}(x_1, x_2) = \langle x_1 x_2 | \hat{\rho}^{(2)} | x_1 x_2 \rangle$ is obtained by a partial trace over all but two bosons of the N -body density operator. A many-body state characterized by $|g^{(2)}(x_1, x_2)| = 1$ is termed fully second order coherent or uncorrelated, while if $|g^{(2)}(x_1, x_2)|$ takes values larger (smaller) than unity it is referred to as correlated (anti-correlated). Fig. 2 (e₁) presents $|g^{(2)}(x_1, x_2)|$ for $k_1 = 0.2$ and $\phi = \pi/4$. An anti-correlated (correlated) behavior occurs in the left and central (right, see in particular the substructures where $|g^{(2)}(x_1, x_1)| > 1$) well, while all the off-diagonal elements are correlated. This indicates that two particles reside in the right well and only one in each of the remaining wells, confirming once more the existence of the Mott-like state $|1, 1, 2\rangle$. The same behavior, in terms of $|g^{(2)}(x_1, x_2)|$, is observed for C_{int} with $k_1 = 0.2$ and $\phi = \pi/2$ but this time $|g^{(2)}(x_1, x_2)| > 1 (< 1)$ in the middle (outer) well [Fig. 2 (f₁)] resulting in the Mott-like state $|1, 2, 1\rangle$. Note that particle localization within regions of a vanishing scattering length has already been reported for inhomogeneously interacting bosons in a box potential [34].

Concluding, a spatially-dependent interaction strength enables for the emergence of Mott-like correlations (besides the inherent superfluid character due to $\nu > 1$) or even the possibility to shift the particles to a preferred direction. Taking advantage of the different spatial interaction profiles offers the opportunity to prepare certain ground state configurations. For instance, concerning larger lattice systems a sequence of inhomogeneous Mott-like states such as a double occupation for every second well can be achieved.

IV. DYNAMICS FOLLOWING A QUENCH OF THE PERIOD OF THE INTERACTION STRENGTH

In the present section the nonequilibrium dynamics upon a sudden change of the wavevector k_1 of the spatially-dependent interaction strength C_{int} is examined. The system consists of four bosons confined in a triple well and it is initialized in the ground state with spatial interaction strength C_{int} characterized by the parameters $g = 1$, $k_1 = 0$, $a = 2$ and $\phi = 0$. The initial many-body state is an admixture of the number states $|1, 2, 1\rangle$, $|1, 1, 2\rangle$, $|2, 1, 1\rangle$, and $|1, 3, 0\rangle$, $|0, 3, 1\rangle$ with the $|1, 2, 1\rangle$, $|1, 3, 0\rangle$ and $|0, 3, 1\rangle$ possessing the dominant contribution due to the hard-wall boundary conditions.

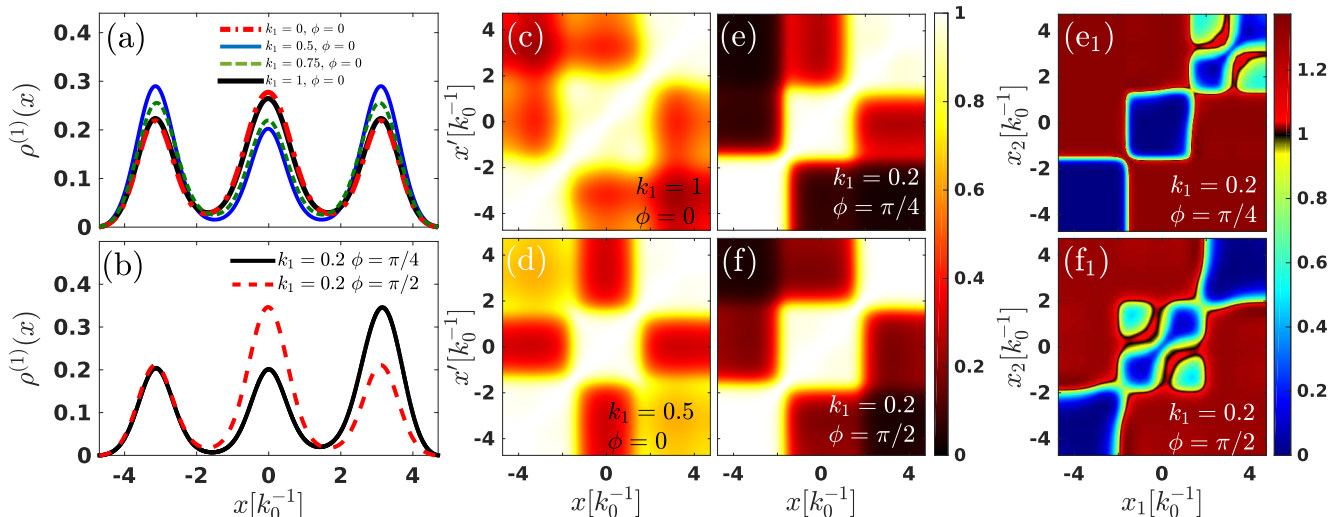


Figure 2. One-body density $\rho^{(1)}(x)$ for either varying (a) wavevector k_1 or (b) phase ϕ of the spatial interaction strength C_{int} (see legends). The remaining parameters that characterize C_{int} are $g = 1$ and $a = 2$. (c)-(f) The corresponding first order coherence $|g^{(1)}(x, x')|$ for the selected ground states shown in (a) and (b) (see legends). (e₁), (f₁) The two-body coherence function $|g^{(2)}(x_1, x_2)|$ for the ground state configurations illustrated in (e) and (f) respectively. The system consists of four bosons confined in a triple well.

A. Tunneling properties

To infer about the system's dynamical response upon quenching k_1 we first rely on the fidelity evolution $F(t; k_1) = |\langle \Psi(0) | \Psi(t; k_1) \rangle|^2$ which provides the overlap between the initial (ground) and the time-evolving wavefunction [63–65]. Fig. 3 (a) illustrates $F(t; k_1)$ for varying wavevector k_1 . The dynamics is characterized by enhanced response regions ($F(t; k_1) \ll 1$) centered around $k_1 = d/2$ with $d = 1, 3, 5, 7$ denoted by *I*, *II*, *III* and *IV* respectively in Fig. 3 (a) and regions of low response ($F(t; k_1) \approx 1$) located around integer values of k_1 . In the former case bosons in different wells are subject to distinct spatially averaged interaction strengths, while in the latter case all wells share on average the same interaction strength [see also Eq. (2) and Fig. 1]. Within the enhanced response regions $F(t; k_1)$ exhibits an oscillatory behavior in time which gradually transforms from a multifrequency pattern for small k_1 values (e.g. region *I*) to a single frequency one for increasing k_1 (e.g. see region *III* and the discussion below). In addition, with increasing k_1 the enhanced response regions gradually loose amplitude [e.g. $F(t; k_1 \approx 3.5) \approx 0.9$] due to the fact that the averaged spatially-dependent interaction strength tends to a homogeneous configuration.

To assign the tunneling modes triggered by a quench of k_1 we employ the fidelity spectrum $F(\omega; k_1) = \text{Re} \left\{ \frac{1}{\pi} \int dt F(t; k_1) e^{i\omega t} \right\}$ [44, 45], see Fig. 3 (b). As can be observed, tunneling occurs only within the enhanced response regions and the number of participating modes strongly depends on the magnitude of k_1 . Within the *I* region ($k_1 \approx 0.5$) five distinct tunneling modes appear indicated by the frequency branches α_1 -

α_5 in Fig. 3 (b). The aforementioned modes can be energetically categorized as follows. The most dominant process (see branch α_1) refers to single-particle tunneling e.g. $|1, 2, 1\rangle \rightleftharpoons |1, 1, 2\rangle$. Interestingly enough the second order tunneling mode $|1, 2, 1\rangle \rightleftharpoons |2, 0, 2\rangle$ (see branch α_2) occurs at smaller frequencies (for an explanation see the discussion below). Moreover, the frequency branches α_3 and α_4 correspond to transitions between the SP and T modes and in particular to e.g. $|1, 1, 2\rangle \rightleftharpoons |1, 0, 3\rangle$ (single-particle tunneling) and $|0, 3, 1\rangle \rightleftharpoons |1, 1, 2\rangle$ (atom pair tunneling [50–52]) respectively. Finally, the highest frequency mode α_5 refers to an interband transition and will be addressed in the next subsection. Turning to region *II* we observe the occurrence of the same tunneling modes as in *I* but overall shifted to smaller frequencies while the interband mode α_5 disappears. More importantly, the second order tunneling mode indicated by α_2 (α_4) possesses here a notably higher (reduced) frequency when compared to region *I* being also larger (smaller) than the α_1 (α_3) [see also the discussion below]. Inspecting the response regions *III* and *IV* we deduce that only the single atom tunneling mode α_1 survives, being however significantly weakened due to the almost homogeneous interaction strengths (C_{int}) that are formed for these wavevectors. To examine the robustness of the above-mentioned tunneling modes in the case of a smaller interaction offset g , we present in the inset (b₁) $F(\omega; k_1)$ for $g = 0.1$. As shown, due to the weak interaction offset only the single-particle tunneling mode α_1 survives possessing an overall smaller frequency when compared to the $g = 1$ case.

To obtain a basic understanding on the existence of the tunneling modes induced by the quench, we employ

a crude measure for the spatially averaged interaction energy [see Eq. (4) below] of a particular single-particle density distribution. As already mentioned in Sec. III different spatial configurations (symmetric around $x = 0$) of the interaction strength with respect to k_1 cause only parity symmetric (with respect to the central well) number states to be energetically equal. Focussing exclusively on the lowest band interwell tunneling, we roughly approximate the spatially averaged interaction energy of a particular particle configuration characterized by the number state $|\vec{n}\rangle = |n_1, n_2, n_3\rangle$ as

$$\bar{E}_{|\vec{n}\rangle}^{int}(g, a, k_1, \phi) = \sum_{i=1}^m \frac{n_i(n_i - 1)}{2(d_i - d'_i)^2} \int_{d_i}^{d'_i} dx C_{int}(x; g, a, k_1, \phi). \quad (4)$$

n_i refers to the number of bosons located at the i -th well, d_i, d'_i denote the edges of the i -th well and N is the total number of bosons. Then, the spatially averaged interaction energy difference of the different Fock states (modes) is approximately determined by $\Delta\bar{E}^{int} = \bar{E}_{|\vec{n}\rangle}^{int} - \bar{E}_{|\vec{n}'\rangle}^{int}$. For the tunneling modes participating in our system, the corresponding spatially averaged energy differences, $\Delta\bar{E}^{int}$ are illustrated in Fig. 3 (c). Referring to the different modes $\Delta\bar{E}^{int}(k_1)$ schematically resembles the energetic order of the frequency branches depicted in Fig. 3 (b) but does not provide any quantitative values as within our approximation we do not take into account the explicit form of the corresponding Wannier function. Moreover using $\Delta\bar{E}^{int}(k_1)$ the appearance of weak and strong response regions can be explained only in some limited cases. Indeed, for integer values of k_1 C_{int} is on average the same for each well, i.e. the repulsion of the atoms within each well is alike, and therefore $\Delta\bar{E}^{int}(k_1 = n \in \mathbb{N}) \rightarrow 0$ for the states $|1, 2, 1\rangle$, $|2, 1, 1\rangle$ and $|1, 1, 2\rangle$. As a consequence the single-particle tunneling mode α_1 is suppressed during the dynamics. However, the absence of higher order tunneling processes such as α_2 - α_5 for $k = n \in \mathbb{N}$ can not be understood utilizing $\Delta\bar{E}^{int}$ [see Fig. 3 (c)]. On the contrary $\Delta\bar{E}^{int}$ for $k = (n + 1)/2$ with $n \in \mathbb{N}$ captures qualitatively at least the behavior of the observed frequency spectra see e.g. the exchange of the α_1 (α_3) and α_2 (α_4) modes which is energetically favored. In addition, for these k_1 values an interaction imbalance between the middle and outer wells (e.g. for $k_1 = 0.5$ an interaction peak appears in the middle well) takes place giving rise to several tunneling modes.

An effective way to manipulate the tunneling frequencies (within the regions I-IV) is to tune the spatial interaction strength by means of the inhomogeneity parameter a or the interaction offset g . $F(\omega; k_1)$ for $a = 5$ and $g = 1, \phi = 0$ is shown in Fig. 3 (d). Besides α_4 , all the previously observed tunneling modes (α_1 - α_3 and α_5) appear in the fidelity spectrum but are found to be shifted to larger frequencies. The absence of the α_4 mode is caused by the fact that for increasing a the $|1, 3, 0\rangle$ contribution in the ground state becomes negligible and

therefore the corresponding tunneling process α_4 is suppressed. The observed shift of the branches α_1 - α_3 and α_5 can also be understood in terms of $\Delta\bar{E}^{int}(a, k_1)$ which acquires larger values for increasing a and fixed k_1 as shown in Fig. 3 (c) for the frequency branch α_1 . Finally, we investigate the influence of the interaction offset g on the quench induced tunneling modes, see Fig. 3 (e) for fixed $k_1 = 0.5, a = 1$ and $\phi = 0$. All five interaction dependent modes (α_1 - α_5) occur but importantly here only the single-particle mode α_1 survives for small $g < 0.5$ as well as for strong $g > 3$ interaction offsets. The latter indicates a suppression of the interwell tunneling dynamics which is highly altered in the strongly interacting regime [66, 67]. Summarizing, a quench of the wavevector of the spatially-dependent interaction strength induces a multitude of tunneling modes which can be further amplified, diminished or shifted by adjusting individually parameters of the interaction profile.

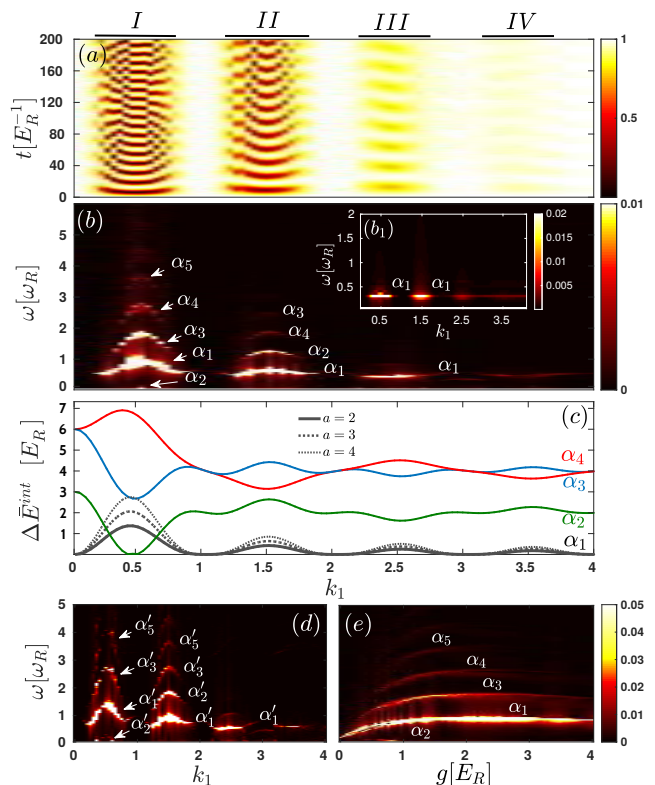


Figure 3. (a) Fidelity evolution $F(t; k_1)$ for varying wavevector k_1 of the spatially-dependent interaction strength C_{int} for $g = 1, a = 2, \phi = 0$ and (b) the corresponding spectrum $F(\omega; k_1)$. Inset (b₁) presents $F(\omega; k_1)$ for $g = 0.1$ while all other system parameters are the same as in (a). (c) Average interaction energy difference $\Delta\bar{E}^{int}$ [see also Eq. (4)] for the tunneling branches shown in (b) that correspond to different number state transitions. (d) $F(\omega; k_1)$ for $a = 5, g = 1, \phi = 0$ and varying k_1 . (e) $F(\omega; g)$ for $k_1 = 0.5, a = 2, \phi = 0$ and varying interaction offset g . In all cases the system is initially prepared in the corresponding ground state of four bosons in a triple well.

B. Breathing dynamics

Having discussed in detail the lowest band tunneling dynamics triggered by quenching the wavevector of C_{int} , we next investigate the corresponding excitation to higher band (interband) processes. The dominant mode here, that contains admixtures of excited band states corresponds to a breathing mode. The latter refers to an expansion and contraction of the atomic cloud [68, 69] and due to the lattice symmetry (parity symmetry with respect to $x = 0$) it is expected to be more prone within the central well [42, 43]. To track this mode we measure the position variance in the middle well (denoted by the index M) $\sigma_M^2(t) = \langle \Psi(t) | \hat{x}_M^2 | \Psi(t) \rangle - \langle \Psi(t) | \hat{x}_M | \Psi(t) \rangle^2$. The one-body operators correspond to $\hat{x}_M = \int_{-\pi/2}^{\pi/2} dx x \hat{\Psi}^\dagger(x) \hat{\Psi}(x)$ and $\hat{x}_M^2 = \int_{-\pi/2}^{\pi/2} dx x^2 \hat{\Psi}^\dagger(x) \hat{\Psi}(x)$ where $\hat{\Psi}(x)$ [$\hat{\Psi}^\dagger(x)$] is the field operator that annihilates [creates] a boson at position x . To quantify the frequency spectrum of the breathing mode we inspect $\sigma_M^2(\omega; k_1) = \text{Re} \{ 1/\pi \int dt \sigma_M^2(t) e^{i\omega t} \}$ with varying wavevector in Fig. 4. Three distinct k_1 -dependent frequency branches can be observed. The energetically lowest branch β_1 is linked to the most dominant interwell tunneling mode $|1, 2, 1\rangle \rightleftharpoons |1, 1, 2\rangle$ [see also Fig. 3 (b)]. The appearance of this mode in the spectrum is attributed to the fact that the tunneling can induce a change in the width of the local wavepacket. The branch β_2 refers to the interband process $|1 \otimes 1^{(2)}, 1, 1\rangle \rightleftharpoons |1, 2, 1\rangle \rightleftharpoons |1, 1, 1 \otimes 1^{(2)}\rangle$ which indicates the occurrence of a global interwell breathing mode induced by the over-barrier transport (i.e. the probability for a single-particle to possess enough energy to overcome the lattice barrier). It fluctuates around $\omega \approx 3.5$ as k_1 is increased exhibiting maxima and minima within the enhanced and weak response areas respectively. Finally, the branch β_3 indicates the participation of even energetically higher excitation processes such as $|1, 2, 1\rangle \rightleftharpoons |1, 1, 1 \otimes 1^{(4)}\rangle$. It is located around $\omega \approx 5.6$ showing a k_1 -dependent behavior similar to β_2 . The underlying process that triggers the aforementioned global breathing mode can be summarized as follows. Following a quench on the wavevector of C_{int} the interaction imbalance between the central and outer wells becomes more pronounced leading to an over-barrier transport of one boson from the middle to the outer wells. Then, this boson performs a collision with the preexisting atom and a subsequent single excitation to the second energy band takes place, inducing this way the breathing mode. It is important to note at this point that the breathing mode can be excited more efficiently upon quenching the wavevector of a spatially-dependent interaction strength as compared to a homogeneous interaction quench [42, 43]. In this latter case the contribution of states higher than the second band is almost absent and can be triggered only for very strong interaction strength quenches i.e. $g > 3.5$ [45]. However even in this case the breathing frequency is mainly insensitive to the interaction quench amplitude. To further study the dependence

of the breathing mode on the interaction offset g of C_{int} , we present in the inset of Fig. 4 $\sigma_M^2(\omega)$ for $g = 0.1$ (the other parameters of C_{int} are the same as before). As shown all excited states disappear and only the lowest band tunneling mode persists, since such a small offset is insufficient to induce over-barrier transport.

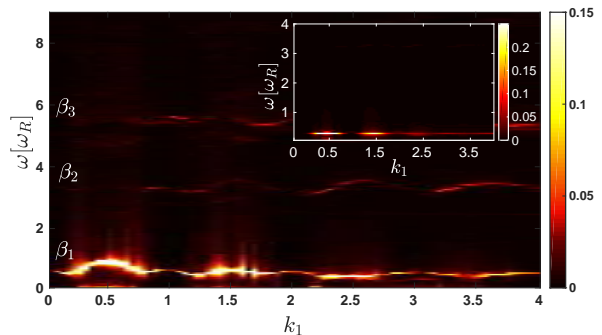


Figure 4. Spectrum of the variance $\sigma_M^2(\omega; k_1)$ for increasing wavevector k_1 of C_{int} with $g = 1$, $a = 2$ and $\phi = 0$. The inset shows $\sigma_M^2(\omega; k_1)$ for the interaction offset $g = 0.1$ and varying wavevector k_1 . The remaining system parameters are the same as above. In both cases the system is initialized in the ground state of four bosons confined in a triple well.

V. QUENCH OF THE PHASE OF THE INTERACTION STRENGTH

Let us now examine the dynamics upon a sudden change of the phase ϕ of the spatially-dependent interaction strength C_{int} . Following this quench protocol an interaction imbalance between all wells of the lattice is induced resulting in a directed tunneling dynamics (see also below). The system (four bosons in a triple well) is initially prepared in the ground state with C_{int} characterized by $g = 1$, $k_1 = 0.2$, $a = 2$ and $\phi = 0$. Then the spatially averaged in each well C_{int} possesses a maximum value around the central well and resembles an almost linear gradient. We remark here that for larger k_1 values being comparable to the lattice wavevector k_0 a phase quench does not produce a substantial dynamical response. The dominant contribution in the initial many-body state stems from the number state $|1, 2, 1\rangle$.

A. Tunneling dynamics

To examine the response of the system induced by a quench of the phase ϕ of the interaction strength C_{int} we invoke the fidelity evolution $F(t; \phi) = |\langle \Psi(0) | \Psi(t; \phi) \rangle|^2$, see Fig. 5 (a). Due to the underlying periodicity of C_{int} [see also Eq. (2)] we restrict our study to the phase interval $[0, \pi/2]$. Recall here that for $\phi = 0$ ($\phi = \pi/4$) the spatially averaged in each well interaction strength exhibits a maximum around the central (left) well, while at

$\phi = \pi/2$ we encounter a corresponding minimum in the middle well [see also Fig. 1]. The system is significantly perturbed i.e. $F(t; \phi) \neq 1$ (unperturbed, $F(t; \phi) \approx 1$) for $\pi/16 < \phi < \pi/2$ ($\phi < \pi/16$) where the quench induced spatial interaction imbalance becomes significant (negligible). The underlying interaction imbalance is strongest within the range $\pi/8 \leq \phi \leq 3\pi/8$ (maximized at $\phi = \pi/4$) and as a consequence the system is strongly driven out-of-equilibrium. $F(t; \phi)$ exhibits oscillations which possess the largest amplitude in the vicinity of $\phi \approx \pi/4$.

To identify the participating modes triggered by the phase quench in C_{int} we inspect the fidelity spectrum $F(\omega; \phi)$ shown in Fig. 5 (b). Three distinct tunneling pathways occur in the spectrum, denoted by γ_1 , γ_2 and γ_3 , which can be linked to first and second order transport. In particular, the two lowest-lying phase-dependent frequency branches refer to the first order processes $|1, 2, 1\rangle \rightleftharpoons |1, 1, 2\rangle$ (γ_1) and $|1, 2, 1\rangle \rightleftharpoons |2, 1, 1\rangle$ (γ_2) respectively. The above-mentioned tunneling processes that would otherwise (for C_{int} with $\phi = 0$) be energetically equal are well separated here as a consequence of the employed quench protocol. Indeed quenching the phase of C_{int} the prevailing interatomic interaction is shifted from the middle to the left well. Therefore the atoms initially located at the left site experience increasing repulsion after the quench rendering the single-particle tunneling from the middle to the right well energetically favorable (branch γ_1). In this way a directed tunneling process can be achieved. Another interesting observation here is that the frequencies of the tunneling modes γ_1 and γ_2 start to merge into a single one for $3\pi/8 < \phi < \pi/2$ as the corresponding spatially averaged interaction strength in the left and right wells becomes comparable within this phase interval. Finally, we encounter the second order tunneling process $|1, 2, 1\rangle \rightleftharpoons |2, 0, 2\rangle$ (indicated by the branch γ_3) which is more pronounced for $\pi/4 < \phi < \pi/2$ where the interaction imbalance is most pronounced when compared to the $0 < \phi < \pi/4$ phase interval.

In an attempt to steer the above-mentioned tunneling modes or even trigger higher-lying ones we present in Fig. 5 (c) $F(\omega; \phi)$ for a larger inhomogeneity amplitude $a = 5$. The resulting lowest band tunneling modes (γ'_1 , γ'_2 and γ'_3) are the same as before but they are located at higher frequencies, they become stronger and the frequency gap between each two is more pronounced when compared to the case of $a = 2$. In addition we observe the existence of the higher lying frequency branch γ'_4 which refers to the interband transition $|1, 2, 1\rangle \rightleftharpoons |1, 1, 1 \otimes 1^{(2)}\rangle$. This mode located in the vicinity of $\phi = \pi/2$ is caused by the enhanced over-barrier transport occurring for these quench amplitudes. Note that such an interband transition is also inherently related to the considered large interaction inhomogeneity being, in general, suppressed for smaller inhomogeneities, see for instance Fig. 5 (b). In the following subsection, we explicitly address how to excite such higher band states for varying inhomogeneity

a.

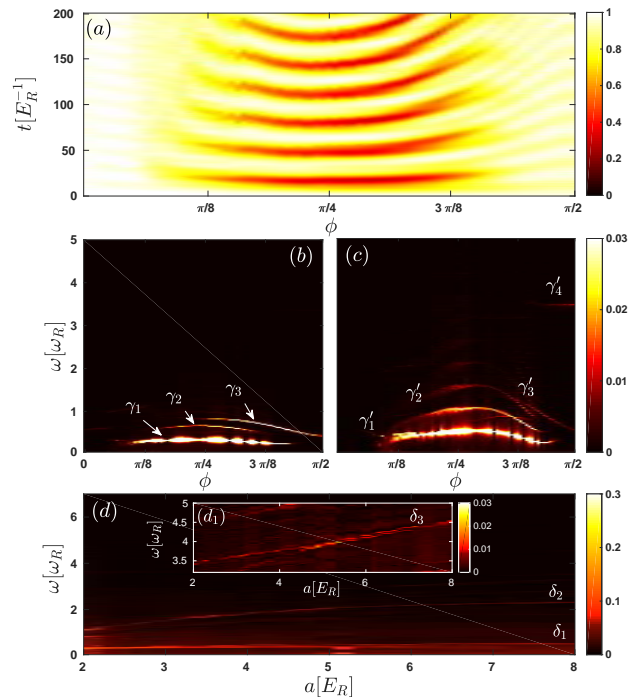


Figure 5. Fidelity evolution $F(t; \phi)$ for a varying phase ϕ of the interaction strength C_{int} with $a = 2$, $g = 1$ and $k_1 = 0.2$. The corresponding spectra $F(\omega; \phi)$ for inhomogeneity (b) $a = 2$ and (c) $a = 5$. (d) Spectrum of the intrawell asymmetry $\Delta\rho_R(\omega)$ and the variance $\sigma_M^2(\omega)$ [inset (d₁)] for increasing inhomogeneity a . The spatially-dependent interaction profile C_{int} is characterized by $g = 1$, $\phi = \pi/8$ and $k_1 = 0.2$. In all cases the system is initially prepared in the ground state of four bosons in a triple well.

B. Excitation processes

Having discussed in detail the tunneling mechanisms upon a phase quench, we next investigate the possibility of triggering interband transitions. As already mentioned above the phase quench shifts the interaction profile C_{int} in space. Here C_{int} initially ($\phi = 0$) exhibits a maximum in the central well and after quenching ϕ this maximum moves to the left well thus inducing the aforementioned tunneling dynamics. In addition the sudden change of ϕ yields a high probability for the delocalized particle to overcome the lattice barrier (over-barrier transport) and move to the neighboring well in which the minimum of the postquench C_{int} occurs. The resulting over-barrier transport is consequently responsible for mainly two higher band excited modes, namely the global breathing [42, 70, 71] and the local cradle [42, 43] modes. It is important to mention here that the cradle mode occurs also upon a wavevector quench but it is greatly suppressed when compared to the phase quench

scenario. In this latter case the interaction imbalance between individual wells is stronger resulting in an enhanced over-barrier transport and thus a prone cradle process. The cradle mode represents a dipole-like intrawell oscillation in the outer wells of the finite lattice (for more details on the generation and properties of this mode see [42, 43]). Since the parity symmetry within the outer well where it takes place is broken, it can be quantified by the corresponding intrawell asymmetry of the wavefunction. Since here we are interested in the right well dynamics the aforementioned asymmetry is defined as $\Delta\rho_R(t) = \rho_{R,1}(t) - \rho_{R,2}(t)$, where $\rho_{R,1}(t)$ and $\rho_{R,2}(t)$ denote the spatially integrated densities of the left and the right half sector of the well. To trace this mode we rely on $\Delta\rho_R(\omega)$. Finally, the global breathing mode refers to the contraction and expansion of the entire bosonic cloud being induced by the over-barrier transport. Due to the lattice symmetry [see also Sec. IV B] the global breathing mode is expected to be more prone in the central well and therefore $\sigma_M^2(\omega)$ provides an adequate measure for this mode.

As both of the above described modes are initialized by the over-barrier transport which in turn depends on the inhomogeneity a it would be instructive to study how they are affected by adjusting a . Let us therefore inspect them by focussing on a specific phase quench from $\phi = 0$ to $\phi = \pi/8$ and considering fixed $k_1 = 0.2$ and $g = 1$ for varying a . Fig. 5 (d) presents $\Delta\rho_R(\omega; a)$ and $\sigma_M^2(\omega; a)$ [see the inset (d₁)] for increasing a . Regarding the cradle mode (see branch δ_2), it can be linked to the interband transition $|1, 2, 1\rangle \rightleftharpoons |1, 1, 1 \otimes 1^{(1)}\rangle$ and it is greatly affected by the considered inhomogeneity amplitude a . This latter behavior is expected as an increasing a triggers all the more the over-barrier transport. In particular, its characteristic frequency (branch δ_2) increases for larger inhomogeneity amplitudes a . The observed energetically lowest branch δ_1 corresponds to the tunneling process $|1, 2, 1\rangle \rightleftharpoons |1, 1, 2\rangle$ which is only weakly a -dependent. On the other hand, the global breathing mode [see branch δ_3 in the $\sigma_M^2(\omega; a)$] refers to the interband tunneling $|1, 2, 1\rangle \rightleftharpoons |1, 1, 1 \otimes 1^{(2)}\rangle$ and it increases almost linearly for varying a due to the consequent enhanced interaction imbalance between the adjacent wells. Summarizing, by tuning the inhomogeneity of the spatially-dependent interaction strength we can manipulate the frequencies of both excited higher band modes.

To generalize our findings, below, we demonstrate that the main characteristics of the dynamical response upon quenching either the wavevector or the phase of the spatially-dependent interaction strength remain robust also in the case of a five well lattice with filling $\nu > 1$. It is important to remark here that for fillings $\nu < 1$ a corresponding quench of the spatial interaction profile does not alter significantly the initial (ground) state of the system (results not shown due to brevity) as the overlap between the individual bosons is weak.

VI. QUENCH DYNAMICS IN A FIVE WELL OPTICAL LATTICE

Let us consider six bosons confined in a five well finite optical lattice. The system is initially prepared in its ground state where the corresponding spatial interaction strength [see also Eq. (2)] is characterized by $g = 1$, $\phi = 0$, $a = 2$, $k_1 = 0$ [$a = 3$, $k_1 = 0.05$] for the wavevector [phase] quench. Then, the initial state is an admixture of the available lowest band states from which the main contribution stems from the Wannier number states $|1, 1, 2, 1, 1\rangle$, $|1, 2, 1, 1, 1\rangle$ and $|1, 1, 1, 2, 1\rangle$.

To induce the dynamics we perform a quench either on the wavevector k_1 or the phase ϕ of the initial interaction strength. Fig. 6 (a) presents $F(t; k_1)$ following a wavevector quench. As in the triple well case, the dynamics exhibits enhanced [weak] response regions namely $F(t; k_1) \ll 1$ [$F(t; k_1) \approx 1$] in the neighborhood of $k_1 = d/2$ with $d = 1, 3, \dots$ [$k_1 = n \in \mathbb{N}$] due to the large [small] quench induced interaction imbalance of bosons residing in the different wells. However, the enhanced response areas appear to be wider with respect to k_1 when compared to the triple well case. Moreover, in these strong response regions $F(t; k_1)$ undergoes oscillations in time possessing a multitude of frequencies and large amplitudes for small k_1 's which tend to a single frequency oscillation of small amplitude for increasing k_1 . This latter behavior is again (as in the case of the triple well) caused by the tendency of C_{int} to an almost spatially homogeneous interaction strength on average for large k_1 's. Focussing on a phase quench, see Fig. 6 (b), the obtained response resembles the triple well case [compare Fig. 6 (b) with Fig. 5 (a)]. Indeed, the system is driven far away from its initial state i.e. $F(t; \phi) \neq 1$ exhibiting an oscillatory behavior for $\pi/16 < \phi < \pi/2$ where the quench induced spatial interaction imbalance between distinct lattice regions becomes significant. This interaction imbalance is maximum at $\phi = \pi/4$ for which the oscillations of $F(t; \phi)$ possess the largest amplitude.

In both quench scenarios, tunneling and over-barrier transport between the distinct wells of the finite lattice can be observed. To visualize the spatially resolved system dynamics we invoke $\delta\rho^{(1)}(x, t) = \rho^{(1)}(x, t) - \langle \rho^{(1)}(x) \rangle_T$, being the deviation of the one-body density from its time average $\langle \rho^{(1)}(x) \rangle_T = \int_0^T \rho^{(1)}(x, t) / T$ over the considered propagation time T . In this sense, $\delta\rho^{(1)}(x, t)$ encompasses the temporal fluctuations of the one-body density around its mean along the finite lattice [42, 43]. Figs. 6 (c), (d) present $\delta\rho^{(1)}(x, t)$ following a quench of the wavevector, from $k_1 = 0$ to $k_1 = 0.75$, and the phase, from $\phi = 0$ to $\phi = \pi/4$, respectively. Regarding the wavevector quench, see Fig. 6 (c), we observe that predominantly a tunneling dynamics takes place which refers to the transfer of population from the middle to the outer wells. Moreover, the inner well dynamics is mainly described by two excited modes. Specifically, the middle well exhibits a breathing like mode due to the lattice symmetry, while in the outer wells the cradle mode

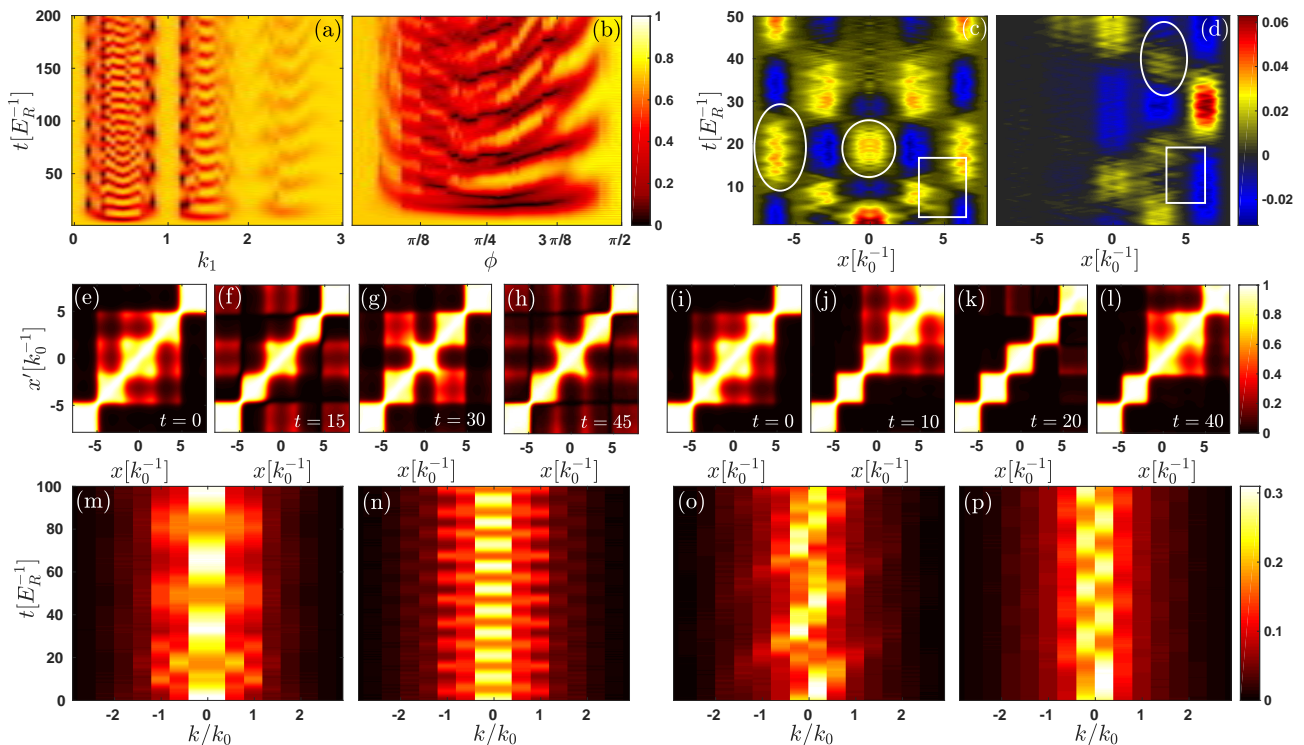


Figure 6. Fidelity evolution following a quench of (a) the wavevector k_1 and (b) the phase ϕ of the spatial interaction strength C_{int} . One-body density fluctuations $\delta\rho^{(1)}(x, t)$ for (c) a wavevector quench from $k_1 = 0$ to $k_1 = 0.75$ and (d) a phase quench from $\phi = 0$ to $\phi = \pi/4$. One-body coherence for distinct time instants (see legend) (e)-(f) [(i)-(l)] after a sudden change of the magnitude of the wavevector [phase] as in (c) [(d)]. (m)-(p) Momentum distribution of the one-body density matrix during the evolution. (m), (n) [(o), (p)] correspond to quenches from $k_1 = 0$ [$\phi = 0$] to $k_1 = 0.75$ and $k_1 = 0.5$ [$\phi = \pi/4$ and $\phi = \pi/8$] respectively. The horizontal axis represents the momenta in units of the inverse lattice vector $k_0 = \pi/l$. For all cases referring to wavevector [phase] quenches the remaining system parameters correspond to $g = 1$, $a = 2$ and $\phi = 0$ [$a = 3$, $k_1 = 0.05$]. The setup consists of six bosons confined in a five well lattice. The ellipses, circles and rectangles in (c), (d) indicate the cradle, breathing and over-barrier transport respectively.

is manifested as a dipole-like oscillation of the localized wavepacket which is generated by a direct over-barrier transport as a consequence of the quench. Turning to the phase quench scenario, illustrated in Fig. 6 (d), a directed population transfer from the middle well to the right side of the lattice located at $0 < x < 7.8$ (tunneling mode) and back occurs. Additionally, the induction of over-barrier transport caused by the quench gives rise to the cradle mode within the right side wells.

To provide a link between the quench induced tunneling dynamics and the coherence properties of the system we study $|g^{(1)}(x, x'; t)|$ at distinct time instants during the evolution [61, 62]. As already mentioned in Sec. III, $|g^{(1)}(x, x'; t)|$ is bound to the range $[0, 1]$ and measures the proximity of the many-body state to a product mean-field state for a fixed set of coordinates x, x' . Figs. 6 (e)-(h) present $|g^{(1)}(x, x'; t)|$ for distinct time instants following a wavevector quench from $k_1 = 0$ to $k_1 = 0.75$. Initially, $t = 0$, all bosons reside in the three central wells [see also Fig. 6 (c)] which are partially incoherent with each other, e.g. $|g^{(1)}(x = 2, x' = -4; t)| \approx 0.6$ as depicted in Fig. 6 (e). During evolution, an atomic portion

gradually tunnels to the edge wells with the remaining atoms residing in the central well resulting in a low population of its nearest neighbors ($-4.7 < x < -1.57$ and $1.57 < x < 4.7$) ones, see for instance Fig. 6 (c) at $t = 15$. These most outer populated wells appear to be partly incoherent [Fig. 6 (f)] with each other (e.g. $|g^{(1)}(x = 6, x' = -6; t = 15)| \approx 0.3$) as well as with the central well ($|g^{(1)}(x = 0, x' = -6; t = 15)| \approx 0.5$). A revival of the tunneling process with population transfer from the central to the proximal to it outer wells occurs at later evolution times, e.g. at $t = 30$ [Fig. 6 (g)]. In turn, a partial coherence between these wells [e.g. $|g^{(1)}(x = 4, x' = -4; t = 30)| \approx 0.6$ in Fig. 6 (g)] is observed. Then the atoms move again to the most outer wells, e.g. at $t = 45$, where the system's coherence properties [Fig. 6 (h)] are similar to $t = 15$. Next, we focus on the coherence properties upon quenching the phase of C_{int} , shown in Figs. 6 (i)-(l). The initial ($t = 0$) partially incoherent region consists of the three middle wells [Fig. 6 (i)]. Then, it shifts across the diagonal of $|g^{(1)}(x, x'; t)|$ [at $t = 10$, see Fig. 6 (j)] including the two outer right ($1.57 < x < 7.8$) and the central well. Finally, it turns

back [at $t = 40$, see Fig. 6 (*l*)] occupying the middle and its nearest neighbor ($1.57 < x < 4.7$) right well. As before, this behavior resembles the corresponding tunneling dynamics, see Fig. 6 (*d*). Concluding from the above, we can infer that quenching the spatial interaction strength it is possible to induce either site selective partial coherence or even completely shift certain partially incoherent regions following the tunneling dynamics. Such a site selective coherence has been recently demonstrated for the ground state of a many-body bosonic ensemble trapped in a tilted triple well [72].

Finally, we inspect whether a certain multitude of momenta is populated during the dynamics as a consequence of the employed quench protocol. To achieve the latter we rely on, the experimentally accessible via time-of-flight measurements [4, 73, 74], one-body momentum distribution

$$n(k, t) = \frac{1}{2\pi} \int \int dx dx' \rho^{(1)}(x, x', t) e^{-ik(x-x')t}. \quad (5)$$

$\rho^{(1)}(x, x', t)$ is the one-body reduced density matrix which is obtained by tracing out all the bosons but one in the N -body density matrix. The time evolution of the momentum distribution for six bosons confined in a five well lattice potential after a quench of the wavevector of C_{int} from $k_1 = 0$ to $k_1 = 0.75$ and $k_1 = 0.5$ is depicted in Figs. 6 (*m*), (*n*) respectively. As it can be seen, under this quench protocol $n(k, t)$ features in time a periodically modulated pattern in which distinct momenta are populated. In particular, $n(k, t)$ forms a gradually transformed in time broad Gaussian like distribution centered around $k_0 = 0$ with edges either at $\pm k_0/2 = 1.57$ or $\pm 3k_0/2 = 4.71$ where in both cases all momenta in between are activated. The oscillation frequency between the above-mentioned momentum structures changes with respect to the quench amplitude, e.g. it is larger at $k_1 = 0.5$ than $k_1 = 0.75$, reflecting this way the system's dynamical response [see also Fig. 6 (*a*)] and more specifically the tunneling dynamics. We remark here that similar periodically modulated patterns in the momentum distribution during the evolution take place when considering multiple interaction quench sequences in few boson homogeneously interacting ensembles trapped in an optical lattice [45]. Following a sudden change of the phase of C_{int} , see Figs. 6 (*o*), (*m*) for a quench from $\phi = 0$ to $\phi = \pi/4$ and $\phi = \pi/8$ respectively, $n(k, t)$ shows a completely different behavior. Due to the phase shift of the interaction strength a tendency for directed tunneling to the right side of the lattice ($0 < x < 7.8$) occurs, see also Fig. 6 (*d*). The latter essentially guides first the consecutive population of $k_0 = 0$, $k_0/2 = 1.57$ and $k_0 = 3.14$ and subsequently of the exactly opposite momenta. This process repeats during the evolution. The different quench amplitudes impact mainly the speed of the alternating activation of momenta and to a lesser extent the magnitude of their population, compare Figs. 6 (*o*) and (*m*).

VII. CONCLUSIONS

We have investigated the ground state properties and in particular the nonequilibrium quantum dynamics of few boson ensembles experiencing a spatially modulated interaction strength and confined in a finite lattice potential. To profit from the competition between delocalization and on-site interaction effects we focus on setups possessing fillings larger than unity, thus also avoiding suppression of tunneling. The employed spatial interaction strength is of sinusoidal type and it is characterized by its modulation wavevector, inhomogeneity amplitude, interaction offset and phase.

Before delving into the dynamics, we trace the impact of the wavevector and the phase individually on the ground state properties of the system. The inhomogeneity amplitude in most cases is kept fixed being of the order of half the lattice depth, while the interaction offset is unity. For small values of the wavevector the spatially in each well averaged interaction strength is larger within the central well when compared to the outer ones, while it becomes the same for incrementing spatial periodicity. This behavior causes a spatial redistribution of the atoms from the outer to the central wells for increasing wavevectors. In all cases, the ensemble remains superfluid. On the other hand, phase shifts yield an interaction imbalance between all lattice wells and enables us to displace the single-particle density distribution in a preferred direction achieving Mott-like states.

Next, we analyze the system's dynamical response upon quenching either the wavevector or the phase of the spatial interaction strength. Following a sudden change of the wavevector the dynamics is characterized by enhanced response regions, located at fractional values of the wavevector, in which bosons at distinct wells are subjected to different spatially averaged interaction strengths. For incrementing wavenumbers these enhanced response regions become gradually less transparent as the respective interaction profile tends to a homogeneous configuration. The quench on the wavevector of the spatially-dependent interaction strength yields the excitation of a multitude of tunneling modes consisting of single and two particle transport. These modes can be further amplified or shifted by adjusting the interaction offset or the inhomogeneity amplitude respectively. A quench induced breathing dynamics is also observed characterized by interband tunneling processes which possess mainly a single excitation to the second or fourth excited band. Inspecting the momentum distribution we show that a periodic population transfer of momenta during the dynamics takes place, while the one-body coherence function reveals that partially coherent regions occur between the wells that are predominantly populated during the evolution.

The phase quench imposes an interaction strength imbalance between all wells yielding a directed transport along the finite lattice as it accounts for a spatial shift of the entire interaction profile. The induced transport

consists of single-particle and atom pair tunneling. More importantly and in contrast to the wavevector quench, a phase quench allows for the discrimination of the tunneling modes which would be otherwise energetically equal. A characteristic process of the latter type corresponds for instance to single-particle lowest band tunneling from the middle to the left or the right well. For larger inhomogeneity amplitudes these modes become more discernible as a function of the phase parameter, namely their energy difference is intensified, while for increasing interaction offset their suppression is observed. The directional transport is also reflected in the evolution of the one-body momentum distribution and the coherence function. In the former case a directed consecutive population of higher momenta occurs, while in the latter case the predominantly populated wells form a partially incoherent region which is shifted in the preferred tunneling direction. Besides the above described tunneling dynamics, the phase quench yields a noticeable over-barrier transport which in turn induces a global breathing motion of the entire bosonic cloud and a cradle mode in the outer wells. Both modes are related to single-particle interband processes to the first or second excited band respectively, and are found to be enhanced for incrementing inhomogeneity amplitude.

There are several directions that one might pursue as possible extensions of the present work. An intriguing prospect would be to study the periodically driven dynamics upon shaking the optical lattice and investigate how the properties of the corresponding parametrically induced resonances are altered when compared to the homogeneously interacting case [75]. Another possible path is to explore the nonequilibrium dynamics of bosonic binary mixtures experiencing such spatially dependent interactions. Here it is interesting to unravel whether a phase separation process can be achieved after quenching the wavevector of the interaction profile and even analyze the triggered excitation modes.

APPENDIX: THE COMPUTATIONAL QUANTUM DYNAMICS APPROACH MCTDHB

To simulate the nonequilibrium dynamics and calculate the stationary properties of the spatially interacting bosons we solve the many-body Schrödinger equation $(i\hbar\partial_t - H)|\Psi(t)\rangle = 0$, by employing the Multi-Configuration Time-Dependent Hartree method for Bosons (MCTDHB) [47, 48, 76]. This method has been applied extensively in several nonequilibrium bosonic settings, see e.g. [42–45, 70, 75–79]. We remark that within our implementation we use the Multi-Layer Multi-Configuration Time-Dependent Hartree method for bosonic and fermionic Mixtures (ML-MCTDHX) [80, 81]. The latter consists an extended version of the MCTDHB and is particularly suitable for treating multi-component ultracold systems, while for the case of a single bosonic species it reduces to MCTDHB. MCTDHB is

based on the usage of a time-dependent (t-d) and variationally optimized many-body basis set, which enables for the optimal truncation of the total Hilbert space. The expansion of the many-body wavefunction relies on a linear combination of t-d permanents $|\vec{n}\rangle$ and t-d weights $A_{\vec{n}}(t)$

$$|\Psi(t)\rangle = \sum_{\vec{n}} A_{\vec{n}}(t) |\vec{n}\rangle. \quad (6)$$

The bosonic number states $|\vec{n}\rangle = |n_1, n_2, \dots, n_M; t\rangle$, built upon t-d single-particle functions (SPFs) $|\phi_i(t)\rangle$, $i = 1, 2, \dots, M$, with M being the number of the considered SPFs. The summation \vec{n} is taken over all the possible combinations n_i such that the total number of bosons N is conserved. Moreover, the SPFs are expanded within a time-independent primitive basis $\{|k\rangle\}$ of dimension M_{pr} . Within our implementation a sine discrete variable representation has been used as a primitive basis for the SPFs. We remark here that in the case of $M = 1$ the many-body wavefunction is given by a single permanent $|n_1 = N; t\rangle$ and the method reduces to the t-d Gross Pitaevskii mean-field approximation.

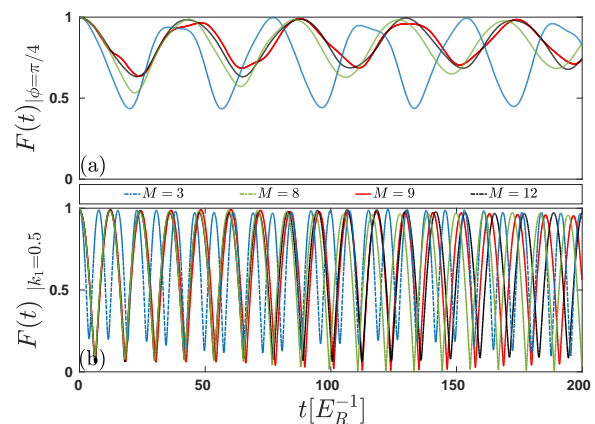


Figure 7. $F(t)$ for different number of SPFs (see legend) following a quench on (a) the phase ϕ from $\phi = 0$ to $\phi = \pi/4$ and (b) the wavevector k_1 from $k_1 = 0$ to $k_1 = 0.5$.

To obtain the t-d N -body wavefunction $|\Psi(t)\rangle$ under the influence of the Hamiltonian \hat{H} we determine the equations of motion [47, 48, 76] for the coefficients $A_{\vec{n}}(t)$ and the SPFs $|\phi_i(t)\rangle$ following e.g. the Dirac-Frenkel [82, 83] variational principle, $\langle \delta\Psi | i\partial_t - \hat{H} | \Psi \rangle = 0$. These equations consist of $\frac{(N+M-1)!}{N!(M-1)!}$ linear equations of motion for $A_{\vec{n}}(t)$ being coupled to the M non-linear integrodifferential equations of motion for the SPFs. To prepare the system in the ground state of the Hamiltonian \hat{H} we utilize the so-called improved relaxation scheme [70], which is briefly outlined below. Namely, we employ a certain number of SPFs $\{|\phi_i^{(0)}\rangle\}$ and diagonalize the Hamiltonian within the basis spanned by the SPFs. Setting the n -th obtained eigenvector as the $A_{\vec{n}}^{(0)}$ -vector we propagate the SPFs in imaginary time within a finite time interval $d\tau$

and update the SPFs to $\{|\phi_i^{(1)}\rangle\}$. The above-mentioned steps are repeated until the energy of the state converges within the prescribed accuracy.

To accurately perform the numerical integration of the MCTDHB equations of motion the overlap criteria $|\langle\Psi|\Psi\rangle - 1| < 10^{-9}$ for the total wavefunction and the SPFs $|\langle\varphi_i|\varphi_j\rangle - \delta_{ij}| < 10^{-10}$ are imposed. Moreover, we increase the number of variationally optimized SPFs and primitive basis states observing a systematic convergence of our results. For instance, we have used $M = 9$, $M_{pr} = 300$ for the triple well and $M = 10$, $M_{pr} = 400$ for the five well respectively. Let us next briefly demonstrate the convergence behaviour of our triple-well simulations for an increasing number of SPFs. To achieve the latter we employ the extensively used, here, fidelity evolution upon quenching either the wavevector or the phase of the spatially-dependent interaction strength C_{int} . Fig. 7 presents $F(t)$ for a sudden phase shift from $\phi = 0$ to $\phi = \pi/4$ [see Fig. 7 (a)] and a wavevector quench from $k_1 = 0$ to $k_1 = 0.5$ [see Fig. 7 (b)] for different number of SPFs. For reasons of completeness we remark that these quench amplitudes refer to enhanced response regions of the respective quench protocol. In both cases a system-

atic convergence of $F(t)$ is showcased for an increasing number of SPFs and in particular for $M > 8$. Indeed following a phase quench, see Fig. 7 (a), the maximum deviation observed in $F(t)$ between the 9 and 12 SPF cases is of the order of 8%. Turning to the wavevector quench, presented in Fig. 7 (b), an admittedly better degree of convergence is observed throughout the evolution as the relative difference of $F(t)$ between 9 and 12 SPFs lies below 5% and becomes at most 9% for long propagation times $t > 160$. An auxiliary indicator for the obtained numerical accuracy is provided by the population of the lowest occupied natural orbital which is kept below 0.1% (not shown here for brevity).

ACKNOWLEDGEMENTS

The authors gratefully acknowledge financial support by the Deutsche Forschungsgemeinschaft (DFG) in the framework of the SFB 925 “Light induced dynamics and control of correlated quantum systems”. S. I. M thanks G. C. Katsimiga for fruitful discussions.

-
- [1] M. Lewenstein, A. Sanpera, V. Ahufinger, B. Damski, A. Sen, and U. Sen, *Adv. in Phys.* **56**, 243 (2007).
- [2] V.I. Yukalov, *Laser Phys.* **19**, 110 (2009).
- [3] M. Lewenstein, A. Sanpera, and V. Ahufinger, *Ultracold Atoms in Optical Lattices: Simulating Quantum Many-body Systems* (Oxford University Press, Oxford, 2012).
- [4] I. Bloch, J. Dalibard, and W. Zwerger, *Rev. Mod. Phys.* **80**, 885 (2008).
- [5] G. Zürn, F. Serwane, T. Lompe, A.N. Wenz, M.G. Ries, J.E. Bohn, and S. Jochim, *Phys. Rev. Lett.* **108**, 075303 (2012).
- [6] F. Serwane, G. Zürn, T. Lompe, T.B. Ottenstein, A.N. Wenz, and S. Jochim, *Science* **332**, 336 (2011).
- [7] A. N. Wenz, G. Zürn, S. Murmann, I. Brouzos, T. Lompe, and S. Jochim, *Science* **342**, 457 (2013).
- [8] A. M. Kaufman, B. J. Lester, M. Foss-Feig, M. L. Wall, A. M. Rey, and C. A. Regal, *Nature* **527**, 208 (2015).
- [9] S. Inouye, M. R. Andrews, J. Stenger, H. J. Miesner, D. M. Stamper-Kurn, and W. Ketterle, *Nature* **392**, 151 (1998).
- [10] C. Chin, R. Grimm, P. Julienne, and E. Tiesinga, *Rev. Mod. Phys.* **82**, 1225 (2010).
- [11] P. O. Fedichev, Yu. Kagan, G. V. Shlyapnikov, and J. T. M. Walraven, *Phys. Rev. Lett.* **77**, 2913 (1996).
- [12] M. Theis, G. Thalhammer, K. Winkler, M. Hellwig, G. Ruff, R. Grimm, and J. H. Denschlag, *Phys. Rev. Lett.* **93**, 123001 (2004).
- [13] D. M. Bauer, M. Lettner, C. Vo, G. Rempe, and S. Dürr, *Phys. Rev. A* **79**, 062713 (2009).
- [14] M. Lettner, D. Bauer, C. Vo, G. Rempe, and S. Duerr, *Nature Phys.* **5**, 339 (2009).
- [15] R. Yamazaki, S. Taie, S. Sugawa, and Y. Takahashi, *Phys. Rev. Lett.* **105**, 050405 (2010).
- [16] M. Yan, B. J. DeSalvo, B. Ramachandhran, H. Pu, and T. C. Killian, *Phys. Rev. Lett.* **110**, 123201 (2013).
- [17] L. W. Clark, L. C. Ha, C. Y. Xu, and C. Chin, *Phys. Rev. Lett.* **115**, 155301 (2015).
- [18] S. G. Ali, S. K. Roy, and B. Talukdar, *Eur. Phys. J. D* **59**, 269 (2010).
- [19] A. I. Nicolin, A. Balaz, J. B. Sudharsan, and R. Radha, *Rom. J. Phys.* **59**, 204 (2014).
- [20] G. A. Sekh, *Phys. Lett. A* **376**, 1740 (2012).
- [21] Y. V. Kartashov, B. A. Malomed, and L. Torner, *Rev. Mod. Phys.* **83**, 247 (2011).
- [22] L. J. Garay, J. R. Anglin, J. I. Cirac, and P. Zoller, *Phys. Rev. Lett.* **85**, 4643 (2000).
- [23] I. Carusotto, S. Fagnocchi, A. Recati, R. Balbinot, and A. Fabbri, *New J. Phys.* **10**, 103001 (2008).
- [24] P. G. Kevrekidis, R. Carretero-González, and D. J. Frantzeskakis, *Int. J. Mod. Phys. B* **31**, 1742013 (2017).
- [25] M. I. Rodas-Verde, H. Michinel, and V. M. Pérez-García, *Phys. Rev. Lett.* **95**, 153903 (2005).
- [26] F. Tsitoura, P. Krüger, P. G. Kevrekidis, and D. J. Frantzeskakis, *Phys. Rev. A* **91**, 033633 (2015).
- [27] C. Hang, and V. V. Konotop, *Phys. Rev. A* **81**, 053849 (2010).
- [28] M. Salerno, V. V. Konotop, and Y. V. Bludov, *Phys. Rev. Lett.* **101**, 030405 (2008).
- [29] G. Theocharis, P. Schmelcher, P. G. Kevrekidis, and D. J. Frantzeskakis, *Phys. Rev. A* **72**, 033614 (2005).
- [30] F. Kh. Abdullaev and M. Salerno, *J. Phys. B* **36**, 2851 (2003).
- [31] G. Theocharis, P. Schmelcher, P. G. Kevrekidis, and D. J. Frantzeskakis, *Phys. Rev. A* **74**, 053614 (2006).
- [32] Y. V. Bludov, V. A. Brazhnyi, and V. V. Konotop, *Phys. Rev. A* **76**, 023603 (2007).

- [33] D. Hocker, J. Yan, and H. Rabitz, *Phys. Rev. A* **93**, 053612 (2016).
- [34] V. M. Perez-Garcia, arXiv [nlin/0612028](https://arxiv.org/abs/0612028) (2006).
- [35] F. K. Abdullaev, A. Gammal, M. Salerno, and L. Tomio, *Phys. Rev. A* **77**, 023615 (2008).
- [36] A. Balaž, R. Paun, A. I. Nicolin, S. Balasubramanian, and R. Ramaswamy, *Phys. Rev. A* **89**, 023609 (2014).
- [37] A. I. Streltsov, *Phys. Rev. A* **88**, 041602 (2013).
- [38] U. R. Fischer, A. U. Lode, and B. Chatterjee, *Phys. Rev. A* **91**, 063621 (2015).
- [39] B. Chatterjee, I. Brouzos, S. Zöllner, and P. Schmelcher, *Phys. Rev. A* **82**, 043619 (2010).
- [40] B. Chatterjee, I. Brouzos, L. Cao, and P. Schmelcher, *J. Phys. B: At. Mol. Opt. Phys.* **46**, 085304 (2013).
- [41] S. I. Mistakidis, G. M. Koutentakis, and P. Schmelcher, *Chem. Phys.* (2018).
- [42] S. I. Mistakidis, L. Cao and P. Schmelcher, *J. Phys. B: At., Mol. Opt. Phys.* **47**, 225303 (2014).
- [43] S. I. Mistakidis, L. Cao and P. Schmelcher, *Phys. Rev. A* **91**, 033611 (2015).
- [44] S. I. Mistakidis, and P. Schmelcher, *Phys. Rev. A* **95**, 013625 (2017).
- [45] J. Neuhaus-Steinmetz, S. I. Mistakidis, and P. Schmelcher, *Phys. Rev. A* **95**, 053610 (2017).
- [46] H. Gimperlein, S. Wessel, J. Schmiedmayer, and L. Santos, *Phys. Rev. Lett.* **95**, 170401 (2005).
- [47] O. E. Alon, A. I. Streltsov and L. S. Cederbaum, *J. Chem. Phys.* **127**, 154103 (2007).
- [48] O. E. Alon, A. I. Streltsov and L. S. Cederbaum, *Phys. Rev. A* **77**, 033613 (2008).
- [49] O. Dutta, M. Gajda, P. Hauke, M. Lewenstein, D.S. Lühmann, B. A. Malomed, T. Sowiński, J. Zakrzewski, *Rep. Prog. Phys.* **78**, 066001 (2015).
- [50] S. Fölling, S. Trotzky, P. Cheinet, M. Feld, R. Saers, A. Widera, T. Müller, and I. Bloch, *Nature* **448**, 1029 (2007).
- [51] F. Meinert, M. J. Mark, E. Kirilov, K. Lauber, P. Weinmann, M. Gröbner, A. J. Daley, and H.C. Nägerl, *Science* **344**, 1259 (2014).
- [52] Y. A. Chen, S. Nascimbene, M. Aidelsburger, M. Atala, S. Trotzky, and I. Bloch, *Phys. Rev. Lett.* **107**, 210405 (2011).
- [53] L. Cao, I. Brouzos, S. Zöllner, and P. Schmelcher, *New J. Phys.* **13**, 033032 (2011).
- [54] H. Sakaguchi, and B.A. Malomed, *Phys. Rev. E*, **72**, 046610 (2005).
- [55] P. Zupancic, P. M. Preiss, R. Ma, A. Lukin, M. E. Tai, M. Rispoli, R. Islam, and M. Greiner, *Opt. Express* **24**, 13881 (2016).
- [56] S. A. Goorden, J. Bertolotti, and A. P. Mosk, *Opt. Express*, **22**, 17999 (2014).
- [57] A. T. Papageorge, A. J. Kollár, and B. L. Lev, *Opt. Express*, **24**, 11447 (2016).
- [58] D. Jaksch, C. Bruder, J. I. Cirac, C. W. Gardiner, and P. Zoller, *Phys. Rev. Lett.* **81**, 3108 (1998).
- [59] M. J. Mark, E. Haller, K. Lauber, J. G. Danzl, A. J. Daley, and H.-C. Nägerl, *Phys. Rev. Lett.* **107**, 175301 (2011).
- [60] R. J. Glauber, *Phys. Rev.* **130**, 2529 (1963).
- [61] M. Naraschewski, and R. J. Glauber, *Phys. Rev. A* **59**, 4595 (1999).
- [62] K. Sakmann, A. I. Streltsov, O. E. Alon, and L. S. Cederbaum, *Phys. Rev. A* **78**, 023615 (2008).
- [63] L.C. Venuti, and P. Zanardi, *Phys. Rev. A* **81**, 022113 (2010).
- [64] T. Gorin, T. Prosen, T. H. Seligman, and M. Žnidarič, *Phys. Rep.* **435**, 33 (2006).
- [65] S. Campbell, M. García-March, T. Fogarty, and T. Busch, *Phys. Rev. A* **90**, 013617 (2014).
- [66] A. Smerzi, S. Fantoni, S. Giovanazzi, and S. R. Shenoy, *Phys. Rev. Lett.* **79**, 4950 (1997).
- [67] M. Albiez, R. Gati, J. Fölling, S. Hunsmann, M. Cristiani, and M. K. Oberthaler, *Phys. Rev. Lett.* **95**, 010402 (2005).
- [68] J. W. Abraham, K. Balzer, D. Hochstuhl, and M. Bonitz, *Phys. Rev. B* **86**, 125112 (2012).
- [69] J. W. Abraham, and M. Bonitz, *Contributions to Plasma Physics* **54**, 27 (2014).
- [70] G. M. Koutentakis, S. I. Mistakidis, and P. Schmelcher, *Phys. Rev. A* **95**, 013617 (2017).
- [71] W. Tschischik, R. Moessner, and M. Haque, *Phys. Rev. A* **88**, 063636 (2013).
- [72] S. Dutta, M.C. Tsatsos, S. Basu, and A.U. Lode, arXiv:[1802.02407](https://arxiv.org/abs/1802.02407) (2018).
- [73] R. Bücker, J. Grund, S. Manz, T. Berrada, T. Betz, C. Koller, U. Hohenester, T. Schumm, A. Perrin, and J. Schmiedmayer, *Nat. Phys.* **7**, 608 (2011).
- [74] S. Will, D. Iyer, and M. Rigol, *Nat. Commun.* **6**, 6009 (2015).
- [75] S. I. Mistakidis, T. Wulf, A. Negretti, and P. Schmelcher, *J. Phys. B: At., Mol. Opt. Phys.* **48**, 244004 (2015).
- [76] A. I. Streltsov, O. E. Alon, and L. S. Cederbaum, *Phys. Rev. Lett.* **99**, 030402 (2007).
- [77] A. I. Streltsov, K. Sakmann, O. E. Alon, and L. S. Cederbaum, *Phys. Rev. A* **83**, 043604 (2011).
- [78] O. E. Alon, A. I. Streltsov, and L. S. Cederbaum, *Phys. Rev. A* **76**, 013611 (2007).
- [79] O. E. Alon, A. I. Streltsov, and L. S. Cederbaum, *Phys. Rev. A* **79**, 022503 (2009).
- [80] L. Cao, V. Bolsinger, S. I. Mistakidis, G. M. Koutentakis, S. Krönke, J. M. Schurer, and P. Schmelcher, *J. Chem. Phys.* **147**, 044106 (2017).
- [81] S. Krönke, L. Cao, O. Vendrell, and P. Schmelcher, *New J. Phys.* **15**, 063018 (2013).
- [82] J. Frenkel, in *Wave Mechanics* 1st ed. (Clarendon Press, Oxford, 1934), pp. 423-428.
- [83] P. A. Dirac, (1930, July). *Proc. Camb. Phil. Soc.* **26**, 376. Cambridge University Press.

4.1.6 Quench-Induced Resonant Tunneling Mechanisms of Bosons in an Optical Lattice with Harmonic Confinement

Quench-induced resonant tunneling mechanisms of bosons in an optical lattice with harmonic confinement

G. M. Koutentakis,^{1,2} S. I. Mistakidis,¹ and P. Schmelcher^{1,2}

¹Zentrum für Optische Quantentechnologien, Universität Hamburg, Luruper Chaussee 149, 22761 Hamburg, Germany

²The Hamburg Centre for Ultrafast Imaging, Universität Hamburg, Luruper Chaussee 149, 22761 Hamburg, Germany

(Received 21 October 2016; published 18 January 2017)

The nonequilibrium dynamics of small boson ensembles in a one-dimensional optical lattice is explored upon a sudden quench of an additional harmonic trap from strong to weak confinement. We find that the competition between the initial localization and the repulsive interaction leads to a resonant response of the system for intermediate quench amplitudes, corresponding to avoided crossings in the many-body eigenspectrum with varying final trap frequency. In particular, we show that these avoided crossings can be utilized to prepare the system in a desired state. The dynamical response is shown to depend on both the interaction strength as well as the number of atoms manifesting the many-body nature of the tunneling dynamics.

DOI: [10.1103/PhysRevA.95.013617](https://doi.org/10.1103/PhysRevA.95.013617)

I. INTRODUCTION

Recent experimental advances in ultracold atomic gases have provided novel ways to examine the static properties and the nonequilibrium dynamics of correlated many-body systems [1–5]. In particular, optical lattice potentials are a prominent feature of ultracold experiments, as they allow for the study of the correlated tunneling dynamics and its dependence on the interparticle interaction [5–9]. Systems consisting of small ensembles of atoms offer the opportunity, both theoretically [8,9] and experimentally [10,11], to identify and track microscopic (quantum) mechanisms due to their finite size and the absence of finite temperature effects. On the other hand, quantum quenches [8,9,12–17] enable us to study the dependence of the dynamical response on the perturbation amplitude applied to an equilibrium system. Therefore, quenched finite systems in combination with the appropriate lattice geometries can lead to new quantum effects, especially when the translational invariance of the lattice is broken.

A well-studied model that breaks the translational invariance consists of a lattice potential with an imposed harmonic trap [5,18–23]. Concerning the dynamics, the ballistic expansion rate of a bosonic Mott insulator trapped in such a composite trap after a quench of the trap frequency to a lower value has been shown to depend on the interparticle interaction [5]. Furthermore, it has been demonstrated [18] that in the limit of low filling factors the dynamics is equivalent to harmonically trapped bosons with a lattice-dependent effective mass. Both of the above-mentioned effects emerge when the harmonic confinement is relatively weak compared to the interparticle repulsion. However, a so far largely unexplored theme is the competition between the harmonic confinement and the interaction strength, which favors different spatial configurations. An intriguing question would therefore be whether this competition can be exploited to obtain a high level of controllability of such a system and, as a consequence, whether the out-of-equilibrium dynamics can be utilized to achieve specific state preparations.

In the present work we consider a small ensemble of bosons confined in an optical lattice subjected to an additional strong harmonic confinement and investigate the dynamics induced by a quench from strong to weak confinement. We

first analyze the many-body eigenspectrum for varying trap frequency, revealing the existence of narrow and wide avoided crossings between the many-body eigenstates. The dynamics of the interacting bosons shows distinct regions of weak and strong dynamical response. In particular, for increasing quench amplitude the system exhibits regions of a pronounced response in the vicinity of wide avoided crossings and sharper response peaks being a consequence of the corresponding narrow avoided crossings. Finally, it is shown that we can achieve specific state preparation by utilizing the narrow avoided crossings. Appropriately selecting the postquench trap frequency it is possible to couple the initial state to a desired final one, allowing for a low-frequency and efficient population transfer between the two eigenstates. Finally, the quench-induced many-body dynamics changes significantly with varying particle number and interparticle repulsion, as the positions and widths of the avoided crossings are shifted, giving rise to further variability and controllability of the dynamics. The results presented in this work are obtained by employing the multiconfiguration time-dependent Hartree method for bosons (MCTDHB) [24,25].

The structure of the paper is as follows. In Sec. II we provide the underlying theoretical framework of our work. Section III presents our triple-well results, both for the static case and for the quench-induced dynamics. In Sec. IV we present the generalization of our results for multiwell traps and, finally, in Sec. V we summarize and give an outlook. Appendix describes our computational method.

II. THEORETICAL FRAMEWORK

In the present section we shall briefly discuss our theoretical framework. First, we introduce the many-body Hamiltonian (see Sec. II A) of our system. Then, the wave function representation in terms of a time-independent number state basis (Sec. II B) is outlined. Finally, the basic observables (Sec. II C) used for the interpretation of the dynamics are explained.

A. Hamiltonian

The many-body Hamiltonian of N bosons trapped in a one-dimensional (1D) lattice potential with an imposed harmonic

trap reads

$$H = \sum_{i=1}^N \left(-\frac{\hbar^2}{2m} \frac{\partial^2}{\partial x_i^2} + V_0 \sin^2(kx_i) + \frac{m\omega^2}{2} x_i^2 \right) + g \sum_{i=1}^N \sum_{j=i+1}^N \delta(x_i - x_j), \quad (1)$$

where x_i denotes the position of the i th particle. The optical lattice potential is characterized by its depth V_0 and the corresponding wave number k . The imposed harmonic trap (parallel to lattice axis) depends on its frequency ω and confines the particles around the origin $x = 0$. The effective 1D coupling strength of the contact interaction $g = \frac{2\hbar^2\alpha}{ma_{\perp}^2} (1 - \frac{|\xi(1/2)\alpha|}{\sqrt{2}a_{\perp}})^{-1}$ [26] can be manipulated via the

transverse harmonic oscillator length $a_{\perp} = \sqrt{\frac{\hbar}{M\omega_{\perp}}}$ (belonging to the strongly confined dimensions) [27,28] or by the 3D s -wave scattering length α via a Feshbach resonance [29,30].

To induce the dynamics we utilize the following scheme: The system is initially prepared in the ground state of the many-body Hamiltonian [see Eq. (1)]. Then, at $t = 0$ we instantaneously change the trap frequency ω to a lower value and let the system evolve under the new Hamiltonian.

Throughout this work we shall employ the recoil energy $E_R = \hbar^2 k^2 / (2m)$, the inverse wave vector k^{-1} and the bosonic mass m as the units of the energy, length, and mass, respectively. Hard-wall boundary conditions are imposed at $x_{\pm} = \pm S\pi/2k^{-1}$, where S denotes the number of lattice sites. The depth of the lattice is fixed to $V_0 = 9E_R$, thus including three localized single-particle states.

B. Number state expansion

Using MCTDHB we calculate the many-body wave function $|\Psi(t)\rangle$ with respect to a time-dependent basis consisting of variationally optimized single-particle functions (SPFs), (for more information see Appendix and Refs. [24,25]). However, for the analysis of our results it is preferable to project the numerically obtained $|\Psi(t)\rangle$ in a time-independent number state basis of single-particle states localized on each lattice site. These localized states are constructed using the subset of delocalized eigenstates with b nodes for each lattice site, i.e., $|\psi_i^{(b)}\rangle_{g=0}$, $i \in \{1, \dots, S\}$. In the absence of a harmonic confinement this subset of eigenstates belong to the b th Bloch band of the system. To obtain a set of localized states we diagonalize the band-projected position operator $\hat{X}^{(b)} = \hat{P}^{(b)} \hat{x} \hat{P}^{(b)}$, where the operator $\hat{P}^{(b)} = \sum_{k=1}^S |\psi_i^{(b)}\rangle_{g=0} \langle \psi_i^{(b)}|_{g=0}$ projects onto the band b [31–33]. In the following, we refer to the eigenstates $|\phi_s^{(b)}\rangle$, $s \in \{1, \dots, S\}$ of $\hat{X}^{(b)}$ as the single-band Wannier states of the deformed lattice. The corresponding N -body number state basis reads

$$\left| \bigotimes_{b_1} n_1^{(b_1)}, \dots, \bigotimes_{b_S} n_S^{(b_S)} \right\rangle = \sum_{i=1}^{N!} \frac{\hat{\mathcal{P}}_i \left(\bigotimes_{j=1}^N |\phi_{s_j}^{(b_j)}\rangle \right)}{\sqrt{N! \prod_{b,s} n_s^{(b)}!}}, \quad (2)$$

where the operator $\hat{\mathcal{P}}_i$ performs the i th permutation of N elements and $n_s^{(b)}$ refers to the number occupation of the Wannier state $|\phi_s^{(b)}\rangle$. To simplify the notation we shall make the

following assumptions. We omit the superscript if no Wannier state or only the Wannier states belonging to the zeroth band are occupied, and decompose the occupation number as $n^{(b_1)} \otimes n^{(b_2)} \otimes \dots$ if more than a single Wannier state localized in a certain well is occupied. For instance, $|1^{(0)}, 1^{(0)} \otimes 1^{(1)}, 1^{(2)}\rangle$ refers to the four-particle state of the triple-well where the ground states of the left and the middle well, the first excited state of the middle well, as well as the second excited state of the right well are each occupied by one boson. For later convenience we also denote by $|\vec{n}\rangle_S$ ($|\vec{n}\rangle_A$) the parity symmetric (antisymmetric) combination of the states $|\vec{n}\rangle = |\bigotimes n_1, \bigotimes n_2, \dots, \bigotimes n_S\rangle$ and $|\bigotimes n_S, \bigotimes n_{S-1}, \dots, \bigotimes n_1\rangle$.

In the presence of a harmonic confinement, the Wannier number states are not uniquely ordered with respect to their energy expectation value, as argued in the following. Indeed, let us consider a system of four bosons in a triple well. For strong harmonic confinement and $g = 0$ there are five number state subsets: $h_0 = \{|0, 4, 0\rangle\}$, $h_1 = \{|1, 3, 0\rangle_{S,A}\}$, $h_2 = \{|2, 2, 0\rangle_{S,A}, |1, 2, 1\rangle\}$, $h_3 = \{|3, 1, 0\rangle_{S,A}, |2, 1, 1\rangle_{S,A}\}$, and $h_4 = \{|4, 0, 0\rangle_{S,A}, |3, 0, 1\rangle_{S,A}, |2, 0, 2\rangle\}$ ordered in increasing energy. On the other hand, for an interacting gas with vanishing harmonic confinement there are four subsets of number states energetically ordered by the multiplicity of bosons that reside in each well: single pairs $i_{SP} = \{|2, 1, 1\rangle, \odot\}$, double pairs $i_{DP} = \{|2, 2, 0\rangle, \odot\}$, triplets $i_T = \{|3, 1, 0\rangle, \odot\}$, and quadruplets $i_Q = \{|4, 0, 0\rangle, \odot\}$, where \odot stands for site permutations. Note that, for interaction energies of the order of the band gap, also higher band excitations must be considered.

From the above example it becomes evident that a reordering of the number states in energy takes place as the system passes from the one limiting case to the other. For instance, the state $|0, 4, 0\rangle$ belonging to the classes h_0 and i_Q , is the most favorable state for strong confinement but, at the same time, the most unfavorable for strong interactions. As we shall see, this corresponding reordering process is the main reason for the resonant dynamics in the quenched system.

C. Observables

Let us now briefly introduce a few basic observables to be utilized in the following analysis, which are based on the one-body density $\rho^{(1)}(x; t)$. To quantify the time evolution of interwell and intrawell modes we use the average position of the bosons in a spatial region D , $D = \{x \in (x_i, x_f)\}$

$$\langle x \rangle_D(t) = \langle \Psi(t) | \hat{x}_D | \Psi(t) \rangle = \frac{1}{N_D} \int_{x_i}^{x_f} dx x \rho^{(1)}(x; t), \quad (3)$$

where $N_D = \int_{x_i}^{x_f} dx \rho^{(1)}(x; t)$ is the particle number within D , $\hat{x}_D = \int_{x_i}^{x_f} dx x \hat{\Psi}^\dagger(x) \hat{\Psi}(x)$ refers to a one-body operator, and $\hat{\Psi}(x)$ is the field operator. This quantity offers a measure for the collective displacement of the atoms (see Ref. [34] for the dipole mode) within a prescribed region of the lattice.

Further, we introduce the position variance in a spatial region D

$$\sigma_{x,D}^2(t) = \langle \Psi(t) | \hat{x}_D^2 | \Psi(t) \rangle - \langle \Psi(t) | \hat{x}_D | \Psi(t) \rangle^2 = \frac{1}{N_D} \int_{x_i}^{x_f} dx x^2 \rho^{(1)}(x; t) - \langle x \rangle_D^2(t), \quad (4)$$

which measures the expansion and contraction of the atomic cloud (see Ref. [35] for the breathing mode) within D . Note the appearance of the one-body operator $\hat{x}_D^2 = \int_{x_i}^{x_f} dx x^2 \hat{\Psi}^\dagger(x) \hat{\Psi}(x)$. The position variance over the whole lattice $\sigma_{x,L}^2(t)$ quantifies a global breathing mode, composed of intersite tunneling and intrasite breathing and dipole modes, which contribute altogether to the total contraction and expansion of the atomic cloud. $\sigma_{x,L}^2(t)$ thus offers a measure for the net dynamical response of the system.

To measure the impact of the quench we also define the time-averaged position variance

$$\begin{aligned} \overline{\sigma_{x,L}^2} - \sigma_{x,L}^2(0) &\equiv \frac{1}{T} \int_0^T dt [\sigma_{x,L}^2(t) - \sigma_{x,L}^2(0)] \\ &\equiv \sum_{i>j} \text{Re}(c_i^* \langle \Psi_i | \hat{x}_L^2 | \Psi_j \rangle_\omega c_j), \end{aligned} \quad (5)$$

which describes how far the system is in average from its initial state. Here, $|\Psi_i\rangle_\omega$ is the i th excited stationary eigenstate of the postquench Hamiltonian and $|\Psi\rangle = \sum_i c_i |\Psi_i\rangle_\omega$ holds. We have also used the parity symmetry, which implies $\langle x \rangle_L(t) = \langle x \rangle_L(0) = 0$ (since the initial state is the ground state of the Hamiltonian before the quench). Finally, the temporal variance of the position variance

$$\begin{aligned} \Delta_T \{\sigma_{x,L}^2\} &\equiv \frac{1}{T} \int_0^T dt (\sigma_{x,L}^2(t) - \overline{\sigma_{x,L}^2})^2 \\ &\equiv \frac{1}{2} \sum_{i>j} |c_i^* \langle \Psi_i | \hat{x}_L^2 | \Psi_j \rangle_\omega c_j|^2 \end{aligned} \quad (6)$$

quantifies how much the state fluctuates around its average configuration during the evolution. $\Delta_T \{\sigma_{x,L}^2\}$ thus measures the intensity of the dynamical processes and of defect formations following a quench. The theoretical limit $T \rightarrow \infty$ is replaced in practice by a finite evolution time T where $\overline{\sigma_{x,L}^2}$ and $\Delta_T \{\sigma_{x,L}^2\}$ have converged.

III. QUENCH DYNAMICS WITHIN A TRIPLE WELL

As a prototype system exhibiting characteristic quench-induced dynamics, we use a system of four harmonically trapped bosons in a triple-well potential. We first investigate the eigenspectra of the system with varying trap frequency (Sec. III A), which are subsequently related to the dynamics induced by the quench (Sec. III B).

A. Eigenspectra

The eigenstate spectrum of the Hamiltonian of Eq. (1) depends on both the trap frequency ω and the interaction strength g (see also Sec. II B). To interpret the dynamics caused by a quench of the frequency ω of the imposed harmonic trap we analyze how the eigenstate spectrum depends on ω .

Figure 1(a) shows the ω dependence of the eigenenergies for $g = 1 E_R k^{-1}$. For later convenience we denote each of the even-parity eigenstates as $|\Psi_i\rangle$, where $i \in \{0, \dots, 8\}$ refers to their energetical order for a given ω . In the following, we focus on the even-parity part of the spectrum $|\Psi_i\rangle$ [see Fig. 1(a)], which contains the ground state $|\Psi_0\rangle$. At $\omega = 0$ the number states within each class (i_X , $X = SP, DP, T, Q$) are very close

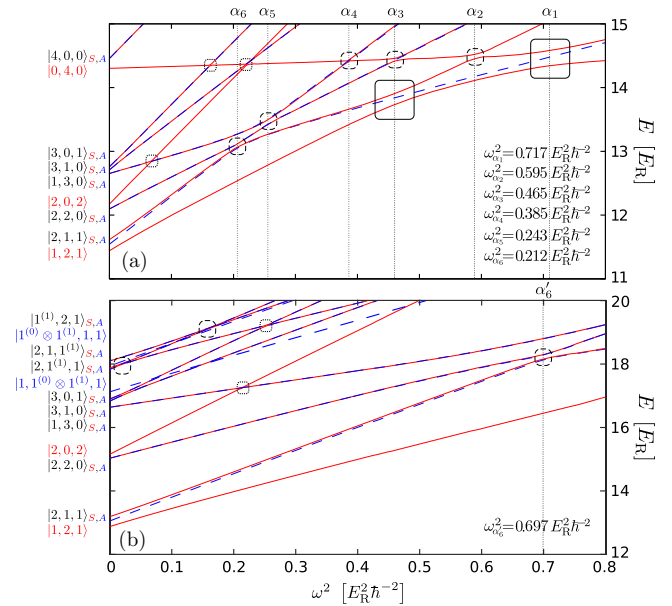


FIG. 1. Dependence of the eigenenergies of the Hamiltonian of Eq. (1) on the trap frequency ω^2 for a system consisting of $N = 4$ bosons trapped in a triple well with additional harmonic confinement. The lowest (a) 15 eigenenergies for $g = 1 E_R k^{-1}$ and (b) 20 eigenenergies for $g = 4 E_R k^{-1}$ are shown. Solid (dashed) lines represent even (odd) parity eigenstates. Very narrow crossings (width smaller than $4 \times 10^{-3} E_R^2 \hbar^{-2}$) are denoted by dotted boxes, narrow avoided crossings are indicated by dashed boxes and wide avoided crossings are denoted by solid boxes. α_i , $i = 1, \dots, 6$ indicate the position of each avoided crossing (see legend). The dominant number state contribution of each eigenstate at $\omega = 0$ is indicated on the left-hand side of each figure.

in energy, their minor energetical difference being caused by the respective avoided crossings (and the boundary conditions of the triple well), and thus the eigenstates are a superposition of the corresponding Wannier number states. In particular, each of the eigenstates possesses a dominant contribution from a particular Wannier number state of class i_X [presented on the left-hand side of Fig. 1(a)]. For $\omega > 0$, the eigenenergies increase linearly (proportional to the number of bosons in the side wells) with ω^2 . The population of the dominant contribution of each eigenstate increases with ω^2 (at the expense of the contribution of other number states that belong to the same class) up to the point of complete dominance and therefore saturation. This behavior with increasing ω^2 occurs unless we encounter an avoided crossing with another eigenstate. Indeed, as it can be seen in Fig. 1(a) at such avoided crossings (being denoted by $C \in \{\alpha_i\}$, $i = 1, \dots, 6$) the two involved eigenstates exchange their character and therefore corresponding dominant Wannier number states. Indicative of this process is the fact that for $\omega^2 > \omega_C^2$ the linear ω^2 dependence of the eigenstates is restored and the corresponding slopes have been exchanged. Moreover, the avoided crossings α_6 and α_5 due to their proximity exhibit a slightly different behavior being referred to in the following as a composite avoided crossing $\{\alpha_6 \alpha_5\}$. We note that the avoided crossings, which involve the ground state $|\Psi_0\rangle$ are much wider (wide avoided crossings) compared to those involving excited

states (narrow avoided crossings). Despite the appearance of the above-mentioned avoided crossings there are also very narrow avoided crossings possessing a corresponding width smaller than $4 \times 10^{-3} E_R^2 \hbar^{-2}$.

To interpret the eigenspectrum we employ the corresponding (three-site, lowest-band) Bose-Hubbard model (BHM) [36,37]

$$\hat{H}_{\text{BHM}} = -J(\hat{a}_1^\dagger \hat{a}_2 + \hat{a}_2^\dagger \hat{a}_3 + \text{H.c.}) + \sum_{i=1}^3 [\epsilon(i-2)^2 + e_0] \hat{n}_i + \frac{U}{2} \sum_{i=1}^3 \hat{n}_i (\hat{n}_i - 1), \quad (7)$$

where \hat{a}_i (\hat{a}_i^\dagger) denotes the annihilation (creation) operator that annihilates (creates) a particle in the state $|\phi_i^{(0)}\rangle$ (e.g., $i = 1$ refers to the leftmost well) and $\hat{n}_i = \hat{a}_i^\dagger \hat{a}_i$ corresponds to the particle number operator. The Hubbard parameters J , U , ϵ , and e_0 refer to the intersite hopping, intrasite interaction, site offset energy, and the zero point energy of the ensemble, respectively. We remark that all of the presented results are obtained within the MCTDHB framework for the continuum space Hamiltonian of Eq. (1) and we only refer to discrete models [BHM, see Eq. (7)], to interpret and compare our findings.

The classification in terms of the interparticle interaction (i_X) provides information on the energy expectation value of the corresponding states for a vanishing harmonic confinement. Furthermore, the classification in terms of strong harmonic confinement provides information on how the energy of each Wannier number state depends on the trap frequency, i.e., $E\{h_d\}(\omega) = E\{h_d\}|_{\omega=0} + d\epsilon$ ($\epsilon \propto \omega^2$). For instance, at $J = 0$ all the crossings become exact [since all individual n_i are conserved, see Eq. (7)] and we can evaluate the expected position for each one, e.g., the states $|1,2,1\rangle$ and $|1,3,0\rangle_S$ are expected to cross at $\epsilon = 4U$. For $J \neq 0$ these exact crossings become avoided and their widths can be approximated by the coupling between the involved states, e.g., $\langle 1,2,1 | \hat{H}_{\text{BHM}} | 1,3,0 \rangle_S = -\sqrt{3}/2J$, [see the wide avoided crossing in Fig. 1(a) at $\omega^2 = \omega_{\alpha_5}^2$]. Narrow avoided crossings emerge from higher order transitions yielding a nonlinear coupling in J , e.g., although $\langle 0,4,0 | \hat{H}_{\text{BHM}} | 1,2,1 \rangle = 0$ these states are coupled by the higher-order transition $|0,4,0\rangle \stackrel{J}{\leftarrow} |1,3,0\rangle_S \stackrel{J}{\leftarrow} |1,2,1\rangle$ leading to a coupling $\propto J^2$. Here, the hopping $J \ll U$, and therefore the corresponding avoided crossing observed at $\omega^2 = \omega_{\alpha_2}^2$ [see Fig. 1(a)] is much narrower. On the other hand, the composite avoided crossing $\{\alpha_6\alpha_5\}$ can be interpreted as follows: At $\omega_{\alpha_6}^2$ a comparatively narrow avoided crossing between the eigenstates $|\Psi_1\rangle$ and $|\Psi_2\rangle$ takes place (exchange between the Wannier number states $|2,1,1\rangle_S$ and $|2,2,0\rangle_S$). A wide avoided crossing involving the eigenstates $|\Psi_1\rangle$ and $|\Psi_3\rangle$ follows at $\omega_{\alpha_6}^2 \leq \omega^2 \leq \omega_{\alpha_5}^2$ (exchange between the Wannier number states $|1,3,0\rangle_S$, $|2,1,1\rangle_S$). Finally, at $\omega_{\alpha_5}^2$ a second narrow avoided crossing takes place between the eigenstates $|\Psi_2\rangle$ and $|\Psi_3\rangle$ (exchange between the number states $|2,1,1\rangle_S$ and $|2,2,0\rangle_S$). This behavior stems from the fact that all these three states are degenerate for $J = 0$, $\epsilon = U$, while for finite J the coupling between $|2,1,1\rangle_S$ and $|1,3,0\rangle_S$ can

be neglected. To connect our Hamiltonian [Eq. (1)] with the employed BHM [see Eq. (7)] we mention here that the studied case of $V_0 = 9E_R$ and $g = 1E_R k^{-1}$ corresponds to the BHM Hamiltonian with parameters $U \sim 0.13E_R$, $J \sim 1.5 \times 10^{-2} E_R$, yielding a ratio $U/J \sim 8.5$. The offset induced by the imposed harmonic oscillator potential corresponds to $\epsilon/\omega^2 \sim 0.55\hbar^2/E_R$. Finally, it can be shown that the energy of the $|0,4,0\rangle$ state depends on the trap frequency as $\sim 1 + \frac{\omega^2}{4V_0}$, related to the zero point energy e_0 [see Eq. (7)].

For larger interaction strength, the many-body states, as shown in Fig. 1(b), become energetically higher due to the higher interaction energy among the bosons. Note that a certain number of states with higher band excitations possess lower energies from states of the lowest band, e.g., the state $|0,4,0\rangle$ does not participate in the lowest twenty eigenstates of the Hamiltonian with $g = 4E_R k^{-1}$ [see Fig. 1(b)]. Indeed, for $g = 4E_R k^{-1}$ the BHM can still be applied since: (i) there is no coupling to higher band excitations via hopping terms of the form $-J_{ij}^{b,b'} a_i^{(b)} a_j^{(b')} = 0$ due to the orthogonality of the single-particle Bloch states that belong to different bands, and (ii) in the interaction part of the Hamiltonian, intraband on-site interaction terms due to $U_{i,i,i}^{b,b,b'} a_i^{(b)} a_i^{(b)} a_i^{(b)}$, where $|b-b'| = 2j+1$, $j \in \mathbb{N}$ vanish because of parity symmetry within the corresponding well [38]. This manifests itself in Fig. 1(b) by the absence of avoided crossings between states with higher band excitations (first excited band) and states with all particles in the zeroth band (see, for instance, the very narrow avoided crossing at $\omega^2 = 0.25E_R^2 \hbar^{-2}$ involving the states $|\Psi_7\rangle$ and $|\Psi_8\rangle$). The energies of the latter possess a similar dependence on the frequency ω^2 as for $g = 1E_R k^{-1}$ but the position in terms of ω^2 of the avoided crossings between these states [see Fig. 1(a)] has increased approximately three times the original value for $g = 1E_R k^{-1}$. The dependence of the eigenenergies involving higher band excitations is linear in ω^2 with the proportionality factor $\epsilon^{(1)} = \epsilon$, see for instance $|\Psi_0\rangle$ and $|\Psi_8\rangle$ within the frequency interval $\omega^2 \in [0.1, 0.25E_R^2 \hbar^{-2}]$. Furthermore, the states with higher band excitations show both narrow and wide avoided crossings, e.g., see the narrow avoided crossing at $\omega^2 = 0.02E_R^2 \hbar^{-2}$ involving the states $|\Psi_8\rangle$ and $|\Psi_9\rangle$ and the wide avoided crossing at $\omega^2 \in [0.02, 0.16E_R^2 \hbar^{-2}]$ between the states $|\Psi_8\rangle$ and $|\Psi_{10}\rangle$. The narrow avoided crossings refer to intraband tunneling within the ground band while the wide avoided crossings are related to interband tunneling within the first excited band. Finally, let us also note that the narrow avoided crossings between (the parity symmetric) states with higher band excitations comprise a composite avoided crossing [see the dashed boxes at $\omega^2 \sim 0.02E_R^2 \hbar^{-2}$ and $\omega^2 \sim 0.16E_R^2 \hbar^{-2}$ in Fig. 1(b)] similar to the $\{\alpha_6\alpha_5\}$ avoided crossing observed for the ground band [see Fig. 1(a)].

Non-negligible widths of avoided crossings between states of the ground band and those having a contribution from the first excited band can in principle be achieved by shifting the center of the harmonic trap. This is equivalent to a lattice tilt [39] where the parity symmetry of the system is broken and states of different parity become coupled. According to Figs. 1(a), 1(b) the states with different parity, e.g., $|\vec{n}\rangle_S$ and $|\vec{n}\rangle_A$ are near degenerate, except for the case of avoided crossings, and consequently we expect that the spectrum is slightly altered for the case of broken parity symmetry.

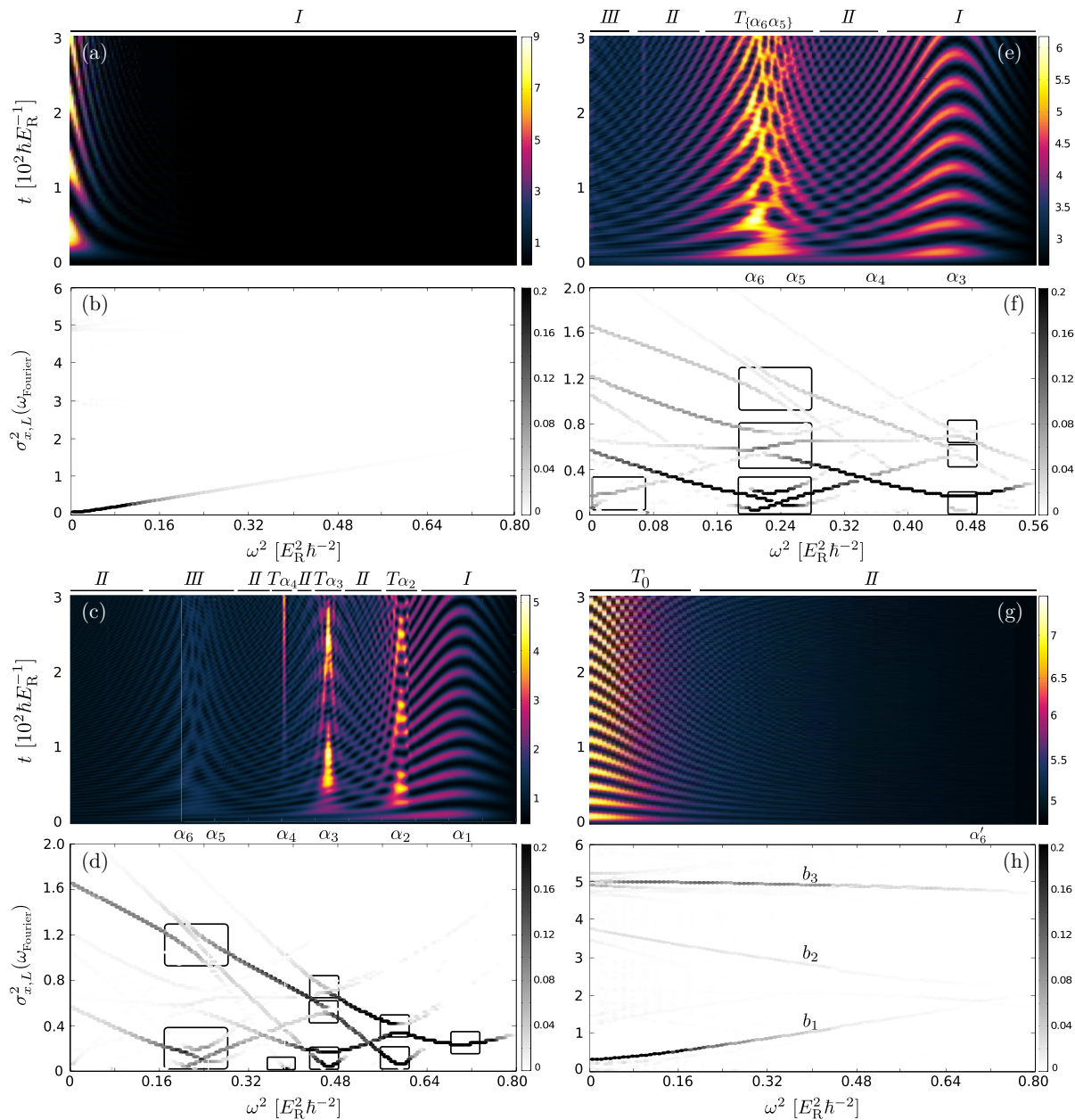


FIG. 2. (a), (c), (e), (g) Time evolution of $\sigma_{x,L}^2(t)$ and (b), (d), (f), (h) the corresponding spectra $\sigma_{x,L}^2(\omega_{\text{Fourier}})$, as a function of the trap frequency ω^2 after the quench. The system parameters used in each case correspond to (a), (b) $g = 0E_R k^{-1}$, $\omega_i^2 = 0.8E_R^2 \hbar^{-2}$ (initial trap frequency), (c), (d) $g = 1E_R k^{-1}$, $\omega_i^2 = 0.8E_R^2 \hbar^{-2}$, (e), (f) $g = 1E_R k^{-1}$, $\omega_i^2 = 0.58E_R^2 \hbar^{-2}$, and (g), (h) $g = 4E_R k^{-1}$, $\omega_i^2 = 0.8E_R^2 \hbar^{-2}$. α_i , $i = 1, \dots, 6$ denote the positions of the corresponding avoided crossings (see also Fig. 1). Note that on top of each of the (a), (c), (e), (h) subfigures regions I , II , III , T_C with $C \in \{\alpha_i\}$, are presented. In (d), (f) the branches are organized by solid boxes denoted in Table I as segment $\alpha_{i,j}$, where the index $j = 1, 2, 3$ introduces an energetically increasing order.

B. Quench-induced dynamics

After having examined the basic properties of the eigenstate spectrum we proceed by investigating the many-body dynamics when the system is subjected to an abrupt quench of the trap frequency ω to lower values.

For a strongly confined system initialized in the noninteracting ground state ($|\Psi\rangle \sim \prod |\phi_c^{(0)}\rangle$, c stands for the middle well) the dynamical response of the system (for varying final trap frequency ω) is shown in Fig. 2(a) via $\sigma_{x,L}^2(t)$ [see Eq. (4)]. This response can be described by the two single-particle

states, i.e., by $|\phi_c^{(0)}\rangle$ and the symmetric state $\frac{1}{\sqrt{2}}(|\phi_l^{(0)}\rangle + |\phi_r^{(0)}\rangle)$ (l, r stand for the left and right wells respectively). For $\omega^2 > 0.08E_R^2 \hbar^{-2}$ we have $\sigma_{x,L}^2(t) \approx \sigma_{x,L}^2(0)$ showing that the system is unaffected by the quench and all the particles remain essentially localized in the center well ($\sim |\phi_c^{(0)}\rangle$). Only for quenches to very low trapping frequencies $\omega^2 < 0.08E_R^2 \hbar^{-2}$, see in Fig. 2(a) the particles diffuse to the outer wells and as a consequence the variance fluctuates significantly with time. The spectrum of the variance $\sigma_{x,L}^2(\omega_{\text{Fourier}})$, presented in Fig. 2(b), is dominated by a single frequency for all quenches,

TABLE I. Energy differences and the corresponding main tunneling processes for each branch that appear in the spectra of Fig. 2(d), 2(f). Each avoided crossing is denoted by $\alpha_i, i = 1, \dots, 6$, while 0 refers to the avoided crossings located at $\omega = 0$. The branches are categorized into segments being denoted by a second subscript index j , i.e., $\alpha_{i,j}, j = 1, 2, 3$. The energy difference of a given branch is denoted by $E_{km} \equiv E_k - E_m$ followed by the corresponding main tunneling processes and the respective frequency domains.

$\{\alpha_6\alpha_5\}$		α_3	α_2
E_{21}	$ 1,3,0\rangle_S \rightleftharpoons 2,2,0\rangle_S$	$\omega^2 > \omega_{\alpha_5}^2$	
$\{\alpha_6\alpha_5\}_1 E_{32}$	$ 2,1,1\rangle_S \rightleftharpoons 2,2,0\rangle_S$	$\omega^2 < \omega_{\alpha_5}^2$	
	$ 2,1,1\rangle_S \rightleftharpoons 2,2,0\rangle_S$	$\omega^2 > \omega_{\alpha_6}^2$	$\alpha_{3,1} E_{32} 2,2,0\rangle_S \rightleftharpoons 0,4,0\rangle$
	$ 1,3,0\rangle_S \rightleftharpoons 2,2,0\rangle_S$	$\omega^2 < \omega_{\alpha_6}^2$	$\alpha_{2,1} E_{21} 1,2,1\rangle \rightleftharpoons 0,4,0\rangle$
E_{31}	$ 1,3,0\rangle_S \rightleftharpoons 2,2,0\rangle_S$	$\omega^2 \in (\omega_{\alpha_6}^2, \omega_{\alpha_5}^2)$	$\omega^2 \approx \omega_{\alpha_2}^2$
E_{10}	$ 1,3,0\rangle_S \rightleftharpoons 1,2,1\rangle$	$\omega^2 > \omega_{\alpha_6}^2$	
$\{\alpha_6\alpha_5\}_2 E_{20}$	$ 2,1,1\rangle_S \rightleftharpoons 1,2,1\rangle$	$\omega^2 < \omega_{\alpha_6}^2$	$E_{10} 1,3,0\rangle_S \rightleftharpoons 0,4,0\rangle$
	$ 2,2,0\rangle_S \rightleftharpoons 1,2,1\rangle$	$\omega^2 \in (\omega_{\alpha_6}^2, \omega_{\alpha_5}^2)$	$\omega^2 > \omega_{\alpha_2}^2$
	$ 2,2,0\rangle_S \rightleftharpoons 1,2,1\rangle$	$\omega^2 \notin (\omega_{\alpha_6}^2, \omega_{\alpha_5}^2)$	$\omega^2 < \omega_{\alpha_2}^2$
E_{30}	$ 2,1,1\rangle_S \rightleftharpoons 1,2,1\rangle$	$\omega^2 > \omega_{\alpha_5}^2$	$\alpha_{2,2} E_{20} 1,3,0\rangle_S \rightleftharpoons 1,2,1\rangle$
	$ 1,3,0\rangle_S \rightleftharpoons 1,2,1\rangle$	$\omega^2 < \omega_{\alpha_5}^2$	$ 1,3,0\rangle_S \rightleftharpoons 0,4,0\rangle$
E_{43}	$ 1,3,0\rangle_S \rightleftharpoons 0,4,0\rangle$	$\omega^2 < \omega_{\alpha_5}^2$	
$\{\alpha_6\alpha_5\}_3 E_{42}$	$ 1,3,0\rangle_S \rightleftharpoons 0,4,0\rangle$	$\omega^2 \in (\omega_{\alpha_6}^2, \omega_{\alpha_5}^2)$	$E_{20} 1,3,0\rangle_S \rightleftharpoons 0,4,0\rangle$
E_{41}	$ 1,3,0\rangle_S \rightleftharpoons 0,4,0\rangle$	$\omega^2 > \omega_{\alpha_6}^2$	$\omega^2 > \omega_{\alpha_3}^2$
		$\alpha_{3,2} E_{21} 2,2,0\rangle_S \rightleftharpoons 1,3,0\rangle_S$	$\omega^2 < \omega_{\alpha_3}^2$
		$ 0,4,0\rangle \rightleftharpoons 1,2,1\rangle$	$\omega^2 > \omega_{\alpha_3}^2$
		$E_{31} 1,3,0\rangle_S \rightleftharpoons 0,4,0\rangle$	$\omega^2 < \omega_{\alpha_3}^2$
		$E_{20} 1,3,0\rangle_S \rightleftharpoons 0,4,0\rangle$	$\omega^2 > \omega_{\alpha_3}^2$
		$ 2,2,0\rangle_S \rightleftharpoons 1,2,1\rangle$	$\omega^2 < \omega_{\alpha_3}^2$
		$E_{30} 1,2,1\rangle \rightleftharpoons 0,4,0\rangle$	$\omega^2 < \omega_{\alpha_3}^2$
α_4		α_1	0
$\alpha_{4,1} E_{43}$	$ 2,1,1\rangle_S \rightleftharpoons 0,4,0\rangle$	$\omega^2 \approx \omega_{\alpha_4}^2$	$E_{10} 2,1,1\rangle_S \rightleftharpoons 1,2,1\rangle$
			$\omega \approx 0$
		$\alpha_{1,1} E_{10} 1,3,0\rangle_S \rightleftharpoons 0,4,0\rangle$	$E_{23} 2,2,0\rangle_S \rightleftharpoons 2,0,2\rangle$
		$\omega^2 \approx \omega_{\alpha_1}^2$	$\omega \approx 0$

and this frequency corresponds to the Rabi frequency involving the energy difference between the two aforementioned states.

Figure 2(c) presents $\sigma_{x,L}^2(t)$ as a function of ω^2 for intermediate interactions $g = 1E_R k^{-1}$. Here, the ground state is dominated by the $|0,4,0\rangle$ number state for the initial trap frequency $\omega_i^2 = 0.8$ [see Fig. 1(a)]. Regions of qualitatively different dynamical response with varying final trap frequency ω^2 are manifest, denoted as *I*, *II*, *III*, and T_C in Fig. 2(c), thereby showing also a prominent difference from the $g = 0$ case [see Fig. 2(a)]. Within the region denoted as type *I* ($\omega^2 > \omega_{\alpha_2}^2$) $\sigma_{x,L}^2(t)$ fluctuates prominently with time, indicating the presence of the global breathing mode. Here the fluctuations of $\sigma_{x,L}^2(t)$ are still characterized by a single frequency [see Fig. 2(d)], and correspond to the Rabi oscillation region studied also in Ref. [18]. The regions of type T_C (associated with a corresponding avoided crossing *C*) are characterized by a small frequency and high-amplitude response during the evolution. Regions of type *II* appear in between the regions of type T_C , e.g., $\omega_{\alpha_3}^2 < \omega^2 < \omega_{\alpha_2}^2$. Here, the variance $\sigma_{x,L}^2(t)$ evolves with a multitude of frequencies while its amplitude is diminished compared to the case of regions *I* and T_C . Finally, within the region *III* (linked to the composite avoided crossing $\{\alpha_6\alpha_5\}$) of relatively strong response emerges.

To gain more insight into the existence of the regions *II*, *III*, and T_C , we employ $\sigma_{x,L}^2(\omega_{\text{Fourier}})$ shown in Fig. 2(d). The connection of each of the branches observed in Fig. 2(d) to the related eigenenergy differences is presented in detail in Table I. We remark that only branches involving the state $|0,4,0\rangle$ (being the dominant Wannier number state contribution of the initial state) are contributing significantly. The region *I* is formed due to the avoided crossing α_1 [see Fig. 1(a)] and the bosons perform Rabi tunneling oscillations between the number states

$|0,4,0\rangle$ and $|1,3,0\rangle_S$ (see segment $\alpha_{1,1}$ in Table I). Turning to the region T_{α_2} we observe that the dynamical response of the system is dominated by the low-frequency second-order tunneling process $|1,2,1\rangle \rightleftharpoons |0,4,0\rangle$ (see segment $\alpha_{2,1}$ in Table I). The formation of regions *II* ($\omega_{\alpha_3}^2 \leq \omega^2 \leq \omega_{\alpha_2}^2$) is caused by the fact that the tunneling modes $|1,2,1\rangle \rightleftharpoons |0,4,0\rangle$, $|1,3,0\rangle_S \rightleftharpoons |1,2,1\rangle$, and $|1,3,0\rangle_S \rightleftharpoons |0,4,0\rangle$ (see segments $\alpha_{2,1}$ and $\alpha_{2,2}$ in Table I) possess a similar amplitude [see also Fig. 2(d)] and the interference of these modes is destructive (on average) resulting in a weakened dynamical response. At T_{α_3} ($\omega^2 = \omega_{\alpha_3}^2$) a low-frequency second-order tunneling mode $|2,2,0\rangle_S \rightleftharpoons |0,4,0\rangle$ (see segment $\alpha_{3,1}$ in Table I) is observed. For larger quenches, i.e., $\omega^2 < \omega_{\alpha_3}^2$, the eigenstate dominated by $|0,4,0\rangle$ does not couple with the remaining states of the eigenspectrum [see also Fig. 1(a)]. Then, most of the processes appearing within this trap frequency regime are associated with the small $|1,3,0\rangle_S$ contribution to the initial state. The above give rise to the region *II* which encompasses the T_{α_4} and *III* regions. The T_{α_4} region is dominated by a low-frequency mode being the third-order process $|2,1,1\rangle_S \rightleftharpoons |0,4,0\rangle$ (see segment $\alpha_{4,1}$). Note that even for very low detuning ($\omega^2 \neq \omega_{\alpha_4}^2$) from the crossing α_4 , this third-order process vanishes because: (i) the width of the avoided crossing α_4 is extremely narrow and (ii) the state $|2,1,1\rangle_S$ has no contribution to the initial state. Finally, within the region *III* that appears near the crossing $\{\alpha_6\alpha_5\}$ [see Figs. 2(c), 2(d)] the relevant low-frequency tunneling processes are $|2,1,1\rangle_S \rightleftharpoons |2,2,0\rangle_S$ and $|1,3,0\rangle_S \rightleftharpoons |2,2,0\rangle_S$ (see segment $\{\alpha_6\alpha_5\}_1$ in the appropriate regions and also Table I). Here, the prominent dynamics of the state $|1,3,0\rangle_S$ gives rise to a slightly increased response of the system in comparison to region *II*.

To examine the case of the composite avoided crossing $\{\alpha_6\alpha_5\}$ we initialize the system to the ground state $|\Psi_0\rangle$

($g = 1E_R k^{-1}$ and $\omega_i^2 = 0.560E_R^2 \hbar^{-2}$) being dominated by the Wannier number state $|1,3,0\rangle_S$. Figure 2(e) shows $\sigma_{x,L}^2(t)$ for different final trapping frequencies ω . For $\omega^2 > \omega_{\alpha_4}^2$ the system undergoes Rabi oscillations of varying amplitude [region *I* in Fig. 2(e)]. As the quench amplitude increases the system transits smoothly via the region *II* where the amplitude of the Rabi oscillations decreases to the region $T_{\{\alpha_6\alpha_5\}}$ where the response of the system is prominent. Note here that the region $T_{\{\alpha_6\alpha_5\}}$ is broader than the previously mentioned regions of type T_C . Finally, for $\omega^2 < \omega_{\alpha_6}^2$ (region *II*) the response of the system becomes multimode and the fluctuations of $\sigma_{x,L}^2(t)$ are diminished.

To identify the corresponding microscopic processes, Fig. 2(f) presents $\sigma_{x,L}^2(\omega_{\text{Fourier}})$. The region *I* is dominated by the tunneling mode $|1,3,0\rangle_S \rightleftharpoons |1,2,1\rangle$ (see segment $\alpha_{3,1}$) and it is related to the wide avoided crossing α_3 [see solid boxes in Fig. 1(a)]. As the quench amplitude increases the region *II* appears for similar reasons as in the case of $\omega_i = 0.8$ and $\omega^2 \in (\omega_{\alpha_3}, \omega_{\alpha_2})$. Within the region $T_{\{\alpha_6\alpha_5\}}$ the behavior of the system can be summarized as follows. For $\omega^2 > \omega_{\alpha_5}^2$, the process $|1,3,0\rangle_S \rightleftharpoons |2,2,0\rangle_S$ dominates the dynamics, while at $\omega^2 \approx \omega_{\alpha_5}^2$ the additional mode $|2,1,1\rangle_S \rightleftharpoons |2,2,0\rangle_S$ appears. Next, at $\omega_{\alpha_6}^2 \leq \omega^2 \leq \omega_{\alpha_5}^2$ the latter mode possesses two distinct frequencies, while the process $|1,3,0\rangle_S \rightleftharpoons |2,2,0\rangle_S$ possesses a higher frequency than in the case of $\omega^2 > \omega_{\alpha_5}^2$. Finally, at $\omega^2 \approx \omega_{\alpha_5}^2$ the low-amplitude mode $|2,1,1\rangle_S \rightleftharpoons |2,2,0\rangle_S$ corresponds to a single frequency and the process $|1,3,0\rangle_S \rightleftharpoons |2,2,0\rangle_S$ dominates the dynamics. Concluding, the response of the system at $T_{\{\alpha_6\alpha_5\}}$ depends strongly on the postquench trap frequency. For $\omega^2 < \omega_{\alpha_6}^2$ a region *II* appears similarly to the case of $\omega_i = 0.8$ and $\omega^2 < \omega_{\alpha_3}$. For $\omega \approx 0$ two additional branches of low frequency appear, which correspond to the avoided crossings between $|1,2,1\rangle$ and $|2,1,1\rangle_S$ and between $|2,2,0\rangle$ and $|2,0,2\rangle_S$ (see segment $0_{1,1}$). These modes do not involve the major contribution to the initial state $|1,3,0\rangle_S$ and consequently possess very small amplitude (region *III*).

For higher interactions (here $g = 4E_R k^{-1}$), the dynamical response of the system, shown in Fig. 2(g) via $\sigma_{x,L}^2(t)$, after a quench on ω ($\omega_i^2 = 0.8E_R^2 \hbar^{-2}$) shows a qualitatively different behavior from the case of intermediate interactions. The initial state is dominated by $|1,2,1\rangle$ and possesses significant contributions from higher band excitations, e.g., $|1,1^{(0)}\rangle \otimes |1^{(2)},1\rangle$ and $|1,2^{(1)},1\rangle$ [40]. The system is essentially unperturbed for $\omega^2 > 0.16E_R^2 \hbar^{-2}$ and the evolution is characterized by multiple frequencies (see region *II*). Remarkably enough even for small quench amplitudes regions of Rabi oscillations [see Figs. 2(a), 2(c), 2(e)] are absent. Only for quenches to $\omega \approx 0$, a prominent response is observed [region T_0 in Fig. 2(g)]. Figure 2(h) presents $\sigma_{x,L}^2(\omega_{\text{Fourier}})$ where we observe (in contrast to the case of intermediate interactions) the appearance of only a few branches. The most dominant branch (denoted as b_1) refers to the tunneling mode $|1,2,1\rangle \rightleftharpoons |2,1,1\rangle_S$ while the second branch (denoted as b_2) corresponds to the process $|1,2,1\rangle \rightleftharpoons |1,3,0\rangle_S$. These tunneling modes appear due to the avoided crossing at $\omega = 0$ [see Fig. 1(b)]. Finally, the third branch (denoted as b_3) corresponds to the dipole mode $|1,2,1\rangle \rightleftharpoons |1^{(1)},2,1\rangle_S$. This dipole mode is induced by the minor shift of the side well caused by the quench and it is of single particle nature [41]. We remark here that in the case

of strong interactions the tunneling dynamics is suppressed allowing the dipole mode to possess a prominent role in the course of the evolution (see branch b_3).

A natural next step is to investigate whether abrupt quenches can be used for state preparation. To achieve this goal let us examine the occupation of specific number states, i.e., $N\{|\vec{n}\rangle\}(t) = |\langle \vec{n} | \Psi(t) \rangle|^2$ during the evolution within the above-mentioned dynamical regions (see also Fig. 2). Figures 3(a)–3(d) show the dynamics of a system initialized in the ground state ($\omega_i^2 = 0.8E_R^2 \hbar^{-2}$, $g = 1E_R k^{-1}$) dominated by the number state $|0,4,0\rangle$ while in Figs. 3(e), 3(f) we consider the case ($\omega_i^2 = 0.56E_R^2 \hbar^{-2}$, $g = 1E_R k^{-1}$) in which the $|1,3,0\rangle_S$ possesses the dominant contribution to the ground state. Figure 3(a) shows $N\{|\vec{n}\rangle\}(t)$ for a quench within the region *I* and near the avoided crossing α_1 . A population transfer from the number state $|0,4,0\rangle$ to $|1,3,0\rangle_S$ (see segment $\alpha_{1,1}$ in Table I) following Rabi oscillations is observed. Additional contributions stemming mainly from the state $|2,2,0\rangle_S$ are negligible. On the other hand, Fig. 3(b) presents $N\{|\vec{n}\rangle\}(t)$ for a quench within the region T_{α_2} . The dominant tunneling process corresponds to $|0,4,0\rangle \rightleftharpoons |1,2,1\rangle$ (see segment $\alpha_{2,1}$), while the additional high-frequency tunneling modes $|1,3,0\rangle_S \rightleftharpoons |0,4,0\rangle$, $|1,3,0\rangle_S \rightleftharpoons |1,2,1\rangle$ coexist. As a consequence $|1,3,0\rangle_S$ possesses a significant occupation during the dynamics. Figure 3(c) shows $N\{|\vec{n}\rangle\}(t)$ for a quench within the region T_{α_3} . The main population transfer takes place between the number states $|0,4,0\rangle$ and $|2,2,0\rangle_S$ (see segment $\alpha_{3,1}$). The influence of additional contributions to the initial state is smaller because: (i) the frequency of the main tunneling mode $|0,4,0\rangle \rightleftharpoons |2,2,0\rangle_S$ is much lower than the frequency of the tunneling modes that couple the dominant state $|0,4,0\rangle$ with $|1,3,0\rangle_S$ and $|1,2,1\rangle$ and (ii) the tunneling mode $|1,3,0\rangle_S \rightleftharpoons |1,2,1\rangle$ (see segment $\alpha_{3,1}$) is pronounced due to the wide avoided crossing α_3 . Figure 3(d) presents $N\{|\vec{n}\rangle\}(t)$ for a quench within the region T_{α_4} . We observe that the main population transfer takes place between the number states $|0,4,0\rangle$ and $|2,1,1\rangle_S$. The frequency of the corresponding tunneling mode (see segment $\alpha_{4,1}$) is much lower compared to the other cases shown in Fig. 3 and also compared to the remaining tunneling processes, e.g., $|1,3,0\rangle_S \rightleftharpoons |2,2,0\rangle_S$, that appear in Fig. 3(d). Figure 3(e) shows $N\{|\vec{n}\rangle\}(t)$ for a system initialized at $\omega_i^2 = 0.56E_R^2 \hbar^{-2}$ and following a quench within the region T_{α_3} . In this case, Rabi oscillations between the number states $|1,3,0\rangle_S$ and $|1,2,1\rangle$ (see segment $\alpha_{3,1}$) are observed. Finally, Fig. 3(f) illustrates $N\{|\vec{n}\rangle\}(t)$ (same initial state) for a quench within the region $T_{\{\alpha_6\alpha_5\}}$. Here, there are three dominant states, namely $|1,3,0\rangle_S$, $|2,2,0\rangle_S$, and $|2,1,1\rangle_S$, which are coupled via the tunneling modes $|1,3,0\rangle_S \rightleftharpoons |2,2,0\rangle_S$ and $|2,2,0\rangle_S \rightleftharpoons |2,1,1\rangle_S$ (see segment $\{\alpha_6\alpha_5\}_1$). The total state of the system $|\Psi(t)\rangle$ is dominated within different time intervals by each of the above-mentioned number states. Concluding from the above, we note that it is possible to employ an abrupt quench of the trap frequency and achieve state preparation to one of the number states $|1,3,0\rangle_S$, $|1,2,1\rangle$, $|2,2,0\rangle_S$, and $|2,1,1\rangle_S$, with an adequate population $|\langle \vec{n} | \Psi(t) \rangle|^2 \geq 0.6$ (see the vertical dashed lines in Fig. 3) by choosing properly the total evolution time. This implies that multimode evolution can be used for state preparation, as long as, the frequency of the desired transition is much lower than the competing population transfer processes during the dynamics.

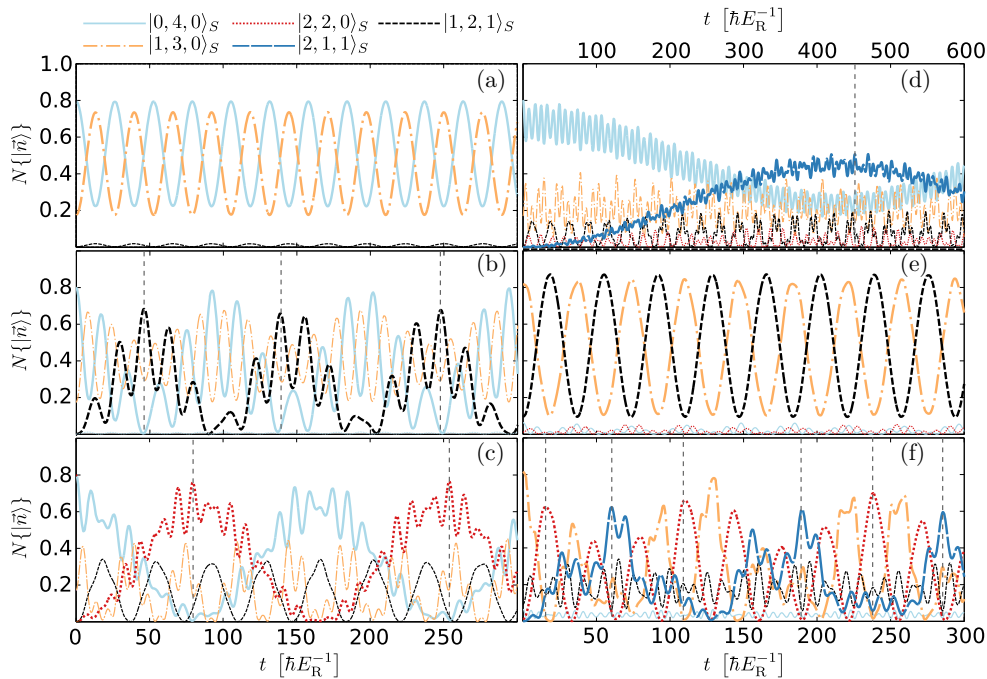


FIG. 3. Evolution of the dominant number state populations [see the legend above (a)] for $N = 4$ interacting bosons ($g = 1E_Rk^{-1}$) confined in a triple well with additional harmonic confinement ($\omega_i^2 = 0.8E_R^2\hbar^{-2}$). The dynamics is induced via a quench of the trap frequency to (a) $\omega^2 = 0.745E_R^2\hbar^{-2}$ (region I), (b) $\omega^2 = 0.58E_R^2\hbar^{-2}$ (region T_{α_2}), (c) $\omega^2 = 0.48E_R^2\hbar^{-2}$ (region T_{α_3}), and (d) $\omega^2 = 0.385E_R^2\hbar^{-2}$ (region T_{α_4}). Note that the scaling of the time axis in (d) is different from the other cases and appears on top of the figure. The evolution of the number state populations is also shown for a quench from $\omega_i^2 = 0.56E_R^2\hbar^{-2}$ to (e) $\omega^2 = 0.48E_R^2\hbar^{-2}$ (region I) and (f) $\omega^2 = 0.265E_R^2\hbar^{-2}$ (region $T_{\{\alpha_6\alpha_5\}}$). For the identification of the different regions see Fig. 2.

To examine the dependence of the intensity of the dynamical processes on the quench amplitude, we employ $\Delta_T\{\sigma_{x,L}^2\}$ [see Eq. (II C)] being a measure of the time-averaged dynamical response, which depends solely on the parameters of the system. Figure 4 presents $\Delta_T\{\sigma_{x,L}^2\}$ as a function of the postquench trap frequency ω^2 for different values of the relevant physical parameters.

Figure 4(a) exhibits $\Delta_T\{\sigma_{x,L}^2\}$ with varying quench amplitude for different interaction strengths g . In the noninteracting case [see also Fig. 2(a)] the mean response of the system after a quench of the trap frequency is close to zero for a wide range of final trapping frequencies ($\omega^2 > 0.08E_R^2\hbar^{-2}$). However, for large quench amplitudes ($\omega^2 < 0.08E_R^2\hbar^{-2}$) the mean response increases strongly as the state $|\phi_c^{(0)}\rangle$ couples to the state $(|\phi_\ell^{(0)}\rangle + |\phi_r^{(0)}\rangle)/\sqrt{2}$. For the case of intermediate interactions ($g = 1E_Rk^{-1}$) and initial trap frequency $\omega_i^2 = 0.8E_R^2\hbar^{-2}$ [see also Fig. 2(c)] we observe, as expected, that the different regions of dynamical response (i.e., I , II , III , T_C) yield a distinct averaged response. In particular, for quenches within the region I the mean response of the system increases until it reaches its maximum value at $\omega^2 = \omega_{\alpha_1}^2$. For $\omega^2 < \omega_{\alpha_1}^2$ the mean response of the system decreases. The T_{α_2} region appears as a peak in $\Delta_T\{\sigma_{x,L}^2\}$ because the interwell tunneling mode $|0,4,0\rangle \rightleftharpoons |1,2,1\rangle$ becomes resonant. For $\omega_{\alpha_3}^2 < \omega^2 < \omega_{\alpha_2}^2$ the first region of type II appears and $\Delta_T\{\sigma_{x,L}^2\}$ exhibits a local minimum. As $\omega^2 \sim \omega_{\alpha_3}^2$ the mean response increases (at the T_{α_3} region) exhibiting a narrow peak followed by a region II where the response is minimized. This process is repeated

for $\omega^2 \sim \omega_{\alpha_4}^2$ within the region T_{α_4} . The response peak at T_{α_4} is much narrower compared to the peaks in regions T_{α_3} and T_{α_2} since the resonant tunneling process $|0,4,0\rangle \rightleftharpoons |2,1,1\rangle_S$ is of third order. Furthermore, the mean response of the system remains small for $\omega^2 < \omega_{\alpha_4}^2$, with the only remarkable feature being the slightly increased response observed in region III .

For $g = 1E_Rk^{-1}$ and $\omega_i^2 = 0.56E_R^2\hbar^{-2}$ [see also Fig. 2(e)] a different overall dynamical response is observed. The region of type I exhibits a similar behavior as for $\omega_i^2 = 0.8E_R^2\hbar^{-2}$ but in this case the region II follows the region I for decreasing ω^2 without the appearance of a T region. For $\omega^2 \approx \omega_{\alpha_5}^2$, an increase in the mean response is observed as the system approaches the $T_{\{\alpha_6\alpha_5\}}$ region. In contrast to the other T_C regions the $T_{\{\alpha_6\alpha_5\}}$ covers a wide range of trapping frequencies ω^2 and exhibits a response peak at $\omega^2 = \omega_{\alpha_5}^2$ due to the tunneling mode $|1,3,0\rangle_S \rightleftharpoons |2,2,0\rangle_S$ (see wide part of the crossing $\{\alpha_6\alpha_5\}$). Finally, for larger quench amplitudes the response is minimized and increases slightly only at $\omega = 0$ within the region III . For high interactions ($g = 4E_Rk^{-1}$) and initial trap frequency $\omega_i^2 = 0.8E_R^2\hbar^{-2}$ the dynamical response of the system is completely different from the case of intermediate interactions. The initial state of the system is dominated by $|1,2,1\rangle$ (which is also the main contribution to the ground state for $\omega^2 < \omega_i^2$). The system remains essentially unperturbed except for quenches in the proximity of $\omega \approx 0$ where an increasing response is observed due to the existence of the tunneling mode $|1,2,1\rangle \rightleftharpoons |2,1,1\rangle_S$ (see T_0 region).

Figure 4(b) presents a comparison of $\Delta_T\{\sigma_{x,L}^2\}$ obtained within the mean-field approximation and the corresponding

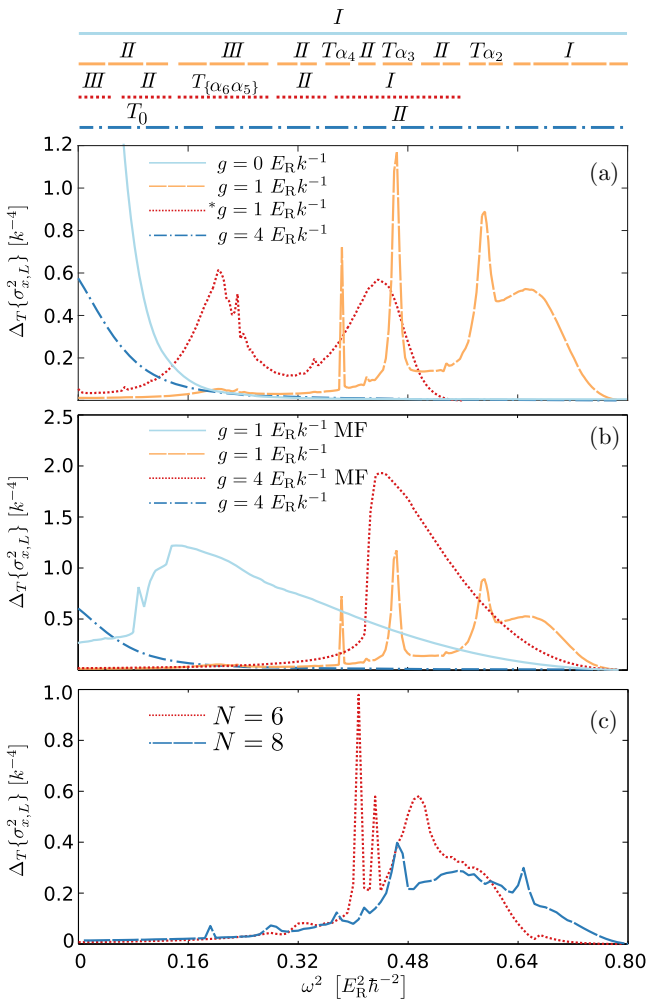


FIG. 4. $\Delta_T\{\sigma_{x,L}\}$ as a function of the postquench frequency ω^2 . Comparison between (a) different interaction strengths g (see legend), (b) the mean-field (MF) and MCTDHB results (see legend), and (c) different particle numbers $N = 6, 8$ (see legend) for $g = 0.5 E_R k^{-1}$. The symbol * denotes that the system is initialized in the ground state for $\omega_{i,*}^2 = 0.56 E_R^2 \hbar^{-2}$ instead of $\omega_i^2 = 0.8 E_R^2 \hbar^{-2}$ being used otherwise.

MCTDHB result, i.e., taking into account the correlations. As it is clearly visible the two dynamical responses differ significantly. In particular, for intermediate interactions ($g = 1$), the mean-field response of the system possesses a higher amplitude in comparison to the correlated case and continues to increase also beyond the regions T_C . Only for $\omega^2 < \omega_{\alpha_3}^2$ it finally decreases almost abruptly to a small but finite value (which is still larger than the corresponding MCTDHB value). A similar behavior is observed for higher interaction strengths. Here, the mean-field approach overestimates even more the dynamical response of the system as a consequence of the increased interparticle repulsion. We conclude that the multiple resonant behavior obtained within the correlated approach can not be captured by the mean-field approximation and consequently correlations between particles are crucial for the dynamics.

Obviously, the behavior of the system depends strongly on the particle number, since for different values of the latter the eigenstates and spectrum change overall. Figure 4(c)

presents $\Delta_T\{\sigma_{x,L}^2\}$ for the particle numbers $N = 6, 8$ and $g = 0.5 E_R k^{-1}$. Both cases show a qualitatively similar response to the $N = 4$ case presented in Fig. 4(a). Indeed, high response peaks appear also here, indicating the existence of avoided crossings in the corresponding many-body spectrum. The overall response (see, e.g., the response peaks) is altered with the number of particles, manifesting the many-body nature of the induced dynamics.

To verify the applicability of our results for larger systems, in the following section, we shall consider multiwell setups consisting of a finite optical lattice and additional harmonic confinement. Then, we shall demonstrate that the character of the diffusion dynamics induced by a quench of the frequency of the imposed harmonic trap shows similar characteristics to the triple-well case.

IV. DYNAMICS IN MULTIWELL TRAPS

Let us consider four bosons confined in a seven-well lattice with additional harmonic confinement. The system is initially prepared in the ground state for $g = 1 E_R k^{-1}$ and $\omega_i^2 = 0.56 E_R^2 k^{-2}$, where all the particles are mainly localized in the center of the trap. The initial state is dominated by Wannier number states of the form $|0, 0, 1, 3, 0, 0, 0\rangle_S$. Figure 5(a) shows the dynamics of the ensemble after a quench of the trap frequency to zero. We observe that even in this extreme case the atoms remain essentially localized within the region of the triple well. In particular, a small portion of the particle density tunnels away from the central well and reaches the edge of the triple-well region (where the boson gas is mainly localized) at $t \sim 100 \hbar E_R^{-1}$ and subsequently expands ballistically beyond the three core sites [see Fig. 5(a)].

To explore the mean dynamical response of the system Fig. 5(b) illustrates $\Delta_T\{\sigma_{x,3}^2\}$ (where 3 stands for the integration over the three core sites) for varying final trap frequency. To perform a direct comparison with the case of the triple well we also show the mean response of the latter with equal system parameters. A similar behavior between the two cases is observed. However, we observe two deviations. First, the corresponding response peaks are slightly shifted to a lower value of ω^2 . This effect can be explained by the artificial energy offset that the hard-wall boundary conditions introduce to the side wells with respect to the middle well. Indeed, this energy offset is reduced in the seven-well case. Second, an increase of $\Delta_T\{\sigma_{x,3}^2\}$ for $\omega \rightarrow 0$ is observed (see region II). This is due to the portion of atoms that expand beyond the triple-well region (the dominant tunneling mode corresponds to $|0, 0, 2, 1, 1, 0, 0\rangle_S \equiv |0, 1, 1, 1, 1, 0, 0\rangle_S$). Indeed, as can be seen from Fig. 5(a) the unbound atomic density expands, then scatters at the hard-wall boundaries and finally reenters the triple well. This process enhances the amplitude of $\sigma_{x,3}^2$ and as a consequence the corresponding temporal variance.

To investigate the dynamical response Fig. 5(c) presents $\sigma_{x,L}^2(t)$ for different final trap frequencies. It is shown that for a quench to $\omega^2 = 0$ the portion of the density, which is unbound to the triple-well region expands ballistically. Indeed, $\sigma_{x,L}^2(t)$ after some critical value [$\sigma_{x,L}^2(t_0 = 100) \approx 5 k^{-2}$] becomes linear for a finite time interval ($100 < t < 300 \hbar E_R^{-1}$). Furthermore, for quenches within the region of a response

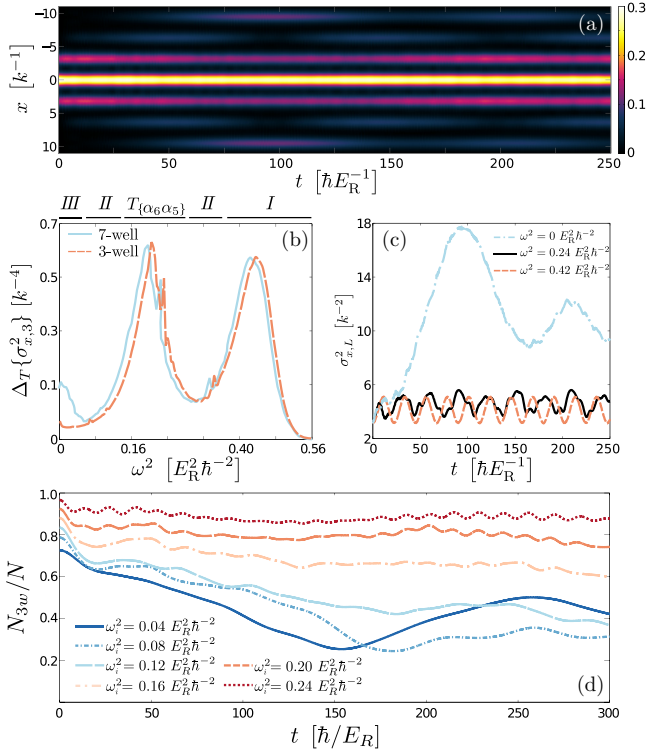


FIG. 5. (a) $\sqrt{\rho^{(1)}(x;t)}$ for $N = 4$ interacting bosons ($g = 1E_R k^{-1}$) confined in a seven-well lattice with additional harmonic confinement. The initial trap frequency is $\omega_i^2 = 0.56E_R^2 \hbar^{-2}$ and we quench to $\omega = 0$. (b) $\Delta_T\{\sigma_{x,3w}^2\}$ with respect to the postquench ω^2 for the triple well and the seven well setup (see legend) with the same parameter values, i.e., $\omega_i^2 = 0.56E_R^2 \hbar^{-2}$ and $g = 1E_R k^{-1}$. (c) $\sigma_{x,L}^2(t)$ for varying final trap frequency (see legend) for the seven-well setup. (d) Evolution of the density fraction within the triple-well region (N_{3w}/N) for a fifteen-well with an imposed harmonic trap. The system is initialized in the ground state with $N = 5$, $g = 1E_R k^{-1}$ for varying initial trap frequency, ω_i^2 (see legend), and the dynamics is induced by a quench to $\omega^2 = 0.016E_R^2 \hbar^{-2}$.

peak [e.g., see region T_{α_5} at $\omega^2 \sim 0.25E_R^2 \hbar^{-2}$ in Fig. 1(a)] or Rabi oscillations (e.g., see region I at $\omega^2 \sim 0.40E_R^2 \hbar^{-2}$) the amplitude of $\sigma_{x,L}^2(t)$ is smaller than the critical one, thus showing the absence of a ballistically expanding fragment.

To further characterize the expansion dynamics we consider $N = 5$ bosons confined in a fifteen-well lattice potential with an imposed harmonic trap. The dynamics, shown in Fig. 5(d), is induced by a quench of the trap frequency and in particular we study quenches that refer to the same final trap frequency ($\omega^2 = 0.016E_R^2 \hbar^{-2}$) but a different initial one. To compare the expansion dynamics we measure the fraction of the particle density within the three core sites during the dynamics, i.e., $N_{3w}(t)/N = \frac{1}{N} \int_{-3\pi/2}^{3\pi/2} dx \rho^{(1)}(x;t)$. Figure 5(d) shows that the above fragment of the particle density gets suppressed with increasing initial trap frequency. This indicates that an initially strongly confined bosonic ensemble remains after a quench of the trap frequency confined near the sites it was initially trapped into, which is a manifestation of the well-known self-trapping effect [42–44].

V. CONCLUSIONS AND OUTLOOK

We have investigated the eigenspectra and in particular the out-of-equilibrium quantum dynamics for a small ensemble of bosons confined in a lattice potential with an imposed harmonic trap. We hereby focus on the case of a strong harmonic confinement where the eigenstates become well separated and are dominated by a single Wannier number state.

In the noninteracting case, a significant tunneling dynamics is observed only for the case of a small final harmonic trapping. For intermediate interactions multiple avoided crossings with varying ω appear in the eigenspectrum, which can be exploited to reveal a rich dynamics after quenching the trap frequency. For relatively small quench amplitudes we observe Rabi oscillations caused by the wide avoided crossings between the ground and the first excited states. However, by using intermediate quench amplitudes we can utilize narrow avoided crossings involving solely excited states to selectively couple the initial state to a desired final state. The induced dynamics is characterized by multiple frequencies, one of which is particularly slow and can be used to drive the system to a desired final state. For large quench amplitudes a multimode and low-amplitude dynamical response is realized. In this case the number state with the dominant contribution to the initial state is an eigenstate of the final system (low-amplitude dynamical response), while the remaining contributions to the initial state give rise to the observed multimode dynamics. The deterministic preparation of the system in a desired Wannier number state is hindered by the fact that more tunneling modes are induced from additional contributions to the initial state. The case of stronger interparticle interactions with admixtures of a single excitation to the first excited band that do not couple in the eigenstate spectrum have been explored. The avoided crossings appear at higher trap frequencies and are narrower. The dynamics is different from the case of weak interactions, with higher band effects being more prominent and interwell tunneling being suppressed.

Let us comment on possible experimental implementations of our setup. In a corresponding ultracold gas experiment strongly interacting bosons are trapped in a one-dimensional superlattice. This superlattice can be formed by two retro-reflected laser beams from which the first one possesses a large wave number and intensity (forming each supercell) compared to the second (forming each cell of the supercell). The above-mentioned wave numbers should be commensurate. In this way, the potential landscape near the center of each supercell is similar to the one considered in the present study. Such a system may be implemented either by the use of holographic masks [45] or by the modulation of the wave number, e.g., using accordion lattices [46]. The trap frequency and the barrier height can be manipulated independently via the intensity of the lattice beams, and, finally, the interparticle interaction can be modulated via a magnetic Feshbach resonance. The corresponding static and dynamical properties of this state can then be measured with the recently developed single-site resolved imaging techniques [45,47–49]. A experimental alternative would be to prepare $2N$ fermionic ^6Li atoms in a microtrap [10], condense them into N Li_2 bosonic Feshbach molecules [50] and create a multiwell trap by switching on further microtraps [11].

The above-mentioned findings suggest that bosonic systems confined in a lattice potential with a superimposed harmonic trap can be used for state preparation in the limit of strong harmonic confinement. A natural continuation of the present work is to consider time-dependent quench protocols, such as linear quenches or pulsed sequences consisting of abrupt quenches, that may yield a substantial improvement on the state preparation, e.g., by exploiting the Landau-Zener mechanism [51–53]. Another prospect is to study the case where the parity symmetry is broken by a shift of the harmonic oscillator relative to the lattice. In this case states of opposite parity couple and one can induce transitions between states of the zeroth band and states in the first excited band. In this context novel kinds of dynamics such as Bloch-like oscillations [54–56] and the cradle mode [8,9] can be imprinted to the system. Finally, another interesting perspective is the study of nonintegrability since the many-body spectrum of the considered system shows a plethora of avoided crossings even in the few-body case. The latter might be a precursor of the advent of thermalization [57] for larger particle numbers and system sizes.

ACKNOWLEDGMENTS

The authors thank M. Kurz, G. Zürn, C. V. Morfonios, A. V. Zampetaki, and H.-D. Meyer for helpful discussions. This work has been financially supported by the excellence cluster “The Hamburg Centre for Ultrafast Imaging - Structure, Dynamics and Control of Matter at the Atomic Scale” and by the SFB 925 “Light induced dynamics and control of correlated quantum systems” of the Deutsche Forschungsgemeinschaft (DFG).

APPENDIX: COMPUTATIONAL METHOD: MCTDHB

Our approach to solve the many-body Schrödinger equation $(i\hbar\partial_t - H)\Psi(x,t) = 0$ relies on the multiconfiguration time-dependent Hartree method for bosons [24,25] (MCTDHB). MCTDHB has been applied extensively in the literature for the treatment of single species structureless bosons (see, e.g., Refs. [58–60]). The key idea of MCTDHB lies on the usage of a time-dependent (t-d) and variationally optimized many-body basis set, which allows for the optimal truncation of the total Hilbert space. The ansatz for the many-body wave function is taken as a linear combination of t-d permanents $|\vec{n}(t)\rangle$, with time-dependent weights $A_{\vec{n}}(t)$. Each t-d permanent is expanded in terms of M t-d variationally optimized single-particle functions (SPFs) $|\phi_j(t)\rangle$. For the numerical implementation the SPFs are expanded within a primitive basis $\{|k\rangle\}$ of dimension M_p . The time-evolution of the N -body wave function under the effect of the Hamiltonian \hat{H} reduces to the determination of the A -vector coefficients and the SPFs, which in turn follow the variationally obtained equations of motion [24,25]. Let us note here that in the limiting case of $M = 1$, the method reduces to the t-d Gross-Pitaevski equation, while for the case of $M = M_p$, the method is equivalent to a full configuration interaction approach to the Schrödinger equation within the basis $\{|k\rangle\}$.

For our implementation we have used a sine discrete variable representation (sin-DVR) as a primitive basis for the SPFs. A sin-DVR intrinsically introduces hard-wall

boundaries at both ends of the potential. To obtain the n th many-body eigenstate we rely on the so-called improved relaxation scheme. This scheme can be summarized as follows: (i) initialize the system with an ansatz set of SPFs $\{|\phi_i^{(0)}\rangle\}$; (ii) diagonalize the Hamiltonian within a basis spanned by the SPFs; (iii) set the n th obtained eigenvector as the $A^{(0)}$ vector; (iv) propagate the SPFs in imaginary time within a finite time interval $d\tau$; (v) update the SPFs to $\{|\phi_i^{(1)}\rangle\}$; and (vi) repeat steps (ii)–(v) until the energy of the state converges within the prescribed accuracy. To study the dynamics, we propagate the wave function by utilizing the appropriate Hamiltonian within the MCTDHB equations of motion. Finally, let us remark that our implementation has been performed by employing the multilayer multiconfiguration Hartree method for bosons [61,62] (ML-MCTDHB), which reduces to MCTDHB for the case of a single bosonic species as considered here.

To verify the numerical convergence of our simulations, we impose the following overlap criteria: (i) $|\langle\Psi|\Psi\rangle - 1| < 10^{-8}$ and (ii) $|\langle\phi_i|\phi_j\rangle - \delta_{ij}| < 10^{-9}$ for the total wave function and the SPFs respectively. Furthermore, we increase the number of SPFs and primitive basis states observing a systematic convergence of our results. For instance, we have used $M_p = 300$, $M = 9$ for the triple well, $M_p = 560$, $M = 7$ for the seven well and $M_p = 600$, $M = 6$ for the fifteen well. In the following, we shall briefly demonstrate the convergence behavior concerning our triple-well simulations either with an increasing number of SPFs M (and fixed number of $M_p = 300$ grid points) or for a varying number of grid points M_p and a fixed number of SPFs, $M = 9$. In particular, the fulfillment of the above two conditions is presented below for two different quenches, namely from $\omega_i^2 = 0.80E_R^2\hbar^{-2}$ to $\omega^2 = 0.40E_R^2\hbar^{-2}$, $g = 1E_R\hbar^{-1}$ and from $\omega_i^2 = 0.80E_R^2\hbar^{-2}$ to $\omega^2 = 0.464E_R^2\hbar^{-2}$ and $g = 1E_R\hbar^{-1}$. For reasons of completeness, note that the first of the aforementioned quenches [see Figs. 6(a), 6(b)] lie within the region II (low dynamical response), and the second [see Figs. 6(c), 6(d)] in the region T_{α_3} (resonant dynamical response). Employing the time-evolution of our main observable, i.e., the position variance $\sigma_{x,L}^2(t)$ [see Eq. (4)], we show [see Figs. 6(a), 6(c)] that it does not alter significantly for varying number of grid points. In particular, even in the case of $M_p = 200$ the corresponding differences from the results with $M_p = 300$ [e.g., presented also in Fig. 2(d)] are negligible. Remarkably enough, the maximum deviation observed in $\sigma_{x,L}^2(t)$, for a quench lying within the region T_{α_3} [see Fig. 6(c)], calculated using 250 and 300 grid points respectively, is of the order of 2.0% for long evolution times ($t > 250$). In addition, we also present for the same quench amplitudes as above, the long time propagation of $\sigma_{x,L}^2(t)$ for different numbers of SPFs [see Figs. 1(b), 1(d)]. It is observed that in the case of $M = 3$ and $M = 6$ strong deviations from the case with $M = 9$ occur, while the cases $M = 9$ and $M = 12$ are almost indistinguishable. For instance, the maximum deviation observed in $\sigma_{x,L}^2(t)$, for a quench lying in the region T_{α_3} [see Fig. 6(c)], calculated using nine and twelve SPFs respectively, is of the order of 5.0% for long evolution times ($t > 200$). We remark that the same analysis has also been performed for the seven- and fifteen-well case (omitted here for brevity) showing a similar behavior. An additional criterion for ensuring the convergence of our simulations is the population of the lowest occupied SPF, which is kept below 0.01%.

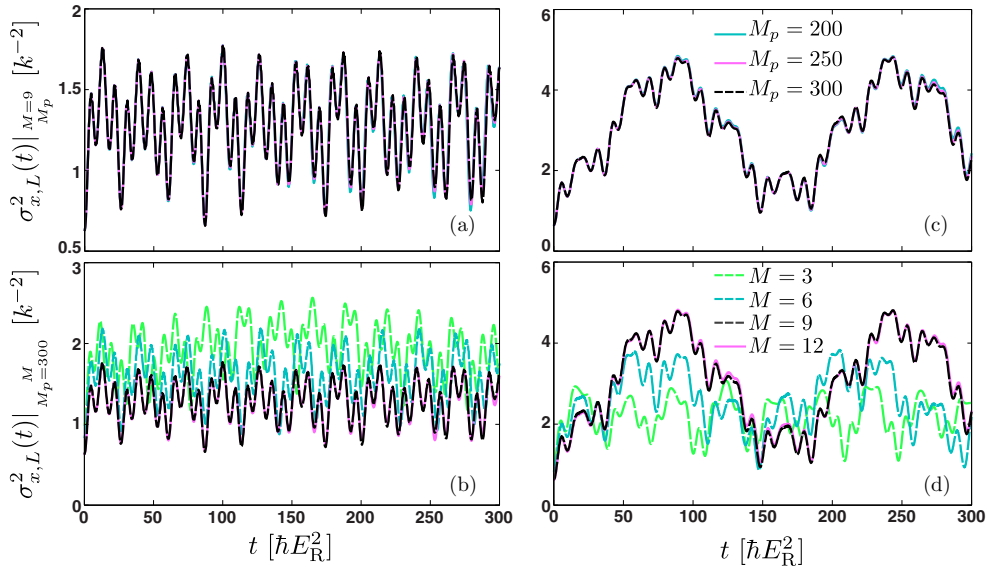


FIG. 6. $\sigma_{x,L}^2(t)$ for a quench from $\omega_i^2 = 0.80E_R^2\hbar^{-2}$ to $\omega^2 = 0.40E_R^2\hbar^{-2}$ and $g = 1E_Rk^{-1}$ for (a) different number of grid points M_p and $M = 9$ SPFs, (b) different number of SPFs M and $M_p = 300$ grid points. (c), (d) The same as (a), (b) but for a quench from $\omega_i^2 = 0.80E_R^2\hbar^{-2}$ to $\omega^2 = 0.464E_R^2\hbar^{-2}$.

- [1] I. Bloch, J. Dalibard, and W. Zwerger, *Rev. Mod. Phys.* **80**, 885 (2008).
- [2] A. Polkovnikov, K. Sengupta, A. Silva, and M. Vengalattore, *Rev. Mod. Phys.* **83**, 863 (2011).
- [3] M. Weidemüller, A. Hemmerich, A. Görlitz, T. Esslinger, and T. W. Hänsch, *Phys. Rev. Lett.* **75**, 4583 (1995).
- [4] C. L. Hung, X. Zhang, L. C. Ha, S. K. Tung, N. Gemelke, and C. Chin, *New J. Phys.* **13**, 075019 (2011).
- [5] J. P. Ronzheimer, M. Schreiber, S. Braun, S. S. Hodgman, S. Langer, I. P. McCulloch, F. Heidrich-Meisner, I. Bloch, and U. Schneider, *Phys. Rev. Lett.* **110**, 205301 (2013).
- [6] F. Meinert, M. J. Mark, E. Kirilov, K. Lauber, P. Weinmann, M. Gröbner, A. J. Daley, and H. C. Nägerl, *Science* **344**, 1259 (2014).
- [7] S. Fölling, S. Trotzky, P. Cheinet, M. Feld, R. Saers, A. Widera, T. Müller, and I. Bloch, *Nature (London)* **448**, 1029 (2007).
- [8] S. I. Mistakidis, L. Cao, and P. Schmelcher, *J. Phys. B: At. Mol. Opt. Phys.* **47**, 225303 (2014).
- [9] S. I. Mistakidis, L. Cao, and P. Schmelcher, *Phys. Rev. A* **91**, 033611 (2015).
- [10] F. Serwane, G. Zürn, T. Lompe, T. B. Ottenstein, A. N. Wenz, and S. Jochim, *Science* **332**, 336 (2011).
- [11] S. Murmann, A. Bergschneider, V. M. Klinkhamer, G. Zürn, T. Lompe, and S. Jochim, *Phys. Rev. Lett.* **114**, 080402 (2015).
- [12] M. Cheneau, P. Barmettler, D. Poletti, M. Endres, P. Schaub, T. Fukuhara, C. Gross, I. Bloch, C. Kollath, and S. Kuhr, *Nature (London)* **481**, 484 (2012).
- [13] S. S. Natu and E. J. Mueller, *Phys. Rev. A* **87**, 053607 (2013).
- [14] D. Chen, M. White, C. Borries, and B. DeMarco, *Phys. Rev. Lett.* **106**, 235304 (2011).
- [15] H. Elmar, R. Hart, M. J. Mark, J. G. Danzl, L. Reichsöllner, M. Gustavsson, M. Dalmonte, G. Pupillo, and H.-C. Nägerl, *Nature (London)* **466**, 597 (2010).
- [16] K. W. Mahmud, L. Jiang, P. R. Johnson, and E. Tiesinga, *New J. Phys.* **16**, 103009 (2014).
- [17] S. Campbell, M. A. García-March, T. Fogarty, and T. Busch, *Phys. Rev. A* **90**, 013617 (2014).
- [18] W. Tschischik, R. Moessner, and M. Haque, *Phys. Rev. A* **88**, 063636 (2013).
- [19] M. Rigol, G. G. Batrouni, V. G. Rousseau, and R. T. Scalettar, *Phys. Rev. A* **79**, 053605 (2009).
- [20] G. G. Batrouni, V. Rousseau, R. T. Scalettar, M. Rigol, A. Muramatsu, P. J. H. Denteneer, and M. Troyer, *Phys. Rev. Lett.* **89**, 117203 (2002).
- [21] V. A. Kashurnikov, N. V. Prokof'ev, and B. V. Svistunov, *Phys. Rev. A* **66**, 031601(R) (2002).
- [22] C. Kollath, U. Schollwöck, J. von Delft, and W. Zwerger, *Phys. Rev. A* **69**, 031601(R) (2004).
- [23] S. Wessel, F. Alet, M. Troyer, and G. G. Batrouni, *Phys. Rev. A* **70**, 053615 (2004).
- [24] O. E. Alon, A. I. Streltsov, and L. S. Cederbaum, *J. Chem. Phys.* **127**, 154103 (2007).
- [25] O. E. Alon, A. I. Streltsov, and L. S. Cederbaum, *Phys. Rev. A* **77**, 033613 (2008).
- [26] M. Olshanii, *Phys. Rev. Lett.* **81**, 938 (1998).
- [27] J. I. Kim, V. S. Melezhik, and P. Schmelcher, *Phys. Rev. Lett.* **97**, 193203 (2006).
- [28] P. Giannakeas, F. K. Diakonou, and P. Schmelcher, *Phys. Rev. A* **86**, 042703 (2012).
- [29] R. A. Duine and H. T. Stoof, *Phys. Rep.* **396**, 115 (2004).
- [30] C. Chin, R. Grimm, P. Julienne, and E. Tiesinga, *Rev. Mod. Phys.* **82**, 1225 (2010).
- [31] S. Kivelson and J. R. Schrieffer, *Phys. Rev. B* **25**, 6447 (1982).
- [32] U. Bissbort, F. Deuretzbacher, and W. Hofstetter, *Phys. Rev. A* **86**, 023617 (2012).

- [33] J. Enders, Master thesis, Goethe-Universität, 2014 (unpublished).
- [34] W. Kohn, *Phys. Rev.* **123**, 1242 (1961).
- [35] J. W. Abraham and M. Bonitz, *Contrib. Plasma Phys.* **54**, 27 (2014).
- [36] M. P. A. Fisher, P. B. Weichman, G. Grinstein, and D. S. Fisher, *Phys. Rev. B* **40**, 546 (1989).
- [37] D. Jaksch, C. Bruder, J. I. Cirac, C. W. Gardiner, and P. Zoller, *Phys. Rev. Lett.* **81**, 3108 (1998).
- [38] We remark that at the region of the exact crossing [see the dotted box at $\omega^2 \sim 0.21 E_R^2 \hbar^{-2}$ in Fig. 1(b)], the $|2, 1^{(1)}, 1\rangle_{S,A}$ dominated eigenstate acquires a contribution from the state $|3, 0, 1\rangle_{S,A}$ of the order of $\sim 10\%$. This coupling is caused by the small tilt of the side wells, which weakly breaks the corresponding parity symmetry. This, however, does not lead to any considerable alterations in the many-body spectrum.
- [39] C. A. Parra-Murillo, J. Madroñero, and S. Wimberger, *Phys. Rev. A* **88**, 032119 (2013).
- [40] States with two excited particles in the second band do not contribute significantly to the dynamics as they are energetically far from states belonging to the ground band.
- [41] The dipole mode is mathematically explained by the unitary transformation $|\vec{n}\rangle(\omega_i) \xrightarrow{U} |\vec{n}\rangle(\omega)$, which maps the Wannier basis from ω_i to ω and imprints a coherentlike state to each boson initially residing in a side well.
- [42] A. Smerzi, S. Fantoni, S. Giovanazzi, and S. R. Shenoy, *Phys. Rev. Lett.* **79**, 4950 (1997).
- [43] S. Raghavan, A. Smerzi, S. Fantoni, and S. R. Shenoy, *Phys. Rev. A* **59**, 620 (1999).
- [44] M. Albiez, R. Gati, J. Fölling, S. Hunsmann, M. Cristiani, and M. K. Oberthaler, *Phys. Rev. Lett.* **95**, 010402 (2005).
- [45] J. F. Sherson, C. Weitenberg, M. Endres, M. Cheneau, I. Bloch, and S. Kuhr, *Nature (London)* **467**, 68 (2010).
- [46] T. Li, H. Kelkar, D. Medellin, and M. Raizen, *Opt. Express* **16**, 5465 (2008).
- [47] P. M. Preiss, R. Ma, M. E. Tai, J. Simon, and M. Greiner, *Phys. Rev. A* **91**, 041602(R) (2015).
- [48] T. Fukuhara, S. Hild, J. Zeiher, P. Schauß, I. Bloch, M. Endres, and C. Gross, *Phys. Rev. Lett.* **115**, 035302 (2015).
- [49] M. Miranda, R. Inoue, Y. Okuyama, A. Nakamoto, and M. Kozuma, *Phys. Rev. A* **91**, 063414 (2015).
- [50] S. Sala, G. Zürn, T. Lompe, A. N. Wenz, S. Murmann, F. Serwane, S. Jochim, and A. Saenz, *Phys. Rev. Lett.* **110**, 203202 (2013).
- [51] L. D. Landau, *Phys. Z. Sowjetunion* **2**, 46 (1932).
- [52] C. Zener, *Proc. Roy. Soc. Lond. A* **137**, 696 (1932).
- [53] E. C. G. Stueckelberg, *Helv. Phys. Acta* **5**, 370 (1932).
- [54] M. Ben Dahan, E. Peik, J. Reichel, Y. Castin, and C. Salomon, *Phys. Rev. Lett.* **76**, 4508 (1996).
- [55] O. Morsch, J. H. Müller, M. Cristiani, D. Ciampini, and E. Arimondo, *Phys. Rev. Lett.* **87**, 140402 (2001).
- [56] S. Kling, T. Salger, C. Grossert, and M. Weitz, *Phys. Rev. Lett.* **105**, 215301 (2010).
- [57] M. Rigol, V. Dunjko, and M. Olshanii, *Nature (London)* **452**, 854 (2008).
- [58] A. I. Streltsov, K. Sakmann, O. E. Alon, and L. S. Cederbaum, *Phys. Rev. A* **83**, 043604 (2011).
- [59] O. E. Alon, A. I. Streltsov, and L. S. Cederbaum, *Phys. Rev. A* **76**, 013611 (2007).
- [60] O. E. Alon, A. I. Streltsov, and L. S. Cederbaum, *Phys. Rev. A* **79**, 022503 (2009).
- [61] L. Cao, S. Krönke, O. Vendrell, and P. Schmelcher, *J. Chem. Phys.* **139**, 134103 (2013).
- [62] S. Krönke, L. Cao, O. Vendrell, and P. Schmelcher, *New J. Phys.* **15**, 063018 (2013).

4.2 Driven Lattices

4.2.1 Resonant Quantum Dynamics of Few Ultracold Bosons in Periodically Driven Finite Lattices

PAPER

Resonant quantum dynamics of few ultracold bosons in periodically driven finite lattices

To cite this article: S I Mistakidis *et al* 2015 *J. Phys. B: At. Mol. Opt. Phys.* **48** 244004

View the [article online](#) for updates and enhancements.

Related content

- [Interaction quench induced multimode dynamics of finite atomic ensembles](#)
S I Mistakidis, L Cao and P Schmelcher
- [Interaction-driven interband tunneling of bosons in the triple well](#)
Lushuai Cao, Ioannis Brouzos, Sascha Zöllner *et al.*
- [Floquet engineering with quasienergy bands of periodically driven optical lattices](#)
Martin Holthaus

Recent citations

- [Phases, many-body entropy measures, and coherence of interacting bosons in optical lattices](#)
R. Roy *et al*
- [Variance of an anisotropic Bose-Einstein condensate](#)
Shachar Klaiman *et al*
- [Uncertainty product of an out-of-equilibrium Bose-Einstein condensate](#)
S Klaiman *et al*

Resonant quantum dynamics of few ultracold bosons in periodically driven finite lattices

S I Mistakidis¹, T Wulf¹, A Negretti^{1,2} and P Schmelcher^{1,2}

¹Zentrum für Optische Quantentechnologien, Universität Hamburg, Luruper Chaussee 149, D-22761 Hamburg, Germany

²The Hamburg Centre for Ultrafast Imaging, Universität Hamburg, Luruper Chaussee 149, D-22761 Hamburg, Germany

E-mail: smistaki@physnet.uni-hamburg.de

Received 4 June 2015

Accepted for publication 4 September 2015

Published 3 November 2015



CrossMark

Abstract

The out-of-equilibrium dynamics of finite ultracold bosonic ensembles in periodically driven one-dimensional optical lattices is investigated. Our study reveals that the driving enforces the bosons in different wells to oscillate in-phase and to exhibit a dipole-like mode. A wide range from weak-to-strong driving frequencies is covered and a resonance-like behavior of the intra-well dynamics is discussed. In the proximity of the resonance a rich intraband excitation spectrum is observed. The single particle excitation mechanisms are studied in the framework of Floquet theory elucidating the role of the driving frequency. The impact of the interatomic repulsive interactions is examined in detail yielding a strong influence on the tunneling period and the excitation probabilities. Finally, the dependence of the resonance upon a variation of the tunable parameters of the optical lattice is examined. Our analysis is based on the *ab initio* multi-configuration time-dependent Hartree method for bosons.

Keywords: ultracold atoms, periodic driving, nonequilibrium quantum dynamics

(Some figures may appear in colour only in the online journal)

1. Introduction

Ultracold atomic quantum gases in optical lattices have reached an unprecedented degree of control providing direct experimental access to a plethora of non-equilibrium phenomena [1–4]. This control includes the modulation of the interparticle interactions via confinement-induced, magnetic and optical Feshbach resonances [5–10], the design of arbitrarily shaped optical traps with variable lattice depths, and the ability to move time-periodically or even accelerate the entire lattice structure. This level of control and accuracy over the system parameters has opened the possibility to simulate and study quantum many-body phenomena in part inspired from condensed matter physics [11]. For instance, when accelerating an optical lattice, representative processes are Bloch-oscillations [12–16], Wannier–Stark ladders [17, 18], Landau–Zener tunneling [16, 18] and photon assisted

tunneling [19], to name only a few. A promising technique is the lattice shaking which has been used in order to address, for example, the coherent control of the superfluid to Mott insulator phase transition [20], parametric amplification of matter waves [21], four-wave mixing [22, 23], topological states of matter [24], hybridized band structure [21, 25], and even the engineering of artificial gauge fields [26]. More recently it has been shown [27, 28] that one can use lattice shaking to probe coherent band coupling and realize the formation of ferromagnetic domains. Moreover, the dynamics induced by shaking an optical lattice can lead to an admixture of excited orbitals [29] and constitutes an emergent branch of modern quantum physics.

A substantial part of the previous studies has been primarily focused on the renormalization of the physics due to driving, the mean-field approach [14] for weak interactions, where the Gross–Pitaevskii equation is still valid, and a linear

response treatment [30]. However, a relatively large modulation of the strength or of the frequency of the driving as well as strong interactions calls for alternative methods which can take into account higher-orbitals. Indeed, the inclusion of higher-band contributions introduces new degrees of freedom and as a result additional physical processes come into play. Hereby, a sinusoidal shaking of the optical lattice is a natural starting point which induces an in-phase dipole mode on each site. An interesting and so far largely unexplored direction is the study of the interplay between higher bands for the intra-well mode and the inter-well tunneling dynamics with respect to the driving frequency, and the investigation of the effect of the interatomic interactions in the overall process. In this way, it is natural to start with the investigation of the few body analogue in order to achieve a more comprehensive understanding of the microscopic properties of the strongly driven interacting system. Although the major part of the presented results is devoted to the case of four bosons in a triple-well setup, we provide strong evidence that our findings are still applicable for larger lattice systems and larger particle numbers.

Motivated by the recent experimental progress [26, 27] we investigate in the present work the effects that a periodically driven one-dimensional optical lattice can introduce in a small ensemble of ultracold bosons. The dynamical response of the system for a wide range of driving frequencies is studied by means of the concept of fidelity or autocorrelation function. Even though we consider a scenario with a deep lattice such that the tunneling modes have a minor influence on the overall dynamics, a quite rich excitation spectrum is found. We note that such intra-band excitations, which lead to a coupling between the two lowest energy bands, have been exploited in order to realize single- and two-qubit gates, where the quantum bit has been encoded in the localized Wannier functions of the two lowest energy bands of each lattice site [31]. In order to analyze the intra-well dynamics we employ the one-body reduced density matrix. The Fourier spectrum of the local one-body density as well as of the on-site density oscillations are employed in order to obtain insights into the excited intra-well modes. We find a resonant behavior of the dipole mode indicating that the intra-well dynamics can be controlled by adjusting the driving frequency. Moreover, the magnification of the intra-well generated mode at resonance is also manifested in the population of additional lattice momenta. Our investigation of the resonances is supported by a Floquet analysis for the effective single-particle degree of freedom. This allows us to further explore the on-site dynamics and the inter-well tunneling that occur due to the driving. Including interatomic interactions for larger atom numbers, we analyze similarities and differences with respect to the single-particle description. The above outlined findings are confirmed for different filling factors, lattice potentials, and boundary conditions. To solve the underlying many-body Schrödinger equation we apply the *ab initio* multiconfiguration time-dependent Hartree method for bosons (MCTDHB) [32, 33] which is especially designed to treat the driven out-of-equilibrium quantum dynamics of interacting bosons.

This article is organized as follows. In section 2 we introduce our setup and the multi-band expansion. Section 3 contains the driven quantum dynamics first from a single-particle perspective, by performing a Floquet analysis, and second by inspecting the dynamics of a small bosonic ensemble including repulsive interactions. We summarize our findings and provide an outlook in section 4. The appendix briefly outlines our computational method.

2. Hamiltonian and multi-band expansion

This section is devoted to a brief presentation of the theoretical framework of our study. In particular, we shall briefly discuss the driven optical lattice, the underlying many-body Hamiltonian, and the concept of multi-band expansion. The latter will be a useful tool in order to understand the excitations involved in the dynamics.

2.1. Modeling the periodically-driven potential

The periodic driving of an optical lattice can be accomplished in two different ways. Retroreflecting mirrors that are used to form the lattice can be moved periodically in space or, alternatively, a frequency difference between counter-propagating laser beams can be induced by means of acousto-optical modulators [27] which renders the lattice time-dependent. Here, we model the driven optical lattice with a sinusoidal function of the form

$$V_{\text{sh}}(x, t) = V_0 \sin^2[k_0(x - A \sin \omega_D t)]. \quad (1)$$

Such a potential has been implemented in the experiment in [21]. It is characterized by the barrier depth V_0 , a lattice wave-vector $k_0 = \frac{\pi}{l}$, where l denotes the distance between successive potential minima, the amplitude A and the frequency $\omega_D = 2\pi/T_D$ of the driving field. In an experiment k_0 is the wave vector of the laser beams which form the optical lattice, while its depth V_0 can be tuned by adjusting the laser's intensity.

2.2. The Hamiltonian

The Hamiltonian of N identical ultracold bosons of mass M confined in a driven one-dimensional m -well optical lattice reads

$$H = \sum_{i=1}^N -\frac{\hbar^2}{2M} \frac{\partial^2}{\partial x_i^2} + V_{\text{sh}}(x_i, t) + \sum_{i < j} V_{\text{int}}(x_i - x_j), \quad (2)$$

where $V_{\text{int}}(x_i - x_j) = g_{1D} \delta(x_i - x_j)$ denotes the short-range contact interaction potential between particles located at position x_i , $i = 1, 2, \dots, N$. In the ultracold regime the interaction is well described by s -wave scattering whose effective one-dimensional coupling strength [5] is given by $g_{1D} = \frac{2\hbar^2 a_0}{M a_{\perp}^2} \left(1 - \frac{|\zeta(1/2)| a_0}{\sqrt{2} a_{\perp}}\right)^{-1}$. Here $a_{\perp} = \sqrt{\frac{\hbar}{M \omega_{\perp}}}$ is the transverse harmonic oscillator length with ω_{\perp} the frequency of the two-dimensional confinement, while a_0 denotes the free space three-dimensional s -wave scattering length. In this way,

the interaction strength can be tuned either via a_0 with the aid of Feshbach resonances [9, 10], or via the transversal confinement frequency ω_\perp [34, 35].

For the sake of simplicity and computational convenience, we rescale the Hamiltonian (2) in units of the recoil energy $E_R = \frac{\hbar^2 k_0^2}{2M}$. Then, the corresponding length, time and frequency scales are given in units of k_0^{-1} , $\omega_R^{-1} = \hbar E_R^{-1}$ and ω_R respectively. In our simulations we have used a sufficiently large lattice depth with values ranging from $V_0 = 4.5 E_R$ to $8.0 E_R$ such that each well includes three localized single-particle Wannier states. In particular, due to the deep optical lattice and small driving amplitudes (in comparison to the lattice constant) mainly used in our simulations highly energetic excitations above the barrier are excluded and as a consequence heating processes can be minimized. The confinement of the bosons in the m -well system is imposed by the use of hard-wall boundary conditions at positions $x_\sigma = \pm \frac{m\pi}{2k_0}$, where the potential is maximum. In addition, we set also $\hbar = M = k_0 = 1$ and the coupling strength becomes $g = \frac{s_{\text{D}}}{E_R}$, while A represents the dimensionless driving amplitude. The rescaled shaken triple well is given by $V_{\text{sh}}(x_i, t) = V_0 \sin^2(x_i - A \sin \omega_D t)$ with the hard wall boundaries located at $x_\sigma = \pm 3\pi/2$.

2.3. The multi-band expansion

The understanding of the spatial localization of states in lattice systems makes the use of multi-band Wannier number states crucial as it includes the information of excited bands and allows us to interpret both intraband and interband processes. In general, this representation is valid when the lattice potential is deep enough such that the Wannier states between different wells have a very small overlap for not too high energetic excitation. In the present case where the potential is periodically driven, the above description can still be used as long as the driving amplitude is small enough in comparison to the lattice constant l , i.e. $A \ll l$. In this way, each localized Wannier function can be still adapted and assigned to a certain well and the respective band-mixing is fairly small. For large displacements one should use a time-dependent Wannier basis in order to ensure that the corresponding on-site Wannier states are well-adapted to each well during the driving.

To introduce the formalism, let us consider a system consisting of N bosons, m -wells and k localized single particle bands [36, 37]. Then, the expansion of the many-body bosonic wavefunction in terms of the number states of non-interacting bosons reads

$$|\Psi\rangle = \sum_{\{N_i\}, \mathbf{I}} C_{\{N_i\}, \mathbf{I}} |N_1, N_2, \dots, N_m\rangle_{\mathbf{I}}, \quad (3)$$

where $|N_1, N_2, \dots, N_m\rangle_{\mathbf{I}}$ is the multiband Wannier number state and the element N_i denotes the number of bosons being localized in the i th well satisfying the constraint $\sum_{i=1}^m N_i = N$. The summation is performed over the different configurations of the N bosons according to their energetic order denoted by the index \mathbf{I} . In particular, the index \mathbf{I} corresponds

to a high dimensional quantity $\mathbf{I} = (I_1, I_2, \dots, I_m)$ which contains m elements each of them being a k -component vector. More precisely, the q th element can be written as $\mathbf{I}_q = (I_q^{(1)}, I_q^{(2)}, \dots, I_q^{(k)})$, where $I_q^{(k)}$ refers to the number of bosons located at the q th well and k th band, satisfying the constraint $\sum_{q=1}^m \sum_{i=1}^k I_q^{(i)} = N$. Within the above notation one can investigate, among others, the probability of $N_0 < N$ bosons to be in an excited band or to find a specific number state configuration. Indeed, suppose the case of $N_0 < N$ bosons excited in the i th band while the rest $N - N_0$ lie in lower bands. Then, it must hold $I_1^{(j)} = I_2^{(j)} = \dots = I_m^{(j)} = 0$ for every $j > i$, while $I_1^{(i)} + I_2^{(i)} + \dots + I_m^{(i)} = N_0$ and $I_1^{(1)} + \dots + I_m^{(1)} = N - N_0$ for every $j_1 < i$.

Let us consider an example of a system with four bosons ($N = 4$) confined in a triple well ($m = 3$) which includes three bands ($k = 3$). Then, for instance, the state $|1, 2, 1\rangle_{\mathbf{I}}$ with $\mathbf{I} = (\mathbf{I}_L, \mathbf{I}_M, \mathbf{I}_R)$, and $\mathbf{I}_L = \mathbf{I}_R = (0, 1, 0)$, $\mathbf{I}_M = (0, 1, 1)$ denotes a state for which in the left (right) well one boson occupies the first excited band, whereas in the middle well one boson is localized in the first excited and one in the second excited band. As a final attempt, here, we make a link between the ground state and its dominant spatial configuration in terms of the aforementioned multiband expansion. To do that, let us choose again a system consisting of four bosons in a triple well as it will be used extensively in the following. It is known that, in general, the ground state configuration depends on the interaction strength, while for the present system, i.e. $N = 4$ and $m = 3$, the on-site interaction effects will always be prominent. For the non-interacting case ($g = 0$) the dominant spatial configuration of the system is $|1, 2, 1\rangle_{\mathbf{I}}$, with $I_L = I_R = (1, 0, 0)$ and $I_M = (2, 0, 0)$ due to the hard-wall boundaries which render the middle and outer sites non-equivalent. In the course of increasing interaction a tendency towards a uniform population of each site, e.g. for $g = 0.2$, due to the repulsion of the bosons is observed. In this region the system is described by a superposition of lowest-band states which are predominantly of single-pair occupancy, e.g. $|1, 2, 1\rangle_{\mathbf{I}}$, $|2, 1, 1\rangle_{\mathbf{I}}$, and double-pair occupancy, e.g. $|2, 2, 0\rangle_{\mathbf{I}}$. For further increasing repulsion, e.g. $g = 0.4$, a trend towards the repopulation of the central well is noted. As we enter the strong interaction regime, e.g. $g = 1.5$, the state consists of a particle in the first excited-band being on a commensurate background of localized particles which lie in the zeroth band and the dominant ground state configuration is $|1, 2, 1\rangle_{\mathbf{I}}$, with $I_L = I_R = (1, 0, 0)$ and $I_M = (1, 1, 0)$. Finally, for strong interparticle repulsion, e.g. $g = 3$, the contribution from the higher-band states becomes more prominent and the corresponding ground state configuration is characterized by an admixture of zeroth- and excited-band states.

3. Driven quantum dynamics

This section is devoted to a detailed analysis of the bosonic dynamics in a driven optical lattice. At the beginning, a general overview of the effect of the driving on the finite bosonic ensemble with respect to the driving frequency is

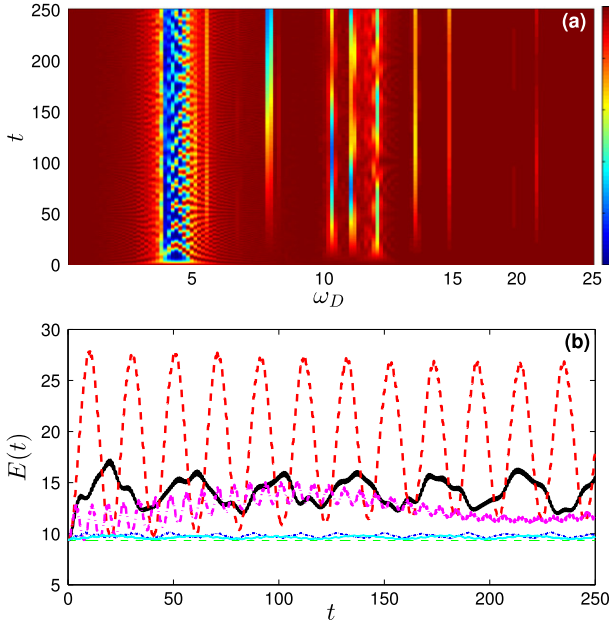


Figure 1. (a) Time evolution of the fidelity $F_{\omega_D}(t)$ as a function of the driving frequency ω_D (measured in units of ω_R). (b) Time evolution of the expectation value of the Hamiltonian (2) (measured in units of the recoil energy E_R) for various driving frequencies $\omega_D = 0.4$ (green thin dashed line), $\omega_D = 4.0$ (black thick solid line), $\omega_D = 4.5$ (red thick dashed line), $\omega_D = 5.25$ (magenta thick dashed-dotted line), $\omega_D = 11.0$ (blue thin dashed-dotted line), and $\omega_D = 13.375$ (light-blue thin solid line). The driving amplitude is $A = 0.05$, while the initial state corresponds to the ground state of four weakly interacting bosons with $g = 0.1$ confined in a triple-well. Time unit is ω_R^{-1} .

given. Subsequently, a Floquet analysis is employed in order to investigate the underlying single-particle physics. Finally, we focus on specific interaction effects.

3.1. Dynamical response

Let us explore the dynamical response or sensitivity of the system with respect to the driving frequency ω_D . In order to investigate the stability of the system against the perturbations induced by the shaking (see equation (1)), we first analyse the fidelity [38] between the initial state and the state evolved at time t : $F_{\omega_D}(t) = |\langle \Psi(0) | \Psi(t) \rangle|^2$, where the dependence on ω_D is implicit in the time evolved state $\Psi(t)$. Here we will consider a system of four bosons in a triple-well with $g = 0.1$, whose ground state (i.e. the initial state $\Psi(0)$) corresponds to a superfluid state, as the filling factor is not commensurable and we do not encounter the formation of a Mott insulating state. In terms of its dominant spatial configuration our system initially consists (see also section 2.3) of two bosons in the middle well and two others each of them localized in one of the outer wells, i.e. the state $|1, 2, 1\rangle_I$, with $I_L = I_R = (1, 0, 0)$ and $I_M = (2, 0, 0)$ has the most prominent contribution. Figure 1(a) shows $F_{\omega_D}(t)$ as a function of the driving frequency ω_D . The dynamics are characterized by three main regions with respect to ω_D , where the system is driven far from the initial state, while for the remaining frequency

regions (red sections in figure 1(a)) the evolved state is essentially unperturbed by the driving. In the first region, between $4.0 < \omega_D < 5.5$, the minimal overlap in the course of the dynamics drops down to 0.1, whereas in the second ($7.0 < \omega_D < 8.0$) and third ($10.0 < \omega_D < 15.0$) regions the system maximally departs from the initial state with a percentage on the order of 50% and 65%, respectively. The emergence of these dynamical regions strongly depends on the parameters of the optical lattice. For instance, for smaller lattice depths the aforementioned regions will be wider, because of the smaller potential energy, which favors a possible deviation of the system from the initial state.

Let us inspect the time evolution of the total energy $E(t) = \langle \Psi(t) | \hat{H} | \Psi(t) \rangle$. Figure 1(b) shows $E(t)$ for various driving frequencies ω_D . For driving frequencies where $F_{\omega_D} \simeq 1$ (e.g. $\omega_D \in \{1, 3\}$, see also figure 1(a)) the dependence of the energy on the driving frequency is weak and it is essentially constant during the time evolution. On the other hand, for the regions where $F_{\omega_D} \ll 1$, $E(t)$ increases initially and it shows an oscillatory behavior. In particular, for $\omega_D = 4.5$ the total energy exhibits an oscillatory (almost periodic) pattern which can also be observed in the corresponding fidelity evolution. This driving frequency will be referred to in the following as critical and denoted by ω_D^c , that is, the driving frequency for which $\min_{t \in [0, T]} F_{\omega_D}(t)$ is minimal. Indeed, as we shall see below, the most interesting dynamics of the system takes place close to this frequency.

Finally, let us inspect the response of the system to the driving from a one-body perspective via the single-particle density $\rho_1(x, t) = \int dx_2 \dots dx_N |\Psi(x, x_2, \dots, x_N; t)|^2$. Figure 2 illustrates the evolution of the one-body density for different driving frequencies ω_D , but with the same amplitude A . The driving leads to oscillations of the particles densities in every site. As can be observed by having a glance at figure 2(a), the one-body density shows a weak response for driving frequencies away from the critical region $\omega_D \in [4, 5.5]$, while for $\omega_D = \omega_D^c$ (see figure 2(b)) we observe the periodic formation of enhanced density oscillations being accompanied by a broadening of each intra-well ensemble. The peculiar behavior of the bosonic ensemble observed for $\omega_D = \omega_D^c$ is characterized by three processes and time scales: (i) the internal fast oscillations of the density; (ii) the large amplitude oscillations of the density in each well of period ~ 14 ; (iii) the tunneling between the wells with a period of about 200. All these features will be analyzed in detail in the following subsections both at the single particle and many-body level.

3.2. Single particle dynamics

Here we investigate to what extent the previously presented results can be understood in the limit of zero interaction among the particles by means of Floquet theory. Specifically, we are interested in two distinct features of the dynamics observed in figure 2(b): first, the on-site dynamics and, especially, its resonance-like dependence on the driving frequency ω_D , and second, the inter-well tunneling dynamics which are enhanced at certain values of ω_D .

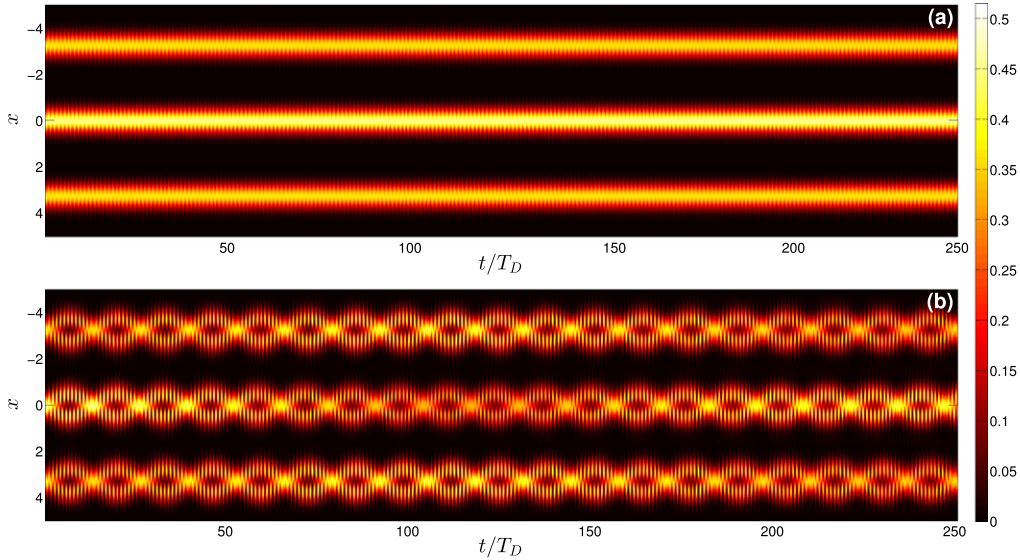


Figure 2. Time evolution of the one-body density $\rho_1(x, t)$ in a triple-well potential for different driving frequencies: (a) $\omega_D = 2.0$ (top panel) and (b) $\omega_D = 4.5$ (lower panel). The driving amplitude is fixed to the value $A = 0.05$, while the initial state corresponds to the ground state of four weakly interacting bosons with $g = 0.1$. The spatial extent of the lattice is expressed in units of k_0^{-1} , while the time units are rescaled in terms of the driving period T_D .

3.2.1. Floquet theory. To be self-contained, we start by summing up the main notions of Floquet theory. Because of the temporal periodicity of the single particle Hamiltonian employed throughout this work (equation (2) with $g = 0$ and $N = 1$), every solution of the time-dependent Schrödinger equation (TDSE) takes the form of a Floquet mode (FM) $\Psi_\alpha(x, t)$ which in turn can be written as: $\Psi_\alpha(x, t) = e^{-i\epsilon_\alpha t/\hbar} \Phi_\alpha(x, t)$ with the real quasi energy (QE) $\epsilon_\alpha \in [-\hbar\omega_D/2, +\hbar\omega_D/2]$ and with $\Phi_\alpha(x, t) = \Phi_\alpha(x, t + T_D)$ respecting the temporal periodicity of the Hamiltonian [39]. The FMs are eigenvectors of the time evolution operator over one driving period

$$U(T_D + t_0, t_0)\Psi_\alpha(x, t_0) = e^{-i\epsilon_\alpha T_D/\hbar}\Psi_\alpha(x, t_0). \quad (4)$$

This property is of particular interest as it allows for a stroboscopic time evolution of an arbitrary initial state $\Psi(x, t_0)$ once the FMs of a system are known. To show this, we exploit the fact that the FMs constitute an orthonormal basis for the solution space of the TDSE [40] and expand $\Psi(x, t_0)$ at the initial time $t = t_0$ as

$$\Psi(x, t_0) = \sum_{\alpha} C_{\alpha}(t_0)\Psi_{\alpha}(x, t_0) \quad (5)$$

with the corresponding coefficients $C_{\alpha}(t_0)$. By applying the one period evolution operator $U(T_D + t_0, t_0)$ on both sides of equation (5) for m times and by virtue of equation (4), we readily obtain the stroboscopic time evolution of $\Psi(x, t_0)$ as

$$\Psi(x, t_0 + mT) = \sum_{\alpha} C_{\alpha}(t_0)e^{-i\epsilon_{\alpha}mT_D/\hbar}\Psi_{\alpha}(x, t_0). \quad (6)$$

Numerically, we obtain the FMs for a given initial time t_0 by calculating the eigenvectors of the one period evolution operator $U(T_D + t_0, t_0)$ (see equation (4)). We refer the interested reader to [41] for a detailed description of the employed computational scheme.

Finally, let us note that equation (6) already reveals some interesting features of the time evolution in periodically driven systems as we shall see in the following. Imagine that only a single FM, say $\Psi_0(x, t)$, is populated. The stroboscopic evolution of the probability density is thus given as $|\Psi(x, mT_D)|^2 = |C_0|^2|\Psi_0(x, 0)|^2$. Hence, $|\Psi(x, t)|^2$ is again periodic with period T_D and the only time dependence arises from the explicit time dependence of the FM, which is commonly referred to as ‘micro-motion’. This situation changes if the initial state populates multiple FMs. In this case one encounters interference terms in $|\Psi(x, mT_D)|^2$ between the different FMs in the form of $\sim e^{im(\epsilon_{\alpha} - \epsilon_{\beta})T_D/\hbar}$. Thus, the quasi energies ϵ_{α} in periodically driven systems play a comparable role in the time evolution as the energy eigenvalues do in time-independent setups.

3.2.2. On-site dynamics in the single well. To begin with, we shall investigate the observed on-site dynamics (see figure 2(b)), and in particular their dependence on the driving frequency ω_D . To this end, we simplify the setup studied in section 3.1 to just a single well of the lattice potential. Hence, the potential is given by $V_{\text{sh}}(x, t) = V_0 \sin^2(x - A \sin(\omega_D t))$ for $x \in (-\pi, +\pi]$ and we impose periodic boundary conditions at $x = \pm\pi$ in order to mimic the situation in an extended lattice. We choose as initial state $\Psi(x, 0)$ the single particle density as shown in figure 2(b) at $t = 0$ within the central potential well. The time evolution is then obtained by expanding $\Psi(x, 0)$ in terms of the FMs of the system and by making use of equation (6). As a result, we find that we can reproduce some of the main features of the on-site dynamics shown in figures 2(a) and (b), namely, we observe resonantly enhanced on-site oscillations in an interval of the driving frequencies around $\omega_D \approx 4.5$. Following the discussion in [42], further insight into this effect can be

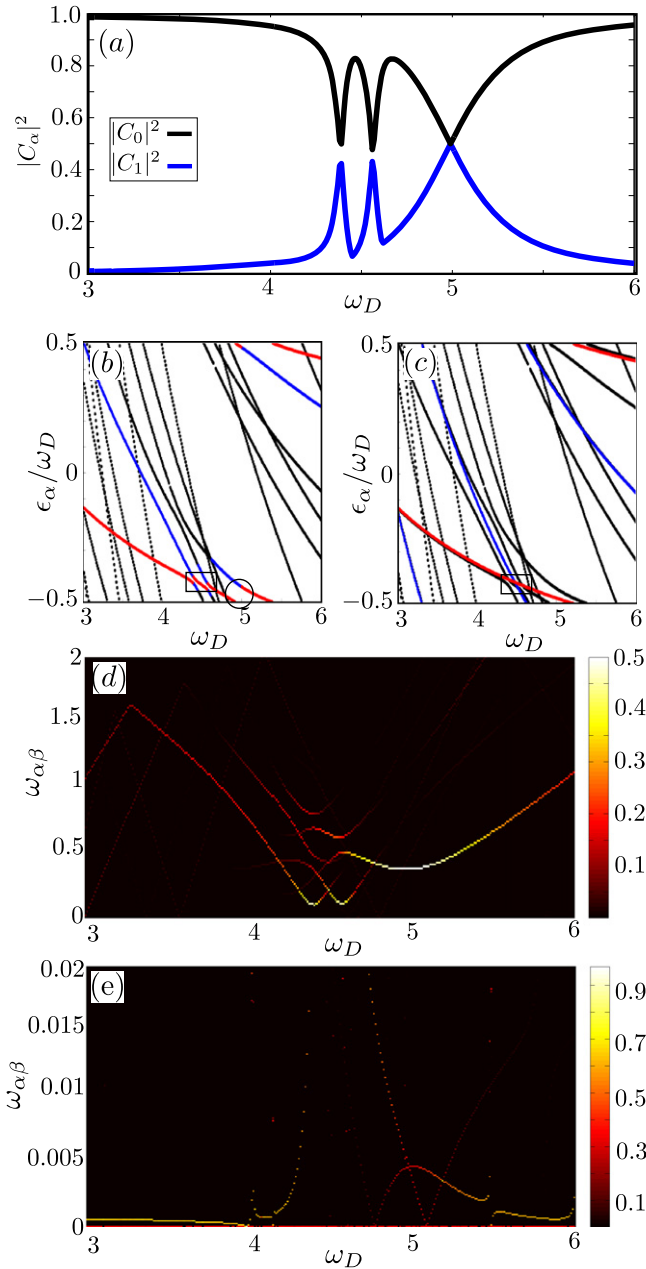


Figure 3. On-site dynamics for a single particle. (a) Populations $|C_0|^2$ and $|C_1|^2$ of the two most populated FMs. (b) QE spectrum as a function of the driving frequency ω_D (measured in units of ω_R). Highlighted are the most (red) and second most (blue) populated FMs. The rectangular area indicates the narrow avoided crossings, while the circle highlights the area where a broad avoided crossing among the FMs appears with respect to the driving frequency. (c) In black is again the QE spectrum (same as in (b)). Additionally, we show the most (red) and second most (blue) populated states of the static, i.e. undriven, lattice. For comparison, we depict again the black rectangle at the same position as in (b). (d) Frequencies $\omega_{\alpha\beta}$ of the on-site dynamics as a function of the driving frequency (see main text). (e) Same as (d), but in the triple well setup (shown is only the extract of small frequencies $\omega_{\alpha\beta} \ll \omega_D$ which corresponds to tunneling dynamics). In all panels $A = 0.05$.

obtained by studying the population of the FMs by the initial state as a function of ω_D . We therefore sort the FMs Ψ_α according to their overlap with the initial state and label the mode with the largest overlap as Ψ_0 , the mode with the

second largest overlap as Ψ_1 , etc. In figure 3(a) the coefficients of the two most populated FMs, $|C_0|^2$ and $|C_1|^2$ are shown as a function of the driving frequency. Apparently, both at small frequencies ($\omega_D \lesssim 4$) and at large ones ($\omega_D \gtrsim 5.5$) only a single FM is notably populated, while $|C_0|^2$ and $|C_1|^2$ become comparable at distinct driving frequencies (e.g. at $\omega_D \approx 5$). According to our discussion above, in cases when $|C_0|^2$ is close to one, and thus only a single FM is populated, the stroboscopic time evolution, as given by equation (6), becomes, to a good approximation, time periodic with the period of the driving T_D . Note that this agrees with the observation of figure 2(a), that away from the resonance frequencies, the single particle density merely performs oscillations whose period matches T_D . This corresponds precisely to the previously described micro-motion arising from the explicit time dependence of the FM $\Psi_0(x, t)$.

On resonance, when $|C_0|^2 \approx |C_1|^2$, the evolution of $|\Psi(x, 0)|^2$ includes, besides the micro-motion, an interference term between Ψ_0 and Ψ_1 , whose period is dictated by the corresponding quasi energies and is given by: $T_{\text{osc}}/T_D = \hbar\omega_D/(\epsilon_1 - \epsilon_0)$. Indeed, we find that this term is responsible for the observed on-site mode with a period of ~ 14 lattice oscillations (compare figure 2(b)). Up to now, however, it is not yet clear why Ψ_1 is resonantly populated at certain frequencies. In order to provide an answer to this question we follow the argumentation in [42] and consider the dependence of the QE spectrum on the driving frequency ω_D as shown in figure 3(b). Highlighted are the two most populated modes at each ω_D (blue and red dots) revealing avoided crossings of these two modes at the frequencies where a resonant enhancement of $|C_1|^2$ was observed in figure 2(b). Hence, at these values of ω_D the FMs Ψ_0 and Ψ_1 are resonantly coupled by the driving which results in an increase of $|C_1|^2$ and ultimately to the section in 3.1 describing on-site dynamics.

In the following we provide insight into the question why we observe Floquet resonances at driving frequencies around $\omega_D \sim 4.5$. Let us start by noting that, by means of appropriate unitary transformations, the single particle Hamiltonian with a potential as given in equation (1) can be recast into the form:

$$\tilde{H} = -\frac{\hbar^2}{2m} \frac{\partial^2}{\partial x^2} + V_0 \sin^2(k_0 x) + V_D \sin(\omega_D t)x, \quad (7)$$

where the amplitude of the oscillating term is given by $V_D = mA\omega_D^2$. That is, the transformed Hamiltonian takes the form of a static lattice plus a time-dependent perturbation whose strength is determined by V_D . For the used parameters of $m = 1$ and $A = 0.05$ and for the range of considered frequencies of $3 \lesssim \omega_D \lesssim 6$ we get that the amplitude V_D of the time-dependent term is of order one. Hence, it can be seen as a small perturbation compared to the static term of strength $V_0 = 15$ and we can expect that the QEs of the driven lattice setup can be estimated by the actual energies of the undriven lattice. Resonances would then be expected whenever the energy difference between two notably populated eigenstates of the static system matches an integer multiple of $\hbar\omega_D$. In fact we find that the energies of the three energetically lowest

states of even parity are given by $E_0 \approx 2.6$, $E_1 \approx 11.6$ and $E_2 = 16.9$. Naively, we expect driving induced resonances whenever the ground state is resonantly coupled to one of the excited states. Indeed we find $E_1 - E_0 \approx 2 \times 4.5$ and $E_2 - E_0 \approx 3 \times 4.8$. Thus, following this line of argument, at driving frequencies of approximately $\omega_D = 4.5$ the ground state of the unperturbed lattice is coupled via a 2 (3) photon process to the first (second) excited states. In order to justify this simplified picture we show the energies E_0 and E_1 on top of the QE spectrum of the driven lattice (see figure 3(c)). Away from any resonances, both energies are almost identical to the QEs of the corresponding Floquet states, so, for example, the red line is practically on top of an underlying black line. Closer to the resonance region, we see of course deviations of the QEs from the mere energies of the undriven lattice as the different states are coupled by the driving.

Finally, figure 3(d) provides an overview over the possibly observed frequencies in the on-site dynamics at various driving frequencies. Shown are the frequencies associated with all possible interference terms between the FMs weighted by their overlap with the initial state. More precisely, we calculate $\omega_{\alpha\beta} = (\epsilon_\alpha - \epsilon_\beta)/\hbar$ for all pairs of FMs at a given driving frequency and determine the color coding by computing the product $|C_\alpha^* C_\beta|$. Hence, the frequency $\omega_{\alpha\beta}$ appears in figure 3(d) only when both of the corresponding FMs Ψ_α and Ψ_β have appreciable overlap with the initial state. In agreement with the discussion concerning figure 3(b) we observe pronounced on-site oscillations only within an interval of driving frequencies $4.0 \lesssim \omega_D \lesssim 5.5$. In particular, the two narrow avoided crossings around $\omega_D^c \approx 4.5$ (see the rectangular in figure 3(b)) yield low frequency on-site dynamics, whereas the comparably broad avoided crossing at $\omega_D \approx 5$ (see the circle in figure 3(b)) results in a much faster on-site oscillation.

3.2.3. Tunneling dynamics in the triple well. Besides the on-site dynamics, figure 2(b) revealed a pronounced tunneling between the lattice sites at certain driving frequencies. Similar to the previous section, we analyze this effect in the following by applying Floquet theory for the single particle dynamics. We choose the same setup as before, that is, $V_{\text{sh}}(x, t) = V_0 \sin^2(x - A \sin(\omega_D t))$, with the same initial state, i.e. essentially a Gaussian centered around the potential well at $x = 0$, but with the difference that the periodic boundary conditions are imposed at $x = \pm 2\pi$ (instead of at $x = \pm \pi$ as we did before). In this way we allow for tunneling of the wave packet into the two neighboring lattice sites. As for the on-site dynamics, we provide an overview over the observable frequencies in the temporal evolution in figure 3(e) (in close analogy to figure 3(d)). Note that, since the tunneling dynamics observed in section 3.1 occurs on much longer timescales as compared to the on-site dynamics, we only show the extract of the regime of small frequencies, i.e. $\omega_{\alpha\beta} \ll \omega_D$. Furthermore, because no on-site dynamics occur with timescales matching the extremely small frequencies of $\lesssim 0.02$, all the frequencies depicted in figure 3(e) are indeed associated with an inter-well tunneling mode. In accordance with the observation made

in the many-particle simulations (see figure 2(b)) we observe a strong increase of the frequencies associated with the tunneling dynamics in the range of driving frequencies of $4 \lesssim \omega_D \lesssim 5.5$. Away from this resonance, for example at $\omega_D = 2.5$, the only notable tunneling mode corresponds to an interference term of two FMs which oscillates with a period of $T_{\text{osc}}/T_D \approx 3300$ and could therefore not be observed in the simulations performed in section 3.1. Within the regime of resonant driving, e.g. at $\omega_D = 4.5$, the frequency of the tunneling mode is increased strongly and the associated oscillation period becomes $T_{\text{osc}}/T_D \approx 200$ matching the observed tunneling mode in the weakly interacting regime (see figure 2(b)).

3.3. Interband tunneling and excitation processes

In the previous section we have shown that most of the features of the (effective) single-particle dynamics of figure 2 can be explained via a non-interacting Floquet theory. As we shall see now, however, the full dynamics presents a rich excitation spectrum ascribable to the particles interaction, especially in the strong interaction regime. Thus, we investigate the tunneling and excitation probabilities of the dominant particle configurations, for different driving frequencies ω_D , by means of the multiband expansion introduced in section 2.3. More precisely, we compute and analyze the probabilities, during the dynamics, defined as

$$|C_{\{N_i\};\mathbf{I}}|^2 = |\mathbf{I}\langle N_1, N_2, N_3 | \Psi(t) \rangle|^2. \quad (8)$$

The case $I_m^{(k)} = 0 \forall k > 1$ refers to the lowest-band inter-well tunneling dynamics. The initial state of the system corresponds to the ground state of four weakly interacting bosons with $g = 0.1$ in a triple well, while the dominant number state configuration (see also section 2.3) is $|1, 2, 1\rangle_{\mathbf{I}}$ with $I_L = I_R = (1, 0, 0)$ and $I_M = (2, 0, 0)$. In this way, a lowest-band tunneling process can take place among the initial state and: (a) another state of single-pair occupancy, e.g. $|2, 1, 1\rangle_{\mathbf{I}}$ ($I_L = (2, 0, 0)$ and $I_M = I_R = (1, 0, 0)$); (b) a state with double-pair occupancy, e.g. $|2, 2, 0\rangle_{\mathbf{I}}$ ($I_L = I_M = (2, 0, 0)$ and $I_R = (0, 0, 0)$); (c) a state with triple occupancy, e.g. $|3, 1, 0\rangle_{\mathbf{I}}$ ($I_L = (3, 0, 0)$, $I_M = (1, 0, 0)$, $I_R = (0, 0, 0)$); or (d) a state with quartic occupancy, e.g. $|4, 0, 0\rangle_{\mathbf{I}}$ ($I_L = (4, 0, 0)$ and $I_M = I_R = (0, 0, 0)$). However, from the system preferred tunneling processes form a hierarchy according to the energetical difference between the initial and final state. For instance, a tunneling process to another state of single-pair occupancy will be more preferable than to a state of double-pair occupancy, etc. Figure 4(a) shows the tunneling probability to the energetically closest number state, which is $|2, 1, 1\rangle_{\mathbf{I}}$ (or $|1, 1, 2\rangle_{\mathbf{I}}$) with $I_L = (2, 0, 0)$ and $I_M = I_R = (1, 0, 0)$ (or $I_L = I_M = (1, 0, 0)$ and $I_R = (2, 0, 0)$), i.e. $|D_{\{N_i\};\mathbf{I}}|^2 = |\mathbf{I}\langle 2, 1, 1 | \Psi(t) \rangle|^2$ with $I_L = (2, 0, 0)$ and $I_M = I_R = (1, 0, 0)$, for various driving frequencies. As is shown, for $\omega_D < \omega_D^c$ this tunneling mode has a small amplitude and it is quite insensitive to ω_D as intuitively expected from the fact that the evolved-state is essentially unperturbed by the driving (see also figure 1(a)). For $\omega_D \approx \omega_D^c$, however, the amplitude of the oscillations is

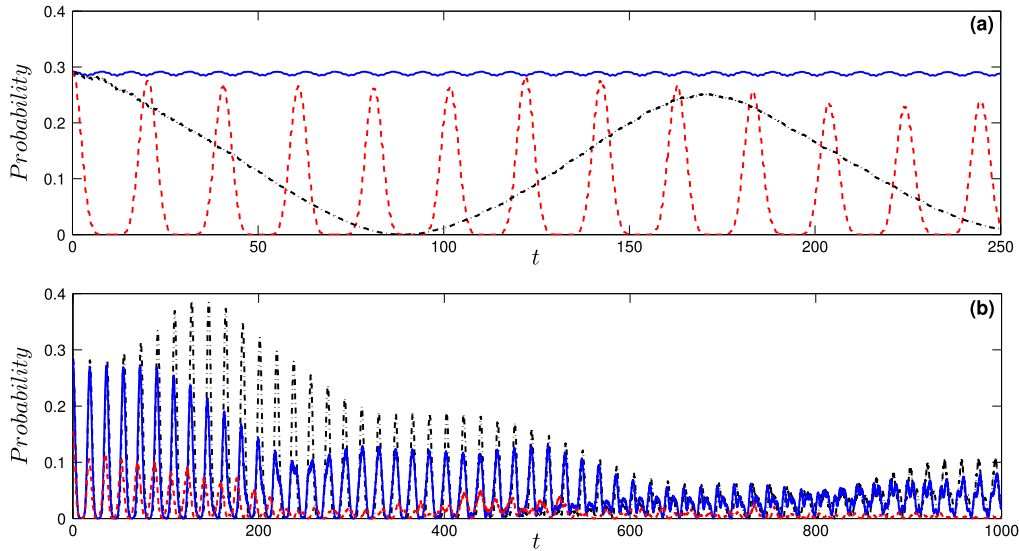


Figure 4. (a) Tunneling probability (see main text) $|D_{\{N_i\};\mathbf{I}}|^2 = |\langle \mathbf{I} | \Psi(t) \rangle|^2$ with $I_L = (2, 0, 0)$ and $I_R = I_M = (1, 0, 0)$ as a function of time for different driving frequencies $\omega_D = 0.5$ (blue solid line), $\omega_D = 4.5$ (red dashed line) and $\omega_D = 11.0$ (black dashed–dotted line). The most significant contribution of the interband tunneling mode is between the state $|2, 1, 1\rangle_{\mathbf{I}}$ (with $I_L = (2, 0, 0)$ and $I_R = I_M = (1, 0, 0)$) and the initial $|1, 2, 1\rangle_{\mathbf{I}}$ (with $I_M = (2, 0, 0)$ and $I_R = I_L = (1, 0, 0)$). (b) Inter-well tunneling probability $|D_{\{N_i\};\mathbf{I}}|^2$ at resonance for different values of the interatomic interaction $g = 0.1$ (black dashed–dotted line), $g = 0.5$ (blue solid line) and $g = 2.0$ (red dashed line). In all panels $A = 0.05$. The time evolution is expressed in units of ω_R^{-1} .

significantly larger indicating an enhancement of the tunneling (see also figures 2(b) and 3(e)), whereas when $F_{\omega_D} \ll 1$ and $\omega_D > \omega_D^c$ ($\omega_D = 11.0$ curve in figure 4(a)) the oscillations occur with a larger period. The fact that it oscillates with a larger time period can be traced back to the behavior of the fidelity at $\omega_D = 11$. Indeed, for short times ($\omega_D = 11.0$) the system stays in the initial ground state and after some time the fidelity starts to decrease, differently from the situation at $\omega_D = 4.5$, where the system deviates from the initial state on much shorter time scales. Concerning the remaining tunneling modes, i.e. tunneling to higher energetical states that belong to the lowest-band (see discussion above), they are negligible as they provide a very small contribution even for $\omega_D = \omega_D^c$. The latter has already been seen in the last subsection, but it can also be shown with the use of the multi-band analysis. On the other hand, figure 4(b) presents again the tunneling probability $|D_{\{N_i\};\mathbf{I}}|^2$ for the energetically closest lowest-band states (i.e. the same as figure 4(a)) when the driving frequency is at resonance for different interaction strengths g . For weak to intermediate interactions the tunneling amplitude decreases and for strong interactions, e.g. $g = 2.0$, a destruction of the tunneling is observed for long time scales.

Now, let us consider the excitation dynamics. In this case it holds $I_m^{(k)} \neq 0$ for $k > 1$. To this aim, we have analyzed the probability of finding all the four bosons in the zeroth-band. The latter can be expressed via equation (8) as $|B_{\{N_i\};\mathbf{I}}|^2 = \sum_{\mathbf{I}} |\langle N_1, N_2, N_3 | \Psi(t) \rangle|^2 = \sum_{\mathbf{I}} |C_{\{N_i\};\mathbf{I}}|^2$, where the summation is performed over the excitation indices $\mathbf{I} = (I_L, I_M, I_R)$ which, in terms of the multiband expansion, obey the constraints $I_L^{(1)} + I_M^{(1)} + I_R^{(1)} = N$ and $I_L^{(j)} = I_M^{(j)} = I_R^{(j)} = 0$ for all $j > 1$. In particular, figure 5(a) shows the probability $|B_{\{N_i\};\mathbf{I}}|^2$ for all the bosons to reside in the zeroth-band for various driving frequencies ω_D and a fixed amplitude

$A = 0.05$ during the time evolution. At the critical driving frequency a complete depopulation of the zeroth-band at some specific time intervals is observed. In particular, this probability exhibits revivals, which are connected with the enhancement of the (amplitude) oscillations of the single-particle density (see also figure 2(b)). On the other hand, for driving frequencies different from the critical frequency the respective probability of all the bosons occupying the zeroth-band is rather large and is indeed dominant. However contributions from excited configurations cannot be neglected, especially in the regions $7.0 < \omega_D < 8.0$ and $10.0 < \omega_D < 15.0$, where the system significantly departs from the initial state (see also figures 1(a) and 5(a) red dashed line). Furthermore, figure 5(b) presents the probability, at the critical driving frequency, of obtaining a state of $N_0 \leq 4$ particles in the first-excited band and the remaining to be in the zeroth-band. The latter can be expressed as $|Q_{\{N_i\};\mathbf{I}}|^2 = \sum_{\mathbf{I}} |C_{\{N_i\};\mathbf{I}}|^2$, where the summation index $\mathbf{I} = (I_L, I_M, I_R)$ obeys the constraints $I_L^{(1)} + I_M^{(1)} + I_R^{(1)} = N - N_0$, $I_L^{(2)} = I_M^{(2)} = I_R^{(2)} = N_0$ and $I_L^{(j)} + I_M^{(j)} + I_R^{(j)} = 0$ for all $j > 2$. Indeed, the interplay between the four possible excitation scenarios from the zeroth to the first excited-band (i.e. one-particle excitation, two-particle excitation, etc) in the course of the dynamics is illustrated in a transparent way. It is observed that the complete depopulation of the zeroth-band is mainly accompanied by the excitation of three or all the four bosons in the first-excited band. For long evolution times, the zeroth-band possesses a low population and states with one or two bosons in the first excited-band are mainly populated. The states with the most significant contribution are of the type $|1, 2, 1\rangle_{\mathbf{I}}$ with $I_L = I_R = (0, 1, 0)$ and $I_M = (0, 2, 0)$ or $I_M = (1, 1, 0)$. We note that a small contribution comes from the state $|1, 2, 1\rangle_{\mathbf{I}}$ with $I_L = I_R = (0, 1, 0)$ and $I_M = (0, 1, 1)$. This clearly shows

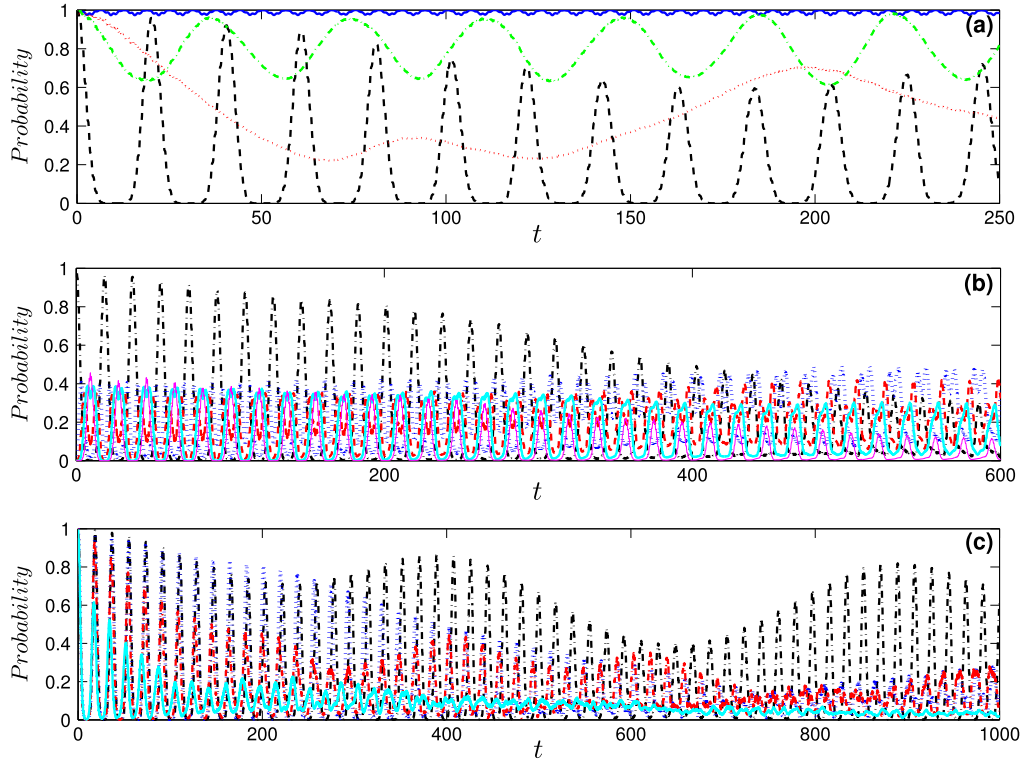


Figure 5. (a) Probability $|B_{\{N_i\};\mathbf{I}}|^2$ (see main text) of all bosons being in the zeroth-band during the evolution for different driving frequencies $\omega_D = 2.0$ (blue solid line), $\omega_D = 4.5$ (black dashed line), $\omega_D = 10.25$ (red dotted line) and $\omega_D = 11.75$ (green dashed-dotted line). (b) Comparison of different excitation scenarios at $\omega_D = 4.375$. The black dashed-dotted line refers to the probability of all the bosons being in the zeroth-band while the blue dotted, red dashed, light-blue thick solid and magenta thin solid line refer to the probability of having one, two, three or four bosons, respectively, in the first-excited band. (c) Probability $|B_{\{N_i\};\mathbf{I}}|^2$ of all the bosons being in the zeroth-band for $\omega_D = \omega_D^c$, but with different interparticle repulsion $g = 0$ (black dashed-dotted), $g = 0.1$ (blue dotted line), $g = 0.5$ (red dashed-dotted line) and $g = 2.0$ (light-blue solid line). In all panels $A = 0.05$. The time evolution is expressed in units of ω_R^{-1} .

that the most prominent excitation process in our system originates from the energy difference between each of the above states and $|1, 2, 1\rangle_I$ with $I_L = I_R = (1, 0, 0)$ and $I_M = (2, 0, 0)$, namely the (initial) ground state configuration.

Finally, in order to explore the impact of the interactions on the dynamics, figure 5(c) shows the probability $|B_{\{N_i\};\mathbf{I}}|^2$ for long evolution times of all the bosons being in the zeroth-band for different interparticle repulsion at the driving frequency $\omega_D = \omega_D^c$. For the non-interacting case the population of the zeroth-band shows revivals even for long time scales, while, as the interaction strength is turned on, the corresponding probability presents a decaying envelope. This envelope behavior is a pure effect of the interactions and reflects also the initial ground state configuration (see the discussion in section 2.3) which strongly depends on the interparticle interactions. As can be seen for increasing repulsion between the particles the probability of the system remaining in the zeroth-band, in the course of the dynamics, decays on increasingly shorter time scales and the system is dominated by different types of excitations, as expected intuitively.

3.4. Characteristics of the resonant behavior

To characterize the overall process with respect to the driving frequency, we compute the spectrum of the local one-body

density

$$\rho_\alpha(\omega) = \frac{1}{\pi} \int_0^T dt \rho_\alpha(t) e^{i\omega t}, \quad (9)$$

where $\rho_\alpha(t) = \int_{d_\alpha}^{d'_\alpha} dx \rho_1(x, t)$ denotes the spatially over a single well integrated single-particle density at every time instant t . The index $\alpha = L, M, R$ corresponds to the left, middle or right well respectively, whereas the limits of the wells are denoted by d_α, d'_α . Note that in the present case all the components of $\rho_\alpha(\omega)$, i.e. $\rho_L(\omega), \rho_M(\omega)$ and $\rho_R(\omega)$, are equivalent due to the considered large lattice depths and the employed driving scheme which enforces the bosons among different wells to oscillate in-phase. Figure 6 shows the above spectrum, where five dominant branches (denoted as (1)–(5) in the figure) can be observed. The lowest branch denoted as (1) in figure 6 (in the range $\omega \in [0, 0.02]$) refers to the intraband tunneling being restricted to the energetically closest number states, e.g. from $|1, 2, 1\rangle_I$ ($I_M = (2, 0, 0), I_L = I_R = (1, 0, 0)$) to $|2, 1, 1\rangle_I$ ($I_L = (2, 0, 0), I_M = I_R = (1, 0, 0)$). This branch is hardly visible in figure 6 due to the presented wide range of frequencies that have been taken into account in order to visualize all the dynamical frequencies of the system. In addition, the next lowest branch (denoted as (2)) at $\omega_D \in [4, 5]$ and $\omega \in [0.05, 1]$ corresponds to the large amplitude density oscillations (see also figure 2(b)). These

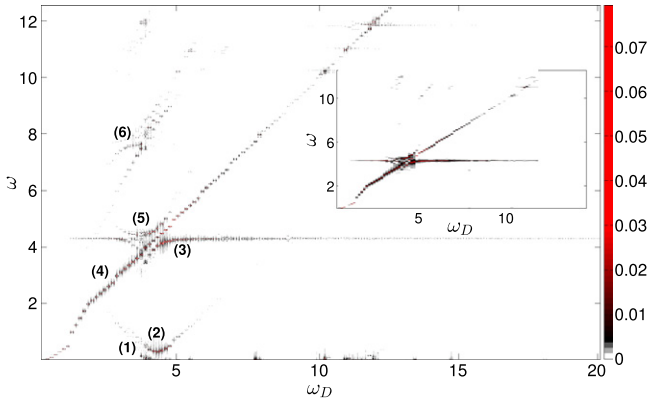


Figure 6. Local one-body density spectrum $\rho_L(\omega)$ (for the left well) as a function of the driving frequency ω_D (measured in units of ω_R). The driving amplitude has been chosen $A = 0.05$. Inset: the spectrum of the intra-well oscillations calculated via $\Delta\rho_L(t)$ (see also main text).

mode frequencies have already been predicted via the Floquet analysis in section 3.2 (see figures 3(d) and (e)). To investigate in some detail the intra-well wavepacket dynamics the quantity $\Delta\rho_\alpha(t) = \rho_{\alpha,1}(t) - \rho_{\alpha,2}(t)$ is employed. Here, each well is divided from the center into two equal parts, namely left and right, with $\rho_{\alpha,1}(t)$, $\rho_{\alpha,2}(t)$ being the corresponding integrated densities at time t . The index $\alpha = L, M, R$ stands for the left, middle and right well, respectively. To determine the frequencies of this mode we calculate the spectrum $\Delta\rho_L(\omega) = \frac{1}{\pi} \int dt \Delta\rho_L(t) e^{i\omega t}$. The inset of figure 6 presents the corresponding spectrum, thus showing the emergent frequencies of the intra-well oscillations as a function of the driving frequency ω_D . We observe that the spectrum $\Delta\rho_L(\omega)$ follows the evolution of the upper three branches (denoted by (3)–(5)) of the spectrum of $\rho_L(\omega)$, whereas in the region of the resonance the intra-well oscillation measured via $\Delta\rho_L(t)$ features a beating dynamics, as expected. Hence, away from the region around the critical driving frequency the generated dipole mode possesses three different frequencies, while close to ω_D^c the intra-well dynamics come into a resonance. Therefore, one can induce this resonant intra-well dynamics by adjusting the driving frequency. Finally, let us comment on the existence of some higher frequency components, e.g. branch (6) in figure 6, which correspond to very fast intrawell oscillations (i.e. $\omega \ll \omega_D$) and possess a low amplitude (in comparison to the previous branches (1)–(5)).

In turn, we shall visualize the above mentioned resonance and inspect how it depends on the lattice parameters. To this aim, the minimal occupancy, during the evolution time T , of the zeroth-band $\min_{t \in [0, T]} P_0(t) = \min_{t \in [0, T]} \sum_{\mathbf{I}} |\langle N_1, N_2, N_3 | \Psi(t) \rangle|^2$, with the energetical indices $I_L^{(1)} + I_M^{(1)} + I_R^{(1)} = N$ and $I_L^{(j)} = I_M^{(j)} = I_R^{(j)} = 0$ for every $j > 1$ is used. Employing the above quantity one can show that far from resonance there are regions with non-negligible excitations, i.e. $\min_{t \in [0, T]} P_0 < 1$ (e.g. at $\omega_D = 11.0$; see also figure 1(a)) as well as regions where $\min_{t \in [0, T]} P_0 \approx 1$ (e.g. $\omega_D = 2.0$ in figure 1(a)). Now let us analyze the dependence

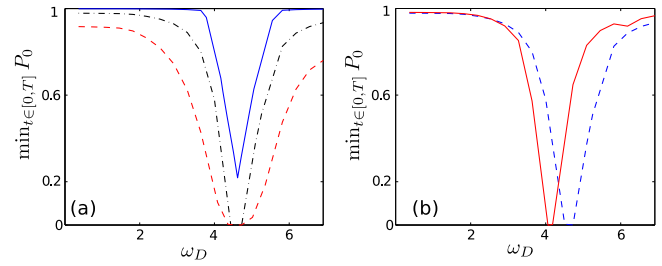


Figure 7. (a) Profile of the resonance for various driving amplitudes $A = 0.01$ (blue solid line), $A = 0.05$ (black dashed–dotted line) and $A = 0.1$ (red dashed line) obtained from the $\min_{t \in [0, T]} P_0(t)$ and T being some fixed long evolution time as a function of the driving frequency. (b) Same as (a) with $A = 0.05$, but for different barrier heights $V_0 = 9.0$ (red solid line) and $V_0 = 12.0$ (blue dashed line). The system consists of four bosons confined in a triple-well with interparticle interaction $g = 0.1$.

of $\min_{t \in [0, T]} P_0$ on the driving frequency around ω_D^c . Firstly we study the dependence of the resonance on the driving amplitude. In figure 7(a) we show for an increasing driving amplitude the minimum of $\min_{t \in [0, T]} P_0$ as a function of the frequency ω_D which broadens and eventually reaches zero, meaning that the zeroth-band has been completely depopulated (see also figure 5(a)). On the other hand, for small amplitudes the value of the minimum of $\min_{t \in [0, T]} P_0$ is non-zero and in the limit $A \rightarrow 0$ its dependence on the driving frequency disappears. Instead, in figure 7(b) we show how the minimal population of the zeroth-band ($\min_{t \in [0, T]} P_0$) varies as a function of the lattice depth. For an increasing lattice depth it is known that the energy gaps among the different energy levels become larger. This phenomenon can intuitively be understood in terms of a tight-binding approximation. For simplicity let us assume only a nearest neighbor coupling $J \propto \int dx W_s(x) \left[\frac{p^2}{2m} + V_0 \sin^2(x) \right] W_{s+1}(x)$ between the sites s and $s + 1$, where $W_s(x)$ are the on-site localized Wannier states. Then, within this approximation, which is valid for a relatively deep potential, the resulting eigenvalues are $E_{k-1} = E_0^{\text{on-site}} - 2J \cos\left(\frac{k\pi}{N+1}\right)$ ($k = 1, 2, \dots, N$), where $E_0^{\text{on-site}}$ are the on-site energies. Thus, the resonance can be tuned at will, i.e. for a decreasing lattice depth the ω_D^c is negatively shifted, as is confirmed by the numerical results of figure 7(b). Finally, let us comment on the dependence of the position of the resonance on the interparticle interaction strength g . Indeed, in order to investigate whether there is such a dependence, various interaction strengths (for the same particle number $N = 4$), e.g. $g = 0.1$, $g = 1.0$ and $g = 3.0$, have been considered (omitted here for brevity) and it was found that the position of the resonance is essentially unaffected.

In the following, let us inspect the momentum distribution with varying driving frequencies with the aim of understanding whether signatures of a parametric amplification of matter-waves can be observed. The momentum distribution is a routinely employed observable in atomic quantum gas experiments as it is accessible via time-of-flight measurements [4]. This quantity can be calculated as the

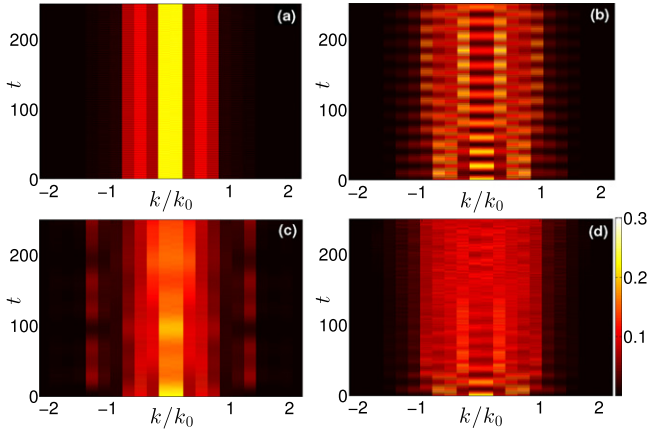


Figure 8. Momentum distribution of the one-body density as a function of time (measured in units of ω_R^{-1}) for $g = 0.1$ and different driving frequencies (a) before the critical frequency $\omega_D = 2.0$, (b) at the critical frequency $\omega_D = \omega_D^c = 4.5$ and (c) at $\omega_D = 8.0$. (d) The case of strong interparticle repulsion for $g = 2.0$ and $\omega_D = \omega_D^c$. The horizontal axis represents the lattice momenta in units of the inverse lattice vector $k_0 = \pi/l$. In all panels $A = 0.05$.

Fourier transformation of the one-body reduced density matrix as

$$n(k, t) = \frac{1}{2\pi} \int \int dx dx' \rho_1(x, x'; t) e^{-ik(x-x')}. \quad (10)$$

Here $\rho_1(x, x'; t)$ denotes the one-body reduced density matrix, being obtained by tracing out all the bosons but one in the density of the N -body system. The panels (a)–(c) of figure 8 present the time evolution of the momentum distribution for different driving frequencies before, on, and after the resonance. As can be noted, exactly at the resonance the momentum distribution exhibits a special pattern, that is, some additional lattice momenta are periodically activated during the dynamics. In particular, it is observed that the modes $\pm \frac{k_0}{2} \simeq \pm 1.57$, $\pm k_0 \simeq \pm 3.14$, $\pm \frac{3k_0}{2} \simeq \pm 4.713$ are populated, whereas out of resonance only the $\pm k_0$ modes are significantly populated. The population of the $\pm k_0/2, \pm 3k_0/2$ modes at $\omega_D = \omega_D^c$ is reminiscent of the parametric amplification of matter-wave phenomenon, as observed experimentally in [21]. However, an exact correspondence with [21] cannot be made due to the very different setup of our system, i.e. its finite size and the hard wall boundaries. A detailed study of this process, also for higher particle numbers and lattice potentials, would be desirable, but it is clearly beyond the scope of this work. Furthermore, figure 8(d) shows the momentum distribution at resonance, but for a strong interparticle repulsion $g = 2.0$. The expected periodic pattern for large evolution times is blurred as an effect of the strong interaction which decreases the degree of coherence.

Finally, in order to demonstrate that our findings are of general character we investigate a larger lattice system with a filling factor smaller than unity. Specifically, the case of five bosons in a twelve-well finite lattice has been considered. Concerning the ground state with filling factor $\nu < 1$, the most important aspect is the spatial redistribution of the atoms as the interaction strength increases. Indeed, as the repulsion

increases from the non-interacting to the weak interaction regime the atoms are pushed from the central to the outer sites which gain and lose population in the course of increasing g .

In the following, the shaking dynamics applied at $t = 0$ to the ground state of the five bosons which are trapped in the twelve-well potential in the weak interaction regime ($g = 0.1$) is explored. The emergent non-equilibrium behavior shows similar characteristics as in the previous setup with filling $\nu > 1$, i.e. the occurrence of an intrawell dipole and an interwell tunneling mode. Interestingly, at the same frequency $\omega_D = \omega_D^c = 4.5$ a resonance of the intra-well dynamics is observed. Figure 9 presents the one-body density evolution exactly at the critical point ω_D^c . As in the case for setups with filling $\nu > 1$, the formation of enhanced density oscillations at each site is observed, which is in relation to the time periods where the zeroth-band is completely depopulated during the evolution. Employing a corresponding number state analysis the significant contribution of two kinds of number states has been confirmed: (a) either $I_1^{(1)} + \dots + I_{12}^{(1)} = N - 1$, $I_1^{(3)} = \dots = I_{12}^{(3)} = 0$ and one with $I_k^{(2)} = 1$ for $k = 1, \dots, 12$ or (b) $I_1^{(1)} + \dots + I_{12}^{(1)} = N - 1$, $I_1^{(2)} = \dots = I_{12}^{(2)} = 0$ and a certain $I_k^{(3)} = 1$ for $k = 1, \dots, 12$. Notice that the same kind of number states have been found to contribute significantly also in the dynamics of four bosons in the triple-well. The above mentioned observations suggest a generalization of the observed phenomena to larger systems as well. Indeed, the same shaken scheme has been tested in different systems (omitted here for brevity), e.g. ten bosons in a triple-well, six bosons in five wells, etc, confirming that the above observed resonant-like behavior of the bosonic ensemble occurs in each setup.

4. Conclusions and outlook

The correlated non-equilibrium quantum dynamics of few-body bosonic ensembles induced by the driving of a finite-size optical lattice has been investigated. Our work focuses particularly on the regimes of large lattice depths and small driving amplitudes. This choice has been made in order to limit the degree of excitations that would otherwise lead to heating processes. Starting from the ground state of a weak or strongly interacting small ensemble, we have examined in detail the time evolution of the system induced by periodically driving the optical lattice. We find that the dynamical evolution of the system is governed by two main modes: the inter-well tunneling and the intra-well dipole-like mode. The dynamical behavior of the system in the non-interacting regime has been firstly analyzed via Floquet theory, that is, at the single-particle level, providing an accurate interpretation of the observed processes. For large particle numbers and large interaction strengths, however, such a single-particle description was not sufficient anymore to provide an exhaustive explanation of the observed dynamics, and a multi-band Wannier number state expansion has been employed.

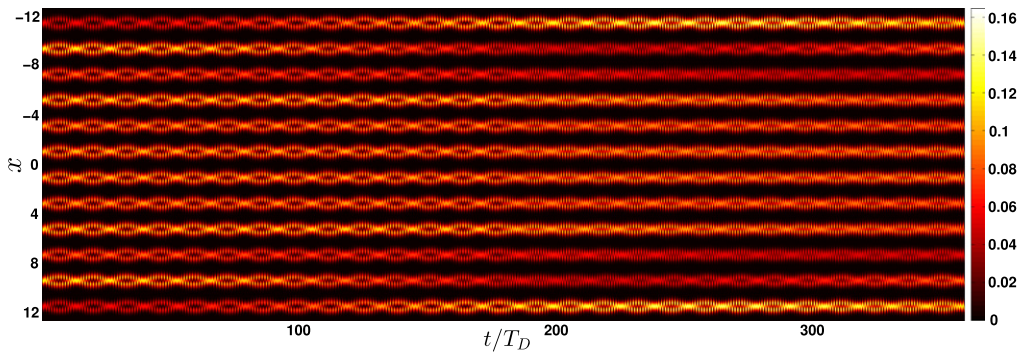


Figure 9. Time evolution of the one-body density $\rho_1(x, t)$ in a twelve-well potential for $\omega_D = 4.5$. The driving amplitude is fixed to the value $A = 0.05$, while the initial state corresponds to the ground state of five weakly interacting bosons with $g = 0.1$. The spatial extent of the lattice is expressed in units of k_0^{-1} , while the time units are rescaled in terms of the driving period T_D .

The inter-well tunneling mode is weak as a consequence of the deep optical lattice and the small driving amplitude. On the other hand, the local dipole mode has been identified from the intra-well oscillations of bosons in the individual wells. Remarkably enough, it has been found that by tuning the driving frequency the intra-well dynamics experiences a resonant-like behavior. This is manifested, for example, by the enhanced oscillations in the one-body density evolution or from the periodic population of additional lattice momenta in the momentum distribution of the one-body density. Additionally, on a single-particle level in terms of Floquet theory, it has been shown that in the proximity of the resonance the first two FMs possess the main contribution, while away from resonance the dynamics can be described with the inclusion of the first FM. To explain the enhanced population of the second FM at resonance the corresponding quasienergy spectrum has been employed, revealing avoided-crossings between the first two FMs at certain driving frequencies. To obtain the frequencies which refer to the on-site and tunneling dynamics, the corresponding frequencies associated with the interference terms between the FMs have been employed showing pronounced on-site oscillations and an enhancement of the inter-well tunneling mode in the vicinity of the resonance. Considering an ensemble of few-bosons we examined the influence of the interatomic interactions both for the inter- and intra-well generated modes. Indeed, it has been found that the repulsion affects each of the aforementioned modes, yielding a destruction of the inter-well tunneling for strong interactions and an enhancement of the excitations (i.e. the contribution of higher-band states). Moreover, in the spectrum of the local one-body density with respect to the driving frequency all the relative dynamical frequencies, e.g. on-site oscillations and tunneling period have been identified. Finally, the occurrence of the above resonance seems to be universal in a periodically driven lattice as it is independent of the filling factor, the boundary conditions or the interparticle repulsion.

We would like to underline the fact that, contrary to related studies based, for example, on effective model Hamiltonians or lattice calculations with tensor network methods, our many-body analysis based on the *ab initio* MCTDHB method has the advantage of providing the

complete system wavefunction in space and time. Thus, it enables us to accurately identify the involved intra- and inter-well band excitations.

Let us comment on possible future investigations. Although in the present work we did not employ the multi-layer structure of the multi-layer multiconfiguration time-dependent Hartree method for bosons (ML-MCTDHB) method, our *ab initio* approach is well suited to describe the dynamics of multi bosonic species. Given this, a first natural extension would be to study the driven dynamics of mixtures consisting of different bosonic species in order to unravel the induced excitation modes or to devise schemes for selective transport of an individual bosonic component. In relation to the present study, it would be interesting to simulate the parametrical amplification of matter-waves with interesting applications, like the generation of four-wave mixing, entanglement production, but also for fundamental tests of quantum mechanics with massive particles like the Hong–Ou–Mandel experiment, as recently performed with a Bose–Einstein condensate [23].

Acknowledgments

SM thanks the Hamburgisches Gesetz zur Förderung des wissenschaftlichen und künstlerischen Nachwuchses (HmbNFG) for a PhD Scholarship. PS gratefully acknowledges funding by the Deutsche Forschungsgemeinschaft (DFG) in the framework of the SFB 925 ‘Light induced dynamics and control of correlated quantum systems’. AN gratefully acknowledges discussions with Klaus Mølmer related to four-wave mixing.

Appendix. The computational method: ML-MCTDHB and MCTDHB

Our computational approach to solve the many-body Schrödinger equation of the interacting bosons relies on the ML-MCTDHB [43, 44] which constitutes an *ab initio* method for the calculation of stationary properties and in particular the non-equilibrium quantum dynamics of bosonic systems of

different species. For a single species it reduces to MCTDHB which has been established in [32, 33, 45] and applied extensively [45–48]. The wavefunction is represented by a set of variationally optimized time-dependent orbitals which implies an optimal truncation of the Hilbert space by employing a time-dependent moving basis where the system can be instantaneously optimally represented by the corresponding time-dependent permanents. To be self contained let us briefly introduce the basic concepts of the method and discuss the main ingredients of our implementation.

Within the MCTDHB method the TDSE $(i\hbar\partial_t - H)\Psi(x, t) = 0$ is solved as an initial value problem $|\Psi(0)\rangle = |\Psi_0\rangle$. The many-body wavefunction which is expanded in terms of the bosonic number states $|n_1, n_2, \dots, n_M; t\rangle$, based on time-dependent single-particle functions (SPFs) $|\phi_i(t)\rangle$, $i = 1, 2, \dots, M$, reads

$$|\Psi(t)\rangle = \sum_{\vec{n}} C_{\vec{n}}(t) |n_1, n_2, \dots, n_M; t\rangle. \quad (\text{A1})$$

Here M is the number of SPFs and the summation \vec{n} is over all the possible particle combinations n_i such that the total number of bosons is conserved and equal to N . To determine the time-dependent wave function $|\Psi(t)\rangle$ we need the equations of motion for the coefficients $C_{\vec{n}}(t)$ and of the SPFs $|\phi_i(t)\rangle$. Following the Dirac–Frenkel [49, 50] variational principle, i.e. $\langle\delta\Psi| i\partial_t - \hat{H} |\Psi\rangle = 0$ we end up with the well-known MCTDHB equations of motion [32, 33, 45, 51] consisting of a set of M nonlinear integro-differential equations of motion for the orbitals which are coupled to the $\frac{(N+M-1)!}{N!(M-1)!}$ linear equations of motion for the coefficients.

For our numerical implementation a discrete variable representation (DVR) for the SPFs and a sin-DVR, which intrinsically introduces hard-wall boundaries at both edges of the potential, has been employed. The preparation of the initial state has been performed by using the so-called relaxation method in terms of which one obtains the lowest eigenstates of the corresponding m -well setup. The key idea is to propagate some trial wave function $\Psi^{(0)}(x)$ by the non-unitary operator $e^{-H\tau}$. This is equivalent to an imaginary time propagation and for $\tau \rightarrow \infty$, the propagation converges to the ground state, as all other contributions (i.e. $e^{-E_n\tau}$) are exponentially suppressed. In turn, we periodically drive the optical lattice and study the evolution of $\Psi(x_1, x_2, \dots, x_N; t)$ in the m -well potential within MCTDHB. To ensure the convergence of our simulations we have used up to nine single particle functions thereby observing a systematic convergence of our results for sufficiently large spatial grids. An additional criterion that confirms the achieved convergence is the population of the lowest occupied natural orbital kept in each case below 0.1%.

References

- [1] Goldman N and Dalibard J 2014 *Phys. Rev. X* **4** 031027
- [2] Goldman N, Dalibard J, Aidelsburger M and Cooper N R 2015 *Phys. Rev. A* **91** 033632
- [3] Morsch O and Oberthaler M 2006 *Rev. Mod. Phys.* **78** 179
- [4] Bloch I, Dalibard J and Zwerger W 2008 *Rev. Mod. Phys.* **80** 885
- [5] Olshani M 1998 *Phys. Rev. Lett.* **81** 938
- [6] Grimm R, Weidemüller M and Ovchinnikov Y B 2000 *Adv. At. Mol. Opt. Phys.* **42** 95–170
- [7] Santos L, Baranov M A, Cirac J I, Everts H U, Fehrmann H and Lewenstein M 2004 *Phys. Rev. Lett.* **93** 030601
- [8] Inouye S, Goldwin J, Olsen M L, Ticknor C, Bohn J L and Jin D S 2004 *Phys. Rev. Lett.* **93** 183201
- [9] Köhler T, Goral K and Julienne P S 2006 *Rev. Mod. Phys.* **78** 1311
- [10] Chin C, Grimm R, Julienne P and Tiesinga E 2010 *Rev. Mod. Phys.* **82** 1225
- [11] Lewenstein M, Sanpera A and Ahufinger V 2012 *Ultracold Atoms in Optical Lattices: Simulating Quantum Many-body Systems* (Oxford: Oxford University Press)
- [12] Choi D I and Niu Q 1999 *Phys. Rev. Lett.* **82** 2022
- [13] Dahan M B, Peik E, Reichel J, Castin Y and Salomon C 1996 *Phys. Rev. Lett.* **76** 4508
- [14] Morsch O, Müller J H, Cristiani M, Ciampini D and Arimondo E 2001 *Phys. Rev. Lett.* **87** 140402
- [15] Peik E, Dahan M B, Bouchoule I, Castin Y and Salomon C 1997 *Phys. Rev. A* **55** 2989
- [16] Cristiani M, Morsch O, Müller J H, Ciampini D and Arimondo E 2002 *Phys. Rev. A* **65** 063612
- [17] Wilkinson S R, Bharucha C F, Madison K W, Niu Q and Raizen M G 1996 *Phys. Rev. Lett.* **76** 4512
- [18] Niu Q, Zhao X G, Georgakis G A and Raizen M G 1996 *Phys. Rev. Lett.* **76** 4504
- [19] Sias C, Lignier H, Singh Y P, Zenesini A, Ciampini D, Morsch O and Arimondo E 2008 *Phys. Rev. Lett.* **100** 040404
- [20] Eckardt A, Weiss C and Holthaus M 2005 *Phys. Rev. Lett.* **95** 260404
- [21] Gemelke N, Sarajlic E, Bidet Y, Hong S and Chu S 2005 *Phys. Rev. Lett.* **95** 170404
- [22] Hilligsøe K M and Mølmer K 2005 *Phys. Rev. A* **71** 041602
- [23] Lopes R, Imanaliev A, Aspect A, Cheneau M, Boiron D and Westbrook C I 2015 *Nature* **520** 7545
- [24] Zheng W and Zhai H 2014 *Phys. Rev. A* **89** 061603
- [25] Lignier H, Sias C, Ciampini D, Singh Y, Zenesini A, Morsch O and Arimondo E 2007 *Phys. Rev. Lett.* **99** 220403
- [26] Struck J, Ölschläger C, Weinberg M, Hauke P, Simonet J, Eckardt A, Lewenstein M, Sengstock K and Windpassinger P 2012 *Phys. Rev. Lett.* **108** 225304
- [27] Parker C V, Ha L C and Chin C 2013 *Nat. Phys.* **9** 769–74
- [28] Choudhury S and Mueller E J 2014 *Phys. Rev. A* **90** 013621
- [29] Sträter C and Eckardt A 2015 *Phys. Rev. A* **91** 053602
- [30] Iucci A, Cazalilla M A, Ho A F and Giamarchi T 2006 *Phys. Rev. A* **73** 041608
- [31] Schneider P I and Saenz A 2012 *Phys. Rev. A* **85** 050304
- [32] Alon O E, Streltsov A I and Cederbaum L S 2007 *J. Chem. Phys.* **127** 154103
- [33] Alon O E, Streltsov A I and Cederbaum L S 2008 *Phys. Rev. A* **77** 033613
- [34] Kim J I, Melezhik V S and Schmelcher P 2006 *Phys. Rev. Lett.* **97** 193203
- [35] Giannakeas P, Diakonou F K and Schmelcher P 2012 *Phys. Rev. A* **86** 042703
- [36] Mistakidis S I, Cao L and Schmelcher P 2014 *J. Phys. B: At. Mol. Opt. Phys.* **47** 225303
- [37] Mistakidis S I, Cao L and Schmelcher P 2014 *Phys. Rev. A* **91** 033611

- [38] Gorin T, Prosen T, Seligman T H and Žnidarič M 2006 *Phys. Rep.* **435** 33
- [39] Tannor D J 2007 *Introduction to Quantum Mechanics: A Time-Dependent Perspective* (Mill Valley, CA: University Science Books)
- [40] Grifoni M and Hänggi P 1998 *Phys. Rep.* **304** 229–354
- [41] Wulf T, Petri C, Liebchen B and Schmelcher P 2014 *Phys. Rev. E* **90** 042913
- [42] Wulf T, Liebchen B and Schmelcher P 2015 *Phys. Rev. A* **91** 043628
- [43] Cao L, Krönke S, Vendrell O and Schmelcher P 2013 *J. Chem. Phys.* **139** 134103
- [44] Krönke S, Cao L, Vendrell O and Schmelcher P 2013 *New J. Phys.* **15** 063018
- [45] Streltsov A I, Alon O E and Cederbaum L S 2007 *Phys. Rev. Lett.* **99** 030402
- [46] Streltsov A I, Sakmann K, Alon O E and Cederbaum L S 2011 *Phys. Rev. A* **83** 043604
- [47] Alon O E, Streltsov A I and Cederbaum L S 2007 *Phys. Rev. A* **76** 013611
- [48] Alon O E, Streltsov A I and Cederbaum L S 2009 *Phys. Rev. A* **79** 022503
- [49] Frenkel J (ed) 1934 *Wave Mechanics* 1st edn (Oxford: Clarendon Press) pp 423–8
- [50] Dirac P A 1930 *Proc. Camb. Phil. Soc.* vol 26 (Cambridge: Cambridge University Press) pp 376–85
- [51] Broeckhove J, Lathouwers L, Kesteloot E and van Leuven P 1988 *Chem. Phys. Lett.* **149** 547

4.2.2 Mode Coupling of Interaction Quenched Ultracold Few-Boson Ensembles in Periodically Driven Lattices

Mode coupling of interaction quenched ultracold few-boson ensembles in periodically driven latticesS. I. Mistakidis¹ and P. Schmelcher^{1,2}¹*Zentrum für Optische Quantentechnologien, Universität Hamburg, Luruper Chaussee 149, 22761 Hamburg, Germany*²*The Hamburg Centre for Ultrafast Imaging, Universität Hamburg, Luruper Chaussee 149, 22761 Hamburg, Germany*

(Received 11 April 2016; published 24 January 2017)

The out-of-equilibrium dynamics of interaction quenched finite ultracold bosonic ensembles in periodically driven one-dimensional optical lattices is investigated. It is shown that periodic driving enforces the bosons in the outer wells of the finite lattice to exhibit out-of-phase dipolelike modes, while in the central well the atomic cloud experiences a local breathing mode. The dynamical behavior is investigated with varying driving frequencies, revealing resonantlike behavior of the intrawell dynamics. An interaction quench in the periodically driven lattice gives rise to admixtures of different excitations in the outer wells, enhanced breathing in the center, and amplification of the tunneling dynamics. We then observe multiple resonances between the inter- and the intrawell dynamics at different quench amplitudes, with the position of the resonances being tunable via the driving frequency. Our results pave the way for future investigations of the use of combined driving protocols in order to excite different inter- and intrawell modes and to subsequently control them.

DOI: [10.1103/PhysRevA.95.013625](https://doi.org/10.1103/PhysRevA.95.013625)**I. INTRODUCTION**

Ultracold atoms in optical lattices offer an ideal platform for simulating certain problems of condensed matter physics and constitute many-body systems exhibiting a diversity of physical phenomena. In particular, the understanding of the nonequilibrium dynamics of strongly correlated many-body systems in optical lattices is currently one of the most challenging problems for both theory and experiment. This dynamics is typically triggered by an external periodic driving [1–4] or an instantaneous change (quench) of a Hamiltonian parameter [5]. Remarkable dynamical phenomena employing periodic driving [1,2] of the optical lattice include Bloch oscillations [6–8], realization of the superfluid-to-Mott insulator phase transition [9], topological states of matter [10], artificial gauge fields [11], realization of ferromagnetic domains [12,13], and even applications to quantum computation [14]. On the other hand, quench dynamics enables us to explore, among others, the light-cone effect in the spreading of correlations [15,16], the Kibble-Zurek mechanism [17,18], and the question of thermalization [19,20]. Driving or quenches can also be used in order to generate energetically low-lying collective modes, such as the dipole [21,22] or the breathing [23–27] mode. In general, a sudden displacement or a periodic shaking of the external trap induces a dipole oscillation of the atomic cloud, while a quench of the frequency of the trap excites a breathing mode of the cloud. These modes constitute a main probe both for theoretical investigations, to understand and interpret the nonequilibrium dynamics, and for experiments, as they can be used in order to measure key quantities of trapped many-body systems [23].

Recently, increasing effort has been devoted to controlling the atomic motion in optical lattices by subjecting them to time-periodic external driving [28–31] and investigating the optimal driving protocol [32–34]. In this direction, it is important to carefully explore and design the relevant driving protocol to transfer the energy to the desired final degrees of freedom. To trigger or even control a certain type of (collective) modes of the dynamics, widely used techniques in the literature constitute either periodic driving

of the lattice potential, e.g., a lattice shaking, or a quench of a parameter of the system, e.g., a lattice amplitude quench or an interaction quench. In the former case a tunable local dipole mode and a resonant intrawell dynamics were recently explored by shaking an optical lattice [35]. On the other hand, in the latter case it has been shown [36] that a sudden increase in the interparticle repulsion in a nondriven lattice induces a rich interwell as well as intrawell dynamics which can be coupled and consequently mixed for certain quench amplitudes. However, for decreasing repulsive forces [37] the accessible interwell tunneling channels are far fewer compared to the excited intrawell modes, and in particular, no resonant dynamics can be observed. From the above analysis it becomes evident that a crucial ingredient for the design and further control of the dynamics is the choice of the driving protocol of the system: By using different driving schemes, different types of excited modes are induced, i.e., different energetical channels can be triggered. In this direction, an intriguing question is how a combination of periodic driving and interaction quenches can be used to steer the dynamics of the system and, as a consequence, the coupling of the interwell and intrawell modes. Such an investigation will, among other things, permit us to gain a deeper understanding of the underlying microscopic mechanisms and will allow us to activate certain energy channels by using specific driving protocols for control of the different processes.

In the spirit of the above-posed question we investigate in the present work the quantum dynamics of interaction quenched few-boson ensembles trapped in periodically driven finite optical lattices. Concerning the periodic driving, vibration of the optical lattice is employed. This scheme, in contrast to shaking, induces out-of-phase dipole modes among the outer wells and a local breathing mode in the central well of the finite lattice. We cover the dynamics of the periodically driven lattice with varying driving frequencies in the complete range from adiabatic to high-frequency driving. In particular, we observe for the intermediate-driving-frequency regime, being intractable by current state of the art analytical methods [1,2], resonantlike behavior of the intrawell dynamics. This resonance is accompanied by a rich excitation spectrum

and an enhanced interwell tunneling compared to adiabatic or high-intensity driving and it is mainly of single-particle character. Indeed, it survives upon increasing interaction, obtaining faint additional features, the most remarkable being the cotunneling of an atom pair [31,38]. To induce a correlated many-body dynamics we employ an interaction quench on top of the driven lattice, thus opening energetically higher inter-well and intrawell channels. As a consequence, the interwell tunneling is amplified even for adiabatic driving, and admixtures of excitations possessing breathinglike and dipolelike components are generated. Remarkably enough, as a function of the quench amplitude, the system experiences multiple resonances between the inter- and the intrawell dynamics. This observation indicates the high degree of controllability of the system, especially for the excited modes under such a combination of driving protocols, and it is arguably one of our central results. To the best of our knowledge, this multifold mode coupling behavior unraveled with a composite driving protocol has not been reported before. Moreover, the position of the above-mentioned resonances is tunable via the driving frequency, allowing for further control of the mode coupling in optical lattices. Finally, the realization of intensified loss of coherence caused either by the resonant driving or by a quench on top of the driving is an additional indicator of the observed phenomena. To obtain a comprehensive understanding of the microscopic properties of the strongly driven and interacting system, we focus on the few-body dynamics in small lattices (specifically, four bosons in a triple-well setup). However, we provide strong evidence that our findings apply equally to larger lattice systems and particle numbers. All calculations to solve the underlying many-body Schrödinger equation are performed by employing the multiconfiguration time-dependent Hartree method for bosons (MCTDHB) [39,40], which is especially designed to treat the out-of-equilibrium quantum dynamics of interacting bosons under time-dependent modulations.

This work is organized as follows. In Sec. II we explain our setup and introduce the multiband expansion and the basic observables that we use in order to interpret the dynamics. Section III presents the effects resulting from an interaction quench of a driven triple well for filling factors larger than unity. Section IV presents the dynamics for filling factors smaller than unity. We summarize our findings and give an outlook in Sec. V. In Appendix A the nonequilibrium dynamics induced by a driven harmonic oscillator and simultaneously an interaction quenched bosonic cloud is briefly outlined. Appendix B briefly comments on the resonant response of the driven lattice, and finally, Appendix C describes our computational method.

II. SETUP AND ANALYSIS TOOLS

In the present section we briefly report on our theoretical framework. First, we introduce the protocol of the driven optical lattice and the many-body Hamiltonian. Second, the wave-function representation in terms of a multiband expansion and some basic observables for the understanding of the inter- and intrawell modes of the dynamics are introduced.

A. Setup and Hamiltonian

To model a lattice vibration, with amplitude δ and angular frequency $\omega_D = 2\pi f_D$, a spatiotemporal sinusoidal modulation is used to generate a lattice potential of the form

$$V_{\text{br}}(x; t) = V_0 \sin^2[k_x(1 + \delta \sin(\omega_D t))x], \quad (1)$$

with lattice depth V_0 and wave vector $k_x = \frac{\pi}{l}$, where l denotes the distance between successive potential minima. Such a potential can be realized, e.g., via acousto-optical modulators [12], which induce a frequency difference among counterpropagating laser beams. The Hamiltonian of N identical bosons of mass M following an interaction quench protocol upon the driven one-dimensional (1D) lattice reads

$$H(x; t) = \sum_{i=1}^N \frac{p_i^2}{2M} + V_{\text{br}}(x_i; t) + g_{\text{1D}}^{(f)} \sum_{i<j} \delta(x_i - x_j), \quad (2)$$

where $g_{\text{1D}}^{(f)} = \delta g + g_{\text{1D}}^{(\text{in})}$, with $g_{\text{1D}}^{(\text{in})}$ and $g_{\text{1D}}^{(f)}$ being the initial and final interaction strengths, respectively, and δg denotes the corresponding perturbation. The short-range interaction potential between particles located at positions x_i is modeled by a Dirac delta function. The interaction is well described by s -wave scattering and the effective 1D coupling strength [41] becomes $g_{\text{1D}} = \frac{2\hbar^2 a_0}{M a_{\perp}^2} (1 - \frac{|k(1/2)l a_0|}{\sqrt{2} a_{\perp}})^{-1}$. The transversal length scale is $a_{\perp} = \sqrt{\frac{\hbar}{M \omega_{\perp}}}$, with ω_{\perp} the frequency of the confinement, while a_0 denotes the 3D s -wave scattering length. The interaction strength can be tuned either via a_0 with the aid of Feshbach resonances [42,43] or via the transversal confinement frequency ω_{\perp} [44–46].

In the following, for reasons of universality, Hamiltonian (2) is rescaled in units of the recoil energy $E_R = \frac{\hbar^2 k_x^2}{2M}$. Then the corresponding length, time, and frequency scales are given in units of k_x^{-1} , $\omega_R^{-1} = \hbar E_R^{-1}$, and ω_R , respectively. For our simulations we have used a sufficiently large lattice depth, of the order of $V_0 = 10.0 E_R$, such that each well includes three localized single-particle Wannier states. The confinement of the bosons in the m -well system is imposed by the use of hard-wall boundary conditions at the appropriate position $x_{\sigma} = \pm \frac{m\pi}{2k_x}$. Finally, for computational convenience we set $\hbar = M = k_x = 1$ and therefore all quantities below are given in dimensionless units.

B. Wave-function representation and basic observables

To understand the microscopic properties and analyze the dynamics, the notion of noninteracting multiband Wannier number states is employed. The presently used lattice potential is deep enough for the Wannier states between different wells to have a very small overlap for not too high energetic excitation. In the case of a periodically driven potential the above description can still be valid if the driving amplitude is low enough in comparison to the lattice constant l , i.e., $\delta \ll l$, such that each localized Wannier function is assigned to a certain well and the respective band mixing is fairly small. For $\delta \gg l$ the use of a time-dependent Wannier basis is more adequate. Summarizing, for a system with N bosons, m wells, and j localized single-particle states [36,37] the expansion of

the many-body bosonic wave function reads

$$|\Psi\rangle = \sum_{\{N_i\}, \{I_i\}} C_{\{N_i\}, \{I_i\}} |N_1^{(I_1)}, N_2^{(I_2)}, \dots, N_m^{(I_m)}\rangle, \quad (3)$$

where $|N_1^{(I_1)}, N_2^{(I_2)}, \dots, N_m^{(I_m)}\rangle$ is the multiband Wannier number state, the element $N_i^{(I_i)} = |n_i^{(1)}\rangle \otimes |n_i^{(2)}\rangle \otimes \dots \otimes |n_i^{(j)}\rangle$ denotes the number of bosons being localized in the i th well, and I_i indexes the corresponding energetic excitation order. In particular, $|n_i^{(k)}\rangle$ refers to the number of bosons which reside at the i th well and k th band, satisfying the closed subspace constraint $\sum_{i=1}^m \sum_{k=1}^j n_i^{(k)} = N$. For instance, in a setup with $N = 4$ bosons confined in a triple well, i.e., $m = 3$, which includes $k = 3$ single-particle states, the state $|1^{(0)} \otimes 1^{(1)}, 1^{(0)}, 1^{(0)}\rangle$ indicates that in every well one boson occupies the zeroth excited band, but in the left well there is one extra boson localized in the first excited band. For this setup it is also important to note that one can realize four energetic classes of number states, namely, the quadruple mode $\{|4^{(I_1)}, 0^{(I_2)}, 0^{(I_3)}\rangle + \text{c}\}$ (Q), the triple mode $\{|3^{(I_1)}, 1^{(I_2)}, 0^{(I_3)}\rangle + \text{c}\}$ (T), the double-pair mode $\{|2^{(I_1)}, 2^{(I_2)}, 0^{(I_3)}\rangle + \text{c}\}$ (DP), and the single-pair mode $\{|2^{(I_1)}, 1^{(I_2)}, 1^{(I_3)}\rangle + \text{c}\}$ (SP), where c stands for all corresponding permutations. It is important to note that, for later convenience, we consider only the corresponding subclass with isoenergetic states and not all members, which would also include energetically unequal number states, e.g., for the single-pair mode $\{|2^{(I_1)}, 1^{(I_2)}, 1^{(I_3)}\rangle, |1^{(I_1)}, 2^{(I_2)}, 1^{(I_3)}\rangle, |1^{(I_1)}, 1^{(I_2)}, 2^{(I_3)}\rangle\}$. Also, in the present consideration for a given set of excitation indices $\mathbf{I} = (I_1, I_2, I_3)$, the above-mentioned class of number states we are focusing on has similar on-site energies and will contribute significantly to the same eigenstates. Indexing each such class by α , we adopt the more compact notation $|q\rangle_{\alpha; \mathbf{I}}$ for characterization of the eigenstates in terms of number states, where the index q refers to the spatial occupation. For instance, $\{|q\rangle_{3; \mathbf{I}}\}$ with $\mathbf{I} = (1, 0, 0)$ represent the eigenstates which are dominated by the set of triple-pair states $\{|3^{(1)}, 1^{(0)}, 0^{(0)}\rangle, |0^{(0)}, 3^{(1)}, 1^{(0)}\rangle, |1^{(0)}, 0^{(0)}, 3^{(1)}\rangle, |1^{(0)}, 3^{(1)}, 0^{(0)}\rangle, |0^{(0)}, 1^{(0)}, 3^{(1)}\rangle, |3^{(1)}, 0^{(0)}, 1^{(0)}\rangle\}$, and the index q runs from 1 to 6.

Below, a few basic observables which refer to the inter- and intrawell generated modes are introduced and their expansion in terms of the multiband number state basis is given. Note that henceforth we denote by $|\Psi(0)\rangle = \sum_{q; \alpha; \mathbf{I}} C_{\alpha; \mathbf{I}}^q |q\rangle_{\alpha; \mathbf{I}}$ the initial wave function in terms of the eigenstates $|q\rangle_{\alpha; \mathbf{I}}$ of the final Hamiltonian. A time-resolved measure for the impact of the external driving on the system is provided via the fidelity $F_{\{\lambda_i\}}(t) = |\langle \Psi(0) | \Psi_{\{\lambda_i\}}(t) \rangle|^2$, which is the overlap between the time evolved and the initial (ground) state. Note the dependence of the fidelity on the set of parameters $\{\lambda_i\}$, e.g., the driving frequency ω_D , the interaction strength g , and the particle number N . The expansion of the fidelity reads

$$F_{\{\lambda_i\}}(t) = \sum_{q_1; \alpha; \mathbf{I}} |C_{\alpha; \mathbf{I}}^{q_1}|^4 + \sum_{q_1, q_2; \alpha, \beta; \mathbf{I}} |C_{\alpha; \mathbf{I}}^{q_1}|^2 \times |C_{\beta; \mathbf{I}}^{q_2}|^2 \cos(\epsilon_{\alpha; \mathbf{I}}^{q_1} - \epsilon_{\beta; \mathbf{I}}^{q_2})t. \quad (4)$$

The second term on the right-hand side of the above expression contains the energy difference between two distinct number states and therefore offers to be a measure of the tunneling process. The indices α and β indicate a particular number-

state group [36], q_i is the intrinsic index within each group, \mathbf{I} corresponds to the respective energetic level, and ϵ refers to the corresponding on-site energy of a particular number state and energetic level.

For investigation of the intrawell dynamics it is appropriate to employ a local density analysis. To measure the instantaneous spreading of the cloud in the i th well we define the operator of the second moment $\sigma_i^2(t) = \langle \Psi | (x - R_{\text{CM}}^{(i)})^2 | \Psi \rangle$ [49]. Here $R_{\text{CM}}^{(i)} = \int_{d_i}^{d_i'} dx (x - x_0^{(i)}) \rho_i(x) / \int_{d_i}^{d_i'} dx \rho_i(x)$ refers to the coordinate of the center of mass [47,48], $x_0^{(i)}$ denotes the central point of the i th well under investigation, and d_i and d_i' correspond to the instantaneous limits of the wells, whereas $\rho_i(x)$ is the respective single-particle density. Then the expansion of the second moment for the middle well in terms of the eigenstates of the final Hamiltonian reads

$$\begin{aligned} \sigma_M^2(t) &= \sum_{\alpha; q_1; \mathbf{I}} |C_{\alpha; \mathbf{I}}^{q_1}|^2 \langle q_1 | (x - R_{\text{CM}}^{(i)})^2 | q_1 \rangle_{\alpha; \mathbf{I}} \\ &+ 2 \sum_{q_1 \neq q_2} \text{Re}(C_{\beta; \mathbf{I}}^{*q_1} C_{\alpha; \mathbf{I}}^{q_2})_{\beta; \mathbf{I}} \langle q_1 | (x - R_{\text{CM}}^{(i)})^2 | q_2 \rangle_{\alpha; \mathbf{I}} \\ &\times \cos(\omega_{\beta; \mathbf{I}}^{q_1} - \omega_{\alpha; \mathbf{I}}^{q_2})t. \end{aligned} \quad (5)$$

Finally, as a measure of the dipole motion the intrawell asymmetry $\Delta\rho_a(t) = \rho_{a,1}(t) - \rho_{a,2}(t)$ is introduced. Here, a particular well a (in a triple well $a = L, M, R$ stands for the left, middle, and right wells, respectively) is divided from the center point into two equal sections, with $\rho_{a,1}(t)$ and $\rho_{a,2}(t)$ being the respective integrated densities of the left and right parts during the evolution. The expectation value of the asymmetry operator is expressed as

$$\begin{aligned} \langle \Psi | \Delta\rho(t) | \Psi \rangle &= \sum_{q_1; \alpha; \mathbf{I}} |C_{\alpha; \mathbf{I}}^{q_1}|^2 \langle q_1 | \Delta\rho | q_1 \rangle_{\alpha; \mathbf{I}} \\ &+ 2 \sum_{q_1 \neq q_2} \text{Re}(C_{\alpha; \mathbf{I}}^{*q_1} C_{\beta; \mathbf{I}}^{q_2})_{\mathbf{I}; \alpha} \langle q_1 | \Delta\rho | q_2 \rangle_{\beta; \mathbf{I}} \\ &\times \cos[(\omega_{\alpha; \mathbf{I}}^{q_1} - \omega_{\beta; \mathbf{I}}^{q_2})t]. \end{aligned} \quad (6)$$

C. First-order coherence

The spectral representation of the reduced one-body density matrix [50–52] reads

$$\rho(x, x'; t) = \sum_{\alpha=1}^M n_{\alpha}(t) \varphi_{\alpha}(x, t) \varphi_{\alpha}^*(x', t), \quad (7)$$

where $\varphi_{\alpha}(x, t)$ are the so-called natural orbitals and M corresponds to the considered number of orbitals. The population eigenvalues $n_{\alpha}(t) \in [0, 1]$ characterize the fragmentation of the system [53–55,57]: For only one macroscopically occupied orbital the system is said to be condensed; otherwise it is fragmented.

To quantify the degree of first-order coherence during the dynamics, the normalized spatial first-order correlation function $g^{(1)}(x, x'; t)$ is defined:

$$g^{(1)}(x, x'; t) = \frac{\rho(x, x'; t)}{\sqrt{\rho_1(x; t) \rho_1(x'; t)}}. \quad (8)$$

It is known that for $|g^{(1)}(x, x'; t)|^2 < 1$ the corresponding visibility of interference fringes in an interference experiment is less than 100% and this case is referred to as loss of coherence. On the contrary, when $|g^{(1)}(x, x'; t)|^2 = 1$ the fringe visibility of the interference pattern is maximal and is referred to as full coherence. The above quantity depends strongly on the various parameters of the Hamiltonian, and an investigation of the aforementioned dependence is reported in Sec. IV.

III. INTERACTION QUENCH DYNAMICS ON A DRIVEN LATTICE FOR FILLING FACTOR $\nu > 1$

To analyze the dynamics of our system, it is instructive first to comment on the relation between the ground state and its dominant interaction-dependent spatial configuration employing the multiband expansion. Let us consider a setup with four bosons in a triple well (which is our workhorse). Within the weak-interaction regime $0 < g < 0.1$ the dominant spatial configuration of the system is $|1^{(0)}, 2^{(0)}, 1^{(0)}\rangle$, while states of double-pair occupancy, e.g., $|2^{(0)}, 2^{(0)}, 0^{(0)}\rangle$, and triple-pair occupancy, e.g., $|1^{(0)}, 3^{(0)}, 0^{(0)}\rangle$, possess a small contribution. In the intermediate-interaction regime $0.1 < g < 1.0$ the system is described by a superposition of the lowest band states, which are predominantly of single-pair occupancy, e.g., $|1^{(0)}, 2^{(0)}, 1^{(0)}\rangle$, $|2^{(0)}, 1^{(0)}, 1^{(0)}\rangle$, and double-pair occupancy, e.g., $|2^{(0)}, 2^{(0)}, 0^{(0)}\rangle$, while energetically higher states than the first excited band start to be occupied. For further increasing repulsion, e.g., $1.0 < g < 5.0$, the excited states gain more population and the corresponding ground-state configuration is characterized by an admixture of ground-band (predominantly of single-pair occupancy) and excited-band (to the first and even to the second band) states.

In the following, we investigate the effect of an interaction quench upon a periodically driven finite lattice. Note that we consider interaction quenches imposed at $t = 0$ or after a short transient time. The resulting dynamics is qualitatively the same. We refer, for brevity, to the effect of an interaction quench performed at $t = 0$, i.e., when the periodic driving also starts. To be more specific, below we first explore the effect of an interaction quench for various driving frequencies and compare the induced dynamics with an unquenched system. Subsequently, the dynamics for a fixed driving frequency with varying quench amplitudes is investigated. We remark that in each case we consider quench amplitudes for which the induced above-barrier transport is suppressed.

A. Case I: Interaction quench dynamics for different driving frequencies

We explore the effect of an interaction quench on top of a periodically driven triple-well potential with four bosons in the weak-interaction regime ($g = 0.05$), where the dominant spatial configuration of the ground state corresponds to states of single-pair occupancy, e.g., $|1^{(0)}, 2^{(0)}, 1^{(0)}\rangle$. To demonstrate the difference between the dynamics of the quenched and that of the unquenched bosonic ensemble let us first investigate the response of an explicitly driven system, i.e., with $\delta g = 0$. Figure 1(a) shows $F_{\{\omega_D\}}(t)$ (see also Sec. II B) with varying ω_D . It is observed that for $0 < \omega_D < 1.5$ (nearly adiabatic driving) or very intense driving $\omega_D > 12.0$ the system remains

essentially unperturbed. In between, an interesting stripe pattern occurs. To be self-contained, in the following, let us classify the frequency intervals

$$\Delta\omega_{D_1} \equiv [2.0, 6.0] \quad \text{and} \quad \Delta\omega_{D_2} \equiv [7.0, 11.0], \quad (9)$$

where the time-evolved state of the periodically driven system deviates significantly from the initial (ground) state. Indeed, for $\omega_D \in \Delta\omega_{D_1} \equiv [2.0, 6.0]$ the minimal overlap during the dynamics drops down to 0.1, whereas for $\omega_D \in \Delta\omega_{D_2} \equiv [7.0, 11.0]$ the system maximally departs from the initial state by a percentage of the order of 30%. To probe the effect of the interactions and of the driving frequency on the overall dynamics, the inset in Fig. 1(a) illustrates $\bar{F}_{\{\omega_D\}} = \int_0^T dt F_{\{\omega_D\}}(t)/T$ (T denotes the considered evolution time) at $\omega_D = 1.5$ and at $\omega_D = 2.75 \in \Delta\omega_{D_1}$ for different initial interactions and particle number. Focusing on the same driving frequency ω_D and a large interparticle interaction we observe that the mean response of the system decreases as a function of the particle number and therefore the system can be driven more efficiently out of equilibrium. The same observation holds for a fixed interaction strength and particle number but a driving frequency below and in the region $\Delta\omega_{D_1}$, e.g., for $N = 4$, $g = 3$, $\bar{F}_{\{\omega_D=1.5\}} = 0.9405$, while $\bar{F}_{\{\omega_D=2.75\}} = 0.1202$. Let us now inspect how an interaction quench distorts the fidelity evolution. Figure 1(b) shows $F_{\{\omega_D, \delta g\}}(t)$ for $\delta g = 2.0$ (performed at $t = 0$, i.e., simultaneously with the driving) with varying ω_D . It is observed that the combination of driving and interaction quench brings the system significantly out of equilibrium for every driving frequency. To understand the effect of the quench on the system let us compare Fig. 1(b) with Fig. 1(a) for the fidelity evolution of the driven but unquenched system. Indeed, an interaction quench introduces more energy into the system, and as a consequence the final evolving state deviates significantly from the initial one even in the region of adiabatic driving, e.g., $\omega_D = 0.5$, or high-frequency driving, e.g., $\omega_D = 14.0$, as shown in Fig. 1(b). For instance, $\bar{F}_{\{\omega_D=1.0, \delta g=0\}} = 0.98$ and $\bar{F}_{\{\omega_D=1.0, \delta g=2.0\}} = 0.81$, while $\bar{F}_{\{\omega_D=14.0, \delta g=0\}} = 0.92$ and $\bar{F}_{\{\omega_D=14.0, \delta g=2.0\}} = 0.78$. Finally, as an estimate we report that according to our simulations the deviation of \bar{F} between the unquenched and the quenched system ranges from 12% to 70%.

To analyze the role of dynamical fragmentation [55,56] [see Eq. (7)], Fig. 1(c) shows the deviation from unity, $\lambda(t) = 1 - n_1(t)$, during the evolution of the first natural population for different driving frequencies ω_D and no quench. Note here that even $\lambda(0) \neq 0$, i.e., as a result of the finite repulsion the initial state possesses a small degree of fragmentation. As shown, $\lambda(t)$ is always significantly above 0, confirming the fragmentation process. Focusing on different ω_D 's we note that the temporal average of the fragmentation, i.e., $\bar{\lambda} = \int dt \lambda(t)/T$, increases if $\omega_D \in \Delta\omega_{D_1} \cup \Delta\omega_{D_2}$, while for the regions where $F_{\{\omega_D\}} \simeq 1$ it decreases but never tends to a perfectly condensed state. Note also that for $\omega_D \notin \Delta\omega_{D_1} \cup \Delta\omega_{D_2}$, $\lambda(t)$ possesses low-amplitude oscillations, whereas for $\omega_D \in \Delta\omega_{D_1} \cup \Delta\omega_{D_2}$ the external driving introduces high-amplitude variations in $\lambda(t)$. As expected the interparticle repulsion supports the fragmentation process [see $\lambda(t)$ for $\omega_D = 3.0$, $g = 1.0$ and $\delta g = 0.0$ in Fig. 1(c)]. The effect of an interaction quench on the fragmentation process is

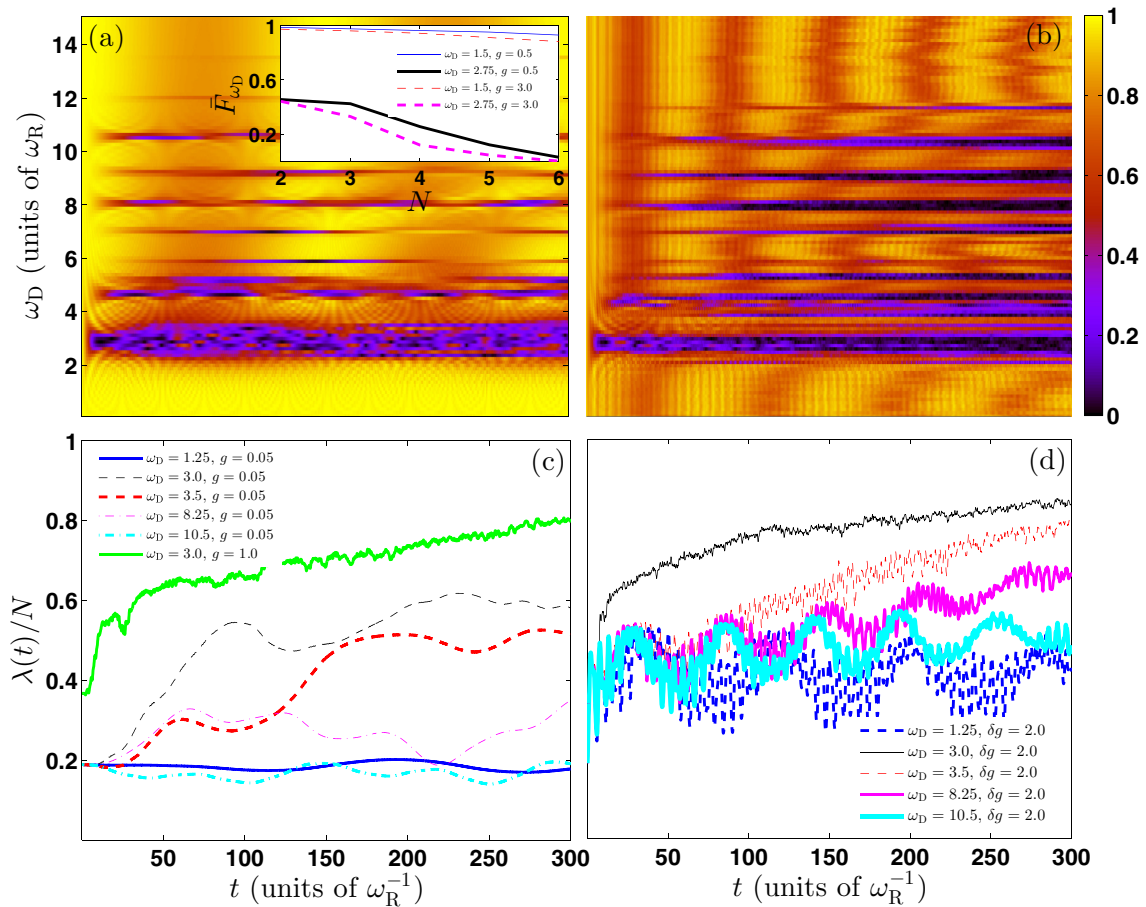


FIG. 1. (a) Time evolution of the fidelity $F_{\{\omega_D\}}(t)$ as a function of the driving frequency ω_D . The driving amplitude is $\delta = 0.03$ and the initial state corresponds to the ground state of four weakly interacting bosons with $g = 0.05$ confined in a triple well. Inset: Mean response $\bar{F}_{\{\omega_D\}}$ at $\omega_D = 0.75$ and at $\omega_D = 2.75$ for different interparticle repulsions, $g = 0.5$ and $g = 3.0$, as a function of the particle number N (see legend). (b) Same as (a), but for a fixed interaction quench, with amplitude $\delta g = 2.0$, on top of the driven triple well. (c) Deviation from unity of the first natural occupation number, i.e., $\lambda(t) = 1 - n_1(t)$, during the evolution for different driving frequencies ω_D (see legend). The effect of a stronger interparticle repulsion for $g = 1.0$ at $\omega_D = 3.0$ in the fragmentation process is also shown. (d) The same as (c), but for a fixed interaction quench, $\delta g = 2.0$, upon the driving.

shown in Fig. 1(d) employing $\lambda(t)$ for $\delta g = 2.0$ and the same driving frequencies as in Fig. 1(c). A tendency toward a higher fragmented state for every ω_D , at least for certain time periods, is manifest. Comparing $\lambda(t)$ for ω_D below $\Delta\omega_{D_1}$, in the unquenched case, we observe that the interaction quench introduces high-amplitude variations, while for $\omega_D \in \Delta\omega_{D_1} \cup \Delta\omega_{D_2}$, $\lambda(t)$ shows a monotonic increase towards a fully fragmented state. Thus, in conclusion, the fragmentation process under an interaction quench is enhanced, which is attributed to the consequent rise in the interparticle repulsion.

To identify the effect of an interaction quench on the one-body level, Fig. 2 compares $\rho_1(x, t)$ without and with an interaction quench on top of the periodically driven triple well for $\omega_D = 0.75$ and amplitude $\delta = 0.03$. Without quench, the one-body density [see Fig. 2(a)] shows a weak response, a local dipole mode in the outer wells, and a local breathing mode [hardly visible in Fig. 2(a) due to weak driving] in the central well due to the combination of the parity of the lattice (odd number of sites) and the driving scheme. The dynamics in the central well shows a compression and decompression, while the outer wells are shaken (for a lattice with an even

number of sites the generated intrawell mode will be solely a local dipole mode). As shown, by performing a quench [see Fig. 2(b)] at $\delta g = 2.0$, the breathinglike mode in the central well is enhanced, while in the outer wells the cloud exhibits admixtures of excitations consisting of a dipole and a breathing component. Focusing on the dynamics of the left well it is obvious that the atomic cloud oscillates inside the well with a varying amplitude, i.e., it performs an oscillation with a simultaneous compression and decompression. Finally, the interwell tunneling mode, which is manifested as a direct population transport from the middle to the outer wells and accompanies the whole process, is amplified. To illustrate explicitly the evolution of the atomic cloud in each well we follow the $\rho_1(x, t) = 0.25$ of the local density, shown as the thick white line on top of the density. It is shown that in the central well the cloud compresses and decompresses during the evolution, while in the outer wells the cloud oscillates, also changing its width (in Appendix A, this mode is generated in a harmonic trap for a deeper understanding).

To obtain a quantitative understanding of the interwell tunneling dynamics, let us investigate the spectrum of the fidelity,

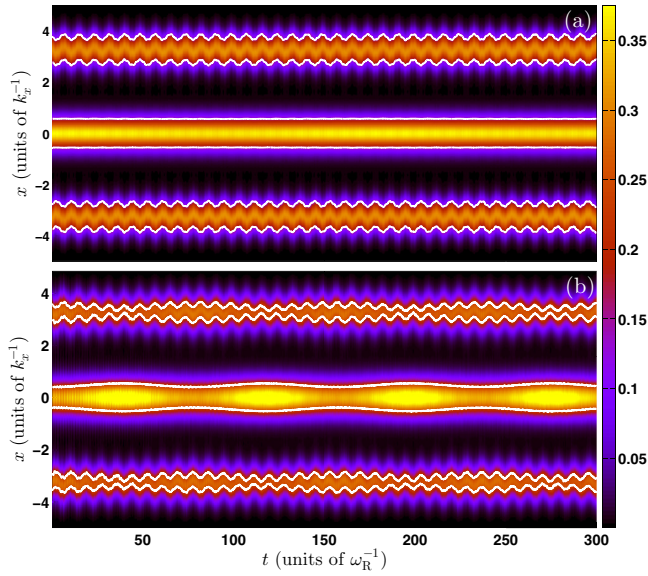


FIG. 2. Time evolution of the one-body density $\rho_1(x,t)$ caused by a periodically driven triple well with (a) $\omega_D = 0.75$ and (b) a simultaneous interaction quench with amplitude $\delta g = 2.0$. White contours, at $\rho_1(x,t) = 0.25$, are plotted on top in order to facilitate a comparison of the atomic motion between the unquenched (a) and the quenched (b) systems. The driving amplitude is fixed at the value $\delta = 0.03$ and the initial state corresponds to the ground state of four weakly interacting bosons with $g = 0.05$.

i.e., $F_{\{\omega_D, \delta g\}}(\omega) = \frac{1}{\pi} \int dt F_{\{\omega_D, \delta g\}}(t) e^{i\omega t}$ [see also Eq. (4)]. Figure 3(a) shows the tunneling spectrum of both the unquenched (see black line) and the quenched (see red line) systems with respect to the driving frequency. Indeed, employing Eq. (4) we obtain that for the unquenched system the dominant tunneling process for every ω_D corresponds to tunneling within the SP mode [e.g., between state $|2^{(0)}, 1^{(0)}, 1^{(0)}\rangle$ and state $|1^{(0)}, 2^{(0)}, 1^{(0)}\rangle$]. It is important here to note that for $\omega_D \in \Delta\omega_{D1}$ additional tunneling modes from the SP to the DP mode [e.g., from $|1^{(0)}, 2^{(0)}, 1^{(0)}\rangle$ to $|2^{(0)}, 2^{(0)}, 0^{(0)}\rangle$] and from the SP to the T mode [e.g., from $|1^{(0)}, 2^{(0)}, 1^{(0)}\rangle$ to $|3^{(0)}, 1^{(0)}, 0^{(0)}\rangle$] can be generated. To illustrate this fact we depict in the inset in Fig. 3(a) the probabilities $A_1(t) = |\langle 2^{(0)}, 1^{(0)}, 1^{(0)} | \Psi(t) \rangle|^2$, $A_2(t) = |\langle 2^{(0)}, 2^{(0)}, 0^{(0)} | \Psi(t) \rangle|^2$, and $A_3(t) = |\langle 3^{(0)}, 1^{(0)}, 0^{(0)} | \Psi(t) \rangle|^2$ at $\omega_D = 2.75$. It is shown that $A_2(t)$ and $A_3(t)$, although suppressed in comparison to $A_1(t)$, possess significant populations. We remark here that a similar tunneling procedure corresponding to atom-pair tunneling has been observed for few atoms confined in a driven double well in Ref. [31]. However, for the quenched system the tunneling takes place only within the SP mode, while the remaining tunneling modes are suppressed, due to the quench, even for $\omega_D \in \Delta\omega_{D1}$. To illustrate the effect on the tunneling dynamics of an interaction quench upon the driven lattice, Fig. 3(b) shows the probability $A_1(t)$ for both the unquenched and the quenched system for various driving frequencies. As shown the effect of the quench depends on the driving frequency. Indeed, for $\omega_D \leq \min(\Delta\omega_{D1})$ the quench decreases the frequency of the tunneling branch [see the open red circles in Fig. 3(a), which correspond to the interaction quenched fidelity spectrum]

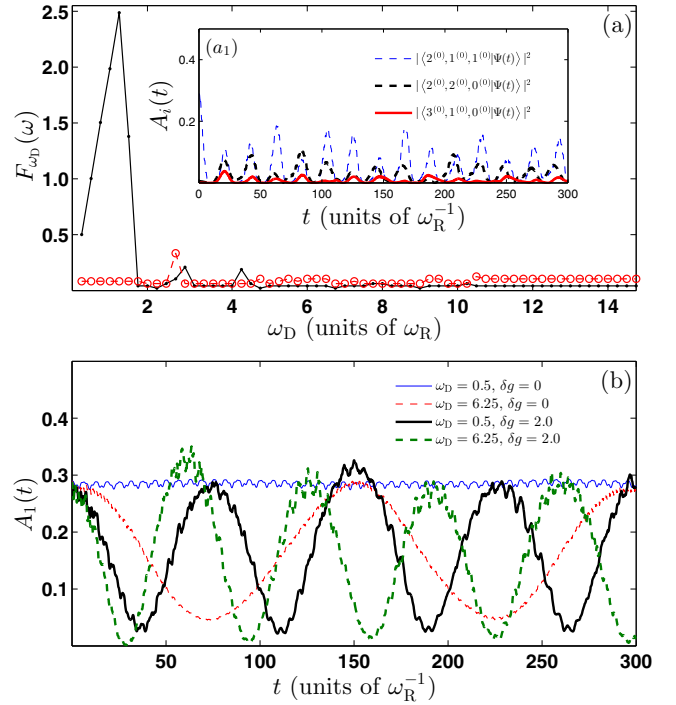


FIG. 3. (a) Spectrum of the fidelity $F_{\{\omega_D\}}(\omega)$ as a function of the driving frequency ω_D . Black dots correspond to $F_{\{\omega_D, \delta g=0.0\}}(\omega)$, i.e., to the unquenched system, while open red circles refer to $F_{\{\omega_D, \delta g=2.0\}}(\omega)$, i.e., to the case of a simultaneous interaction quench with amplitude $\delta g = 2.0$ on top of the driving. Inset (a₁): Tunneling probabilities $A_1(t)$, $A_2(t)$, and $A_3(t)$ (see text and legend) at $\omega_D = 2.75$. (b) Comparison of the single-particle tunneling probabilities $A_1(t)$ in a periodically driven triple well without and with a simultaneous interaction quench for various driving frequencies ω_D (see legend). The driving amplitude is fixed at the value $\delta = 0.03$ and the initial state corresponds to the ground state of four weakly interacting bosons with $g = 0.05$.

and leads to a significant enhancement of the amplitude of this tunneling branch [e.g., see the blue and black lines in Fig. 3(b)]. The latter is a consequence of the fact that the interaction quench injects energy into the system. However, for $\omega_D > \max(\Delta\omega_{D1})$ the tunneling branch is quite insensitive to the quench because both the frequency and the amplitude of the tunneling probability are slightly higher [see Figs. 3(a) and 3(b)].

To determine the frequencies of the local dipole mode in the outer wells we calculate the spectrum $\Delta\rho_L(\omega) = \frac{1}{\pi} \int dt \Delta\rho_L(t) e^{i\omega t}$. The analysis of the corresponding breathing component is performed in the next subsection, where we examine in more detail the effects of the quench dynamics. Figure 4(a) presents $\Delta\rho_L(\omega)$, where two emergent frequency branches [denoted (a₁) and (a₂) in the spectrum] of the intrawell oscillations are visible. It is observed that for driving frequencies $\omega_D \in [0, 0.5]$ the intrawell dipole mode possesses two distinct frequencies which come into resonance in the region $\omega_D \in [2, 3]$ and then, for $\omega_D > 3.0$, are again well separated. To gain insight into the impact of an interaction quench, performed on top of the driving, on the intrawell density oscillations, Fig. 4(b) shows $\Delta\rho_L(t)$ at resonance

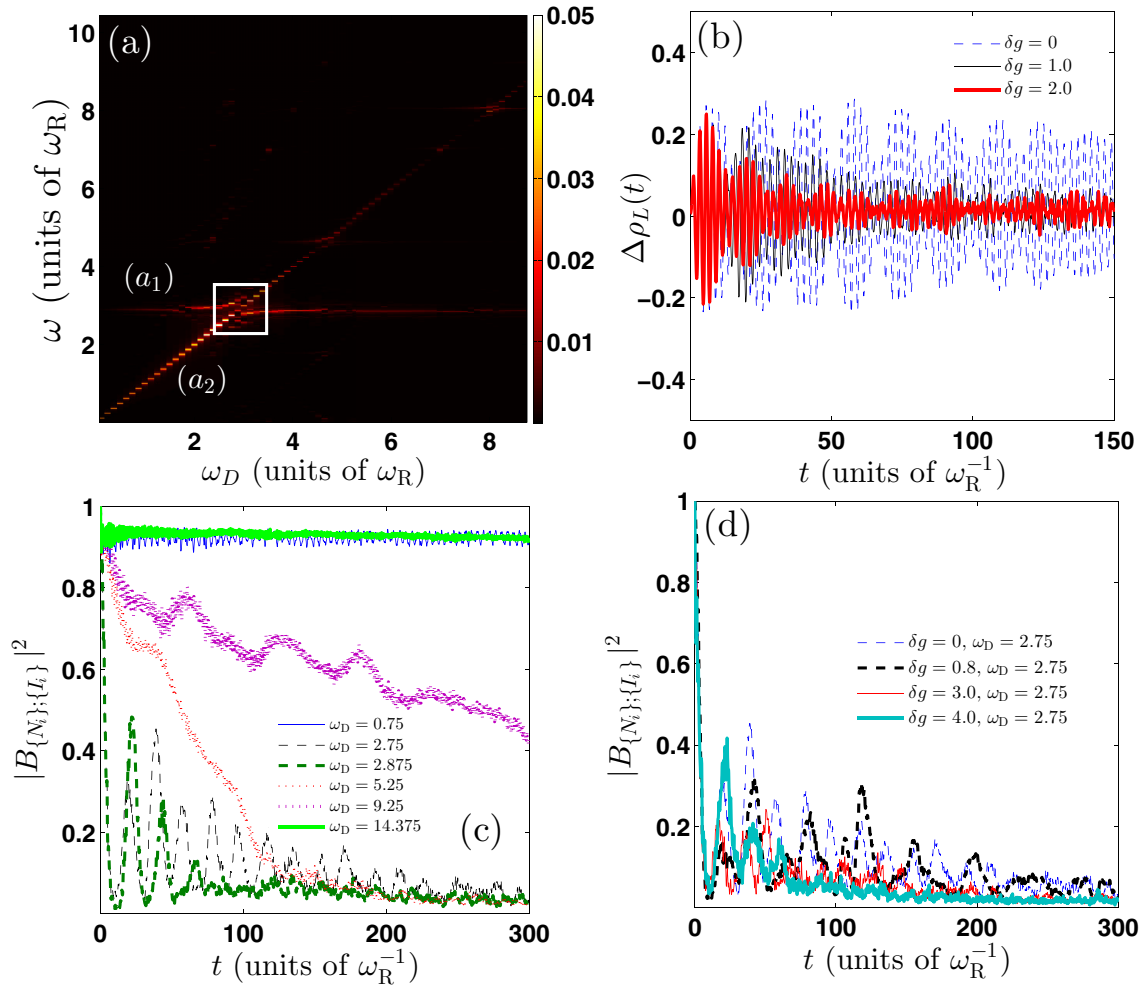


FIG. 4. (a) Spectrum of the intrawell asymmetry for the left well $\Delta\rho_L(\omega)$ in a driven triple well, with respect to the driving frequency ω_D . The white rectangle indicates the region of resonance. (b) Intrawell asymmetry evolution $\Delta\rho_L(t)$ at resonance ($\omega_D = 2.875$) employing different interaction quenches (see legend). (c) Excitation probability $|B_{\{N_i\};\{I_i\}}|^2$ (see text) during the evolution for different driving frequencies ω_D . (d) The same as (c), at $\omega_D = 2.75$, for different quenches on the interparticle repulsion (see legend). The driving amplitude is fixed at the value $\delta = 0.03$, while the initial state corresponds to the ground state of four weakly interacting bosons with $g = 0.05$.

($\omega_D = 2.875$) for different quench amplitudes, namely, at $\delta g = 0.0, 1.0$, and 2.0 . As expected (resonance) $\Delta\rho_L(t)$ features a beating dynamics but with an increasingly decaying envelope with increasing quench amplitude, which is a direct effect of the interactions. A similar dephasing behavior holds for the other ω_D 's, where $\Delta\rho_L(t)$ does not exhibit a beating pattern. Concerning the width of the resonant region different amplitudes of the interaction quench lead to a slight broadening of the resonant region. According to our calculations for the case with $\delta g = 0$ the resonant frequency region corresponds to $\omega_D \in [2, 3]$, while for $\delta g = 1.0$ and $\delta g = 2.0$ the corresponding regions are $\omega_D \in [1.8, 3.2]$ and $\omega_D \in [1.5, 3.5]$, respectively. Summarizing, one can induce this resonant intrawell dynamics by adjusting the driving frequency and by applying an interaction quench to increase the width of the resonance and manipulate the amplitude of the intrawell oscillations.

From another perspective the above-mentioned resonant behavior can be illustrated by employing the occupation of the zeroth band of the triple well during evolution. The probability

of finding all four bosons within the zeroth band (employing the multiband expansion) reads

$$|B_{\{N_i\};\{I_i\}}(t)|^2 = \sum_{\{I_i\}} |\langle N_1^{(I_1)}, N_2^{(I_2)}, N_3^{(I_3)} | \Psi(t) \rangle|^2, \quad (10)$$

where the summation is performed over the excitation indices with the imposed constraints $\sum_{i=1}^3 n_i^{(1)} = N$ and $\sum_{i=1}^3 \sum_{j=2}^3 n_i^{(j)} = 0$ [see also Eq. (3)]. Figure 4(c) shows the probability $|B_{\{N_i\};\{I_i\}}(t)|^2$ of all the bosons residing in the zeroth band for various driving frequencies ω_D and a fixed amplitude $\delta = 0.03$. At resonance a complete depopulation of the zeroth band at some specific time intervals is observed. To be more precise, this probability exhibits a revival-like behavior on short time scales and decays as time evolves [see, in particular, the dashed black curve in Fig. 4(c)]. The local minima of $|B_{\{N_i\};\{I_i\}}(t)|^2$ are connected to the enhancement of the amplitude of the oscillations of the single-particle density (see also Appendix B). On the other hand, for driving frequencies away from $\Delta\omega_D$, the respective probability that

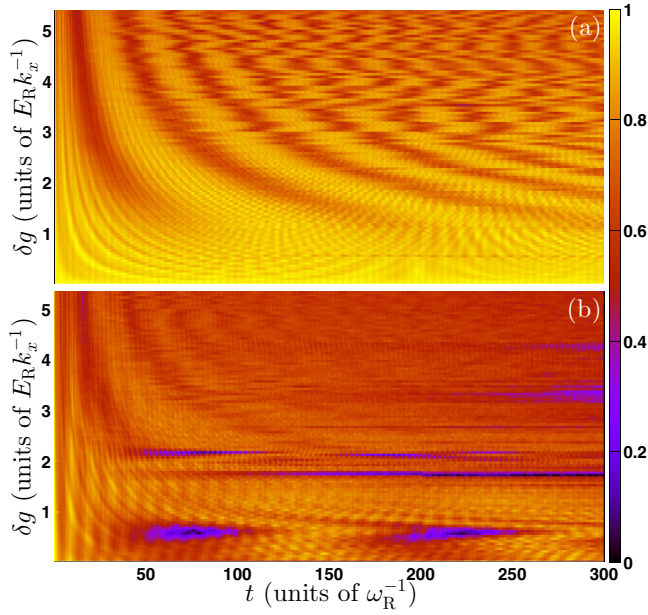


FIG. 5. Time evolution of the fidelity $F_{\{\omega_D, \delta g\}}(t)$ in a periodically driven triple well with (a) $\omega_D = 0.75$ and (b) $\omega_D = 2.75$ as a function of the quench amplitude. The driving amplitude is $\delta = 0.03$, while the initial state corresponds to the ground state of four weakly interacting bosons with $g = 0.05$.

all the bosons will occupy the zeroth band is rather high and is indeed dominant. However, significant contributions, e.g., at $\omega_D = 5.25$ or $\omega_D = 9.25$ [see Fig. 4(c)] from excited configurations cannot be neglected, especially in the regions $\Delta\omega_{D_1}$ and $\Delta\omega_{D_2}$, where the system departs from the initial state [see also Fig. 1(a)] in a prominent way. Finally, in order to explore the impact of the interaction quench at resonance, Fig. 4(d) shows $|B_{\{N_i\};\{L_i\}}(t)|^2$ for different quench amplitudes at $\omega_D = 2.75$. It is observed that for larger interaction quenches, this probability exhibits a more strongly decaying envelope, which is a pure effect of the interactions. As shown, for increasing quench amplitude the probability that the system will remain in the zeroth band, in the course of the dynamics, decays on increasingly shorter time scales and the system is dominated by different types of excitations, e.g., two, three, or four particles distributed in the first and second excited bands, as expected intuitively.

B. Case II: Periodically driven dynamics for different interaction quench amplitudes

In the following, we examine the impact of the quench amplitude δg , focusing on two driving frequency regions, i.e., for an almost-adiabatic periodic driving and in the vicinity of the resonance [see also Fig. 1(a)]. To obtain an overview of the dynamical response, Figs. 5(a) and 5(b) show the fidelity evolution with respect to δg , for fixed driving frequencies $\omega_D = 0.75$ and $\omega_D = 2.75$, respectively. As expected, for higher quench amplitudes the time-evolved final state deviates from the initial (ground) state in a prominent way. For instance, $\bar{F}_{\{\omega_D=0.75, \delta g=0\}} = 0.95$ and $\bar{F}_{\{\omega_D=0.75, \delta g=4.0\}} = 0.6$, while $\bar{F}_{\{\omega_D=2.75, \delta g=0\}} = 0.7$ and $\bar{F}_{\{\omega_D=2.75, \delta g=4.0\}} = 0.4$. Next,

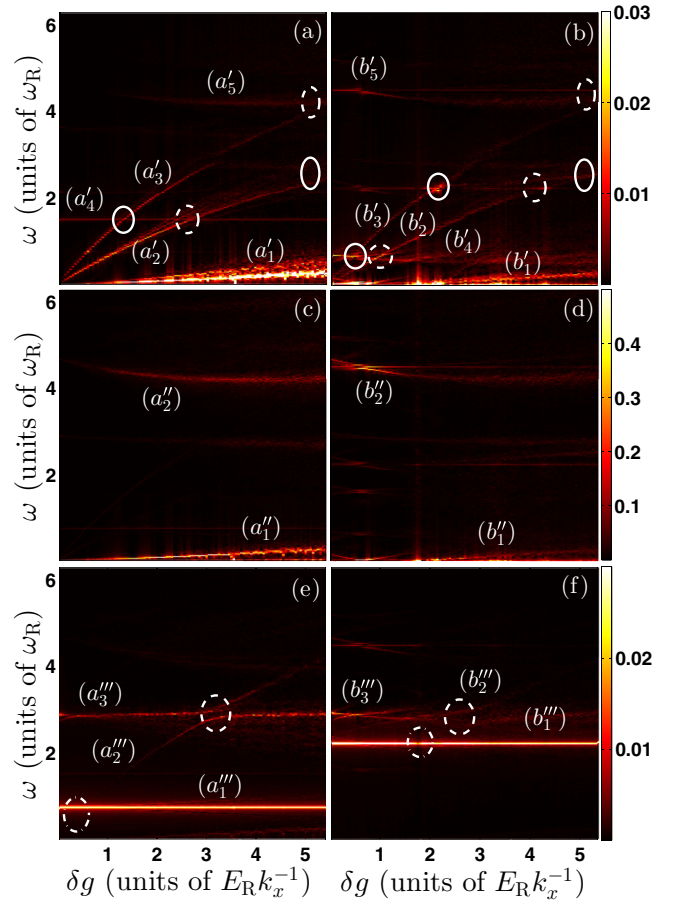


FIG. 6. The following are shown as a function of the quench amplitude δg : the fidelity spectrum $F_{\{\omega_D, \delta g\}}(\omega)$ for (a) $\omega_D = 0.75$ and (b) $\omega_D = 2.75$; the spectrum of the local-breathing mode $[\sigma_M^2(\omega)]$ for the middle well of a periodically driven triple well with (c) $\omega_D = 0.75$ and (d) $\omega_D = 2.75$; and the spectrum of the local-dipole mode $[\Delta\rho_L(\omega)]$ for the left well of a driven triple well with (e) $\omega_D = 0.75$ and (f) $\omega_D = 2.75$. Solid and dashed ellipses indicate the positions of the resonances between the tunneling and the breathing or dipole branches (see text). The driving amplitude is $\delta = 0.03$, while the initial state corresponds to the ground state of four weakly interacting bosons with $g = 0.05$.

let us proceed with a more detailed analysis in order to probe the effect of an interaction quench on the interwell tunneling dynamics and the intrawell excited modes.

To examine the tunneling dynamics, Fig. 6(a) presents the fidelity spectrum $F_{\{\delta g\}}(\omega) = \frac{1}{\pi} \int dt F_{\{\delta g\}}(t)$ as a function of the quench amplitude. Three interwell tunneling branches ($a'_1 - a'_3$) can be identified. The lowest branch (a'_1), which dominates for strong quench amplitudes, refers to the energy difference $\Delta\epsilon$ within the energetically lowest-band states of the SP mode, e.g., from the initial state $|1^{(0)}, 2^{(0)}, 1^{(0)}\rangle$ to a final state $|2^{(0)}, 1^{(0)}, 1^{(0)}\rangle$. The second branch (a'_2) corresponds to tunneling between the SP and the DP modes, e.g., from $|1^{(0)}, 2^{(0)}, 1^{(0)}\rangle$ to $|2^{(0)}, 2^{(0)}, 0^{(0)}\rangle$. The third branch (a'_3) refers to a tunneling process among the SP and T modes, e.g., from $|1^{(0)}, 2^{(0)}, 1^{(0)}\rangle$ to $|3^{(0)}, 1^{(0)}, 0^{(0)}\rangle$. The remaining interwell tunneling branches, which correspond to transitions of

energetically higher different modes, are negligible in comparison to the aforementioned, and therefore we can hardly identify them in Fig. 6(a). To probe the effect of the driving frequency on the tunneling spectrum, Fig. 6(b) shows $F_{\{\delta g\}}(\omega)$ at $\omega_D = 2.75$ (i.e., at resonance of an explicitly driven triple well) with varying quench amplitude. The three observed tunneling branches ($b'_1 - b'_3$) refer to the same transitions, i.e., between the same number states as addressed above, but they are slightly shifted to higher frequencies as a consequence of the higher driving frequency. The remaining branches, e.g., a'_4 and b'_4 , that are visible in the spectrum, which show more prominent deviations for the different driving frequencies, correspond to other modes and interband transitions and are explained below.

To identify the frequencies of the local breathing mode we resort to the second moment $\sigma_i^2(\omega) = \frac{1}{\pi} \int dt \sigma_i^2(t) e^{i\omega t}$ for each well [see Sec. II B and Eq. (5)]. Focusing on the left well, which possesses a breathing component [see also Fig. 2(b)] we calculate the frequency spectrum of $\sigma_L^2(\omega)$, which matches the branch a'_4 in the fidelity spectrum [see Fig. 6(a)]. Most importantly this frequency branch resonates with two distinct tunneling branches at different quench amplitudes, namely, at $\delta g \approx 1.0$ with branch a'_3 [see the ellipse in Fig. 6(a)] and at $\delta g \approx 2.8$ with branch a'_2 [see the dashed ellipse in Fig. 6(a)] of the tunneling. Turning to the middle well, Fig. 6(c) presents $\sigma_M^2(\omega)$, thus showing two main peaks ($a'_1 - a'_2$) with respect to the quench amplitude. The lowest of these peaks refers to a tunneling mode [see also Fig. 6(a)] identified from the energy difference within the energetically lowest states of the SP mode. The appearance of this peak in the spectrum is due to the fact that the tunneling can induce a modulation of the width of the local wave packet. The second peak, located at $\omega_2 \approx 4.5$, refers to an interband process, i.e., to a transition from $|1^{(0)}, 2^{(0)}, 1^{(0)}\rangle$ to $|1^{(0)}, 1^{(0)} \otimes 1^{(2)}, 1^{(0)}\rangle$. Inspecting now more carefully the fidelity spectrum in Fig. 6(a) we observe that the latter breathing frequency branch a'_2 [denoted a'_5 in Fig. 6(a)] comes into resonance with the highest-tunneling-frequency branch (a'_3) at high quench amplitudes $\delta g \approx 5.2$. However, this tunneling branch is not visible in Fig. 6(c) due to its low amplitude in comparison to the breathing (a'_2) branch. To comment on the dependence of the breathing peak (a'_2) on the interaction quench we observe that it is more sensitive to δg for $0.0 < g_f < 2.5$; otherwise it is approximately constant. To probe the effect of the driving frequency on the breathing branch of the middle well, Fig. 6(d) illustrates the spectrum of $\sigma_M^2(\omega)$ with respect to a varying δg for $\omega_D = 2.75$. The respective breathing branches, denoted b'_1 and b'_2 in the figure, are slightly disturbed in comparison to the case with $\omega_D = 0.75$. Concerning the first one, we have commented on its deviation in our discussion of Figs. 6(a) and 6(b). Focusing now on the highest-frequency branch of the breathing a significant alteration is observed: for low quench amplitudes, $0.0 < \delta g < 0.8$, it possesses a single frequency, while for $\delta g > 0.8$ the branch splits into two, with slightly different frequencies. The first is near the corresponding frequency for $\omega_D = 0.75$ but slightly larger, while the second is larger than both. Finally, let us quantitatively examine the dipole component in the outer wells by employing the frequency spectrum $\Delta\rho_L(\omega) = \frac{1}{\pi} \int dt \Delta\rho_L(t) e^{i\omega t}$ for various quench amplitudes. Figure 6(e) shows $\Delta\rho_L(\omega)$, where we

can identify three dominant peaks (denoted $a''_1 - a''_3$), which are located at $\omega''_1 \approx 1.2$, $\omega''_3 \approx 2.5$, while ω''_2 is quench dependent. The steady frequency branches (a''_1 and a''_3) correspond to the dipole mode and refer to interband transitions, e.g., from $|1^{(0)}, 2^{(0)}, 1^{(0)}\rangle$ to $|1^{(0)} \otimes 1^{(1)}, 1^{(0)}, 1^{(0)}\rangle$ or to $|1^{(0)} \otimes 1^{(2)}, 1^{(0)}, 1^{(0)}\rangle$, respectively. On the other hand, the quench-dependent frequency peak (a''_2) is related to the third interwell tunneling mode [denoted a'_3 in Fig. 6(a)]. As shown in Fig. 6(e) the latter branch a''_2 experiences two resonances with each dipole branch at different quench amplitudes, namely, at $\delta g \approx 0.7$ with the lowest-frequency dipole branch (a''_1) and at $\delta g \approx 3.0$ with the higher-frequency dipole branch a''_3 . Moreover, upon examining the fidelity spectrum once again [Fig. 6(a)] more carefully, it is observed that the highest-frequency dipole branch experiences a resonance with the second interwell tunneling mode (a'_2) at $\delta g \approx 5.0$. In order to reach a conclusion on the dependence of the dipole branches on the driving frequency we show in Fig. 6(f) the $\Delta\rho_L(\omega)$ at $\omega_D = 2.75$. As shown the lower-frequency dipole branch (a''_1) is strongly dependent on the driving frequency [see branch b''_1 in Fig. 6(f)], while the higher-frequency branch (a''_3) is essentially unaffected. Most importantly, the aforementioned resonant behavior still exists for $\omega_D = 2.75$ but in this case two more resonances appear in the spectrum [see Fig. 6(b)] due to a shift of the lowest-frequency dipole branch. These resonances are located at $\delta g \approx 2.1$ and $\delta g \approx 4.0$ and refer to a coupling among the second (b'_2) and third (b'_3) tunneling branches with the lowest-frequency dipole branch.

In the next section, we proceed to the investigation of a system with filling $\nu < 1$ in order to generalize our findings. In particular, by considering a setup with 11 wells and five particles we demonstrate that the above-discussed resonant behavior for the intrawell dynamics induced by an explicitly driven potential is present also here. Subsequently, we explore the impact of an interaction quench.

IV. QUENCH DYNAMICS IN THE DRIVEN LATTICE FOR FILLING FACTOR $\nu < 1$

Here we concentrate on a larger lattice system characterized by a filling factor smaller than unity, namely, we consider the case of five bosons trapped in an 11-well potential. To understand and interpret the dynamics let us first briefly comment on the ground-state properties of the system. An important property of the ground state is the spatial redistribution of the atoms as the interparticle repulsion increases. The noninteracting ground state ($g = 0$) is the product of the single-particle eigenstates spreading across the entire lattice, while the presence of the hard-wall boundaries renders the neighborhood of the central well of the potential slightly more populated. Increasing the repulsion within the weak-interaction regime the atoms are pushed to the outer sites, which gain and lose population in the course of increasing g [58].

In the following, let us first focus on the driven bosonic dynamics induced, at $t = 0$, by a vibrating 11-well potential to the ground state of five repulsively interacting bosons with $g = 0.05$. Figures 7(a) and 7(b) demonstrate the response of the system at the one-body level for different driving frequencies ω_D , but the same driving amplitude $\delta = 0.03$.

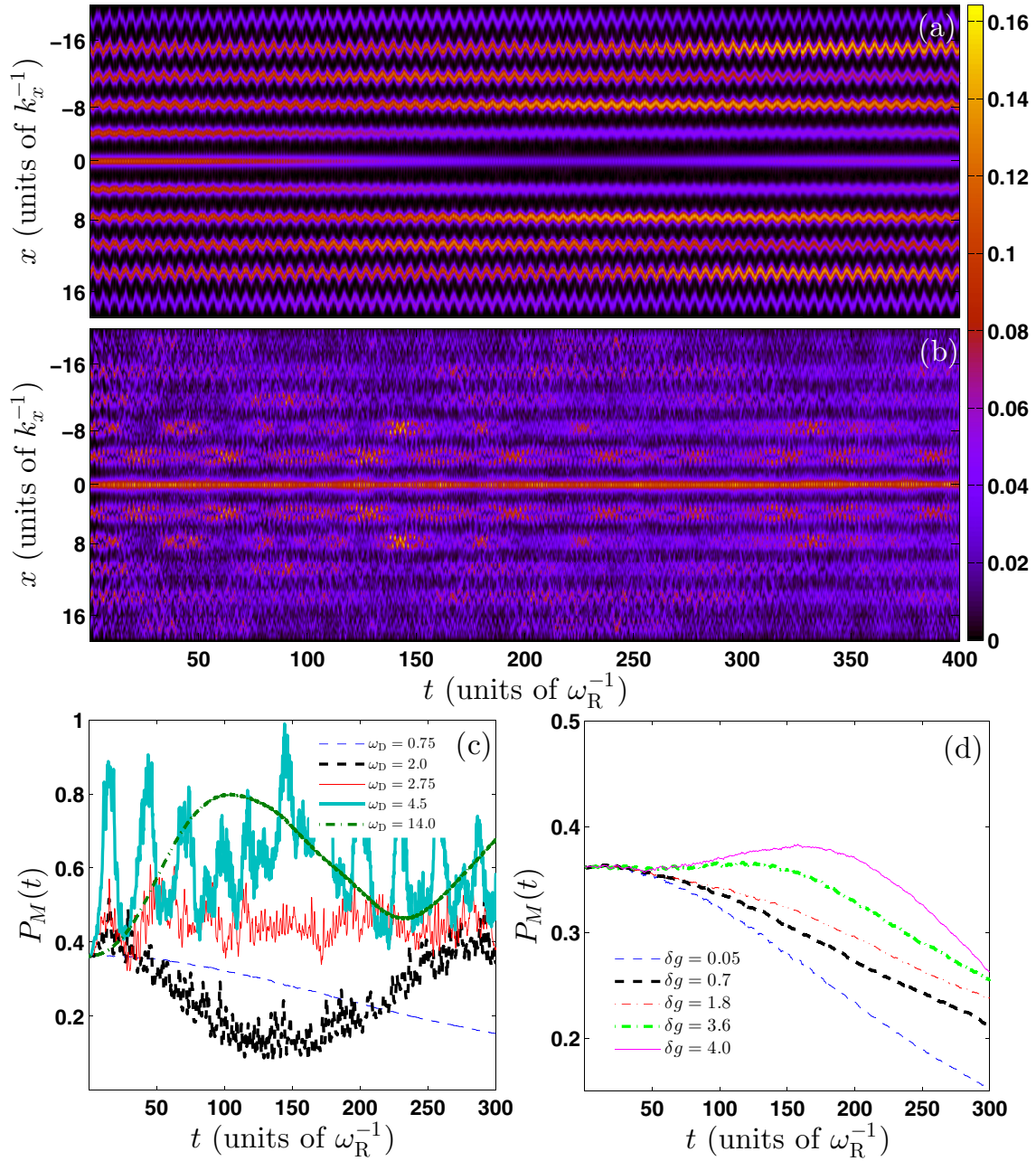


FIG. 7. Time evolution of the one-body density $\rho_1(x,t)$ in a periodically driven 11-well potential for different driving frequencies: (a) $\omega_D = 1.25$ and (b) $\omega_D = 2.875$. The driving amplitude is fixed at the value $\delta = 0.03$, while the initial state corresponds to the ground state of five weakly interacting bosons with $g = 0.05$. (c) Probability of finding all the bosons in the central well [$P_M(t)$] during the evolution for different driving frequencies ω_D (see legend). (d) The same as (c), but for $\omega_D = 0.75$ and different quench amplitudes δg (see legend).

The overall out-of-equilibrium behavior shows characteristics to those in the case of the triple well, i.e., the occurrence of out-of-phase dipolelike modes among the outer wells of the lattice, a local-breathing mode in the central well, and an interwell tunneling mode accompanying the dynamics. In addition, a transition from nonresonant [Fig. 7(a)] to a resonant intrawell dynamics [Fig. 7(b)] upon adjusting ω_D is observed at the same frequency, $\omega_D = 2.875$, as in the triple-well case. This resonant behavior is again manifested [Fig. 7(b)] in the one-body density evolution as the formation of enhanced density oscillations at each site, being further

related to a gradual depopulation of the zeroth band during evolution. In terms of the significant contributing number states we can infer that out of resonance the dynamics can well be described by the set of lowest-band states (with a small contribution from the excited-band states), while at resonance the inclusion of number states which obey the constraints $\sum_{i=1}^{11} n_i^{(1)} = N - 1$, $n_i^{(3)} = 0$, and $n_i^{(2)} = 1$ for $k = 1, \dots, 11$ is necessary. Contributions from excited states to the second band, i.e., $\sum_{i=1}^{11} n_i^{(1)} = N - 1$, $n_i^{(2)} = 0$, and $n_i^{(3)} = 1$ for $k = 1, \dots, 11$ also exist, but they are negligible in comparison to the excitations of the first excited band.

Another important observation here is that upon tuning the driving frequency ω_D close to resonance the tunneling dynamics is modified. To explicate the latter, we employ, as a measure of the interwell tunneling, the spatially integrated middle-well density $P_M(t) = \int_{-\pi/2}^{\pi/2} dx \rho_1(x,t)$, shown in Fig. 7(c) for different driving frequencies, namely, before, exactly at, and after the resonance. Approaching $\omega_D = 2.875$ from below, diffusion to the outer wells is observed. In the region of $\omega_D = 2.875$ the tunneling dynamics is slowed down, i.e., the occupation of the middle well fluctuates around a mean value. For $\omega_D > 2.875$ the tunneling process is modified and a tendency for the particles to concentrate in the central well is observed. Employing a corresponding number-state analysis we can infer that for $\omega_D > 2.875$, states with a higher occupancy in the central well gain prominence. The same behavior of the tunneling dynamics (before and after the resonance) is also observed in the triple-well case. Furthermore, let us inspect the influence of an interaction quench on top of the driven lattice. As expected intuitively, with increasing interaction quench the tunneling process decreases. Figure 7(d) shows $P_M(t)$ for different interaction quench amplitudes on top of the periodically driven lattice with $\omega_D = 0.75$ (i.e., away from resonance). It is observed that $P_M(t)$ becomes steady for increasingly longer times as we increase δg , thus indicating a decrease in the corresponding interwell tunneling dynamics. Finally, note that due to the low filling the admixing modes, induced after an interaction quench on the periodically driven lattice, in the outer wells are hardly visible and therefore not shown here.

Let us further investigate the signature of the resonant regions as well as the effect of the interaction quench on top of the periodically driven lattice by exploring the first-order correlation function [see Eq. (8)], in coordinate space, which quantifies the degree of spatial coherence of the interacting system [51]. It is important to stress that, within the single-orbital Gross-Pitaevskii theory, the quantum wave packet remains coherent at all times, in contrast to a many-body calculation, where it exhibits prominent time-varying structures which in turn indicate the rise of fragmentation in the system as the correlations between particles increase. From this point of view we expect a strong influence on the change in the spatial distribution of the atoms in the lattice either due to the resonant driving or as a consequence of the interaction quench. Focusing on low driving frequencies ($\omega_D = 0.75$) within the weakly interacting regime ($g = 0.05$) we observe spread of the coherence [Figs. 8(a)–8(d)] through the lattice sites as time evolves. The diagonal elements are always perfectly coherent and their first neighbors remain close to unity throughout the time evolution. The off-diagonal elements are partially coherent and oscillate around the value 0.5, while for comparatively long evolution times a site-selective, off-diagonal, long-range order appears [see Fig. 8(d)]. Turning our attention to the resonant driving [see Figs. 8(e)–8(h)] a different behavior throughout the time evolution is observed: On short time scales, only the diagonal elements remain coherent and the off-diagonal is partially coherent. As time evolves, a substantial loss of coherence is observed even on the diagonal, while the off-diagonal elements exhibit a much more prominent and complex structure. A direct comparison at equal times of the correlation functions for nonresonant and resonant

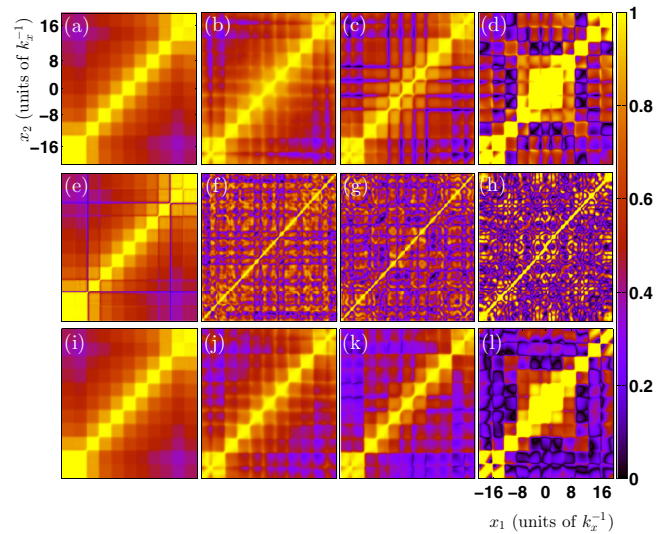


FIG. 8. One-body coherence function at different instants in time ($t_1 = 1.0$, $t_2 = 56.0$, $t_3 = 123.0$, and $t_4 = 193.0$) during the evolution caused by a periodically driven 11-well potential with (a)–(d) $\omega_D = 0.75$ and (e)–(h) $\omega_D = 3.0$. (i)–(l) Evolution of the one-body coherence in a periodically driven potential with $\omega_D = 0.75$ and a simultaneous interaction quench with amplitude $\delta g = 1.0$. The driving amplitude is fixed at the value $\delta = 0.03$ and the initial state corresponds to the ground state of five weakly interacting bosons with $g = 0.05$.

driving shows that resonant driving and loss of coherence go hand in hand. On the other hand, by performing an interaction quench on top of the driving, the coherence [see Figs. 8(i)–8(l)] is unity along the diagonal, while for sufficiently long evolution times it tends to vanish away from the diagonal. Finally, note that the off-diagonal contributions tend to fade out (but never vanish completely, even for stronger quenches, since the particles always remain delocalized) with increasing quench amplitude and a tendency toward concentration close to the diagonal is observed at equal times. This indicates that the strength of the interaction between particles strongly affects the correlations; the stronger the interparticle repulsion, the stronger the loss of coherence. As a concluding remark we can infer that either the resonant driving or a quench on top of the driving entails an intensified loss of coherence.

V. CONCLUSIONS AND OUTLOOK

In the present work, the few-body correlated nonequilibrium quantum dynamics of an interaction quenched bosonic cloud in an external periodically driven finite-size optical lattice has been investigated. The effect of an interaction quench on top of the driven lattice has been analyzed. We focus on large lattice depths and low driving amplitudes in order to limit the degree of excitations that could lead to the creation of cradle motion [37] or even to heating processes. Starting from the ground state of a weakly interacting small atomic ensemble, we examine in detail the time evolution of the system in a periodically driven optical lattice by a simultaneous interaction quench.

It has been shown that for the case of the periodically driven lattice one can induce out-of-phase local dipole modes in the

outer wells, while a local breathing mode can be generated in the central well. This is in direct contrast with the shaken lattice, where only in-phase dipole modes are excited. A wide range of driving frequencies has been considered in order to unravel the range from adiabatic to high-frequency driving. We observe that within the intermediate-frequency regimes, being intractable by current analytical methods, the system can be driven to a far out-of-equilibrium state compared to other driving-frequency regions. In particular, resonance of the intrawell dynamics occurs with enhanced tunneling dynamics, thus opening energetically higher-lying interwell tunneling channels. A prominent signature of the resonant regions as well as the effect of the interaction is provided via the study of the time dependence of the first-order coherence, where intensified loss of coherence is observed. This loss of coherence constitutes an independent signature of the resonant regions, allowing us to study it from another perspective and, potentially, to measure it in experiments. Following an interaction quench on top of the periodically driven lattice for various driving frequencies, we can trigger more effectively the interwell as well as the intrawell dynamics and steer the system towards strongly out-of-equilibrium regimes. Here, the tunneling as well as the local breathing mode in the middle well is amplified, while in the outer wells the atomic cloud experiences an admixture of a dipole and a breathing component. This admixture leads to simultaneous oscillations around the minimum of the well as well as a contraction and expansion in the course of the dynamics. Our analysis shows that one can use the interaction quench to manipulate the tunneling frequency, rendering single-particle tunneling dominant even at resonance. Concerning the on-site modes it is shown that an interaction quench can be used in order to manipulate their amplitude oscillations, yielding also a strong influence on the excitation dynamics.

Subsequently, the dynamics of the periodically driven lattice (i.e., for a fixed driving frequency) as a function of the quench amplitude has been studied. In particular, the tunneling contains three modes, the breathing possesses two frequency branches, and the corresponding admixture three branches: one from the breathing component and two which refer to the dipole component. Furthermore, five resonances between the interwell tunneling dynamics and the intrawell dynamics have been revealed. The interwell tunneling experiences a resonance with the breathing component of the central well, two resonances with the breathing component of the outer wells, and two resonances with the dipole component of the outer wells. These resonances can further be manipulated via the frequency of the periodic driving. As a result, the combination of different driving protocols can excite different inter- and intrawell modes as well as manifest various energetically higher components of a mode. Most importantly, the observed resonances between different inter- and intrawell modes demonstrate the richness of the system, while their dependence on various system parameters, e.g., the driving frequency, shows the tunability of the system. The above-mentioned realization of multiple resonances constitutes arguably one of the central results of our investigation, which, to the best of our knowledge, has never been reported in such a setting.

Finally, let us comment on possible future extensions of the present work. Our analysis reveals that a combination of

different driving protocols can induce admixtures of excited modes which, in the present case, correspond to admixtures of dipolelike and breathinglike modes. In this direction, it would be a natural next step to find the optimal pulse of the interaction quench protocol in order to induce a perfectly shaped squeezed state. Also, the understanding and prediction of the long-time dynamics imposing an interaction quench on a driven lattice at different transient times is certainly of interest.

ACKNOWLEDGMENTS

The authors thank C. V. Morfonios for fruitful discussions. The authors gratefully acknowledge funding by the Deutsche Forschungsgemeinschaft (DFG) in the framework of SFB 925 (“Light induced dynamics and control of correlated quantum systems”).

APPENDIX A: HARMONIC OSCILLATOR—ADMIXTURES OF DIPOLELIKE AND BREATHINGLIKE MODES

In the present Appendix we briefly demonstrate the creation of admixtures of excitations consisting of a dipole and a breathing component in the dynamics of a bosonic ensemble confined in a 1D harmonic oscillator. Let us first comment on the creation of each of the above excited modes separately. It is well known that a quench of the frequency of the harmonic oscillator or of the interatomic repulsive interaction induces a breathing-mode oscillation of the atomic cloud. On the other hand, a sudden displacement or a periodic driving, e.g., shaking, of the harmonic oscillator can induce a dipole mode in the atomic cloud. However, a combination of the above techniques can induce more complicated modes in the dynamics [59] and requires computational methods which can take into account higher orbitals, i.e., correlations. Here, we aim at illuminating this scenario by examining the evolution of an atomic cloud consisting of six bosons initially ($t < 0$) prepared in the ground state of a harmonic oscillator potential. Subsequently ($t > 0$) the cloud is subjected to a periodic driving and a simultaneous quench of the interatomic repulsive interaction. Thus, the Hamiltonian that governs the dynamics reads

$$H = \sum_{i=1}^N \left(\frac{p_i^2}{2M} + V_D(x_i; t) \right) + g_f \sum_{i < j} \delta(x_i - x_j), \quad (\text{A1})$$

where the periodic driving of the harmonic oscillator is modeled via the time-dependent potential $V_D(x; t) = \frac{\omega^2}{2} (x - A \sin(\omega_D t))^2$ and $\delta g = g_f - g_{in}$ denotes the quench amplitude. Figure 9(a) illustrates the dynamics of the atomic cloud on the single-particle level by employing the one-body density. It is observed that the cloud not only oscillates inside the external trap but also changes its shape during the oscillation. This is a clear signature that the induced mode is different from a pure dipole mode or a pure breathing mode but it is an admixture of the above-mentioned excitations. To indicate this fact explicitly we illustrate in Fig. 9(b) the profiles of the one-body density at certain instants in time during the evolution. The cloud compresses and decompresses (caused by the interaction quench) during its oscillation (caused by the driven oscillator) inside the external harmonic trap. On the contrary, a cloud which is only subjected to the above

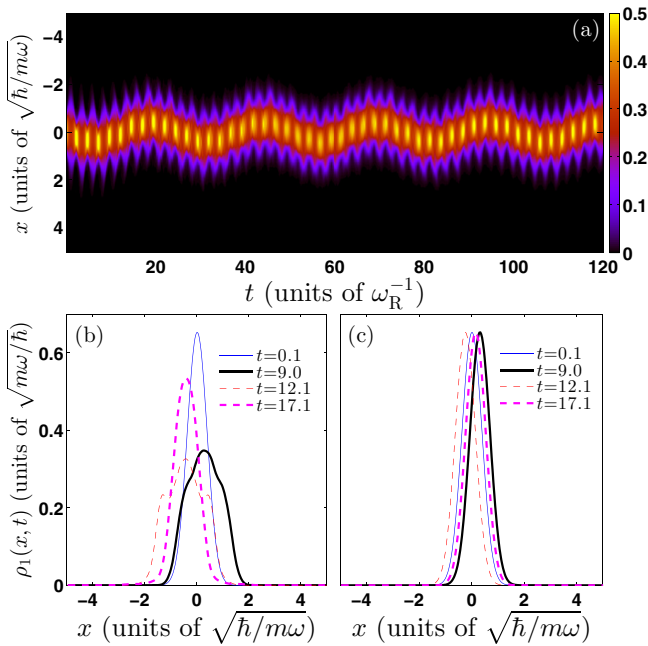


FIG. 9. (a) Time evolution of the one-body density $\rho_1(x,t)$ caused by a periodically driven harmonic trap with $\omega_D = 0.25$ and a simultaneous interaction quench with amplitude $\delta g = 1.6$. The driving amplitude is fixed to the value $A = 0.6$, while the initial state corresponds to the ground state of six weakly interacting bosons with $g = 0.05$. We also illustrate the one-body density profiles at certain instants in time (see legend) during the evolution of the periodically driven oscillator with (b) $\delta g = 1.6$ and (c) $\delta g = 0$.

external driving [see Fig. 9(c)] performs the well-known dipole oscillation and the wave packet exhibits oscillations with a constant width and amplitude.

APPENDIX B: REMARKS ON THE RESONANT INTRAWELL DYNAMICS OF THE DRIVEN LATTICE

In the present Appendix we briefly comment on the characteristics of the resonant dynamics of the driven lattice from a one-body perspective. Indeed, Fig. 10(a) presents $\rho_1(x,t)$ at $\omega_D = 2.75$. The overall dynamics exhibits enhanced density modulations being manifest as internal fast oscillations and high-amplitude oscillations in each well of period ~ 20 . The interwell tunneling is also enhanced in comparison to that at small ω_D 's [see Fig. 2(a)]. A similar intrawell resonant behavior was observed in Ref. [35], where enhanced and in-phase oscillating dipoles were revealed. On the contrary, here, we observe enhanced and out-of-phase oscillating dipole modes as well as an amplified breathing mode in the center. Thus, exploiting the presently used driving scheme we have the possibility of opening an additional energetic channel. To quantify that the driven lattice induced dynamical features are independent of the interaction strength g or the particle number N , we calculate the deviation of the local density oscillation from its mean value, i.e., $\Lambda = \int_0^T dt |\Delta\rho_\alpha(t) - \overline{\Delta\rho_\alpha}|/T$, where $\overline{\Delta\rho_\alpha} = \int_0^T dt \Delta\rho_\alpha(t)/T$ denotes the mean oscillation amplitude over the considered propagation time T and $\Delta\rho_\alpha(t)$ refers to the intrawell wave-packet asymmetry. Figure 10(b)

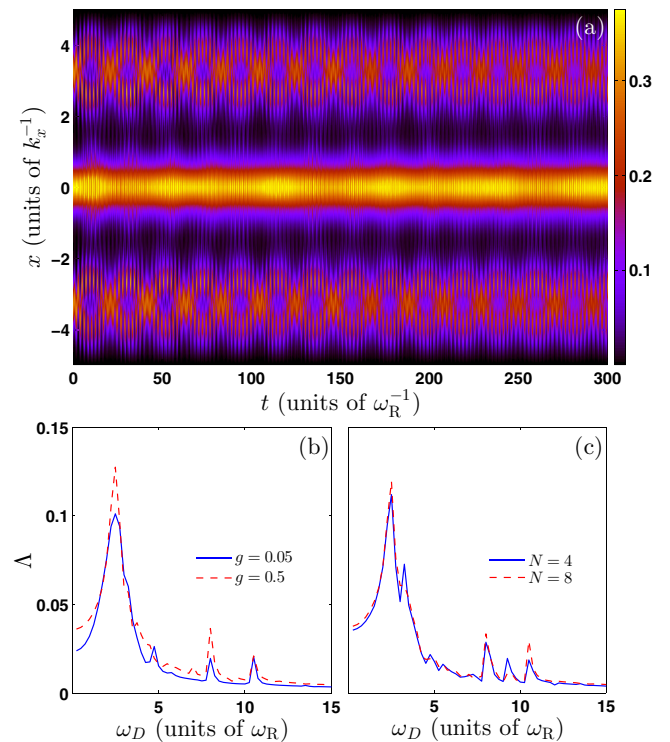


FIG. 10. (a) Time evolution of the one-body density $\rho_1(x,t)$ in a triple well for $\omega_D = 2.75$. The driving amplitude is fixed at the value $\delta = 0.03$, while the initial state corresponds to the ground state of four weakly interacting bosons with $g = 0.05$. (b) Mean oscillation amplitude Λ of the left well for $N = 4$ bosons as a function of the driving frequency ω_D for different interparticle repulsions (see legend). (c) The same as (b), but for fixed interaction $g = 0.2$ and different particle numbers (see legend).

shows the mean amplitude of the intrawell oscillation for the left well as a function of the driving frequency ω_D for different interaction strengths g but the same particle number. The mean amplitude with a varying ω_D increases up to $\omega_D = 2.875$, where it exhibits a peak (position of the resonance) and then decreases again, exhibiting several smaller peaks at frequencies where the system is driven far from equilibrium [see also Fig. 1(a)]. Comparing the dynamics for different interactions it is observed that the ensemble exhibits the same overall behavior but the mean oscillation amplitude is slightly higher (for higher interactions), especially in the region of the central peak. This is a direct interaction effect, since the system possesses more energy. On the other hand, in order to investigate whether the above results are independent of the particle number the same quantity (Λ) is shown in Fig. 10(c) for varying particle numbers, namely, $N = 4$ and 8 . The mean amplitude presents the same overall behavior with respect to the driving frequency ω_D but it is also slightly larger for increasing particle number, with a maximal deviation of the order of 30%.

APPENDIX C: THE COMPUTATIONAL APPROACH—MULTICONFIGURATION TIME-DEPENDENT HARTREE METHOD FOR BOSONS

To solve the many-body Schrödinger equation ($i\hbar\partial_t - H)\Psi(x,t) = 0$ of the interacting bosons as an

initial value problem $|\Psi(0)\rangle = |\Psi_0\rangle$, we employ the MCTDHB [39,40,60]. The latter constitutes an efficient and accurate method for both the stationary properties and the nonequilibrium quantum dynamics of systems consisting of a single bosonic species and has already been applied for a wide set of problems (see, e.g., [60–63]). The wave function is represented by a set of variationally optimized time-dependent orbitals, which implies an optimal truncation of the Hilbert space by employing a time-dependent moving basis where the system can be instantaneously optimally represented by time-dependent permanents. Thus, the many-body wave function, which is expanded in terms of the bosonic number states $|n_1, n_2, \dots, n_M; t\rangle$, based on time-dependent single-particle functions (SPFs) $|\phi_i(t)\rangle$, $i = 1, 2, \dots, M$, reads

$$|\Psi(t)\rangle = \sum_{\vec{n}} C_{\vec{n}}(t) |n_1, n_2, \dots, n_M; t\rangle. \quad (\text{C1})$$

Here M is the number of SPFs and the summation \vec{n} is over all the possible combinations n_i such that the total number of bosons N is conserved. Note that in the limit in which M approaches the number of grid points the above expansion is equivalent to a full configuration interaction approach. However, in the case of $M = 1$ the many-body wave function is given by a single permanent $|n_1 = N; t\rangle$ and the method reduces to the time-dependent Gross-Pitaevskii equation. To determine the time-dependent wave function $|\Psi(t)\rangle$ we need the equations of motion for the coefficients $C_{\vec{n}}(t)$ and the SPFs $|\phi_i(t)\rangle$. Following, e.g., the Dirac-Frenkel [64,65] variational principle, i.e., $\langle \delta\Psi | i\partial_t - \hat{H} | \Psi \rangle = 0$, we end up with the well-known MCTDHB equations of motion [39,40,60], consisting of a set of M nonlinear integrodifferential equations of motion for the orbitals which are coupled to the $\frac{(N+M-1)!}{N!(M-1)!}$ linear equations of motion for the coefficients. Finally, let us remark that in terms of our implementation we use an extended version of the MCTDHB referred to in the literature as the multilayer multi-configuration time-dependent Hartree method for bosons (ML-MCTDHB) [66,67]. This package is particularly suitable for treating systems consisting of different bosonic species, while for the case of a single species it reduces to the MCTDHB.

For our numerical implementation a discrete variable representation for the SPFs and a sine-discrete variable representation, which intrinsically introduces hard-wall boundaries at both edges of the potential, have been employed. The preparation of the initial state has been performed by using the so-called relaxation method in terms of which one obtains the lowest eigenstates of the corresponding m -well setup. The key idea is to propagate some trial wave function $\Psi^{(0)}(x)$ by the nonunitary operator $e^{-H\tau}$. This is equivalent to an imaginary time propagation, and for $\tau \rightarrow \infty$ the propagation converges to the ground state, as all other contributions (i.e., $e^{-E_n\tau}$) are exponentially suppressed. In turn, we periodically drive the optical lattice and perform a quench of the strength of the interparticle repulsion and study the evolution of $\Psi(x_1, x_2, \dots, x_N; t)$ in the m -well potential within the MCTDHB.

Within our simulations the overlap criteria $|\langle \Psi | \Psi \rangle - 1| < 10^{-9}$ and $|\langle \varphi_i | \varphi_j \rangle - \delta_{ij}| < 10^{-10}$ are fulfilled for the total wave function and the SPFs, respectively. Furthermore, to ensure the convergence of our simulations we have used up to 12 (11) optimized SPFs for the triple (11) well, thereby observing

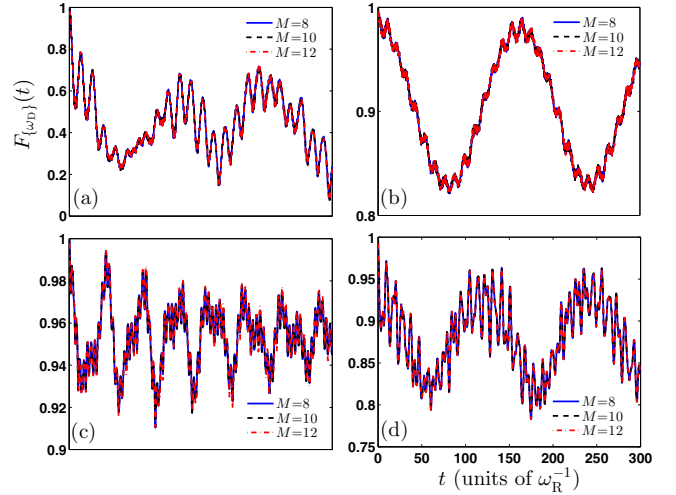


FIG. 11. Fidelity evolution $F_{\omega_D}(t)$ of a periodically driven triple well with (a) $\omega_D = 2.5$ and (b) $\omega_D = 7.5$ with an increasing number of SPFs (see legend). (c), (d) $F_{\omega_D}(t)$ for various SPFs (see legend) with a simultaneous interaction quench of amplitude (c) $\delta g = 0.5$ and (d) $\delta g = 2.0$ on top of the periodically driven triple well with $\omega_D = 0.75$.

a systematic convergence of our results for sufficiently large spatial grids. In particular, we have used 350 spatial grid points in the case of the triple well and 800 spatial grid points for the 11-well potential. In the following, let us briefly demonstrate the convergence procedure concerning our simulations either with an increasing number of SPFs (and a fixed number of 350 grid points) or with a varying number of grid points and a fixed number of SPFs, $M = 12$. Figure 11 shows the fidelity evolution for different numbers of SPFs, namely, $M = 8$, 10, and 12, for the driven triple well at driving frequencies

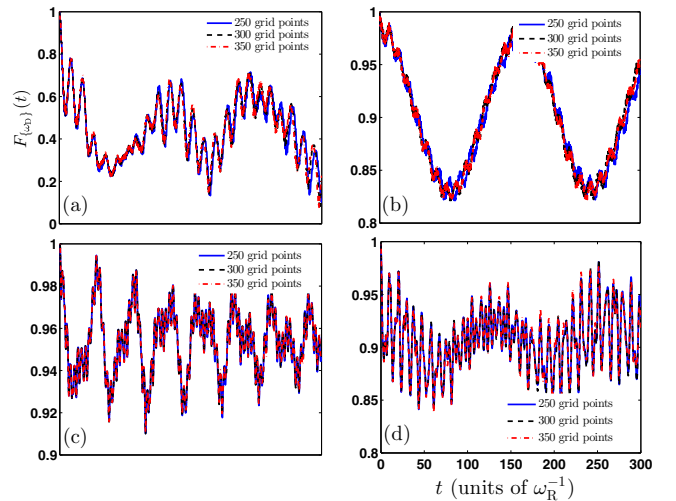


FIG. 12. Fidelity evolution $F_{\omega_D}(t)$ of a periodically driven triple well with (a) $\omega_D = 2.5$ and (b) $\omega_D = 7.5$ with an increasing number of grid sizes (see legend). (c), (d) $F_{\omega_D}(t)$ for various grid sizes (see legend) with a simultaneous interaction quench of amplitude (c) $\delta g = 0.5$ and (d) $\delta g = 2.0$ on top of the periodically driven triple well with $\omega_D = 0.75$.

$\omega_D = 2.5$, $\omega_D = 7.5$ [see Figs. 11(a) and 11(b), respectively], and $F_{\omega_D}(t)$ by employing simultaneous interaction quenches with amplitudes $\delta g = 0.5$, $\delta g = 2.0$ on top of the driving, $\omega_D = 0.75$ [see Figs. 11(c) and 11(d), respectively]. A systematic convergence of the fidelity evolution (for $M > 8$) is observed for increasing numbers of SPFs. For instance, the maximum deviation (at $\omega_D = 2.5$) observed in the fidelity evolution [see Fig. 11(a)] calculated using 8 and 12 SPFs, respectively, is of the order of 0.3% at large evolution times ($t > 200$). Furthermore, in order to show the convergence with an increasing number of grid points Fig. 12 presents the fidelity evolution of the driven triple well at $\omega_D = 2.5$ and $\omega_D = 7.5$ [see Figs. 12(a) and 12(b), respectively] and by

performing interaction quenches with $\delta g = 0.5$ and $\delta g = 2.0$ on top of the driven triple well, $\omega_D = 0.75$ [see Figs. 12(c) and 12(d), respectively]. Again, we observe convergence for an increasing number of grid points (especially for grid sizes that contain more than 300 spatial grid points). For instance, the maximum deviation (at $\omega_D = 2.5$) observed in the fidelity evolution [see Fig. 12(a)] calculated using 300 and 350 grid points, respectively (and 12 SPFs), is of the order of 0.1% at large evolution times ($t > 250$). The same analysis was also performed for the 11-well case (omitted here for brevity) showing the same behavior. Another criterion that confirms the achieved convergence is the population of the lowest-occupied natural orbital, kept in each case below 0.1%.

-
- [1] N. Goldman and J. Dalibard, *Phys. Rev. X* **4**, 031027 (2014).
 [2] N. Goldman, J. Dalibard, M. Aidelsburger, and N. R. Cooper, *Phys. Rev. A* **91**, 033632 (2015).
 [3] O. Morsch and M. Oberthaler, *Rev. Mod. Phys.* **78**, 179 (2006).
 [4] I. Bloch, J. Dalibard, and W. Zwerger, *Rev. Mod. Phys.* **80**, 885 (2008).
 [5] A. Polkovnikov, K. Sengupta, A. Silva, and M. Vengalattore, *Rev. Mod. Phys.* **83**, 863 (2011).
 [6] M. Ben Dahan, E. Peik, J. Reichel, Y. Castin, and C. Salomon, *Phys. Rev. Lett.* **76**, 4508 (1996).
 [7] O. Morsch, J. H. Müller, M. Cristiani, D. Ciampini, and E. Arimondo, *Phys. Rev. Lett.* **87**, 140402 (2001).
 [8] T. Hartmann, F. Keck, H. J. Korsch, and S. Mossmann, *New J. Phys.* **6**, 2 (2004).
 [9] A. Eckardt, C. Weiss, and M. Holthaus, *Phys. Rev. Lett.* **95**, 260404 (2005).
 [10] W. Zheng and H. Zhai, *Phys. Rev. A* **89**, 061603 (2014).
 [11] J. Struck, C. Ölschläger, M. Weinberg, P. Hauke, J. Simonet, A. Eckardt, M. Lewenstein, K. Sengstock, and P. Windpassinger, *Phys. Rev. Lett.* **108**, 225304 (2012).
 [12] C. V. Parker, L. C. Ha, and C. Chin, *Nat. Phys.* **9**, 769 (2013).
 [13] S. Choudhury and E. J. Mueller, *Phys. Rev. A* **90**, 013621 (2014).
 [14] P. I. Schneider and A. Saenz, *Phys. Rev. A* **85**, 050304 (2012).
 [15] M. Cheneau, P. Barmettler, D. Poletti, M. Endres, P. Schau, T. Fukuhara, C. Gross, I. Bloch, C. Kollath, and S. Kuhr, *Nature* **481**, 484 (2012).
 [16] S. S. Natu and E. J. Mueller, *Phys. Rev. A* **87**, 053607 (2013).
 [17] W. H. Zurek, U. Dorner, and P. Zoller, *Phys. Rev. Lett.* **95**, 105701 (2005).
 [18] D. Chen, M. White, C. Borries, and B. DeMarco, *Phys. Rev. Lett.* **106**, 235304 (2011).
 [19] M. Rigol, V. Dunjko, and M. Olshanii, *Nature* **452**, 854 (2008).
 [20] E. Altman and A. Auerbach, *Phys. Rev. Lett.* **89**, 250404 (2002).
 [21] W. Kohn, *Phys. Rev.* **123**, 1242 (1961).
 [22] M. Bonitz, K. Balzer, and R. van Leeuwen, *Phys. Rev. B* **76**, 045341 (2007).
 [23] J. W. Abraham and M. Bonitz, *Contrib. Plasma Phys.* **54**, 27 (2014).
 [24] S. Bauch, K. Balzer, C. Henning, and M. Bonitz, *Phys. Rev. B* **80**, 054515 (2009).
 [25] J. W. Abraham, K. Balzer, D. Hochstuhl, and M. Bonitz, *Phys. Rev. B* **86**, 125112 (2012).
 [26] R. Schmitz, S. Krönke, L. Cao, and P. Schmelcher, *Phys. Rev. A* **88**, 043601 (2013).
 [27] S. Peotta, D. Rossini, M. Polini, F. Minardi, and R. Fazio, *Phys. Rev. Lett.* **110**, 015302 (2013).
 [28] H. Lignier, C. Sias, D. Ciampini, Y. Singh, A. Zenesini, O. Morsch, and E. Arimondo, *Phys. Rev. Lett.* **99**, 220403 (2007).
 [29] C. Sias, H. Lignier, Y. P. Singh, A. Zenesini, D. Ciampini, O. Morsch, and E. Arimondo, *Phys. Rev. Lett.* **100**, 040404 (2008).
 [30] E. Haller, R. Hart, M. J. Mark, J. G. Danzl, L. Reichsöllner, and H. C. Nägerl, *Phys. Rev. Lett.* **104**, 200403 (2010).
 [31] Y.-A. Chen, S. Nascimbène, M. Aidelsburger, M. Atala, S. Trotzky, and I. Bloch, *Phys. Rev. Lett.* **107**, 210405 (2011).
 [32] S. Rosi, A. Bernard, N. Fabbri, L. Fallani, C. Fort, M. Inguscio, T. Calarco, and S. Montangero, *Phys. Rev. A* **88**, 021601 (2013).
 [33] C. Brif, R. Chakrabarti, and H. Rabitz, in *Advances in Chemical Physics*, edited by S. A. Rice and A. R. Dinner (Wiley, New York, 2012), Vol. 148, pp. 1–76.
 [34] C. Brif, R. Chakrabarti, and H. Rabitz, *New J. Phys.* **12**, 075008 (2010).
 [35] S. I. Mistakidis, T. Wulf, A. Negretti, and P. Schmelcher, *J. Phys. B* **48**, 244004 (2015).
 [36] S. I. Mistakidis, L. Cao, and P. Schmelcher, *J. Phys. B* **47**, 225303 (2014).
 [37] S. I. Mistakidis, L. Cao, and P. Schmelcher, *Phys. Rev. A* **91**, 033611 (2015).
 [38] S. Fölling, S. Trotzky, P. Cheinet, M. Feld, R. Saers, A. Widera, T. Müller, and I. Bloch, *Nature (London)* **448**, 1029 (2007).
 [39] O. E. Alon, A. I. Streltsov, and L. S. Cederbaum, *J. Chem. Phys.* **127**, 154103 (2007).
 [40] O. E. Alon, A. I. Streltsov, and L. S. Cederbaum, *Phys. Rev. A* **77**, 033613 (2008).
 [41] M. Olshanii, *Phys. Rev. Lett.* **81**, 938 (1998).
 [42] T. Köhler, K. Goral, and P. S. Julienne, *Rev. Mod. Phys.* **78**, 1311 (2006).
 [43] C. Chin, R. Grimm, P. Julienne, and E. Tiesinga, *Rev. Mod. Phys.* **82**, 1225 (2010).
 [44] J. I. Kim, V. S. Melezhik, and P. Schmelcher, *Phys. Rev. Lett.* **97**, 193203 (2006).
 [45] P. Giannakeas, F. K. Diakonou, and P. Schmelcher, *Phys. Rev. A* **86**, 042703 (2012).
 [46] P. Giannakeas, V. S. Melezhik, and P. Schmelcher, *Phys. Rev. Lett.* **111**, 183201 (2013).

- [47] S. Klaiman and O. E. Alon, *Phys. Rev. A* **91**, 063613 (2015).
- [48] S. Klaiman, A. I. Streltsov, and O. E. Alon, *Phys. Rev. A* **93**, 023605 (2016).
- [49] J. P. Ronzheimer, M. Schreiber, S. Braun, S. S. Hodgman, S. Langer, I. P. McCulloch, F. Heidrich-Meisner, I. Bloch, and U. Schneider, *Phys. Rev. Lett.* **110**, 205301 (2013).
- [50] U. M. Titulaer and R. J. Glauber, *Phys. Rev.* **140**, B676 (1965).
- [51] M. Naraschewski and R. J. Glauber, *Phys. Rev. A* **59**, 4595 (1999).
- [52] K. Sakmann, A. I. Streltsov, O. E. Alon, and L. S. Cederbaum, *Phys. Rev. A* **78**, 023615 (2008).
- [53] R. W. Spekkens and J. E. Sipe, *Phys. Rev. A* **59**, 3868 (1999).
- [54] S. Klaiman, N. Moiseyev, and L. S. Cederbaum, *Phys. Rev. A* **73**, 013622 (2006).
- [55] E. J. Mueller, T. L. Ho, M. Ueda, and G. Baym, *Phys. Rev. A* **74**, 033612 (2006).
- [56] K. Sakmann, A. I. Streltsov, O. E. Alon, and L. S. Cederbaum, *Phys. Rev. A* **89**, 023602 (2014).
- [57] O. Penrose and L. Onsager, *Phys. Rev.* **104**, 576 (1956).
- [58] I. Brouzos, S. Zöllner, and P. Schmelcher, *Phys. Rev. A* **81**, 053613 (2010).
- [59] O. I. Streltsova, O. E. Alon, L. S. Cederbaum, and A. I. Streltsov, *Phys. Rev. A* **89**, 061602 (2014).
- [60] A. I. Streltsov, O. E. Alon, and L. S. Cederbaum, *Phys. Rev. Lett.* **99**, 030402 (2007).
- [61] A. I. Streltsov, K. Sakmann, O. E. Alon, and L. S. Cederbaum, *Phys. Rev. A* **83**, 043604 (2011).
- [62] O. E. Alon, A. I. Streltsov, and L. S. Cederbaum, *Phys. Rev. A* **76**, 013611 (2007).
- [63] O. E. Alon, A. I. Streltsov, and L. S. Cederbaum, *Phys. Rev. A* **79**, 022503 (2009).
- [64] J. Frenkel, *Wave Mechanics*, 1st ed. (Clarendon Press, Oxford, UK, 1934), pp. 423–428.
- [65] P. A. Dirac, *Proc. Cambridge Philos. Soc.* **26**, 376 (1930).
- [66] L. Cao, S. Krönke, O. Vendrell, and P. Schmelcher, *J. Chem. Phys.* **139**, 134103 (2013).
- [67] S. Krönke, L. Cao, O. Vendrell, and P. Schmelcher, *New J. Phys.* **15**, 063018 (2013).

4.3 Quench Dynamics in Binary Mixtures

4.3.1 Correlation Effects in the Quench-Induced Phase Separation Dynamics of a Two-Species Ultracold Quantum Gas

PAPER • OPEN ACCESS

Correlation effects in the quench-induced phase separation dynamics of a two species ultracold quantum gas

To cite this article: S I Mistakidis *et al* 2018 *New J. Phys.* **20** 043052

View the [article online](#) for updates and enhancements.



PAPER

Correlation effects in the quench-induced phase separation dynamics of a two species ultracold quantum gas

OPEN ACCESS

RECEIVED

10 December 2017

REVISED

3 April 2018

ACCEPTED FOR PUBLICATION

9 April 2018

PUBLISHED

25 April 2018

Original content from this work may be used under the terms of the [Creative Commons Attribution 3.0 licence](#).

Any further distribution of this work must maintain attribution to the author(s) and the title of the work, journal citation and DOI.

S I Mistakidis^{1,4}, G C Katsimiga¹, P G Kevrekidis²  and P Schmelcher^{1,3}¹ Zentrum für Optische Quantentechnologien, Universität Hamburg, Luruper Chaussee 149, D-22761 Hamburg, Germany² Department of Mathematics and Statistics, University of Massachusetts Amherst, Amherst, MA 01003-4515, United States of America³ The Hamburg Centre for Ultrafast Imaging, Universität Hamburg, Luruper Chaussee 149, D-22761 Hamburg, Germany⁴ Author to whom any correspondence should be addressed.E-mail: smistaki@physnet.uni-hamburg.de**Keywords:** quench dynamics, phase separation, correlations effects, dark–antidark solitary waves, single-shot images, multi-component BECs**Abstract**

We explore the quench dynamics of a binary Bose–Einstein condensate crossing the miscibility–immiscibility threshold and vice versa, both within and in particular beyond the mean-field approximation. Increasing the interspecies repulsion leads to the filamentation of the density of each species, involving shorter wavenumbers and longer spatial scales in the many-body (MB) approach. These filaments appear to be strongly correlated and exhibit domain-wall structures. Following the reverse quench process multiple dark–antidark solitary waves are spontaneously generated and subsequently found to decay in the MB scenario. We simulate single-shot images to connect our findings to possible experimental realizations. Finally, the growth rate of the variance of a sample of single-shots probes the degree of entanglement inherent in the system.

1. Introduction

The realm of atomic Bose–Einstein condensates (BECs) has offered over the past two decades a fertile testbed for the examination of phenomena involving the role of nonlinearity in wave dynamics and phase transitions [1–6]. Phase separation dynamics in the case of multi-component BECs has held a prominent role among the relevant studies and is a topic that by now has been summarized in various reviews [1, 2, 4, 7]. Nevertheless, the majority of the relevant studies has focused on a mean-field (MF) description, while the role of many-body (MB) effects in such transitions is much less understood.

Since the early days of the experimental realization of BECs, experimental achievements include binary mixtures of e.g. two hyperfine states of ²³Na [8] and of ⁸⁷Rb [9]. Progress of the experimental control over the relevant multi-component settings enabled detailed observations of phase separation phenomena and related dynamical manifestations [10–18]. In recent years, external coupling fields have been utilized to control and modify the thresholds for mixing–demixing dynamics in pseudo-spinor (two-component) [19, 20] and even in spinor systems [21]. Moreover, the quench dynamics across the phase separation transition has been a focal point of studies examining the scaling properties of suitable correlation functions and associated universality properties [22–24].

More recently the inclusion of correlations in multi-component few boson systems enabled a microscopic characterization of their static properties. A variety of novel features have been realized in these settings such as altered phase separation processes [25–28], composite fermionization [29–31], or even the crossover between the two [32, 33]. Also the dynamical properties of such MB ultracold mixtures have been studied including, among others, the dependence of the tunneling dynamics on the mass ratio [34, 35] or the intra- and interspecies interactions [36], as well as the emergence of Anderson’s orthogonality catastrophe upon quenching the interspecies repulsion [37]. On the other hand, far less emphasis has been placed on the MB character of the quench-induced phase separation phenomenology. It is the latter apparent gap in the literature that the present work aims at addressing for both few-particle and larger bosonic ensembles.

To incorporate the quantum fluctuations due to correlations [38–41] emerging when quenching the binary BEC system, we bring to bear the multi-layer multi-configuration time-dependent Hartree method for bosons (ML-MCTDHB) [42, 43] designed for simulating the quantum dynamics of bosonic mixtures. We explore different scenarios, emphasizing the case where the interspecies interaction is quenched from the miscible to the immiscible regime (positive quench) or vice versa (negative quench). We find significant variations in the MB scenario in comparison to the MF one. In the positive quench scenario the unstable dynamics leads to the filamentation of the density of each species and the dominant wavenumber associated with the emerging phase separated state appears to generically be higher in the MF case. The one- and the two-body correlation functions indicate the presence of correlations between the filaments of the same or different species signaling the presence of fragmentation and entanglement respectively. In particular, strong one-body correlations appear between non-parity symmetric (with respect to the trap center) filaments formed indicating their tendency of localization. These filaments are found to be strongly anti-correlated at the two-body level indicating a negligible probability of finding two bosons of the same species one residing in an outer and one in an inner filament. More importantly, combining the behavior of one- and two-body correlations supports the formation of domain-walls i.e. interfaces that separate these distinct filaments [44–46].

In sharp contrast to the above dynamical manifestation of the phase separation, in the negative quench scenario multiple dark–antidark (DAD), i.e. density humps on top of the BEC background, solitary waves [47, 48] are spontaneously generated both within and beyond the MF approximation. At the MB level many decay events, at the early stages of the dynamics, increase the production of DAD solitary waves with the product of each decay being a slow and a fast DAD structure [49]. The latter increase results in multiple collisions and interference events between these matter waves, and most of them are lost during evolution. Furthermore, in both the positive and the negative quench scenarios, single-shot simulations, utilized here for the first time for binary mixtures, offer a link to potential experimental realizations of the above-observed dynamics. In particular, the growth rate of the variance of single-shots resembles the growth rate of the entanglement inherent in the system. Additionally, deviations between the variances of the two species reveal the fragmented nature of the binary system. Last, but not least the case of quenches within the immiscible regime, are explored showcasing the one-dimensional (1D) analog of the so-called ‘ball’ and ‘shell’ structure appearing in higher-dimensional binary BECs [12].

Our presentation is structured as follows. In section 2, we provide the details of the binary setup and the corresponding MB ansatz, briefly addressing the ML-MCTDHB approach. In section 3 we examine the different quench scenarios focusing on the miscible to immiscible quench as well as the reverse quench dynamics. Section 4 provides a summary of our findings and a number of proposed directions for future study. In appendix A we present the details of the single-shot procedure, and in appendix B we show how the quench-induced phase separation dynamics is altered for small particle numbers. Finally, in appendix C we address the convergence of the ML-MCTDHB results.

2. Setup and MB ansatz

To explore the correlated out-of-equilibrium quantum dynamics in a relevant experimental setting, we consider a binary bosonic gas trapped in a 1D harmonic oscillator potential. The MB Hamiltonian consisting of N_A, N_B bosons with masses m_A, m_B for the species A, B respectively, reads

$$H = \sum_{\sigma=A,B} \sum_{i=1}^{N_\sigma} \left[-\frac{\hbar^2}{2m_\sigma} \left(\frac{d}{dx_i^\sigma} \right)^2 + \frac{1}{2} m_\sigma \omega_\sigma^2 (x_i^\sigma)^2 \right] + \sum_{\sigma=A,B} g_{\sigma\sigma} \sum_{i<j} \delta(x_i^\sigma - x_j^\sigma) + g_{AB} \sum_{i=1}^{N_A} \sum_{j=1}^{N_B} \delta(x_i^A - x_j^B). \quad (1)$$

In the s -wave scattering limit [1] both the intra and interspecies interactions are modeled by a contact potential, where the effective coupling constants are denoted by g_{AA}, g_{BB} , and g_{AB} respectively. Experimentally $g_{\sigma\sigma}$ can be tuned either via the three-dimensional scattering length with the aid of Feshbach resonances [50, 51] or via the corresponding transversal confinement frequency and the resulting confinement-induced resonances [52, 53]. Moreover, here we assume that both species possess the same mass, i.e. $m_A = m_B = m$, and are confined in the same external potential, i.e. $\omega_A = \omega_B = \Omega$. Throughout this work the trapping frequency is fixed to $\Omega = 0.1 \approx 2\pi \times 20$ Hz assuming a transversal confinement $\omega_\perp = 2\pi \times 200$ Hz. Furthermore, we fix the intraspecies interactions to $g_{AA} = 1.004$ and $g_{BB} = 0.9544$, which are the values for a binary BEC of ^{87}Rb atoms prepared in the internal states $|F = 1, m_F = -1\rangle$ and $|F = 2, m_F = 1\rangle$ [15], while g_{AB} is left to arbitrarily vary upon a quench taking values within the interval $g_{AB} = [0, 2]$. We remark that in the following the Hamiltonian

of equation (1) is rescaled in harmonic oscillator units, $\tilde{H} = H/(\hbar\Omega)$. Then the corresponding length, energy, time, and interaction strength are given in units of $\sqrt{\hbar/(0.1m\Omega)}$, $\hbar\Omega$, $(\Omega/0.1)^{-1}$, and $g'_{\sigma\sigma'} = g_{\sigma\sigma'}\sqrt{m/\hbar^3 10\Omega}$, respectively.

Within the MF approximation all particle correlations are neglected. Such a simplification allows for expressing the MB wavefunction of a binary system as a product state of the respective MF wavefunctions

$$\Psi_{\text{MF}}(\vec{x}^A, \vec{x}^B; t) = \Psi_{\text{MF}}^A(\vec{x}^A; t)\Psi_{\text{MF}}^B(\vec{x}^B; t) = \prod_{i=1}^{N_A} \frac{\phi^A(x_i^A; t)}{\sqrt{N_A}} \prod_{i=1}^{N_B} \frac{\phi^B(x_i^B; t)}{\sqrt{N_B}}, \quad (2)$$

where $\vec{x}^\sigma = (x_1^\sigma, \dots, x_{N_\sigma}^\sigma)$ denote the spatial $\sigma = A, B$ species coordinates, N_σ is the number of σ species atoms and $\phi^\sigma(x_i^\sigma; t)$ refers to the time-evolved wavefunction for the σ species within the MF approximation. Employing a variational principle, e.g. the Dirac–Frenkel one [54, 55], for the ansatz of equation (2) we obtain the corresponding equations of motion in the form of the well-studied system of coupled Gross–Pitaevskii equations [1, 2].

The binary BEC is a bipartite composite system residing in the Hilbert space $\mathcal{H}^{AB} = \mathcal{H}^A \otimes \mathcal{H}^B$, with \mathcal{H}^σ being the Hilbert space of the σ species. To incorporate correlations between the different (inter-) or the same (intra-) species, M distinct species functions for each species are introduced obeying $M \leq \min(\dim(\mathcal{H}^A), \dim(\mathcal{H}^B))$. Then the MB wavefunction Ψ_{MB} can be expressed according to the truncated Schmidt decomposition [56] of rank M

$$\Psi_{\text{MB}}(\vec{x}^A, \vec{x}^B; t) = \sum_{k=1}^M \sqrt{\lambda_k(t)} \Psi_k^A(\vec{x}^A; t)\Psi_k^B(\vec{x}^B; t). \quad (3)$$

The Schmidt weights $\lambda_k(t)$ in decreasing order are referred to as the natural species populations of the k th species function Ψ_k^σ of the σ species. We remark that $\{\Psi_k^\sigma\}$ forms an orthonormal N_σ -body wavefunction set in a subspace of \mathcal{H}^σ . To quantify the presence of interspecies correlations or entanglement we use the eigenvalues λ_k of the species reduced density matrix $\rho^{N_\sigma}(\vec{x}^\sigma, \vec{x}'^\sigma; t) = \int d^{N_{\sigma'}} x^{\sigma'} \Psi_{\text{MB}}^*(\vec{x}^\sigma, \vec{x}'^\sigma; t)\Psi_{\text{MB}}(\vec{x}^\sigma, \vec{x}'^\sigma; t)$, where $\vec{x}^\sigma = (x_1^\sigma, \dots, x_{N_\sigma}^\sigma)$, and $\sigma \neq \sigma'$. When only one (multiple) eigenvalue(s) of ρ^{N_σ} is (are) macroscopic the system is referred to as non-entangled (species entangled or interspecies correlated). It is also evident from equation (3) that the system is entangled⁵ [57] when at least two distinct $\lambda_k(t)$ are finite, further implying that the MB state cannot be expressed as a direct product of two states stemming from \mathcal{H}^A and \mathcal{H}^B . In this manner, $1 - \lambda_1(t)$ offers a measure for the degree of the system’s entanglement. Moreover, a particular configuration of A species $\Psi_k^A(\vec{x}^A; t)$ is accompanied by a particular configuration of B species $\Psi_k^B(\vec{x}^B; t)$ and vice versa. Indeed, measuring one of the species states e.g. $\Psi_{k'}^A$ collapses the wavefunction of the other species to $\Psi_{k'}^B$ thus manifesting the bipartite entanglement [58, 59]. Concluding, the above MB wavefunction ansatz Ψ_{MB} constitutes an expansion in terms of different interspecies modes of entanglement, where $\sqrt{\lambda_k(t)}\Psi_k^A(\vec{x}^A; t)\Psi_k^B(\vec{x}^B; t)$ corresponds to the k th entanglement mode.

To include interparticle correlations we further expand each of the species functions $\Psi_k^\sigma(\vec{x}^\sigma; t)$ using the permanents of m^σ distinct time-dependent single particle functions (SPFs) namely $\varphi_1, \dots, \varphi_{m^\sigma}$

$$\Psi_k^\sigma(\vec{x}^\sigma; t) = \sum_{\substack{n_1, \dots, n_{m^\sigma} \\ \sum n_i = N}} c_{k,(n_1, \dots, n_{m^\sigma})}(t) \times \sum_{i=1}^{N_\sigma!} \mathcal{P}_i \left[\prod_{j=1}^{n_1} \varphi_1(x_j; t) \cdots \prod_{j=1}^{n_{m^\sigma}} \varphi_{m^\sigma}(x_j; t) \right]. \quad (4)$$

Here, $c_{k,(n_1, \dots, n_{m^\sigma})}(t)$ are the time-dependent expansion coefficients of a particular permanent, \mathcal{P} is the permutation operator exchanging the particle configuration within the SPFs, and $n_i(t)$ denotes the occupation number of the SPF $\varphi_i(\vec{x}; t)$. Following the Dirac–Frenkel [54, 55] variational principle for the generalized ansatz (see equations (3), (4)) yields the ML-MCTDHB equations of motion⁶ [42, 43]. These consist of a set of M^2 ordinary (linear) differential equations of motion for the coefficients $\lambda_k(t)$, coupled to a set of $M \left(\frac{(N_A + m^A - 1)!}{N_A!(m^A - 1)!} + \frac{(N_B + m^B - 1)!}{N_B!(m^B - 1)!} \right)$ nonlinear integrodifferential equations for the species functions, and $m_A + m_B$ nonlinear integrodifferential equations for the SPFs.

According to the above MB expansion, the one-body reduced density matrix of σ species can be expanded in different modes (see equation (3))

⁵ Commonly used measures to quantify bipartite entanglement are the von-Neumann entropy, $S[\Psi_{\text{MB}}(t)] = -\sum_k \lambda_k(t) \log(\lambda_k(t))$, and the concurrence $D[\Psi_{\text{MB}}(t)] = 2\sum_{i < j} \sqrt{\lambda_i(t)\lambda_j(t)}$. Here, $\rho^\sigma(t) = \sum_k \lambda_k(t) |\Psi_k^\sigma(t)\rangle \langle \Psi_k^\sigma(t)|$ refers to the N -body density matrix and $\Psi_k^\sigma(t)$ denotes the k th species function of the σ species. Note that both measures vanish in the non-entangled case.

⁶ The general ML-MCTDHB ansatz for a bosonic mixture consisting of an arbitrary number of components has been introduced in [42]. Here, we utilize the Schmidt decomposition that holds for binary mixtures.

$$\begin{aligned}\rho^{(1),\sigma}(x, x'; t) &= \int d^{N_\sigma-1} \bar{x}^\sigma d^{N_{\sigma'}} x^{\sigma'} \times \Psi_{\text{MB}}^*(x, \bar{x}^\sigma, \bar{x}^{\sigma'}; t) \Psi_{\text{MB}}(x', \bar{x}^\sigma, \bar{x}^{\sigma'}; t) \\ &= \sum_{k=1}^M \lambda_k(t) \rho_k^{(1),\sigma}(x, x'; t),\end{aligned}\quad (5)$$

where $\sigma \neq \sigma'$, $\bar{x}^\sigma = (x_1^\sigma, x_2^\sigma, \dots, x_{N_\sigma-1}^\sigma)$, and $\rho_i^{(1),\sigma}(x, x'; t) = \int d^{N_\sigma-1} \bar{x}^\sigma \Psi_i^*(x, \bar{x}^\sigma; t) \Psi_i(x', \bar{x}^\sigma; t)$ denotes the one-body density matrix of the i th species function. Note here that the system is termed intraspecies correlated or fragmented if multiple eigenvalues of $\rho^{(1),\sigma}(x, x')$ are macroscopically occupied, otherwise is said to be fully coherent or condensed.

The eigenfunctions of the one-body density matrix $\rho^{(1),\sigma}(x, x')$ are the so-called natural orbitals $\phi_i^\sigma(x; t)$. Here we consider them to be normalized to their corresponding eigenvalues, n_i^σ (natural populations)

$$n_i^\sigma(t) = \int dx |\phi_i^\sigma(x; t)|^2. \quad (6)$$

It can be shown that when $\Psi_{\text{MB}}(\bar{x}^A, \bar{x}^B; t) \rightarrow \Psi_{\text{MF}}(\bar{x}^A, \bar{x}^B; t)$ the corresponding natural populations obey $n_1^\sigma(t) = N^\sigma$, $n_{i \neq 1}^\sigma(t) = 0$ and then the first natural orbital $\phi_1^\sigma(x^\sigma; t)$ reduces to the MF wavefunction $\phi^\sigma(x^\sigma; t)$. Therefore, $1 - n_1^\sigma(t)$ serves as a measure of the degree of the σ species fragmentation [60, 61].

3. Interaction quench dynamics

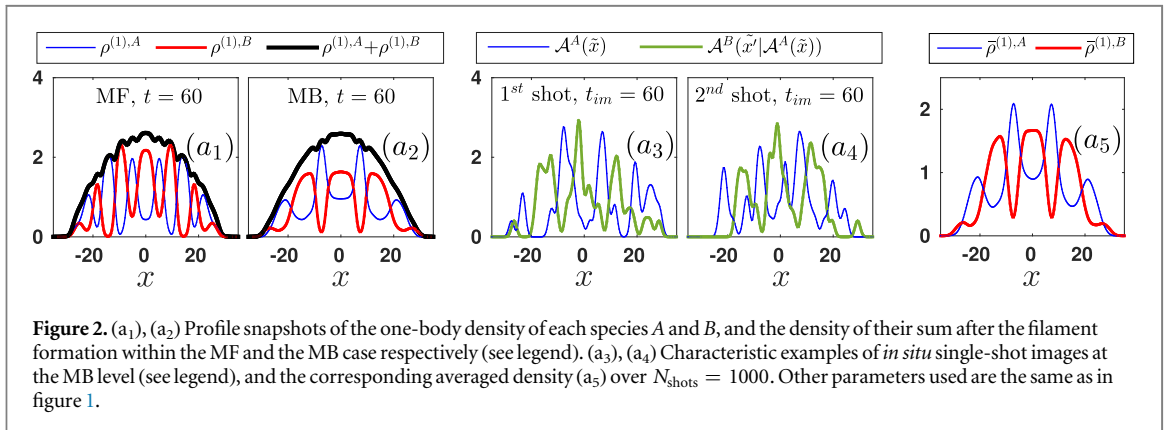
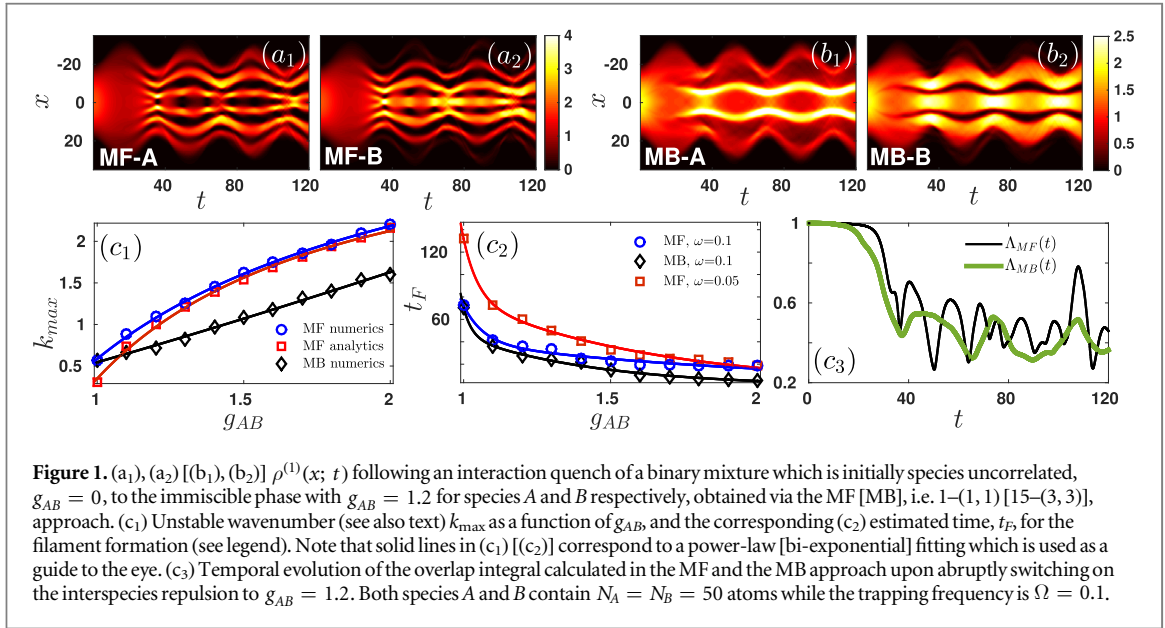
In the following the quench-induced phase separation dynamics of a binary repulsively interacting BEC is investigated both within and beyond the MF approximation. In particular, interspecies interaction quenches are performed from the miscible to the immiscible regime of interactions and vice versa. Recall [62] that species separation in the absence of a trap occurs for $g_{AB}^2 \geq g_{AA}g_{BB}$, while the two species overlap when the above inequality is not fulfilled [15]. It is relevant to note, however, that for sufficiently strong trapping—a scenario not considered here—the above condition is suitably modified [63]. In that case, the g_{AB} needed to induce immiscibility can become substantially larger, as it needs to overcome the restoring, and hence implicitly miscibility favoring, effect of the trap.

First we find the ground state of the system in both the MF and the MB case for fixed intra and interspecies interactions namely $g_{AA} = 1.004$, $g_{BB} = 0.9544$, and $g_{AB} = 0$. To initialize the dynamics we then abruptly vary the interspecies coefficient within the interval $g_{AB} = [0, 2]$, in the dimensionless units adopted herein. Notice that e.g. $g_{AB} = 0$ corresponds to two decoupled overlapping BECs formed around the center of the harmonic trap. With the above choice of parameters the critical point, i.e. the miscibility–immiscibility threshold, in the absence of the trap, is $g_{AB} \approx 0.9789$. The number of particles in each species is fixed to $N_A = N_B = N/2 = 50$, with N being the total number of particles of the system. Dynamical phase separation for smaller bosonic ensembles is addressed in appendix B.

3.1. Quench dynamics to the immiscible regime

As a first step an interaction quench of an initially species uncorrelated (since $g_{AB} = 0$) mixture towards the immiscible regime with $g_{AB} = 1.2$ is performed, driving the system abruptly out-of-equilibrium and letting it dynamically evolve. As shown in figure 1, the initial ground state quickly becomes deformed and breaks into multiple filaments within the MF approach, depicted in figures 1(a₁) and (a₂), as well as in the MB case shown in figures 1(b₁) and (b₂). The dramatic phase separation observed between the two species, and depicted for $t = 60$ in the density profiles of figures 2(a₁), (a₂), results in a different number of filaments formed, the latter being greater within the MF approximation. This suggests that the wavenumber associated with the emergence and growth of these filaments is larger in the MF regime. Notice that in both cases the filaments of the two species locate alternately while the total density does not change dramatically after the filament formation. Additionally here, the first species is found to be expelled further off of the trap center when compared to the second species since this configuration is energetically preferable by virtue of $g_{AA} > g_{BB}$. Besides the filamentation of its density, each species performs collective oscillations that result in an expansion and contraction of the bosonic cloud. Namely a breathing mode [30, 64] possessing a frequency $\omega_{\text{br}} = 2\pi/T \approx 0.2 \equiv 2\Omega$. Finally we remark that for a stronger post-quench repulsion, g_{AB} , an increased number of filaments is observed and a more dramatic phase separation takes place, occurring much faster when compared to smaller g_{AB} values.

In all cases, the dominant wavenumber associated with the above-observed unstable dynamics when entering the phase separated regime, is found to be higher in the MF approach when compared to the MB scenario. To quantify the distinct features of the manifestation of the phase separation dynamics within the two approaches we start by considering the stability properties of a homogeneous binary system of length L . Within the MF approximation the spectrum of quasi-particle excitations consists of two branches Ω_\pm , that in the case of equal masses between the bosons read [65]



$$\Omega_{\pm}^2 = \frac{k^2}{2} \left[\frac{k^2}{2} + n(g_{AA} + g_{BB} \pm \sqrt{(g_{AA} - g_{BB})^2 + 4g_{AB}^2}) \right], \quad (7)$$

where $n = N/2L$ denotes the linear atom density [66]. It turns out that if $g_{AB}^2 > g_{AA}g_{BB}$, i.e. in the immiscible regime of interactions, Ω_{-} becomes imaginary and gives rise to long wavelength modes that grow exponentially in time rendering the homogeneous binary system unstable [67]. For $g_{AB}^2 < g_{AA}g_{BB}$ both branches Ω_{\pm}^2 of equation (7) remain positive implying that the binary system is stable within this miscible regime. The two species remain then mutually overlapped and undergo a breathing dynamics. Turning to $g_{AB}^2 > g_{AA}g_{BB}$, the most unstable $k = k_{\text{max}}$ modes, corresponding to $\max\{\text{Im}(\Omega_{-})\}$, are presented in figure 1(c₁) for varying g_{AB} . For the numerical identification of k_{max} we calculate the spectrum, $\tilde{\rho}^{(1)}(k; \omega)$, of the binary system in both the MF and the MB level. Among the modes that appear in this spectrum, we identify as the fastest growing one the mode that maximizes the growth rate $\omega = \omega_{\text{max}}$. As is evident in figure 1(c₁), our numerical findings are in very good agreement with the analytical predictions within the MF approximation (except for very small values of g_{AB}). Note here, that we have checked the validity of our calculations for different trapping frequencies within the local density approximation (see discussion below). The unstable modes identified within the MB approach involve considerably shorter k_{max} values which result in longer spatial scales for the filament formation (and thus consist of fewer filaments formed). For example the wavelength obtained in the MF case depicted in figure 1(c₁) for $g_{AB} = 1.2$ is $\lambda_{\text{MF}} = 2\pi/k_{\text{max}} \approx 5.76$ ($k_{\text{max}} \approx 1.09$) while at the MB level we get the value $\lambda_{\text{MB}} \approx 8.73$ ($k_{\text{max}} \approx 0.72$). The observed difference of k_{max} between the MF and MB evolution can be attributed to the participation of additional MB excitations which lie beyond the linear response theory as demonstrated, e.g., in [68] for single component setups.

Additionally, having identified the wavenumber associated with the fastest growth, we can also infer the time at which the filament formation occurs. We have estimated this time, namely $t = t_F$, by identifying the time at which the amplitude of this wavenumber, $k = k_{\text{max}}$, starts to grow. The formation time, t_F , is illustrated in figure 1(c₂) for increasing g_{AB} and is fitted by a bi-exponential function. It is evident that close to the

miscibility–immiscibility threshold ($g_{AB} \approx 1$) both approaches coincide, while deviations between the two become apparent as we increase the interspecies interactions. Note also that decreasing the trapping strength towards the homogeneous case alters the time scale at which the instability manifests itself, the more, the closer we are to the above threshold.

To quantify the degree of phase separation we evaluate the overlap integral [69, 70]

$$\Lambda(t) = \frac{\left[\int dx \rho^{(1),A}(x; t) \rho^{(1),B}(x; t) \right]^2}{\left[\int dx (\rho^{(1),A}(x; t))^2 \right] \left[\int dx (\rho^{(1),B}(x; t))^2 \right]}, \quad (8)$$

where, $\Lambda(t) = 1$ [$\Lambda(t) = 0$] denotes complete [zero] overlap of the two species upon abruptly driving the system out-of-equilibrium. As depicted in figure 1(c₃) the transition to immiscibility is signaled at slightly earlier times in the MB approach with the overlap between the two species being about 50% on average, while being almost 60% on average within the MF approximation. Moreover, the abrupt quench protocol entails rapid oscillations in the MF case when compared to the smoother drop down towards immiscibility observed in the MB scenario. It is worth mentioning at this point, that the same overall phenomenology is observed even upon linearly quenching the system between the same initial and final g_{AB} values (results not shown here for brevity). The key outcome in this case is that the filamentation process is signaled at times proportional to the ramping time used resulting to a larger $\Lambda(t)$ when compared to the abrupt quench protocol.

3.2. Single-shot simulations

As a next step we elaborate on how the MB character of the dynamics can be inferred by performing *in situ* single-shot absorption measurements [71]. Such measurements probe the spatial configuration of the atoms which is dictated by the MB probability distribution. An experimental image refers to a convolution of the spatial particle configuration with a point spread function. The latter describes the response of the imaging system to a point-like absorber (atom). Relying on the MB wavefunction being available within ML-MCTDHB we mimic the above-mentioned experimental procedure and simulate such single-shot images for both species A [namely $\mathcal{A}^A(\tilde{x}; t_{\text{im}})$] and species B [i.e. $\mathcal{A}^B(\tilde{x}' | \mathcal{A}^A(\tilde{x}); t_{\text{im}})$] at each instant of the evolution (for more details see appendix A) when we consecutively image first the A and then the B species. We remark that the employed point spread function (being related to the experimental resolution), consists of a Gaussian possessing a width $w = 1 \ll l \approx 3.2$.

Figures 2(a₃), (a₄) illustrate the first and the second simulated *in situ* single-shot images at $t_{\text{im}} = 60$ for both species, namely $\mathcal{A}^A(\tilde{x}; t_{\text{im}} = 60)$, and $\mathcal{A}^B(\tilde{x}' | \mathcal{A}^A(\tilde{x}); t_{\text{im}} = 60)$. It is evident that in both shots the two species exhibit a phase separated behavior resembling this way the overall tendency observed in the one-body density (see also figure 2(a₂)). However, a direct observation of the one-body density in a single-shot image is not possible due to the small particle number of the considered binary bosonic gas, $N_A = N_B = 50$, as well as the presence of multiple orbitals in the system. The MB state builds upon a superposition of multiple orbitals (see equations (4) and (5)) and therefore imaging an atom alters the MB state of the remaining atoms and hence their one-body density. This is in direct contrast to a MF product state, composed from a single macroscopic orbital, where the imaging of an atom does not affect the distribution of the rest (see also the discussion below for the corresponding variance). Note also here that the above-mentioned single-shot images are reminiscent of the experimental images obtained in a two-dimensional (2D) geometry when examining the phase separation process [13]. To reproduce the one-body density of the system one needs to rely on an average of several single-shot images. Indeed, figure 2(a₅) shows within the MB approach the obtained average, $\bar{\rho}^{(1),\sigma}$, over $N_{\text{shots}} = 1000$ images for both species, namely $\bar{A}^A(\tilde{x}; t_{\text{im}}) = (1/N_{\text{shots}}) \sum_{k=1}^{N_{\text{shots}}} \mathcal{A}_k^A(\tilde{x}; t_{\text{im}})$ and $\bar{A}^B(\tilde{x}' | \mathcal{A}^A(\tilde{x}); t_{\text{im}}) = (1/N_{\text{shots}}) \sum_{k=1}^{N_{\text{shots}}} \mathcal{A}_k^B(\tilde{x}' | \mathcal{A}^A(\tilde{x}); t_{\text{im}})$ respectively. As expected, a direct comparison of this averaging and the actual one-body density obtained within the MB approach (see figures 2(a₂) and (a₅)) reveals that they are almost identical. Finally, let us remark here that similar observations can be made when performing the single-shot procedure initially for the B and then for the A species.

Let us now investigate whether the presence of correlations can be deduced from the time evolution of the variance $\mathcal{V}(t)$ of a sample of single-shot measurements [72–74]. As before, we mainly focus on the scenario where the imaging is performed first on the A and then on the B species, but the same results can be obtained for the reverse consecutive imaging process. The variance of a set of single-shot measurements $\{\mathcal{A}_k^A(\tilde{x})\}_{k=1}^{N_{\text{shots}}}$ concerning the A species reads

$$\mathcal{V}^A(t_{\text{im}}) = \int d\tilde{x} \frac{1}{N_{\text{shots}}} \sum_{k=1}^{N_{\text{shots}}} [\mathcal{A}_k^A(\tilde{x}; t_{\text{im}}) - \bar{A}_k^A(\tilde{x}; t_{\text{im}})]^2. \quad (9)$$

In the same manner, one defines the variance of a set of single-shots $\{\mathcal{A}_k^B(\tilde{x}' | \mathcal{A}^A(\tilde{x}))\}_{k=1}^{N_{\text{shots}}}$ referring to the B species

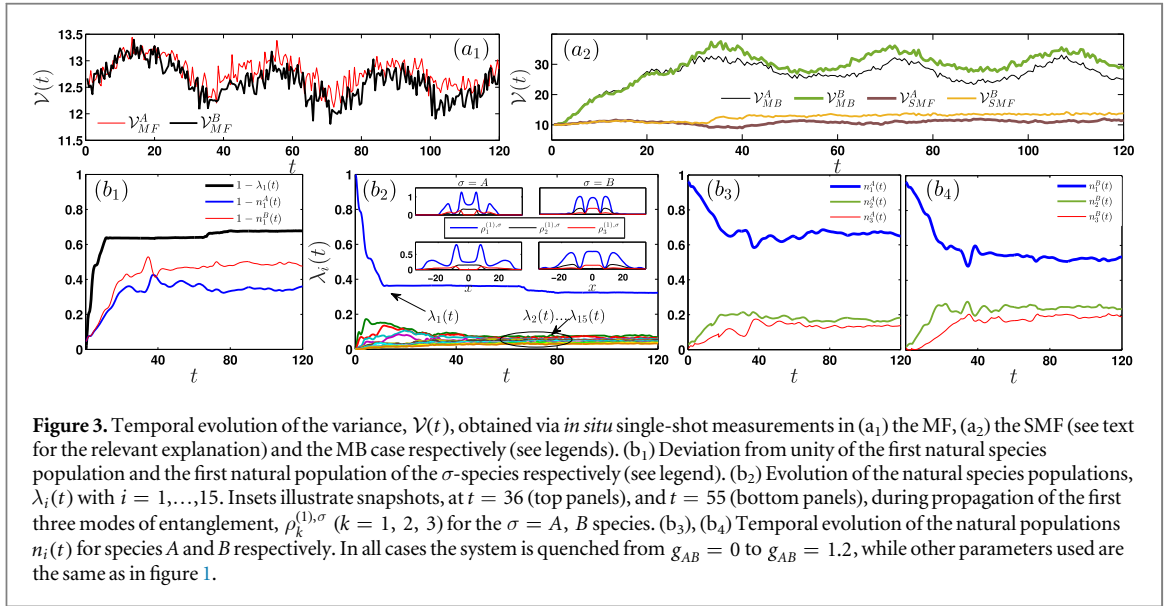


Figure 3. Temporal evolution of the variance, $\mathcal{V}(t)$, obtained via *in situ* single-shot measurements in (a₁) the MF, (a₂) the SMF (see text for the relevant explanation) and the MB case respectively (see legends). (b₁) Deviation from unity of the first natural species population and the first natural population of the σ -species respectively (see legend). (b₂) Evolution of the natural species populations, $\lambda_i(t)$ with $i = 1, \dots, 15$. Insets illustrate snapshots, at $t = 36$ (top panels), and $t = 55$ (bottom panels), during propagation of the first three modes of entanglement, $\rho_k^{(1),\sigma}$ ($k = 1, 2, 3$) for the $\sigma = A, B$ species. (b₃), (b₄) Temporal evolution of the natural populations $n_i(t)$ for species A and B respectively. In all cases the system is quenched from $g_{AB} = 0$ to $g_{AB} = 1.2$, while other parameters used are the same as in figure 1.

$$\mathcal{V}^B(t_{\text{im}}) = \int d\tilde{x}' \frac{1}{N_{\text{shots}}} \times \sum_{k=1}^{N_{\text{shots}}} [\mathcal{A}_k^B(\tilde{x}' | \mathcal{A}_k^A(\tilde{x}); t_{\text{im}}) - \bar{\mathcal{A}}_k^B(\tilde{x}' | \mathcal{A}_k^A(\tilde{x}); t_{\text{im}})]^2. \quad (10)$$

Figures 3(a₁), (a₂) present both $\mathcal{V}^A(t)$ and $\mathcal{V}^B(t)$ with $w = 1$, and $N_{\text{shots}} = 1000$ at the MF and the MB level respectively. As it can be seen, at the MF approximation $\mathcal{V}_{\text{MF}}^A(t)$ and $\mathcal{V}_{\text{MF}}^B(t)$ remain almost constant exhibiting small amplitude oscillations which essentially resemble the breathing motion that both species feature. However, when inter and intraspecies correlations are taken into account $\mathcal{V}_{\text{MB}}^A(t)$ and $\mathcal{V}_{\text{MB}}^B(t)$ show a completely different behavior. In particular, an increasing tendency is observed at the initial stages of the unstable dynamics, while after the filament formation ($t_F \approx 27$), $\mathcal{V}_{\text{MB}}^\sigma(t)$ undergoes large amplitude oscillations reflecting the global breathing of each bosonic cloud. More importantly, the aforementioned increasing tendency of the variance resembles the growth rate of the entanglement, (see $1 - \lambda_1(t)$ in figure 3(b₁)) and the corresponding discussion below. The above resemblance can be explained as follows. In a perfect condensate, i.e. $\lambda_1(t) = 1$ and $n_1^\sigma(t) = 1$, $\mathcal{V}_{\text{MF}}^\sigma(t)$ is almost constant during the dynamics as all the atoms in the corresponding single-shot measurement are picked from the same SPF $\varphi^\sigma(t)$ (see also equation (2)). The only relevant information that is imprinted in $\mathcal{V}_{\text{MF}}^\sigma(t)$ concerns the global motion, here the breathing mode, of the entire cloud. It is also worth mentioning here that $\mathcal{V}_{\text{MF}}^A(t) \approx \mathcal{V}_{\text{MF}}^B(t)$ during the MF evolution, testifying the absence of both inter and intraspecies correlations. The observed negligible differences between $\mathcal{V}_{\text{MF}}^A(t)$, and $\mathcal{V}_{\text{MF}}^B(t)$ (hardly visible in figure 3(a₁)) are caused by the slight deviations in the magnitude of the breathing motion that each species undergoes.

On the contrary, for a MB system where entanglement and fragmentation are present due to the inclusion of inter and intraspecies correlations, the corresponding MB state consists of an admixture of various mutually orthonormal species functions $\Psi_k^A(t)$ and $\Psi_k^B(t)$ respectively, $k = 1, 2, \dots, 15$ (see equation (3)) each of them building upon different mutually orthonormal SPFs $\varphi_i^A(t)$ and $\varphi_i^B(t)$ respectively, $i = 1, 2, 3$ (see also equation (4)). In this way, the corresponding single-shot variance is drastically altered from its MF counterpart as the atoms are picked from the above-mentioned superposition and thus their distribution in the cloud depends strongly on the position of the already imaged atoms [71, 72, 75], see also appendix A. To fairly discern between the impact of the inter and intraspecies correlations on the variance we first inspect $\mathcal{V}^\sigma(t)$ when neglecting the entanglement between the species (this approach will be referred in the following as species MF approximation (SMF)). Namely we calculate $\mathcal{V}_{\text{SMF}}^\sigma(t)$ assuming that the N_σ -body state of each species is described by only one species function ($\Psi_k^A(t) = \Psi_k^B(t) = 0$ for $k \neq 1$) that builds upon distinct SPFs $\varphi_i^A(t)$ and $\varphi_i^B(t)$, $i = 1, 2, 3$. As shown in figure 3(a₂) during the filamentation process $\mathcal{V}_{\text{SMF}}^\sigma(t)$ increases slightly and $\mathcal{V}_{\text{SMF}}^A(t) \approx \mathcal{V}_{\text{SMF}}^B(t)$ while at later time instants $\mathcal{V}_{\text{SMF}}^A(t) < \mathcal{V}_{\text{SMF}}^B(t)$. This latter deviation is attributed to the different degree of fragmentation ($1 - n_1^\sigma(t)$, see e.g. figure 3(b₁)) that each species possesses after the filamentation process $t > 27$. Having identified that the presence of fragmentation essentially causes a slight increase on the single-shot variance and more importantly gives rise to deviations between the $\mathcal{V}_{\text{SMF}}^\sigma(t)$'s of the two species we can elaborate on the impact of the entanglement when also interspecies correlations are taken into account. In the MB case $\mathcal{V}_{\text{MB}}^\sigma(t)$ shows a remarkable increasing tendency during the filamentation process highlighting this way the presence of entanglement in the system. Indeed, the increase of entanglement (evident in $1 - \lambda_1^\sigma(t)$) and consequently of the variance can be attributed to the build up of higher-order superpositions during the filamentation process. Since the absorption imaging destroys the entanglement between the species, we expect that the single-shot images heavily depend on the first few imaged atoms giving rise to pronounced

$\mathcal{V}_{\text{MB}}^\sigma(t)$. We further remark that this increasing tendency of the variance becomes more pronounced (reduced) for larger (smaller) quench values (results not included for brevity). Moreover, during the filamentation process $\mathcal{V}_{\text{MB}}^A(t) \approx \mathcal{V}_{\text{MB}}^B(t)$ but after their formation $\mathcal{V}_{\text{MB}}^A(t) < \mathcal{V}_{\text{MB}}^B(t)$. This latter deviation can be attributed to the different degree of fragmentation that builds up during evolution in each of the two species (compare $1 - n_1^\sigma(t)$ for $t \geq 40$ illustrated in figure 3(b₁)). We finally note that the above-described overall increasing behavior of $\mathcal{V}_{\text{MB}}^A(t)$ and $\mathcal{V}_{\text{MB}}^B(t)$ is robust also for smaller samplings of single-shot measurements, e.g. $N_{\text{shots}} = 100$, or different widths, e.g. $w = 0.5$, (results not shown here for brevity).

3.3. Correlation dynamics

The degree of entanglement is encoded in the species functions of the binary system, i.e. $\Psi_k^\sigma(\vec{x}^\sigma; t)$, with $\sigma = A, B$, being weighted by the $\lambda_k(t)$ coefficients. We remind the reader that if $\lambda_1(t) = 1$ and $\lambda_i(t) = 0$ ($i = 2, \dots, k$) then the non-entangled limit is reached while if $\lambda_k(t) \neq 0$ the more modes are occupied the more strongly entangled the binary system (see footnote 4). In particular, by considering the evolution of the natural occupations $\lambda_k(t)$, depicted in figure 3(b₂) it is observed that from the beginning of the quench-induced dynamics the occupation of the initial single mode (non-entangled) wavefunction reduces rapidly and higher-lying modes become spontaneously populated. Notice that before the filament formation, e.g. at $t \approx 13$, $\lambda_1 \approx 0.37$ and $\lambda_2 \approx \lambda_3 \approx 0.12$, while after the breaking ($t \approx 27$) the amplitude of the higher-lying modes drops below 0.1 and remains in this ballpark till the end of the propagation. The insets depict selected time instants during the phase separation process of the first three modes of entanglement: namely, just after the breaking (upper insets in figure 3(b₂)) and the consequent filamentation of the MB wavefunction, and for larger propagation times (lower insets in figure 3(b₂)) corresponding to $\Lambda(t) \approx 0.5$ during evolution (see also figure 1(c₃)). In all cases the leading order mode weighted by λ_1 , and the first two of the higher-lying modes that are predominantly occupied, weighted by λ_2 and λ_3 respectively, are shown for both the A and B species. As it is evident, the dominant mode clearly captures all the filaments formed for both species. The second mode for species A builds a hump at the location centered around the density dip of the first mode, while it also follows the outer filaments formed, and the corresponding third mode mostly supports the inner filaments. As far as the B species is concerned the above-observed phenomenology is somewhat reversed. Notice that, the second mode mostly follows the outer filaments, and the third mode is found to be predominantly associated with the filaments developed closer to the trap center.

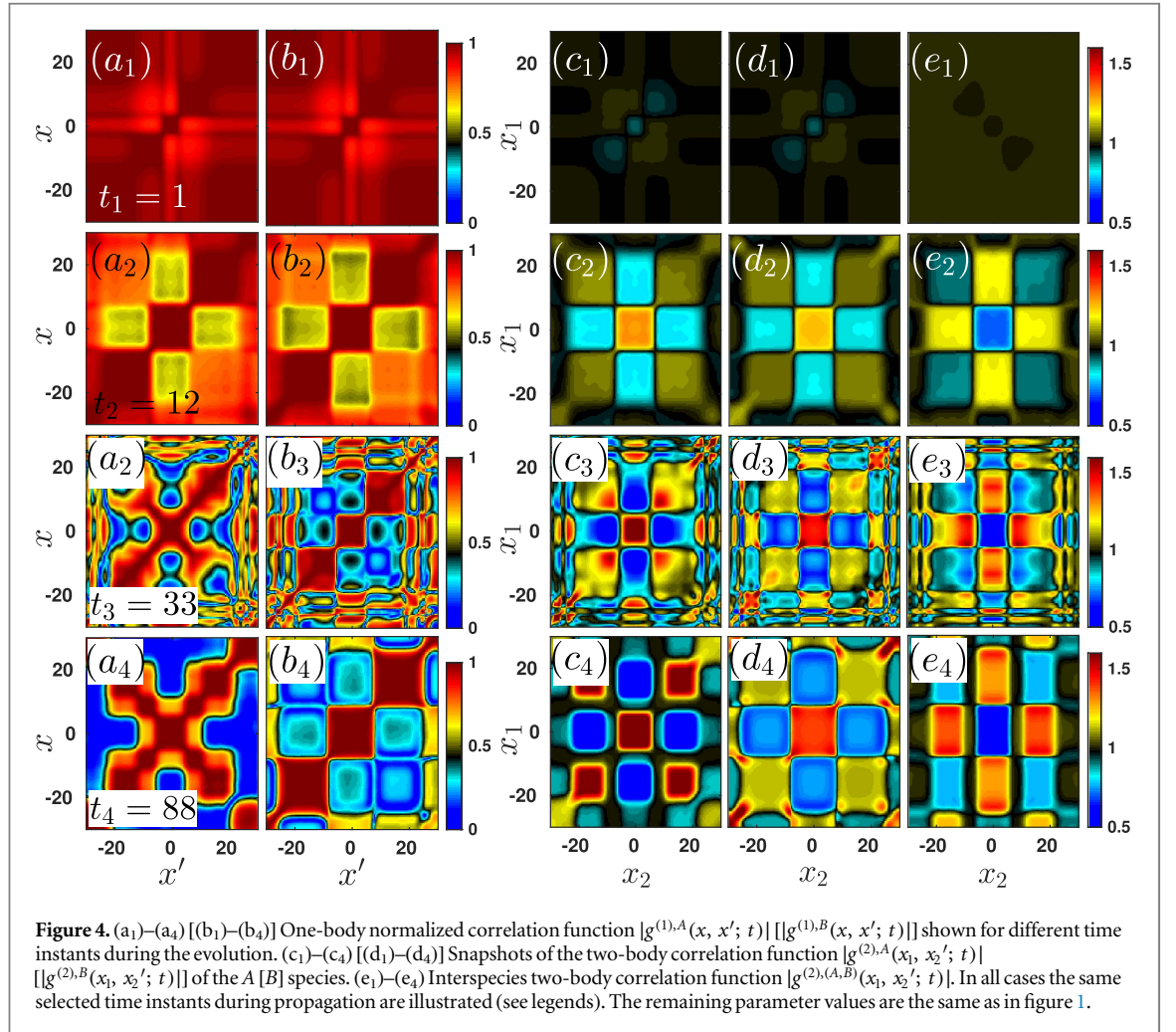
To further elaborate on the MB nature of the observed quench dynamics we next examine the population of the natural orbitals shown in figures 3(b₃), (b₄). The occupations of the three natural orbitals used for each of the two species are significant from the early stages of the dynamics, with the two lower-lying orbitals being monotonically ordered, acquiring lower populations during evolution.

As already discussed in section 2 the non-negligible population of both λ_k and n_k^σ ($k > 1$) signifies the presence of inter- and intraspecies correlations respectively. To identify the degree of intraspecies correlations at the one-body level during the quench dynamics, we employ the normalized spatial first order correlation function [76, 77]

$$g^{(1),\sigma}(x, x'; t) = \frac{\rho^{(1),\sigma}(x, x'; t)}{\sqrt{\rho^{(1),\sigma}(x; t)\rho^{(1),\sigma}(x'; t)}}. \quad (11)$$

This quantity measures essentially the proximity of the MB state to a MF (product) state for a fixed set of coordinates x, x' . $\rho^{(1),\sigma}(x, x'; t)$ is the one-body reduced density matrix of the σ species (see also equation (5)) and $\rho^{(1),\sigma}(x; t) \equiv \rho^{(1),\sigma}(x, x' = x; t)$. Furthermore, $|g^{(1),\sigma}(x, x'; t)|$ takes values within the range $[0, 1]$. Note that, two different spatial regions R, R' , with $R \cap R' = \emptyset$, exhibiting $|g^{(1),\sigma}(x, x'; t)| = 0$, $x \in R, x' \in R'$ ($|g^{(1),\sigma}(x, x'; t)| = 1$, $x \in R, x' \in R'$) are referred to as fully incoherent (coherent). The absence of one-body correlations in the condensate is indicated by $|g^{(1),\sigma}(x, x'; t)| = 1$ for every x, x' while the case that at least two distinct spatial regions are partially incoherent i.e. $|g^{(1),\sigma}(x, x'; t)| < 1$ signifies the emergence of correlations.

Figures 4(a₁)–(a₄) and [(b₁)–(b₄)] present $|g^{(1),A}(x, x'; t)|$ [$|g^{(1),B}(x, x'; t)|$] for different time instants during the dynamics, namely before and after the filamentation process. At initial time instants (see figures 4(a₁), (a₂) and (b₁), (b₂)) where the density deformation sets in, one-body correlations begin to develop. For instance $|g^{(1),\sigma}(x, x'; t)| \approx 0.5$ between the central and the outer BEC regions (in which the filaments are formed later on, see e.g. at $x \approx 0, x' \approx 15$ at $t = 12$), while $|g^{(1),\sigma}(x, x'; t)| \approx 0.8$ among the outer regions ($x = -x' \approx 15$ at $t = 12$). An augmented character of $|g^{(1),\sigma}(x, x'; t)|$ for increasing distances (e.g. for fixed $x \approx 0$, towards $x' \approx 25$ at $t = 7$) is also observed. For later evolution times, i.e. after the filamentation process, a significant build up of one-body correlations occurs for both species. Referring to $|g^{(1),A}(x, x'; t)|$, see figures 4(a₃), (a₄), we observe that each filament is perfectly coherent with itself (see the diagonal elements), while a small amount of correlations occurs between the inner filaments ($|g^{(1),A}(x \approx 6, x' \approx -6; t = 33)| \approx 0.9$) or the outer ones ($|g^{(1),A}(x \approx 14, x' \approx -14; t = 33)| \approx 0.8$). More importantly, strong correlations appear between neighboring inner and outer filaments as well as among an inner (outer) filament and its long distance outer (inner) one ($|g^{(1),A}(x, x'; t)| \approx 0.5$) signaling their independent nature. Finally, significant losses of coherence



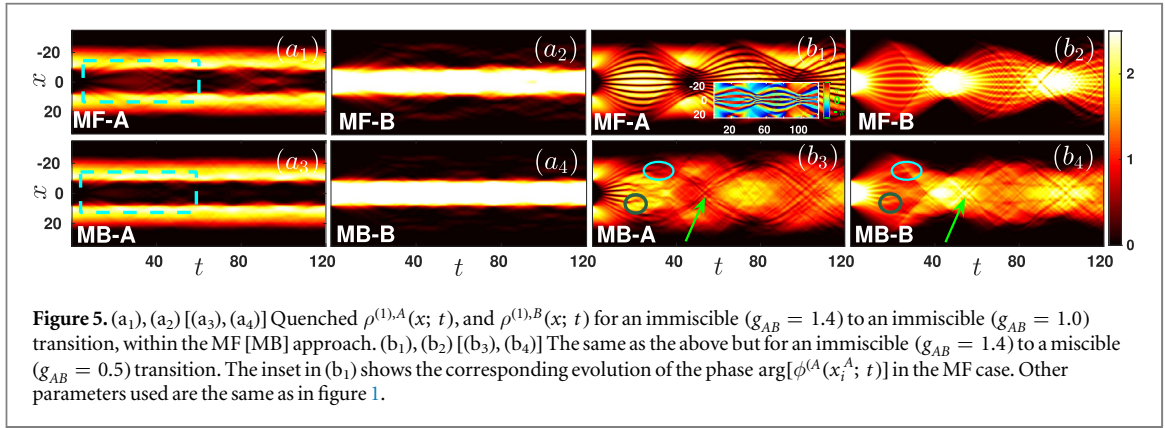
are observed between the inner (outer) filaments and the central dip. Turning to $|g^{(1),B}(x, x'; t)|$, see figures 4(b₃), (b₄), it is evident that strong correlations appear among each outer and the central filaments (see e.g. $x \approx 10$, $x' \approx 0$ at $t = 33$) as well as between the outer ones ($x = -x' \approx 10$ at $t = 33$). This latter behavior is manifested by the almost vanishing off-diagonal elements of $|g^{(1),B}(x, x'; t)|$ after the filamentation process, indicating a tendency of localization of each filament formed.

Having discussed in detail the significance of one-body intraspecies correlations, we next quantify the degree of second order intra- and interspecies correlations by inspecting the normalized two-body correlation function [77]

$$g^{(2),\sigma\sigma'}(x_1, x_2; t) = \frac{\rho^{(2),\sigma\sigma'}(x_1, x_2; t)}{\rho^{(1),\sigma}(x_1; t)\rho^{(1),\sigma'}(x_2; t)}. \quad (12)$$

$\rho^{(2),\sigma\sigma'}(x_1, x_2; t) = \langle \Psi_{\text{MB}}(t) | \Psi^{\dagger,\sigma}(x_1)\Psi^{\dagger,\sigma'}(x_2)\Psi^\sigma(x_1)\Psi^\sigma(x_2) | \Psi_{\text{MB}}(t) \rangle$ is the diagonal two-body reduced density matrix referring to the probability of measuring two particles located at positions x_1, x_2 at time t . $\Psi^{\dagger,\sigma}(x_i)$ [$\Psi^\sigma(x_i)$] is the bosonic field operator that creates (annihilates) a σ species boson at position x_i . Regarding the same (different) species, i.e. $\sigma = \sigma'$ ($\sigma \neq \sigma'$), $|g^{(2),\sigma\sigma'}(x_1, x_2; t)|$ accounts for the intraspecies (interspecies) two-body correlations and is also experimentally accessible via *in situ* density density fluctuation measurements [78–80]. We remark here that a perfectly condensed MB state leads to $|g^{(2),\sigma\sigma'}(x_1, x_2; t)| = 1$ and it is termed fully second order coherent or uncorrelated. However, if $|g^{(2),\sigma\sigma'}(x_1, x_2; t)|$ takes values smaller (larger) than unity the state is referred to as anti-correlated (correlated).

Let us first comment on the intraspecies two-body correlated character of the dynamics. Focusing on $|g^{(2),AA}(x_1, x_2; t)|$ we observe a consecutive formation of two-body correlations during the dynamics, see figures 4(c₁)–(c₄). Besides a bunching tendency (smaller for the inner filaments) of two bosons to lie within each filament (see the diagonal elements), a correlated behavior is observed among two parity symmetric outer ones (see e.g. $x_1 = -x_2 = 14$ at $t = 33$). In addition, an outer filament is anti-correlated both with an inner one ($x_1 \approx 14$, $x_2 \approx 6$ at $t = 33$) as well as with the central dip ($x_1 \approx 14$, $x_2 \approx 0$). Combining this latter behavior with the above suppression of $|g^{(1),A}(x, x'; t)|$ between the filaments, implies the formation of domain-wall-like structures between the area of central filaments and an outer one. Another interesting observation here is that the region between neighboring inner and outer filaments (e.g. $x_1 \approx 16$ at $t = 33$) is strongly correlated



(anti-correlated) with its parity symmetric one. Similar observations can also be made for the $|g^{(2),BB}(x_1, x_2; t)|$, see figures 4(d₁)–(d₄). Evidently, it is preferable for two bosons to reside within each filament (see the diagonals) or one in each of the outer filaments (e.g. $x_1 = -x_2 \approx 10$, $t = 33$). The central filament is anti-correlated with the outer ones throughout the dynamics and since $|g^{(1),BB}(x, x'; t)| \rightarrow 0$ in the same region, the formation of a domain-wall-like structure between a central and an outer filament can be inferred.

As a next step we inspect the interspecies correlation dynamics via $|g^{(2),AB}(x_1, x_2; t)|$, see figures 4(e₁)–(e₄). Here, an outer *A* species filament ($x_1 \approx 14$ at $t = 33$) is anti-correlated (correlated) with the corresponding *B* species outer located at $x_2 \approx 10$ (central at $x_2 = 0$). However, an inner *A* species filament ($x_1 \approx 5$ at $t = 33$) is correlated (anti-correlated) with the respective *B* species outer (central) one. Moreover, we find that the central dip of the *A* species exhibits a correlated (anti-correlated) behavior with the outer (central) *B* species filaments. Summarizing the outcome of $|g^{(2),AB}(x_1, x_2; t)|$ is two-fold. The fact $|g^{(2),AB}(x_1, x_2; t)| \neq 1$ indicates the entangled character of the MB binary system. Additionally, the presence of anti-correlations between the inner and outer filaments of *A* and *B* species respectively (or vice versa) supports the phase separation process being imprinted as domain-walls at the two-body level.

3.4. Reverse quench dynamics

Up to now we explored cases which involve transitions from the miscible to the immiscible phase, by initializing the dynamics from the species uncorrelated ($g_{AB} = 0$) case and abruptly switching on the interspecies repulsion. Our aim here, is to consider the reverse process, namely initialize the system from a species correlated ground state with $g_{AB} = 1.4$, i.e. deep in the immiscible regime of interactions, and suddenly reduce g_{AB} . A characteristic example of an immiscible to immiscible transition with post-quench value $g_{AB} = 1.0$ is realized in figures 5 (a₁)–(a₄). Notice that the phase separated species remain as such at all times with species *A* forming two humps symmetrically placed around the center of the trap. Closer inspection of the central almost zero density region, suggests that two hardly visible density dips are spontaneously formed in the regions indicated by dashed rectangles in figures 5(a₁) and (a₃) for the MF and the MB case respectively. These density dips interact with the density peaks created in this species right at their phase boundary, and via this interaction multiple interference fringes can be seen around the center of the trap in both approaches. It is these events which are more pronounced in the MF than in the MB approach, that result in the differences measured in the overlap between the two species. In particular as shown in figure 6(b), $\Lambda_{MF}(t) \approx 0.35$ on average, while $\Lambda_{MB}(t) \lesssim 0.05$ during evolution, which is significantly smaller. The location of these dips is also the location of a ‘giant’ density hump formed in species *B*. It is also worth mentioning at this point that the evolved phase separated state formed here, consists the 1D analog of the so-called ‘ball’ and ‘shell’ state that forms in higher-dimensional binary BECs [12].

However a far more rich dynamical behavior of the binary system is observed when the two immiscible species are abruptly quenched towards the miscible regime, with the post-quench value $g_{AB} = 0.5$. Such a situation is illustrated in figures 5(b₁), (b₂) [(b₃), (b₄)] within the MF [MB] approach. The quench dynamics leads to the formation of multiple DAD solitary waves [47, 48] both in the MF and in the MB approach. In the former case, the DAD structures are directly discernible and can be seen to interact and perform oscillations, splitting and recombining within the parabolic trap, in a way reminiscent of the one-component dark solitons in the experiments of [81, 82]. To verify the nature of these structures we further depict as an inset in figure 5(b₁) the spatio-temporal evolution of the phase, where the phase jumps corresponding to the location of each dark soliton shown in the density can be easily seen. In contrast to that, in the MB scenario the dynamical evolution of these DAD structures is less transparent, since the system in this case is strongly correlated and the background at which the solitons are formed is highly excited. Recall that dark-bright states are prone to decay in the presence of quantum fluctuations [49] into faster (traveling towards the periphery of the cloud) and slower (remaining closer to the trap center) solitary waves. A similar dynamical phenomenology is also observed here

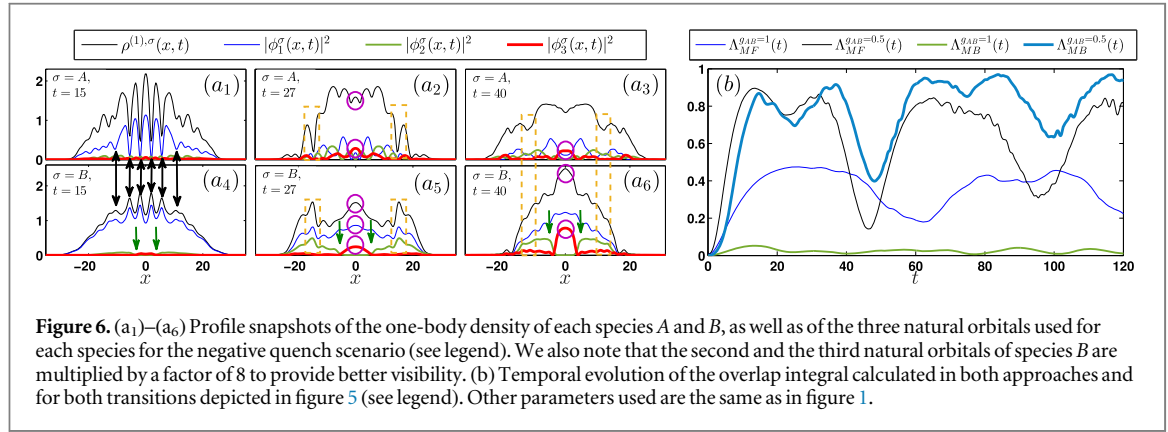


Figure 6. (a₁)–(a₆) Profile snapshots of the one-body density of each species A and B, as well as of the three natural orbitals used for each species for the negative quench scenario (see legend). We also note that the second and the third natural orbitals of species B are multiplied by a factor of 8 to provide better visibility. (b) Temporal evolution of the overlap integral calculated in both approaches and for both transitions depicted in figure 5 (see legend). Other parameters used are the same as in figure 1.

for the above-mentioned DAD states. Indeed, at the early stages of the dynamics several decay events occur. Two case examples of such a decay are marked with circles in figures 5(b₃), (b₄) corresponding to an initially fast and an initially slow DAD pair respectively. This way in the MB case the number of the solitary waves formed increases when compared to the initial stages of the dynamics and thus multiple collision events occur during propagation. We can clearly distinguish a collision event closer to the trap center at $t_F^{MB} \approx 27$ which results to a merger. On the other hand, the corresponding fast moving DAD states reach at different times the periphery of the cloud and thus multiple collision events occur at different times during evolution. A case example of such a collision is indicated with arrows in figures 5(b₃), (b₄).

To expose the multi-orbital nature of the above dynamics, both the one-body density as well as the different orbital contributions are depicted in figures 6(a₁)–(a₆) at initial ($t = 15$), intermediate ($t = 27$) and larger evolution times ($t = 40$). Notice that at initial times the two species are still phase separated, while the first orbital predominantly describes the MB dynamics of the system. Here, we can easily measure the number of DAD solitary waves that are initially formed, illustrated with two-directional arrows in figures 6(a₁) and (a₄), by observing that each density dip created in species A, figure 6(a₁), is filled by a density hump (on top of the BEC background) developed in species B, figure 6(a₄), and vice versa. Furthermore, it is found that consecutive orbitals within the same species also follow the above-described phenomenology with a clearly visible domain-wall [4, 44] formed between the second and the third orbital of species B (see arrows in green in figures 6(a₄)–(a₆)). For intermediate times the merging of the most inner solitary states discussed above is indicated with circles in figures 6(a₂), (a₅). Notice the pronounced density hump that occurs in species B around the center of the trap, being supported by all three orbitals developed in this species. Additionally, also the faster DAD solitary waves are monitored in this time slice, where again it is observed that these states are supported by all orbitals used in each of the two species being marked with dashed rectangles. However, at larger propagation times and since we ‘kicked’ the system towards miscibility, multiple interference events more pronounced in species B, result to a dephasing of these matter wave patterns and most of these states are lost as can be seen in figures 6(a₃), (a₆), rendering the two species mostly overlapped. Notice the increasing tendency towards miscibility with the overlap integral (see again here figure 6(b)) for $g_{AB} = 0.5$ reaching its maximum value, $\Lambda_{MB}(t \geq 60) \approx 0.95$, at large propagation times, when compared to the MF approximation. In the latter case, $\Lambda_{MF}(t) \approx 0.85$ is reached from the early stages of the dynamics remaining on average almost the same as time progresses.

To conclude our investigation, let us also briefly comment on the manifestation of the MB correlated character of the quench-induced dynamics with the aid of *in situ* single-shot measurements. Figures 7(a), (b) present the first and the second simulated *in situ* single-shot images at $t_{im} = 15$ for both species, with the DAD structures being clearly imprinted in both shots. Notice that the two species are almost completely overlapped resembling the overall tendency observed in the averaged, over $N_{shots} = 1000$, one-body density illustrated in figure 7(c). By inspecting the corresponding variances (see also equations (9) and (10)) during the evolution shown in figure 7(d), we observe that within the MF $\mathcal{V}_{MF}^A(t)$ and $\mathcal{V}_{MF}^B(t)$ exhibit a small amplitude oscillatory behavior reflecting the global breathing motion of each cloud. Interestingly enough the oscillation amplitudes of $\mathcal{V}_{MF}^A(t)$ and $\mathcal{V}_{MF}^B(t)$ differ further, due to the difference in the magnitude of the breathing that each species undergoes (see also figures 5(b₁), (b₂)). In sharp contrast to the above, the variances within the MB approach differ drastically from their MF counterparts. Indeed, both $\mathcal{V}_{MB}^A(t)$ and $\mathcal{V}_{MB}^B(t)$ show an overall increasing tendency indicating, as in the positive quench scenario, the presence of entanglement (see also the corresponding discussion in section 3.2). $\mathcal{V}_{MB}^A(t)$ and $\mathcal{V}_{MB}^B(t)$ deviate significantly as a result of the strong intraspecies correlations. We should bear in mind that the initial pre-quenched state is both strongly fragmented and entangled on the MB level. Therefore, in this strongly correlated scenario both fragmentation as well as entanglement are greatly manifested in the evolution of the variance of a set of single-shot measurements.

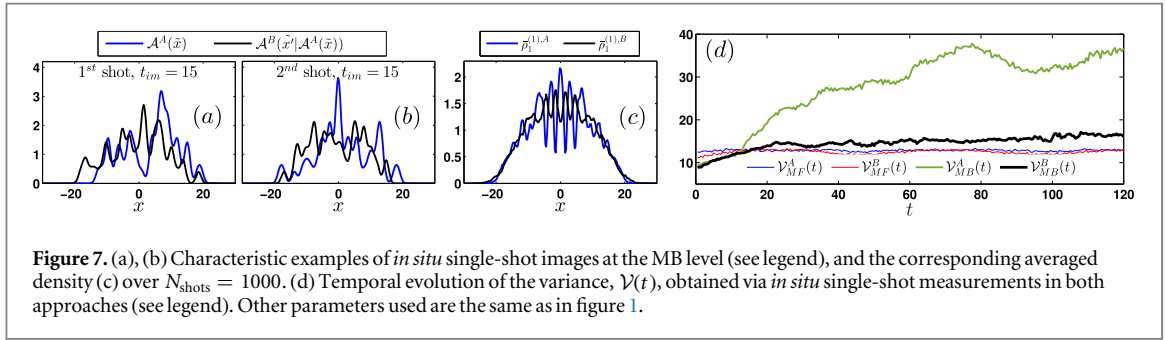


Figure 7. (a), (b) Characteristic examples of *in situ* single-shot images at the MB level (see legend), and the corresponding averaged density (c) over $N_{shots} = 1000$. (d) Temporal evolution of the variance, $\mathcal{V}(t)$, obtained via *in situ* single-shot measurements in both approaches (see legend). Other parameters used are the same as in figure 1.

4. Conclusions

In the present work we explored the quench-induced phase separation dynamics of an inhomogeneous repulsively interacting binary BEC both within and beyond the MF approximation including multiple orbitals. To achieve such a miscible to immiscible transition (positive quench case) the intraspecies interactions are held fixed and the system is abruptly driven out-of-equilibrium by switching on the interspecies repulsion. Quench dynamics leads to the filamentation of the density of each of the two species and also in both approaches (MF and MB) while the filaments formed perform collective oscillations of the breathing-type. The wavenumbers associated with the observed growth are identified to be shorter in the MB case for all g_{AB} values that we have checked, whilst our numerical findings at the MF level are in very good agreement with the analytical predictions available in this limit, as regards the instability growth rate. It is found that increasing the interspecies repulsion, not only accelerates the filamentation process but also increases the number of filaments formed in both approaches, occurring faster on the MB level. Additionally, stronger interspecies repulsion leads to almost complete phase separation being more pronounced in the MB scenario. We further note, that upon fixing the interspecies repulsion while decreasing significantly the system size (few boson case) phase separation is absent in the MB case while still present at the MF limit.

Detailed correlation analysis at the one- and the two-body level bear the signature of the phase separation process as the miscibility–immiscibility threshold is crossed. On the one-body level significant losses of coherence are observed, verifying the fragmented nature of the system, between filaments residing around the center of the trap with the longer distant ones lying at the periphery of the bosonic cloud. At the two-body level domain-wall-like structures are revealed, since the inner filaments in both species are found to be anti-correlated with their respective outer ones. These domain-walls support the fact that for smaller interspecies interactions, but well inside the immiscible regime, we never observe perfect demixing of the two species. Furthermore, and even more importantly, the presence of both entanglement and fragmentation are related to the variance of single-shot images, that are utilized for the first time in the current effort for binary systems, offering a direct way for the experimental realization of the observed dynamics. In particular, it is found that the growth rate of the variance resembles the growth rate of the entanglement. The fragmentation of the binary system is captured by the deviations in the variance measured in the course of the dynamics with respect to each of the two species.

Interestingly enough, when considering the reverse (negative) quench scenario, namely quenching from the immiscible towards the miscible regime multiple DAD solitary waves are spontaneously generated in both approaches and they are found to decay in the MB case [49]. The evolution of the variance of single-shot measurements reveals enhanced entanglement, since the system in this case is strongly correlated on the MB level. Finally, for transitions inside the immiscible regime we retrieve the 1D analog of the so-called ‘ball’ and ‘shell’ structure that appears in higher-dimensional binary BECs [12, 83].

There are multiple directions that are of interest for future work along the lines of the current effort. A systematic study of the dynamical phase separation process following a time-dependent protocol (e.g. a linear quench) presents one of the major computational challenges for further study. In particular, in such a scenario one can explore the domain formation crossing the critical point with different velocities and thus testing the Kibble–Zurek mechanism [66] in the presence of quantum fluctuations. However, to examine the latter, a major challenge that it is imperative to overcome is that of considering low atom numbers, in order to explore the associated thermodynamic limit, avoiding the potential influence of finite size effects. Another straight forward direction is to consider the corresponding already experimentally realized [13] 2D setting, and examine how the MF properties are altered in the presence of quantum fluctuations. Also of great interest would be to consider the quench dynamics of spinor BECs, for which phase separation processes are of ongoing interest at the MF limit [84] and also investigate the relevant MB aspects.

Acknowledgments

SIM and PS gratefully acknowledge financial support by the Deutsche Forschungsgemeinschaft (DFG) in the framework of the SFB 925 ‘Light induced dynamics and control of correlated quantum systems’. PGK gratefully acknowledges the support of NSF-PHY-1602994 and the Alexander von Humboldt Foundation. SIM and GCK would like to thank G M Koutentakis for fruitful discussions.

Appendix A. Single-shot measurements in binary bosonic mixtures

As in the single component case, the single-shot simulation procedure relies on a sampling of the MB probability distribution [71, 72, 75]. The latter is available within the ML-MCTDHB framework. However, in a two species BEC and when inter and intraspecies correlations are taken into account, the entire single-shot procedure is significantly altered when compared to the single component case. Here, the role of entanglement between the species manifested by the Schmidt decomposition (see equation (3)) and in particular the Schmidt coefficients λ_k ’s play a crucial role concerning the image ordering.

For instance, to image first the A and then the B species we consecutively annihilate all the N_A particles. Focusing first on a certain imaging time instant, t_{im} , a random position is drawn according to the constraint $\rho_{N_A}^{(1)}(x_1') > l_1$ where l_1 refers to a random number within the interval $[0, \max\{\rho_{N_A}^{(1)}(x; t_{\text{im}})\}]$. Then we project the $(N_A + N_B)$ -body wavefunction to the $(N_A - 1 + N_B)$ -body one, by employing the operator $\frac{1}{\mathcal{N}}(\hat{\Psi}_A(x_1') \otimes \hat{\mathbb{I}}_B)$, where $\hat{\Psi}_A(x_1')$ denotes the bosonic field operator that annihilates an A species boson at position x_1' and \mathcal{N} is the normalization constant. The latter process directly affects the λ_k ’s (entanglement weights) and thus despite the fact that the B species has not been imaged yet, both $\rho_{N_A-1}^{(1)}(t_{\text{im}})$ and $\rho_{N_B}^{(1)}(t_{\text{im}})$ change. This can be easily understood by employing once more the Schmidt decomposition. Indeed after this first measurement the MB wavefunction reads

$$|\tilde{\Psi}_{\text{MB}}^{N_A-1, N_B}(t_{\text{im}})\rangle = \sum_i \sqrt{\tilde{\lambda}_{i, N_A-1}(t_{\text{im}})} |\tilde{\Psi}_{i, N_A-1}^A(t_{\text{im}})\rangle |\Psi_i^B(t_{\text{im}})\rangle, \quad (\text{A1})$$

where $|\tilde{\Psi}_{i, N_A-1}^A\rangle = \frac{1}{N_i} \hat{\Psi}_A(x_1') |\Psi_i^A\rangle$ is the $N_A - 1$ species wavefunction. $N_i = \sqrt{\langle \Psi_i^A | \hat{\Psi}_A^\dagger(x_1') \hat{\Psi}_A(x_1') | \Psi_i^A \rangle}$ denotes the normalization factor and $\tilde{\lambda}_{i, N_A-1} = \lambda_i N_i / \sum_i \lambda_i N_i^2$ are the Schmidt coefficients that refer to the $(N_A - 1 + N_B)$ -body wavefunction. The above-mentioned procedure is repeated for $N_A - 1$ steps and the resulting distribution of positions $(x'_1, x'_2, \dots, x'_{N_A-1})$ is convoluted with a point spread function leading to a single-shot $\mathcal{A}^A(\tilde{x}) = \sum_{i=1}^{N_A} e^{-\frac{(\tilde{x}-x_i')^2}{2w^2}}$ for the A species. Here \tilde{x} refers to the spatial coordinates within the image and w is the width of the point spread function. It is worth mentioning also at this point that before annihilating the last of the N_A particles, the MB wavefunction has the form

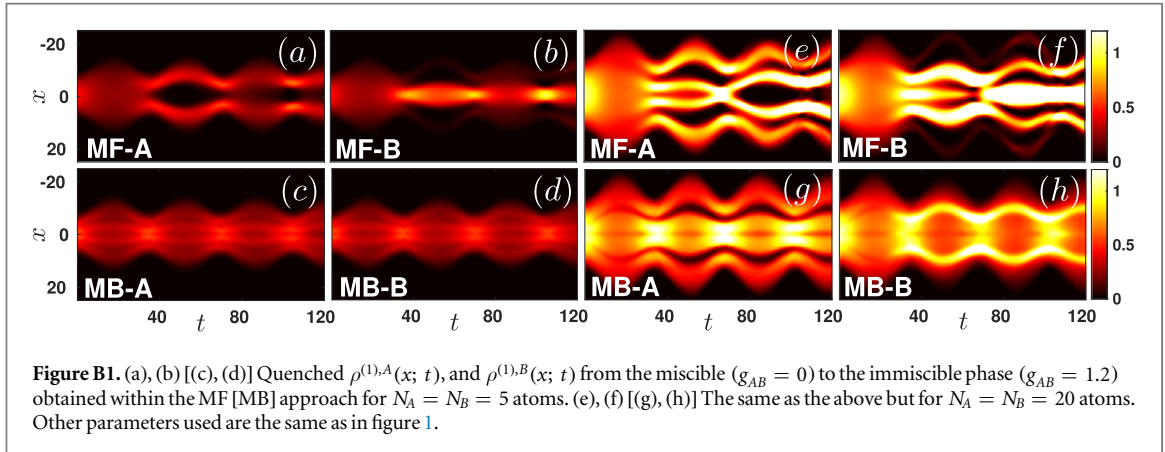
$$|\tilde{\Psi}_{\text{MB}}^{1, N_B}(t_{\text{im}})\rangle = \sum_i \sqrt{\tilde{\lambda}_{i, 1}(t_{\text{im}})} |\Phi_{i, 1}^A(t_{\text{im}})\rangle |\Psi_i^B(t_{\text{im}})\rangle, \quad (\text{A2})$$

where $|\Phi_{i, 1}^A(t_{\text{im}})\rangle$ denotes a single particle wavefunction characterizing the A species. Then, it can be easily shown that annihilating the last A species particle the MB wavefunction reads

$$|\tilde{\Psi}_{\text{MB}}^{0, N_B}(t_{\text{im}})\rangle = |0\rangle \otimes \sum_i \frac{\sqrt{\tilde{\lambda}_{i, 1}(t_{\text{im}})} \langle x | \Phi_{i, 1}^A \rangle}{\sum_j \sqrt{\tilde{\lambda}_{j, 1}(t_{\text{im}})} |\langle x | \Phi_{j, 1}^A \rangle|^2} |\Psi_i^B(t_{\text{im}})\rangle, \quad (\text{A3})$$

where $\langle x | \Phi_{j, 1}^A \rangle$ is the single particle orbital of the j th mode. After this last step the entanglement between the species has been destroyed and the wavefunction of the B species $|\Psi_{\text{MB}}^{N_B}(t_{\text{im}})\rangle$ corresponds to the second term of the cross product on the right hand side of equation (A3). In this way, it becomes evident that $|\Psi_{\text{MB}}^{N_B}(t_{\text{im}})\rangle$ obtained after the annihilation of all N_A atoms is a non-entangled N_B -particle MB wavefunction and its corresponding single-shot procedure is the same as in the single species case [71]. The latter is well-established (for details see [71, 72]) and therefore it is only briefly outlined below. Referring to $t = t_{\text{im}}$ we first calculate $\rho_{N_B}^{(1)}(x; t_{\text{im}})$ from the MB wavefunction $|\Psi_{N_B}\rangle \equiv |\Psi(t_{\text{im}})\rangle$. Then, a random position x_1'' is drawn obeying $\rho_{N_B}^{(1)}(x_1''; t_{\text{im}}) > l_2$ where l_2 is a random number in the interval $[0, \rho_{N_B}^{(1)}(x; t_{\text{im}})]$. Next, one particle located at a position x_1'' is annihilated and $\rho_{N_B-1}^{(1)}(x; t_{\text{im}})$ is calculated from $|\Psi_{N_B-1}\rangle$. To proceed, a new random position x_2'' is drawn from $\rho_{N_B-1}^{(1)}(x; t_{\text{im}})$. Following this procedure for $N_B - 1$ steps we obtain the distribution of positions $(x''_1, x''_2, \dots, x''_{N_B-1})$ which is then convoluted with a point spread function resulting in a single-shot $\mathcal{A}^B(x' | \mathcal{A}^A(\tilde{x}))$.

We remark here that the same overall procedure can be followed in order first to image the B and then the A species. Such an imaging process results in the corresponding single-shots $\mathcal{A}^B(\tilde{x})$ and $\mathcal{A}^A(\tilde{x}' | \mathcal{A}^B(\tilde{x}))$.



Appendix B. Few boson case

Here, we explore the dependence of a miscible–immiscible transition, from $g_{AB} = 0$ to $g_{AB} = 1.2$, on the total number of atoms, N , of the binary system. Initially we consider a binary system consisting of $N = 40$ atoms, which is almost half the total number of particles considered in the main text ($N = 100$), and as a next step a mixture with $N = 10$ bosons, i.e. an order of magnitude smaller cloud, is studied. Our findings are summarized in figure B1. At the MF level depicted in figures B1(a), (b) and (e), (f) for $N = 10$ and $N = 40$ respectively, we find that the number of filaments formed depends on the number of atoms present in the system and for larger particle numbers more filaments are formed. In sharp contrast to the above dynamics, for small particle numbers, i.e. $N = 10$, phase separation is not observed in the MB approach (while it is transparent at the MF level in the form of a ball and shell configuration); instead an enhanced miscibility region is evident in figures B1(c), (d). Alterations of the miscibility–immiscibility threshold due to the presence of quantum pressure effects in confined BECs have been reported in [63, 85, 86] but at the MF level. Remarkably here, and also in contrast to the MF approximation four, instead of two, almost equally populated filaments are dynamically formed in both the A and the B species shown respectively in figures B1(c) and (d), but the two species remain overlapping at all times. Additionally, the interparticle repulsion between the species leads to breathing-type oscillations of the particle densities.

As the number of particles is increased, namely for $N = 40$, the one-body density evolution of the A species shown in figures B1(e), (g) for the MF and the MB scenario respectively also differ. In particular, while in both approaches four filaments are formed, they are found to be significantly broader in the MB case. This broadening together with the breathing that the cloud undergoes, leads to a collision of the inner filaments in a periodic manner, being more pronounced in the MB case when compared to the single merging, and repulsion observed at around $t \approx 70$ in the MF approach of figure B1(e). Moreover, the disparity between the two approaches becomes rather transparent when further inspecting the spatio-temporal evolution of the density of species B illustrated in figures B1(f), (h) for the MF and the MB case respectively. Interestingly here, in the MB scenario only two filaments are formed located alternately in regions that correspond to density dips of species A , restoring the phase separation process absent for smaller particle numbers. However, the central filament created in the MF approach (see for comparison figure B1(f)) is clearly absent in the MB case, resulting in this way in a larger overlap between the two gases at the MB level.

Appendix C. Remarks on convergence

Let us first briefly comment on the main features of our computational methodology, ML-MCTDHB, and then showcase the convergence of our results. ML-MCTDHB [42, 43] constitutes a flexible variational method for solving the time-dependent MB Schrödinger equation of bosonic mixtures. It relies on expanding the total MB wavefunction with respect to a time-dependent and variationally optimized basis, which enables us to capture the important correlation effects using a computationally feasible basis size. Finally, its multi-layer ansatz for the total wavefunction allows us to account for intra- and interspecies correlations when simulating the dynamics of bipartite systems. For our simulations, we use a primitive basis consisting of a sine discrete variable representation containing 800 grid points. To perform the simulations into a finite spatial region, we impose hard-wall boundary conditions at the positions $x = \pm 50$. Note that the Thomas-Fermi radius of each bosonic cloud is of the order of 20 and we never observe appreciable densities beyond $x = \pm 30$. Therefore the location of the imposed boundary conditions is inconsequential for our simulations. The truncation of the total system's

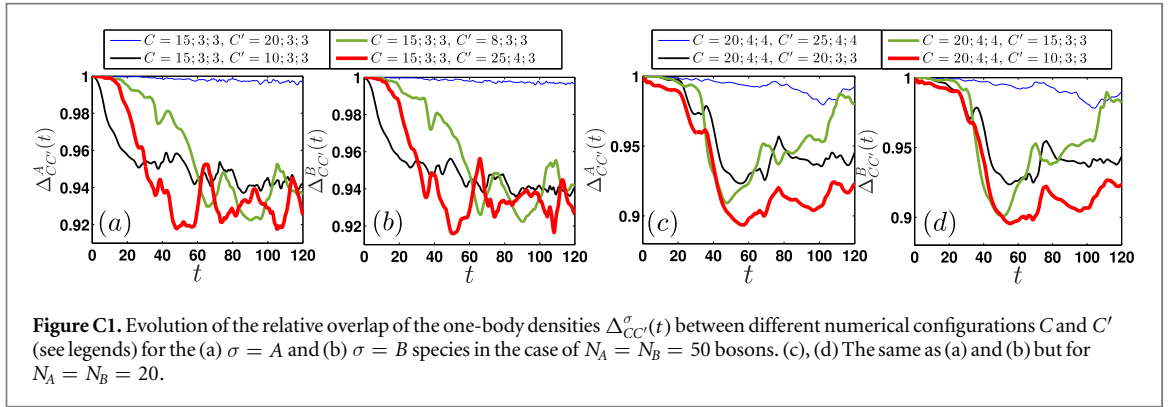


Figure C1. Evolution of the relative overlap of the one-body densities $\Delta_{CC'}^\sigma(t)$ between different numerical configurations C and C' (see legends) for the (a) $\sigma = A$ and (b) $\sigma = B$ species in the case of $N_A = N_B = 50$ bosons. (c), (d) The same as (a) and (b) but for $N_A = N_B = 20$.

Hilbert space, namely the order of the considered approximation, is indicated by the used numerical configuration space $C = (M; m_A; m_B)$. Here, $M = M_A = M_B$ refers to the number of species functions and m_A, m_B denote the amount of SPFs for each of the species. In the limit $M = m_A = m_B = 1$ the ML-MCTDHB expansion reduces to the MF ansatz. Finally, in order to guarantee the accurate performance of the numerical integration for the ML-MCTDHB equations of motion the following overlap criteria $|\langle \Psi | \Psi \rangle - 1| < 10^{-10}$ and $|\langle \varphi_i | \varphi_j \rangle - \delta_{ij}| < 10^{-10}$ have been imposed for the total wavefunction and the SPFs respectively.

Next, we demonstrate the order of convergence of our results and thus the level of our MB truncation scheme. To show that our MB results (more specifically the quantities and observables considered here) are numerically converged, we inspect for the σ species the overlap $\Delta_{CC'}^\sigma(t) = 1 - \delta_{CC'}^\sigma(t)$ between the one-body densities $\rho_i^{(1),\sigma}(x, t)$, where $i = C, C'$, obtained within the different numerical configurations $C = (M; m_A; m_B)$ and $C' = (M'; m'_A; m'_B)$

$$\delta_{CC'}^\sigma(t) = \frac{1}{N_\sigma} \int_R dx (\rho_C^{(1),\sigma}(x, t) - \rho_{C'}^{(1),\sigma}(x, t)). \quad (\text{C1})$$

N_σ denotes the number of σ species bosons and $R = [-30, 30]$ corresponds to the spatially integrated domain in which there is finite density. In this way, we track the relative error between the different approximations C, C' and infer about convergence when $\Delta_{CC'}^\sigma(t)$ becomes to a certain degree insensitive upon increasing either the number of species functions M or the SPFs m_A, m_B . $\Delta_{CC'}^\sigma$ is bounded within the interval $[0, 1]$, where in the case of $\Delta_{CC'}^\sigma = 1$ [$\Delta_{CC'}^\sigma = 0$] the two densities completely overlap [phase separate] and therefore the C, C' approximations yield the same [deviating] results. Figures C1(a), (b) present $\Delta_{CC'}^A(t)$ and $\Delta_{CC'}^B(t)$ respectively, for $N_A = N_B = 50$ and post-quench interspecies interaction $g_{AB} = 1.2$. Here, we keep always $C = (15; 3; 3)$ fixed and examine the convergence upon varying either M' or m'_A, m'_B . As it can be seen, upon increasing the number of species functions from $M = 15$ to $M = 20$, i.e. $C = (15; 3; 3)$ and $C' = (20; 3; 3)$, $\Delta_{CC'}^A(t)$ [$\Delta_{CC'}^B(t)$] exhibits negligible deviations being smaller than 1% throughout the dynamics. Therefore convergence is guaranteed with respect to M . However, for increasing number of SPFs $\Delta_{CC'}^\sigma(t)$ is more sensitive. Indeed, by considering $C' = (25; 4; 3)$ corresponding to a total number of coefficients 625 025 [instead of 44 805 that refer to the $C = (15; 3; 3)$] the deviation obtained from $\Delta_{CC'}^A(t)$ [$\Delta_{CC'}^B(t)$] reaches a maximum value of the order of 8% at large propagation times. We should note here that further increase of the number of SPFs is computationally prohibitive for this number of particles as the considered number of configurations becomes significantly larger. The same observations can also be obtained from $\Delta_{CC'}^\sigma(t)$ of a mixture consisting of $N_A = N_B = 20$ bosons, see figures C1(c), (d), when considering $C = (20; 4; 4)$. For completeness we note that fragmentation becomes enhanced all the more as the particle number is reduced. To conclude upon convergence concerning the species functions we show $\Delta_{CC'}^A(t)$ [$\Delta_{CC'}^B(t)$] in figures C1(c) [(d)]. It is observed that $\Delta_{CC'}^A(t)$ [$\Delta_{CC'}^B(t)$] between $C = (20; 4; 4)$ and $C' = (25; 4; 4)$ testifies negligible deviations which become at most 2.2% at long evolution times. In the same manner, convergence occurs for a varying number of SPFs in both species. For instance, $\Delta_{CC'}^A(t)$ [$\Delta_{CC'}^B(t)$] between $C' = (20; 3; 3)$ and $C = (20; 4; 4)$ shows a maximum deviation of the order of 7% for large evolution times. Similar observations can be deduced also for the case of even smaller particle numbers, and the reverse quench scenario (not included here for brevity reasons). To summarize, according to the above systematic investigations, the considered orbital configurations provide adequate approximations for the description of the non-equilibrium correlated dynamics.

ORCID iDs

P G Kevrekidis  <https://orcid.org/0000-0002-7714-3689>

References

- [1] Pethick C J and Smith H S 2002 *Bose–Einstein Condensation in Dilute Gases* (Cambridge: Cambridge University Press)
- [2] Pitaevskii L P and Stringari S 2003 *Bose–Einstein Condensation* (Oxford: Oxford University Press)
- [3] Kevrekidis P G, Frantzeskakis D J and Carretero-González R (ed) 2008 *Emergent Nonlinear Phenomena in Bose–Einstein Condensates. Theory and Experiment* (Berlin: Springer)
- [4] Kevrekidis P G, Frantzeskakis D J and Carretero-González R 2015 *The Defocusing Nonlinear Schrödinger Equation* (Philadelphia, PA: SIAM)
- [5] Carr L D 2010 *Understanding Quantum Phase Transitions* (Boca Raton, FL: CRC Press)
- [6] Proukakis N, Gardiner S, Davis M and Szymanska M 2013 *Quantum Gases: Finite Temperature and Non-Equilibrium Dynamics* (London: Imperial College Press)
- [7] Kawaguchi Y and Ueda M 2012 *Phys. Rep.* **250** 253
- [8] Stamper-Kurn D M, Andrews M R, Chikkatur A P, Inouye S, Miesner H-J, Stenger J and Ketterle W 1998 *Phys. Rev. Lett.* **80** 2027
- [9] Hall D S, Matthews M R, Ensher J R, Wieman C E and Cornell E A 1998 *Phys. Rev. Lett.* **81** 1539
- [10] Stenger J, Inouye S, Stamper-Kurn D M, Miesner H-J, Chikkatur A P and Ketterle W 1998 *Nature* **396** 345
- [11] Schweikhard V, Coddington I, Engels P, Tung S and Cornell E A 2004 *Phys. Rev. Lett.* **93** 210403
- [12] Mertes K M, Merrill J W, Carretero-González R, Frantzeskakis D J, Kevrekidis P G and Hall D S 2007 *Phys. Rev. Lett.* **99** 190402
- [13] Papp S B, Pino J M and Wieman C E 2008 *Phys. Rev. Lett.* **101** 040402
- [14] Anderson R P, Ticknor C, Sidorov A I and Hall B V 2009 *Phys. Rev. A* **80** 023603
- [15] Egorov M, Opanchuk B, Drummond P, Hall B V, Hannaford P and Sidorov A I 2013 *Phys. Rev. A* **87** 053614
- [16] Tojo S, Taguchi Y, Masuyama Y, Hayashi T, Saito H and Hirano T 2010 *Phys. Rev. A* **82** 033609
- [17] Eto Y, Takahashi M, Kunimi M, Saito H and Hirano T 2016 *New J. Phys.* **18** 073029
- [18] Eto Y, Takahashi M, Nabeta K, Okada R, Kunimi M, Saito H and Hirano T 2016 *Phys. Rev. A* **93** 033615
- [19] Nicklas E, Strobel H, Zibold T, Gross C, Malomed B A, Kevrekidis P G and Oberthaler M K 2011 *Phys. Rev. Lett.* **107** 193001
- [20] Nicklas E, Muessel W, Strobel H, Kevrekidis P G and Oberthaler M K 2015 *Phys. Rev. A* **92** 053614
- [21] Lin Y-J, Jiménez-García K and Spielman I B 2011 *Nature* **471** 83
- [22] Nicklas E, Karl M, Höfer M, Johnson A, Muessel W, Strobel H, Tomkovic J, Gasenzer T and Oberthaler M K 2015 *Phys. Rev. Lett.* **115** 245301
- [23] Karl M, Cakir H, Halimeh J C, Oberthaler M K, Kastner M and Gasenzer T 2017 *Phys. Rev. E* **96** 022110
- [24] Bisset R N, Wilson R M and Ticknor C 2015 *Phys. Rev. A* **91** 053613
- [25] García-March M A, Juliá-Díaz B, Astrakharchik G E, Boronat J and Polls A 2014 *Phys. Rev. A* **90** 063605
- [26] Cazalilla M A and Ho A F 2003 *Phys. Rev. Lett.* **91** 150403
- [27] Alon O E, Streltsov A I and Cederbaum L S 2006 *Phys. Rev. Lett.* **97** 230403
- [28] García-March M A and Busch T 2013 *Phys. Rev. A* **87** 063633
- [29] Zöllner S, Meyer H D and Schmelcher P 2008 *Phys. Rev. A* **78** 013629
- [30] Pyzh M, Krönke S, Weitenberg C and Schmelcher P 2018 *New J. Phys.* **20** 015006
- [31] Hao Y and Chen S 2009 *Phys. Rev. A* **80** 043608
- [32] García-March M A, Juliá-Díaz B, Astrakharchik G E, Busch T, Boronat J and Polls A 2013 *Phys. Rev. A* **88** 063604
- [33] García-March M A, Juliá-Díaz B, Astrakharchik G E, Busch T, Boronat J and Polls A 2014 *New J. Phys.* **16** 103004
- [34] Pflanzner A C, Zöllner S and Schmelcher P 2009 *J. Phys. B: At. Mol. Opt. Phys.* **42** 231002
- [35] Pflanzner A C, Zöllner S and Schmelcher P 2010 *Phys. Rev. A* **81** 023612
- [36] Chatterjee B, Brouzos I, Cao L and Schmelcher P 2012 *Phys. Rev. A* **85** 013611
- [37] Campbell S, García-March M A, Fogarty T and Busch T 2014 *Phys. Rev. A* **90** 013617
- [38] Mistakidis S I, Cao L and Schmelcher P 2014 *J. Phys. B: At. Mol. Opt. Phys.* **47** 225303
- [39] Mistakidis S I, Cao L and Schmelcher P 2015 *Phys. Rev. A* **91** 033611
- [40] Mistakidis S I, Wulf T, Negretti A and Schmelcher P 2015 *J. Phys. B: At. Mol. Opt. Phys.* **48** 244004
- [41] Mistakidis S I and Schmelcher P 2017 *Phys. Rev. A* **95** 013625
- [42] Cao L, Krönke S, Vendrell O and Schmelcher P 2013 *J. Chem. Phys.* **139** 134103
- [43] Cao L, Bolsinger V, Mistakidis S I, Koutentakis G M, Krönke S, Schurer J M and Schmelcher P 2017 *J. Chem. Phys.* **147** 044106
- [44] Trippenbach M, Góral K, Rządźewski K, Malomed B A and Band Y B 2000 *J. Phys. B: At. Mol. Opt. Phys.* **33** 4017
- [45] Filatrella G, Malomed B A and Salerno M 2014 *Phys. Rev. A* **90** 043629
- [46] De S, Campbell D L, Price R M, Putra A, Anderson B M and Spielman I B 2014 *Phys. Rev. A* **89** 033631
- [47] Danaïla I, Khamehchi M A, Gokhroo V, Engels P and Kevrekidis P G 2016 *Phys. Rev. A* **94** 053617
- [48] Kevrekidis P G, Nistazakis H E, Frantzeskakis D J, Malomed B A and Carretero-González R 2004 *Eur. Phys. J. D* **28** 181–5
- [49] Katsimiga G C, Koutentakis G M, Mistakidis S I, Kevrekidis P G and Schmelcher P 2017 *New J. Phys.* **19** 073004
- [50] Köhler T, Goral K and Julienne P S 2006 *Rev. Mod. Phys.* **78** 1311
- [51] Chin C, Grimm R, Julienne P and Tiesinga E 2010 *Rev. Mod. Phys.* **82** 1225
- [52] Olshani M 1998 *Phys. Rev. Lett.* **81** 938
- [53] Kim J I, Melezhik V S and Schmelcher P 2006 *Phys. Rev. Lett.* **97** 193203
- [54] Frenkel J 1934 *Wave Mechanics* 1st edn (Oxford: Clarendon) pp 423–8
- [55] Dirac P A 1930 *Proc. Camb. Phil. Soc.* **26** 376
- [56] Horodecki R, Horodecki P, Horodecki M and Horodecki K 2009 *Rev. Mod. Phys.* **81** 865
- [57] Roncaglia M, Montorsi A and Genovese M 2014 *Phys. Rev. A* **90** 062303
- [58] Peres A 2006 *Quantum Theory: Concepts and Methods* vol 57 (Berlin: Springer)
- [59] Lewenstein M, Bruß D, Cirac J I, Kraus B, Kus’ M, Samsonowicz J, Sanpera A and Tarrach R 2000 *J. Mod. Opt.* **47** 2481
- [60] Mueller E J, Ho T L, Ueda M and Baym G 2006 *Phys. Rev. A* **74** 033612
- [61] Penrose O and Onsager L 1956 *Phys. Rev.* **104** 576
- [62] Ao P and Chui S T 1998 *Phys. Rev. A* **58** 4836
- [63] Navarro R, Carretero-González R and Kevrekidis P G 2009 *Phys. Rev. A* **80** 023613
- [64] Abraham J W and Bonitz M 2014 *Contrib. Plasma Phys.* **54** 27
- [65] Tommasini P, de Passos E J V, de Toledo Piza A F R, Hussein M S and Timmermans E 2003 *Phys. Rev. A* **67** 023606
- [66] Sabbatini J, Zurek W H and Davis M J 2011 *Phys. Rev. Lett.* **107** 230402
- [67] Timmermans E 1998 *Phys. Rev. Lett.* **81** 5718

- [68] Grond J, Streltsov A I, Lode A U, Sakmann K, Cederbaum L S and Alon O E 2013 *Phys. Rev. A* **88** 023606
- [69] Jain P and Boninsegni M 2011 *Phys. Rev. A* **83** 023602
- [70] Bandyopadhyay S, Roy A and Angom D 2017 *Phys. Rev. A* **96** 043603
- [71] Sakmann K and Kasevich M 2016 *Nat. Phys.* **12** 451
- [72] Lode A U and Bruder C 2017 *Phys. Rev. Lett.* **118** 013603
- [73] Chatterjee B and Lode A U 2017 arXiv:1708.07409
- [74] Koutentakis G M, Mistakidis S I and Schmelcher P in preparation
- [75] Katsimiga G C, Mistakidis S I, Koutentakis G M, Kevrekidis P G and Schmelcher P 2017 *New J. Phys.* **19** 123012
- [76] Naraschewski M and Glauber R J 1999 *Phys. Rev. A* **59** 4595
- [77] Sakmann K, Streltsov A I, Alon O E and Cederbaum L S 2008 *Phys. Rev. A* **78** 023615
- [78] Tavares P E S, Fritsch A R, Telles G D, Hussein M S, Impens F, Kaiser R and Bagnato V S 2016 arXiv:1606.01589
- [79] Tsatsos M C, Nguyen J H V, Lode A U J, Telles G D, Luo D, Bagnato V S and Hulet R G 2017 arXiv:1707.04055
- [80] Endres M et al 2013 *Appl. Phys. B* **113** 27
- [81] Weller A, Ronzheimer J P, Gross C, Esteve J, Oberthaler M K, Frantzeskakis D J, Theocharis G and Kevrekidis P G 2008 *Phys. Rev. Lett.* **101** 130401
- [82] Theocharis G, Weller A, Ronzheimer J P, Gross C, Oberthaler M K, Kevrekidis P G and Frantzeskakis D J 2010 *Phys. Rev. A* **81** 063604
- [83] Bisset R N, Kevrekidis P G and Ticknor C 2018 *Phys. Rev. A* **97** 023602
- [84] Gautam S and Adhikari S K 2014 *Phys. Rev. A* **90** 043619
- [85] Pattinson R W, Billam T P, Gardiner S A, McCarron D J, Cho H W, Cornish S L, Parker N G and Proukakis N P 2013 *Phys. Rev. A* **87** 013625
- [86] Wen L, Liu W M, Cai Y, Zhang J M and Hu J 2012 *Phys. Rev. A* **85** 043602

4.3.2 Many-Body Expansion Dynamics of a Bose-Fermi Mixture Confined in an Optical Lattice

Many-body expansion dynamics of a Bose-Fermi mixture confined in an optical latticeP. Siegl,¹ S. I. Mistakidis,¹ and P. Schmelcher^{1,2}¹*Zentrum für Optische Quantentechnologien, Universität Hamburg, Luruper Chaussee 149, 22761 Hamburg, Germany*²*The Hamburg Centre for Ultrafast Imaging, Universität Hamburg, Luruper Chaussee 149, 22761 Hamburg, Germany*

(Received 21 March 2018; revised manuscript received 8 May 2018; published 31 May 2018)

We unravel the correlated nonequilibrium dynamics of a mass balanced Bose-Fermi mixture in a one-dimensional optical lattice upon quenching an imposed harmonic trap from strong to weak confinement. Regarding the system's ground state, the competition between the inter- and intraspecies interaction strength gives rise to the immiscible and miscible phases characterized by negligible and complete overlap of the constituting atomic clouds, respectively. The resulting dynamical response depends strongly on the initial phase and consists of an expansion of each cloud and an interwell tunneling dynamics. For varying quench amplitude and referring to a fixed phase, a multitude of response regimes is unveiled, being richer within the immiscible phase, which are described by distinct expansion strengths and tunneling channels.

DOI: [10.1103/PhysRevA.97.053626](https://doi.org/10.1103/PhysRevA.97.053626)**I. INTRODUCTION**

Recent experimental advances in ultracold atomic gases offer the opportunity to realize mixtures of bosons and fermions with the aid of sympathetic cooling [1–5]. These mixtures serve as prototypical examples in which the interacting particles obey different statistics [6,7]. For instance and in sharp contrast to bosons, *s*-wave interactions among spin-polarized fermions are prevented due to the Pauli exclusion principle. The complex interplay of Bose-Bose and Bose-Fermi interactions led to numerous theoretical studies of Bose-Fermi (BF) mixtures such as their phase separation process [8,9], stability conditions [10,11], and collective excitations [12,13].

Moreover, BF mixtures confined in optical lattices unveiled a variety of intriguing quantum phases including, among others, exotic Mott-insulator and superfluid phases [14–17], charge-density waves [17,18], supersolid phases [19,20], and polaronlike quasiparticles [18,21]. A commonly used model to describe the properties of such mixtures, e.g., pairing of fermions with bosons or bosonic holes for attractive and repulsive interspecies interactions, respectively [17,22], is the lowest-band BF Hubbard model [23,24]. A celebrated problem that has been intensively studied concerns the effect of the fermions on the mobility of the bosons. Heavier or lighter fermions mediate long-range interactions between the bosons or act as impurities, inducing a shift of the bosonic superfluid-to-Mott transition [25] caused by the contribution of energetically higher than the lowest-band states. This behavior indicated that more involved approximations than the lowest-band BF Hubbard model need to be considered for an adequate explanation of the superfluid-to-Mott transition [26–28].

Despite the importance of the system's static properties, a particularly interesting but largely unexplored research direction in BF mixtures is to investigate their nonequilibrium quantum dynamics by employing a quantum quench [29,30]. Referring to lattice systems, the simplest scenario to explore is the expansion dynamics of the trapped atomic cloud after quenching the frequency of an imposed harmonic oscillator.

Such studies have already been performed mainly for bosonic ensembles unraveling the dependence of the expansion on the interatomic interactions. For instance, it has been shown that the expansion is enhanced for noninteracting or hard-core bosons [31], while for low filling systems, a global breathing mode is induced [32]. Detailing the dynamics on the microscopic level, a resonant dynamical response has been revealed which is related to avoided crossings in the many-body (MB) eigenspectrum [33]. A peculiar phenomenon, called quasicondensation, arises during the expansion of hard-core bosons enforcing a temperature-dependent long-range order in the system [34–38]. Moreover, the expansion velocities of fermionic and bosonic Mott insulators have been found to be the same irrespectively of the interaction strength [39]. However, a systematic study of the expansion dynamics in particle-imbalanced BF mixtures still lacks. In such a scenario, it would be particularly interesting to examine how interspecies correlations, which reflect the initial phase of the system [40–44], modify the expansion dynamics of the mixture. Another intriguing prospect is to investigate, when residing within a specific phase, whether different response regimes can be triggered upon varying the quench amplitude. To address these intriguing questions, we employ the multilayer multiconfigurational time-dependent Hartree method for atomic mixtures (ML-MCTDHX) [45,46], which is a multiorbital treatment that enables us to capture the important inter- and intraspecies correlation effects.

We investigate a BF mixture confined in a one-dimensional optical lattice with an imposed harmonic trap. Operating within the weak-interaction regime, we show that the interplay of the intra- and interspecies interactions leads to different ground-state phases regarding the degree of miscibility in the mixture, namely, to the miscible and the immiscible phases where the bosonic and the fermionic single-particle densities are completely and zero overlapping, respectively. To trigger the dynamics, the BF mixture is initialized within a certain phase and a quench from strong to weak confinement is performed. Each individual phase exhibits a characteristic

response composed of an overall expansion of both atomic clouds and an interwell tunneling dynamics. Referring to the immiscible phase, a resonantlike response of both components occurs at moderate quench amplitudes, which is reminiscent of the single-component case [33]. A variety of distinct response regimes is realized for decreasing confinement strength. Bosons perform a breathing dynamics or solely expand, while fermions tunnel between the outer wells, located at the edges of the bosonic cloud, or exhibit a delocalized behavior over the entire lattice. To gain further insight into the MB expansion dynamics, the contribution of the higher-lying orbitals is analyzed and their crucial role in the course of the evolution is showcased. Inspecting the dynamics of each species on both the one- and the two-body level, we observe that during the evolution, the predominantly occupied wells are one-body incoherent and mainly two-body anticorrelated with each other; while within each well, a correlated behavior, for bosons, and an anticorrelated one, for fermions, occurs. Furthermore, it is shown that the immiscible phase gives rise to a richer response when compared to the miscible phase for varying quench amplitude. Finally, it is found that for increasing height of the potential barrier, the expansion dynamics of the BF mixture is suppressed, while for mass imbalanced mixtures, the heavier component is essentially unperturbed.

This work is organized as follows. In Sec. II, we introduce our setup, the employed MB wave-function ansatz, and the basic observables of interest. Section III presents the ground-state properties of our system. In Secs. IV and V, we focus on the quench-induced expansion dynamics of the BF mixture within the immiscible and the miscible correlated phases, respectively. We summarize our findings and present an outlook in Sec. VI. Appendix A presents the correlation dynamics during the expansion of the BF mixture within the immiscible phase, and in Appendix B we show the impact of several system parameters on the expansion dynamics. Appendix C contains a discussion regarding the convergence of our numerical ML-MCTDHX simulations.

II. THEORETICAL FRAMEWORK

A. Setup and many-body ansatz

We consider a BF mixture consisting of N_F spin-polarized fermions and N_B bosons each of mass M . This system can be to a good approximation realized by considering, e.g., a mixture of isotopes of ^7Li and ^6Li [47] or ^{171}Yb and ^{172}Yb [48,49]. The mixture is confined in a one-dimensional optical lattice with an imposed harmonic confinement of frequency ω , and the MB Hamiltonian reads

$$H = \sum_{i=1}^{N_F+N_B} \left[-\frac{\hbar^2}{2M} \frac{\partial^2}{\partial x_i^2} + \frac{M}{2} \omega^2 x_i^2 + V_0 \sin^2(kx_i) \right] + g_{FB} \sum_{i=1}^{N_F} \sum_{j=1}^{N_B} \delta(x_i^F - x_j^B) + g_{BB} \sum_{1 \geq i \geq j \geq N_B} \delta(x_i^B - x_j^B). \quad (1)$$

The lattice potential is characterized by its depth V_0 and periodicity $l = \pi$ (with $k = \pi/l$). Within the ultracold s -wave scattering limit, the inter- and intraspecies interac-

tions are adequately modeled by contact interactions scaling with the effective one-dimensional coupling strength $g_{\sigma\sigma'}$, where $\sigma, \sigma' = B, F$ for bosons or fermions, respectively. The effective one-dimensional coupling strength [50] $g_{\sigma\sigma'}^{1D} = \frac{2\hbar^2 a_{\sigma\sigma'}^s}{\mu a_{\perp}^3} [1 - |\zeta(1/2)| a_{\sigma\sigma'}^s / \sqrt{2} a_{\perp}]^{-1}$, where ζ denotes the Riemann zeta function and μ is the corresponding reduced mass. The transversal length scale is $a_{\perp} = \sqrt{\hbar/\mu\omega_{\perp}}$, and ω_{\perp} is the frequency of the transversal confinement, while $a_{\sigma\sigma'}^s$ denotes the free-space s -wave scattering length within or between the two species. $g_{\sigma\sigma'}$ is tunable by $a_{\sigma\sigma'}^s$ via Feshbach resonances [51,52] or by means of ω_{\perp} [50,53]. S -wave scattering is prohibited for spinless fermions due to their antisymmetry [6,7] and thus they are considered to be noninteracting among each other. The MB Hamiltonian is rescaled in units of the recoil energy $E_R = \frac{\hbar^2 k^2}{2M}$. Then, the corresponding length, time, frequency, and interaction strength scales are given in units of k^{-1} , $\omega_R^{-1} = \hbar E_R^{-1}$, ω_R , and $2E_R k^{-1}$, respectively. To limit the spatial extension of our system, we impose hard-wall boundary conditions at $x_{\pm} = \pm \frac{19}{2} \pi$. For convenience, we also shall set $\hbar = M = k = 1$ and therefore all quantities below are given in dimensionless units.

Our system is initially prepared in the ground state of the MB Hamiltonian where the harmonic trap frequency is $\omega = 0.1$ and the lattice depth $V_0 = 3$. Due to the imposed harmonic trap, initially the mixture experiences a localization tendency towards the central wells which is stronger for decreasing g_{BB} . To induce the dynamics, we instantaneously change at $t = 0$ the trapping frequency ω to lower values and let the system evolve in time. Note that reducing ω predominantly favors the tunneling of both components to the outer wells as the corresponding energy offset between distinct wells becomes smaller. In this way, after the quench, the mixture is prone to expand.

To solve the underlying MB Schrödinger equation, we employ ML-MCTDHX [45,46]. The latter, in contrast to the mean-field (MF) approximation, relies on expanding the MB wave function in a time-dependent and variationally optimized basis, enabling us to take into account inter- and intraspecies correlations. To include interspecies correlations, we first introduce M distinct species functions for each component, namely, $\Psi_k^{\sigma}(\vec{x}^{\sigma}; t)$, where $\vec{x}^{\sigma} = (x_1^{\sigma}, \dots, x_{N_{\sigma}}^{\sigma})$ denote the spatial ($\sigma = F, B$)-species coordinates and N_{σ} is the number of σ -species atoms. Then, the MB wave function Ψ_{MB} can be expressed according to the truncated Schmidt decomposition [54] of rank M ,

$$\Psi_{MB}(\vec{x}^F, \vec{x}^B; t) = \sum_{k=1}^M \sqrt{\lambda_k(t)} \Psi_k^F(\vec{x}^F; t) \Psi_k^B(\vec{x}^B; t), \quad (2)$$

where the Schmidt coefficients $\lambda_k(t)$ are referred to as the natural species populations of the k th species function. The system is entangled [55] or interspecies correlated when at least two distinct $\lambda_k(t)$ are nonzero and therefore the MB state cannot be expressed as a direct product of two states. In this entangled case, a particular fermionic configuration $\Psi_k^F(\vec{x}^F; t)$ is accompanied by a particular bosonic configuration $\Psi_k^B(\vec{x}^B; t)$, and vice versa. As a consequence, measuring one of the species states, e.g., $\Psi_{k'}^F$, collapses the wave function of the other species to $\Psi_{k'}^B$, thus manifesting the bipartite entanglement [56,57].

Moreover, in order to account for interparticle correlations, each of the species functions $\Psi_k^\sigma(\vec{x}^\sigma; t)$ is expanded using the determinants or permanents of m^σ distinct time-dependent fermionic or bosonic single-particle functions (SPFs), $\varphi_1, \dots, \varphi_{m^\sigma}$, respectively,

$$\Psi_k^\sigma(\vec{x}^\sigma; t) = \sum_{\substack{n_1, \dots, n_{m^\sigma} \\ \sum n_i = N}} c_{k, (n_1, \dots, n_{m^\sigma})}(t) \sum_{i=1}^{N_{\sigma!}} \text{sign}(\mathcal{P}_i)^\zeta \mathcal{P}_i \times \left[\prod_{j=1}^{n_1} \varphi_1(x_j; t) \cdots \prod_{j=1}^{n_{m^\sigma}} \varphi_{m^\sigma}(x_j; t) \right]. \quad (3)$$

Here, $\zeta = 0, 1$ for the case of bosons and fermions, respectively, and $\text{sign}(\mathcal{P}_i)$ denotes the sign of the corresponding permutation. \mathcal{P} is the permutation operator exchanging the particle configuration within the SPFs. $c_{k, (n_1, \dots, n_{m^\sigma})}(t)$ are the time-dependent expansion coefficients of a particular determinant for fermions or permanent for bosons, and $n_i(t)$ denotes the occupation number of the SPF $\varphi_i(\vec{x}; t)$. Note that the bosonic subsystem is termed intraspecies correlated if more than one eigenvalue is substantially occupied, otherwise it is said to be fully coherent [58,59]. In the same manner, the fermionic species possesses beyond Hartree-Fock intraspecies correlations if more than N_F eigenvalues occur. Employing the Dirac-Frenkel variational principle [60,61] for the MB ansatz [see Eqs. (2) and (3)] yields the ML-MCTDHX equations of motion [45]. These consist of M^2 linear differential equations of motion for the coefficients $\lambda_i(t)$, which are coupled to a set of $\binom{M(N_B+m^B-1)}{m^B-1} + \binom{m^F}{N_F}$ nonlinear integrodifferential equations for the species functions and $m^F + m^B$ integrodifferential equations for the SPFs. Finally, it is also worth mentioning that ML-MCTDHX can operate in different approximation orders, e.g., it reduces to the MF Gross-Pitaevskii equation in the case of $M = m^F = m^B = 1$.

B. Observables of interest

Let us next briefly introduce the main observables that will be used for the interpretation of the expansion dynamics on both the one- and two-body level. To measure the collective expansion and contraction dynamics [31,33] of the σ -species atomic cloud, we rely on the position variance,

$$\Sigma_{x,\sigma}^2(t) = \langle \Psi_{MB}(t) | \hat{x}_\sigma^2 | \Psi_{MB}(t) \rangle - \langle \Psi_{MB}(t) | \hat{x}_\sigma | \Psi_{MB}(t) \rangle^2. \quad (4)$$

Here, $\hat{x}_\sigma = \int_D dx x \sigma \hat{\Psi}_\sigma^\dagger(x) \hat{\Psi}_\sigma(x)$ and $\hat{x}_\sigma^2 = \int_D dx x^2 \hat{\Psi}_\sigma^\dagger(x) \hat{\Psi}_\sigma(x)$ are one-body operators, with $\hat{\Psi}_\sigma(x)$ denoting the σ -species field operator, and D is the spatial extent of the lattice. We remark that the aforementioned position variance, evaluated over the entire lattice, essentially quantifies a global breathing mode composed of interwell tunneling and intrawell breathing modes, offering in this way a measure for the system's dynamical response.

To elaborate on the intensity of the resulting dynamical response for the σ species, we define the time-averaged

position variance,

$$\bar{\Sigma}_{x,\sigma}^2 = \frac{1}{T} \int_0^T [\Sigma_{x,\sigma}^2(t) - \Sigma_{x,\sigma}^2(0)], \quad (5)$$

which describes the mean deviation of the system from its initial (ground) state. $\Sigma_{x,\sigma}^2(0)$ refers to the position variance of the σ species for the initial state at $t = 0$, while T is the considered finite evolution time in which $\bar{\Sigma}_{x,\sigma}^2$ has converged to a certain value.

The one-body reduced density matrix of the σ species, $\rho^{(1),\sigma}(x, x'; t) = \langle \Psi_{MB}(t) | \Psi_\sigma^\dagger(x') \Psi_\sigma(x) | \Psi_{MB}(t) \rangle$, provides the probability to find a σ -species particle simultaneously at positions x and x' at a certain time instant t , while $\rho^{(1),\sigma}(x; t) \equiv \rho^{(1),\sigma}(x, x' = x; t)$ is the σ -species single-particle density [62]. The eigenfunctions of the σ -species one-body density matrix, $\rho^{(1),\sigma}(x, x')$, are the so-called σ -species natural orbitals, $\phi_i^\sigma(x; t)$, which are normalized to their corresponding eigenvalues,

$$n_i^\sigma(t) = \int dx |\phi_i^\sigma(x; t)|^2. \quad (6)$$

$n_i^\sigma(t)$ are known as the natural populations of the σ species [58,59]. Finally, the diagonal two-body reduced density matrix $\rho^{(2),\sigma\sigma'}(x, x'; t) = \langle \Psi_{MB}(t) | \Psi_{\sigma'}^\dagger(x') \Psi_\sigma^\dagger(x) \Psi_\sigma(x) \Psi_{\sigma'}(x') | \Psi_{MB}(t) \rangle$ refers to the probability of finding two atoms located at positions x and x' at time t .

III. INITIAL-STATE CHARACTERIZATION

Depending on the ratio between the interspecies (g_{FB}) and intraspecies (g_{BB}) interaction strength, the BF mixture forms two phases characterized by the miscibility of the bosonic and fermionic clouds [8,63–65]. Here, we typically restrict ourselves to weak inter- and intraspecies interactions and consider a BF mixture consisting of $N_B = 20$ bosons and $N_F = 2$ spin-polarized fermions confined in a 19-well optical lattice. Tuning $\frac{g_{FB}}{g_{BB}}$, we identify different ground-state configurations, namely, the miscible and the immiscible correlated phases (see below). We remark that by operating within the aforementioned weak-interaction regime and besides realizing the above phases, we showcase that the inclusion of correlations is of substantial importance in order to accurately describe the expansion dynamics of the BF mixture. Effects of stronger interaction strengths, such as the Tonks-Girardeau regime, might be of great importance but lie beyond our scope.

For $g_{BB} > g_{FB}$ and for $g_{BB} = 1.0$ and $g_{FB} = 0.05$, we realize the miscible phase where the single-particle densities of bosons and fermions are overlapping; see Fig. 1(a). In particular, the bosonic and fermionic single-particle densities in the three central wells overlap completely, while the outer wells are mainly populated by bosons. The broadening of the bosonic one-body density distribution is anticipated due to the strong g_{BB} . The aforementioned miscibility character of $\rho^{(1),\sigma}(x)$, favoring certain spatial regions, leads to the characterization of the phase as miscible. On the two-body level, the corresponding $\rho^{(2),BB}(x, x')$ [see inset (a₁) of Fig. 1] demonstrates that two bosons are likely to populate most of the available wells, while two fermions [see $\rho^{(2),FF}(x, x')$ in the inset (a₂) of Fig. 1] cannot reside in the same well but

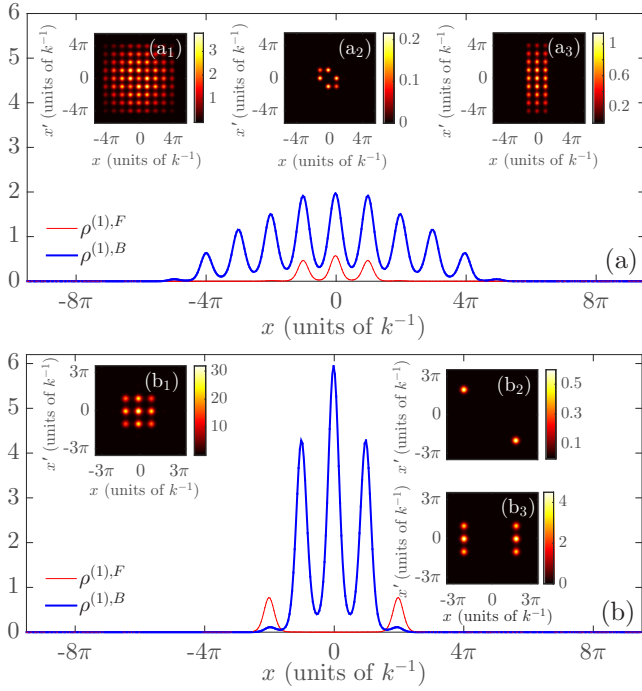


FIG. 1. Fermionic (red line) and bosonic (blue line) ground-state one-body densities for (a) $g_{BB} = 1.0$, $g_{FB} = 0.05$ (miscible phase) and (b) $g_{BB} = 0.05$, $g_{FB} = 0.2$ (immiscible phase). Insets (a₁) and (a₂) show the two-body reduced density matrix of the bosons and fermions, respectively, for the miscible phase. Insets (b₁) and (b₂) show the same quantities as (a₁) and (a₂), but for the immiscible phase. Insets (a₃) and (b₃) depict the interspecies two-particle reduced density matrix in the miscible and immiscible regime, respectively.

are rather delocalized over the three central wells. Finally, the elongated shape of $\rho^{(2),FB}(x, x')$ [see inset (a₃) of Fig. 1] further indicates the miscibility of the two components within the three central wells and their vanishing overlap in the outer lattice wells.

Turning to the regime of $g_{FB} > g_{BB}$, namely, for $g_{BB} = 0.05$ and $g_{FB} = 0.2$, we enter the immiscible phase characterized by almost perfectly separated fermionic and bosonic single-particle densities; see Fig. 1(b). As shown, $\rho^{(1),B}(x) \neq 0$ for the three central wells (i.e., $x \in [-3\pi/2, 3\pi/2]$) and therefore one boson is delocalized in this region. However, $\rho^{(1),F}(x) \neq 0$ only for the nearest neighbors of the three central wells, namely, $x \in [3\pi/2, 5\pi/2]$ and $x \in [-5\pi/2, -3\pi/2]$. The latter indicates that each fermion is localized in one of these neighboring wells. The above observations are also supported by the intraspecies two-body reduced density matrices [44]. Indeed, $\rho^{(2),BB}(x, x') \neq 0$ [see inset (b₁) of Fig. 1] for the three central wells, implying that it is likely for two bosons to reside within this spatial region. However, $\rho^{(2),FF}(x, x') \neq 0$ [see inset (b₂) of Fig. 1] only for the antidiagonal elements that refer to the nearest neighbors ($-5\pi/2 < x < -3\pi/2$ and $3\pi/2 < x < 5\pi/2$) of the three central wells. Therefore, each fermion populates only one of these wells. The diagonals of $\rho^{(2),FB}(x, x)$ depicted in the inset (b₃) of Fig. 1 are almost zero, reflecting in this way the phase-separated character of the state.

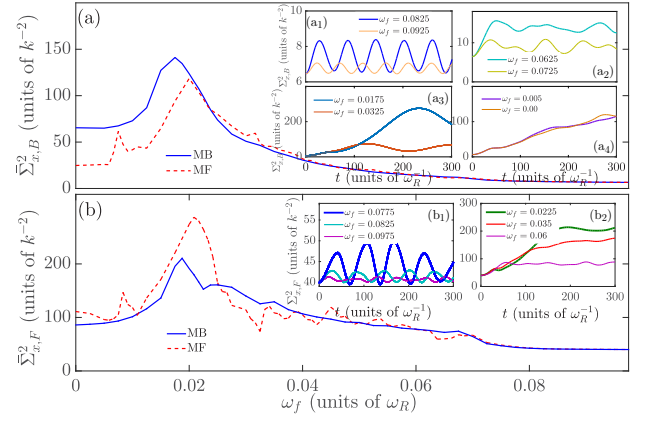


FIG. 2. (a) Bosonic and (b) fermionic mean variance $\bar{\Sigma}_{x,\sigma}^2$ in the immiscible phase for varying postquench harmonic trap frequency ω_f . (a₁)–(a₄) Position variance $\Sigma_{x,B}(t)$ as a function of time within the characteristic four different bosonic response regimes. (b₁), (b₂) $\Sigma_{x,F}(t)$ within the characteristic two distinct fermionic response regimes. Initially the system is in the ground state of $N_B = 20$ bosons and $N_F = 2$ fermions with $g_{BB} = 0.05$, $g_{FB} = 0.2$, which are confined in a 19-well lattice potential with an imposed harmonic trap of frequency $\omega = 0.1$.

IV. QUENCH DYNAMICS IN THE IMMISCIBLE PHASE

Focusing on the immiscible phase, we study the expansion dynamics induced by a quench of the harmonic-oscillator frequency to smaller values. To gain an overview of the system's mean dynamical response, we resort to the σ -species time-averaged position variance $\bar{\Sigma}_{x,\sigma}^2$ [see also Eq. (5)], which essentially measures the expansion strength of the atomic cloud. Figures 2(a) and 2(b) present $\bar{\Sigma}_{x,B}^2$ and $\bar{\Sigma}_{x,F}^2$, respectively, with varying final trap frequency ω_f . It is observed that the expansion strength strongly depends on ω_f and exhibits a maximum value in the vicinity of $\omega_f = 0.0175$. Therefore, both the bosonic and the fermionic cloud do not show their strongest expansion when completely releasing the harmonic trap, i.e., at $\omega_f = 0$, but rather at moderate quench amplitudes. For either $\omega_f < 0.0175$ or $\omega_f > 0.0175$, an essentially monotonic decrease of $\bar{\Sigma}_{x,\sigma}^2$ occurs (see also below for a more detailed description of the dynamics). Alterations of the overall dynamical response can be achieved by tuning the height of the potential barrier or the mass ratio of the two species (see Appendix B). The above-mentioned resonantlike behavior is reminiscent of the expansion dynamics of single-component bosons trapped in a composite lattice and subjected to a quench of the imposed harmonic trap from strong to weak confinement [33]. In this latter case, a resonant response of the system for intermediate quench amplitudes occurs and it is related to the avoided crossings in the MB eigenspectrum with varying ω_f . The occurrence of the resonantlike response of the BF mixture suggests that also in the present case, such avoided crossings could be responsible for the appearance of the maximum at $\omega_f = 0.0175$. However, due to the large particle numbers considered herein, a direct calculation of the corresponding MB eigenspectrum is not possible.

To elaborate in more detail on the characteristics of the dynamical response, we invoke the position variance $\Sigma_{x,\sigma}^2(t)$

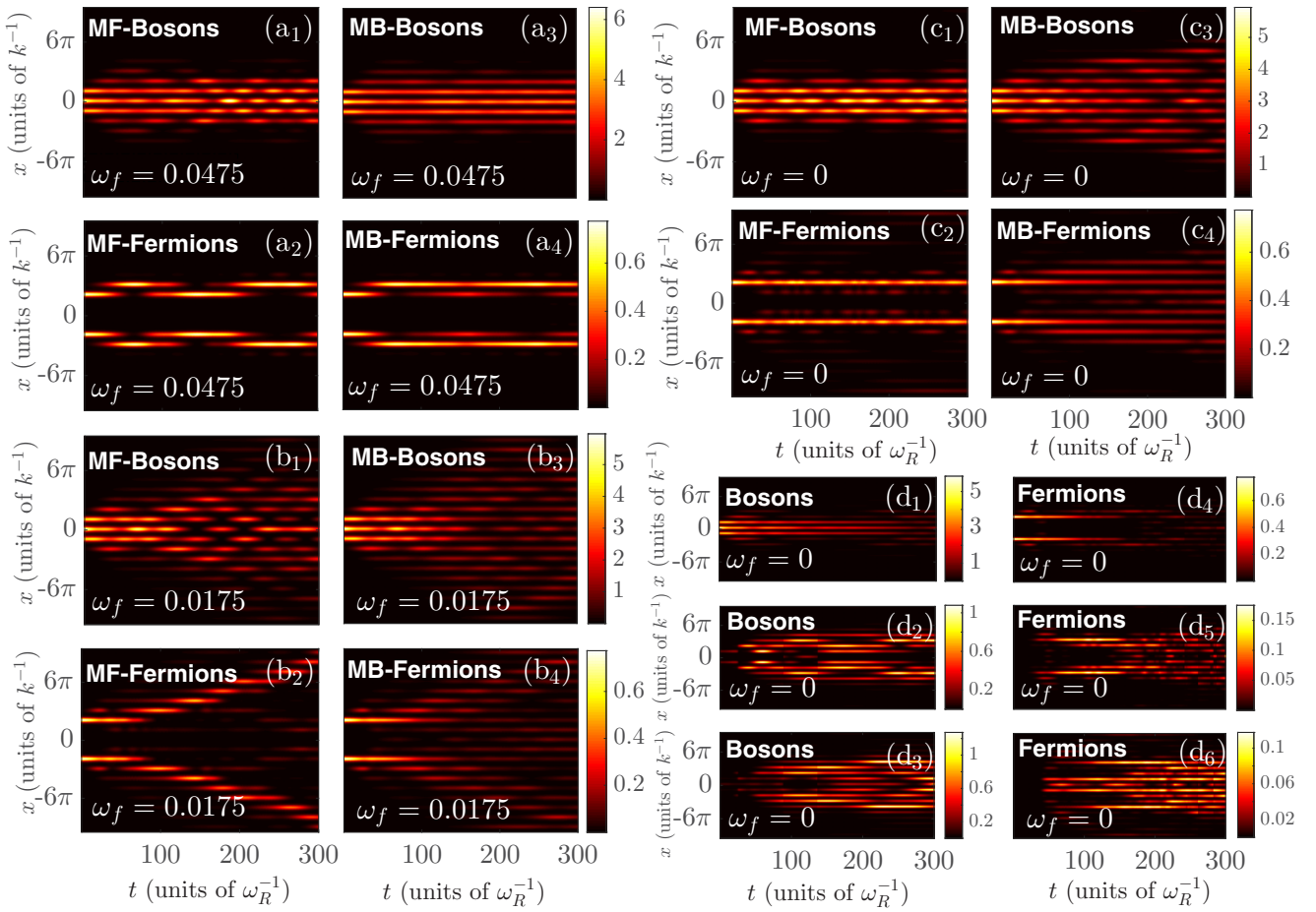


FIG. 3. The one-body density evolution within the MF approach is presented in (a₁) bosons and (a₂) fermions after a quench to $\omega_f = 0.0475$. (b₁), (b₂) and (d₁), (d₂) present the same quantities as above, but for a quench to $\omega_f = 0.0175$ and $\omega_f = 0.0$, respectively. One-body density evolution within the MB approach for (a₃) bosons and (a₄) fermions after a quench to $\omega_f = 0.0475$. (b₃), (b₄) and (c₃), (c₄) present the same quantities as (a₃) and (a₄), but for a quench to $\omega_f = 0.0175$ and $\omega_f = 0.0$, respectively. (d₁)–(d₃) The one-body density, in the course of the dynamics, of the first, second, resummed third, and fourth bosonic orbitals of (c₃). (d₄)–(d₆) The resummed one-body density evolution of the first and second, third and fourth, and fifth to eighth fermionic orbitals of (c₄). The system is initialized in the ground state of $N_B = 20$ bosons and $N_F = 2$ fermions with $g_{BB} = 0.05$, $g_{FB} = 0.2$ and is confined in a 19-well lattice potential with an imposed harmonic trap of frequency $\omega = 0.1$.

[see Eq. (4)] and the single-particle density $\rho^{(1),\sigma}(x,t)$ of the σ species during the evolution [31]. Recall that by quenching the harmonic-oscillator frequency to lower values, we mainly trigger the tunneling dynamics towards the outer lattice wells as their corresponding energy offset is reduced. Focusing on the bosonic species, we can identify four distinct response regimes, each one exhibiting a characteristic expansion; see Figs. 2(a₁)–2(a₄). Within the first regime located at $0.0775 \leq \omega_f \leq 0.1$, the bosonic cloud undergoes a regular periodic expansion and contraction dynamics [see the oscillatory behavior of $\Sigma_{x,B}^2(t)$ in Fig. 2(a₁)], which is identified as a global breathing mode [32,33]. The oscillation amplitude (frequency) of $\Sigma_{x,B}^2(t)$ increases (decreases) for smaller ω_f 's lying within this region. In the second response regime ($0.0525 \leq \omega_f < 0.0755$), the cloud initially expands within a short evolution time ($t < 50$) and then performs irregular oscillations possessing multiple frequencies [Figs. 2(a₂) and 3(a₃)]. The third response regime ($0.015 \leq \omega_f \leq 0.05$) is characterized by an initial expansion of the bosons until a maximum value is reached. Then the

ensemble undergoes a contraction and followup expansion [Figs. 2(a₃) and 3(b₃)]. For $\omega_f < 0.015$, defining the fourth regime, the atoms strictly expand in an approximately linear manner [Figs. 2(a₄) and 3(c₄)], reaching a maximum value at very long evolution times $t > 600$ (not shown here). Their expansion velocity and amplitude are significantly reduced when compared to the third response regime, resulting in this way in the smaller expansion strength shown in Fig. 2(a).

Turning to the fermionic subsystem, we can realize two different response regimes; see Figs. 2(b₁) and 2(b₂). The first occurs within the same range of ω_f 's as the corresponding bosonic one and $\Sigma_{x,F}^2(t)$ performs regular oscillations [Fig. 2(b₁)]. The second one appears for $\omega_f < 0.0775$, thus covering the range of quench amplitudes that leads to the second, third, and fourth bosonic response regimes. Here, $\Sigma_{x,F}^2(t)$ increases monotonically for a short evolution time, reaching a maximum around which it oscillates with a small amplitude. To further visualize the dynamics of the mixture, we inspect $\rho^{(1),F}(x,t)$. It is observed that for $\omega_f > 0.03$, the

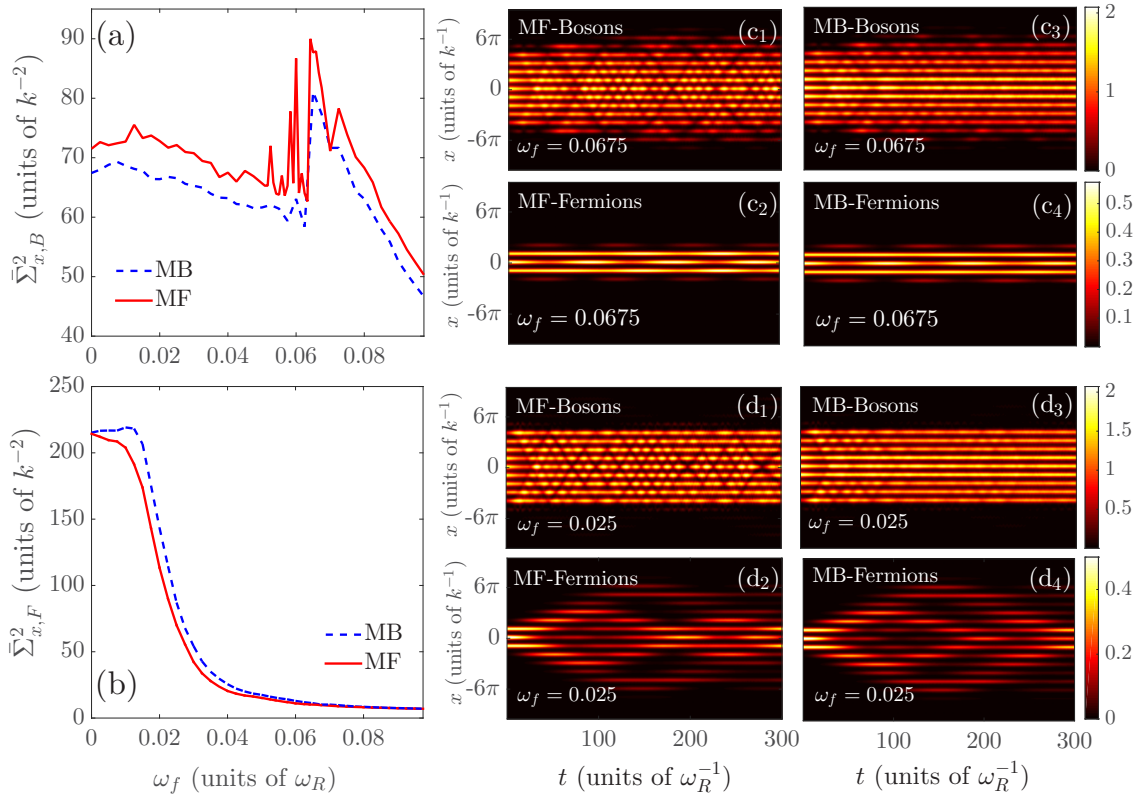


FIG. 4. (a) Bosonic and (b) fermionic mean variance $\bar{\Sigma}_{x,\sigma}^2$ of a BF mixture in the miscible phase for varying postquench harmonic trap frequency ω_f . Evolution of the one-body density within the MF approach for the constituting (c₁) bosons and (c₂) fermions following a quench to $\omega_f = 0.0675$. (d₁),(d₂) The same as above, but for $\omega_f = 0.025$. One-body density evolution within the MB approach for the (c₃) bosons and (c₄) fermions following a quench to $\omega_f = 0.0675$. (d₃),(d₄) The same as above, but for $\omega_f = 0.025$. The system is initialized in the ground state of $N_B = 20$ bosons and $N_F = 2$ fermions with $g_{BB} = 1$, $g_{FB} = 0.05$, which is confined in a 19-well lattice potential with an imposed harmonic trap of frequency $\omega = 0.1$.

bosons mainly bunch within the three central wells, forming a material barrier [66,67] that prevents the fermions from tunneling into the inner central wells; see, e.g., Fig. 3(a₄). Then the fermions perform tunneling oscillations between the two outer nearest-neighboring wells located at $-5\pi/2 < x < -\pi/2$ and $\pi/2 < x < 9\pi/2$. On the contrary, for $\omega_f < 0.03$, the bosons undergo a strong expansion over the whole extent of the lattice, thus allowing the fermions to diffuse via tunneling [Figs. 3(b₄) and 3(c₄)].

Identification of the many-body characteristics

To infer about the MB nature of the above-mentioned response regimes, we perform a comparison with the corresponding quench-induced dynamics obtained within the MF (single-orbital) approximation. In the latter case, $\bar{\Sigma}_{x,B}^2$ for varying ω_f [see Fig. 2(a)] shows a qualitatively similar behavior to the MB case. However, the MF result predicts a displaced response maximum to larger values of ω_f and the existence of a secondary maximum at $\omega_f = 0.0075$, which is suppressed in the presence of correlations. Comparing $\bar{\Sigma}_{x,B}^2$ in the MB and the single-orbital approximation, we can deduce that for large quench amplitudes ($\omega_f < 0.02$), the expansion strength is strongly suppressed in the latter case. Moreover, the third and fourth bosonic response regimes identified within

the MB approach are greatly altered in the MF realm. For instance, the slow monotonic expansion of the cloud in the fourth regime [see, e.g., $\rho^{(1),B}(x,t)$ in Fig. 3(c₃)] is substituted by regular tunneling oscillations of the bosons in the five central wells [Fig. 3(c₁)]. Moreover, MF fails to adequately capture the tunneling dynamics. This latter observation is clearly imprinted in the one-body density evolution presented, e.g., in Figs. 3(b₁) and 3(b₃). Additionally here, significant deviations that are not resolvable by inspecting $\bar{\Sigma}_{x,B}^2$ between the two approaches are also present; compare, for instance, Figs. 3(a₁) and 3(a₃). A careful inspection of $\rho^{(1),B}(x,t)$ reveals that in the MB scenario for $\omega_f < 0.0325$, a diffusive tendency of the bosons over the entire lattice takes place for long evolution times; see Figs. 3(b₃) and 3(c₃).

Turning to the fermionic component, and in contrast to the bosonic case, the expansion strength $\bar{\Sigma}_{x,F}^2$ is enhanced in the MF approximation [Fig. 2(b)] when compared to the MB scenario for large quench amplitudes, namely, $\omega_f < 0.025$. This increase of $\bar{\Sigma}_{x,F}^2$ can be attributed to the suppression of the tunneling processes towards the inner central wells and a dominant outward spreading; see, e.g., Fig. 3(b₃). For $\omega_f < 0.025$, the MB approach predicts a strong delocalization of the two fermions over the entire lattice for large evolution times ($t > 250$) with almost all tunneling processes being damped [see, e.g., Figs. 3(b₄) and 3(c₄)]. This result is in

direct contrast to what is observed in the MF case. Here, the fermions show an expansion that is characterized by two almost localized density branches that mainly tunnel to the outer wells [Fig. 3(b₂)] while being almost localized close to the central wells at all times for $\omega_f = 0$ [Fig. 3(c₂)]. A further discussion regarding the correlation dynamics of the BF mixture on both the one- and two-body level is provided in Appendix A.

To gain a deeper understanding of the underlying microscopic properties of the MB dynamics, we next inspect the single-particle density evolution of the participating orbitals $|\phi_i^\sigma(x,t)|^2$ after quenching to $\omega_f = 0$. Figures 3(d₁)–3(d₃) present the corresponding single-particle densities of all four bosonic orbitals. The first and predominantly contributing orbital [Fig. 3(d₁)] shows almost no expansion and a suppressed tunneling dynamics within the five middle wells. The latter behavior resembles, to a certain extent, the single-particle density evolution within the MF approach; see also Fig. 3(c₁). On the other hand, the second [Fig. 3(d₂)] as well as the resummation of the third and fourth [Fig. 3(d₃)] orbital densities indicate an expansion of the bosonic cloud over the entire lattice. Therefore, these contributions are responsible for the above-described broader one-body density distribution of the bosons along the lattice in the MB (compared to MF) case.

To also analyze the fermionic motion, we next examine the single-particle densities of the eight fermionic orbitals; see Figs. 3(d₄)–3(d₆). Recall here that due to the Pauli exclusion principle, each orbital can be occupied by only one fermion and therefore the corresponding MF approximation requires the utilization of two orbitals. The resummed density of the first two fermionic orbitals [Fig. 3(d₄)] for $t < 120$ presents the evolution of two almost localized single-particle density branches located at $x \rightarrow [3\pi/2, 5\pi/2]$ and $x \rightarrow [-5\pi/2, -3\pi/2]$, respectively. Notice here the resemblance to the corresponding MF density [Fig. 3(c₂)] for $t < 120$. However, for longer evolution times, these density branches move towards the inner central lattice wells. In contrast to the above, the resummed single-particle densities of every two consecutively occupied orbitals [Figs. 3(d₅) and 3(d₆)] exhibit a delocalization along the system. Therefore, the diffusive behavior of the fermions during the MB expansion is mainly caused by the presence of these higher-lying orbitals.

V. QUENCH DYNAMICS IN THE MISCIBLE PHASE

To identify the impact of the initial phase on the expansion dynamics, we next examine the response of a BF mixture, which initially resides within the miscible phase (with $g_{BB} = 1$ and $g_{FB} = 0.05$; see also Sec. III), following a quench of the imposed harmonic trap from strong to weak confinement ω_f . The corresponding expansion strength of the σ -species cloud measured via $\bar{\Sigma}_{x,\sigma}^2$ for varying ω_f is presented in Figs. 4(a) and 4(b). $\bar{\Sigma}_{x,B}^2$ increases within the interval $0.065 < \omega_f < 0.1$ for decreasing ω_f and then exhibits a decreasing behavior up to $\omega_f = 0.0625$, below which it shows a slightly increasing tendency up to $\omega_f = 0$. To visualize the emergent bosonic response, we resort to the one-body density evolution $\rho^{(1),B}(x,t)$. The dynamical expansion of the bosonic cloud is mainly suppressed for almost every ω_f [e.g., see, Fig. 4(d₃)], except for $0.065 < \omega_f < 0.072$, a region in which it becomes

non-negligible [Fig. 4(c₂)]. Instead of an expansion, the bosons tunnel between the initially (at $t = 0$) occupied wells and reach an almost steady-state configuration for long evolution times [Figs. 4(c₂) and 4(d₃)]. Despite the aforementioned triggered tunneling modes, the bosonic density reveals a maximal occupation of the three central wells during the dynamics [Figs. 4(c₂) and 4(d₃)]. To identify the effect of correlations on the bosonic expansion, we compare these findings to the MF approximation. The mean expansion strength $\bar{\Sigma}_{x,B}^2$ is similar to what MB theory predicts, but overall shifted to larger values [Fig. 4(a)]. This shift is caused by the absence of the density bunching [e.g., see Figs. 4(c₁) and 4(d₁)] within the three middle wells that occurs in the MB scenario, leading in turn to the smaller $\bar{\Sigma}_{x,B}^2$ observed. Notice also here the highly fluctuating behavior of $\bar{\Sigma}_{x,B}^2$ around $\omega_f = 0.06$, which suggests the presence of several response resonances that are absent in the MB case. Furthermore, in the MF dynamics, an enhanced interwell tunneling is observed when compared to the MB case that remains robust during the evolution [see Figs. 4(c₁), 4(c₂) and 4(d₁), 4(d₃)].

In contrast to bosons, a dramatic (slight) increase of the fermionic mean variance $\bar{\Sigma}_{x,F}^2$ occurs for $\omega_f < 0.04$ ($0.04 < \omega_f < 0.1$) [Fig. 4(b)]. This latter behavior of $\bar{\Sigma}_{x,F}^2$ essentially designates the fermionic expansion strength for distinct ω_f 's, which can be better traced in $\rho^{(1),F}(x,t)$; see Figs. 4(c₄) and 4(d₄). Indeed, for small quench amplitudes, i.e., $0.04 < \omega_f < 0.1$, the fermions expand only slightly [Fig. 4(c₄)]. However, for $\omega_f > 0.04$, they strongly expand, reaching the edges of the surrounding bosonic cloud [Fig. 4(d₃)] where they are partly transmitted and partly reflected moving back towards the central wells [Fig. 4(d₄)]. The same overall phenomenology also holds for the MF case as is evident by inspecting both $\bar{\Sigma}_{x,F}^2$ [Fig. 4(b)] and $\rho^{(1),F}(x,t)$ [compare Figs. 4(c₂), 4(c₄) and 4(d₂), 4(d₄)]. This similarity can be attributed to the weak interspecies interactions, $g_{FB} = 0.05$, which in turn result in reduced interspecies correlations within this miscible regime of interactions.

VI. CONCLUSIONS

We have investigated the ground-state properties and, in particular, the many-body expansion dynamics of a weakly interacting BF mixture confined in a one-dimensional optical lattice with a superimposed harmonic trap. Tuning the ratio between the inter- and intraspecies interaction strengths, we have realized distinct ground-state configurations, namely, the miscible and immiscible phases. These phases are mainly characterized by a complete or strongly suppressed overlap of the bosonic and fermionic single-particle density distributions, respectively.

To induce the dynamics, we perform a quench from strong to weak confinement and examine the resulting dynamical response within each of the above-mentioned phases for varying final harmonic trap frequencies. It is observed that each phase exhibits a characteristic response composed of an overall expansion of both atomic clouds and an interwell tunneling dynamics, which can be further manipulated by adjusting the quench amplitude. Focusing on the immiscible phase, a resonantlike response of both components occurs at

moderate quench amplitudes, in contrast to what is expected upon completely switching off the imposed harmonic trap. A careful inspection of the BF mixture expansion dynamics reveals the existence of different bosonic response regimes accompanied by a lesser amount of fermionic ones for decreasing confinement strength. In particular, we find that for varying quench amplitude, the bosons either perform a breathing dynamics or solely expand, while the fermions tunnel between the nearest-neighbor outer wells that are located at the edges of the bosonic cloud or show a delocalized behavior over the entire lattice, respectively. To identify the many-body characteristics of the expansion dynamics, we compare our findings to the mean-field approximation, where all particle correlations are neglected. Here, it is shown that in the absence of correlations, the tunneling dynamics of both components cannot be adequately captured, the bosonic expansion is suppressed, and the diffusive character of the fermions is replaced by an expansion of two almost localized density branches to the outer wells for large quench amplitudes. These deviations are further elucidated by studying the evolution of the distinct orbitals used, where the first one resembles the mean-field approximation and the higher-orbital contributions are responsible for the observed correlated dynamics. Finally, investigating the one- and two-body coherences for each species, we observe that during the evolution, the predominantly occupied wells are one-body incoherent and two-body anticorrelated among each other, while within each well a correlated behavior for bosons and an anticorrelated one for fermions occurs.

Within the miscible phase, the dynamical response of the BF mixture is greatly altered. The bosonic expansion is significantly suppressed when compared to the immiscible phase and the bosons perform interwell tunneling, reaching an almost steady state for long evolution times. The fermions, on the other hand, expand. When reaching the edges of the surrounding bosonic cloud, they are partly transmitted and partly reflected back towards the central wells. Neglecting correlations, the bosonic tunneling dynamics is found to be enhanced and remains undamped during the evolution, in contrast to the many-body approach, while the fermionic expansion adequately resembles the many-body case.

As a final attempt, we have examined the dependence of the BF mixture expansion strength on the potential barrier height and the mass imbalance between the two components. We find that upon increasing the height of the potential barrier, the expansion dynamics is suppressed, while for mass imbalanced mixtures, the heavy (bosonic) component remains essentially unperturbed.

There are several interesting directions that one might pursue in future studies. A straightforward one would be to explore the dynamics of the BF mixture setup, but now induced by a quench from strong to weak confinement only for the fermionic ensemble, thus leaving the bosons unaffected. In this setting, the bosonic system may act as a filter which completely or partly absorbs the momentum of the expanded fermions depending on the quench amplitude. Yet another intriguing prospect is to examine the dynamics of a dipolar BF mixture under the quench protocol considered herein, and investigate the distinct response regimes that appear for varying quench amplitude or initial phase so as to explore the possibility to induce a ballistic expansion.

ACKNOWLEDGMENTS

S.I.M. and P.S. gratefully acknowledge financial support by the Deutsche Forschungsgemeinschaft (DFG) in the framework of the SFB 925 ‘‘Light induced dynamics and control of correlated quantum systems.’’

APPENDIX A: CORRELATION DYNAMICS IN THE IMMISCIBLE PHASE

To further elaborate on the MB nature of the expansion dynamics of the BF mixture within the immiscible phase, we study the emergent correlation properties of the system on both the one- and two-body level. To estimate the degree of spatial first-order coherence during the expansion dynamics, we employ [68]

$$g^{(1),\sigma}(x, x'; t) = \frac{\rho^{(1),\sigma}(x, x'; t)}{\sqrt{\rho^{(1),\sigma}(x; t)\rho^{(1),\sigma}(x'; t)}}, \quad (\text{A1})$$

where $\rho^{(1),\sigma}(x, x'; t) = \langle \Psi_{MB}(t) | \Psi_{\sigma}^{\dagger}(x') \Psi_{\sigma}(x) | \Psi_{MB}(t) \rangle$ is the one-body reduced density matrix of the σ species. $|g^{(1),\sigma}(x, x'; t)|^2$ takes values within the range $[0, 1]$, while a spatial region with $|g^{(1),\sigma}(x, x'; t)|^2 = 0$ [$|g^{(1),\sigma}(x, x'; t)|^2 = 1$] is referred to as fully incoherent (coherent).

Figures 5(a₁)–5(a₄) and 5(c₁)–5(c₄) present $g^{(1),B}(x, x'; t)$ and $g^{(1),F}(x, x'; t)$, respectively, for distinct time instants during evolution after quenching the system to $\omega_f = 0$. Referring to the bosonic component, we observe that at $t = 0$ (ground

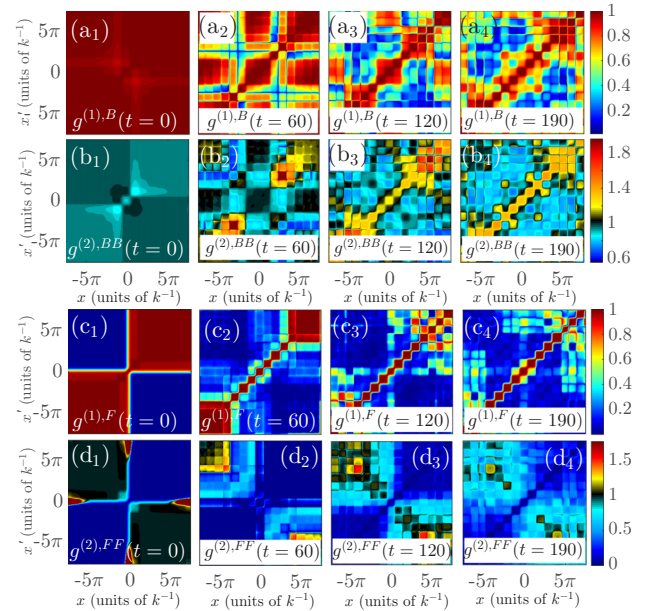


FIG. 5. (a₁)–(a₄) One-body coherence function $g^{(1),B}(x, x'; t)$ shown for different time instants (see legends) during the expansion dynamics within the immiscible phase ($g_{BB} = 0.05$, $g_{FB} = 0.2$). (c₁)–(c₄) The same as above, but for $g^{(1),F}(x, x'; t)$. (b₁)–(b₄) Snapshots of the corresponding two-body bosonic coherence function $g^{(2),BB}(x_1, x_2'; t)$. (d₁)–(d₄) The same as before, but for $g^{(2),FF}(x_1, x_2'; t)$ of the fermionic component. The BF mixture consists of $N_B = 20$ bosons and $N_F = 2$ fermions confined in a 19-well optical lattice with an imposed harmonic trap with initial frequency $\omega = 0.1$.

state), the ensemble is almost perfectly one-body coherent as $g^{(1),B}(x, x'; t) \approx 1$ everywhere [Fig. 5(a₁)]. However, upon quenching, this situation changes drastically and a substantial loss of coherence in the off-diagonal elements of $g^{(1),B}(x, x'; t)$ occurs throughout the dynamics; see Figs. 5(a₂)–5(a₄). The latter implies that the quench operation and loss of coherence go hand in hand. In particular, we can identify three different spatial regions [see, for instance, Fig. 5(a₃)] in which the coherence is mainly preserved. The first one contains the three central wells ($x, x' \in [-3\pi/2, 3\pi/2]$), while the other two regions, not fixed throughout the dynamics, lie in the outer wells (e.g., at $t = 120$, they are located at $x, x' \in [3\pi/2, 9\pi/2]$ and $x, x' \in [-3\pi/2, -9\pi/2]$, respectively). Furthermore, the aforementioned regions coincide with the areas where the different orbital densities contribute significantly to the MB density [Figs. 3(d₁)–3(d₃)]. Indeed, as time evolves, the first region exhibits a contraction [Fig. 5(a₃)] and an expansion [Fig. 5(a₄)], resembling the tunneling oscillations in the first orbital [Fig. 3(d₁)]. The second and third regions travel towards the outer wells [Fig. 5(a₄)] in the course of the dynamics, reflecting the expansion of the second, third, and fourth orbital densities [Figs. 3(d₂) and 3(d₃)]. Finally, a significant loss of coherence takes place [$g^{(1),B}(x, x'; t) \approx 0.2$] between each two of the above-mentioned regions.

To infer about the degree of spatial second-order coherence, we study the normalized two-body correlation function [62],

$$g^{(2),\sigma\sigma'}(x, x'; t) = \frac{\rho^{(2),\sigma\sigma'}(x, x'; t)}{\rho^{(1),\sigma}(x; t)\rho^{(1),\sigma'}(x'; t)}, \quad (\text{A2})$$

where $\rho^{(2),\sigma\sigma'}(x, x'; t) = \langle \Psi_{MB}(t) | \Psi_{\sigma'}^{\dagger}(x') \Psi_{\sigma}^{\dagger}(x) \Psi_{\sigma}(x) \Psi_{\sigma'}(x') | \Psi_{MB}(t) \rangle$ is the diagonal two-body reduced density matrix. When referring to the same (different) species, i.e., $\sigma = \sigma'$ ($\sigma \neq \sigma'$), $g^{(2),\sigma\sigma'}$ accounts for the intraspecies (interspecies) two-body correlations. A perfectly condensed MB state corresponds to $g^{(2),\sigma\sigma'}(x, x'; t) = 1$ and is termed fully second-order coherent or uncorrelated. However, if $g^{(2),\sigma\sigma'}(x, x'; t)$ takes values larger (smaller) than unity, the state is said to be correlated (anticorrelated) [62,69].

In Figs. 5(b₁)–5(b₄) and 5(d₁)–5(d₄), we show $g^{(2),BB}(x, x'; t)$ and $g^{(2),FF}(x, x'; t)$ for different evolution times when quenching the system to $\omega_f = 0$. The bosonic subsystem is initially ($t = 0$) mainly characterized by weak two-body anticorrelations, i.e., $g^{(2),BB}(x, x'; t) < 1$ [Fig. 5(b₁)]. The quench gives rise to new correlation structures; see Figs. 5(b₂)–5(b₄). For instance, a bunching tendency occurs in the diagonal elements, i.e., $g^{(2),BB}(x, x'; t) > 1$, indicating that it is probable for two bosons to reside within the same well during the dynamics. Most importantly, we observe that each of the above-described second and third regions of almost perfect one-body coherence (e.g., see, $x, x' \in [3\pi/2, 9\pi/2]$ and $x, x' \in [-3\pi/2, -9\pi/2]$, respectively, at $t = 120$) are two-body correlated, while they are mainly anticorrelated between each other [e.g., see Fig. 5(b₃)]. Overall, the off-diagonal elements of the $g^{(2),BB}(x, x'; t)$ tend to values smaller than unity, indicating long-range anticorrelations in the system. Comparing $g^{(1),B}(x, x'; t)$ and $g^{(2),BB}(x, x'; t)$, we can infer that when $g^{(2),BB}(x, x'; t) > 1$ [$g^{(2),BB}(x, x'; t) < 1$], the corresponding $g^{(1),B}(x, x'; t) \approx 1$ [$g^{(1),B}(x, x'; t) \leq 0.5$].

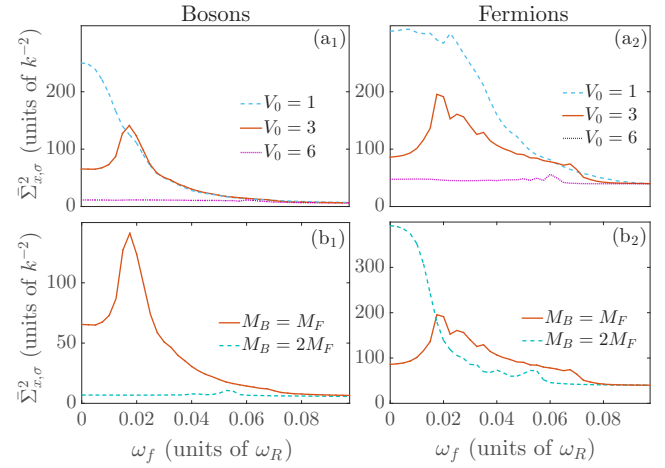


FIG. 6. (a₁), (b₁) Bosonic and (a₂), (b₂) fermionic mean variance $\bar{\Sigma}_{x,\sigma}^2$ corresponding to different system parameters for varying postquench frequency ω_f . $\bar{\Sigma}_{x,\sigma}^2(\omega_f)$ for (a₁), (a₂) distinct potential barrier heights V_0 in units of E_R , and for (b₁), (b₂) different mass ratios of the individual components. In all cases, the BF mixture consists of $N_B = 20$ bosons, $N_F = 2$ fermions, and is confined in a 19-well potential with an imposed harmonic trap of initial frequency $\omega = 0.1$. The system is initialized in its ground state with $g_{BB} = 0.05$ and $g_{FB} = 0.2$.

In contrast to the bosons, initially ($t = 0$) each fermion is localized either in the left ($-20 < x < 0$) or in the right ($0 < x < 20$) part of the lattice [see, also, Fig. 1(c)]. Indeed, $g^{(1),F}(x, x'; t) \approx 1$ and $g^{(2),FF}(x, x'; t) < 1$ [$g^{(1),F}(x, x'; t) = 0$ and $g^{(2),FF}(x, x'; t) \approx 1$] within (between) the left and right part; see Figs. 5(c₁) and 5(d₁), respectively. For later times ($t > 0$), a significant loss of one-body coherence takes place manifested by the almost zero off-diagonal elements in $g^{(1),F}(x, x'; t) \approx 0$ throughout the evolution [Figs. 5(c₂)–5(c₄)]. On the two-body level, we observe the rise of long-range correlations between the parity symmetric expanded parts, e.g., $g^{(2),FF}(x = 7\pi/2, x' = -7\pi/2; t) \approx 1.3$ in Figs. 5(d₂) and 5(d₃), which transform into anticorrelations for long propagation times [Fig. 5(d₄)]. Finally, an anticorrelated behavior occurs within the same part (i.e., right with $x, x' \in [0, 6\pi]$ or left with $x, x' \in [-6\pi, 0]$ in Fig. 5) of the lattice throughout the evolution; see, for instance, $g^{(2),FF}(x = 2\pi, x' = 2\pi; t)$ in Figs. 5(d₂)–5(d₄).

APPENDIX B: CONTROL OF THE EXPANSION DYNAMICS

Having analyzed in detail the expansion dynamics of the BF mixture within the immiscible and miscible correlated phases, let us discuss how the overall dynamics can be altered by adjusting certain initial system parameters.

First we study the effect of the potential barrier height V_0 on the expansion dynamics of an ensemble that resides in the immiscible phase; see Figs. 6(a₁) and 6(a₂). As can be seen, the corresponding expansion strength measured via $\bar{\Sigma}_{x,\sigma}^2$ for both fermions and bosons becomes larger for smaller V_0 values. The latter is a consequence of the fact that interwell as well

as overbarrier tunneling is more favorable for reduced barrier heights [70–74]. Note also here that the resonant expansion located at moderate quench amplitudes (see $\omega_f = 0.0175$) occurs only for $V_0 = 3$. In contrast, for $V_0 = 6$, $\bar{\Sigma}_{x,\sigma}^2$ is almost constant for all ω_f , indicating a negligible response, while at $V_0 = 1$, $\bar{\Sigma}_{x,\sigma}^2$ exhibits an almost monotonic increase for decreasing ω_f . This observation suggests that for fixed ω_f as well as inter- and intraspecies interactions, the expansion strength can be manipulated by tuning the potential barrier height.

Another way to control the expansion dynamics is to consider a mass imbalanced BF mixture that is experimentally realizable by using, e.g., isotopes of ^{40}K and ^{89}Rb [52,75], which possess approximately a mass ratio of 1:2. The system is in this case initialized in the ground state of the lattice with $g_{FB} = 0.2$ and $g_{BB} = 0.05$. Therefore, it resides in the immiscible phase (see also Sec. III) where the two components are phase separated. The degree of this phase separation increases for larger bosonic masses (results not shown here). Comparing a mass balanced ($M_B = M_F$) with a mass imbalanced ($M_B = 2M_F$) system, we observe that the bosonic mass strongly influences both the fermionic and the bosonic dynamics; see Figs. 6(b₁) and 6(b₂). For $M_B = 2M_F$, the bosons are essentially unperturbed for all ω_f , while the fermionic expansion becomes significant for small ω_f . The enhancement of $\bar{\Sigma}_{x,F}^2$ can be explained as follows. First, the tunneling probability to the inner wells is suppressed due to the constantly high bosonic one-body density within the three central wells, which essentially forms an additional material barrier [66,67]. Furthermore, the fermionic cloud can expand ballistically, as the interspecies scattering processes in the outer wells are negligible since the bosonic distribution in these wells is nearly zero.

In summary, we can infer that the fermions exhibit a more pronounced expansion as compared to the bosons. This can be attributed to the fact that the fermions are noninteracting and, as such, they are exposed to less scattering processes when compared to bosons [31]. Moreover, tuning several of the system's parameters allows for a control of the system's expansion dynamics in a systematic fashion.

APPENDIX C: CONVERGENCE OF MANY-BODY SIMULATIONS

In this appendix, we provide a brief overview of our numerical methodology and elaborate on the convergence of our results. ML-MCTDHX [45] is a variational method for solving the time-dependent MB Schrödinger equation of Bose-Bose [65,76], Fermi-Fermi [77,78], and Bose-Fermi mixtures. The MB wave function is expanded with respect to a time-dependent variationally optimized MB basis, which enables us to capture the important correlation effects using a computationally feasible basis size. In this way, we are able to more efficiently span the relevant, for the system under consideration, subspace of the Hilbert space at each time instant with a reduced number of basis states when compared to expansions relying on a time-independent basis. Finally, the multilayer ansatz for the total wave function allows us to account for intra- and interspecies correlations when simulating the dynamics of bipartite systems.

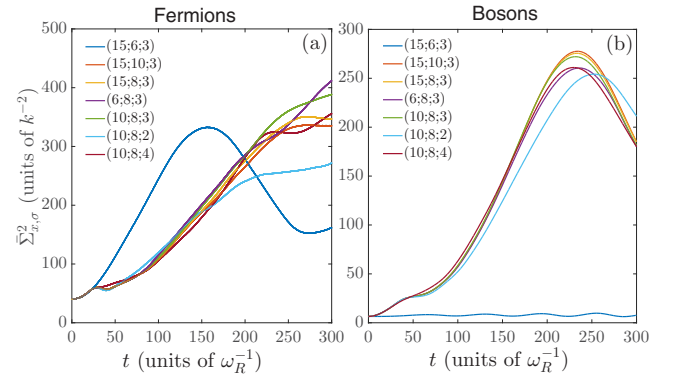


FIG. 7. Evolution of the (a) fermionic and (b) bosonic variance $\bar{\Sigma}_{x,\sigma}^2(t)$ within the immiscible phase ($g_{FB} = 0.2$ and $g_{BB} = 0.05$) for different numerical configurations ($M; m^F; m^B$) (see legend) following a quench to $\omega_f = 0.175$.

Within our simulations, we employ a primitive basis consisting of a sine discrete variable representation including 475 grid points. The Hilbert space truncation, i.e., the order of the used approximation, is indicated by the considered numerical configuration space $C = (M; m^F; m^B)$. Here, $M = M^F = M^B$ (m^F, m^B) denote the number of species (single-particle) functions for each of the species. To maintain the accurate performance of the numerical integration for the ML-MCTDHX equations of motion, we further ensured that $|\langle \Psi | \Psi \rangle - 1| < 10^{-10}$ and $|\langle \varphi_i | \varphi_j \rangle - \delta_{ij}| < 10^{-10}$ for the total wave function and the single-particle functions, respectively.

Next, let us comment on the convergence of our results upon varying the numerical configuration space $C = (M; m^F; m^B)$. To conclude about the reliability of our simulations, we increase the number of species functions and single-particle functions, thus observing a systematic convergence of our results. We remark that all MB calculations presented in the main text rely on the configuration $C = (10; 8; 4)$. To be more concrete, in the following, we demonstrate the convergence procedure for the position variance $\bar{\Sigma}_{x,\sigma}^2(t)$ of the σ species within the immiscible phase ($g_{FB} = 0.2$ and $g_{BB} = 0.05$) for a varying number of species or single-particle functions. Figure 7(a) [Fig. 7(b)] presents $\bar{\Sigma}_{x,F}^2(t)$ [$\bar{\Sigma}_{x,B}^2(t)$] following a quench of the imposed harmonic-oscillator frequency from $\omega = 0.1$ to $\omega_f = 0.0175$. For reasons of completeness, we remark that this quench amplitude refers to a strong response region of the system; see, also, Fig. 2. Regarding the number of the used species functions M , we observe an adequate convergence of both the fermionic and bosonic variance. In particular, comparing the $C = (10; 8; 3)$ and $C = (15; 8; 3)$ approximations, $\bar{\Sigma}_{x,F}^2(t)$ shows a maximal deviation of the order of 10% for large propagation times $t > 250$, while $\bar{\Sigma}_{x,B}^2(t)$ is almost insensitive as the corresponding relative difference is less than 1.5% throughout the evolution. Increasing the number of the fermionic single-particle functions m^F , the maximum deviation observed in $\bar{\Sigma}_{x,F}^2(t)$ [$\bar{\Sigma}_{x,B}^2(t)$] between the $C = (15; 8; 3)$ and $C = (15; 10; 3)$ approximations is of the order of 4% [$< 1\%$]. Turning to the number of bosonic single-particle functions m^B , the relative difference in $\bar{\Sigma}_{x,F}^2(t)$ [$\bar{\Sigma}_{x,B}^2(t)$] between the configurations $C = (10; 8; 3)$ and

$C = (10; 8; 4)$ becomes, at most, 11% [4%] for large evolution times $t > 230$. Finally, we remark that the same analysis has been performed for the convergence within the miscible regime

($g_{BB} = 1.0$, $g_{FB} = 0.05$) for increasing both the number of species M as well as the single-particle functions m^F and m^B (not shown here).

-
- [1] S. Inouye, J. Goldwin, M. L. Olsen, C. Ticknor, J. L. Bohn, and D. S. Jin, *Phys. Rev. Lett.* **93**, 183201 (2004).
- [2] T. Fukuhara, S. Sugawa, Y. Takasu, and Y. Takahashi, *Phys. Rev. A* **79**, 021601 (2009).
- [3] Z. Hadzibabic, C. A. Stan, K. Dieckmann, S. Gupta, M. W. Zwierlein, A. Görlitz, and W. Ketterle, *Phys. Rev. Lett.* **88**, 160401 (2002).
- [4] J. Heinze, S. Götze, J. S. Krauser, B. Hundt, N. Fläschner, D. S. Lühmann, C. Becker, and K. Sengstock, *Phys. Rev. Lett.* **107**, 135303 (2011).
- [5] A. G. Truscott, K. E. Strecker, W. I. McAlexander, G. B. Partridge, and R. G. Hulet, *Science* **291**, 2570 (2001).
- [6] C. J. Pethick and H. Smith, *Bose-Einstein Condensation in Dilute Gases* (Cambridge University Press, Cambridge, 2002).
- [7] M. Lewenstein, A. Sanpera, and V. Ahufinger, *Ultracold Atoms in Optical Lattices: Simulating Quantum Many-body Systems* (Oxford University Press, Oxford, 2012).
- [8] K. K. Das, *Phys. Rev. Lett.* **90**, 170403 (2003).
- [9] L. Viverit, C. J. Pethick, and H. Smith, *Phys. Rev. A* **61**, 053605 (2000).
- [10] M. A. Cazalilla and A. F. Ho, *Phys. Rev. Lett.* **91**, 150403 (2003).
- [11] T. Miyakawa, H. Yabu, and T. Suzuki, *Phys. Rev. A* **70**, 013612 (2004).
- [12] H. Pu, W. Zhang, M. Wilkens, and P. Meystre, *Phys. Rev. Lett.* **88**, 070408 (2002).
- [13] X. J. Liu and H. Hu, *Phys. Rev. A* **67**, 023613 (2003).
- [14] A. Zujev, A. Baldwin, R. T. Scalettar, V. G. Rousseau, P. J. H. Denteneer, and M. Rigol, *Phys. Rev. A* **78**, 033619 (2008).
- [15] O. Dutta and M. Lewenstein, *Phys. Rev. A* **81**, 063608 (2010).
- [16] M. Cramer, J. Eisert, and F. Illuminati, *Phys. Rev. Lett.* **93**, 190405 (2004).
- [17] M. Lewenstein, L. Santos, M. A. Baranov, and H. Fehrmann, *Phys. Rev. Lett.* **92**, 050401 (2004).
- [18] L. Mathey, D. W. Wang, W. Hofstetter, M. D. Lukin, and E. Demler, *Phys. Rev. Lett.* **93**, 120404 (2004).
- [19] H. P. Büchler and G. Blatter, *Phys. Rev. Lett.* **91**, 130404 (2003).
- [20] I. Titvinidze, M. Snoek, and W. Hofstetter, *Phys. Rev. B* **79**, 144506 (2009).
- [21] A. Privitera and W. Hofstetter, *Phys. Rev. A* **82**, 063614 (2010).
- [22] A. B. Kuklov and B. V. Svistunov, *Phys. Rev. Lett.* **90**, 100401 (2003).
- [23] A. Albus, F. Illuminati, and J. Eisert, *Phys. Rev. A* **68**, 023606 (2003).
- [24] A. Sanpera, A. Kantian, L. Sanchez-Palencia, J. Zakrzewski, and M. Lewenstein, *Phys. Rev. Lett.* **93**, 040401 (2004).
- [25] Th. Best, S. Will, U. Schneider, L. Hackermüller, D. van Oosten, I. Bloch, and D. S. Lühmann, *Phys. Rev. Lett.* **102**, 030408 (2009).
- [26] A. Mering and M. Fleischhauer, *Phys. Rev. A* **83**, 063630 (2011).
- [27] D. S. Lühmann, K. Bongs, K. Sengstock, and D. Pfannkuche, *Phys. Rev. Lett.* **101**, 050402 (2008).
- [28] S. Tewari, R. M. Lutchyn, and S. Das Sarma, *Phys. Rev. B* **80**, 054511 (2009).
- [29] A. Polkovnikov, K. Sengupta, A. Silva, and M. Vengalattore, *Rev. Mod. Phys.* **83**, 863 (2011).
- [30] N. Andrei, [arXiv:1606.08911](https://arxiv.org/abs/1606.08911).
- [31] J. P. Ronzheimer, M. Schreiber, S. Braun, S. S. Hodgman, S. Langer, I. P. McCulloch, F. Heidrich-Meisner, I. Bloch, and U. Schneider, *Phys. Rev. Lett.* **110**, 205301 (2013).
- [32] W. Tschischik, R. Moessner, and M. Haque, *Phys. Rev. A* **88**, 063636 (2013).
- [33] G. M. Koutentakis, S. I. Mistakidis, and P. Schmelcher, *Phys. Rev. A* **95**, 013617 (2017).
- [34] L. Vidmar, J. P. Ronzheimer, M. Schreiber, S. Braun, S. S. Hodgman, S. Langer, F. Heidrich-Meisner, I. Bloch, and U. Schneider, *Phys. Rev. Lett.* **115**, 175301 (2015).
- [35] M. Rigol and A. Muramatsu, *Phys. Rev. Lett.* **93**, 230404 (2004).
- [36] L. Vidmar, D. Iyer, and M. Rigol, *Phys. Rev. X* **7**, 021012 (2017).
- [37] W. Xu and M. Rigol, *Phys. Rev. A* **95**, 033617 (2017).
- [38] L. Vidmar, W. Xu, and M. Rigol, *Phys. Rev. A* **96**, 013608 (2017).
- [39] L. Vidmar, S. Langer, I. P. McCulloch, U. Schneider, U. Schollwock, and F. Heidrich-Meisner, *Phys. Rev. B* **88**, 235117 (2013).
- [40] C. K. Lai and C. N. Yang, *Phys. Rev. A* **3**, 393 (1971).
- [41] A. Imambekov and E. Demler, *Ann. Phys.* **321**, 2390 (2006).
- [42] A. Imambekov and E. Demler, *Phys. Rev. A* **73**, 021602 (2006).
- [43] B. Fang, P. Vignolo, M. Gattobigio, C. Miniatura, and A. Minguzzi, *Phys. Rev. A* **84**, 023626 (2011).
- [44] A. S. Dehkharghani, F. F. Bellotti, and N. T. Zinner, *J. Phys. B: At. Mol. Opt. Phys.* **50**, 144002 (2017).
- [45] L. Cao, V. Bolsinger, S. I. Mistakidis, G. M. Koutentakis, S. Krönke, J. M. Schurer, and P. Schmelcher, *J. Chem. Phys.* **147**, 044106 (2017).
- [46] L. Cao, S. Krönke, O. Vendrell, and P. Schmelcher, *J. Chem. Phys.* **139**, 134103 (2013).
- [47] E. V. Kempen, B. Marcelis, and S. J. J. M. F. Kokkelmans, *Phys. Rev. A* **70**, 050701 (2004).
- [48] K. Honda, Y. Takasu, T. Kuwamoto, M. Kumakura, Y. Takahashi, and T. Yabuzaki, *Phys. Rev. A* **66**, 021401 (2002).
- [49] Y. Takasu, K. Maki, K. Komori, T. Takano, K. Honda, M. Kumakura, T. Yabuzaki, and Y. Takahashi, *Phys. Rev. Lett.* **91**, 040404 (2003).
- [50] M. Olshanii, *Phys. Rev. Lett.* **81**, 938 (1998).
- [51] T. Köhler, K. Goral, and P. S. Julienne, *Rev. Mod. Phys.* **78**, 1311 (2006).
- [52] C. Chin, R. Grimm, P. Julienne, and E. Tiesinga, *Rev. Mod. Phys.* **82**, 1225 (2010).
- [53] J. I. Kim, V. S. Melezhik, and P. Schmelcher, *Phys. Rev. Lett.* **97**, 193203 (2006).
- [54] R. Horodecki, P. Horodecki, M. Horodecki, and K. Horodecki, *Rev. Mod. Phys.* **81**, 865 (2009).
- [55] M. Roncaglia, A. Montorsi, and M. Genovese, *Phys. Rev. A* **90**, 062303 (2014).
- [56] A. Peres, *Quantum Theory: Concepts and Methods*, Vol. 57 (Springer Science and Business Media, New York, 2006).

- [57] M. Lewenstein, D. Bruß, J. I. Cirac, B. Kraus, M. Kuś, J. Samsonowicz, A. Sanpera, and R. Tarrach, *J. Mod. Opt.* **47**, 2481 (2000).
- [58] E. J. Mueller, T. L. Ho, M. Ueda, and G. Baym, *Phys. Rev. A* **74**, 033612 (2006).
- [59] O. Penrose and L. Onsager, *Phys. Rev.* **104**, 576 (1956).
- [60] J. Frenkel, in *Wave Mechanics*, 1st ed. (Clarendon Press, Oxford, UK, 1934), pp. 423–428.
- [61] P. A. Dirac, *Proc. Camb. Philos. Soc.* **26**, 376 (1930).
- [62] K. Sakmann, A. I. Streltsov, O. E. Alon, and L. S. Cederbaum, *Phys. Rev. A* **78**, 023615 (2008).
- [63] Z. Akdeniz, P. Vignolo, A. Minguzzi, and M. P. Tosi, *J. Phys. B: At. Mol. Opt. Phys.* **35**, L105 (2002).
- [64] Z. Akdeniz, P. Vignolo, and M. P. Tosi, *J. Phys. B: At. Mol. Opt. Phys.* **38**, 2933 (2005).
- [65] S. I. Mistakidis, G. C. Katsimiga, P. G. Kevrekidis, and P. Schmelcher, *New J. Phys.* **20**, 043052 (2018).
- [66] A. C. Pflanzner, S. Zöllner, and P. Schmelcher, *J. Phys. B: At. Mol. Opt. Phys.* **42**, 231002 (2009).
- [67] A. C. Pflanzner, S. Zöllner, and P. Schmelcher, *Phys. Rev. A* **81**, 023612 (2010).
- [68] M. Naraschewski and R. J. Glauber, *Phys. Rev. A* **59**, 4595 (1999).
- [69] M. C. Tsatsos, J. H. V. Nguyen, A. U. J. Lode, G. D. Telles, D. Luo, V. S. Bagnato, and R. G. Hulet, [arXiv:1707.04055](https://arxiv.org/abs/1707.04055).
- [70] S. I. Mistakidis, L. Cao, and P. Schmelcher, *J. Phys. B: At. Mol. Opt. Phys.* **47**, 225303 (2014).
- [71] S. I. Mistakidis, L. Cao, and P. Schmelcher, *Phys. Rev. A* **91**, 033611 (2015).
- [72] J. Neuhaus-Steinmetz, S. I. Mistakidis, and P. Schmelcher, *Phys. Rev. A* **95**, 053610 (2017).
- [73] S. I. Mistakidis, G. M. Koutentakis, and P. Schmelcher, *Chem. Phys.* (2017), doi:10.1016/j.chemphys.2017.11.022
- [74] T. Plaßmann, S. I. Mistakidis, and P. Schmelcher, [arXiv:1802.06693](https://arxiv.org/abs/1802.06693).
- [75] C. H. Wu, I. Santiago, J. W. Park, P. Ahmadi, and M. W. Zwierlein, *Phys. Rev. A* **84**, 011601 (2011).
- [76] G. C. Katsimiga, G. M. Koutentakis, S. I. Mistakidis, P. G. Kevrekidis, and P. Schmelcher, *New J. Phys.* **19**, 073004 (2017).
- [77] L. Cao, S. I. Mistakidis, X. Deng, and P. Schmelcher, *Chem. Phys.* **482**, 303 (2017).
- [78] G. M. Koutentakis, S. I. Mistakidis, and P. Schmelcher, [arXiv:1804.07199](https://arxiv.org/abs/1804.07199).

Chapter 5

Conclusions and Outlook

In this cumulative dissertation, we have discussed the zero-temperature nonequilibrium quantum dynamics of few repulsively interacting ultracold bosons and mixtures thereof confined in one-dimensional finite lattices. The nonequilibrium situation has been induced either by performing a quench on a Hamiltonian parameter or utilizing a time-periodic modulation of the lattice potential. Focal point of our research has been the characterization of the system's dynamical response including the microscopic mechanisms and correlated origin of the nonequilibrium modes and most importantly their coupling by tuning an appropriate parameter of the employed quench protocol. In this final chapter, an outline of our key findings is provided along with a multitude of interesting directions that could be consecutively pursued in future studies.

Quench Dynamics in Scalar Few-Boson Ensembles:

Regarding the quench dynamics in few scalar bosonic ensembles confined in optical lattices the main focus has been the study of different interaction quench protocols aiming in generating and subsequently characterize and manipulate the desired nonequilibrium modes. A major scope was to obtain a certain degree of control of the dynamics. As a first attempt in [[1]] we investigated the correlated nonequilibrium dynamics of few lattice trapped bosons of incommensurate filling upon considering a sudden raise of the interaction strength. Our investigations incorporated highly non-perturbative scenarios, by means of driving the system to a regime dominated by interparticle interactions instead of kinetic energies. In particular, by considering weak-to-strong interaction quenches enabled us to identify the existence of excited-band modes linked to certain interband processes, namely the well-known breathing mode and the so-called cradle mode with the latter being reported for the first time in the literature. Finally, we revealed the presence of a density-wave tunneling mainly referring to a lowest-band dynamical phenomenon. This density-wave spatial pattern probes the lowest-band tunneling dynamics after the quench comprising of single and atom pair tunneling and can be seen as an effective breathing of the “global wavepacket” reflecting the instantaneous density distribution of the trap. Referring to the intrawell dynamics, we were able besides identifying the aforementioned modes to further characterize and control them. In particular, in the middle well the on-site breathing mode corresponds to the expansion and contraction of the bosonic cloud, while in the outer wells the so-called cradle mode manifests itself as

CONCLUSIONS AND OUTLOOK

a “dipole-like” oscillation of the localized wavepacket. Its generation is accompanied by an initial over-barrier transport of the particles from the central well to the outer ones due to the import of energy into the system and the consequent collisions with the respective atoms in the outer sites. Strikingly enough, we were able to tune the frequency of the energetically highest tunneling branch in resonance with the frequency of the cradle mode, a mechanism that was triggered by varying the quench amplitude and thus enabling us to concretely control the system. A first possible extension of our work is to consider the interaction quench dynamics of few-bosons confined in a two-dimensional finite optical lattice. In such a setting it would be interesting to examine under what circumstances the cradle mode can be generated and consequently whether it can be coupled to the quench-induced tunneling mode [432–434]. A second path is to study the interaction quench dynamics of binary bosonic mixtures confined in an one-dimensional optical lattice [223, 442, 443]. Here one can perform interspecies interaction quenches and cross dynamically the miscibility-immiscibility threshold in a two-directional manner unraveling the emergent defect formation and further characterizing its correlated nature.

After revealing the existence of the cradle mode, a natural next step examined in [[2]] was whether this mode could be excited when quenching the system from strong-to-weak interactions thus exerting energy from the system. An intriguing question here was to explore how the initial ground state configuration, reflected by the filling factor of the system, affects the generation of the quench-induced excited modes or enables us to resonantly couple them. We found that the quench triggers several modes of the system consisting of distinct lowest-band tunneling channels, an on-site breathing and a cradle mode. Conceptual differences concerning the ingredients of each mode and its excitation process when compared to the case of weak-to-strong interaction quenches [[1]] have been demonstrated. Most importantly, it is observed that the cradle mode can be excited only for setups with filling larger than unity following a quench from strong-to-weak interactions. Indeed, due to the strong interparticle repulsion the initial spatial configuration corresponds to one localized boson in each well and one delocalized over the lattice, lying energetically close to the lattice barrier. As a consequence, a sudden decrease of the interaction strength yields a high probability for the delocalized particle to overcome the lattice barrier and move to a neighboring well initializing a cradle process. To excite the cradle mode in setups characterized by filling smaller than unity we enforced the spatial delocalization of the atoms by quenching the height of the potential barrier to lower values, thus driving the system to a region where the kinetic energy of the atoms dominates in comparison to the potential energy. Finally, by considering time-dependent quenches or the modulation of various potential parameters of the Hamiltonian we demonstrated different ways to control the cradle and breathing modes by means of manipulating their frequencies. Our developed understanding on the properties of the quench-induced excitation modes paves the way for developing certain controlling schemes for the nonequilibrium dynamics of such strongly correlated systems. For instance one can investigate the nonequilibrium dynamics of mixtures consisting of different bosonic species in order to selectively transport an individual bosonic component [435, 436]. Another interesting prospect is to study the interaction quench dynamics of few dipolar bosons confined in one-dimensional optical lattices and identify the microscopic origin of the induced excitation modes [444, 445].

To dynamically manipulate the quench-induced excited modes in [[3]] we followed a generalized interaction quench protocol, namely a multiple interaction quench (MIQ), consisting of different sequences of single quenches. The latter, allows the system to dynamically return to its original Hamiltonian within certain time intervals. To characterize the effect of the multiple pulses we studied the interplay between the quench amplitude and the pulse width during the evolution. The quenches excite several interwell tunneling modes and the cradle as well as a breathing mode. We showed that the lowest-band tunneling dynamics consists of three distinct energy channels occurring in the time intervals of increased interaction, whilst for decreasing interaction only one tunneling mode survives. The latter opens the possibility to dynamically manipulate the tunneling dynamics within the different time intervals of the MIQ protocol. Furthermore, the intrawell cradle motion persists during the time evolution as it has already been initialized during the first pulse and therefore the coupling between the cradle mode and one of the tunneling modes, discussed in [[1]] occurs only for the time intervals of increased interactions. The breathing mode exhibited a strong dependence on the instantaneous interatomic repulsion, namely for increasing interactions it possesses an interaction dependent frequency branch otherwise this branch disappears and two new interaction independent frequency branches occur. Moreover, the quench-induced excitation dynamics exhibits an almost linear dependence on the quench amplitude, i.e. for increasing amplitude of the quench the amount of excitations increase monotonically, while on the pulse width it possesses a non-linear dependence. A prominent signature of the impact of the quenches is revealed by resorting to the evolution of the one-body momentum distribution where a periodic population transfer of lattice momenta is observed. A possible future direction would be to apply our protocol to repulsively interacting dipolar systems [438–441] or consider similar modulations of the one-dimensional lattice geometry. Also referring to systems consisting of larger particle numbers and sizes the question whether thermalization [112, 143, 144] occurs for long evolution times after the system has been quenched to its initial Hamiltonian is an intriguing one.

To provide insights into the largely unexplored scaling of few-body defect density in [[4]] we explored the nonequilibrium quantum dynamics following a linear interaction quench (LIQ) protocol in repulsively interacting few-boson ensembles confined in one-dimensional finite optical lattices. We have particularly focussed on unit filling setups such that the ground state of the system for increasing interaction strength exhibits the few-body analogue of the superfluid to a Mott-insulator phase. Inspecting the corresponding many-body eigenspectrum for varying interparticle repulsion we revealed the existence of narrow and wide avoided-crossings between states of the zeroth and first excited-band. Then we performed a LIQ to dynamically cross the phase boundary, with a finite ramp rate, either from weak-to-strong interactions or inversely, covering in both cases the diabatic to nearly adiabatic crossing regimes. When crossing the weak-to-strong interaction regimes we found an enhanced dynamical response at moderate quench rates rather than in the abrupt or almost adiabatic regimes. The resulting lowest-band tunneling dynamics consists of first and second order transport and it can be manipulated by tuning either the interaction strength after the quench or the height of the potential barriers in the optical lattice. Furthermore, a rich interband tunneling dynamics has been identified possessing mainly a single excitation to the first or second excited-band

CONCLUSIONS AND OUTLOOK

of the finite lattice. It has also been shown that following a LIQ the excited to higher-band fraction obeys a bi-exponential decay for decreasing quench rate, being directly related to the diabatic or adiabatic crossing of the transition. For varying height of the potential barrier, the excited to higher-band fraction follows a more complex scaling, namely for diabatic quenches it reduces while for larger ramp times it exhibits a non-linear behavior showing a maximum at a certain height of the potential barrier. Additionally, the higher-band dynamics depends strongly on the postquench state, i.e. when approaching the region of an existing avoided-crossing it exhibits a non-linear growth, while for larger quench amplitudes it increases in an almost linear manner. In contrast to the above, following a LIQ from strong-to-weak interactions the overall dynamical response is reduced and mainly consists of the lowest-band tunneling dynamics. The quench triggers only a few tunneling modes and the excited to higher-band fraction is negligible obeying an exponential decay both with varying ramp time and potential height. Finally, we demonstrated that larger unit filling setups can be driven out-of-equilibrium more efficiently which is a manifestation of the Anderson orthogonality catastrophe. An interesting future research direction would be to investigate the dynamical response induced by a LIQ in repulsively interacting dipolar bosons upon crossing the corresponding superfluid to supersolid transition point [438, 444, 445]. Moreover, the study of bosonic or fermionic spinor ensembles confined in an optical lattice consists an intriguing perspective as the inclusion of the spin degree of freedom enriches the phase diagram and a significantly altered dynamical response is expected to occur [18, 446, 447].

Next, we have studied [[5]] the nonequilibrium quantum dynamics of few-bosons experiencing a spatially modulated interaction strength and confined in a finite lattice potential. In particular, we utilized a spatially modulated interaction strength of sinusoidal type which is characterized by its wavevector, inhomogeneity amplitude, interaction offset and a phase. To exploit the competition between delocalization and on-site interaction effects we focussed on setups possessing fillings larger than unity. Regarding the ground state properties of the system we showed that by tuning either the wavevector or the phase, the density distribution can be effectively displaced to regions of decreasing interaction strength, enabling in particular the existence of Mott-like states after a phase shift of the interaction profile. The dynamics after a quench of the wavevector is characterized by enhanced response regions, located at fractional values of the wavevector, where bosons at different wells are subjected to different spatially averaged interaction strengths. The quench yields the excitation of a multitude of tunneling modes consisting of single and two particle transport which can be manipulated by adjusting the interaction offset or the inhomogeneity amplitude. A breathing dynamics of the bosonic cloud also occurs being associated with interband tunneling processes. Inspecting the momentum distribution reveals a periodic population transfer of momenta during the dynamics, while in the one-body coherence function we observe that partially coherent regions occur between the wells that are predominantly populated during the evolution. On the other hand, a phase quench of the interaction profile yields a directed transport along the finite lattice. The emergent tunneling modes are of single-particle and atom pair character. Most importantly, a phase quench enables us to discriminate energetically, otherwise, degenerate tunneling channels, while for increasing inhomogeneity amplitudes the quench-induced modes become more discernible. This directional transport is also reflected in the one-body

momentum distribution where a directed consecutive population of higher momenta occurs, and in the one-body correlation function where the predominantly populated wells form a partially incoherent region which is shifted in the preferred tunneling direction. Finally, we showed that a phase quench yields a non-negligible over-barrier transport generating a global breathing motion and a cradle mode in the outer wells. These modes refer to single-particle interband processes to the first or second excited-band respectively. An intriguing prospect of the present work would be to examine the periodically driven dynamics upon shaking the optical lattice and subsequently investigate how the properties of the corresponding parametrically induced resonances are altered when compared to the homogeneously interacting case [[7]]. Another possible extension is to explore the nonequilibrium dynamics of bosonic binary mixtures experiencing such spatially dependent interactions and unravel whether a phase separation process can be achieved after quenching the wavevector of the interaction profile [211, 212, 448, 449].

To achieve an initial state preparation and consequently obtain a direct control of the many-body evolution in [[6]] we examined the nonequilibrium dynamics of finite bosonic ensembles confined in a one-dimensional optical lattice upon quenching the frequency of an imposed harmonic trap from strong-to-weak confinement. Calculating the many-body eigenspectrum for varying trap frequency we revealed the existence of narrow and wide avoided-crossings between the many-body eigenstates. Inspecting the quench-induced dynamics for varying final trap frequency we deduced the following. In the non-interacting limit, a pronounced tunneling dynamics occurs only for the case of a small final harmonic trapping frequency. For intermediate interactions different response regimes depending on the postquenched confinement are observed and their occurrence is directly related to the multiple avoided-crossings in the many-body eigenspectrum. More importantly, for intermediate quench amplitudes the narrow avoided-crossings, solely involving excited states, can be utilized to selectively couple the initial state to a desired final state. For large quench amplitudes a multimode dynamical response of small amplitude occurs. Furthermore, we showcase the deterministic preparation of the system in a desired Wannier number state. Finally, for strong interactions the dynamics significantly differs from the case of weak interactions, with higher-band effects being more prominent and lowest-band tunneling being suppressed. This latter behavior is caused by the fact that in the many-body eigenspectrum avoided-crossings exist at higher trapping frequencies and are narrower. Concluding we can infer that an appropriate selection of the postquench confinement enables us to couple the initial state to a desired final one, thus allowing for a low-frequency and efficient population transfer between the two eigenstates. Our findings suggest that bosonic systems confined in a composite potential landscape consisting of a lattice potential and an imposed harmonic trap can be used for state preparation. Then, a natural next step is to consider time-dependent quench protocols, e.g. linear quenches, that may yield a substantial improvement on the state preparation by exploiting the Landau-Zener mechanism [450–452]. Another interesting prospect is to consider the case where the parity symmetry is broken by a shift of the harmonic oscillator relative to the lattice. Here, the states of opposite parity can potentially couple and one can induce transitions between states of the zeroth band and states in the first excited-band revealing, for instance, Bloch oscillations [193–195] or the cradle mode [[1-3]].

Driven Lattices

Another intriguing prospect towards the control of the nonequilibrium dynamics is to consider a time-periodic modulation of the finite optical lattice. In [[7]] we study the nonequilibrium quantum dynamics of finite ultracold bosonic ensembles confined in a shaken one-dimensional optical lattice which is modelled with the sinusoidal function. We focus on large lattice depths and small driving amplitudes in order to limit the degree of induced excitations that would otherwise lead to heating processes. The system is prepared in its weakly or strongly interacting ground state and then it is shaken. We cover a wide range of driving frequencies from adiabatic to highly intense driving. The system's dynamical evolution is mainly governed by the interwell tunneling and the intrawell dipole-like mode associated with a rich excitation spectrum. Remarkably enough, it has been shown that by adjusting the driving frequency the intrawell dynamics experiences a resonant behaviour, elucidating that it can be controlled by tuning the driving frequency. The resonantly driven dynamics is identified e.g. by the periodic formation of enhanced density oscillations (giant dipole oscillations) or from the periodic population of additional lattice momenta in the momentum distribution of the one-body density. Utilizing Floquet theory it has been found that in the proximity of this resonance the first two Floquet modes are dominantly contributing, while away from resonance the dynamics is described by only the first Floquet mode. To explain the enhanced population of the second Floquet mode in the vicinity of the resonance the quasienergy spectrum has been calculated, revealing avoided-crossings between the first two Floquet modes at certain driving frequencies. However, for finite particle numbers and interaction strengths such a single-particle description has been proved to be inadequate for the description of the observed dynamics and a multimode treatment is necessary. It has been shown that the interparticle repulsion significantly affects the dynamics, yielding a destruction of the interwell tunneling in the strongly interacting regime and an enhanced amount of higher-band excitations. Inspecting the spectrum of the one-body density for varying driving frequency we have identified all the involved dynamical frequencies, such as those referring to the intrawell oscillations and the emergent tunneling dynamics. A first natural extension of our work is to study the driven dynamics of binary bosonic mixtures in order to unravel the induced excitation modes within the miscible and immiscible phases [211, 212, 448, 449] or to devise schemes for selective transport of an individual bosonic component [435, 436]. Furthermore, it would be very interesting to simulate the parametric amplification of matter-waves with applications ranging from the generation of four-wave mixing [172–174] to controllable entanglement production.

A step forward to deepen our understanding on the control of the nonequilibrium dynamics is to unravel how a combination of periodic driving and an interaction quench can be used to further steer the dynamics and as a consequence the coupling of the interwell and intrawell modes. These inquiries lead us to our next scientific contribution [[8]] where we investigated the quantum dynamics of interaction quenched few-boson ensembles trapped in one-dimensional periodically driven, vibrating, finite optical lattices. To limit the degree of the induced excitations we employ a deep lattice potential and small driving amplitudes. Starting from the ground state of a weakly interacting few-boson ensemble, we first examined the system's time evolution in the periodically driven finite lattice. To unravel the range from

adiabatic to high frequency driving we cover a wide range of driving frequencies. Our driving scheme induces out-of-phase local dipole modes in the outer wells, and an on-site breathing mode in the central well. Recall that this is in direct contrast with a shaken lattice, where only on-site in-phase dipole modes are generated. It is observed that within the intermediate frequency regime, the system can be driven to a highly nonequilibrium state where a resonance of the intrawell dynamics takes place. The tunneling dynamics within this regime possesses mainly a single-particle character and it survives upon increasing interaction obtaining additional features the most remarkable of which being the co-tunneling of an atom pair [54, 134]. Additionally, within this resonantly driven regime an intensified loss of coherence occurs. To induce a correlated many-body dynamics we then employed an interaction quench upon the periodically driven lattice. In this manner we were able to amplify the tunneling and the on-site breathing mode, while in the outer lattice wells the bosons experienced an admixture of a dipole and a breathing motion. Finally, the dynamics of the periodically driven lattice for a fixed driving frequency and varying quench amplitude has been studied. It has been shown that the combination of different driving protocols can excite different inter- and intrawell modes and manifest various energetically higher components of a mode. Remarkably enough, a multitude of distinct resonances between the lowest-band tunneling dynamics and the intrawell dynamics is revealed. It has been further shown that these resonances can be manipulated via the frequency of the periodic driving, allowing for further control of the mode coupling in optical lattices. Our findings reveal that a combination of different driving protocols can induce admixtures of excited modes which in the present case correspond to admixtures of dipole-like and breathing-like modes. In the same spirit it would be interesting to find the optimal pulse of the interaction quench protocol in order to induce a perfectly shaped squeezed state [138–141]. Finally, the understanding of the long-time dynamics imposing the interaction quench on the driven lattice at different transient times is certainly of interest [112, 437].

Quench Dynamics in Binary Mixtures

Having established a basic understanding of the nonequilibrium dynamics of single-component bosonic ensembles we proceed to our last two scientific contributions in which we investigate the correlation effects in the quench dynamics of multicomponent systems. In this context, quantum correlations possess a crucial role as their interplay gives rise to novel phases of matter and peculiar dynamical phenomena [203–205]. In particular, within [[9]] we examined the quench-induced phase separation dynamics of a harmonically trapped repulsively interacting binary bosonic ensemble both within and beyond the mean-field approximation. The system is initially prepared into the miscible phase. To realize the miscible to immiscible transition the intraspecies interactions are held fixed and the interspecies repulsion is quenched to a finite value. A filamentation of the one-body density during the dynamics of each of the two species takes place. The dominant wavenumber associated with the emerging phase separated state appears to be higher in the mean-field case. Examining the corresponding few-boson systems we found that the phase separation is absent in the many-body case while it is still present within the mean-field approximation. On the one-body level prominent losses of coherence have been observed, verifying the fragmented nature of the system, between filaments residing around the center of the trap with the longer distant ones, lying at the periphery of

CONCLUSIONS AND OUTLOOK

the bosonic cloud. Most importantly, at the two-body level domain-wall-like structures are revealed, since the inner filaments in both species are found to be anti-correlated with their respective outer ones. A direct link with potential experimental realizations of the dynamics has been also provided by utilizing, for the first time for binary mixtures, single-shots simulations. Here, the presence of both the entanglement and the fragmentation has been related to the dynamical evolution of the variance of single-shot images. In particular, it has been observed that the growth rate of the variance resembles the growth rate of the entanglement, while the fragmented nature of the binary system is captured by the deviations in the variance with respect to each of the two species. Following the reverse quench scenario, namely quenching from the immiscible towards the miscible phase multiple dark-antidark solitary waves are spontaneously generated and they are found to decay within the many-body approach [309,310]. Employing the variance of single-shot measurements we showcased the presence of a significant degree of entanglement. Finally quenches within the immiscible regime have been investigated revealing the one-dimensional analogue of the so-called “ball” and “shell” structure that appears in higher-dimensional binary systems [226, 423]. A natural next step would be to unravel the dynamical phase separation process following a time-dependent protocol, e.g. a linear quench, in order to explore the domain formation crossing the critical point with different velocities and thus testing the Kibble-Zurek mechanism [453,454] in the presence of quantum fluctuations. Another interesting prospect is to consider the corresponding already experimentally realized [211] two-dimensional setting, and examine how the mean-field properties are altered in the presence of quantum fluctuations. Additionally, of great interest would be to investigate the quench dynamics of spinor bosons, for which phase separation processes are of ongoing interest even at the mean-field limit [455]. Last but not least a very intriguing future direction is to examine the out-of-equilibrium dynamics of highly particle imbalanced mixtures and subsequently investigate the dynamical formation of the so-called Bose polarons [456–466] e.g. by quenching the interspecies repulsion.

Within our final work [[10]] we examined the quench-induced expansion dynamics of a particle imbalanced Bose-Fermi mixture confined in an one-dimensional optical lattice with an imposed harmonic trap upon considering quenches from strong-to-weak confinement. Inspecting the ground state properties of the system we revealed that by tuning the inter- and intraspecies interaction strengths two distinct ground state configurations can be realized, namely the miscible and immiscible phases being characterized by a complete or vanishing overlap of the bosonic and fermionic single-particle density distributions respectively. Residing within the weak interaction regime, we performed a quench from strong-to-weak confinement and examined the resulting dynamical response within each of the above-mentioned phases for varying final harmonic trap frequency. Within the immiscible phase the dynamical response of both components exhibits a resonant-like response at moderate quench amplitudes. This observation is in accordance with the single-component expansion dynamics discussed in [[6]]. For decreasing confinement different bosonic response regimes occur and accompanied by a lesser amount of fermionic ones. We found that the bosons either perform a breathing dynamics or solely expand, while the fermions tunnel between the nearest neighbor outer wells being located at the edges of the bosonic cloud or show a delocalized

behavior over the entire lattice. It has been further shown that within the single-orbital approximation the tunneling dynamics of both components cannot be adequately captured. Performing a correlation analysis on both the one- and two-body level for each species we have seen that during the evolution the predominantly occupied wells are one-body incoherent and two-body anti-correlated among each other, while within each well a correlated behavior for bosons and an anti-correlated one for fermions occurs. On the other hand, the dynamical response within the miscible phase of the Bose-Fermi mixture is greatly altered when compared to the immiscible one. The bosons perform interwell tunneling reaching an almost steady state for long evolution times, while the fermions expand until the edges of the surrounding bosonic cloud where they are partly transmitted and partly reflected back towards the central wells. Finally, the dependence of the expansion dynamics on the mass imbalance between the two components and the potential barrier height has been examined. We found that for mass imbalanced mixtures the heavy component remains almost unperturbed, while upon increasing the height of the potential barrier the expansion dynamics becomes suppressed. A straightforward extension of the present work is to explore the dynamics of the Bose-Fermi mixture which is induced by a quench from strong-to-weak confinement only for the fermionic ensemble thus letting the bosons unaffected. Here, the bosonic system may act as a filter which absorbs completely or partly the momentum of the expanded fermions depending on the quench amplitude. Another intriguing prospect is to examine the dynamics of a dipolar Bose-Fermi mixture [438–441] under the quench protocol considered herein, and reveal the different response regimes which appear for varying quench amplitude or initial phase so as to explore the possibility to induce a ballistic expansion.

Acknowledgements

First and foremost, I would like to thank the supervisor of my thesis, Professor Peter Schmelcher, for introducing me into the field of Ultracold atoms, his support and guidance in my doctoral research as well as for letting me explore and make mistakes.

I am also very grateful to Professor Panagiotis Kevrekidis for several discussions and the fruitful collaboration. It has also been a great pleasure to work and exchange knowledge with the other members of Professor Schmelcher's group including Georgios, Garyfallia, Johannes, Valentin, Alexandra, Lushuai, Aritra, Sven, Jan, Thomas, Antonio, Thomas, Andrea, Malte, Markus, Christian F., Christian M., Kevin, Fabian and Maxim. I am indebted to Alexandra Zampetaki, Christian Morfonios, Garyfallia Katsimiga and Georgios Koutentakis for proof-reading this thesis. I am heartfully thankful to my friends and colleagues Panos, Christian, Garyfallia, Alexandra and Georgios for many extended and insightful discussions and their support. Outside of my direct scientific environment I had the pleasure to meet many people which with their friendship have contributed to my moments of joy. Many thanks to all of my friends both near and far.

I have been also privileged to work with the incredible graduate students: J. Neuhaus-Steinmetz, T. Plaßmann, P. Siegl and J. Erdmann. Many thanks to all of them for their work and scientific interactions. I am particularly grateful to my closest collaborators and friends Georgios Koutentakis and Garyfallia Katsimiga for their support, work and enlightening discussions. Their contribution and physical insights to all of our common projects were more than significant. Thank you very much for everything! Last but not least I am also grateful to Dr. Antonio Negretti, Dr. Thomas Wulf and Prof. Lushuai Cao for the nice collaborations that we had in the field of driven lattices and quench dynamics.

I am grateful for generous financial support from the University of Hamburg under the PhD Scholarship Hamburgisches Gesetz zur Förderung des wissenschaftlichen und künstlerischen Nachwuchses (HmbNFG) as well as the Deutsche Forschungsgemeinschaft (DFG) in the framework of the SFB 925 "Light induced dynamics and control of correlated quantum systems".

Finally, there is an immense debt I owe to my Parents and my brother. Their support and encouragement allowed for my entire education.

Bibliography

- [1] C.J. Pethick, and H. Smith, Bose-Einstein condensation in dilute gases, Cambridge university press (2002).
- [2] L. Pitaevskii, and S. Stringari, Bose-Einstein condensation and superfluidity, Vol. 164, Oxford University Press (2016).
- [3] P.G. Kevrekidis, D.J. Frantzeskakis, and R. Carretero-González, Emergent nonlinear phenomena in Bose-Einstein condensates: theory and experiment, Vol. 45, Springer Science & Business Media (2007).
- [4] S. Inouye, M.R. Andrews, J. Stenger, H.J. Miesner, D.M. Stamper-Kurn, and W. Ketterle, Observation of Feshbach resonances in a Bose-Einstein condensate, *Nature* **392**, 151 (1998).
- [5] T. Köhler, K. Góral, and P.S. Julienne, Production of cold molecules via magnetically tunable Feshbach resonances, *Rev. Mod. Phys.* **78**, 1311 (2006).
- [6] C. Chin, R. Grimm, P. Julienne, and E. Tiesinga, Feshbach resonances in ultracold gases, *Rev. Mod. Phys.* **82**, 1225 (2010).
- [7] J.I. Kim, V.S. Melezhik, and P. Schmelcher, Suppression of quantum scattering in strongly confined systems, *Phys. Rev. Lett.* **97**, 193203 (2006).
- [8] P. Giannakeas, V.S. Melezhik, and P. Schmelcher, Dipolar confinement-induced resonances of ultracold gases in waveguides, *Phys. Rev. Lett.* **111**, 183201 (2013).
- [9] O. Morsch, and M. Oberthaler, Dynamics of Bose-Einstein condensates in optical lattices, *Rev. Mod. Phys.* **78**, 179 (2006).
- [10] F. Serwane, G. Zürn, T. Lompe, T.B. Ottenstein, A.N. Wenz, and S. Jochim, Deterministic preparation of a tunable few-fermion system, *Science* **332**, 336 (2011).
- [11] G. Zürn, F. Serwane, T. Lompe, A.N. Wenz, M.G. Ries, J.E. Bohn, and S. Jochim, Fermionization of two distinguishable fermions, *Phys. Rev. Lett.* **108**, 075303 (2012).
- [12] A.N. Wenz, G. Zürn, S. Murmann, I. Brouzos, T. Lompe, and S. Jochim, From few to many: Observing the formation of a Fermi sea one atom at a time, *Science* **342**, 457 (2013).
- [13] A.M. Kaufman, B.J. Lester, M. Foss-Feig, M.L. Wall, A.M. Rey, and C.A. Regal, Entangling two transportable neutral atoms via local spin exchange, *Nature* **527**, 208 (2015).
- [14] M. Endres, H. Bernien, A. Keesling, H. Levine, E.R. Anschuetz, A. Krajenbrink, C. Senko, V. Vuletic, M. Greiner, and M.D. Lukin, Atom-by-atom assembly of defect-free one-dimensional cold atom arrays, *Science* **aaah3752**, (2016).

- [15] M. Lewenstein, A. Sanpera, V. Ahufinger, B. Damski, A. Sen, and U. Sen, Ultracold atomic gases in optical lattices: mimicking condensed matter physics and beyond, *Advances In Physics*, **56**, 243 (2007).
- [16] I. Bloch, J. Dalibard, and W. Zwerger, Many-body physics with ultracold gases, *Rev. Mod. Phys.* **80**, 885 (2008).
- [17] V.I. Yukalov, Cold bosons in optical lattices, *Laser Phys.* **19**, 1 (2009).
- [18] M. Lewenstein, A. Sanpera, and V. Ahufinger, *Ultracold Atoms in Optical Lattices: Simulating quantum many-body systems*, Oxford University Press, (2012).
- [19] D. Jaksch, C. Bruder, J.I. Cirac, C.W. Gardiner, and P. Zoller, Cold bosonic atoms in optical lattices, *Phys. Rev. Lett.* **81**, 3108 (1998).
- [20] M.P. Fisher, P.B. Weichman, G. Grinstein, and D.S. Fisher, Boson localization and the superfluid-insulator transition, *Phys. Rev. B* **40**, 546 (1989).
- [21] L. Fallani, J.E. Lye, V. Guarrera, C. Fort, and M. Inguscio, Ultracold atoms in a disordered crystal of light: Towards a bose glass, *Phys. Rev. Lett.* **98**, 130404 (2007).
- [22] B. Damski, J. Zakrzewski, L. Santos, P. Zoller, and M. Lewenstein, Atomic Bose and Anderson glasses in optical lattices, *Phys. Rev. Lett.* **91**, 080403 (2003).
- [23] M. Greiner, O. Mandel, T. Esslinger, T.W. Hänsch, and I. Bloch, Quantum phase transition from a superfluid to a Mott insulator in a gas of ultracold atoms, *Nature* **415**, 39 (2002).
- [24] T. Stöferle, H. Moritz, C. Schori, M. Köhl and T. Esslinger, Transition from a Strongly Interacting 1D Superfluid to a Mott Insulator, *Phys. Rev. Lett.* **92**, 130403 (2004).
- [25] M. Köhl, H. Moritz, T. Stöferle, C. Schori, and T. Esslinger, Superfluid to Mott insulator transition in one, two, and three dimensions, *J. L. Temp. Phys.* **138**, 635 (2005).
- [26] M.J. Mark, E. Haller, K. Lauber, J.G. Danzl, A.J. Daley, and H.C. Nägerl, Precision measurements on a tunable Mott insulator of ultracold atoms, *Phys. Rev. Lett.* **107**, 175301 (2011).
- [27] R. Jördens, N. Strohmaier, K. Günter, H. Moritz, and T. Esslinger, A Mott insulator of fermionic atoms in an optical lattice, *Nature* **455**, 204 (2008).
- [28] U. Schneider, L. Hackermüller, S. Will, T. Best, I. Bloch, T.A. Costi, R.W. Helmes, D. Rasch, and A. Rosch, Metallic and insulating phases of repulsively interacting fermions in a 3D optical lattice, *Science* **322**, 1520 (2008).
- [29] B. Paredes, A. Widera, V. Murg, O. Mandel, S. Fölling, I. Cirac, G.V. Shlyapnikov, T.W. Hänsch, and I. Bloch, Tonks-Girardeau gas of ultracold atoms in an optical lattice, *Nature* **429**, 277 (2004).

BIBLIOGRAPHY

- [30] T. Kinoshita, T. Wenger, and D.S. Weiss, Observation of a one-dimensional Tonks-Girardeau gas, *Science* **305**, 1125 (2004).
- [31] C. Chin, M. Bartenstein, A. Altmeyer, S. Riedl, S. Jochim, J.H. Denschlag, and R. Grimm, Observation of the pairing gap in a strongly interacting Fermi gas, *Science* **305**, 1128 (2004).
- [32] G.B. Partridge, W. Li, R.I. Kamar, Y.A. Liao, and R.G. Hulet, Pairing and phase separation in a polarized Fermi gas, *Science* **311**, 503 (2006).
- [33] V. Gurarie, and L. Radzihovsky, Resonantly paired fermionic superfluids, *Annals of Physics* **322**, 2 (2007).
- [34] J.K. Chin, D.E. Miller, Y. Liu, C. Stan, W. Setiawan, C. Sanner, K. Xu, and W. Ketterle, Evidence for superfluidity of ultracold fermions in an optical lattice, *Nature* **443**, 961 (2006).
- [35] G. Wirth, M. Ölschläger, and A. Hemmerich, Evidence for orbital superfluidity in the P-band of a bipartite optical square lattice, *Nature Phys.* **7**, 147 (2011).
- [36] P. Soltan-Panahi, D.S. Lühmann, J. Struck, P. Windpassinger, and K. Sengstock, Quantum phase transition to unconventional multi-orbital superfluidity in optical lattices, *Nature Phys.* **8**, 71 (2012).
- [37] S. Choudhury, and E.J. Mueller, Absence of the twisted superfluid state in a mean-field model of bosons on a honeycomb lattice, *Phys. Rev. A*, **87**, 033621 (2013).
- [38] M. Ölschläger, G. Wirth, and A. Hemmerich, Unconventional superfluid order in the f band of a bipartite optical square lattice, *Phys. Rev. Lett.* **106**, 015302 (2011).
- [39] N. Gemelke, X. Zhang, C.L. Hung, and C. Chin, In situ observation of incompressible mott-insulating domains in ultracold atomic gases, *Nature* **460**, 995 (2009).
- [40] W. Ketterle, D.S. Durfee, and D.M. Stamper-Kurn, Making, probing and understanding Bose-Einstein condensates, arXiv preprint cond-mat/**9904034** (1999).
- [41] M. Greiner, I. Bloch, O. Mandel, T.W. Hänsch, and T. Esslinger, Exploring phase coherence in a 2D lattice of Bose-Einstein condensates, *Phys. Rev. Lett.* **87**, 160405 (2001).
- [42] S. Fölling, F. Gerbier, A. Widera, O. Mandel, T. Gericke, and I. Bloch, Spatial quantum noise interferometry in expanding ultracold atom clouds, *Nature* **434**, 481 (2005).
- [43] T. Rom, T. Best, D. Van Oosten, U. Schneider, S. Fölling, B. Paredes, and I. Bloch, Free fermion antibunching in a degenerate atomic Fermi gas released from an optical lattice, *Nature* **444**, 733 (2006).

-
- [44] C.L. Hung, X. Zhang, L.C. Ha, S.K. Tung, N. Gemelke, and C. Chin, Extracting density-density correlations from in situ images of atomic quantum gases, *New J. Phys.* **13**, 075019 (2011).
- [45] M. Endres, M. Cheneau, T. Fukuhara, C. Weitenberg, P. Schauß, C. Gross, L. Mazza, M.C. Banuls, L. Pollet, I. Bloch, and S. Kuhr, Observation of correlated particle-hole pairs and string order in low-dimensional Mott insulators, *Science* **334**, 200 (2011).
- [46] M. Cheneau, P. Barmettler, D. Poletti, M. Endres, P. Schauß, T. Fukuhara, C. Gross, I. Bloch, C. Kollath, and S. Kuhr, Light-cone-like spreading of correlations in a quantum many-body system, *Nature* **481**, 484 (2012).
- [47] W.S. Bakr, J.I. Gillen, A. Peng, S. Fölling, and M. Greiner, A quantum gas microscope for detecting single atoms in a Hubbard-regime optical lattice, *Nature* **462**, 74 (2009).
- [48] J.F. Sherson, C. Weitenberg, M. Endres, M. Cheneau, I. Bloch, and S. Kuhr, Single-atom-resolved fluorescence imaging of an atomic mott insulator, *Nature* **467**, 68 (2010).
- [49] C. Weitenberg, M. Endres, J.F. Sherson, M. Cheneau, P. Schauß, T. Fukuhara, I. Bloch, and S. Kuhr, Single-spin addressing in an atomic Mott insulator, *Nature* **471**, 319 (2011).
- [50] C.A. Regal, and D.S. Jin, Measurement of positive and negative scattering lengths in a Fermi gas of atoms, *Phys. Rev. Lett.* **90**, 230404 (2003).
- [51] S. Gupta, Z. Hadzibabic, M.W. Zwierlein, C.A. Stan, K. Dieckmann, C.H. Schunck, E.G.M. Van Kempen, B.J. Verhaar, and W. Ketterle, Radio-frequency spectroscopy of ultracold fermions, *Science* **300**, 1723 (2003).
- [52] D. Clément, N. Fabbri, L. Fallani, C. Fort, and M. Inguscio, Exploring correlated 1D Bose gases from the superfluid to the Mott-insulator state by inelastic light scattering, *Phys. Rev. Lett.* **102**, 155301 (2009).
- [53] P.T. Ernst, S. Götze, J.S. Krauser, K. Pyka, D.S. Lühmann, D. Pfannkuche, and K. Sengstock, Probing superfluids in optical lattices by momentum-resolved Bragg spectroscopy, *Nature Phys.* **6**, 56 (2010).
- [54] S. Fölling, S. Trotzky, P. Cheinet, M. Feld, R. Saers, A. Widera, T. Müller, and I. Bloch, Direct observation of second-order atom tunnelling, *Nature* **448**, 1029 (2007).
- [55] M. Anderlini, P.J. Lee, B.L. Brown, J. Sebby-Strabley, W.D. Phillips, and J.V. Porto, Controlled exchange interaction between pairs of neutral atoms in an optical lattice, *Nature* **448**, 452 (2007).
- [56] S. Trotzky, P. Cheinet, S. Fölling, M. Feld, U. Schnorrberger, A.M. Rey, A. Polkovnikov, E.A. Demler, M.D. Lukin, and I. Bloch, Time-resolved observation and control of superexchange interactions with ultracold atoms in optical lattices, *Science* **319**, 295 (2008).

BIBLIOGRAPHY

- [57] M. Greiner, I. Bloch, O. Mandel, T.W. Hänsch, and T. Esslinger, Exploring phase coherence in a 2D lattice of Bose-Einstein condensates, *Phys. Rev. Lett.* **87**, 160405 (2001).
- [58] L. Tarruell, D. Greif, T. Uehlinger, G. Jotzu, and T. Esslinger, Creating, moving and merging Dirac points with a Fermi gas in a tunable honeycomb lattice, *Nature* **483**, 302 (2012).
- [59] C. Becker, P. Soltan-Panahi, J. Kronjäger, S. Dörscher, K. Bongs, and K. Sengstock, Ultracold quantum gases in triangular optical lattices, *New J. Phys.* **12**, 065025 (2010).
- [60] P. Soltan-Panahi, J. Struck, P. Hauke, A. Bick, W. Plenkers, G. Meineke, C. Becker, P. Windpassinger, M. Lewenstein, and K. Sengstock, Multi-component quantum gases in spin-dependent hexagonal lattices, *Nature Phys.* **7**, 434 (2011).
- [61] G.B. Jo, J. Guzman, C.K. Thomas, P. Hosur, A. Vishwanath, and D.M. Stamper-Kurn, Ultracold atoms in a tunable optical kagome lattice, *Phys. Rev. Lett.* **108**, 045305 (2012).
- [62] O. Dutta, M. Gajda, P. Hauke, M. Lewenstein, D.S. Lühmann, B.A. Malomed, T. Sowiński, and J. Zakrzewski, Non-standard Hubbard models in optical lattices: a review, *Rep. Prog. Phys.* **78**, 066001 (2015).
- [63] M. Łącki, D. Delande, and J. Zakrzewski, Dynamics of cold bosons in optical lattices: effects of higher Bloch bands, *New J. Phys.* **15**, 013062 (2013).
- [64] O. Jürgensen, Extended Hubbard models for ultracold atoms in optical lattices, (2015).
- [65] T.D. Kühner, and H. Monien, Phases of the one-dimensional Bose-Hubbard model, *Phys. Rev. B* **58**, R14741 (1998).
- [66] T.D. Kühner, S.R. White, and H. Monien, One-dimensional Bose-Hubbard model with nearest-neighbor interaction, *Phys. Rev. B* **61**, 12474 (2000).
- [67] P. Sengupta, L.P. Pryadko, F. Alet, M. Troyer, and G. Schmid, Supersolids versus phase separation in two-dimensional lattice bosons, *Phys. Rev. Lett.* **94**, 207202 (2005).
- [68] S. Wessel, Phase diagram of interacting bosons on the honeycomb lattice, *Phys. Rev. B* **75**, 174301 (2007).
- [69] J.Y. Gan, Y.C. Wen, J. Ye, T. Li, S.J. Yang, and Y. Yu, Extended Bose-Hubbard model on a honeycomb lattice, *Phys. Rev. B* **75**, 214509 (2007).
- [70] K.K. Ng, Y.C. Chen, and Y.C. Tzeng, Quarter-filled supersolid and solid phases in the extended Bose-Hubbard model, *J. Phys.: Cond. Matt.* **22**, 185601 (2010).
- [71] J.M. Kurdestany, R.V. Pai, and R. Pandit, The inhomogeneous extended Bose-Hubbard model: A mean-field theory, *Annalen der Physik* **524**, 234 (2012).

-
- [72] M. Maik, P. Hauke, O. Dutta, M. Lewenstein, and J. Zakrzewski, Density-dependent tunneling in the extended Bose-Hubbard model, *New J. Phys.* **15**, 113041 (2013).
- [73] O. Jürgensen, K. Sengstock, and D.S. Lühmann, Twisted complex superfluids in optical lattices, *Sc. Rep.* **5**, 12912 (2015).
- [74] L. Cao, S. Krönke, J. Stockhofe, J. Simonet, K. Sengstock, D.S. Lühmann, and P. Schmelcher, Beyond-mean-field study of a binary bosonic mixture in a state-dependent honeycomb lattice, *Phys. Rev. A* **91**, 043639 (2015).
- [75] P. Buonsante, V. Penna, and A. Vezzani, Fractional-filling loophole insulator domains for ultracold bosons in optical superlattices, *Phys. Rev. A* **70**, 061603 (2004).
- [76] P. Buonsante, and A. Vezzani, Cell strong-coupling perturbative approach to the phase diagram of ultracold bosons in optical superlattices, *Phys. Rev. A* **72**, 013614 (2005).
- [77] I. Danshita, J.E. Williams, C.S. de Melo, and C.W. Clark, Quantum phases of bosons in double-well optical lattices, *Phys. Rev. A* **76**, 043606 (2007).
- [78] D. Muth, A. Mering, and M. Fleischhauer, Ultracold bosons in disordered superlattices: Mott insulators induced by tunneling, *Phys. Rev. A* **77**, 043618 (2008).
- [79] O. Jürgensen, J. Heinze, and D.S. Lühmann, Large-amplitude superexchange of high-spin fermions in optical lattices, *New J. Phys.* **15**, 113017 (2013).
- [80] J.Y. Gan, Y.C. Wen, and Y. Yu, Supersolidity and phase diagram of soft-core bosons on a triangular lattice, *Phys. Rev. B* **75**, 094501 (2007).
- [81] A.J. Leggett, Can a solid be “superfluid”?, *Phys. Rev. Lett.* **25**, 1543 (1970).
- [82] T. Leggett, Superfluidity in a Crystal?, *Science* **305**, 1921 (2004).
- [83] G.G. Batrouni, and R.T. Scalettar, Phase separation in supersolids, *Phys. Rev. Lett.* **84**, 1599 (2000).
- [84] N. Prokof’ev, What makes a crystal supersolid?, *Adv. Phys.* **56**, 381 (2007).
- [85] D.S. Lühmann, O. Jürgensen, and K. Sengstock, Multi-orbital and density-induced tunneling of bosons in optical lattices, *New J. Phys.* **14**, 033021 (2012).
- [86] K. Günter, T. Stöferle, H. Moritz, M. Köhl, and T. Esslinger, Bose-Fermi mixtures in a three-dimensional optical lattice, *Phys. Rev. Lett.* **96**, 180402 (2006).
- [87] S. Ospelkaus, C. Ospelkaus, O. Wille, M. Succo, P. Ernst, K. Sengstock, and K. Bongs, Localization of bosonic atoms by fermionic impurities in a three-dimensional optical lattice, *Phys. Rev. Lett.* **96**, 180403 (2006).
- [88] J. Heinze, S. Götze, J.S. Krauser, B. Hundt, N. Fläschner, D.S. Lühmann, C. Becker, and K. Sengstock, Multiband spectroscopy of ultracold fermions: observation of reduced tunneling in attractive Bose-Fermi mixtures, *Phys. Rev. Lett.* **107**, 135303 (2011).

BIBLIOGRAPHY

- [89] J.E. Hirsch, Inapplicability of the Hubbard model for the description of real strongly correlated electrons, *Physica B: Cond. Matt.* **199**, 366 (1994).
- [90] R. Strack, and D. Vollhardt, Hubbard model with nearest-neighbor and bond-charge interaction: Exact ground-state solution in a wide range of parameters, *Phys. Rev. Lett.* **70**, 2637 (1993).
- [91] O. Jürgensen, F. Meinert, M.J. Mark, H.C. Nägerl, and D.S. Lühmann, Observation of density-induced tunneling, *Phys. Rev. Lett.* **113**, 193003 (2014).
- [92] D. Raventós, T. Graß, M. Lewenstein, and B. Juliá-Díaz, Cold bosons in optical lattices: a tutorial for exact diagonalization, *J. Phys. B: At. Mol. Opt. Phys.* **50**, 113001 (2017).
- [93] J.K. Freericks, and H. Monien, Phase diagram of the Bose-Hubbard model, *EPL* **26**, 545 (1994).
- [94] J.K. Freericks, and H. Monien, Strong-coupling expansions for the pure and disordered bose-hubbard model, *Phys. Rev. B* **53**, 2691 (1996).
- [95] D.S. Rokhsar, and B.G. Kotliar, Gutzwiller projection for bosons, *Phys. Rev. B* **44**, 10328 (1991).
- [96] O. Jürgensen, K. Sengstock, and D.S. Lühmann, Density-induced processes in quantum gas mixtures in optical lattices, *Phys. Rev. A* **86**, 043623 (2012).
- [97] L. Cao, V. Bolsinger, S.I. Mistakidis, G.M. Koutentakis, S. Krönke, J.M. Schurer, and P. Schmelcher, A unified ab initio approach to the correlated quantum dynamics of ultracold fermionic and bosonic mixtures, *J. Chem. Phys.* **147**, 044106 (2017).
- [98] V.J. Bolsinger, S. Krönke, and P. Schmelcher, Beyond mean-field dynamics of ultra-cold bosonic atoms in higher dimensions: facing the challenges with a multi-configurational approach, *J. Phys. B: At. Mol. Opt. Phys.* **50**, 034003 (2017).
- [99] L. Cao, S. Krönke, O. Vendrell, and P. Schmelcher, The multi-layer multi-configuration time-dependent Hartree method for bosons: Theory, implementation, and applications, *J. Chem. Phys.* **139**, 134103 (2013).
- [100] S. Krönke, L. Cao, O. Vendrell, and P. Schmelcher, Non-equilibrium quantum dynamics of ultra-cold atomic mixtures: the multi-layer multi-configuration time-dependent Hartree method for bosons, *New J. Phys.* **15**, 063018 (2013).
- [101] A. Polkovnikov, K. Sengupta, A. Silva, and M. Vengalattore, Colloquium: Nonequilibrium dynamics of closed interacting quantum systems, *Rev. Mod. Phys.* **83**, 863 (2011).
- [102] T. Langen, R. Geiger, and J. Schmiedmayer, Ultracold atoms out of equilibrium, *Annu. Rev. Cond. Mat. Phys.* **6**, 201 (2015).
- [103] A. Mitra, Quantum quench dynamics, *Annu. Rev. Cond. Mat. Phys.* **9**, 245 (2018).

-
- [104] N. Andrei, Quench dynamics in integrable systems, arXiv:**1606.08911** (2016).
- [105] Y. Yanay, and E.J. Mueller, Evolution of coherence during ramps across the Mott-insulator-superfluid phase boundary, *Phys. Rev. A* **93**, 013622 (2016).
- [106] C. Kollath, A.M. Läuchli, and E. Altman, Quench dynamics and nonequilibrium phase diagram of the Bose-Hubbard model, *Phys. Rev. Lett.* **98**, 180601 (2007).
- [107] S. Braun, M. Friesdorf, S.S. Hodgman, M. Schreiber, J.P. Ronzheimer, A. Riera, M. del Rey, I. Bloch, J. Eisert, and U. Schneider, Emergence of coherence and the dynamics of quantum phase transitions, *Proc. Nat. Acad. Sc.* **112**, 3641 (2015).
- [108] F.M. Cucchiatti, B. Damski, J. Dziarmaga, and W.H. Zurek, Dynamics of the Bose-Hubbard model: Transition from a Mott insulator to a superfluid, *Phys. Rev. A* **75**, 023603 (2007).
- [109] P. Navez, and R. Schützhold, Emergence of coherence in the Mott-insulator-superfluid quench of the Bose-Hubbard model, *Phys. Rev. A* **82**, 063603 (2010).
- [110] J.P. Corson, *Dynamics of Quenched Ultracold Quantum Gases*, (2016).
- [111] J.P. Corson, and J.L. Bohn, Ballistic quench-induced correlation waves in ultracold gases, *Phys. Rev. A* **94**, 023604 (2016).
- [112] M. Rigol, V. Dunjko, and M. Olshanii, Thermalization and its mechanism for generic isolated quantum systems, *Nature* **452**, 854 (2008).
- [113] R. Nandkishore, and D.A. Huse, Many-body localization and thermalization in quantum statistical mechanics, *Annu. Rev. Condens. Matter Phys.* **6**, 15 (2015).
- [114] S. Trotzky, Y.A. Chen, A. Flesch, I.P. McCulloch, U. Schollwöck, J. Eisert, and I. Bloch, Probing the relaxation towards equilibrium in an isolated strongly correlated one-dimensional Bose gas, *Nature Phys.* **8**, 325 (2012).
- [115] M. Gring, M. Kuhnert, T. Langen, T. Kitagawa, B. Rauer, M. Schreitl, I. Mazets, D.A. Smith, E. Demler, and J. Schmiedmayer, Relaxation and prethermalization in an isolated quantum system, *Science* 1224953 (2012).
- [116] J. Dziarmaga, Dynamics of a quantum phase transition and relaxation to a steady state, *Adv. Phys.* **59**, 1063 (2010).
- [117] M. Eckstein, M. Kollar, and P. Werner, Thermalization after an interaction quench in the Hubbard model, *Phys. Rev. Lett.* **103**, 056403 (2009).
- [118] C. Gogolin, and J. Eisert, Equilibration, thermalisation, and the emergence of statistical mechanics in closed quantum systems, *Rep. Prog. Phys.* **79**, 056001 (2016).
- [119] T. Langen, R. Geiger, M. Kuhnert, B. Rauer, and J. Schmiedmayer, Local emergence of thermal correlations in an isolated quantum many-body system, *Nature Phys.* **9**, 640 (2013).

BIBLIOGRAPHY

- [120] F.H. Essler, and M. Fagotti, Quench dynamics and relaxation in isolated integrable quantum spin chains, *J. Stat. Mech.: Theory and Experiment*, **2016**, 064002 (2016).
- [121] M.A. Cazalilla, A. Iucci, and M.C. Chung, Thermalization and quantum correlations in exactly solvable models, *Phys. Rev. E* **85**, 011133 (2012).
- [122] M. Fagotti, and M. Collura, Universal prethermalization dynamics of entanglement entropies after a global quench, *arXiv:1507.02678* (2015).
- [123] M. Rigol, and M. Srednicki, Alternatives to eigenstate thermalization, *Phys. Rev. Lett.* **108**, 110601 (2012).
- [124] J. Dziarmaga, Dynamics of a quantum phase transition and relaxation to a steady state, *Adv. Phys.* **59**, 1063 (2010).
- [125] L.W. Clark, L. Feng, and C. Chin, Universal space-time scaling symmetry in the dynamics of bosons across a quantum phase transition, *Science* **354**, 606 (2016).
- [126] R. Schützhold, M. Uhlmann, Y. Xu, and U.R. Fischer, Sweeping from the superfluid to the Mott phase in the Bose-Hubbard model, *Phys. Rev. Lett.* **97**, 200601 (2006).
- [127] B. Gardas, J. Dziarmaga, and W.H. Zurek, Dynamics of the quantum phase transition in the one-dimensional Bose-Hubbard model: Excitations and correlations induced by a quench, *Phys. Rev. B* **95**, 104306 (2017).
- [128] K. Shimizu, Y. Kuno, T. Hirano, and I. Ichinose, Dynamics of a quantum phase transition in the Bose-Hubbard model: Kibble-Zurek mechanism and beyond, *Phys. Rev. A* **97**, 033626 (2018).
- [129] J. Dziarmaga, and W.H. Zurek, Quench in the 1D Bose-Hubbard model: Topological defects and excitations from the Kosterlitz-Thouless phase transition dynamics, *Sc. Rep.* **4**, 5950 (2014).
- [130] J. Beugnon, and N. Navon, Exploring the Kibble-Zurek mechanism with homogeneous Bose gases, *J. Phys. B: At. Mol. Opt. Phys.* **50**, 022002 (2017).
- [131] M. Anquez, B.A. Robbins, H.M. Bharath, M. Boguslawski, T.M. Hoang, and M.S. Chapman, Quantum Kibble-Zurek mechanism in a spin-1 Bose-Einstein condensate, *Phys. Rev. Lett.* **116**, 155301 (2016).
- [132] G. Lamporesi, S. Donadello, S. Serafini, F. Dalfovo, and G. Ferrari, Spontaneous creation of Kibble-Zurek solitons in a Bose-Einstein condensate, *Nature Phys.* **9**, 656 (2013).
- [133] M. Aidelsburger, J.L. Ville, R. Saint-Jalm, S. Nascimbéne, J. Dalibard, and J. Beugnon, Relaxation Dynamics in the Merging of N Independent Condensates, *Phys. Rev. Lett.* **119**, 190403 (2017).

-
- [134] Y.A. Chen, S. Nascimbene, M. Aidelsburger, M. Atala, S. Trotzky, and I. Bloch, Controlling correlated tunneling and superexchange interactions with ac-driven optical lattices, *Phys. Rev. Lett.* **107**, 210405 (2011).
- [135] S. Rosi, A. Bernard, N. Fabbri, L. Fallani, C. Fort, M. Inguscio, T. Calarco, and S. Montangero, Fast closed-loop optimal control of ultracold atoms in an optical lattice, *Phys. Rev. A* **88**, 021601 (2013).
- [136] M.K. Pedersen, J.J.W. Sørensen, M.C. Tichy, and J.F. Sherson, Many-body state engineering using measurements and fixed unitary dynamics, *New J. Phys.* **16**, 113038 (2014).
- [137] S. Van Frank, M. Bonneau, J. Schmiedmayer, S. Hild, C. Gross, M. Cheneau, I. Bloch, T. Pichler, A. Negretti, T. Calarco, and S. Montangero, Optimal control of complex atomic quantum systems, *Sc. Rep.* **6**, 34187 (2016).
- [138] M.C. Tichy, M.K. Pedersen, K. Mølmer, and J.F. Sherson, Nonadiabatic quantum state control of many bosons in few wells, *Phys. Rev. A* **87**, 063422 (2013).
- [139] N. Rach, S. Montangero, and M. Paternostro, Optimal control of many-body non-equilibrium quantum thermodynamics, arXiv:**1605.07476** (2016).
- [140] C. Brif, R. Chakrabarti, and H. Rabitz, Control of quantum phenomena, *Adv. Chem. Phys.* **148**, 1 (2011).
- [141] C. Brif, R. Chakrabarti, and H. Rabitz, Control of quantum phenomena: past, present and future, *New J. Phys.* **12**, 075008 (2010).
- [142] T. Kinoshita, T. Wenger, and D.S. Weiss, A quantum Newton's cradle, *Nature* **440**, 900 (2006).
- [143] S. Hofferberth, I. Lesanovsky, B. Fischer, T. Schumm, and J. Schmiedmayer, Non-equilibrium coherence dynamics in one-dimensional Bose gases, *Nature* **449**, 324 (2007).
- [144] M. Gring, M. Kuhnert, T. Langen, T. Kitagawa, B. Rauer, M. Schreitl, I. Mazets, D.A. Smith, E. Demler, and J. Schmiedmayer, Relaxation and prethermalization in an isolated quantum system, *Science* **337**, 1318 (2012).
- [145] J.P. Ronzheimer, M. Schreiber, S. Braun, S.S. Hodgman, S. Langer, I.P. McCulloch, F. Heidrich-Meisner, I. Bloch, and U. Schneider, Expansion dynamics of interacting bosons in homogeneous lattices in one and two dimensions, *Phys. Rev. Lett.* **110**, 205301 (2013).
- [146] J.P. Ronzheimer, Non-equilibrium dynamics of ultracold atoms in optical lattices, Doctoral dissertation, lmu, (2014).
- [147] C.D. Fertig, K.M. O'hara, J.H. Huckans, S.L. Rolston, W.D. Phillips, and J.V. Porto, Strongly inhibited transport of a degenerate 1D Bose gas in a lattice, *Phys. Rev. Lett.* **94**, 120403 (2005).

BIBLIOGRAPHY

- [148] H. Ott, E. De Mirandes, F. Ferlino, G. Roati, G. Modugno, and M. Inguscio, Collisionally induced transport in periodic potentials, *Phys. Rev. Lett.* **92**, 160601 (2004).
- [149] N. Strohmaier, Y. Takasu, K. Günter, R. Jördens, M. Köhl, H. Moritz, and T. Esslinger, Interaction-controlled transport of an ultracold Fermi gas, *Phys. Rev. Lett.* **99**, 220601 (2007).
- [150] U. Schneider, L. Hackermüller, J.P. Ronzheimer, S. Will, S. Braun, T. Best, I. Bloch, E. Demler, S. Mandt, D. Rasch, and A. Rosch, Fermionic transport and out-of-equilibrium dynamics in a homogeneous Hubbard model with ultracold atoms, *Nature Phys.* **8**, 213 (2012).
- [151] D. Chen, M. White, C. Borries, and B. DeMarco, Quantum quench of an atomic Mott insulator, *Phys. Rev. Lett.* **106**, 235304 (2011).
- [152] D. Chen, M. White, C. Borries, and B. DeMarco, Quantum quench of an atomic Mott insulator, *Phys. Rev. Lett.* **106**, 235304 (2011).
- [153] C. Meldgin, Dynamics of ultracold bosons in a disordered optical lattice, Doctoral dissertation, University of Illinois at Urbana-Champaign, (2016).
- [154] J.C. Halimeh, Frustrated magnetism, quench dynamics, and out-of-equilibrium criticality in quantum many-body lattices, Doctoral dissertation, lmu, (2017).
- [155] G. Rigolin, and G. Ortiz, Adiabatic perturbation theory and geometric phases for degenerate systems, *Phys. Rev. Lett.* **104**, 170406 (2010).
- [156] S.R. Manmana, S. Wessel, R.M. Noack, and A. Muramatsu, Strongly correlated fermions after a quantum quench, *Phys. Rev. Lett.* **98**, 210405 (2007).
- [157] A. Peres, Ergodicity and mixing in quantum theory. I, *Phys. Rev. A* **30**, 504 (1984).
- [158] M. Rigol, Breakdown of thermalization in finite one-dimensional systems, *Phys. Rev. Lett.* **103**, 100403 (2009).
- [159] J.M. Deutsch, Quantum statistical mechanics in a closed system, *Phys. Rev. A* **43**, 2046 (1991).
- [160] M. Srednicki, Chaos and quantum thermalization, *Phys. Rev. E* **50**, 888 (1994).
- [161] G. Biroli, C. Kollath, and A. Laeuchli, Does thermalization occur in an isolated system after a global quantum quench, arXiv:**0907.3731**, (2009).
- [162] J. Grond, A.I. Streltsov, L.S. Cederbaum, and O.E. Alon, Excitation spectra of fragmented condensates by linear response: General theory and application to a condensate in a double-well potential, *Phys. Rev. A* **86**, 063607 (2012).
- [163] J. Grond, A.I. Streltsov, A.U. Lode, K. Sakmann, L.S. Cederbaum, and O.E. Alon, Excitation spectra of many-body systems by linear response: General theory and applications to trapped condensates, *Phys. Rev. A* **88**, 023606 (2013).

-
- [164] O.E. Alon, A.I. Streltsov, and L.S. Cederbaum, Unified view on linear response of interacting identical and distinguishable particles from multiconfigurational time-dependent Hartree methods, *J. Chem. Phys.* **140**, 034108 (2014).
- [165] O.E. Alon, Many-body excitation spectra of trapped bosons with general interaction by linear response, *J. Phys.: Conf. Ser.* **594**, 012039 (2015).
- [166] M. Theisen, and A.I. Streltsov, Many-body excitations and deexcitations in trapped ultracold bosonic clouds, *Phys. Rev. A* **94**, 053622 (2016).
- [167] R. Beinke, S. Klaiman, L.S. Cederbaum, A.I. Streltsov, and O.E. Alon, Many-body effects in the excitation spectrum of weakly interacting Bose-Einstein condensates in one-dimensional optical lattices, *Phys. Rev. A* **95**, 063602 (2017).
- [168] N. Proukakis, S. Gardiner, M. Davis, and M. Szymaska, *Quantum gases: finite temperature and non-equilibrium dynamics*, **1**, World Scientific (2013).
- [169] J. Kinnunen, and P. Törmä, Beyond linear response spectroscopy of ultracold Fermi gases, *Phys. Rev. Lett.* **96**, 070402 (2006).
- [170] N. Goldman, and J. Dalibard, Periodically driven quantum systems: effective Hamiltonians and engineered gauge fields, *Phys. Rev. X* **4**, 031027 (2014).
- [171] N. Goldman, J. Dalibard, M. Aidelsburger, and N.R. Cooper, Periodically driven quantum matter: The case of resonant modulations, *Phys. Rev. A* **91**, 033632 (2015).
- [172] N. Gemelke, E. Sarajlic, Y. Bidel, S. Hong, and S. Chu, Parametric amplification of matter waves in periodically translated optical lattices, *Phys. Rev. Lett.* **95**, 170404 (2005).
- [173] K.M. Hilligsøe, and K. Mølmer, Phase-matched four wave mixing and quantum beam splitting of matter waves in a periodic potential, *Phys. Rev. A* **71**, 041602 (2005).
- [174] R. Lopes, A. Imanaliev, A. Aspect, M. Cheneau, D. Boiron, and C.I. Westbrook, Atomic Hong-Ou-Mandel experiment, *Nature* **520**, 66 (2015).
- [175] C.V. Parker, L.C. Ha, and C. Chin, Direct observation of effective ferromagnetic domains of cold atoms in a shaken optical lattice, *Nature Phys.* **9**, 769 (2013).
- [176] S. Choudhury, and E.J. Mueller, Stability of a Floquet Bose-Einstein condensate in a one-dimensional optical lattice, *Phys. Rev. A* **90**, 013621 (2014).
- [177] W. Zheng, and H. Zhai, Floquet topological states in shaking optical lattices, *Phys. Rev. A* **89**, 061603 (2014).
- [178] A. Eckardt, C. Weiss, and M. Holthaus, Superfluid-insulator transition in a periodically driven optical lattice, *Phys. Rev. Lett.* **95**, 260404 (2005).

BIBLIOGRAPHY

- [179] H. Lignier, C. Sias, D. Ciampini, Y. Singh, A. Zenesini, O. Morsch, and E. Arimondo, Dynamical control of matter-wave tunneling in periodic potentials, *Phys. Rev. Lett.* **99**, 220403 (2007).
- [180] J. Struck, C. Ölschläger, M. Weinberg, P. Hauke, J. Simonet, A. Eckardt, M. Lewenstein, K. Sengstock, and P. Windpassinger, Tunable gauge potential for neutral and spinless particles in driven optical lattices, *Phys. Rev. Lett.* **108**, 225304 (2012).
- [181] J. Struck, M. Weinberg, C. Ölschläger, P. Windpassinger, J. Simonet, K. Sengstock, R. Höppner, P. Hauke, A. Eckardt, M. Lewenstein, and L. Mathey, Engineering Ising-XY spin-models in a triangular lattice using tunable artificial gauge fields, *Nature Phys.* **9**, 738 (2013).
- [182] J. Struck, Artificial Gauge Fields in Driven Optical Lattices-From Frustrated XY Models to Ising Ferromagnetism, (2013).
- [183] M. Aidelsburger, Artificial gauge fields with ultracold atoms in optical lattices, Springer, (2015).
- [184] C. Schori, T. Stöferle, H. Moritz, M. Köhl, and T. Esslinger, Excitations of a superfluid in a three-dimensional optical lattice, *Phys. Rev. Lett.* **93**, 240402 (2004).
- [185] D. Greif, L. Tarruell, T. Uehlinger, R. Jördens and T. Esslinger, Probing Nearest-Neighbor Correlations of Ultracold Fermions in an Optical Lattice, *Phys. Rev. Lett.* **106**, 145302 (2011).
- [186] R. Ma, M. Tai, P. Preiss, W. Bakr, J. Simon and M. Greiner, Photon-Assisted Tunneling in a Biased Strongly Correlated Bose Gas, *Phys. Rev. Lett.* **107**, 095301 (2011).
- [187] W. Bakr, P. Preiss, M. Tai, R. Ma, J. Simon and M. Greiner, Orbital excitation blockade and algorithmic cooling in quantum gases, *Nature* **480**, 500 (2011).
- [188] F. Grossmann, T. Dittrich, P. Jung and P. Hänggi, Coherent destruction of tunneling, *Phys. Rev. Lett.* **67**, 516 (1991).
- [189] F. Großmann and P. Hänggi, Localization in a Driven Two-Level Dynamics, *EPL* **18**, 571 (1992).
- [190] M. Holthaus, Collapse of minibands in far-infrared irradiated superlattices, *Phys. Rev. Lett.* **69**, 351 (1992).
- [191] X.-G. Zhao, The suppression of a Bloch band in a driving laser field, *J. Phys.: Condens. Matter* **6**, 2751 (1994).
- [192] D.I. Choi, and Q. Niu, Bose-Einstein condensates in an optical lattice, *Phys. Rev. Lett.* **82**, 2022 (1999).
- [193] M.B. Dahan, E. Peik, J. Reichel, Y. Castin, and C. Salomon, Bloch oscillations of atoms in an optical potential, *Phys. Rev. Lett.* **76**, 4508 (1996).

-
- [194] O. Morsch, J.H. Müller, M. Cristiani, D. Ciampini, and E. Arimondo, Bloch oscillations and mean-field effects of Bose-Einstein condensates in 1D optical lattices, *Phys. Rev. Lett.* **87**, 140402 (2001).
- [195] M. Cristiani, O. Morsch, J.H. Müller, D. Ciampini, and E. Arimondo, Experimental properties of Bose-Einstein condensates in one-dimensional optical lattices: Bloch oscillations, Landau-Zener tunneling, and mean-field effects, *Phys. Rev. A* **65**, 063612 (2002).
- [196] S.R. Wilkinson, C.F. Bharucha, K.W. Madison, Q. Niu, and M.G. Raizen, Observation of atomic Wannier-Stark ladders in an accelerating optical potential, *Phys. Rev. Lett.* **76**, 4512 (1996).
- [197] Q. Niu, X.G. Zhao, G.A. Georgakis, and M.G. Raizen, Atomic Landau-Zener tunneling and Wannier-Stark ladders in optical potentials, *Phys. Rev. Lett.* **76**, 4504 (1996).
- [198] C. Sträter, and A. Eckardt, Orbital-driven melting of a bosonic Mott insulator in a shaken optical lattice, *Phys. Rev. A* **91**, 053602 (2015).
- [199] M. Reitter, J. Näger, K. Wintersperger, C. Sträter, I. Bloch, A. Eckardt, and U. Schneider, Interaction dependent heating and atom loss in a periodically driven optical lattice, *Phys. Rev. Lett.* **119**, 200402 (2017).
- [200] S. Lellouch, M. Bukov, E. Demler, and N. Goldman, Parametric instability rates in periodically driven band systems, *Phys. Rev. X* **7**, 021015 (2017).
- [201] S. Lellouch, and N. Goldman, Parametric instabilities in resonantly-driven Bose-Einstein condensates, *Quantum Science and Technology*, **3**, 024011 (2018).
- [202] M. Reitter, Scattering processes in interacting Floquet systems, Doctoral dissertation, lmu, (2017).
- [203] C.J. Myatt, E.A. Burt, R.W. Ghrist, E.A. Cornell, and C.E. Wieman, Production of two overlapping Bose-Einstein condensates by sympathetic cooling, *Phys. Rev. Lett.* **78**, 586 (1997).
- [204] D.S. Hall, M.R. Matthews, C.E. Wieman, and E.A. Cornell, Measurements of relative phase in two-component Bose-Einstein condensates, *Phys. Rev. Lett.* **81**, 1543 (1998).
- [205] H.J. Miesner, D.M. Stamper-Kurn, J. Stenger, S. Inouye, A.P. Chikkatur, and W. Ketterle, Observation of metastable states in spinor Bose-Einstein condensates, *Phys. Rev. Lett.* **82**, 2228 (1999).
- [206] T. Mishra, R.V. Pai, and B.P. Das, Phase separation in a two-species Bose mixture, *Phys. Rev. A* **76**, 013604 (2007).
- [207] P. Buonsante, S.M. Giampaolo, F. Illuminati, V. Penna, and A. Vezzani, Mixtures of strongly interacting bosons in optical lattices, *Phys. Rev. Lett.* **100**, 240402 (2008).

BIBLIOGRAPHY

- [208] A.B. Kuklov, and B.V. Svistunov, Counterflow superfluidity of two-species ultracold atoms in a commensurate optical lattice, *Phys. Rev. Lett.* **90**, 100401 (2003).
- [209] A. Hu, L. Mathey, I. Danshita, E. Tiesinga, C.J. Williams, and C.W. Clark, Counterflow and paired superfluidity in one-dimensional Bose mixtures in optical lattices, *Phys. Rev. A* **80**, 023619 (2009).
- [210] A. Hu, L. Mathey, C.J. Williams, and C.W. Clark, Noise correlations of one-dimensional Bose mixtures in optical lattices, *Phys. Rev. A* **81**, 063602 (2010).
- [211] S.B. Papp, J.M. Pino, and C.E. Wieman, Tunable miscibility in a dual-species Bose-Einstein condensate, *Phys. Rev. Lett.* **101**, 040402 (2008).
- [212] S. Tojo, Y. Taguchi, Y. Masuyama, T. Hayashi, H. Saito, and T. Hirano, Controlling phase separation of binary Bose-Einstein condensates via mixed-spin-channel Feshbach resonance, *Phys. Rev. A* **82**, 033609 (2010).
- [213] D.J. McCarron, H.W. Cho, D.L. Jenkin, M.P. Köppinger, and S.L. Cornish, Dual-species Bose-Einstein condensate of ^{87}Rb and ^{133}Cs , *Phys. Rev. A* **84**, 011603 (2011).
- [214] Y. Kawaguchi, and M. Ueda, Spinor Bose-Einstein condensates, *Phys. Rep.* **520**, 253 (2012).
- [215] D.S. Petrov, Quantum mechanical stabilization of a collapsing Bose-Bose mixture, *Phys. Rev. Lett.* **115**, 155302 (2015).
- [216] C.R. Cabrera, L. Tanzi, J. Sanz, B. Naylor, P. Thomas, P. Cheiney, and L. Tarruell, Quantum liquid droplets in a mixture of Bose-Einstein condensates, *Science* **359**, 301 (2018).
- [217] P. Cheiney, C.R. Cabrera, J. Sanz, B. Naylor, L. Tanzi, and L. Tarruell, Bright soliton to quantum droplet transition in a mixture of Bose-Einstein condensates, *arXiv:1710.11079* (2017).
- [218] G. Semeghini, G. Ferioli, L. Masi, C. Mazzinghi, L. Wolswijk, F. Minardi, M. Modugno, G. Modugno, M. Inguscio, and M. Fattori, Self-bound quantum droplets in atomic mixtures, *arXiv:1710.10890* (2017).
- [219] O.E. Alon, A.I. Streltsov, and L.S. Cederbaum, Demixing of bosonic mixtures in optical lattices from macroscopic to microscopic scales, *Phys. Rev. Lett.* **97**, 230403 (2006).
- [220] S. Zöllner, H.D. Meyer, and P. Schmelcher, Composite fermionization of one-dimensional Bose-Bose mixtures, *Phys. Rev. A* **78**, 013629 (2008).
- [221] T. Roscilde, and J.I. Cirac, Quantum emulsion: a glassy phase of bosonic mixtures in optical lattices, *Phys. Rev. Lett.* **98**, 190402 (2007).
- [222] A. Kleine, C. Kollath, I.P. McCulloch, T. Giamarchi, and U. Schollwöck, Spin-charge separation in two-component Bose gases, *Phys. Rev. A* **77**, 013607 (2008).

-
- [223] M.A. Cazalilla, and A.F. Ho, Instabilities in binary mixtures of one-dimensional quantum degenerate gases, *Phys. Rev. Lett.* **91**, 150403 (2003).
- [224] E. Nicklas, M. Karl, M. Höfer, A. Johnson, W. Muessel, H. Strobel, J. Tomkoviö, T. Gasenzer, and M.K. Oberthaler, Observation of scaling in the dynamics of a strongly quenched quantum gas, *Phys. Rev. Lett.* **115**, 245301 (2015).
- [225] M. Karl, H. Cakir, J.C. Halimeh, M.K. Oberthaler, M. Kastner, and T. Gasenzer, Universal equilibrium scaling functions at short times after a quench, *Phys. Rev. E* **96**, 022110 (2017).
- [226] R.N. Bisset, R.M. Wilson, and C. Ticknor, Scaling of fluctuations in a trapped binary condensate, *Phys. Rev. A* **91**, 053613 (2015).
- [227] S. Inouye, J. Goldwin, M.L. Olsen, C. Ticknor, J.L. Bohn, and D.S. Jin, Observation of heteronuclear Feshbach resonances in a mixture of bosons and fermions, *Phys. Rev. Lett.* **93**, 183201 (2004).
- [228] Z. Hadzibabic, C.A. Stan, K. Dieckmann, S. Gupta, M.W. Zwierlein, A. Görlitz, and W. Ketterle, Two-species mixture of quantum degenerate Bose and Fermi gases, *Phys. Rev. Lett.* **88**, 160401 (2002).
- [229] A.G. Truscott, K.E. Strecker, W.I. McAlexander, G.B. Partridge, and R.G. Hulet, Observation of Fermi pressure in a gas of trapped atoms, *Science* **291**, 2570 (2001).
- [230] E.V. Kempen, B. Marcelis, and S.J.J.M.F. Kokkelmans, Formation of fermionic molecules via interisotope Feshbach resonances, *Phys. Rev. A* **70**, 050701 (2004).
- [231] K. Honda, Y. Takasu, T. Kuwamoto, M. Kumakura, Y. Takahashi, and T. Yabuzaki, Optical dipole force trapping of a fermion-boson mixture of ytterbium isotopes, *Phys. Rev. A* **66**, 021401 (2002).
- [232] Y. Takasu, K. Maki, K. Komori, T. Takano, K. Honda, M. Kumakura, T. Yabuzaki, and Y. Takahashi, Spin-singlet Bose-Einstein condensation of two-electron atoms, *Phys. Rev. Lett.* **91**, 040404 (2003).
- [233] K.K. Das, Bose-Fermi mixtures in one dimension, *Phys. Rev. Lett.* **90**, 170403 (2003).
- [234] L. Viverit, C.J. Pethick, and H. Smith, Zero-temperature phase diagram of binary boson-fermion mixtures, *Phys. Rev. A* **61**, 053605 (2000).
- [235] T. Miyakawa, H. Yabu, and T. Suzuki, Peierls instability, periodic Bose-Einstein condensates, and density waves in quasi-one-dimensional boson-fermion mixtures of atomic gases, *Phys. Rev. A* **70**, 013612 (2004).
- [236] H. Pu, W. Zhang, M. Wilkens, and P. Meystre, Phonon spectrum and dynamical stability of a dilute quantum degenerate Bose-Fermi mixture, *Phys. Rev. Lett.* **88**, 070408 (2002).

BIBLIOGRAPHY

- [237] X.J. Liu, and H. Hu, Collisionless and hydrodynamic excitations of trapped boson-fermion mixtures, *Phys. Rev. A* **67**, 023613 (2003).
- [238] A. Zujev, A. Baldwin, R.T. Scalettar, V.G. Rousseau, P.J.H. Denteneer, and M. Rigol, Superfluid and Mott-insulator phases of one-dimensional Bose-Fermi mixtures, *Phys. Rev. A* **78**, 033619 (2008).
- [239] O. Dutta, and M. Lewenstein, Unconventional superfluidity of fermions in Bose-Fermi mixtures, *Phys. Rev. A* **81**, 063608 (2010).
- [240] M. Cramer, J. Eisert, and F. Illuminati, Inhomogeneous atomic Bose-Fermi mixtures in cubic lattices, *Phys. Rev. Lett.* **93**, 190405 (2004).
- [241] M. Lewenstein, L. Santos, M.A. Baranov, and H. Fehrmann, Atomic Bose-Fermi mixtures in an optical lattice, *Phys. Rev. Lett.* **92**, 050401 (2004).
- [242] L. Mathey, D.W. Wang, W. Hofstetter, M.D. Lukin, and E. Demler, Luttinger liquid of polarons in one-dimensional boson-fermion mixtures, *Phys. Rev. Lett.* **93**, 120404 (2004).
- [243] H.P. Büchler, and G. Blatter, Supersolid versus phase separation in atomic Bose-Fermi mixtures, *Phys. Rev. Lett.* **91**, 130404 (2003).
- [244] I. Titvinidze, M. Snoek, and W. Hofstetter, Generalized dynamical mean-field theory for Bose-Fermi mixtures in optical lattices, *Phys. Rev. B* **79**, 144506 (2009).
- [245] A. Privitera, and W. Hofstetter, Polaronic slowing of fermionic impurities in lattice Bose-Fermi mixtures, *Phys. Rev. A* **82**, 063614 (2010).
- [246] M.A. García-March, B. Juliá-Díaz, G.E. Astrakharchik, J. Boronat, and A. Polls, Distinguishability, degeneracy, and correlations in three harmonically trapped bosons in one dimension, *Phys. Rev. A* **90**, 063605 (2014).
- [247] M.A. García-March, and T. Busch, Quantum gas mixtures in different correlation regimes, *Phys. Rev. A* **87**, 063633 (2013).
- [248] M. Pyzh, S. Krönke, C. Weitenberg, and P. Schmelcher, Spectral properties and breathing dynamics of a few-body Bose-Bose mixture in a 1D harmonic trap, *New J. Phys.* **20**, 015006 (2018).
- [249] Y. Hao, and S. Chen, Density-functional theory of two-component Bose gases in one-dimensional harmonic traps, *Phys. Rev. A* **80**, 043608 (2009).
- [250] M.A. García-March, B. Juliá-Díaz, G.E. Astrakharchik, T. Busch, J. Boronat, and A. Polls, Sharp crossover from composite fermionization to phase separation in microscopic mixtures of ultracold bosons, *Phys. Rev. A* **88**, 063604 (2013).
- [251] M.A. García-March, B. Juliá-Díaz, G.E. Astrakharchik, T. Busch, J. Boronat, and A. Polls, Quantum correlations and spatial localization in one-dimensional ultracold bosonic mixtures, *New J. Phys.* **16**, 103004 (2014).

- [252] A.C. Pflanze, S. Zöllner, and P. Schmelcher, Material-barrier tunnelling in one-dimensional few-boson mixtures, *J. Phys. B: At. Mol. Opt. Phys.* **42**, 231002 (2009).
- [253] A.C. Pflanze, S. Zöllner, and P. Schmelcher, Interspecies tunneling in one-dimensional Bose mixtures, *Phys. Rev. A* **81**, 023612 (2010).
- [254] B. Chatterjee, I. Brouzos, L. Cao, and P. Schmelcher, Few-boson tunneling dynamics of strongly correlated binary mixtures in a double well, *Phys. Rev. A* **85**, 013611 (2012).
- [255] S. Campbell, M.A. García-March, T. Fogarty, and T. Busch, Quenching small quantum gases: Genesis of the orthogonality catastrophe, *Phys. Rev. A* **90**, 013617 (2014).
- [256] J. Hubbard, Electron correlations in narrow energy bands, *Proc. R. Soc. Lond. A* **276**, 238 (1963).
- [257] G.F. Gribakin, and V.V. Flambaum, Calculation of the scattering length in atomic collisions using the semiclassical approximation, *Phys. Rev. A* **48**, 546 (1993).
- [258] L.D. Landau, and E.M. Lifshitz, *Quantum Mechanics*, Pergamon, New York (1987).
- [259] W. Krauth, M. Caffarel, and J.P. Bouchaud, Gutzwiller wave function for a model of strongly interacting bosons, *Phys. Rev. B* **45**, 3137 (1992).
- [260] K. Sheshadri, H.R. Krishnamurthy, R. Pandit, and T.V. Ramakrishnan, Superfluid and insulating phases in an interacting-boson model: Mean-field theory and the rpa, *EPL* **22**, 257 (1993).
- [261] D. Van Oosten, P. van der Straten, and H.T.C. Stoof, Quantum phases in an optical lattice, *Phys. Rev. A* **63**, 053601 (2001).
- [262] G.G. Batrouni, R.T. Scalettar, and G.T. Zimanyi, Quantum critical phenomena in one-dimensional Bose systems, *Phys. Rev. Lett.* **65**, 1765 (1990).
- [263] G.G. Batrouni, R.T. Scalettar, G.T. Zimanyi, and A.P. Kampf, Supersolids in the Bose-Hubbard Hamiltonian, *Phys. Rev. Lett.* **74**, 2527 (1995).
- [264] G.G. Batrouni, V. Rousseau, R.T. Scalettar, M. Rigol, A. Muramatsu, P.J.H. Denteneer, and M. Troyer, Mott domains of bosons confined on optical lattices, *Phys. Rev. Lett.* **89**, 117203 (2002).
- [265] P. Niyaz, R.T. Scalettar, C.Y. Fong, and G.G. Batrouni, Ground-state phase diagram of an interacting Bose model with near-neighbor repulsion, *Phys. Rev. B* **44**, 7143 (1991).
- [266] N.W. Ashcroft, and N.D. Mermin, *Solid State Physics*, Philadelphia, PA: Saunders (1976).
- [267] G.K. Campbell, J. Mun, M. Boyd, P. Medley, A.E. Leanhardt, L.G. Marcassa, D.E. Pritchard, and W. Ketterle, Imaging the Mott insulator shells by using atomic clock shifts, *Science* **313**, 649 (2006).

BIBLIOGRAPHY

- [268] M.J. Mark, E. Haller, K. Lauber, J.G. Danzl, A. Janisch, H.P. Büchler, A.J. Daley, and H.C. Nägerl, Preparation and spectroscopy of a metastable Mott-insulator state with attractive interactions, *Phys. Rev. Lett.* **108**, 215302 (2012).
- [269] S. Will, T. Best, U. Schneider, L. Hackermüller, D.S. Lühmann, and I. Bloch, Time-resolved observation of coherent multi-body interactions in quantum phase revivals, *Nature* **465**, 197 (2010).
- [270] F. Meinert, M.J. Mark, E. Kirilov, K. Lauber, P. Weinmann, A.J. Daley, and H.C. Nägerl, Quantum quench in an atomic one-dimensional Ising chain, *Phys. Rev. Lett.* **111**, 053003 (2013).
- [271] M. Anderlini, P.J. Lee, B.L. Brown, J. Sebby-Strabley, W.D. Phillips, and J.V. Porto, Controlled exchange interaction between pairs of neutral atoms in an optical lattice, *Nature* **448**, 452 (2007).
- [272] A. Browaeys, H. Häffner, C. McKenzie, S.L. Rolston, K. Helmerson, and W.D. Phillips, Transport of atoms in a quantum conveyor belt, *Phys. Rev. A* **72**, 053605 (2005).
- [273] M. Köhl, H. Moritz, T. Stöferle, K. Günter, and T. Esslinger, Fermionic atoms in a three dimensional optical lattice: Observing Fermi surfaces, dynamics, and interactions, *Phys. Rev. Lett.* **94**, 080403 (2005).
- [274] T. Müller, S. Fölling, A. Widera, and I. Bloch, State preparation and dynamics of ultracold atoms in higher lattice orbitals, *Phys. Rev. Lett.* **99**, 200405 (2007).
- [275] M. Ölschläger, T. Kock, G. Wirth, A. Ewerbeck, C.M. Smith, and A. Hemmerich, Interaction-induced chiral $p_x ip_y$ superfluid order of bosons in an optical lattice, *New J. Phys.* **15**, 083041 (2013).
- [276] M. Ölschläger, G. Wirth, T. Kock, and A. Hemmerich, Topologically induced avoided band crossing in an optical checkerboard lattice, *Phys. Rev. Lett.* **108**, 075302 (2012).
- [277] T. Best, S. Will, U. Schneider, L. Hackermüller, D. Van Oosten, I. Bloch, and D.S. Lühmann, Role of Interactions in Rb 87 K 40 Bose-Fermi Mixtures in a 3D Optical Lattice, *Phys. Rev. Lett.* **102**, 030408 (2009).
- [278] C. Ospelkaus, S. Ospelkaus, L. Humbert, P. Ernst, K. Sengstock, and K. Bongs, Ultracold heteronuclear molecules in a 3D optical lattice, *Phys. Rev. Lett.* **97**, 120402 (2006).
- [279] B. Pasquiou, G. Bismut, Q. Beaufils, A. Crubellier, E. Maréchal, P. Pedri, L. Vernac, O. Gorceix, and B. Laburthe-Tolra, Control of dipolar relaxation in external fields, *Phys. Rev. A* **81**, 042716 (2010).
- [280] B. Pasquiou, G. Bismut, E. Maréchal, P. Pedri, L. Vernac, O. Gorceix, and B. Laburthe-Tolra, Spin relaxation and band excitation of a dipolar Bose-Einstein condensate in 2D optical lattices, *Phys. Rev. Lett.* **106**, 015301 (2011).

-
- [281] A. De Paz, A. Sharma, A. Chotia, E. Marechal, J.H. Huckans, P. Pedri, L. Santos, O. Gorceix, L. Vernac, and B. Laburthe-Tolra, Nonequilibrium quantum magnetism in a dipolar lattice gas, *Phys. Rev. Lett.* **111**, 185305 (2013).
- [282] P.G. Kevrekidis, and D.J. Frantzeskakis, Solitons in coupled nonlinear Schrödinger models: A survey of recent developments, *Rev. Phys.* **1**, 140 (2016).
- [283] D.J. Frantzeskakis, Dark solitons in atomic Bose–Einstein condensates: from theory to experiments, *J. Phys. A* **43**, 213001 (2010).
- [284] M. Girardeau, and R. Arnowitt, Theory of many-boson systems: Pair theory, *Phys. Rev.* **113**, 755 (1959).
- [285] J. Dziarmaga, and K. Sacha, Bogoliubov theory of a Bose-Einstein condensate in the particle representation, *Phys. Rev. A* **67**, 033608 (2003).
- [286] J. Dziarmaga, and K. Sacha, Depletion of the dark soliton: The anomalous mode of the Bogoliubov theory, *Phys. Rev. A* **66**, 043620 (2002).
- [287] J. Dziarmaga, Z.P. Karkuszewski, and K. Sacha, Images of the dark soliton in a depleted condensate, *J. Phys. B: At. Mol. Opt. Phys.* **36**, 1217 (2003).
- [288] J. Dziarmaga, and K. Sacha, Images of a Bose-Einstein condensate: diagonal dynamical Bogoliubov vacuum, *J. Phys. B: At. Mol. Opt. Phys.* **39**, 57 (2005).
- [289] C.K. Law, P.T. Leung, and M.C. Chu, Quantum fluctuations of coupled dark solitons in a trapped Bose-Einstein condensate, *J. Phys. B: At. Mol. Opt. Phys.* **35**, 3583 (2002).
- [290] C.K. Law, Dynamic quantum depletion in phase-imprinted generation of dark solitons, *Phys. Rev. A* **68**, 015602 (2003).
- [291] R.V. Mishmash, I. Danshita, C.W. Clark, and L.D. Carr, Quantum many-body dynamics of dark solitons in optical lattices, *Phys. Rev. A* **80**, 053612 (2009).
- [292] D. Delande, and K. Sacha, Many-body matter-wave dark soliton, *Phys. Rev. Lett.* **112**, 040402 (2014).
- [293] A. Syrwid, and K. Sacha, Quantum dark solitons in a Bose gas confined in a hard-wall box, *Phys. Rev. A* **96**, 043602 (2017).
- [294] A. Syrwid, M. Brewczyk, M. Gajda, and K. Sacha, Single-shot simulations of dynamics of quantum dark solitons, *Phys. Rev. A* **94**, 023623 (2016).
- [295] A. Weller, J.P. Ronzheimer, C. Gross, J. Esteve, M.K. Oberthaler, D.J. Frantzeskakis, G. Theocharis, and P.G. Kevrekidis, Experimental observation of oscillating and interacting matter wave dark solitons, *Phys. Rev. Lett.* **101**, 130401 (2008).
- [296] G. Theocharis, A. Weller, J.P. Ronzheimer, C. Gross, M.K. Oberthaler, P.G. Kevrekidis, and D.J. Frantzeskakis, Multiple atomic dark solitons in cigar-shaped Bose-Einstein condensates, *Phys. Rev. A* **81**, 063604 (2010).

BIBLIOGRAPHY

- [297] H. Sakaguchi, and B.A. Malomed, Matter-wave solitons in nonlinear optical lattices, *Phys. Rev. E* **72**, 046610 (2005).
- [298] O.V. Borovkova, Y.V. Kartashov, L. Torner, and B.A. Malomed, Bright solitons from defocusing nonlinearities, *Phys. Rev. E* **84**, 035602 (2011).
- [299] T. Busch, and J.R. Anglin, Dark-bright solitons in inhomogeneous Bose-Einstein condensates, *Phys. Rev. Lett.* **87**, 010401 (2001).
- [300] C. Hamner, J.J. Chang, P. Engels, and M.A. Hoefer, Generation of dark-bright soliton trains in superfluid-superfluid counterflow, *Phys. Rev. Lett.* **106**, 065302 (2011).
- [301] D. Yan, J.J. Chang, C. Hamner, P.G. Kevrekidis, P. Engels, V. Achilleos, D.J. Frantzeskakis, R. Carretero-González, and P. Schmelcher, Multiple dark-bright solitons in atomic Bose-Einstein condensates, *Phys. Rev. A* **84**, 053630 (2011).
- [302] A. Álvarez, J. Cuevas, F.R. Romero, C. Hamner, J.J. Chang, P. Engels, P.G. Kevrekidis, and D.J. Frantzeskakis, Scattering of atomic dark-bright solitons from narrow impurities, *J. Phys. B: At. Mol. Opt. Phys.* **46**, 065302 (2013).
- [303] M.R. Matthews, B.P. Anderson, P.C. Haljan, D.S. Hall, C.E. Wieman, and E.A. Cornell, Vortices in a Bose-Einstein condensate, *Phys. Rev. Lett.* **83**, 2498 (1999).
- [304] K.W. Madison, F. Chevy, W. Wohlleben, and J. Dalibard, Vortex formation in a stirred Bose-Einstein condensate, *Phys. Rev. Lett.* **84**, 806 (2000).
- [305] J.R. Abo-Shaeer, C. Raman, J.M. Vogels, and W. Ketterle, Observation of vortex lattices in Bose-Einstein condensates, *Science* **292**, 476 (2001).
- [306] T.W. Neely, E.C. Samson, A.S. Bradley, M.J. Davis, and B.P. Anderson, Observation of vortex dipoles in an oblate Bose-Einstein condensate, *Phys. Rev. Lett.* **104**, 160401 (2010).
- [307] S. Donadello, S. Serafini, M. Tylutki, L.P. Pitaevskii, F. Dalfovo, G. Lamporesi, and G. Ferrari, Observation of solitonic vortices in Bose-Einstein condensates, *Phys. Rev. Lett.* **113**, 065302 (2014).
- [308] E.C. Samson, K.E. Wilson, Z.L. Newman, and B.P. Anderson, Deterministic creation, pinning, and manipulation of quantized vortices in a Bose-Einstein condensate, *Phys. Rev. A* **93**, 023603 (2016).
- [309] G.C. Katsimiga, G.M. Koutentakis, S.I. Mistakidis, P.G. Kevrekidis, and P. Schmelcher, Dark-bright soliton dynamics beyond the mean-field approximation, *New J. Phys.* **19**, 073004 (2017).
- [310] G.C. Katsimiga, S.I. Mistakidis, G.M. Koutentakis, P.G. Kevrekidis, and P. Schmelcher, Many-body quantum dynamics in the decay of bent dark solitons of Bose-Einstein condensates, *New J. Phys.* **19**, 123012 (2017).

-
- [311] M.A. Cazalilla, R. Citro, T. Giamarchi, E. Orignac, and M. Rigol, One dimensional bosons: From condensed matter systems to ultracold gases, *Rev. Mod. Phys.* **83**, 1405 (2011).
- [312] M.A. García-March, B. Juliá-Díaz, G.E. Astrakharchik, J. Boronat, and A. Polls, Distinguishability, degeneracy, and correlations in three harmonically trapped bosons in one dimension, *Phys. Rev. A* **90**, 063605 (2014).
- [313] S.R. White, Density matrix formulation for quantum renormalization groups, *Phys. Rev. Lett.* **69**, 2863 (1992).
- [314] S.R. White, Density-matrix algorithms for quantum renormalization groups, *Phys. Rev. B* **48**, 10345 (1993).
- [315] U. Schollwöck, The density-matrix renormalization group, *Rev. Mod. Phys.* **77**, 259 (2005).
- [316] U. Schollwöck, The density-matrix renormalization group in the age of matrix product states, *Ann. of Phys.* **326**, 96 (2011).
- [317] S.P. Rath, and R. Schmidt, Field-theoretical study of the Bose polaron, *Phys. Rev. A* **88**, 053632 (2013).
- [318] A.G. Volosniev, H.W. Hammer, and N.T. Zinner, Real-time dynamics of an impurity in an ideal Bose gas in a trap, *Phys. Rev. A* **92**, 023623 (2015).
- [319] G. Kordas, S.I. Mistakidis, and A.I. Karanikas, Coherent-state path integrals in the continuum, *Phys. Rev. A* **90**, 032104 (2014).
- [320] G.E. Astrakharchik, and S. Giorgini, Quantum Monte Carlo study of the three-to one-dimensional crossover for a trapped Bose gas, *Phys. Rev. A* **66**, 053614 (2002).
- [321] L.P. Ardila, and S. Giorgini, Impurity in a Bose-Einstein condensate: Study of the attractive and repulsive branch using quantum Monte Carlo methods, *Phys. Rev. A* **92**, 033612 (2015).
- [322] W. Li, and S.D. Sarma, Variational study of polarons in Bose-Einstein condensates, *Phys. Rev. A* **90**, 013618 (2014).
- [323] H.D. Meyer, U. Manthe, and L.S. Cederbaum, The multi-configurational time-dependent Hartree approach, *Chem. Phys. Lett.* **165**, 73 (1990).
- [324] M.H. Beck, A. Jäckle, G.A. Worth, and H.D. Meyer, The multiconfiguration time-dependent Hartree (MCTDH) method: a highly efficient algorithm for propagating wavepackets, *Phys. Rep.* **324**, 1 (2000).
- [325] S. Zöllner, H.D. Meyer, and P. Schmelcher, Ultracold few-boson systems in a double-well trap, *Phys. Rev. A* **74**, 053612 (2006).

BIBLIOGRAPHY

- [326] S. Zöllner, H.D. Meyer, and P. Schmelcher, Correlations in ultracold trapped few-boson systems: Transition from condensation to fermionization, *Phys. Rev. A* **74**, 063611 (2006).
- [327] S. Zöllner, H.D. Meyer, and P. Schmelcher, Excitations of few-boson systems in one-dimensional harmonic and double wells, *Phys. Rev. A* **75**, 043608 (2007).
- [328] S. Zöllner, H.D. Meyer, and P. Schmelcher, Tunneling dynamics of a few bosons in a double well, *Phys. Rev. A* **78**, 013621 (2008).
- [329] A.I. Streltsov, O.E. Alon, and L.S. Cederbaum, Role of excited states in the splitting of a trapped interacting Bose-Einstein condensate by a time-dependent barrier, *Phys. Rev. Lett.* **99**, 030402 (2007).
- [330] O.E. Alon, A.I. Streltsov, and L.S. Cederbaum, Multiconfigurational time-dependent Hartree method for bosons: Many-body dynamics of bosonic systems, *Phys. Rev. A* **77**, 033613 (2008).
- [331] A.I. Streltsov, O.E. Alon, and L.S. Cederbaum, General mapping for bosonic and fermionic operators in Fock space, *Phys. Rev. A* **81**, 022124 (2010).
- [332] A.I. Streltsov, O.E. Alon, and L.S. Cederbaum, General variational many-body theory with complete self-consistency for trapped bosonic systems, *Phys. Rev. A* **73**, 063626 (2006).
- [333] A.I. Streltsov, O.E. Alon, and L.S. Cederbaum, Formation and dynamics of many-boson fragmented states in one-dimensional attractive ultracold gases, *Phys. Rev. Lett.* **100**, 130401 (2008).
- [334] A.I. Streltsov, O.E. Alon, and L.S. Cederbaum, Swift loss of coherence of soliton trains in attractive Bose-Einstein condensates, *Phys. Rev. Lett.* **106**, 240401 (2011).
- [335] A.I. Streltsov, K. Sakmann, O.E. Alon, and L.S. Cederbaum, Accurate multi-boson long-time dynamics in triple-well periodic traps, *Phys. Rev. A* **83**, 043604 (2011).
- [336] K. Sakmann, Exact quantum dynamics of a bosonic Josephson junction. In *Many-Body Schrödinger Dynamics of Bose-Einstein Condensates*, pp. 65-80, Springer, Berlin, Heidelberg (2011).
- [337] K. Sakmann, A.I. Streltsov, O.E. Alon, and L.S. Cederbaum, Exact Quantum Dynamics of a Bosonic Josephson Junction, *Phys. Rev. Lett.* **103**, 220601 (2009).
- [338] K. Sakmann, Quantum dynamics of attractive versus repulsive bosonic Josephson junctions: Bose-Hubbard and full-Hamiltonian results, In *Many-Body Schrödinger Dynamics of Bose-Einstein Condensates*, pp. 81-88, Springer, Berlin, Heidelberg (2011).
- [339] K. Sakmann, A.I. Streltsov, O.E. Alon, and L.S. Cederbaum, Universality of fragmentation in the Schrödinger dynamics of bosonic Josephson junctions, *Phys. Rev. A* **89**, 023602 (2014).

- [340] G.M. Koutentakis, S.I. Mistakidis, and P. Schmelcher, Probing Ferromagnetic Order in Few-Fermion Correlated Spin-Flip Dynamics, arXiv:**1804.07199** (2018).
- [341] L. Cao, S.I. Mistakidis, X. Deng, and P. Schmelcher, Collective excitations of dipolar gases based on local tunneling in superlattices, *Chem. Phys.* **482** 303 (2017).
- [342] R. Horodecki, P. Horodecki, M. Horodecki, and K. Horodecki, Quantum entanglement, *Rev. Mod. Phys.* **81**, 865 (2009).
- [343] M. Horodecki, P. Horodecki, and R. Horodecki, Separability of n -particle mixed states: necessary and sufficient conditions in terms of linear maps, *Phys. Lett. A* **283**, 1 (2001).
- [344] M. Roncaglia, A. Montorsi, and M. Genovese, Bipartite entanglement of quantum states in a pair basis, *Phys. Rev. A* **90**, 062303 (2014).
- [345] S. Krönke, J. Knörzer, and P. Schmelcher, Correlated quantum dynamics of a single atom collisionally coupled to an ultracold finite bosonic ensemble, *New J. Phys.* **17**, 053001 (2015).
- [346] A. Peres, *Quantum theory: concepts and methods*, Vol. **57**, Springer Science & Business Media, (2006).
- [347] M. Lewenstein, D. Bruß, J.I. Cirac, B. Kraus, M. Kuś, J. Samsonowicz, A. Sanpera, and R. Tarrach, Separability and distillability in composite quantum systems—a primer, *J. Mod. Opt.* **47**, 2481 (2000).
- [348] J. Broeckhove, L. Lathouwers, E. Kesteloot, and P. Van Leuven, On the equivalence of time-dependent variational principles, *Chem. Phys. Lett.* **149**, 547 (1988).
- [349] A.D. McLachlan, A variational solution of the time-dependent Schrodinger equation, *Mol. Phys.* **8**, 39 (1964).
- [350] J. Frenkel, in *Wave Mechanics* 1st ed. (Clarendon Press, Oxford, 1934), pp. 423-428.
- [351] P. A. Dirac, *Proc. Camb. Phil. Soc.* **26**, 376, Cambridge University Press (1930).
- [352] E.J. Mueller, T.L. Ho, M. Ueda, and G. Baym, Fragmentation of bose-einstein condensates, *Phys. Rev. A* **74**, 033612 (2006).
- [353] O. Penrose, and L. Onsager, Bose-Einstein condensation and liquid helium, *Phys. Rev.* **104**, 576 (1956).
- [354] R. Roy, A. Gammal, M.C. Tsatsos, B. Chatterjee, B. Chakrabarti, and A.U. Lode, Phases, many-body entropy measures, and coherence of interacting bosons in optical lattices, *Phys. Rev. A* **97**, 043625 (2018).
- [355] S. Dutta, M.C. Tsatsos, S. Basu, and A.U. Lode, Management of the Correlations of Ultracold Bosons in Triple Wells, arXiv:**1802.02407** (2018).

BIBLIOGRAPHY

- [356] J.G. Cosme, C. Weiss, and J. Brand, Center-of-mass motion as a sensitive convergence test for variational multimode quantum dynamics, *Phys. Rev. A* **94**, 043603 (2016).
- [357] J.G. Cosme, Non-equilibrium dynamics from few-to many-body systems, Albany, New Zealand, Doctoral dissertation, Massey University (2017).
- [358] O.E. Alon, A.I. Streltsov, and L.S. Cederbaum, Unified view on multiconfigurational time propagation for systems consisting of identical particles, *J. Chem. Phys.* **127**, 154103 (2007).
- [359] K. Sakmann, and M. Kasevich, Single-shot simulations of dynamic quantum many-body systems, *Nature Phys.* **12**, 451 (2016).
- [360] A.U. Lode, and C. Bruder, Fragmented superradiance of a Bose-Einstein condensate in an optical cavity, *Phys. Rev. Lett.* **118**, 013603 (2017).
- [361] B. Chatterjee, and A.U. Lode, Order parameter and detection for crystallized dipolar bosons in lattices, *arXiv:1708.07409* (2017).
- [362] J.G. Cosme, M.F. Andersen, and J. Brand, Interaction blockade for bosons in an asymmetric double well, *Phys. Rev. A* **96**, 013616 (2017).
- [363] M. Olshanii, Atomic scattering in the presence of an external confinement and a gas of impenetrable bosons, *Phys. Rev. Lett.* **81**, 938 (1998).
- [364] I. Brouzos, S. Zöllner, and P. Schmelcher, Correlation versus commensurability effects for finite bosonic systems in one-dimensional lattices, *Phys. Rev. A* **81**, 053613 (2010).
- [365] C. Kollath, A.M. Läuchli, and E. Altman, Quench dynamics and nonequilibrium phase diagram of the Bose-Hubbard model, *Phys. Rev. Lett.* **98**, 180601 (2007).
- [366] J.S. Bernier, R. Citro, C. Kollath, and E. Orignac, Correlation dynamics during a slow interaction quench in a one-dimensional Bose gas, *Phys. Rev. Lett.* **112**, 065301 (2014).
- [367] F.H. Essler, S. Evangelisti, and M. Fagotti, Dynamical correlations after a quantum quench, *Phys. Rev. Lett.* **109**, 247206 (2012).
- [368] S.S. Natu, and E.J. Mueller, Dynamics of correlations in a dilute Bose gas following an interaction quench, *Phys. Rev. A* **87**, 053607 (2013).
- [369] W. Tschischik, R. Moessner, and M. Haque, Breathing mode in the Bose-Hubbard chain with a harmonic trapping potential, *Phys. Rev. A* **88**, 063636 (2013).
- [370] L.C. Venuti, and P. Zanardi, Unitary equilibrations: Probability distribution of the Loschmidt echo, *Phys. Rev. A* **81**, 022113 (2010).
- [371] T. Gorin, T. Prosen, T.H. Seligman, and M. Žnidarič, Dynamics of Loschmidt echoes and fidelity decay, *Phys. Rep.* **435**, 33 (2006).

-
- [372] J.W. Abraham, and M. Bonitz, Quantum Breathing Mode of Trapped Particles: From Nanoplasmas to Ultracold Gases, *Contributions to Plasma Physics* **54**, 27 (2014).
- [373] J.W. Abraham, K. Balzer, D. Hochstuhl, and M. Bonitz, Quantum breathing mode of interacting particles in a one-dimensional harmonic trap, *Phys. Rev. B* **86**, 125112 (2012).
- [374] J.W. Abraham, M. Bonitz, C. McDonald, G. Orlando, and T. Brabec, Quantum breathing mode of trapped systems in one and two dimensions, *New J. Phys.* **16**, 013001 (2014).
- [375] R. Schmitz, S. Krönke, L. Cao, and P. Schmelcher, Quantum breathing dynamics of ultracold bosons in one-dimensional harmonic traps: Unraveling the pathway from few-to many-body systems, *Phys. Rev. A* **88**, 043601 (2013).
- [376] P. Makotyn, C.E. Klauss, D.L. Goldberger, E.A. Cornell, and D.S. Jin, Universal dynamics of a degenerate unitary Bose gas, *Nature Phys.* **10**, 116 (2014).
- [377] L. Vidmar, S. Langer, I.P. McCulloch, U. Schneider, U. Schollwöck, and F. Heidrich-Meisner, Sudden expansion of Mott insulators in one dimension, *Phys. Rev. B* **88**, 235117 (2013).
- [378] M. Rigol, R.T. Scalettar, P. Sengupta, and G.G. Batrouni, Time-of-flight observables and the formation of Mott domains of fermions and bosons on optical lattices, *Phys. Rev. B* **73**, 121103 (2006).
- [379] P. Sengupta, M. Rigol, G.G. Batrouni, P.J.H. Denteneer, and R.T. Scalettar, Phase coherence, visibility, and the superfluid-Mott-insulator transition on one-dimensional optical lattices, *Phys. Rev. Lett.* **95**, 220402 (2005).
- [380] L. Chen, Z. Zhang, and Z. Liang, Non-equilibrium dynamics of an ultracold Bose gas under multi-pulsed interaction quenches, *Mod. Phys. Lett. B* **30**, 1650367 (2016).
- [381] S. Will, D. Iyer, and M. Rigol, Observation of coherent quench dynamics in a metallic many-body state of fermionic atoms, *Nature Commun.* **6**, 6009 (2015).
- [382] S.R. Clark, and D. Jaksch, Dynamics of the superfluid to Mott-insulator transition in one dimension, *Phys. Rev. A* **70**, 043612 (2004).
- [383] S.D. Huber, E. Altman, H.P. Büchler, and G. Blatter, Dynamical properties of ultracold bosons in an optical lattice, *Phys. Rev. B* **75**, 085106 (2007).
- [384] J.S. Bernier, D. Poletti, P. Barmettler, G. Roux, and C. Kollath, Slow quench dynamics of Mott-insulating regions in a trapped Bose gas, *Phys. Rev. A* **85**, 033641 (2012).
- [385] C.L. Hung, X. Zhang, N. Gemelke, and C. Chin, Slow mass transport and statistical evolution of an atomic gas across the superfluid-mott-insulator transition, *Phys. Rev. Lett.* **104**, 160403 (2010).

BIBLIOGRAPHY

- [386] F.M. Cucchietti, B. Damski, J. Dziarmaga, and W.H. Zurek, Dynamics of the Bose-Hubbard model: Transition from a Mott insulator to a superfluid, *Phys. Rev. A* **75**, 023603 (2007).
- [387] P.W. Anderson, Infrared catastrophe in Fermi gases with local scattering potentials, *Phys. Rev. Lett.* **18**, 1049 (1967).
- [388] M. Knap, A. Shashi, Y. Nishida, A. Imambekov, D.A. Abanin, and E. Demler, Time-dependent impurity in ultracold fermions: Orthogonality catastrophe and beyond, *Phys. Rev. X* **2**, 041020 (2012).
- [389] R. Yamazaki, S. Taie, S. Sugawa, and Y. Takahashi, Submicron spatial modulation of an interatomic interaction in a Bose-Einstein condensate, *Phys. Rev. Lett.* **105**, 050405 (2010).
- [390] S.G. Ali, S.K. Roy, and B. Talukdar, Stability of matter-wave solitons in optical lattices, *EPJ D* **59**, 269 (2010).
- [391] A.I. Nicolin, A. Balaz, J.B. Sudharsan, and R. Radha, Ground state of Bose-Einstein condensates with inhomogeneous scattering lengths, *Rom. J. Phys.* **59**, 204 (2014).
- [392] Y.V. Kartashov, B.A. Malomed, and L. Torner, Solitons in nonlinear lattices, *Rev. Mod. Phys.* **83**, 247 (2011).
- [393] P. G. Kevrekidis, R. Carretero-González, and D. J. Frantzeskakis, *Int. J. Mod. Phys. B* **31**, 1742013 (2017).
- [394] M. I. Rodas-Verde, H. Michinel, and V. M. Pérez-García, Controllable soliton emission from a Bose-Einstein condensate, *Phys. Rev. Lett.* **95**, 153903 (2005).
- [395] F. Tsitoura, P. Krüger, P. G. Kevrekidis, and D. J. Frantzeskakis, Scattering of matter waves in spatially inhomogeneous environments, *Phys. Rev. A* **91**, 033633 (2015).
- [396] C. Hang, and V. V. Konotop, All-optical steering of light via spatial Bloch oscillations in a gas of three-level atoms, *Phys. Rev. A* **81**, 053849 (2010).
- [397] M. Salerno, V. V. Konotop, and Y. V. Bludov, Long-living Bloch oscillations of matter waves in periodic potentials, *Phys. Rev. Lett.* **101**, 030405 (2008).
- [398] G. Theocharis, P. Schmelcher, P. G. Kevrekidis, and D. J. Frantzeskakis, Matter-wave solitons of collisionally inhomogeneous condensates, *Phys. Rev. A* **72**, 033614 (2005).
- [399] F. Kh. Abdullaev and M. Salerno, *J. Phys. B* **36**, 2851 (2003).
- [400] G. Theocharis, P. Schmelcher, P. G. Kevrekidis, and D. J. Frantzeskakis, *Phys. Rev. A* **74**, 053614 (2006).
- [401] Y.V. Bludov, V.A. Brazhnyi, and V.V. Konotop, Delocalizing transition in one-dimensional condensates in optical lattices due to inhomogeneous interactions, *Phys. Rev. A* **76**, 023603 (2007).

- [402] D. Hocker, J. Yan, and H. Rabitz, Optimal nonlinear coherent mode transitions in Bose-Einstein condensates utilizing spatiotemporal controls, *Phys. Rev. A* **93**, 053612 (2016).
- [403] V.M. Perez-Garcia, Nonlinear Suppression of Tunneling and Strong Localization in Bose-Einstein Condensates with Spatially Inhomogeneous Interactions, arXiv preprint nlin/0612028 (2006).
- [404] F.K. Abdullaev, A. Gammal, M. Salerno, and L. Tomio, Localized modes of binary mixtures of Bose-Einstein condensates in nonlinear optical lattices, *Phys. Rev. A* **77**, 023615 (2008).
- [405] A.I. Streltsov, Quantum systems of ultracold bosons with customized interparticle interactions, *Phys. Rev. A* **88**, 041602 (2013).
- [406] U.R. Fischer, A.U. Lode, and B. Chatterjee, Condensate fragmentation as a sensitive measure of the quantum many-body behavior of bosons with long-range interactions, *Phys. Rev. A* **91**, 063621 (2015).
- [407] B. Chatterjee, I. Brouzos, S. Zöllner, and P. Schmelcher, Few-boson tunneling in a double well with spatially modulated interaction, *Phys. Rev. A* **82**, 043619 (2010).
- [408] B. Chatterjee, I. Brouzos, L. Cao, and P. Schmelcher, Ultracold dipolar few-boson ensembles in a triple-well trap, *J. Phys. B: At. Mol. Opt. Phys.* **46**, 085304 (2013).
- [409] M. Theis, G. Thalhammer, K. Winkler, M. Hellwig, G. Ruff, R. Grimm, and J.H. Denschlag, Tuning the scattering length with an optically induced Feshbach resonance, *Phys. Rev. Lett.* **93**, 123001 (2004).
- [410] L.W. Clark, L.C. Ha, C.Y. Xu, and C. Chin, Quantum dynamics with spatiotemporal control of interactions in a stable Bose-Einstein condensate, *Phys. Rev. Lett.* **115**, 155301 (2015).
- [411] P.O. Fedichev, Y. Kagan, G.V. Shlyapnikov, and J.T.M. Walraven, Influence of nearly resonant light on the scattering length in low-temperature atomic gases, *Phys. Rev. Lett.* **77**, 2913 (1996).
- [412] P. Zupancic, P.M. Preiss, R. Ma, A. Lukin, M.E. Tai, M. Rispoli, R. Islam, and M. Greiner, Ultra-precise holographic beam shaping for microscopic quantum control, *Opt. Exp.* **24**, 13881 (2016).
- [413] M. Rigol, G.G. Batrouni, V.G. Rousseau, and R.T. Scalettar, State diagrams for harmonically trapped bosons in optical lattices, *Phys. Rev. A* **79**, 053605 (2009).
- [414] G.G. Batrouni, V. Rousseau, R.T. Scalettar, M. Rigol, A. Muramatsu, P.J.H. Denteneer, and M. Troyer, Mott domains of bosons confined on optical lattices, *Phys. Rev. Lett.* **89**, 117203 (2002).

BIBLIOGRAPHY

- [415] V.A. Kashurnikov, N.V. Prokof'ev, and B.V. Svistunov, Revealing the superfluid-Mott-insulator transition in an optical lattice, *Phys. Rev. A* **66**, 031601 (2002).
- [416] C. Kollath, U. Schollwöck, J. von Delft, and W. Zwerger, Spatial correlations of trapped one-dimensional bosons in an optical lattice, *Phys. Rev. A* **69**, 031601 (2004).
- [417] C. V. Parker, L.C. Ha, and C. Chin, Direct observation of effective ferromagnetic domains of cold atoms in a shaken optical lattice, *Nature Phys.* **9**, 769 (2013).
- [418] P.I. Schneider, and A. Saenz, Quantum computation with ultracold atoms in a driven optical lattice, *Phys. Rev. A* **85**, 050304 (2012).
- [419] M. Egorov, B. Opanchuk, P. Drummond, B.V. Hall, P. Hannaford, and A.I. Sidorov, Measurement of s -wave scattering lengths in a two-component Bose-Einstein condensate, *Phys. Rev. A* **87**, 053614 (2013).
- [420] M. Trippenbach, K. Góral, K. Rzazewski, B. Malomed, and Y.B. Band, Structure of binary Bose-Einstein condensates, *J. Phys. B: At. Mol. Opt. Phys.* **33**, 4017 (2000).
- [421] G. Filatrella, B.A. Malomed, and M. Salerno, Domain walls and bubble droplets in immiscible binary Bose gases, *Phys. Rev. A* **90**, 043629 (2014).
- [422] S. De, D.L. Campbell, R.M. Price, A. Putra, B.M. Anderson, and I.B. Spielman, Quenched binary Bose-Einstein condensates: Spin-domain formation and coarsening, *Phys. Rev. A* **89**, 033631 (2014).
- [423] K.M. Mertes, J.W. Merrill, R. Carretero-González, D.J. Frantzeskakis, P.G. Kevrekidis, and D.S. Hall, Nonequilibrium dynamics and superfluid ring excitations in binary Bose-Einstein condensates, *Phys. Rev. Lett.* **99**, 190402 (2007).
- [424] L. Vidmar, J.P. Ronzheimer, M. Schreiber, S. Braun, S.S. Hodgman, S. Langer, F. Heidrich-Meisner, I. Bloch, and U. Schneider, Dynamical quasicondensation of hard-core bosons at finite momenta, *arXiv:1505.05150* (2015).
- [425] M. Rigol, and A. Muramatsu, Emergence of quasicondensates of hard-core bosons at finite momentum, *Phys. Rev. Lett.* **93**, 230404 (2004).
- [426] L. Vidmar, D. Iyer, and M. Rigol, Emergent eigenstate solution to quantum dynamics far from equilibrium, *Phys. Rev. X* **7**, 021012 (2017).
- [427] W. Xu, and M. Rigol, Expansion of one-dimensional lattice hard-core bosons at finite temperature, *Phys. Rev. A* **95**, 033617 (2017).
- [428] C.K. Lai, and C.N. Yang, Ground-state energy of a mixture of fermions and bosons in one dimension with a repulsive δ -function interaction, *Phys. Rev. A* **3**, 393 (1971).
- [429] A. Imambekov, and E. Demler, Exactly solvable case of a one-dimensional Bose-Fermi mixture, *Phys. Rev. A* **73**, 021602 (2006).

-
- [430] B. Fang, P. Vignolo, M. Gattobigio, C. Miniatura, and A. Minguzzi, Exact solution for the degenerate ground-state manifold of a strongly interacting one-dimensional Bose-Fermi mixture, *Phys. Rev. A* **84**, 023626 (2011).
- [431] A.S. Dehkharghani, F.F. Bellotti, and N.T. Zinner, Analytical and numerical studies of Bose-Fermi mixtures in a one-dimensional harmonic trap, *J. Phys. B: At. Mol. Opt. Phys.* **50**, 144002 (2017).
- [432] D. Fischer, D. Hoffmann, and S. Wimberger, Spectral analysis of two-dimensional Bose-Hubbard models, *Phys. Rev. A* **93**, 043620 (2016).
- [433] V. Alba, M. Haque, and A.M. Läuchli, Entanglement spectrum of the two-dimensional bose-hubbard model, *Phys. Rev. Lett.* **110**, 260403 (2013).
- [434] A. Jreissaty, J. Carrasquilla, and M. Rigol, Self-trapping in the two-dimensional Bose-Hubbard model, *Phys. Rev. A* **88**, 031606 (2013).
- [435] T. Ernst, T. Paul, and P. Schlagheck, Transport of ultracold Bose gases beyond the Gross-Pitaevskii description, *Phys. Rev. A* **81**, 013631 (2010).
- [436] P. Schlagheck, F. Malet, J.C. Cremon, and S.M. Reimann, Transport and interaction blockade of cold bosonic atoms in a triple-well potential, *New J. Phys.* **12**, 065020 (2010).
- [437] M.C. Tsatsos, J.H.V. Nguyen, A.U.J. Lode, G.D. Telles, D. Luo, V.S. Bagnato, and R.G. Hulet, Granulation in an atomic Bose-Einstein condensate, arXiv:**1707.04055** (2017).
- [438] C. Menotti, M. Lewenstein, T. Lahaye, and T. Pfau, Dipolar interaction in ultracold atomic gases, *AIP Conference Proceedings Vol.* **970**, 332 (2008).
- [439] C. Trefzger, C. Menotti, and M. Lewenstein, Ultracold dipolar gas in an optical lattice: The fate of metastable states, *Phys. Rev. A* **78**, 043604 (2008).
- [440] C. Trefzger, C. Menotti, B. Capogrosso-Sansone, and M. Lewenstein, Ultracold dipolar gases in optical lattices, *J. Phys. B: At. Mol. Opt. Phys.* **44**, 193001 (2011).
- [441] B. Chatterjee, I. Brouzos, L. Cao, and P. Schmelcher, Ultracold dipolar few-boson ensembles in a triple-well trap, *J. Phys. B: At. Mol. Opt. Phys.* **46**, 085304 (2013).
- [442] E. Altman, W. Hofstetter, E. Demler, and M.D. Lukin, Phase diagram of two-component bosons on an optical lattice, *New J. Phys.* **5**, 113 (2003).
- [443] B. Gadway, D. Pertot, R. Reimann, and D. Schneble, Superfluidity of interacting bosonic mixtures in optical lattices, *Phys. Rev. Lett.* **105**, 045303 (2010).
- [444] U.R. Fischer, A.U. Lode, and B. Chatterjee, Condensate fragmentation as a sensitive measure of the quantum many-body behavior of bosons with long-range interactions, *Phys. Rev. A* **91**, 063621 (2015).

BIBLIOGRAPHY

- [445] B. Chatterjee, I. Brouzos, L. Cao, and P. Schmelcher, Ultracold dipolar few-boson ensembles in a triple-well trap, *J. Phys. B: At. Mol. Opt. Phys.* **46**, 085304 (2013).
- [446] S. Tsuchiya, S. Kurihara, and T. Kimura, Superfluid-Mott insulator transition of spin-1 bosons in an optical lattice, *Phys. Rev. A*, **70**, 043628 (2004).
- [447] M. Rizzi, D. Rossini, G. De Chiara, S. Montangero, and R. Fazio, Phase diagram of spin-1 bosons on one-dimensional lattices, *Phys. Rev. Lett.* **95**, 240404 (2005).
- [448] F. Zhan, J. Sabbatini, M.J. Davis, and I.P. McCulloch, Miscible-immiscible quantum phase transition in coupled two-component Bose-Einstein condensates in one-dimensional optical lattices, *Phys. Rev. A* **90**, 023630 (2014).
- [449] I.M. Merhasin, B.A. Malomed, and R. Driben, Transition to miscibility in a binary Bose-Einstein condensate induced by linear coupling, *J. Phys. B: At. Mol. Opt. Phys.* **38**, 877 (2005).
- [450] L. D. Landau, *Zur theorie der energieubertragung. II*, *Phys. of the Sov. Un.* **2**, 2 (1932).
- [451] C. Zener, *Non-Adiabatic Crossing of Energy Levels*, *Proceedings of the Royal Society of London A*. **137**, 6 (1932).
- [452] E. C. G. Stueckelberg, *Theorie der unelastischen Stösse zwischen Atomen*, *Helvetica Physica Acta* **5**, 369 (1932).
- [453] J. Sabbatini, W.H. Zurek, and M.J. Davis, Phase separation and pattern formation in a binary Bose-Einstein condensate, *Phys. Rev. Lett.* **107**, 230402 (2011).
- [454] J. Sabbatini, W.H. Zurek, and M.J. Davis, Causality and defect formation in the dynamics of an engineered quantum phase transition in a coupled binary Bose-Einstein condensate, *New J. Phys.* **14**, 095030 (2012).
- [455] S. Gautam, and S.K. Adhikari, Phase separation in a spin-orbit-coupled Bose-Einstein condensate, *Phys. Rev. A* **90**, 043619 (2014).
- [456] F. M. Cucchietti, and E. Timmermans, Strong-Coupling Polarons in Dilute Gas Bose-Einstein Condensates, *Phys. Rev. Lett.* **96**, 210401 (2006).
- [457] S. Palzer, C. Zipkes, C. Sias, and M. Köhl, Quantum Transport through a Tonks-Girardeau Gas, *Phys. Rev. Lett.* **103**, 150601 (2009).
- [458] W. Li, and S. Das Sarma, Variational study of polarons in Bose-Einstein condensates, *Phys. Rev. A* **90**, 013618 (2014).
- [459] J. Levinsen, M. M. Parish, and G. M. Bruun, Impurity in a Bose-Einstein Condensate and the Efimov Effect, *Phys. Rev. Lett.* **115**, 125302 (2015).
- [460] Y. E. Shchadilova, R. Schmidt, F. Grusdt, and E. Demler, Quantum Dynamics of Ultracold Bose Polarons, *Phys. Rev. Lett.* **117**, 113002 (2016).

- [461] R. S. Christensen, J. Levinsen, and G. M. Bruun, Quasiparticle Properties of a Mobile Impurity in a Bose-Einstein Condensate, *Phys. Rev. Lett.* **115**, 160401 (2015).
- [462] F. Grusdt, R. Schmidt, Y. E. Shchadilova, and E. Demler, Strong-coupling Bose polarons in a Bose-Einstein condensate, *Phys. Rev. A* **96**, 013607 (2017).
- [463] R. Schmidt, H. R. Sadeghpour, and E. Demler, Mesoscopic Rydberg Impurity in an Atomic Quantum Gas, *Phys. Rev. Lett.* **116**, 105302 (2016).
- [464] L. A. Peña Ardila, and S. Giorgini, Bose polaron problem: Effect of mass imbalance on binding energy, *Phys. Rev. A* **94**, 063640 (2016).
- [465] N. B. Jørgensen, L. Wacker, K. T. Skalmstang, M. M. Parish, J. Levinsen, R. S. Christensen, G. M. Bruun, and J. J. Arlt, Observation of Attractive and Repulsive Polarons in a Bose-Einstein Condensate, *Phys. Rev. Lett.* **117**, 055302 (2016).
- [466] M.-G. Hu, M. J. Van de Graaff, D. Kedar, J. P. Corson, E. A. Cornell, and D. S. Jin, Bose Polarons in the Strongly Interacting Regime, *Phys. Rev. Lett.* **117**, 055301 (2016).

Eidesstattliche Versicherung

Hiermit erkläre ich an Eides statt, dass ich die vorliegende Dissertationsschrift selbst verfasst und keine anderen als die angegebenen Quellen und Hilfsmittel benutzt habe.

I hereby declare, on oath, that I have written the present dissertation by my own and have not used other than the acknowledged resources and aids.

Hamburg, den